Far-infrared absorption and dispersion studies on methyl iodide solutions

Graham Peter O'Neill

FAR-INFRARED ABSORPTION AND DISPERSION STUDIES ON METHYL IODIDE SOLUTIONS

BY

GRAHAM PETER O'NEILL B.Sc

(GRADUATE SOCIETY)

A THESIS SUBMITTED FOR THE DEGREE OF DOCTOR OF PHILOSOPHY IN THE UNIVERSITY OF DURHAM 1986

When water turns to ice does it
remember one time it was
water?
When ice turns back into
water does it remember it was
ice?

Carl Sandburg 1878-1967

DECLARATION

The material described in this Thesis was carried out by the author in the Department of Chemistry, University of Durham, the National Physical Laboratory, Teddington and University College of Wales, Edward Davies Chemical Laboratories, Aberystwyth, between October 1979 and October 1982. It has not been submitted for any other degree. The work is original except where acknowledged by reference.

ACKNOWLEDGEMENTS

I would like to express my gratitude to Dr. Jack Yarwood and Dr. Jim Birch for their encouragement and guidance. Thanks also to the academic and technical staff of the University Computer Unit, my fellow researchers at Durham and the National Physical Laboratory. I am grateful to Dr. Alun Price at U.C.W. Aberystwyth for the use of microwave equipment and his help and advice.

The Science and Engineering Research Council and the National Physical Laboratory are thanked for financial support.

CONTENTS

ABSTRACT

FAR-INFRARED ABSORPTION AND DISPERSION STUDIES ON METHYL IODIDE SOLUTIONS

A far-infrared dispersive liquid cell has been developed in collaboration with the National Physical Laboratory. This New Liquid Cell enables both the absorption coefficient and refractive index of a liquid to be accurately determined over the complete far-infrared frequency range.

The New Liquid Cell has been used to make dispersive measurements of methyl iodide liquid and methyl iodide in a range of non-polar solvents. These were: carbon disulphide; carbon tetrachloride; n-heptane; n-decane; n-hexadecane and Santotrac 40 (an industrial traction fluid). This data has been combined with microwave measurements, enabling the total orientational correlation functions and the band moments to be determined. Results have also been obtained on the rates of reorientation and static angular correlations of methyl iodide molecules. This information on the liquid dynamics of methyl iodide has been used to elucidate the molecular environment of the solvents using methyl iodide as a probe molecule, which has given evidence for the presence of discrete solute 'pools' within the solvent environment for the longer chain length n-alkanes.

Two theoretical models for molecular reorientation have been fitted to the experimental data. The first, a second order truncation of the Mori formalism though giving a good fit to the experimental far-infrared absorption coefficient and refractive index spectra, gave values for the molecular torques that did not agree with measured values. The second, a physically more meaningful model is based on the motion of a molecule which is described by a gaussian distribution of librational frequencies within a molecular cage, gives molecular torque values that agree well with experimental results.

C H A P T E R 1

INTRODUCTION

1.1 Investigation of Molecular Motion

Molecules in the liquid phase undergo rotational and translational Brownian motion of a random nature due to the thermal energy of the system[1]. This motion governs the encounter and interaction of the molecules, an investigation of which at the molecular level is achieved by measuring a macroscopic property of the system that can be related to the microscopic behaviour of the molecules. Various spectroscopic techniques have been used to obtain this information, the most effective (and the assosiated motions) are, Nuclear Magnetic Resonance (Rotation & Translation), Microwave (Rotation), Far-Infrared (Rotation & Translation), Raman (Vibration & Rotation), Depolarised Rayleigh (Rotation & Translation), Neutron Scattering (Vibration, Rotation & Translation) and Photon correlation spectroscopy(Brownian Motion). The methyl iodide molecule shown schematically in Figure 1.1, is a symmetric top with C_3v symmetry and has a dipole moment of 1.62 Debyes[2] acting along the C_3 axis. The types of motion that the whole molecule can undergo are shown in Figure 1.2. They are:-

a. Rotation or translation parallel to the C_3 axis, this type of motion will not effect the orientation of the dipole.

b. Rotation or translation perpendicular to the C_3 axis, this type of motion will cause a change in orientation of the dipole.

Since the orientation of the dipole changes with whole molecule tumbling motion, measurements of the orientational changes of the dipoles and the rate at which they occur will yield information on the motions and interactions a molecule is undergoing.

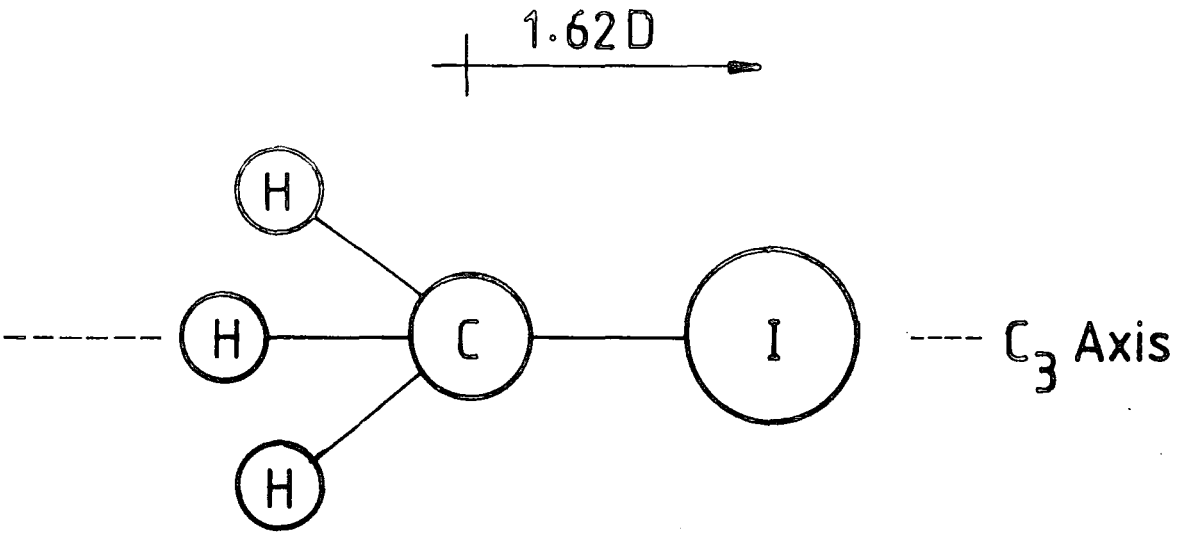

FIGURE 1.1 THE METHYL IODIDE MOLECULE

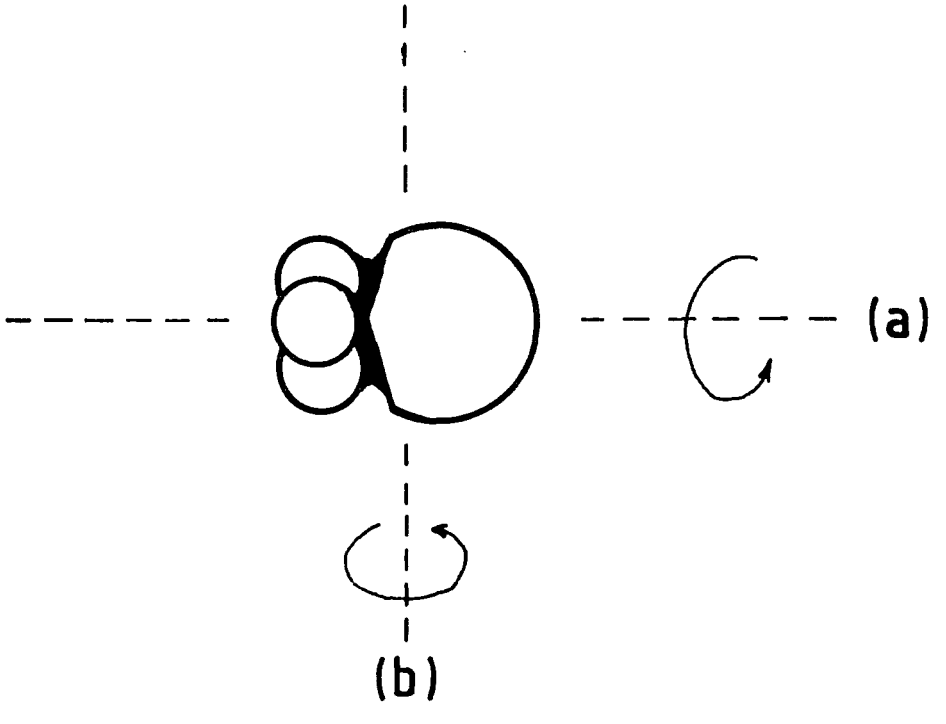

FIGURE 1.2 REORIENTATION OF THE METHYL IODIDE MOLECULE

1.2 Investigations using Methyl Iodide (MeI)

MeI has been extensively studied by Infrared and Raman spectroscopy[3], giving information on the vibrational/rotational motions of the molecule. However, very little work has been reported on the liquid phase dynamics of the molecule via microwave and far-infrared measurements[4,5,6,7] and no dispersive work on dilution studies in the far-infrared has been reported. Other molecules that are similar to MeI that have been studied using microwave and far-infrared measurements are Acetonitrile[8,9], Methyl Chloride[10,11] and methyl flouride[12].

1.2.1 MeI as a Probe Molecule

Information obtained on the microscopic motion of the MeI molecule in the liquid phase, in different solvent environments should yield information on the microscopic nature of the solvent itself. This information would enable the study and development of industrially important liquids such as lubricants and traction fluids. Changing the physical conditions of the system being studied, will give indications of the temperature and pressure performance of these liquids. The microwave and far-infrared region of the spectrum is sensitive to the reorientational motion of polar molecules, and is not complicated by vibrational processes, so is ideal for the study of molecular motion.

1.3 Microwave and Far-Infrared Spectra

If we assume that for a field applied to a dielectric the distortion polarization occurs instantly and the dipolar polarization approaches equilibrium according to exponential law, then

$$P_{Distortion} = (P_{Total} - P_{Induced})[1 - \exp(\frac{-t}{\tau})] \quad \ldots\ldots \quad 1.1$$

where τ is the macroscopic relaxation time.

From Hill[13], when the polarization is complex

$$P = P_{Induced} + P_{Distortion} = P' - iP''$$

$$P(\omega) = \frac{\epsilon(n^2 - 1)F}{4\pi} + \frac{\epsilon(\varepsilon_o - n^2)F}{4\pi(1 + i\omega\tau)} \quad \ldots\ldots \quad 1.2$$

where ω is the angular frequency of the applied field, ϵ the permitivity of free space and n is the internal refractive index defined by Onsager[14], and for the complex permittivity

$$\hat{\varepsilon} = 1 + \frac{4\pi(P' - iP'')}{\epsilon F}$$

$$\hat{\varepsilon} = n^2 + \frac{(\varepsilon_o - n^2)}{(1 + i\omega\tau)} \quad \ldots\ldots \quad 1.3$$

where $\hat{\varepsilon} = \varepsilon^* = \varepsilon' - i\varepsilon''$

If the frequency of the applied field is increased, a point will be reached when dipolar orientation can no longer reach equlibrium within the field oscillation time t, (ie $\tau > t$) at this point the permitivity will begin to decay. Equation 1.3 enables the frequency varying permitivity [$\varepsilon''(\omega)$] and dielectric loss [$\varepsilon'(\omega)$] to be derived

$$\varepsilon'(\omega) = n^2 + \frac{\varepsilon_o - n^2}{1 + \omega^2\tau^2} \qquad \ldots\ldots \quad 1.4$$

$$\varepsilon''(\omega) = \left[\frac{\varepsilon_o - n^2}{1 + \omega^2\tau^2}\right]\omega t \qquad \ldots\ldots \quad 1.5$$

Equations 1.4 and 1.5 are known as the Debye equations and the τ derived from them as the Debye relaxation time normally designated τ_D. The form of ε' and ε'' as a function of ω are shown schematically in Figures 1.3 and 1.4. From these ε' decreases monotonically from ε_o to n^2 with increasing frequency and ε'' is zero at $\omega = 0$, rises to a maximum value of $1/2(\varepsilon_o - n^2)$ at $\omega = 1/\tau_D$, then decreases slowly to zero as ω tends to infinity. So the Debye equations can be used to relate experimentally determined parameters to the macroscopic properties of the system. ε' and ε'' are related to the experimentally measured refractive index $[n(\bar{\nu})]$ and absorption coefficient $[\alpha(\bar{\nu})]$ as follows[15]

$$\varepsilon' = n^2 - K^2 \quad , \quad \varepsilon'' = 2nK$$

where K(the absorption index) = $\frac{\alpha}{4\pi\bar{\nu}}$

and

$$n^2 = \frac{1}{2}\left\{[\varepsilon'^2 + \varepsilon''^2]^{\frac{1}{2}} + \varepsilon'\right\} \qquad \ldots\ldots \quad 1.6$$

$$K^2 = \frac{1}{2}\left\{[\varepsilon'^2 + \varepsilon''^2]^{\frac{1}{2}} - \varepsilon'\right\} \qquad \ldots\ldots \quad 1.7$$

Figure 1.3

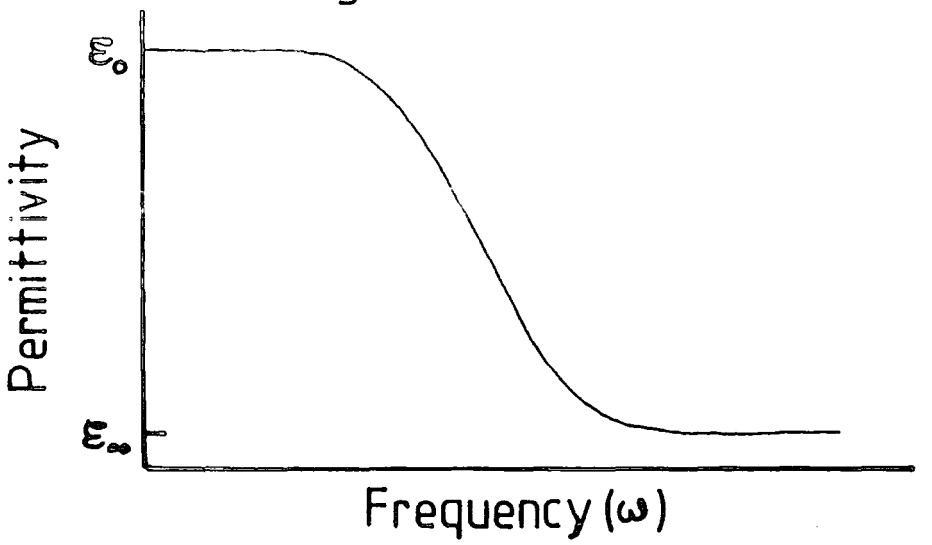

Figure 1.4

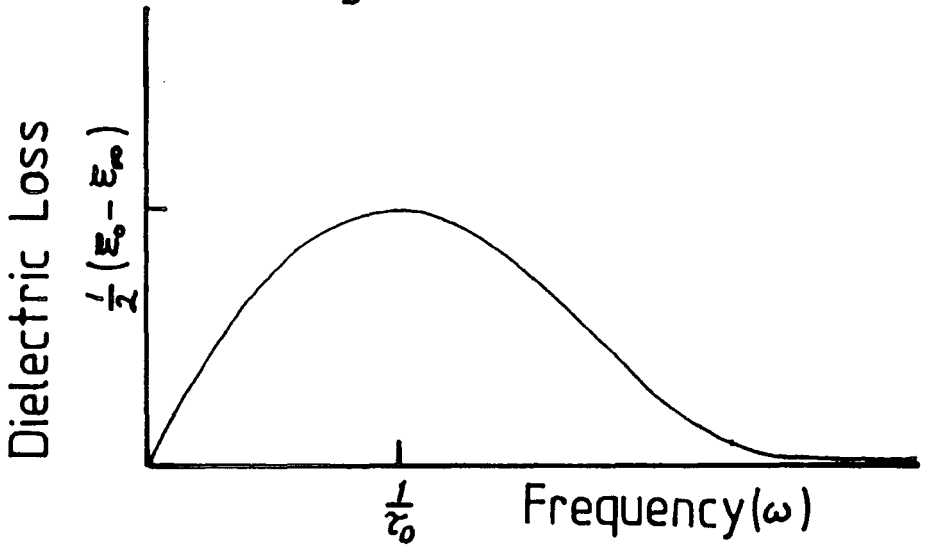

Figure 1.5

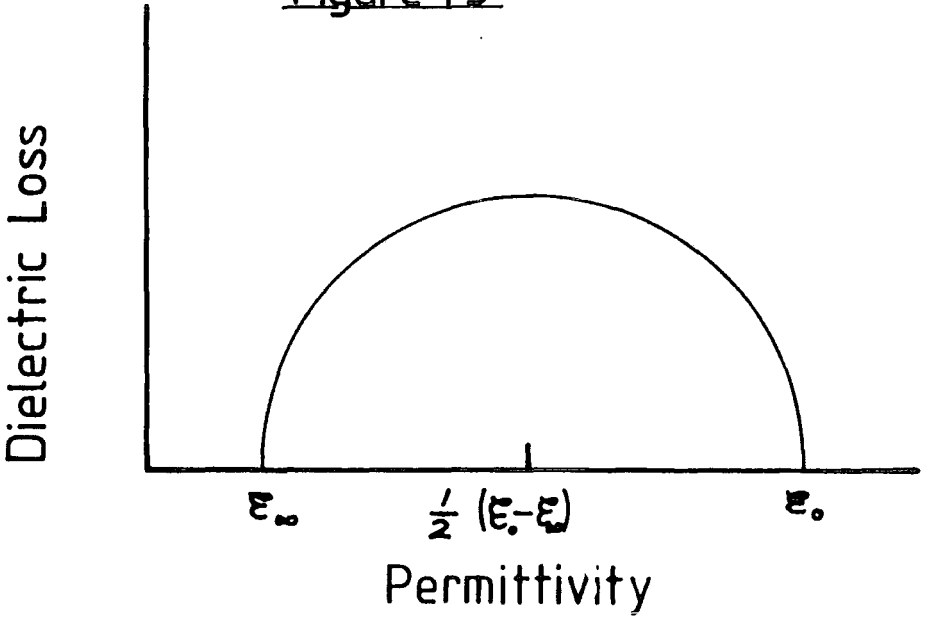

1.3.1 The Debye Semicircle.

The Debye equations have been presented in the following form by Cole and Cole[16]

$$\varepsilon'(\omega) - \frac{1}{2}(\varepsilon_0 - \varepsilon_\infty) = \frac{(\varepsilon_0 - \varepsilon_\infty)(1 - \omega^2\tau_D^2)}{2(1 + \omega^2\tau_D^2)} \quad \ldots\ldots \quad 1.8$$

where from Maxwell $\varepsilon_\infty = n^2$

giving

$$\left[\varepsilon'(\omega) - \frac{1}{2}(\varepsilon_0 + \varepsilon_\infty)\right]^2 + \left[\varepsilon''(\omega)\right]^2 = \left[\frac{1}{2}(\varepsilon_0 - \varepsilon_\infty)\right]^2 \quad \ldots\ldots \quad 1.9$$

Equation 1.9 is the equation of a circle with its centre at $\left[\frac{1}{2}\varepsilon_0 + \varepsilon_\infty, 0\right]$ and a radius of $\frac{1}{2}(\varepsilon_0 - \varepsilon_\infty)$. A Cole-Cole plot is shown schematically in Figure 1.5, this is a very useful way of displaying permittivity and dielectric loss data, but no indication of the frequency range is given.

1.4 The Determination of Molecular Properties

One method by which the molecular properties of a system can be determined from experimental data is by use of the correlation function formalism[17,18].

1.4.1 Correlation Function Formalism.

The correlation function formalism is based on Fluctuation dissipation theory and linear response theory[19]. For a small external force F(u), which is dependent on time u, but not the co-ordinates or

momenta, applied to a system. The response of any quantity B of the system, which is dependent on the co-ordinates and momenta and not directly on time is given by[19]

$$B(u) = B_{Equlibrium} + \int_{-\infty}^{u} dt F(t) \phi_{BA}(u-t) \qquad \ldots\ldots \quad 1.10$$

where $A = -\frac{\Delta H}{F(u)}$, and H is the Hamiltonian of the system

The real function $\phi_{BA}(t)$ the (impulse) response function is dependent only on the correlated time fluctuations of B and A at equilibrium. For a dielectric, where B and A are components of the electric moment of the system equation 1.10 can be written as

$$\phi(t) = -\frac{1}{kT} \frac{d}{dt} \langle M(o) \cdot M(t) \rangle \qquad \ldots\ldots \quad 1.11$$

where $\langle M(0) \cdot M(t) \rangle$ is the autocorrelation function of the property M.

$$\langle M(o) \cdot M(t) \rangle = \int_{-\infty}^{+\infty} M(\tau) M(\tau + t) d\tau \qquad \ldots\ldots \quad 1.12$$

The time dependent dipole-dipole multimolecular correlation function for microwave, far-infrared rotation is given by

$$\phi_{1R}(t) = \langle \sum_{i,j} P_1[u_{ij}(t)] \rangle \qquad \ldots\ldots \quad 1.13$$

where P_1 is the first order Legendre polynomial, which is the solution of the diffusion equation, this describes all the various motions the system is undergoing such as rotation, libration and translation, i and j refer to different molecules and u is a unit rector in the molecular permanent dipole moment axis. Provided absorption measurements cover the microwave and far-infrared frequency ranges,the total correlation function for dipole rotation can be calculated

from[20]

$$\phi^{T}_{1R}(t) = \frac{\langle \sum_{i,j} [u_i(0).u_j(t)] \rangle}{\langle \sum_{i,j} [u_i(0) \,.\, u_j(0)] \rangle}$$

$$= \frac{6kT}{8\pi^3 N\mu_o^2} \int_o^\infty \frac{D(\bar{\nu})\alpha(\bar{\nu})n(\bar{\nu})\exp(2\pi i\bar{\nu}ct)\, d\bar{\nu}}{[1 - \exp(-h\bar{\nu}c/kT)]} \qquad \ldots\ldots \quad 1.14$$

where D(v) is a frequency varying internal field correction factor , α and n are the experimentally determined absorption coefficient and refractive index .In practice only $\alpha(\bar{\nu})$ is determined and $n(\bar{\nu})$ is fixed at the n_D value. Equation 1.14 yields information on molecular properties from the experimentally determined microwave and far-infrared absorption.

1.5 Dielectric Measurements.

In this chapter and in chapter 6 theories that enable the macroscopic and molecular properties of a system to be determined from experimental data are outlined. In all cases to solve the equations fully a knowledge of both the dielectric permittivity and loss data for a system, over the microwave, far-infrared range is required. This data can be obtained from absorption coefficient and refractive index measurements made on liquids, However the common approach is to measure only the absorption spectrum and assume the refractive index is constant at the n_D value. An experimental method that enables both to be measured in one experiment should enable more accurate data on molecular properties to be calculated. The aim of this research has been the development of a simple liquid cell that will enable accurate

measurements of absorption coefficient and refractive index spectra in the far-infrared. Using the cell to make measurements on MeI in a range of solvents and combining this data with the available theories, should provide information on the interactions of the MeI molecule with its local environment, and hence information on that environment. Since it is the short time (non Debye) motion of a system that is most difficult to simulate and this motion is mainly represented in the far-infrared,(see section 6.1) concise n and α measurements over the far-infrared region will also allow stringent tests on models of molecular motion to be made.

C H A P T E R 2

FOURIER TRANSFORM SPECTROSCOPY

2.1 Introduction.

The advantages of Fourier transform spectroscopy over grating or prism instruments[21] make it a very desireable technique to use in the far-infrared. The main advantage, due to the low energy of far-infrared sources, is the throughput (or etendue) of the interferometer which was noticed by Jacquinot[22]. This advantage arises because an interferometer possesses circular symmetry which gives an angular admission advantage over systems that use slits and have no circular symmetry. The angular admission of the interferometer must be limited in order to have a non-zero resolving power, but even so at the same resolving power as a grating instrument the throughput of an interferometer is very much higher[21]. A further advantage (only achieved under conditions of detector noise limitation) is the Fellgett[23] advantage. This is a signal to noise advantage and arises because in an interferometer all frequencies are observed for the total experimental time, whereas in a grating instrument each frequency is observed for only a portion of the total time. Thus if the observation time is T and there are M spectral elements, the signal to noise ratio will be proportional to (T/M) for the grating instrument and T for the interferometer giving a gain of $\sqrt{M}$ for the interferometer.

In the Michelson interferometer shown schematically in Figure 2.1, the energy from the source is incident on the beam devider which results in two beams leaving the beam devider at right angles. The two beams are reflected by the mirrors M_1 and M_2 back to the beam devider, where interference takes place in the recombined beam, which then travels to the detector. When M_1 and M_2 are the same distance

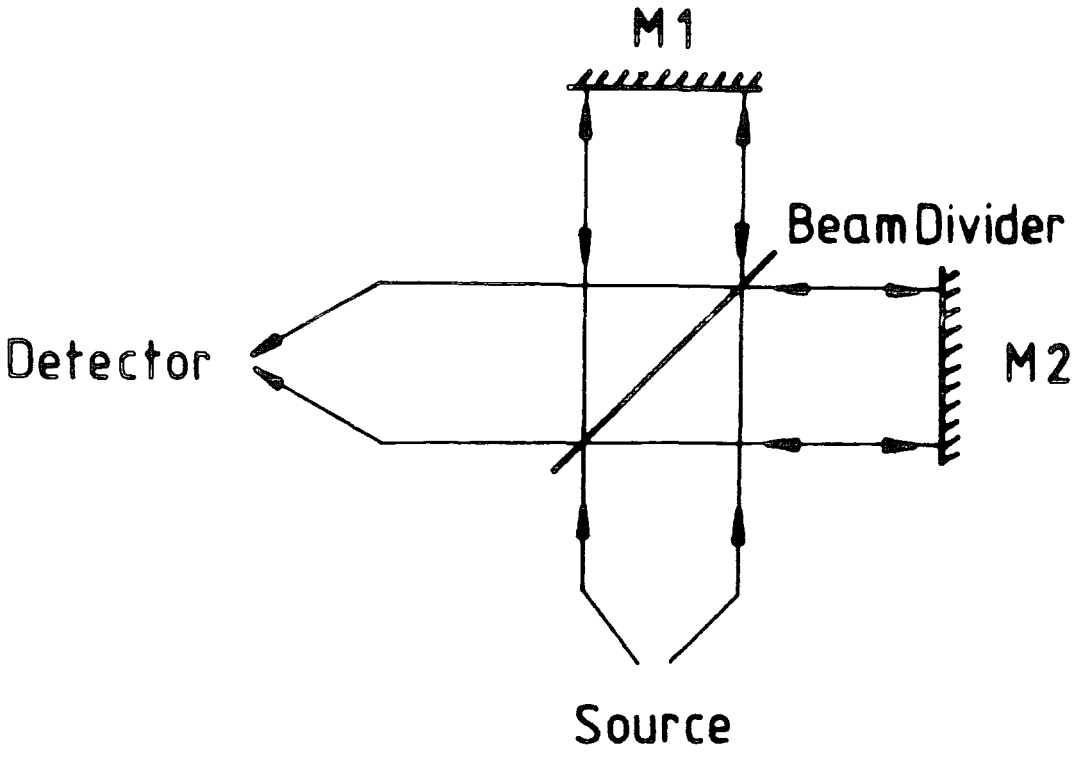

Figure 2.1 The Michelson Interferometer

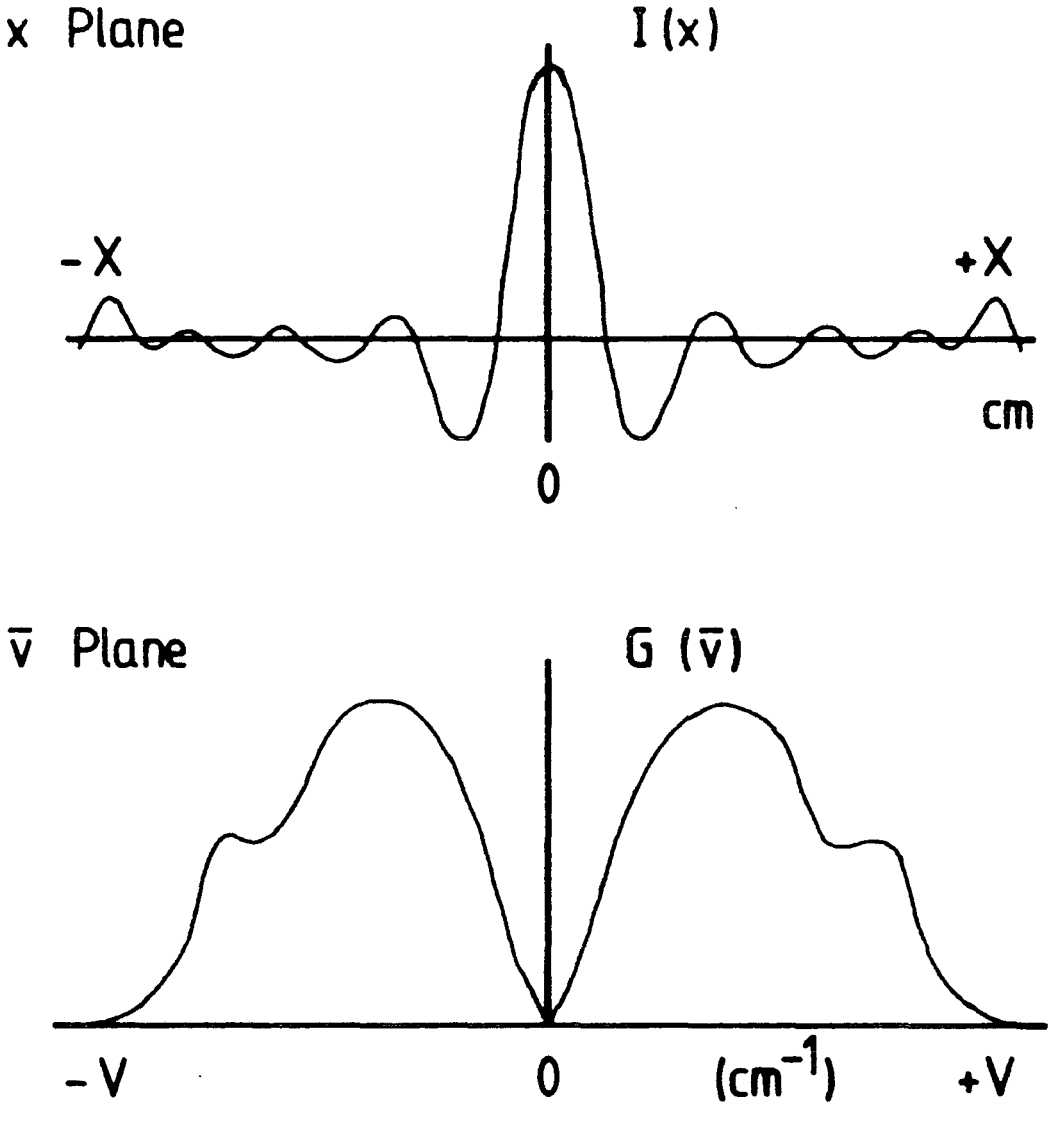

Figure 2.2 Interferogram and instrument energy profiles

from the beam splitter the amplitude and phase of corresponding spectral elements within the two beams will be the same. Under these conditions the recombination of the two beams will produce a grand maximum at the detector. If the distance between the beam splitter and one of the mirrors is changed, the phase of the spectral elements within the two beams will change and an interference pattern will be detected. This pattern is known as an interferogram and is an intensity function of path difference I(x). The general form of the interferogram is dependent on the interferometer energy profile, this relationship is shown schematically in Figure 2.2. The interferogram grand maximum is said to occur at zero path difference (ZPD). The interferogram should be an even function and symmetrical about the ZPD but, because of misalignment, this is not normally the case and the interferogram is made up of an even and odd function. I(x) and $G(\bar{\nu})$ in Figure 2.2 are said to be Fourier transform pairs, that is they are Fourier transforms of each other.

$$G(\bar{\nu}) = \int_{-\infty}^{+\infty} I(x).\exp(-i2\pi\bar{\nu}x)dx \qquad \ldots\ldots 2.1$$

$$I(x) = \int_{-\infty}^{+\infty} G(\bar{\nu}).\exp(i2\pi\bar{\nu}x)d\bar{\nu} \qquad \ldots\ldots 2.2$$

Where the dimensions of $\bar{\nu}$ and x are reciprocally related, $G(\bar{\nu})$ is therefore complex, the real part (I_e) related to the even funtion of I(x) and the imaginary part (I_o) the odd function of I(x).

$$\hat{G}(\bar{\nu}) = \int_{-\infty}^{+\infty} I_e(x)\cos 2\pi\bar{\nu}x\,dx - i\int_{-\infty}^{+\infty} I_o(x)\sin 2\pi\bar{\nu}x\,dx \qquad \ldots\ldots 2.3$$

i.e

$$G(\bar{\nu}) = p(\bar{\nu}) - iq(\bar{\nu}) \qquad \ldots\ldots 2.4$$

If $\mathcal{C}(\bar{\nu})$ is the power amplitude and $\phi(\bar{\nu})$ the phase

$$\hat{G}(\bar{\nu}) = \mathcal{C}(\bar{\nu})\cos\phi(\bar{\nu}) - i\mathcal{C}(\bar{\nu})\sin\phi(\bar{\nu}) \qquad \ldots\ldots 2.5$$

and

$$\mathcal{C}(\bar{\nu}) = [p^2(\bar{\nu}) + q^2(\bar{\nu})]^{\frac{1}{2}} \qquad \ldots\ldots 2.6$$

$$\phi(\bar{\nu}) = \arctan [q(\bar{\nu}) / p(\bar{\nu})] \qquad \ldots\ldots 2.7$$

Therefore the modulus and phase spectra of the energy within the interferometer can be determined from the recorded interferogram. In practice, the interferogram is sampled at discrete intervals Δx and truncated at +X and -X, the Fourier transform integral can then be approximated by a summation.

$$\hat{G}(\bar{\nu}) = \sum_{-X}^{+X} I_e(x)\cos 2\pi\bar{\nu}x\Delta x - i\sum_{-X}^{+X} I_o(x)\sin 2\pi\bar{\nu}x\Delta x \qquad \ldots\ldots 2.8$$

The most widely used interferometer set up for liquid measurements is shown schematically in Figure 2.3. The sample is held between two parallel windows in front of the detector. Measurements made using this method are subject to errors due to difficulties in accurately determining sample pathlengths and the approximate methods of analysis that have to be used[24]. A further disadvantage arises because of the sample position, since both partial beams of the interferometer have recombined before reacting with the sample, they both experience the same attenuation and phase changes on transmission through the sample. This means that the sample phase information is lost to the experiment. Limited information on the sample phase can be inferred by increasing the resolution of the interferogram to include the channel spectrum due to reflections between the windows, but this method of analysis is complicated. Another method if absorption data from 0 to $\simeq$200 cm^{-1} is available would be to use the Kramers-Kronig

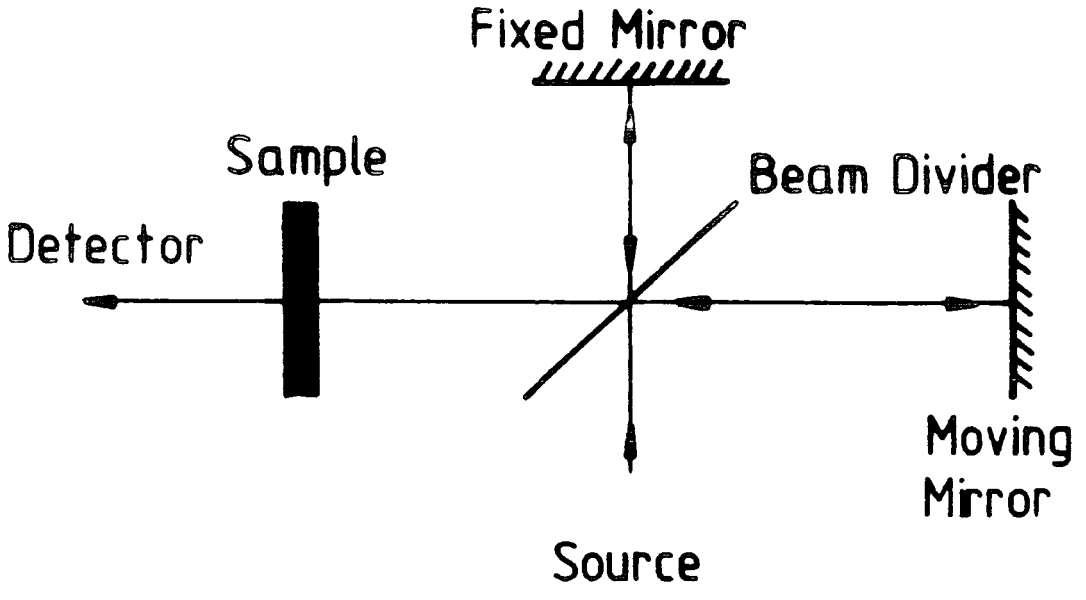

FIGURE 2.3 INTERFEROMETER IN "NORMAL" TRANSMISSION MODE

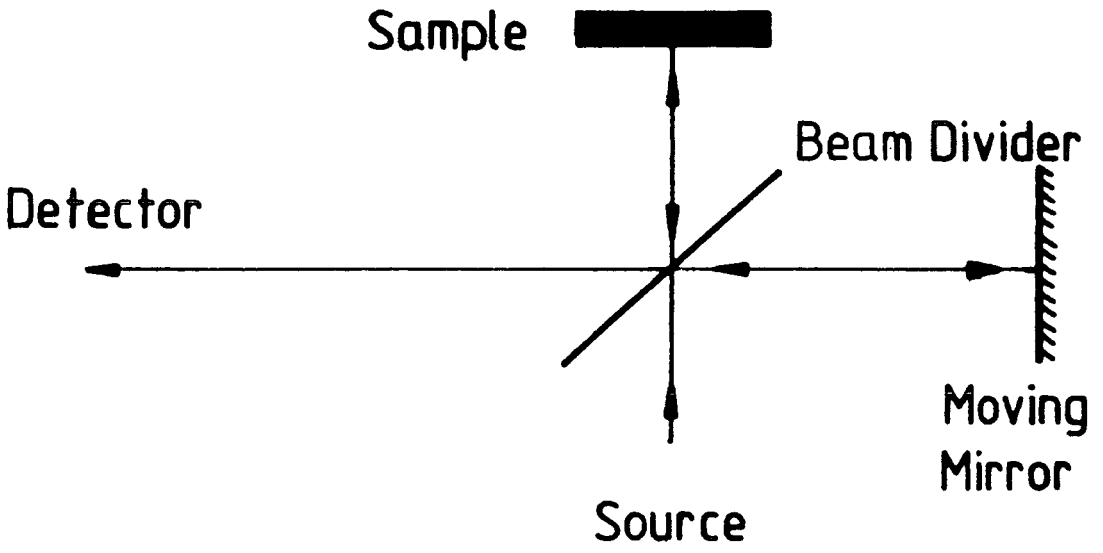

FIGURE 2.4 INTERFEROMETER IN "DISPERSIVE" MODE

relations[8], to obtain the sample phase from the measured attenuation. Alternatively if the sample is placed in one of the "active" interferometer arms as in Figure 2.4 both the attenuation and phase shift due to the sample can be recovered from the recorded interferograms. This is known as Dispersive Fourier Transform Spectrometry (DFTS).

2.2 The Development of DFTS.

In a DFTS experiment the liquid sample is normally contained in a cell that replaces the fixed mirror of an interferometer. The three configurations that have been used are shown schematically in Figure 2.5. The first liquid DFTS measurements were made by Chamberlain et al.[25] on tetrabromoethane using arrangement 2.5(a), which is known as the free liquid layer method. In this cell the liquid forms a gravity held layer above a highly polished flat metal reflector, which replaces the interferometer fixed mirror. The liquid thickness used depends on how absorbing the sample is, due to surface tension effects the minimum thickness is about 100 μm. This limits the range of liquids that can be studied and for highly absorbing liquids arrangement 2.5(b) was developed. This is the reflection technique, where the sample is supported on a transparent window and the window liquid interface is studied. A further development of these two techniques was the development of the enclosed cell shown in 2.5(c) which incorporates both transmission and reflection techniques.

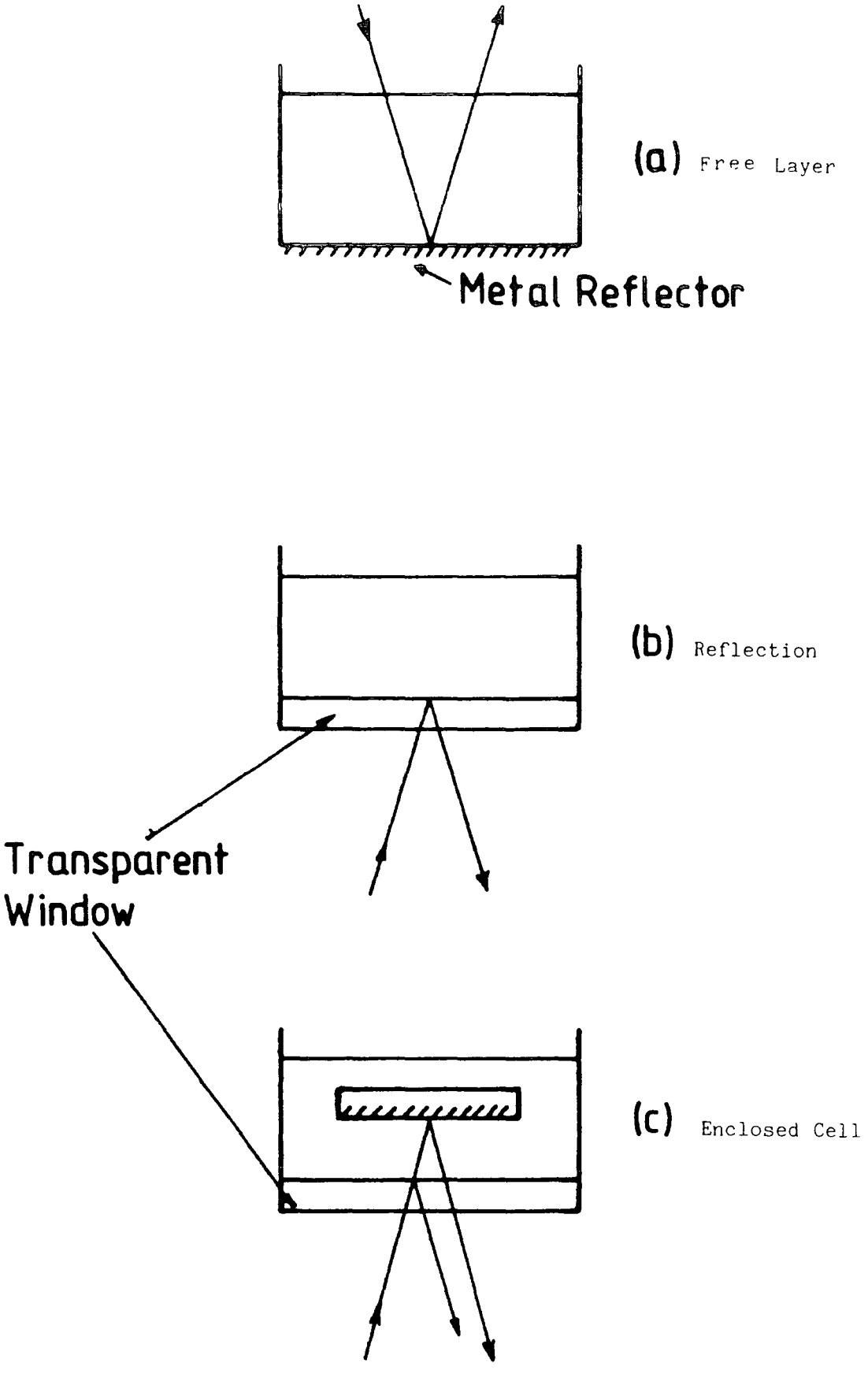

Figure 2.5 DFTS Liquid Cell arrangements

2.3 The Free Layer Method.

In its earliest form this cell was not directly attached to the interferometer but mounted on an adjustable table below it, as in Figure 2.6. This necessitated the addition of windows W_2, W_2' and compensating windows W_1 and W_1' in the moving mirror arm. The large transmission losses due to these windows lead to the cell being directly attached to the interferometer. In the final form shown in figure 2.7 a polystyrene window separated the interferometer vacuum and the liquid sample. The whole interferometer was mounted on an adjustable plate to allow for alignment of the liquid layer.

2.3.1 The Dispersive Interferogram.

When there is no liquid sample above the cell mirror the recorded interferogram will contain one interference signature centred at the ZPD. If a liquid is now poured over the cell mirror to form a plane parallel layer, the incident radiation will now be multiply reflected within this layer. The total reflected ray will therefore be an infinite sum of these internally reflected rays, each of which will interfere with the radiation from the moving mirror arm. Since the reflected rays have different phases the resultant interferogram will contain an interference signature for each internally reflected ray. The internally reflected rays and resultant empty and full cell interferograms are shown in Figure 2.8. The series of reflections M_1, M_2 etc. are usually heavily attenuated above M_1 and not of practical importance. The shift in path difference of the central fringe between the two interferograms ($\bar{x}$) is due to the phase difference introduced by the sample.

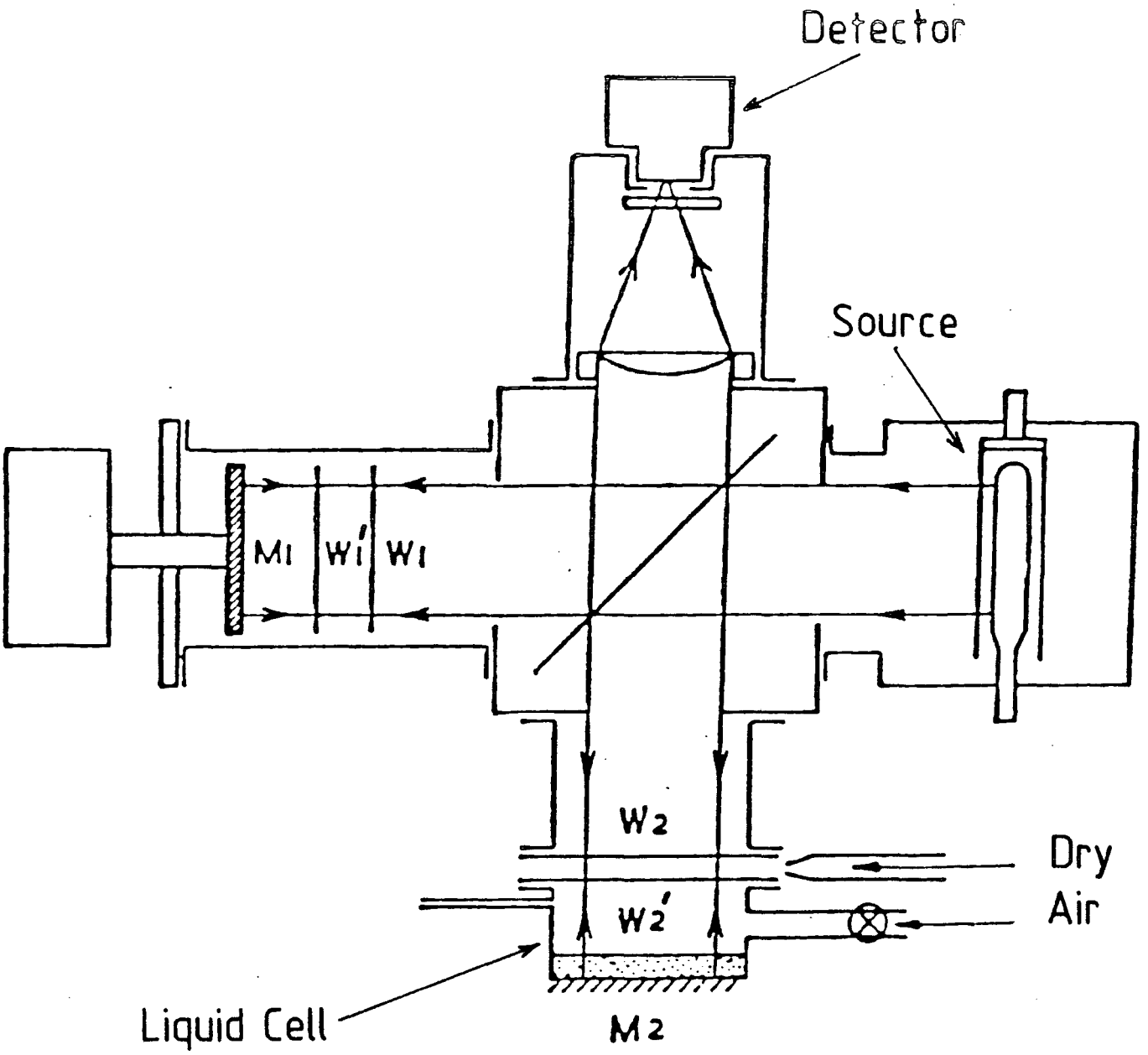

Figure 2.6 Early arrangement for the Free Layer Cell on an NPL Cube interferometer

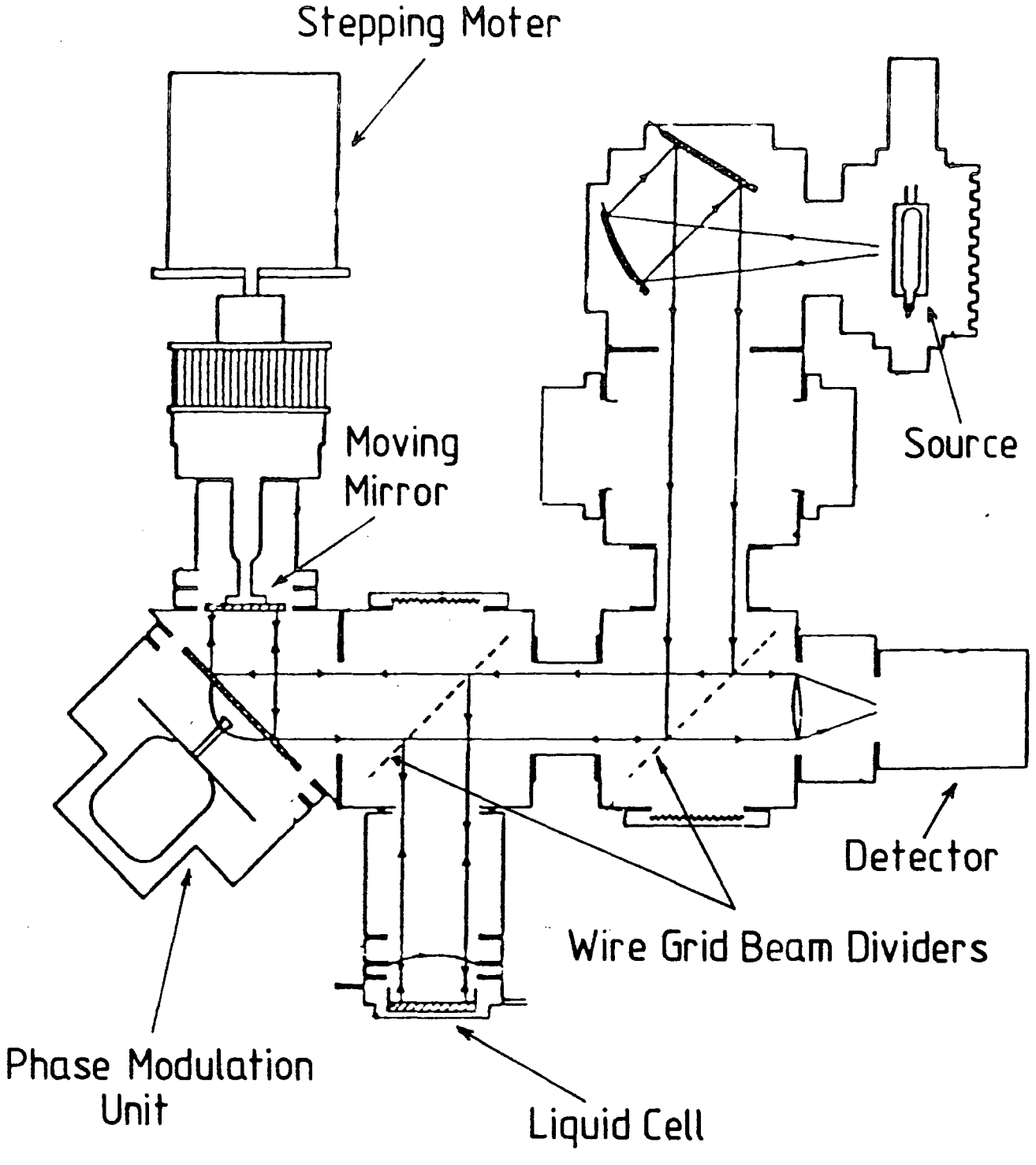

Figure 2.7 Final arrangement for the Free Layer Cell on an NPL interferometer

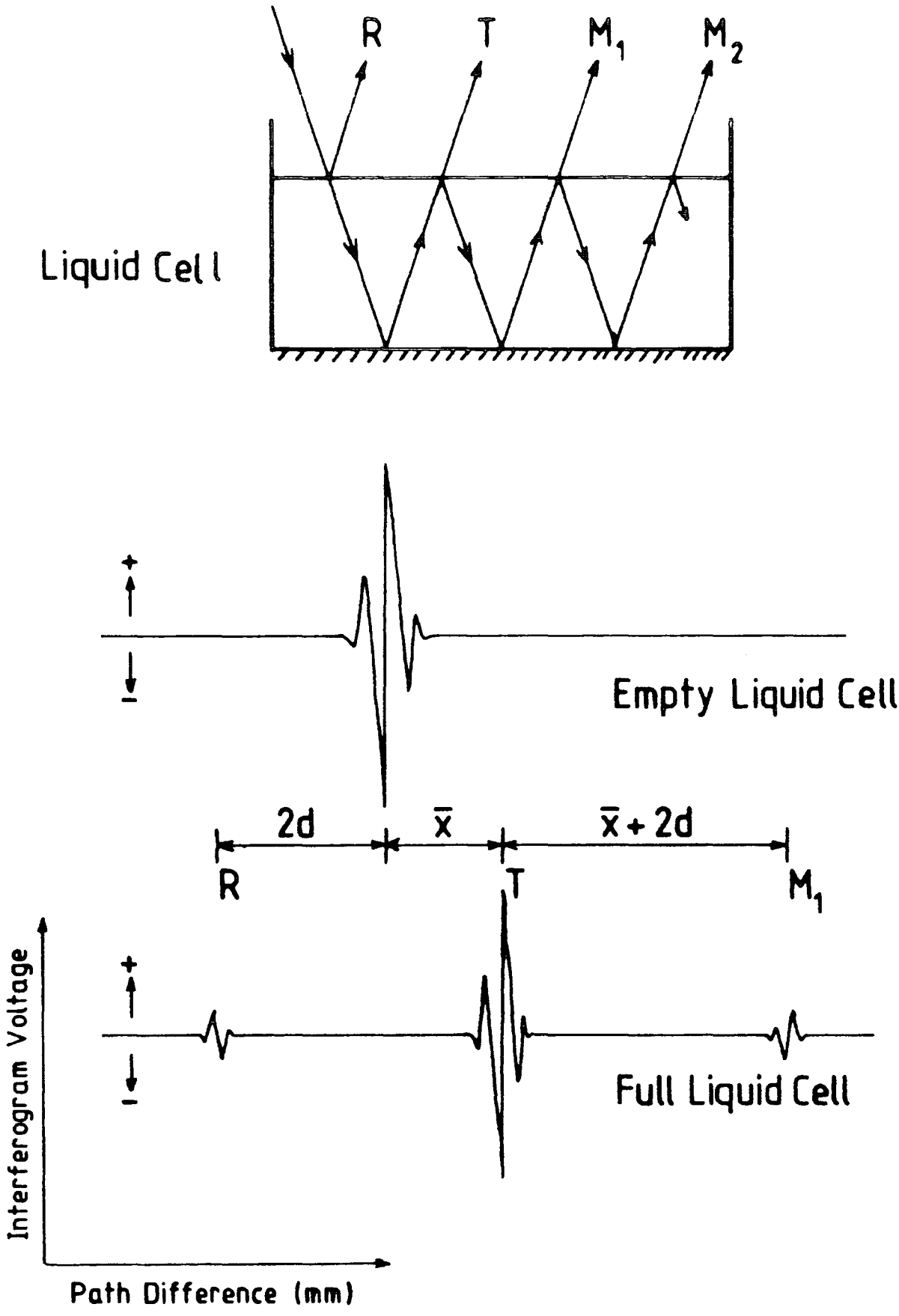

Figure 2.8 Reflections within the Free Layer Cell and resultant interferograms

2.3.2 Method of Analysis.

In the free layer method the liquid optical constants are either obtained from a comparison of full and empty cell interferograms or two liquid thickness measurements. The theory of these measurements and the editing and subtraction techniques necessary to remove the R and M_1 signatures have been discussed in a review by Birch & Parker[15].

2.3.3 Disadvantages.

The disadvantages associated with this type of dispersive cell arise mainly because of the free liquid surface they are:-

i) Liquid pathlengths less than 100 μm cannot be achieved.

ii) Difficulties in obtaining a plane parallel layer.

iii) Evaporation of volatile samples will produce changes in the sample pathlength.

iv) Unknown effects due to surface vibration and gas phase sample above the surface.

v) The sample pathlength cannot be measured directly but must be calculated from full and empty cell interferograms.

vi) The expressions used to obtain the liquid optical constants are not exact.

2.4 The Reflection Technique.

For highly absorbing samples (αmax. >150 Npcm^{-1}) where the free layer method cannot be used, a reflection technique was developed by Chamberlain et al.[26] and Zafar et al.[27]. In this method the interferometer fixed mirror was replaced by an optically flat window so that the sample could be poured on top of the window. This allows the complex reflectivity of the window liquid interface to be measured. Initially a TPX window was used and the reference measurement obtained by replacing the liquid with an equal weight of mercury. In carrying out the analysis it is assumed that the window mercury interface acts as a perfect reflector. Since this technique is dependent on the phase change on reflection at the window liquid interface, it is desirable that there is a large difference between the window and liquid refractive index. The refractive index of TPX is virtually constant at 1.456 throughout the far-infrared[28], which is close to that of air and most liquids. This problem was overcome by using a silicon window[29] which has a refractive index of about 3.41 (see Section 5.4.2a). Since the window/air interface would now have an intense signature, mercury was no longer required for the empty cell measurement.

2.5 Enclosed Dispersive Cells.

To overcome the disadvantages of the free layer method and the necessity to use two cell configurations for measurements, enclosed cells were developed. In these cells the sample was held between a window and mirror, thus removing the disadvantages associated with a free liquid surface. Also since there was a sample window interface

the same cell could be used for the reflection technique for highly absorbing samples. Several enclosed cells of varying complexity have been developed. Although they all overcome the disadvantages of a free layer some suffer from design disadvantages.

2.5.1 The Durham Dispersive Cell.

The cell developed at Durham University by Yarwood et al.[30] was intended to be simple in design and give a high energy throughput. This was achieved by using a large cell mirror, a thin low loss window and spacers to set the liquid pathlength. The cell is shown schematically in Figure 2.9, the main features of the cell are the large fixed mirror A, thin plastic (mylor or polyethylene) window B, the reference mirror and blocking cover, G & H and the cell spacer C. The cell was filled through T using a syringe and an external reservoir was used to maintain the liquid pressure such that there was no bowing of the cell window. The liquid refractive index was determined from a full and empty cell measurement to within $\pm$ 1.0%

2.5.1a Disadvantages.

This cell does overcome most of the disadvantages of the free layer technique, but suffers from further disadvantages due to the simple design, they are:-

i) The whole cell must be dismantled to change the sample pathlength.

ii) The cell can accommodate only small pathlength variations so the

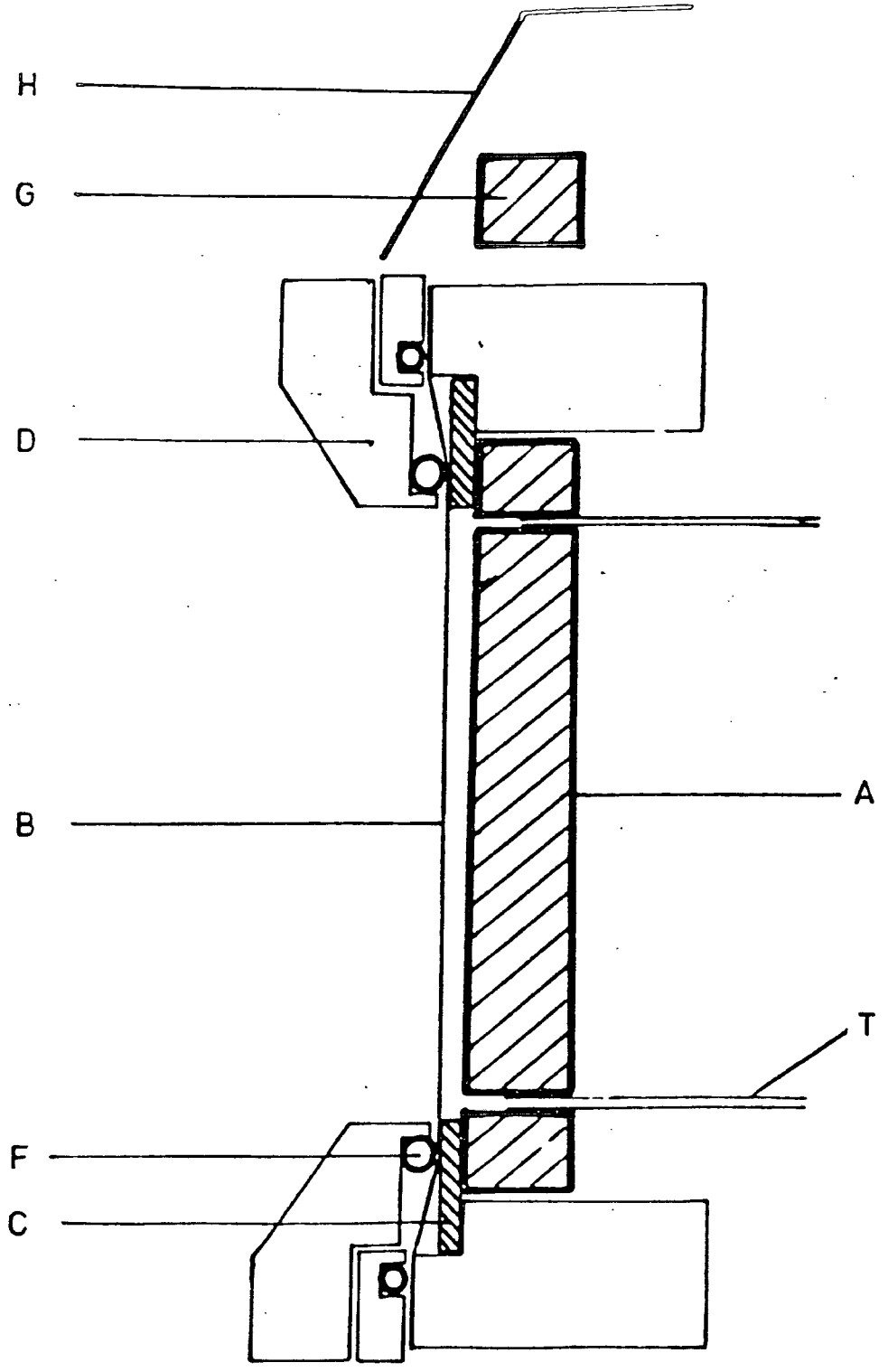

Figure 2.9 The Durham Dispersive Cell

range of liquids that can be studied is limited.

iii) The sample pathlength must be calculated from interferograms.

iv) The level of experimental errors permits only qualitative results.

v) As a thin cell window is used the reflection technique would not be practical.

2.5.2 More Advanced Liquid Cells.

Two variable thickness enclosed liquid cells were developed in collaboration with the National Physical Laboratory (NPL) in the seventies, one by Goulon at the University of Nancy[31,32] and the second at the Ryksuniversiteit, Leiden[33,34,35,36]. Both of these cells were more complicated than the Durham cell, but there is little information in the literature on the cell developed by Goulon. The cell developed at Leiden is shown in Figure 2.9 and has been described in detail by the Leiden group and Birch & Parker[15]. Using the Leiden cell Afsar[31] measured the optical constants of chlorobenzene to the same precision as with the free layer technique. Although this cell does overcome all the disadvantages of the free layer technique and gives the same level of accuracy, it does suffer from a complicated design and the tight fitting piston mechanism was subject to jamming from particulate matter or viscous residues, which occurred because of difficulties in cleaning the cell. Another problem was the difficulty in alignment of the cell mirror to give a plane parallel sample.

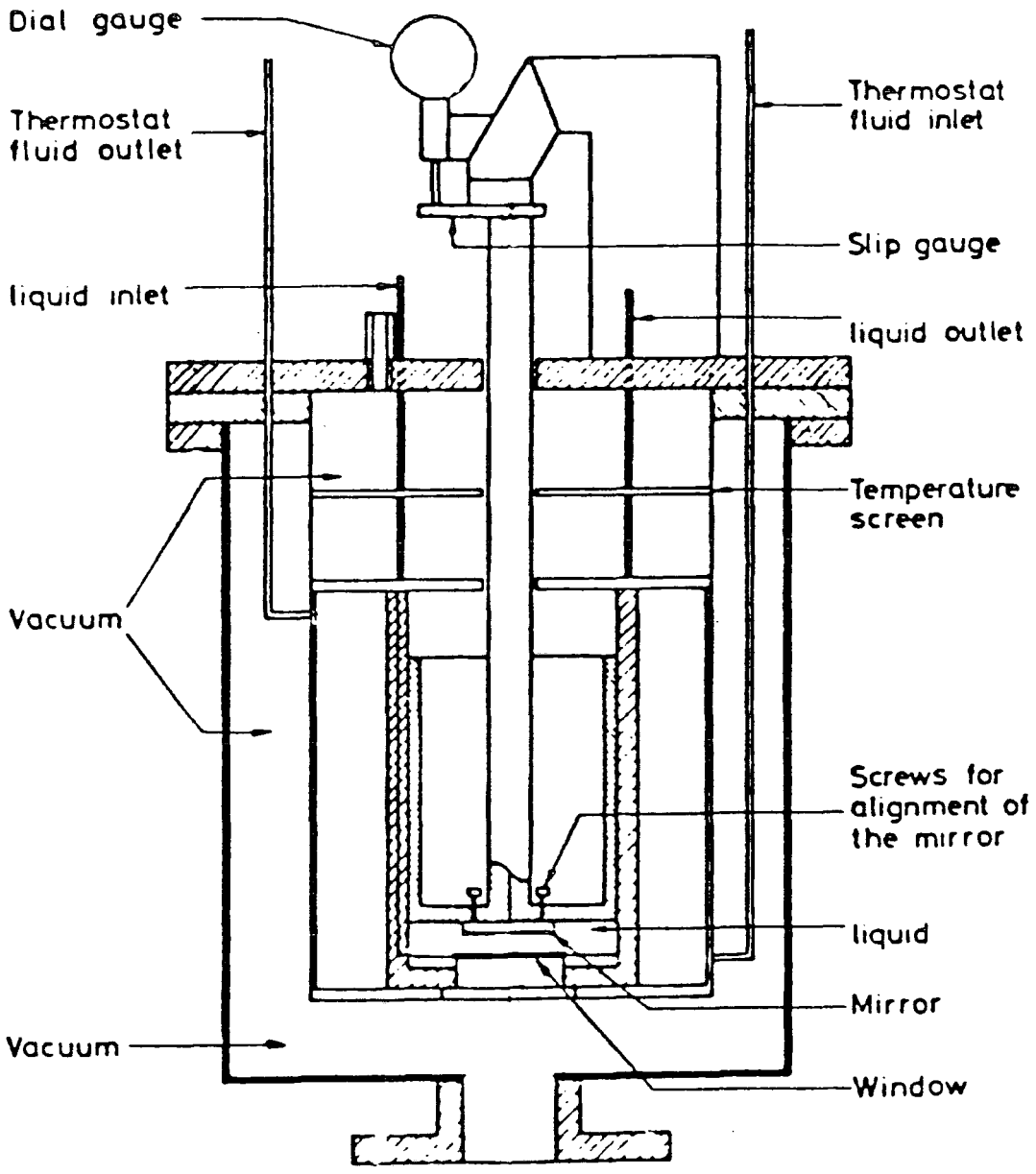

Figure 2.10 The Leiden Dispersive Cell

2.5.3 A New Liquid Cell

A new liquid cell of simple design that avoids the complexities and operational difficulties of the Leiden cell but maintains the measurement capabilities has been developed at the NPL by Birch et al.[37]. The construction of this New Liquid Cell is illustrated in Figure 2.11. It essentially consists of a stainless steel body in the form of a hollow cylinder fitted with a plane parallel single crystal silicon window at its lower end. The silicon was n type with a resistivity of about 0.6 Ω M, a diameter of 60 mm and a thickness of 2.6 mm. In order to minimise the possibility of damage to this brittle material it was supported at its edges between two annular PTFE pads to prevent contact with any of the metal parts of the cell. This restricted the aperture of the cell to 45 mm diameter. The window was held in place by a locking ring which clamped it between the two PTFE pads and forced it against the O-ring seal. This provided a vacuum and liquid seal for the cell, though the PTFE pads normally prevented any liquid coming into contact with the O-ring seal.

The cell mirror was a lapped stainless steel flat which was a tight push fit over the anvil of a non-rotating micrometer. This enabled the distance between the mirror and the window to be varied from a few tens of micrometers to about 45 millimetres. The micrometer was fitted to the top plate of the cell which was firmly clamped down onto the main body of the cell by six equispaced screws three of which screwed into the main body of the cell through clearance holes in the top plate. These were spring loaded to force the rounded ends of the other three screws onto the rim of the main

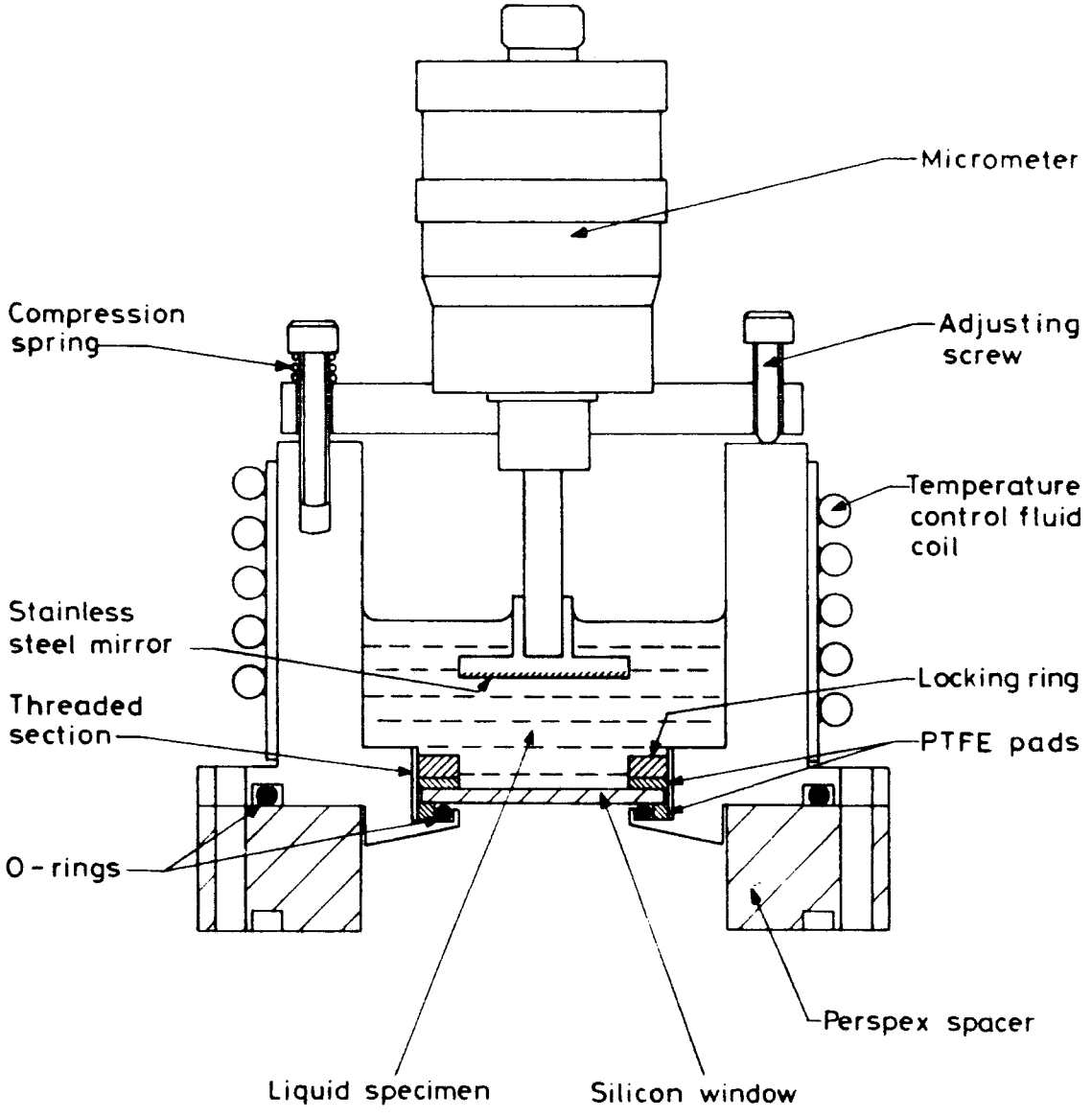

FIGURE 2.11 THE NEW LIQUID CELL

body. Which were screwed through tapped holes in the top plate and were used to align the mirror in the cell. The gap between the top plate and main cell body could be sealed with masking tape when a vapour seal was required. The masking tape was flexible enough to allow for cell alignment and removed the necessity for complicated metal bellows in the cell design. The New Liquid Cell is shown mounted on an interferometer schematically in figure 2.12 and mounted on an NPL cube interferometer in Figures 2.13 and 2.14. The cell is positioned with the window horizontal so that liquid specimens are contained as free standing layers. Liquids are introduced into the cell either through one of the tubes in the top plate or simply poured over the window with the top plate removed. A simple visual test was made to determine that there were no air bubbles left on the cell mirror surface when slowly immersed in a range of the solvents used in these studies for both methods of filling.

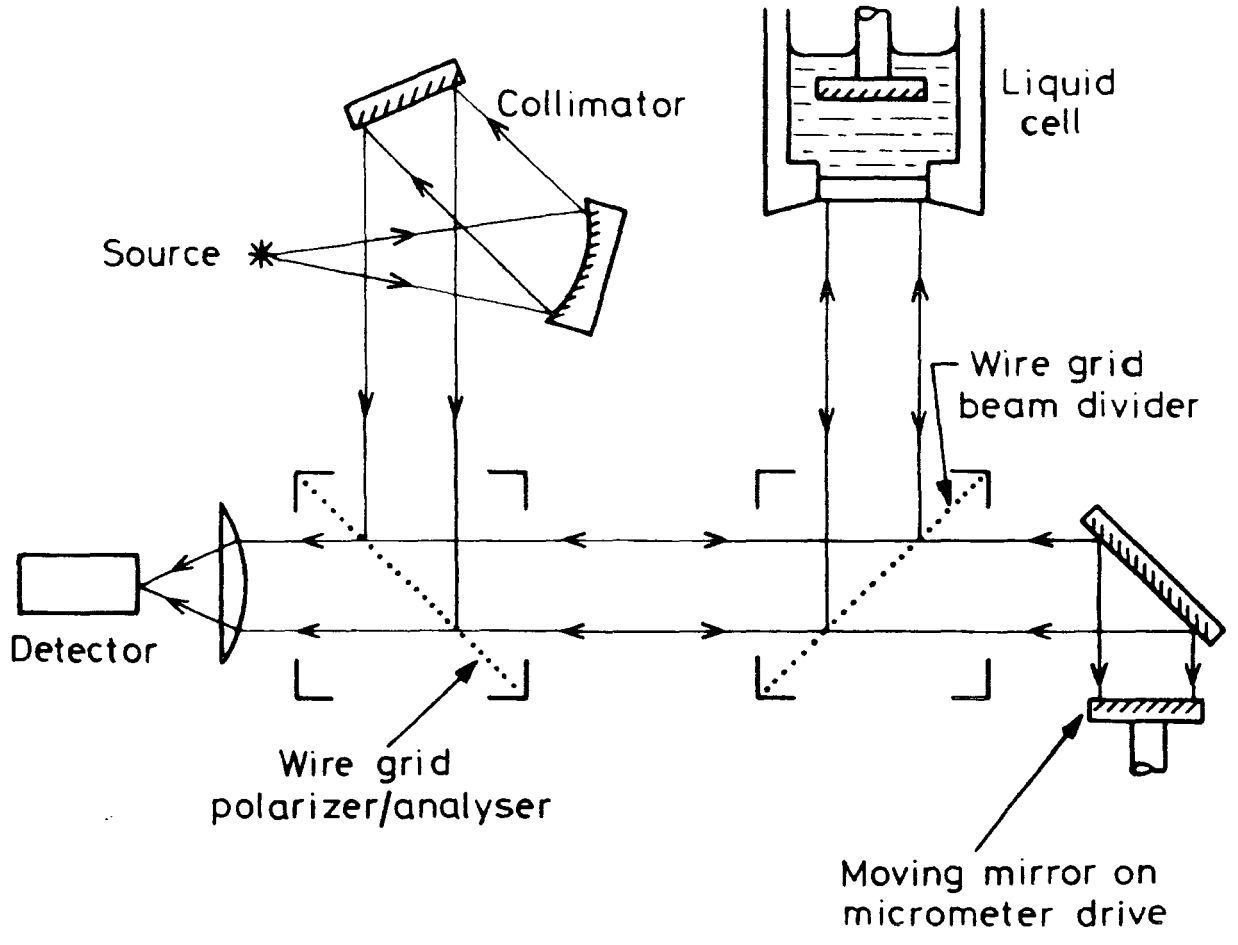

FIGURE 2.12 THE NEW LIQUID CELL / INTERFEROMETER ARRANGEMENT

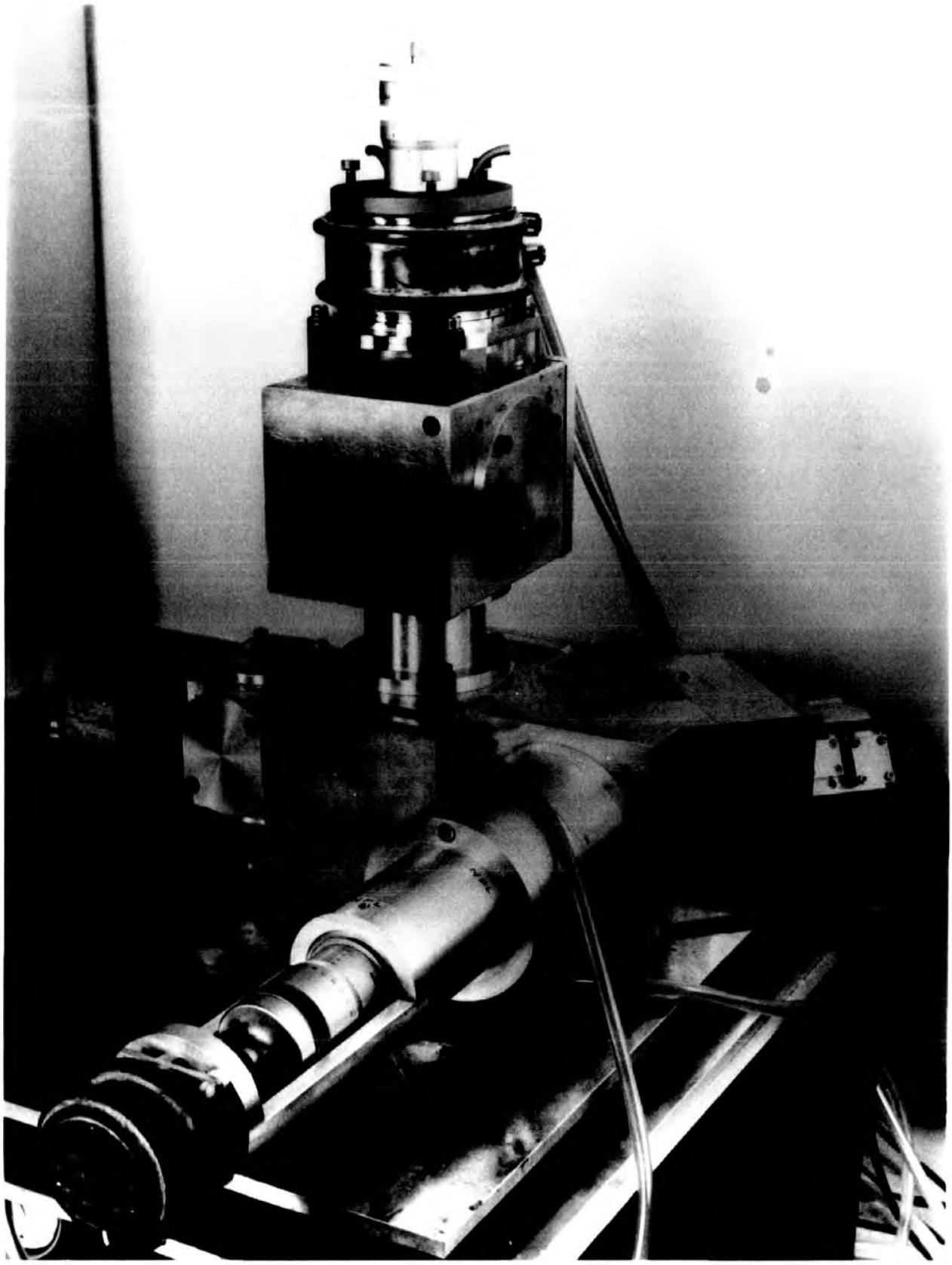

Figure 2.13 The new liquid cell mounted on an NPL interferometer

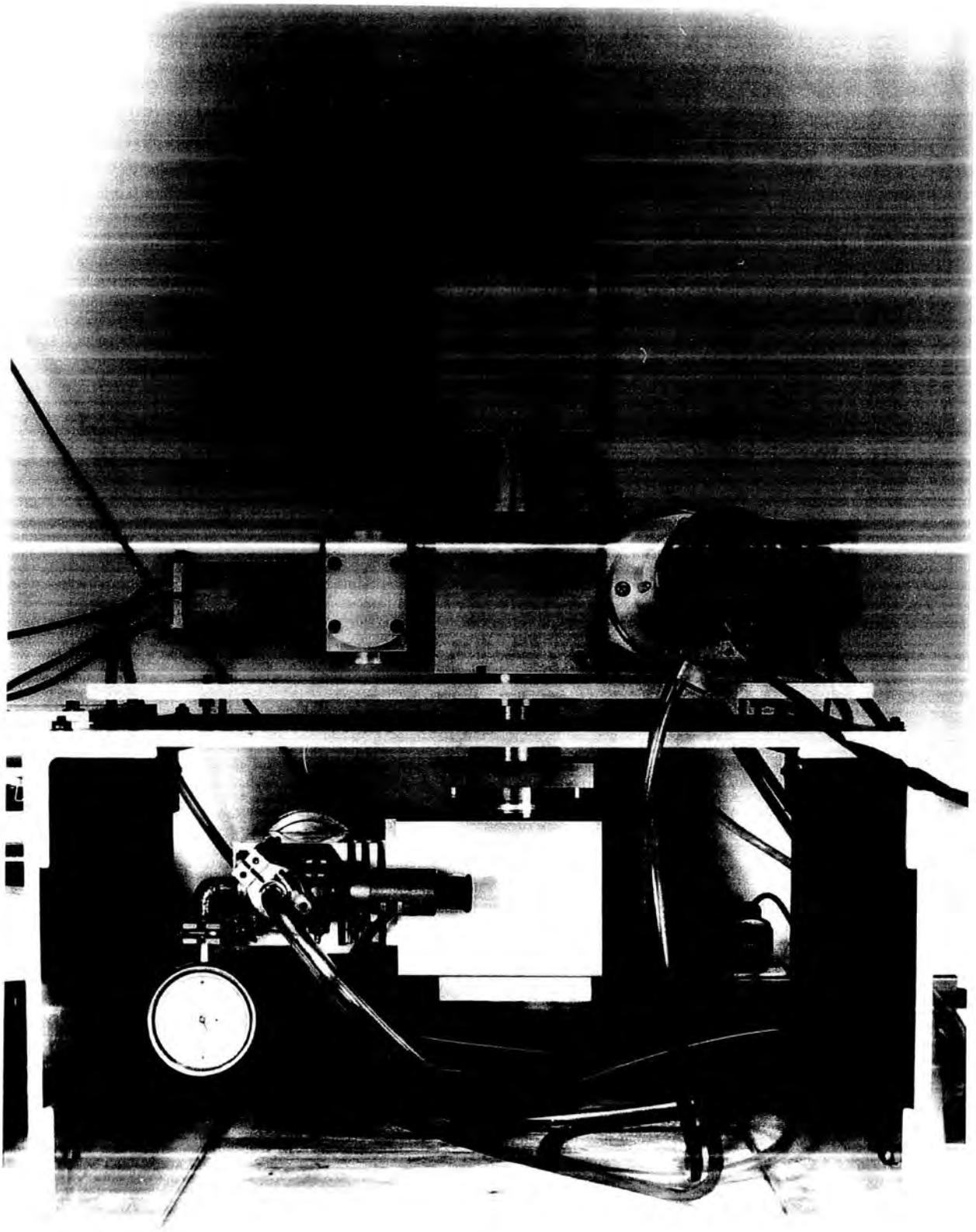

Figure 2.14 The new liquid cell mounted on an NPL interferometer

CHAPTER 3

THEORY OF DISPERSIVE MEASUREMENTS FOR THE NEW LIQUID CELL

3.1 Introduction.

A schematic representation of the three interfaces of the filled New Liquid Cell (described in Chapter 2) and the rays propagating through them is given in Figure 3.1. The rays have been labelled according to the notation of Honijk et al.[33]. Rays A, B, C continue in the same pattern as the previous rays, giving an infinite series of reflections back to the detector. In principle any pair of reflections could be used in a determination of the optical constants of the liquid, but practical considerations limit the number that can be usefully analysed. The first order reflections above (1,1) and all second and higher order reflections (2,0) etc. have poor signal to noise ratios, as can be seen for the empty cell interferogram in Figure 3.2. The reflections used in nearly all cases are therefore combinations of the (0,0), (1,0) and (1,1), but the effects on the (1,1) due to higher order reflections must not be overlooked. These effects are normally overcome by arranging the experimental parameters so that no other reflections are resolved in the (1,1) interferogram range (see Section 4.1.3d).

In order to develop the methods of analysis for the New Liquid Cell it is useful to describe the reflected rays in terms of their complex spectra $\hat{S}$. These are shown for reflections (0,0) to (1,2) in terms of the complex Fresnel reflection, transmission and propagation coefficients[38] in Figure 3.3. The complex Fresnel coefficients are related to the optical properties of the media involved as follows[38]

$$\hat{r}_{xy} = \frac{(\hat{n}_x - \hat{n}_y)}{(\hat{n}_x + \hat{n}_y)} \qquad \ldots\ldots \quad 3.1$$

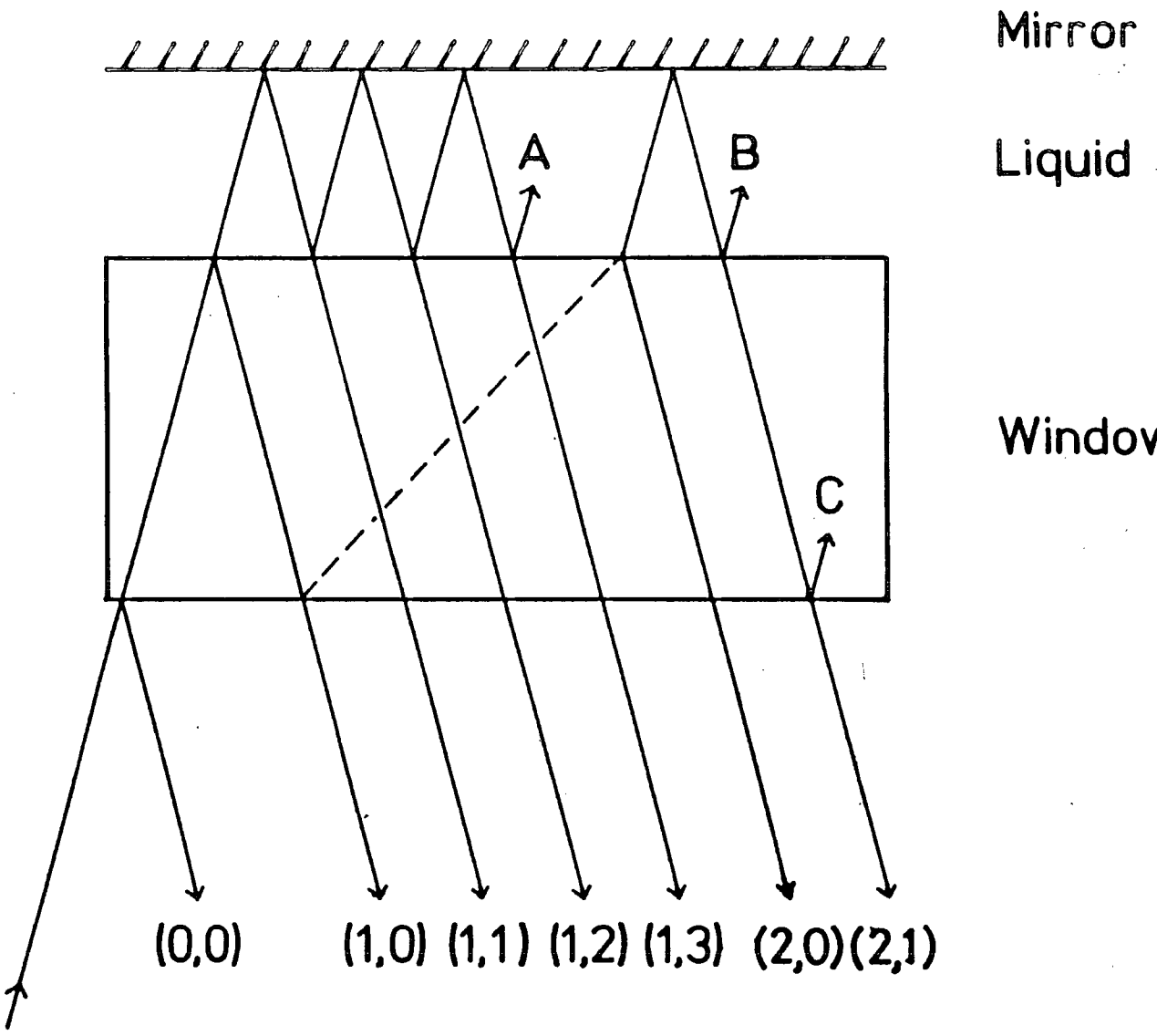

Figure 3.1 ELECTROMAGNETIC RAYS PROPAGATING THROUGH THE NEW LIQUID CELL.

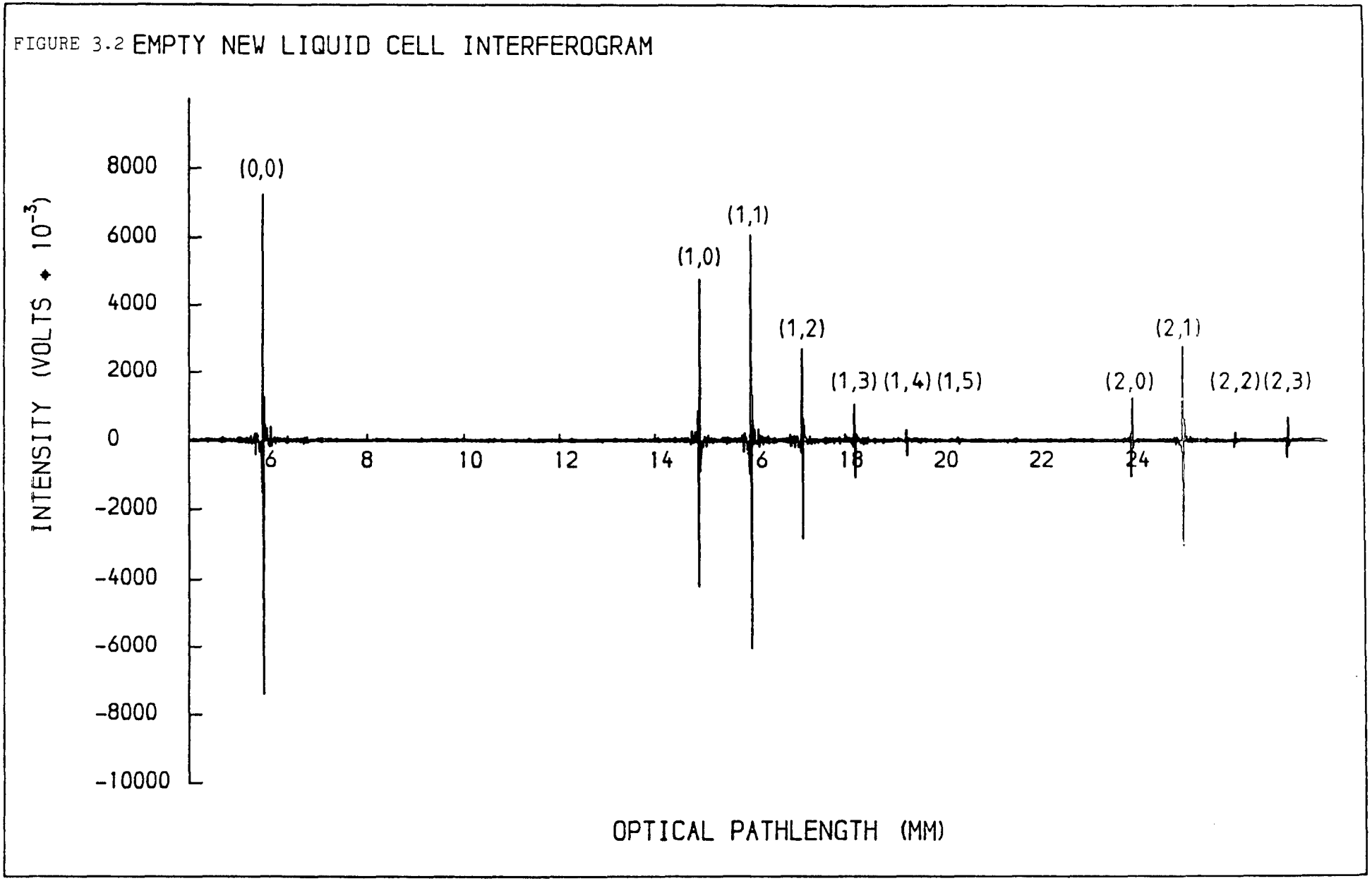
FIGURE 3.2 EMPTY NEW LIQUID CELL INTERFEROGRAM
INTENSITY (VOLTS * 10^{-3})
8000
6000
4000
2000
0
-2000
-4000
-6000
-8000
-10000
(0,0)
(1,0)
(1,1)
(1,2)
(1,3)
(1,4)
(1,5)
(2,0)
(2,1)
(2,2)
(2,3)
6
8
10
12
14
16
18
20
22
24
OPTICAL PATHLENGTH (MM)

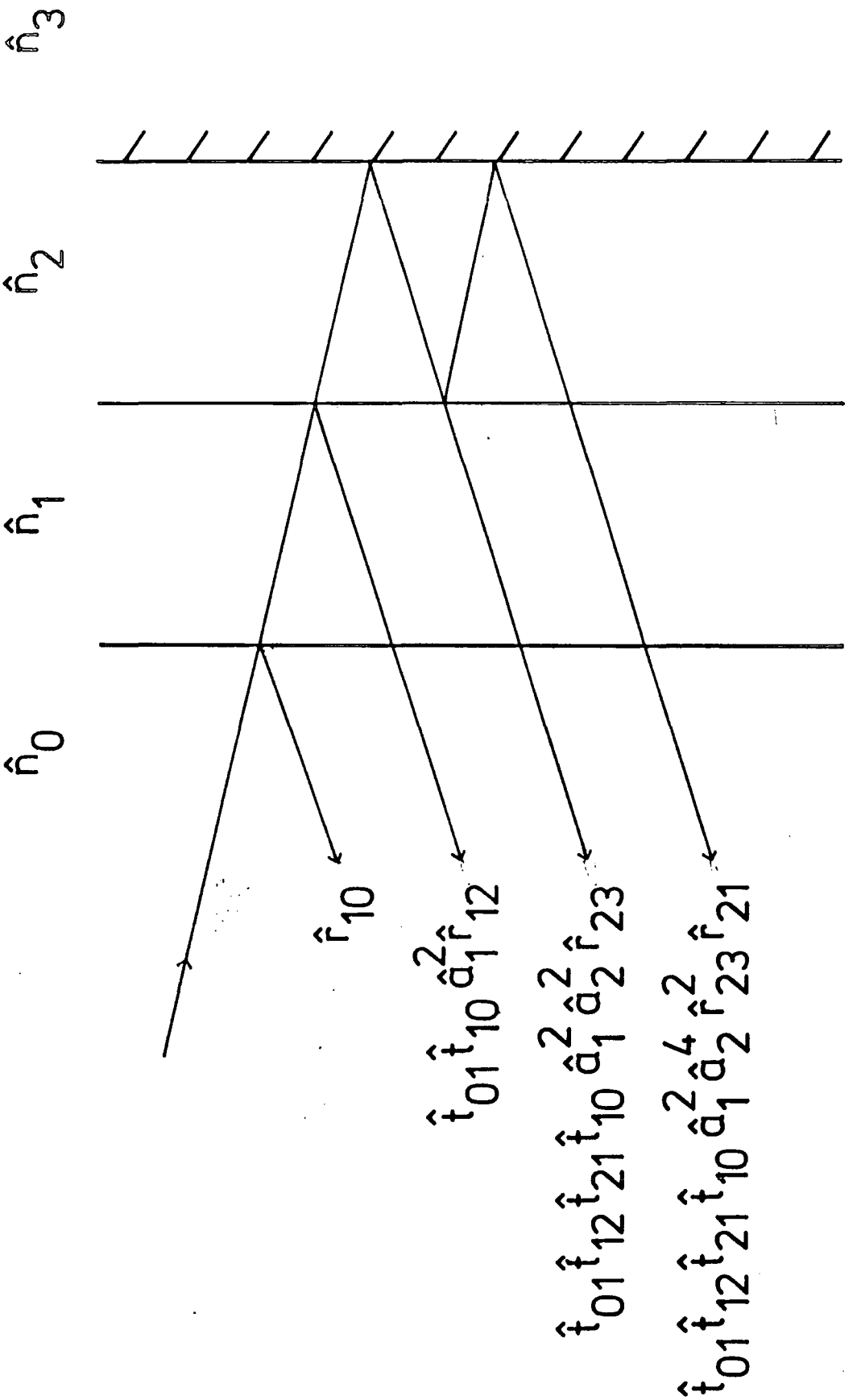

Figure 3.3 COMPLEX FRESNEL REFLECTION, TRANSMISSION AND PROPAGATION COEFFICIENTS FOR REFLECTIONS (0,0) TO (1,0).

where $\hat{r}_{x,y}$ signifies reflection at the interface of media x and y.

$$\hat{r}_{yx} = -\hat{r}_{xy} \qquad \ldots\ldots \quad 3.2$$

$$t_{xy} = \frac{2}{\hat{n}_{xy} + 1} \qquad \ldots\ldots \quad 3.3$$

$$t_{yx} = \hat{n}_{xy}\, t_{xy} \qquad \ldots\ldots \quad 3.4$$

$$\hat{a}_x = \exp(i2\pi\bar{\nu}\hat{n}_x d_x) \qquad \ldots\ldots \quad 3.5$$

where d is the thickness of the medium x.

3.2 Determination of Optical Constants.

The two basic optical arrangements used to measure the optical properties of liquids by DFTS are illustrated schematically in Figure 3.4.a and b. In each case the details of the optical configuration must be taken into account, in order to calculate the optical constants of a liquid from the recorded interferograms. This is achieved by introducing the complex insertion loss

$$\hat{L}(\bar{\nu}) = L(\bar{\nu})\, \exp i\phi_L(\bar{\nu}) \qquad \ldots\ldots \quad 3.6$$

where $L(\bar{\nu})$ is the modulus and $\phi_L(\bar{\nu})$ the phase. $\hat{L}$ is defined by Chamberlain[38] as the complex factor by which the amplitude of a wave is changed, when a reference material such as a vacuum or perfect mirror is replaced by a specimen, see Figure 3.4.c.

Birch & Parker[15] have shown that for a sample placed in one arm of an interferometer, the recorded interferogram may be written as the sum

$$I_s(x) = \int_{-\infty}^{+\infty} \mathcal{C}(\bar{\nu})\cos\phi(\bar{\nu})\cos 2\pi\bar{\nu}x\,d\bar{\nu} + \int_{-\infty}^{+\infty} \mathcal{C}(\bar{\nu})\sin\phi(\bar{\nu})\sin 2\bar{\nu}\pi x\,d\bar{\nu}$$

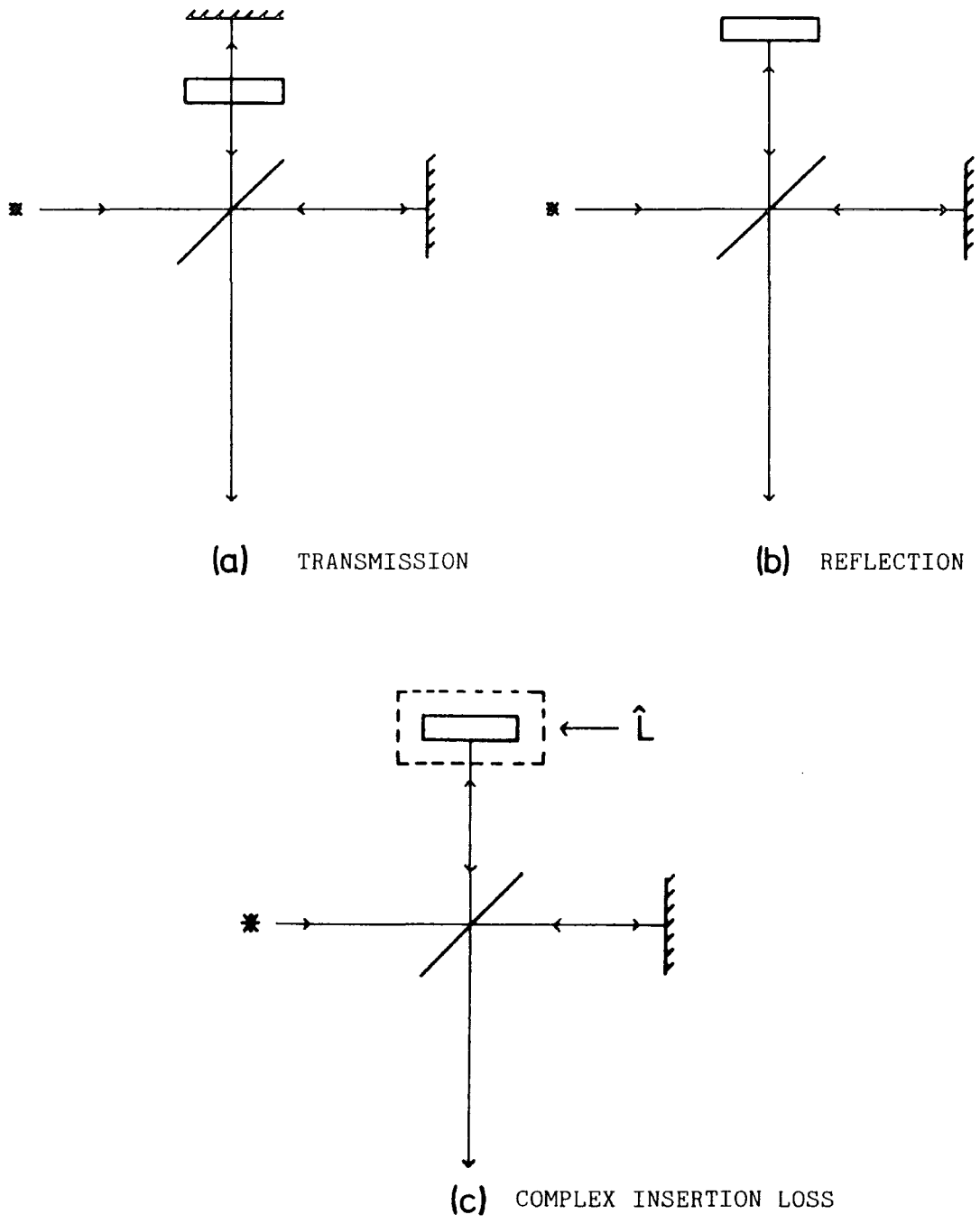

FIGURE 3.4: DFTS ARRANGEMENTS AND THE COMPLEX INSERTION LOSS

of an even part and an odd part (see Section 2.1)

$$\mathcal{C}(\bar{\nu}) = 2\hat{E}_o(\bar{\nu})\hat{E}_o^*(\bar{\nu})L(\bar{\nu}) \quad \ldots\ldots \quad 3.8$$

is the recorded power spectrum and $\phi(\bar{\nu})$ describes the phase difference between the two partial beams within the interferometer.

$$\phi(\bar{\nu}) = \phi_i(\bar{\nu}) + \phi_o(\bar{\nu}) \quad \ldots\ldots \quad 3.9$$

where ϕ_o takes account of any residual phase difference due to lack of symmetry in the interferometer. Cosine and sine transforms of 3.7 give

$$p(\bar{\nu}) = \int_{-\infty}^{+\infty} I_s(x)\cos 2\pi\bar{\nu}x\,dx = \mathcal{C}(\bar{\nu})\cos\phi(\bar{\nu}) \quad \ldots\ldots \quad 3.10$$

$$q(\bar{\nu}) = \int_{-\infty}^{+\infty} I_s(x)\sin 2\pi\bar{\nu}x\,dx = \mathcal{C}(\bar{\nu})\sin\phi(\bar{\nu}) \quad \ldots\ldots \quad 3.11$$

Therefore the complex spectrum obtained by Fourier transformation

$$\hat{S}(\bar{\nu}) = p(\bar{\nu}) + iq(\bar{\nu}) = \mathcal{C}(\bar{\nu})\exp[i\phi(\bar{\nu})] \quad \ldots\ldots \quad 3.12$$

has a modulus

$$\mathcal{C}(\bar{\nu}) = [p^2(\bar{\nu}) + q^2(\bar{\nu})]^{\frac{1}{2}} \quad \ldots\ldots \quad 3.13$$

and phase

$$\phi(\bar{\nu}) = \arctan\frac{[q(\bar{\nu})]}{[p(\bar{\nu})]} \quad \ldots\ldots \quad 3.14$$

When computed numerically $\phi(\bar{\nu})$ is the principal value $-\frac{\pi}{2} \leqslant \phi(\bar{\nu}) \leqslant \frac{\pi}{2}$ this can be extended to $-\pi \leqslant \phi(\bar{\nu}) \leqslant \pi$ by taking into account the signs of p and q. But if $\phi(\bar{\nu})$ is a rapidly changing function, its real value may exceed $\pm\pi$ and phase branching is said to occur[39]. This can be corrected by adding $2M\pi$, where M is an integer (1,2,3 etc.) to the

difference between a sample and background phase spectrum as in Section 3.2.1.

From equations 3.10 to 3.12

$$\mathcal{C}(\tilde{\nu})\exp[i\phi(\tilde{\nu})] = \int_{-\infty}^{+\infty} I_S(x)\exp(i2\pi\tilde{\nu}x)dx \quad \ldots\ldots \quad 3.15$$

From equation 3.8

$$2\hat{E}_O(\tilde{\nu})\hat{E}_O^*(\tilde{\nu})L(\tilde{\nu})\exp[i\phi(\tilde{\nu})] = \int_{-\infty}^{+\infty} I_S(x)\exp(i2\pi\tilde{\nu}x)dx \quad \ldots\ldots \quad 3.16$$

From equation 3.9

$$2\hat{E}_O(\tilde{\nu})\hat{E}_O^*(\tilde{\nu})L(\tilde{\nu})\exp i[\phi_2(\tilde{\nu}) + \phi_O(\tilde{\nu})] = \int_{-\infty}^{+\infty} I_S(x)\exp(i2\pi\tilde{\nu}x)dx \quad 3.17$$

and from equation 3.6

$$2\hat{E}_O(\tilde{\nu})\hat{E}_O^*(\tilde{\nu})\hat{L}(\tilde{\nu})\exp[i\phi_O(\tilde{\nu})] = \int_{-\infty}^{+\infty} I_S(x)\exp(i2\pi\tilde{\nu}x)dx \quad \ldots\ldots \quad 3.18$$

If the sample is removed from the interferometer equation 3.18 becomes

$$2\hat{E}_O(\tilde{\nu})\hat{E}_O^*(\tilde{\nu})\exp[i\phi_O(\tilde{\nu})] = \int_{-\infty}^{+\infty} I_O(x)\exp(i2\pi\tilde{\nu}x)dx \quad \ldots\ldots \quad 3.19$$

Ratioing equations 3.18 and 3.19 will give the complex insertion loss as the ratio of two complex Fourier transforms.

$$L(\tilde{\nu}) = \frac{\int_{-\infty}^{+\infty} I_S(x)\exp(i2\pi\tilde{\nu}x)dx}{\int_{-\infty}^{+\infty} I_O(x)\exp(i2\pi\tilde{\nu}x)dx} \quad \ldots\ldots \quad 3.20$$

or, in a convenient notation

$$\hat{L}(\tilde{\nu}) = \frac{FT\left\{I_S(x)\right\}}{FT\left\{I_O(x)\right\}} \quad \ldots\ldots \quad 3.21$$

where FT $\{\ \}$ is taken to mean the complex Fourier transform of the

quantity in parenthesis.

3.2.1 Transmission Dispersive Fourier Transform Spectrometry (TDFTS).

The optical arrangement used for TDFTS is that of Figure 3.4a, if we consider the reflections within the New Liquid Cell shown in Figure 3.1. The first ray to be transmitted through the liquid sample is the (1,1), which will give rise to an interference signature to higher optical path difference than the (1,0) signature. From equation 3.21 $\hat{L}(\bar{\nu})$ is the ratio of a background and sample complex Fourier transform. These could be obtained by recording (1,1) interferograms for an empty and full cell with the cell mirror in a fixed position. However, any mirror misalignment would give a non-parallel sample and lead to errors in measuring the window mirror pathlength. Also analysis to obtain the liquid optical constants will be complicated, since the reflection and transmission coefficients of the window liquid interface would be different for the two interferograms. A better method is to record interferograms for the full cell with different window-mirror pathlengths. The difference in these pathlengths can be determined accurately and any mirror misalignment would be lost to the experiment. As the window liquid interface is the same for both measurements, its effect on the recorded interferograms will be ratioed out in obtaining $\hat{L}(\bar{\nu})$, simplifying the analysis. Therefore, if two interferograms of the (1,1) signature for liquid pathlengths d_1 and d_2 are recorded, ensuring that neither contain structure due to other interference signatures. From Figure 3.5 point A is the nearest sampled point to the ZPD position of the

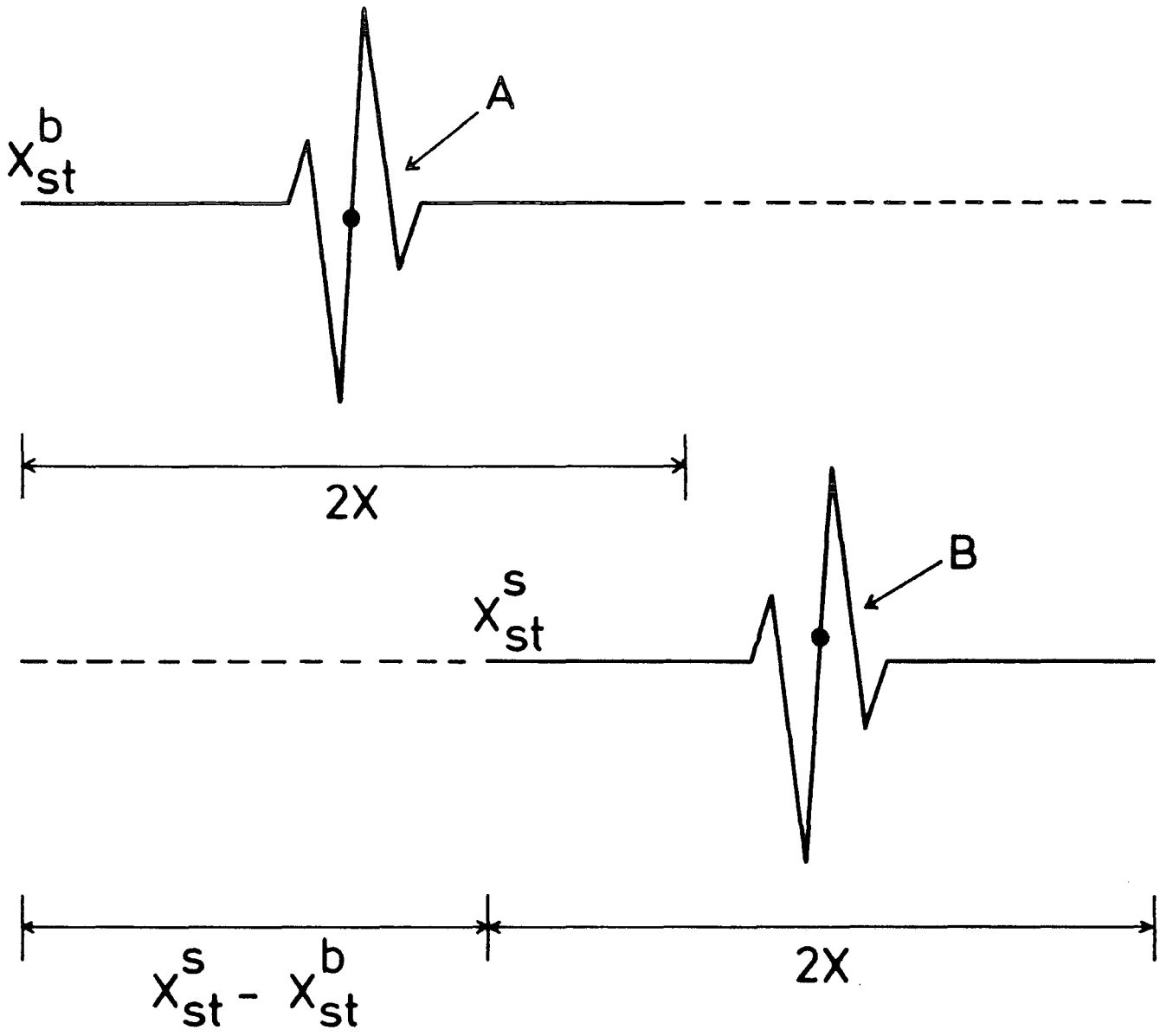

FIGURE 3.5: ZPD POSITIONS FOR A DISPERSIVE EXPERIMENT

first interferogram, and is used as the ZPD in transforming that interferogram over the range 2x. If this position were also used as the ZPD for transformation of the second interferogram, more data than is necessary would have to be recorded, and severe phase branching would occur[40]. This is overcome by taking B, the sampled point nearest to the crossover point of the second interferogram as the ZPD and using the Fourier transform shift theorem[45] to retain the phase of the complex insertion loss.

$$\phi_L(\tilde{\nu}) = \phi_L^{Expt'l}(\tilde{\nu}) + 2\pi\tilde{\nu}(B - A) \qquad \ldots\ldots \quad 3.22$$

where (B-A) is the fringe shift term (FS) of the two interferograms and can be calculated if the moving mirror start point is known for both interferograms.

$$FS = X^s{}_{st} - X^b{}_{st} + \left\{ \text{Sampling Interval x } (ZPD^s - ZPD^b) \right\} \qquad 3.23$$

But (B-A) = 2FS as FS is in moving mirror units, therefore

$$\phi_L(\tilde{\nu}) = \phi_L^{Expt'l}(\tilde{\nu}) + 2\pi\tilde{\nu}2FS \qquad \ldots\ldots \quad 3.24$$

Fourier transforming the two interferograms to obtain their complex spectra and ratioing to obtain the experimental complex insertion loss gives

$$\hat{L}^E(\tilde{\nu}) = \frac{\ell_L^{d2}(\tilde{\nu})\exp i(\phi_L^{d2}(\tilde{\nu}) + 4\pi\tilde{\nu}FS)}{\ell_L^{d1}(\tilde{\nu})\exp i\phi_L^{d1}(\tilde{\nu})} \qquad \ldots\ldots \quad 3.25$$

$$\hat{L}^E(\tilde{\nu}) = \frac{\ell_L^{d2}(\tilde{\nu})\exp i[(\phi_L^{d2}(\tilde{\nu}) - \phi_L^{d1}(\tilde{\nu})) + 4\pi\tilde{\nu}FS]}{\ell_L^{d1}(\tilde{\nu})} \qquad \ldots\ldots \quad 3.26$$

If we now express the complex spectrum of the (1,1) reflection in

terms of the complex transmission, reflection and propagation coefficients of the system, from Figure 3.3

$$\hat{S}(1,1) = \hat{t}_{01}\hat{t}_{12}\hat{t}_{21}\hat{t}_{10}\hat{a}_1^2\hat{a}_2^2\hat{r}_{23} \quad \ldots\ldots \quad 3.27$$

Ratioing the complex spectra corresponding to the two liquid pathlengths will give the theoretical complex insertion loss

$$\hat{L}^T(\bar{\nu}) = \frac{\hat{S}^{d2}(1,1)}{\hat{S}^{d1}(1,1)} \quad \ldots\ldots \quad 3.28$$

$$\hat{L}^T(\bar{\nu}) = \frac{(\hat{t}_{01}\hat{t}_{12}\hat{t}_{21}\hat{t}_{10}\hat{a}_1^2\hat{a}_2^2\hat{r}_{23})^{d2}}{(\hat{t}_{01}\hat{t}_{12}\hat{t}_{21}\hat{t}_{10}\hat{a}_1^2\hat{a}_2^2\hat{r}_{23})^{d1}} \quad \ldots\ldots \quad 3.29$$

The reflection and transmission coefficients will be the same for both pathlengths, as will the propagation coefficient of the cell window, therefore

$$\hat{L}^T(\bar{\nu}) = \frac{(\hat{a}_2^2)^{d2}}{(\hat{a}_2^2)} \quad \ldots\ldots \quad 3.30$$

from equation 3.5

$$\hat{a}_2(\bar{\nu}) = \exp(i2\pi\bar{\nu}n_2(\bar{\nu})d_2^*)\exp(-\tfrac{1}{2}\alpha_2(\bar{\nu})d_2^*) \quad \ldots\ldots \quad 3.31$$

substituting for 3.31 in 3.30

$$\hat{L}^T(\bar{\nu}) = \exp[i4\pi\bar{\nu}n_s(\bar{\nu})\ (d_2 - d_1)]\exp[-\alpha_s(\bar{\nu})\ (d_2 - d_1)] \quad 3.32$$

Comparing the modulus and phase of the experimental and theoretical complex insertion loss in equations 3.26 and 3.32 gives

$$\frac{\mathcal{L}_L^{d2}(\bar{\nu})}{\mathcal{L}_L^{d1}(\bar{\nu})} = \exp[-\alpha_s(\bar{\nu})\ (d_2 - d_1)] \quad \ldots\ldots \quad 3.33$$

and

$$\exp[i(\phi_L^{d2}(\tilde{\nu}) - \phi_L^{d1}(\tilde{\nu})) + 4\pi\tilde{\nu}FS] = \exp[i4\pi\tilde{\nu}n_s(\tilde{\nu})\ (d_2 - d_1)] \quad \ldots\ldots\ 3.34$$

From equations 3.33 and 3.34 the required optical constants of the liquid, can be determined from the experimentally measured modulus and phase spectra.

$$\alpha_s(\tilde{\nu}) = -\frac{1}{d_2 - d_1} \ln\left[\frac{\mathcal{L}^{d_2}(\tilde{\nu})}{\mathcal{L}^{d_1}(\tilde{\nu})}\right] \quad \ldots\ldots\ 3.35$$

and

$$n_s(\tilde{\nu}) = \frac{[\phi_L^{d2}(\tilde{\nu}) - \phi_L^{d1}(\tilde{\nu}) + 2M\pi]}{[4\pi\tilde{\nu}(d_2 - d_1)]} + \frac{FS}{(d_2 - d_1)} \quad \ldots\ldots\ 3.36$$

where $2m\pi$ takes account of any phase branching.

3.2.2 Reflection Dispersive Fourier Transform Spectrometry (RDFTS).

For very absorbing liquid samples, where even for very small liquid pathlengths, the (1,1) signature is virtually totally attenuated. The method of RDFTS, where the (0,0) and (1,0) reflection signatures are used to determine the optical constants of a liquid, can be employed. For this method of analysis the cell window optical constants must be known, in order to calculate the liquid optical constants. Therefore, a separate experiment must first be carried out to determine the optical constants of the window material. This could be achieved by a normal transmission experiment, but small temperature differences of the window between experiments would lead to a systematic error in the liquid absorption coefficient. Therefore, the

method of Passchir et al[42] was followed, and the window optical constants were measured in situ prior to the liquid measurements.

3.2.2a Determination of the New Liquid Cell Window Optical Constants.

If we consider the complex spectra reflected from the lower and upper surfaces of the cell window, these can be represented as follows

$$\hat{S}_{01} = \hat{r}_{01} \qquad \ldots\ldots \quad 3.37$$

From equation 3.2

$$\hat{S}_{12} = \hat{S}_{10} = \hat{r}_{10}\, \hat{a}_1^2\, \hat{t}_{01}\, \hat{t}_{10} \qquad \ldots\ldots \quad 3.38$$

$$\hat{S}_{10} = \hat{r}_{10}\, (1 - \hat{r}_{01})\, (1 - \hat{r}_{10})\, \hat{a}_1^2 \qquad \ldots\ldots \quad 3.39$$

from equation 3.2

$$\hat{S}_{10} = -\hat{r}_{01}\, (1 - \hat{r}_{01})\, (1 - \hat{r}_{01})\, \hat{a}_1^2$$

$$\hat{S}_{10} = (-\hat{r}_{01} - \hat{r}_{01}^2 + \hat{r}_{01}^2 + \hat{r}_{01}^3)\, \hat{a}_1^2$$

$$\hat{S}_{10} = \hat{r}_{01}\, (\hat{r}_{01}^2 - 1)\, \hat{a}_1^2 \qquad \ldots\ldots \quad 3.40$$

The ratio of equations 3.40 and 3.37 will give the complex insertion loss for the cell window

$$\hat{L}(\nu) = \frac{\hat{S}_{10}}{\hat{S}_{01}} = \frac{\hat{r}_{01}\, (\hat{r}_{01}^2 - 1)\, \hat{a}_1^2}{\hat{r}_{01}} \qquad \ldots\ldots \quad 3.41$$

$$\hat{L}(\nu) = (\hat{r}_{01}^2 - 1)\, \hat{a}_1^2 \qquad \ldots\ldots \quad 3.42$$

which is equivalent to equation (2) in Passchir et al.[42]. Since we are dealing with complex quantities $\hat{L}$ can be rewritten in terms of the

modulus and phase of $\hat{r}_{01}$ and $\hat{a}_1$

$$\hat{L}(\nu) = (\hat{r}_{01}^2 \exp(i\, 2\phi_{r_{01}}) - 1) \exp(-\alpha d) \exp(i4\pi n\bar{\nu}d) \quad \ldots\ldots \quad 3.43$$

From complex arithmetic

$$\hat{L}(\bar{\nu}) = [(r_{01}^2 \cos 2\phi_{r_{01}} - 1) + (ir_{01}^2 \sin 2\phi_{r_{01}})] \exp(-\alpha d) \exp(i4\pi n\bar{\nu}d) \quad \ldots\ldots \quad 3.44$$

The modulus of 3.44 is

$$\left|\hat{L}(\tilde{\nu})\right| = [(r_{01}^2 \cos 2\phi_{r_{01}} - 1)^2 + (r_{01}^2 \sin 2\phi_{r_{01}})^2]^{\frac{1}{2}} \exp(-\alpha d)$$

$$\left|\hat{L}(\tilde{\nu})\right| = [(r_{01}^4 \cos^2 2\phi_{r_{01}} - 2r_{01}^2 \cos 2\phi_{r_{01}} + 1) + (r_{01}^4 \sin^2 2\phi_{r_{01}})]^{\frac{1}{2}} \exp(-\alpha d)$$

$$\left|\hat{L}(\tilde{\nu})\right| = \left[[r_{01}^4(\cos^2 2\phi_{r_{01}} + \sin^2 2\phi_{r_{01}}) - 2r_{01}^2 \cos 2\phi_{r_{01}} + 1]\right]^{\frac{1}{2}} \exp(-xd)$$

$$\left|\hat{L}(\tilde{\nu})\right| = \left[[r_{01}^4 - 2r_{01}^2 \cos 2\phi_{r_{01}} + 1]\right]^{\frac{1}{2}} \exp(-\alpha d) \quad \ldots\ldots \quad 3.45$$

and the phase of 3.44 is

$$\mathrm{ph}\left\{\hat{L}(\tilde{\nu})\right\} = 4\pi n\bar{\nu}d + \arctan\left[\frac{r_{01}^2 \sin 2\phi_{r_{01}}}{r_{01}^2 \cos\phi_{r_{01}} - 1}\right] \quad \ldots\ldots \quad 3.46$$

If we consider the value of the first term in equation 3.46 at 50 cm^{-1} letting α = 0.4 cm^{-1}, n = 3.4 and d = 0.3 cm.

$$4\pi n\bar{\nu}d \simeq 640$$

For the second term the denominator is always negative and the numerator positive and near to zero. Considering the size of the first term, the angle represented by the second term can therefore be approximated to π radians. Therefore, equations 3.45 and 3.46 can

be simplified

$$\left|\hat{L}(\bar{\nu})\right| = [r_{01}^4 - 2r_{01}^2 + 1]^{\frac{1}{2}} \exp(-\alpha' d) \qquad \ldots\ldots \quad 3.47$$

$$\text{ph}\left\{\hat{L}(\bar{\nu})\right\} = 4\pi n' \bar{\nu} d + \pi \qquad \ldots\ldots \quad 3.48$$

where α' and n' are the approximate α and n values of the cell window, which can now be calculated.

$$\alpha'(\bar{\nu}) = \frac{1}{d} \frac{\ln[r_{01}^4 - 2r_{01}^2 + 1]^{\frac{1}{2}}}{\left|\hat{L}(\bar{\nu})\right|}$$

$$\alpha'(\bar{\nu}) = \frac{1}{d} \frac{\ln[1 - r_{01}^2]}{\left|\hat{L}(\bar{\nu})\right|} \qquad \ldots\ldots \quad 3.49$$

where

$$r_{01}^2 = \left(\frac{n' - 1}{n' + 1}\right)^2$$

and

$$n'(\bar{\nu}) = \frac{\text{ph}\left\{\hat{L}(\bar{\nu})\right\} - \pi}{4\pi\bar{\nu}d} \qquad \ldots\ldots \quad 3.50$$

The error introduced by the approximation leading to equation 3.47 can be assessed by using the previous n, α and d values at 50 cm^{-1} for a silicon window in equations 3.45 and 3.46, from which

$$\left|\hat{L}(50)\right| = 0.623044 \quad , \quad \text{ph}\left\{\hat{L}(50)\right\} = 644.0264$$

substituting these values in equations 3.49 and 3.50 gives n' = 3.39999 and α' = 0.399996. Therefore, the errors due to approximating the optical constants are insignificant when compared to the experimental errors discussed in Section 5.3.2.1.

3.2.2b Determination of the Liquid Optical Constants.

The optical arrangement used for RDFTS is shown schematically in Figure 3.4b. The first RDFTS measurements[26] were made using a cell containing a TPX window, by comparing the (1,0) signatures obtained for the cell containing mercury and then with an equal weight of liquid. This method was improved by using a silicon window[29,43], since silicon has a high refractive index and gives an intense empty cell (1,0) reflection signature. Therefore, the New Liquid Cell can be used for RDFTS by simply removing the cell mirror assembly. In the original method, as the phase difference of the (1,0) signatures for an empty and full cell were small, the (0,0) signature was included in the recorded interferograms. This enabled the sampling combs of the two interferograms to be aligned, thus reducing any systematic errors due to non-alignment. This method was, however, still subject to systematic and random errors, because two interferograms must be recorded over a relatively long time period. The random errors could be reduced by averaging but this would be difficult since the cell would have to be emptied and cleaned for each measurement.

A new method which reduces the data collection time by half and enables repetitive measurements to be made without emptying the cell, has been developed by Birch & Bennouna[44]. In their analysis they realised that the empty cell interferogram collected in the previous method was redundant since the optical constants of the liquid could be determined by comparing the (0,0) and (1,0) reflection signatures, from a full cell interferogram. Therefore, only one interferogram is recorded for each determination, giving a method of analysis with lower levels of random error and less susceptible to certain

systematic error. Although the interferogram contains both signatures they are transformed separately such that their transform ranges do not overlap. As previously in Section 3.2 the complex insertion loss will be the ratio of the two complex spectra.

$$\hat{L}(\bar{\nu}) = \frac{\hat{S}(1,0)}{\hat{S}(0,0)} \qquad \ldots\ldots \quad 3.51$$

Therefore,

$$\hat{L}(\bar{\nu}) = \frac{\hat{r}_{01}}{\hat{r}_{12}\hat{a}_1^2 t_{01} t_{10}} \qquad \ldots\ldots \quad 3.52$$

since $t_{01}t_{10} = (1 - \hat{r}_{01}^2)$

$$\hat{L}(\bar{\nu}) = \frac{\hat{a}_1^2(1 - \hat{r}_{01}^2)\hat{r}_{12}}{\hat{r}_{01}} \qquad \ldots\ldots \quad 3.53$$

From equation 3.1 substituting for $\hat{r}_{12}$

$$\hat{L}(\bar{\nu}) = \frac{\hat{a}_1^2(1 - \hat{r}_{01}^2)(\hat{n}_1 - \hat{n}_2)}{\hat{r}_{01}(\hat{n}_1 - \hat{n}_2)} \qquad \ldots\ldots \quad 3.54$$

rearranging

$$\hat{L}(\bar{\nu})\hat{r}_{01}\hat{n}_1 + \hat{L}(\bar{\nu})\hat{r}_{01}\hat{n}_2 = \hat{a}_1^2(1 - \hat{r}_{01}^2)\hat{n}_1 - \hat{a}_1^2(1 - \hat{r}_{01}^2)\hat{n}_2$$

$$\hat{L}(\bar{\nu})\hat{r}_{01}\hat{n}_1 + \hat{L}(\bar{\nu})\hat{r}_{01}\hat{n}_2 + \hat{a}_1^2(1 - \hat{r}_{01}^2)\hat{n}_2 = \hat{a}_1^2(1 - \hat{r}_{01}^2)\hat{n}_1$$

$$\hat{L}(\bar{\nu})\hat{r}_{01}\hat{n}_1 + \hat{n}_2(\hat{a}_1^2(1 - \hat{r}_{01}^2) + \hat{L}(\bar{\nu})\hat{r}_{01}) = \hat{a}_1^2(1 - \hat{r}_{01}^2)\hat{n}_1$$

$$\hat{n}_2(\hat{a}_1^2(1 - \hat{r}_{01}^2) + \hat{L}(\bar{\nu})\hat{r}_{01}) = \hat{n}_1(\hat{a}_1^2(1 - \hat{r}_{01}^2) + \hat{L}(\bar{\nu})\hat{r}_{01})$$

$$\hat{n}_2(\bar{\nu}) = \frac{\hat{n}_1\hat{a}_1^2(1 - \hat{r}_{01}^2) + \hat{L}(\bar{\nu})\hat{r}_{01}}{\hat{a}_1^2(1 - \hat{r}_{01}^2) + \hat{L}(\bar{\nu})\hat{r}_{01}} \qquad \ldots\ldots \quad 3.55$$

Therefore, if $\hat{n}_1(\bar{\nu})$, the window optical constants are determined by a separate experiment, see previous section, $\hat{n}_2(\bar{\nu})$ for the liquid can be determined by complex arithmetic using equation 3.55.

3.2.3 Full Interferogram Dispersive Fourier Transform Spectrometry (FIDFTS).

For liquids that are too absorbing for TDFTS experiments but not absorbing enough to carry out an RDFTS experiment the technique of FIDFTS can be used. In this situation because small cell window mirror pathlengths must be used, multiple reflections within the cell are resolved in the interferogram Fourier transform range. Fourier transformation of this type of interferogram will yield a complex spectrum which is made up of contributions from the complex spectra of each resolved reflection. These complex spectra can be expressed in terms of Fresnel reflection, transmission and propagation factors.

$$\hat{S}(0,0) = \hat{r}_{01} \quad \ldots\ldots \quad 3.56$$

$$\hat{S}(1,0) = \hat{r}_{12}\hat{a}_1^2\hat{t}_{01}\hat{t}_{10} \quad \ldots\ldots \quad 3.57$$

$$\hat{S}(1,1) = \hat{r}_{23}\hat{a}_1^2\hat{a}_2^2\hat{t}_{01}\hat{t}_{12}\hat{t}_{21}\hat{t}_{10} \quad \ldots\ldots \quad 3.58$$

$$\hat{S}(1,2) = \hat{r}_{23}^2\hat{r}_{21}\hat{a}_1^2\hat{a}_2^4\hat{t}_{01}\hat{t}_{12}\hat{t}_{21}\hat{t}_{10} \quad \ldots\ldots \quad 3.59$$

$$\hat{S}(1,3) = \hat{r}_{23}^3\hat{r}_{21}^2\hat{a}_1^2\hat{a}_2^6\hat{t}_{01}\hat{t}_{12}\hat{t}_{21}\hat{t}_{10} \quad \ldots\ldots \quad 3.60$$

etc to $\hat{S}(1,n)$

If the Fourier transform range were such that the interferogram contained signatures due to reflections (0,0), (1,0), (1,1), (1,2) and

(1,3) the resultant complex spectrum can be expressed as a sum of the individual complex spectra.

$$\hat{S} = \hat{S}(0,0) + \hat{S}(0,1) + \hat{S}(1,1) + \hat{S}(1,2) + \hat{S}(1,3) \quad \ldots\ldots \quad 3.61$$

If the resolution of the interferogram is such that the reflection from the lower surface of the window is not resolved and the signature due to that from the upper surface is removed by subtraction, the resultant complex spectrum will be of the form

$$\hat{S} = \hat{S}(1,1) + \hat{S}(1,2) + \hat{S}(1,3) \quad \ldots\ldots 3.62$$

The addition of complex spectra can be simplified, if we consider the addition of $\hat{S}_{(1,1)}$ and $\hat{S}_{(1,2)}$ using equations 3.58 and 3.59.

$$\hat{S}(1,1) + \hat{S}(1,2) = \hat{r}_{23}\hat{a}_1^2\hat{a}_2^2 t_{01}t_{12}t_{21}t_{10} + \hat{r}_{23}^2\hat{r}_{21}\hat{a}_1^2\hat{a}_2^4 t_{01}t_{12}t_{21}t_{10}$$

$$\hat{S}(1,1) + \hat{S}(1,2) = t_{01}t_{12}t_{21}t_{10}\hat{a}_1^2(\hat{r}_{23}\hat{a}_2^2 + \hat{r}_{23}^2\hat{r}_{21}\hat{a}_2^4) \quad \ldots\ldots \quad 3.63$$

giving a general formula for first order reflections

$$\hat{S}(1,n) = t_{01}t_{12}t_{21}t_{10}\hat{a}_1^2(\hat{r}_{23}^n\hat{r}_{21}^{n-1}\hat{a}_2^{2n}) \quad \ldots\ldots \quad 3.64$$

In order to obtain the optical constants of a liquid by this method we must record two interferograms with different cell window, mirror pathlengths. From equation 3.21 the complex ratio of these interferograms will give the experimental complex insertion loss

$$\hat{L}^E(\tilde{\nu}) = \frac{\mathcal{C}^s(\tilde{\nu})}{\mathcal{C}^b(\tilde{\nu})}\exp i[(\phi^s(\tilde{\nu}) - \phi^b(\tilde{\nu})) + 4\pi\tilde{\nu}FS] \quad \ldots\ldots \quad 3.65$$

But the ratio of the complex spectra $\hat{S}^s$ and $\hat{S}^b$ is equivalent to the theoretical complex insertion loss

$$\hat{L}^T(\tilde{\nu}) = \frac{\hat{S}^s(1,1) + ... + \hat{S}^s(1,n)}{\hat{S}^b(1,1) + ... + \hat{S}^b(1,n)} \quad ..... \quad 3.66$$

Since the cell window, mirror pathlength is shorter when the background interferogram is recorded, in most cases the background complex spectrum will contain more signatures than the sample complex spectrum. For the case of (1,1) and (1,2) present in the sample and (1,1), (1,2) and (1,3) present in the background interferogram the theoretical complex insertion loss will be

$$\hat{L}^T(\tilde{\nu}) = \frac{[t_{01}t_{12}t_{21}t_{10}\hat{a}_1^2(\hat{r}_{23}\hat{a}_2^2 + \hat{r}_{23}^2\hat{r}_{21}\hat{a}_2^4)]\ (\tilde{\nu})\ \text{Sample}}{[t_{01}t_{12}t_{21}t_{10}\hat{a}_1^2(\hat{r}_{23}\hat{a}_2^2 + \hat{r}_{23}^2\hat{r}_{21}\hat{a}_2^4 + \hat{r}_{23}^3\hat{r}_{21}^2\hat{a}_2^6)]\ (\tilde{\nu})\ \text{Background}} \quad 3.67$$

Since only the $\hat{a}_2$ term will be different for the sample and background equation 3.67 will simplify to

$$\hat{L}^T(\tilde{\nu}) = \frac{[\hat{r}_{23}\hat{a}_2^2 + \hat{r}_{23}^2\hat{r}_{21}\hat{a}_2^4]^s(\tilde{\nu})}{[\hat{r}_{23}\hat{a}_2^2 + \hat{r}_{23}^2\hat{r}_{21}\hat{a}_2^4 + \hat{r}_{23}^3\hat{r}_{21}^2\hat{a}_2^6]^b(\tilde{\nu})} \quad ..... \quad 3.68$$

Equations of the form of 3.68 cannot be explicitly solved for $\hat{n}$ in terms of $\hat{L}^T$. So an iterative method such as the complex secant method[45] can be used to calculate $\hat{n}$ with the desired accuracy. Use of the secant method has been outlined by Birch & Parker[15] and is as follows. The secant method gives an expression for the function f(x)

$$x_{n+1} = x_n - f(x_n)\frac{x_n - x_{n-1}}{f(x_n) - f(x_{n-1})} \quad ..... \quad 3.69$$

Equation 3.69 gives the root of f(x), when $F(x_n)$ equals zero. This can be applied to the complex refractive index to give

$$\hat{n} = \hat{n}'' + (\hat{L}_T'' - \hat{L}_E)\,\frac{(\hat{n}' - \hat{n}'')}{(L_T'' - L_T')} \qquad \ldots\ldots \quad 3.70$$

The method of iteration using equation 3.70 is as follows. $\hat{L}_E$ is calculated at a chosen starting frequency ($\bar{\nu}$) from equation 3.65, $\hat{L}'_T$ is calculated at the same frequency using an equation of the form of 3.68. $\hat{n}'(\bar{\nu})$ for the window must be previously determined as in Section 3.2.2a and $\hat{n}'(\bar{\nu})$ for the liquid must be estimated or obtained from a low resolution Fourier transform. $\hat{n}''(\bar{\nu})$ is obtained by adding a small increment to $\hat{n}'(\bar{\nu})$

$$\hat{n}''(\bar{\nu}) = \hat{n}'(\bar{\nu}) + \delta\hat{n} \qquad \ldots\ldots \quad 3.71$$

and $\hat{n}''$ is used to calculate $\hat{L}_T''$. The refined value $\hat{n}(\bar{\nu})$ is obtained from 3.70 and used to calculate $\hat{L}_T$, which can now be compared with the experimental result.

$$\hat{L}^T(\bar{\nu}) - \hat{L}^E(\bar{\nu}) = \delta\hat{L} \qquad \ldots\ldots \quad 3.72$$

The above procedure is repeated using $\hat{n}(\bar{\nu})$ for $\hat{n}'(\bar{\nu})$ until $\delta\hat{L}$ is within the desired accuracy for the experiment. To continue the analysis to obtain $\hat{n}$ over a desired frequency range, the final refined value obtained for $\hat{n}(\bar{\nu})$ is used as the starting value of $\hat{n}'$ at the next frequency interval.

C H A P T E R 4

EXPERIMENTAL

4.1 Fourier Transform Spectrometry.

4.1.1 General Introduction.

The Beckman FS-720 interferometer used at Durham and the NPL cube interferometers[46], have the same basic optical arrangement as in Figure 2.1 . Both systems use similer types of source, beam dividers and detectors. In the far-infrared the most common source of radiation used is a medium-pressure mercury vapour discharge lamp, which produces brems..trahlung emission[47]. The beam dividers are stretched films of polyethylene terephthalate (melinex), which give a repeating hooped instrument transmission function, the first minimum of which is given by[48,49]

$$\tilde{\nu}_{min} = \frac{1}{2nd\ \cos\theta'} \qquad \ldots\ldots\ 4.1$$

where n is the melinex refractive index ($\simeq$1.6), d the film thickness and θ' the angle of refraction. Wire grid beam dividers[50] are also used in the far-infrared and give an improved instrument transmission profile. The optical arrangement of the interferometer must be altered to implement them, the two most common arrangements are the NPL polarising interferometer[51] and the Martin & Puplett polarising mode[52].

The type of detector used depends on the wavenumber range and sensitivity required in an experiment, the golay cell[53] is generally

used and will cover the range 15 to >4000 cm^{-1}. For greater sensitivity and when measurements below 15 wavenumbers are required cooled detectors are used. The indium antimonide (In SG) detectors of Putley[54] and Rollin[55] cover the ranges 4 to100 and 2 to 40 cm^{-1} and operate at 1.5 and 4K respectively. The germanium bolometer[56,57] operates at 1.8K and will cover the range 2 to 250 cm^{-1}.

In far-infrared interferometry the path difference of the moving mirror is changed slowly and monotonically from -X to +X (see Figure 1.2). This gives an interference record that is generated aperiodically, therefore, for a.c. detection, superimposed modulation of the radiation is required. This can be achieved by amplitude modulation (AM), where the whole of the detected signal is chopped periodically at a set frequency. The disadvantages of this procedure are that about half the radiation is reflected back to the source by the chopper blades, and an unwanted x independent contribution (V_o) is added to the interference function. An alternative is to use phase modulation (PM). The use of PM and its associated advantages in the far-infrared, was first recognised by Chamberlain[58,59,60]. PM is achieved by moving one of the interferometer mirrors sinusoidally with a constant amplitude that is slightly less than the mean wavelength of the radiation detected. In NPL cube interferometers, the PM unit consists of a light mirror mounted on the spider of an

electrically driven heavy duty loudspeaker coil, this is fixed to a 45^{o} cube so that it can be added to either arm of an interferometer as in Figure 2.7 The movement of the mirror imparts a small periodic path difference variation within the interferometer to give a detectable signal. The magnitude of the path difference variation is controlled by the current supplied to the loudspeaker coil. This allows the PM characteristic to be varied to match the beam divider transmission characteristic[58]. In the PM interferograms the ZPD is a zero crossing, in Figure 4.1 both interferograms result from the same conditions but in 4.1b an AM chopper has been added to the system to show the loss in signal intensity due to reflection. To demonstrate the matching of the PM characteristic to the interferometer characteristic the modulus spectra for five interferograms recorded with different PM currents are shown in Figure 4.2. The difference in the transmission profile is because PM effectively convolves the interferometer transmission profile with a Bessel function, which varies with current. This tuneability effect of PM can be used to tailor the instrument transmission profile, within the limits of the beam divider to suit experimental requirements.

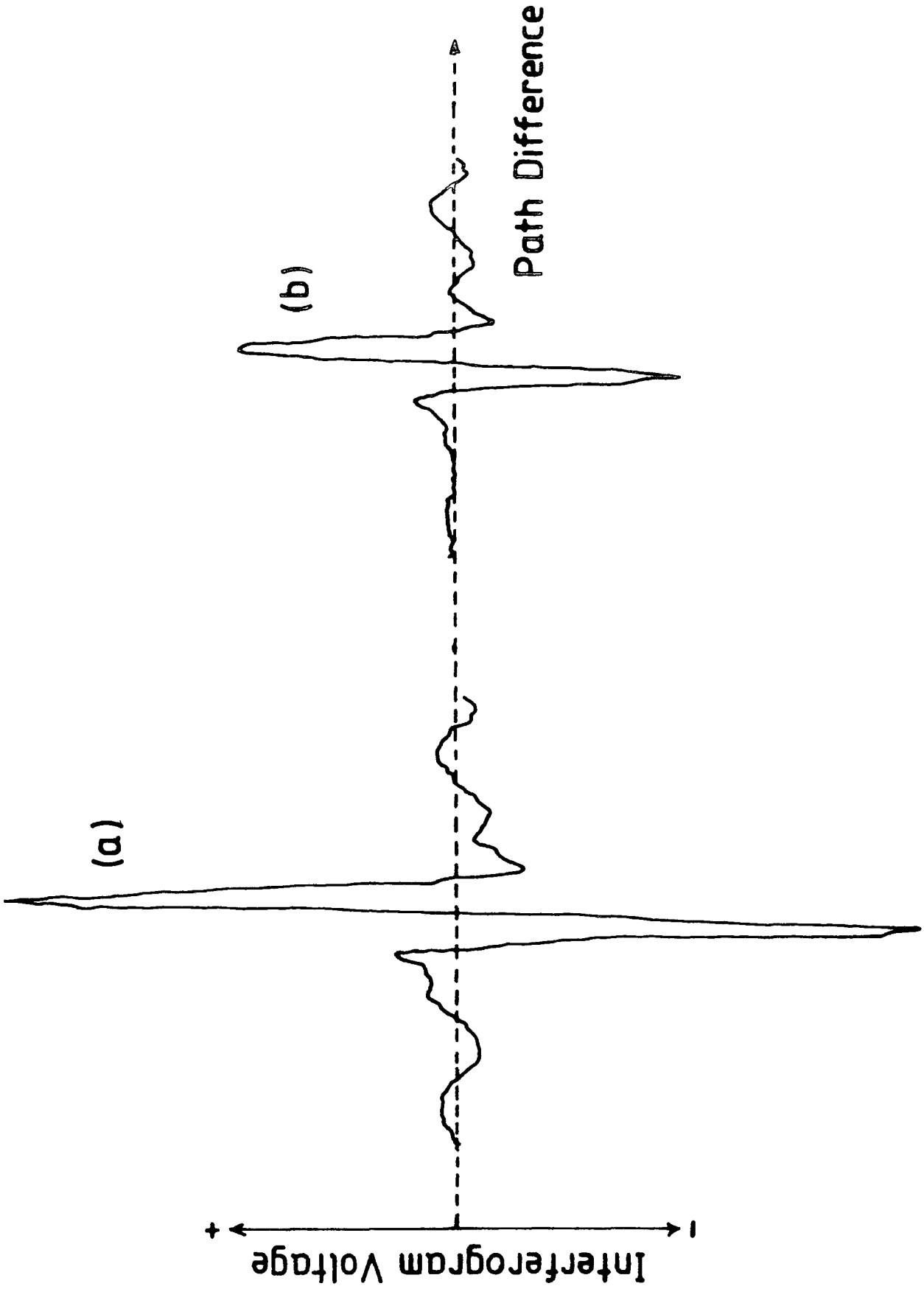

Figure 4.1 Effect of AM chopper on interferogram

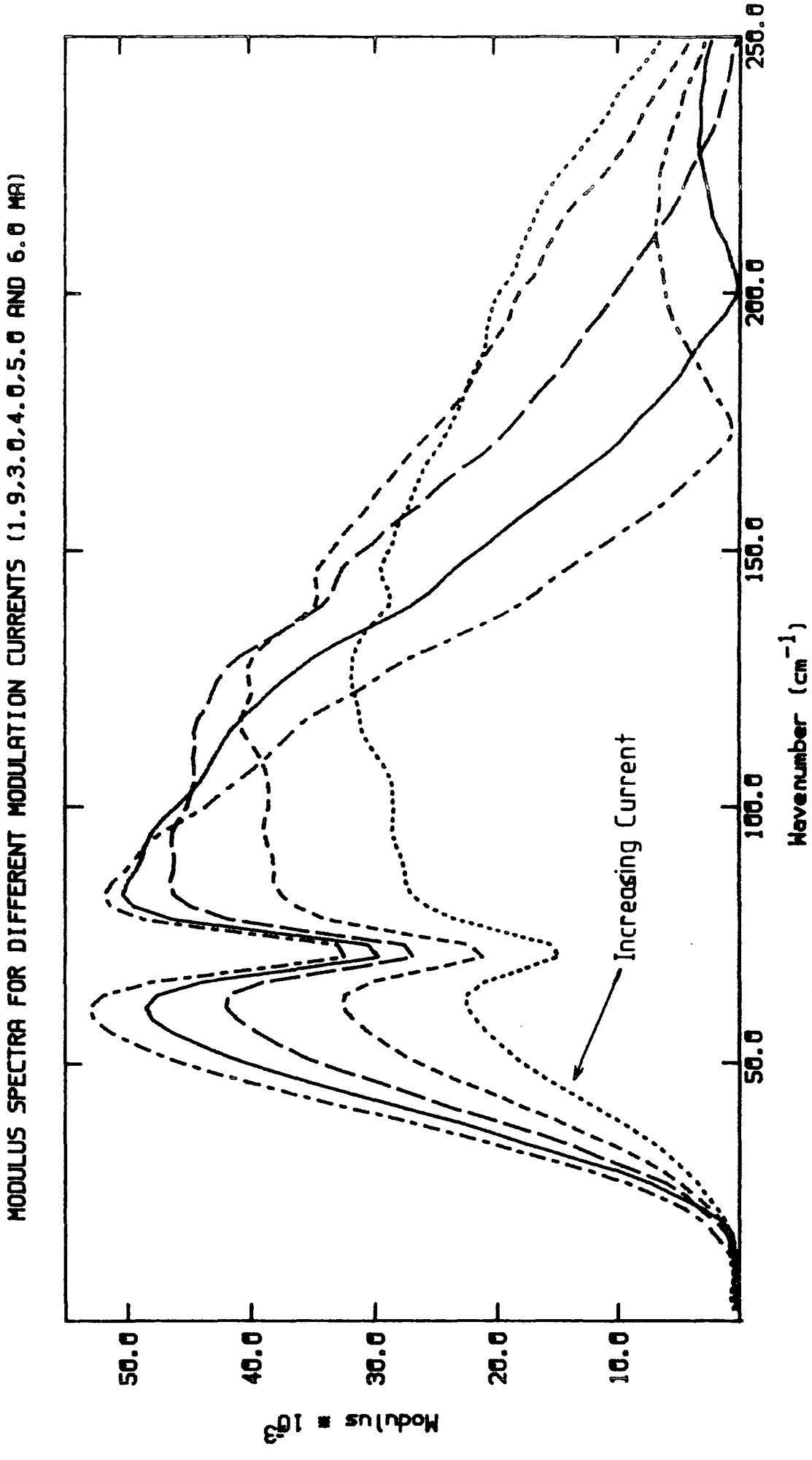

Figure 4.2 Effect of PM current on interferogram energy profile

4.1.2 Experimentally Variable Parameters and Considerations.

The following parameters can be varied to suit the requirements of each FTS experiment.

4.1.2a Resolution.

In interferometry the frequency resolution depends on the range in x over which equation 3.16 is evaluated, if the maximum value of x is X then resolution is given by[21]

$$R = \frac{1}{WX} \qquad \ldots\ldots \quad 4.2$$

where W is determined by the apodisation function used. W = 2 for no weighting. Since equation 3.16 is truncated at $\mp X$, spurious effects can arise in the transformed spectrum. These effects can be reduced or removed by convolving the interferograms with a slowly falling weighting function, this is known as apodisation. The apodisation function used in the Durham fast Fourier transform (FFT) program is:

$$A = \left[\sum_{t=0}^{t=N-1} \cos\left(\frac{\pi}{2} \times \frac{t - M}{M}\right)\right]^2 \qquad \ldots\ldots \quad 4.3$$

$$M = \frac{N}{2} - \frac{1}{2} \qquad \ldots\ldots \quad 4.4$$

where N is the number of transformed points, equation 4.3 is shown in

Figure 4.3 and the effect of apodisation is demonstrated in Figure 4.4. Generally the more effective an apodisation function, the broader the central lobe of the spectral window becomes and the lower the resolution. For equation 4.3 W is approximately 1.

4.1.2b Sampling Interval.

In order to transform an interferogram by digital computation, it must be sampled at discreet intervals of exactly equal size. The interval size is very important; if too large information about the sampled interferogram will be lost, if too small the interferogram will be oversampled and time will be wasted. These effects due to sampling interval can be seen in Figures 4.5 and 4.6. To determine the interval size required to correctly sample an interferogram, the sampling theorem can be used[61]. If the Fourier transform of the interferogram I(x) is G($\tilde{\nu}$) (see Section 2.1) and $\tilde{\nu}_c$ is the wavenumber cutoff value of $\tilde{\nu}$. A function whose Fourier transform is zero for $/\tilde{\nu}/>\tilde{\nu}_c$ is fully specified by sampled values placed at equal intervals not exceeding $(2\ \tilde{\nu}_c)^{-1}$.

A further consideration is the phenomenon of aliasing. Since equations of the form of equation 2.3 are evaluated as truncated summations they can be represented as

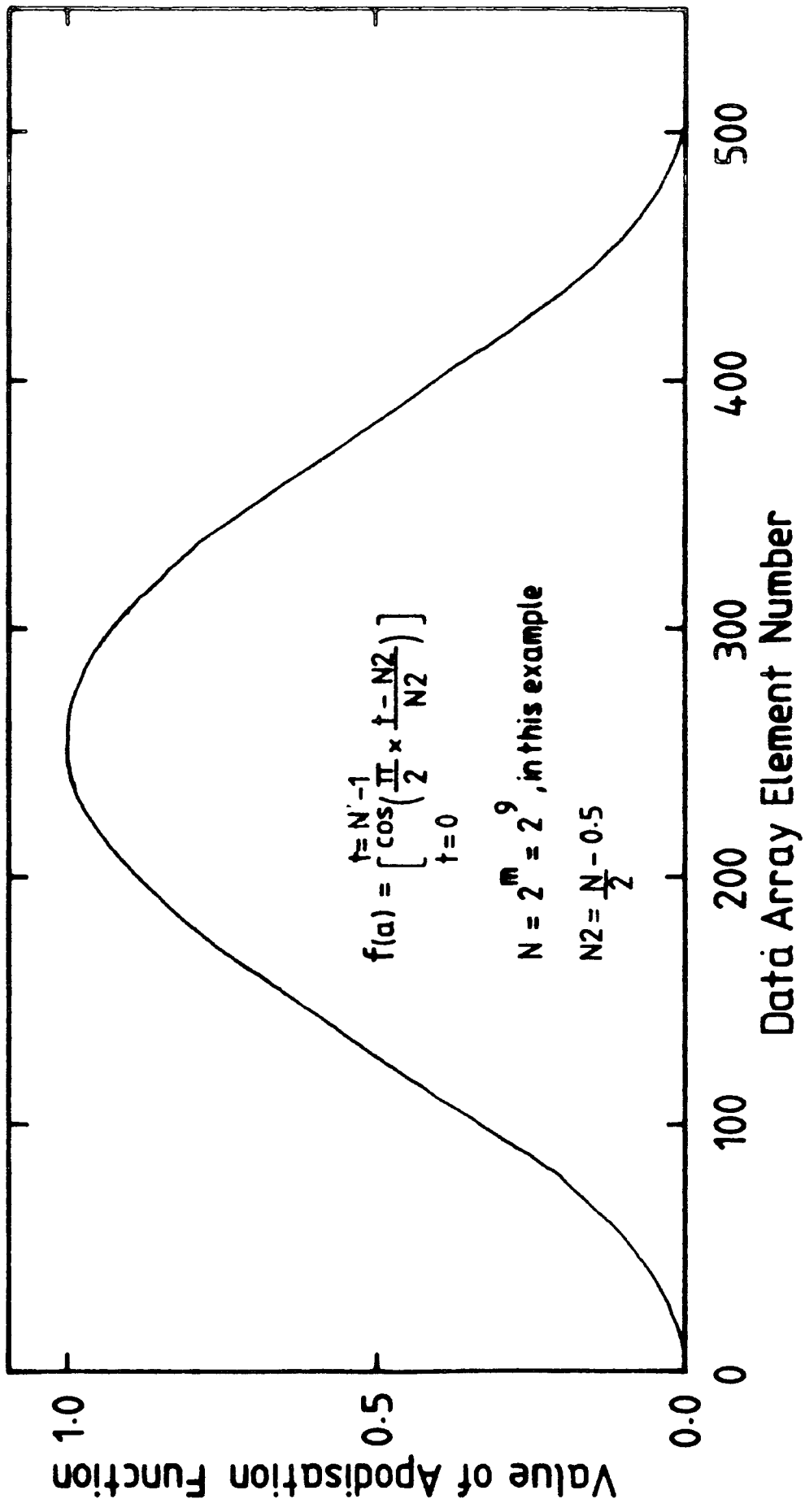

Figure 4.3 Durham apodisation function

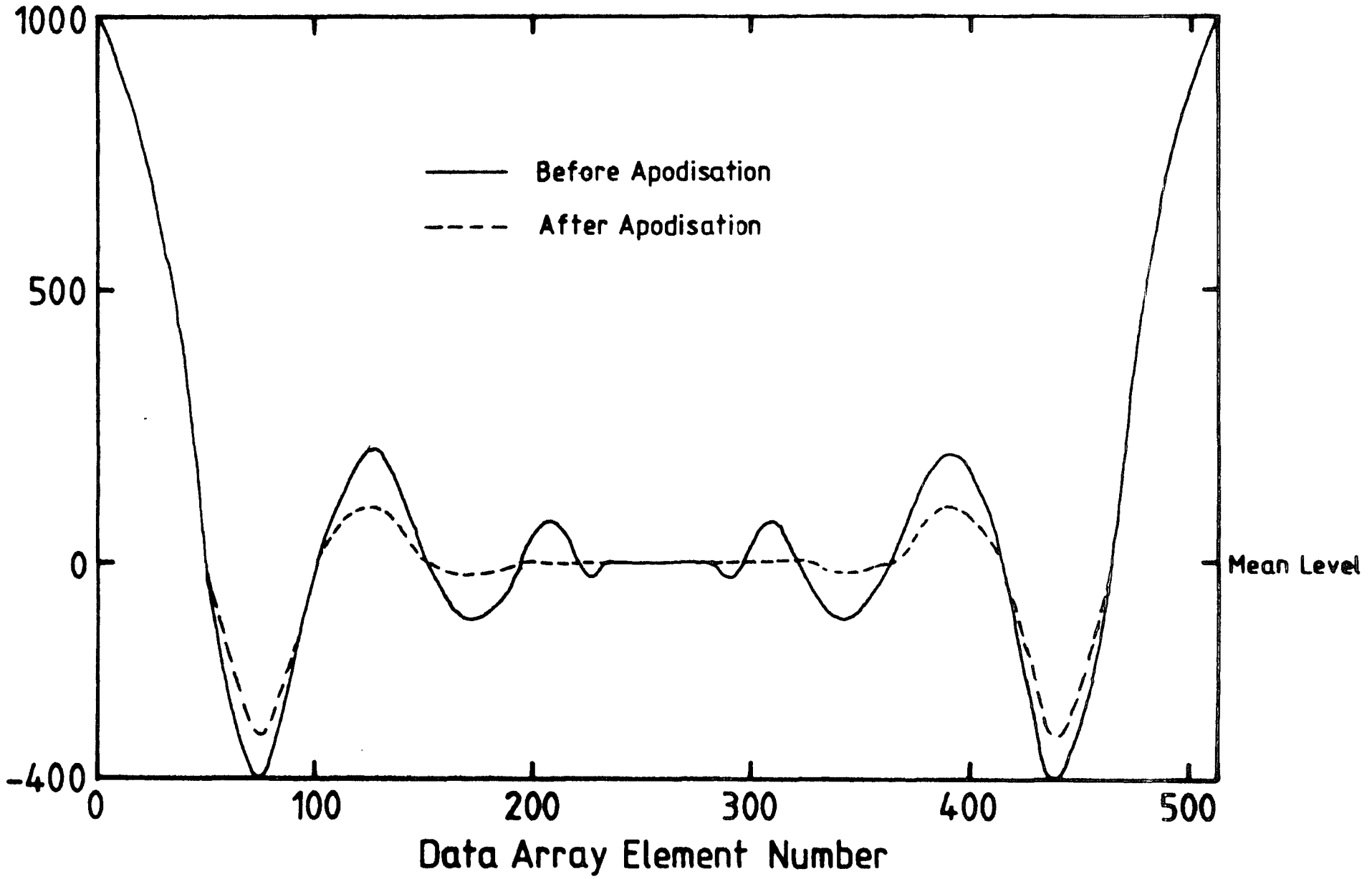

Figure 4.4 Effect of apodisation

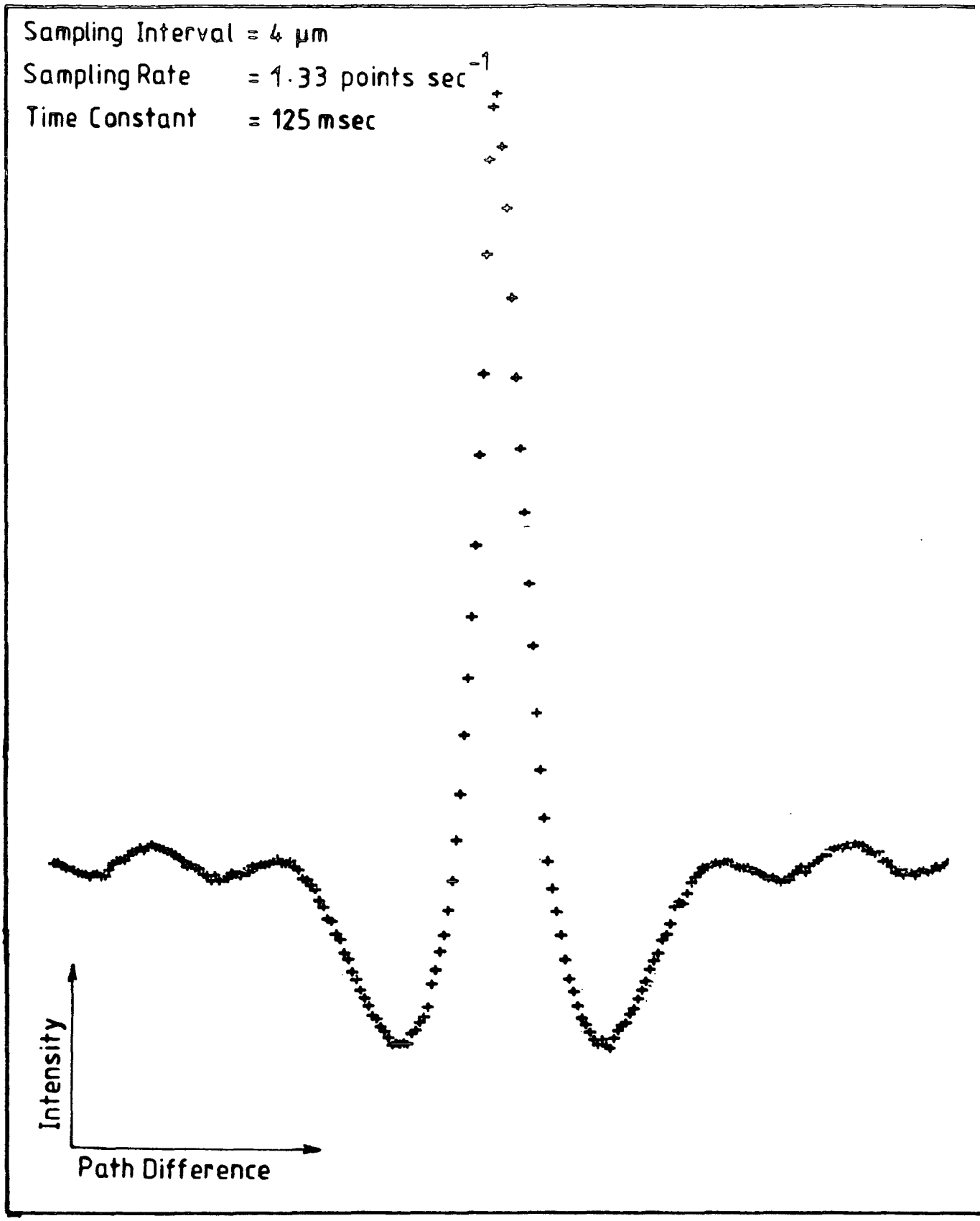

Figure 4.5 Oversampled Interferogram

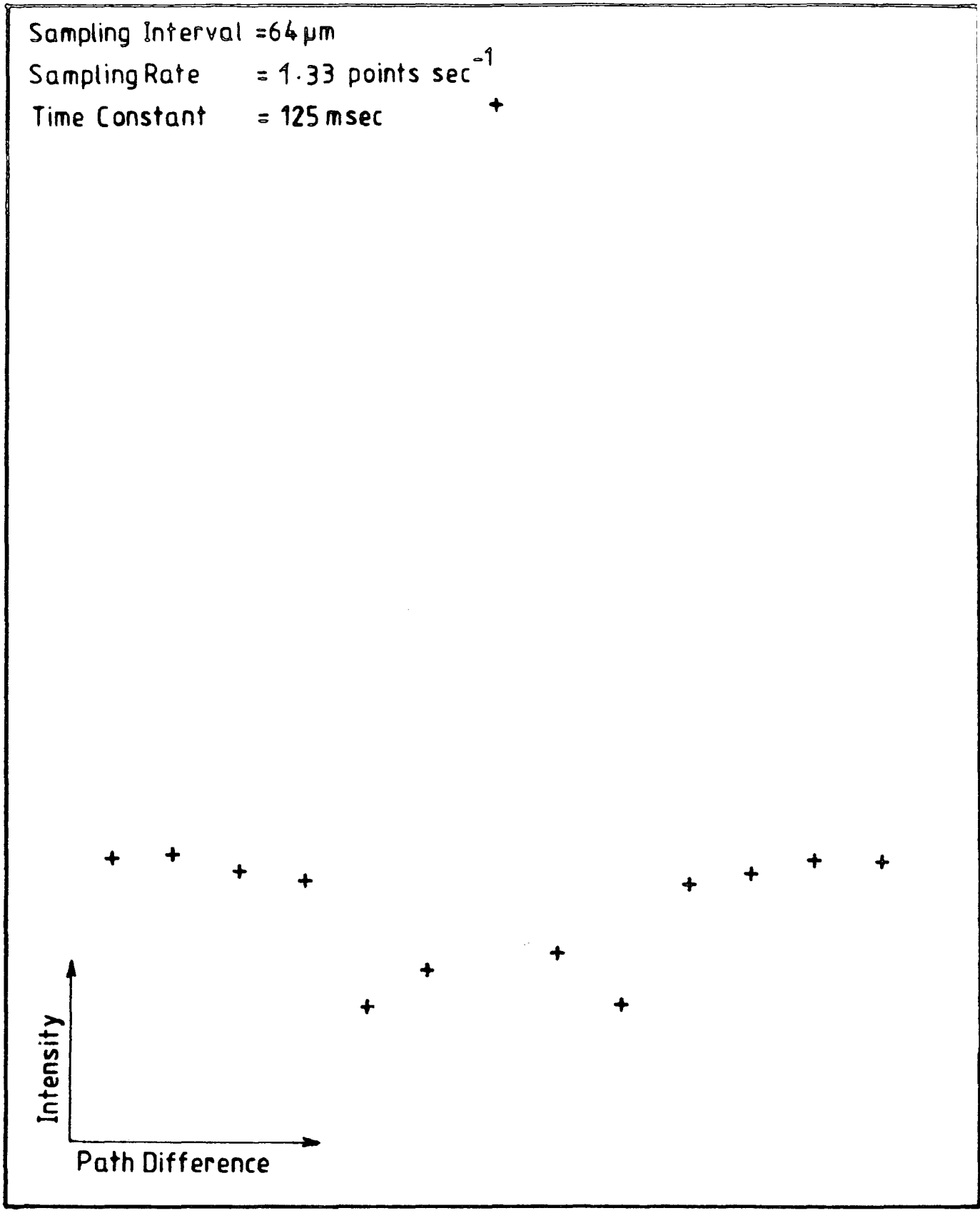

Figure 4.6 Undersampled Interferogram

$$p(\bar{\nu}) = \Delta x \sum_{-D}^{+D} I(\Delta x) \cos 2\pi \bar{\nu} D \Delta x$$

where Δx is the sampling interval. The computed spectrum $p(\bar{\nu})$ will consist of a series of identical spectral profiles (aliases) repeated at $(\Delta x)^{-1}$ (aliasing frequency) in the wavenumber domain. As the aliase that coincides with the required wavenumber region is the only one of interest, the sampling interval must be such that the aliasing frequency is greater than the limit of the wavenumber region of interest. Also higher aliases must be excluded from this wavenumber region by filtering to avoid distortion of the spectral profile by overlapping aliases.

4.1.2c Beam Divider Thickness.

From equation 4.1 the thickness of a beam divider determines the wavenumber range of the interferometer transmission profile. For example to cover a 0 to 250 wavenumber range a 50g (12.5 μm) beam divider will be required.

4.1.2d Filtering.

From Section 4.1.2b all aliases that occur above the first must be removed by filtering. If the wavenumber range required for an experiment is less than the aliasing frequency, it is also desireable

to restrict the bandpass further to remove unwanted frequencies. This is necessary as a multiplex interferometer observes the whole wavenumber range for the time of the experiment, therefore, noise from an unwanted range will be included in the required wavenumber range.

4.1.2e Amplifier Sensitivity and Time Constant.

These parameters should be adjusted to give the maximum signal to noise ratio in the interferogram. It is also desireable to set the sensitivity so that the whole range of the A to D converter is filled by the interferogram maximum and minimum to reduce digitising errors.

4.1.2f Data Collection Rate.

The rate at which an interferogram is sampled should be matched to the amplifier time constant, if too fast the system electronics will not respond in time and information on the sampled interferogram will be lost. The effects of sampling rate can be seen in Figure 4.7 and 4.8, for all data collected at NPL and Durham a collection rate of 3 times the amplifier time constant was used.

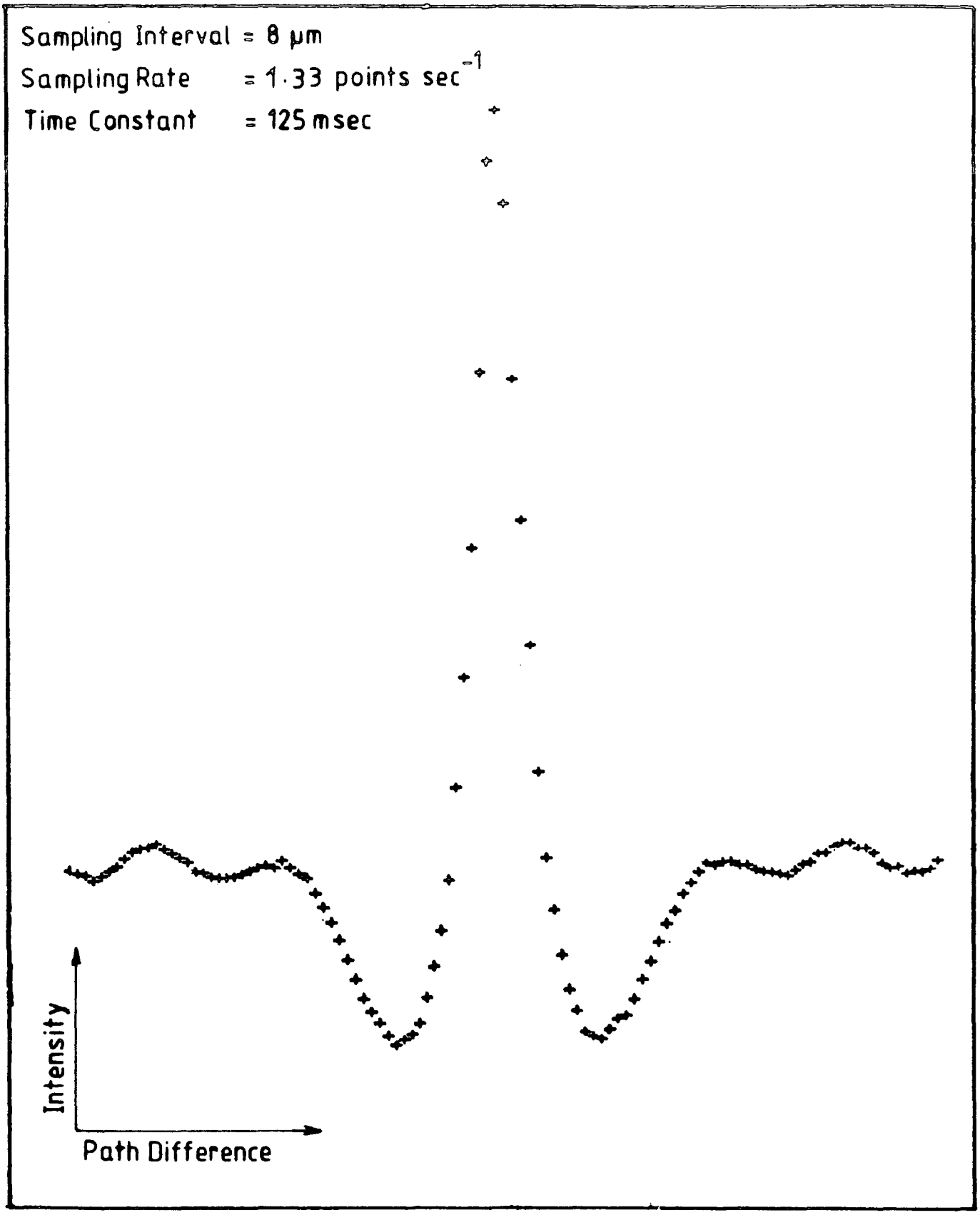

Figure 4.7 Correct sampling rate

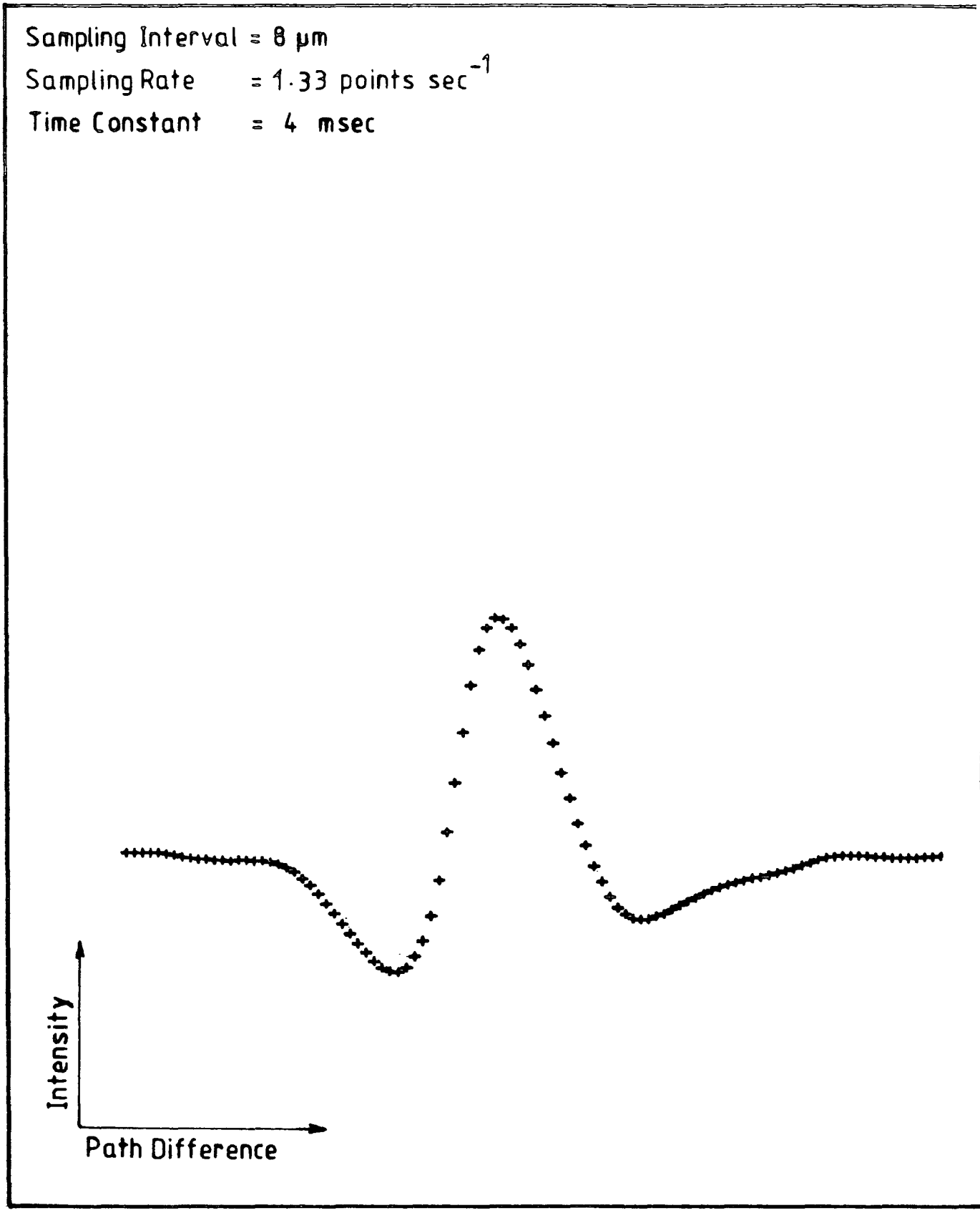

Figure 4.8 Incorrect sampling rate

4.1.2g Sample Preparation.

Solutions were made up prior to carrying out experiments, from spectroscopic grade reagents, that had been dried and stored over molecular sieves. The reagents were supplied by BDH and Aldrich Chemicals.

4.1.3 The New Liquid Cell at The NPL.

4.1.3a Cell and Interferometer Alignment.

With the New Liquid Cell mounted on an NPL cube interferometer as in Figures 2.13 and 2.14, the following procedure was followed to align the cell mirror and interferometer optics.

First, the interferometer optics were aligned by positioning the moving mirror on the peak of the positive or negative lobe resulting from the (0,0) signature. The intensities of both lobes were then maximised in turn using the three adjusting screws of the 45^{o} phase modulation mirror. At the same time the phase of the amplifier was matched to the phase of the modulated mirror by adjusting the amplifier phase to also maximise the two lobes.

The cell mirror was then carefully lowered until it just touched the window and then raised approximately 0.5mm. The moving mirror was then slowly scanned through the position where the (1,1) signature should occur. If the cell mirror was misaligned the (1,1) signature

was not always resolved, in these cases increased amplifier sensitivity and patience were required. Having identified the (1,1) signature, the cell mirror was aligned by maximising the intensity of the (1,1) lobes using the three cell mirror adjusting screws. Alignment was optimum when the intensity of the (1,1) signature for an empty cell was greater than the (1,0) signature but slightly less than the (0,0) signature.

4.1.3b Cell and Interferometer Temperature Control.

Temperature control of liquids within the New Liquid Cell was achieved by a copper coil mounted on a copper strip bolted to the outside of the cell, through which various liquids could be circulated. It was found that a thermocouple fixed to the side of the coil with a piece of plasticine recorded the same temperature as one emersed in the liquid. The interferometer was temperature controlled by using similar copper coils mounted on copper blocks. Initially the interferometer and the New Liquid Cell were maintained at the same temperature, but during temperature studies on carbon tetrachloride it was found that for large differences positive or negative between room temperature and instrument temperature the interferometer phase was not stable due to interferometer dimensional changes. The optimum operating conditions were found to be with the interferometer very

close to room temperature and the liquid cell at the required temperature.

4.1.3c Phase Modulation Current.

From 4.11 the PM current can be used to tailor the interferometer transmission profile to fit the requirements of an experiment, within the beam divider limitations. The variation of the instrument modulus profile with PM current for a 50 gauge beam divider is shown in Figure 4.3. The current at which the PM and instrument characterics are matched corresponds to a maximum in the two major lobes of the phase modulated interferogram. Measurements were normally made with the PM and instrument characteristics matched, but for low frequency measurements, higher PM currents than those for matching were used to push the energy profile to lower frequencies as in figure 4.9.

4.1.3d New Liquid Cell in TDFTS Measurements.

With the interferometer and cell aligned as previously described and a liquid sample in the cell, the following procedure was used to measure the optical constants. The cell mirror was positioned as near to the window back surface as possible, so that the transform range of the (1,1) signature did not contain any resolvable structure due to the (1,0) signature. A background interferogram was then recorded

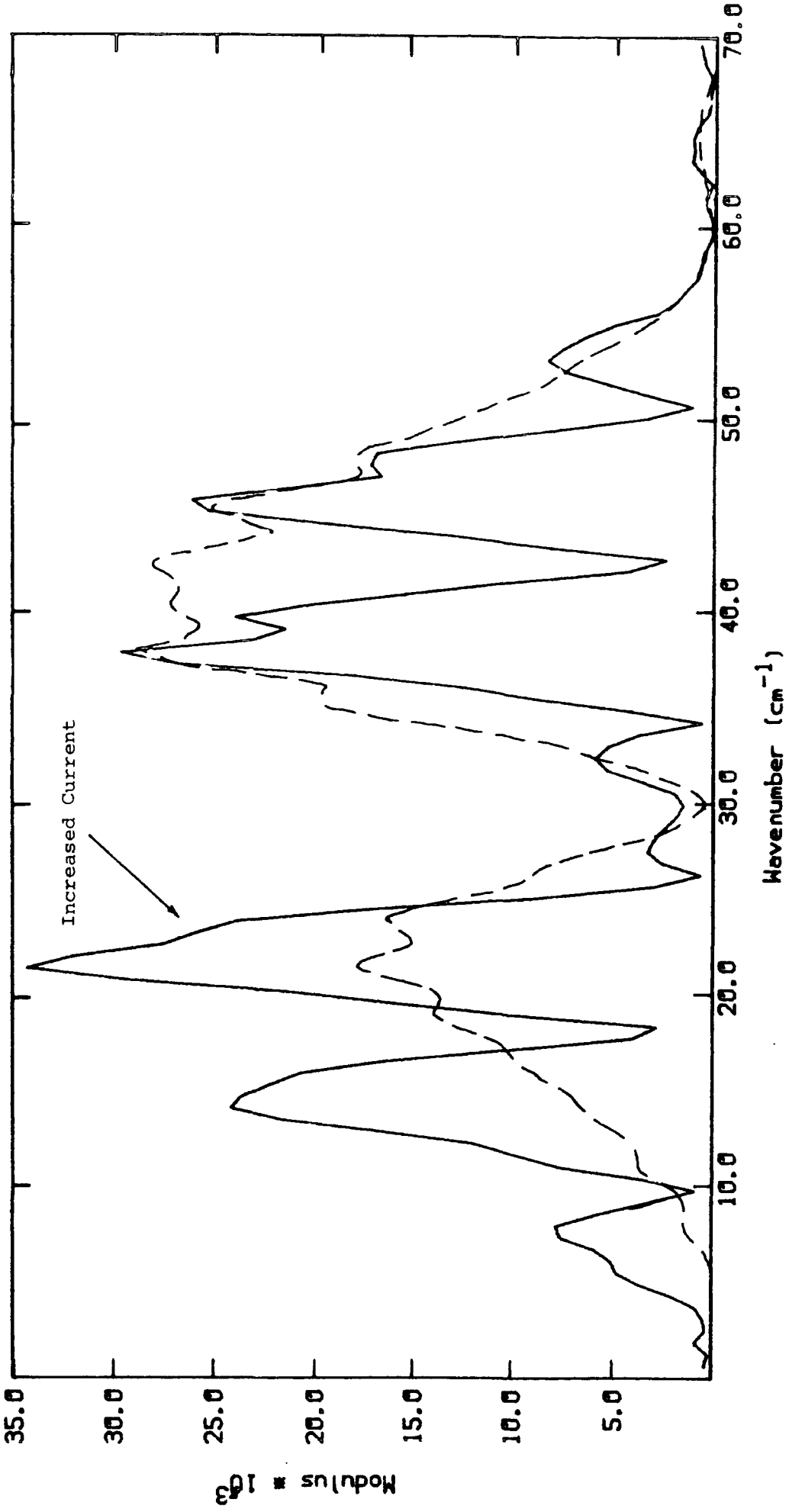

Figure 4.9 Tuning the interferometer energy profile by changing the PM current.

with the cell mirror in this position. The cell mirror was then moved away from the window to a position where the intensity of the (1,1) signature was approximately half that for the background. After ensuring that there was no structure due to the (2,0) or higher window signatures within the transform range for this position, the sample (1,1) interferogram was recorded. The above procedure was repeated three times and in all cases the cell mirror was positioned moving from high to low pathlength to avoid micrometer backlash effects. Each pair of interferograms were then analysed as in Section 3.2.1 to give $n(\bar{\nu})$ and $\alpha(\bar{\nu})$ for the liquid. Spectra for carbon tetrachloride at 25°C obtained using this method are shown in Figures 4.10 and 4.11 the reproducibility for the three determinations is ∓ 0.0001 in refractive index and ∓ 0.02 in absorption coefficient.

For more absorbing liquids, in order to maintain a good signal to noise ratio, the cell mirror had to be positioned closer to the cell window and the (1,0) signature was resolved in the (1,1) signature transform range. In these cases the subtraction technique shown in figure 4.12 was employed. With the cell mirror moved out of range, a background interferogram was recorded over the transform range required for the (1,1) signature. The cell mirror was then placed in the desired position and a second interferogram recorded with the same start position as the first. The first interferogram was then

FIGURE 4.10 CARBON TETRACHLORIDE AT 25.0 DEG C (150/155)

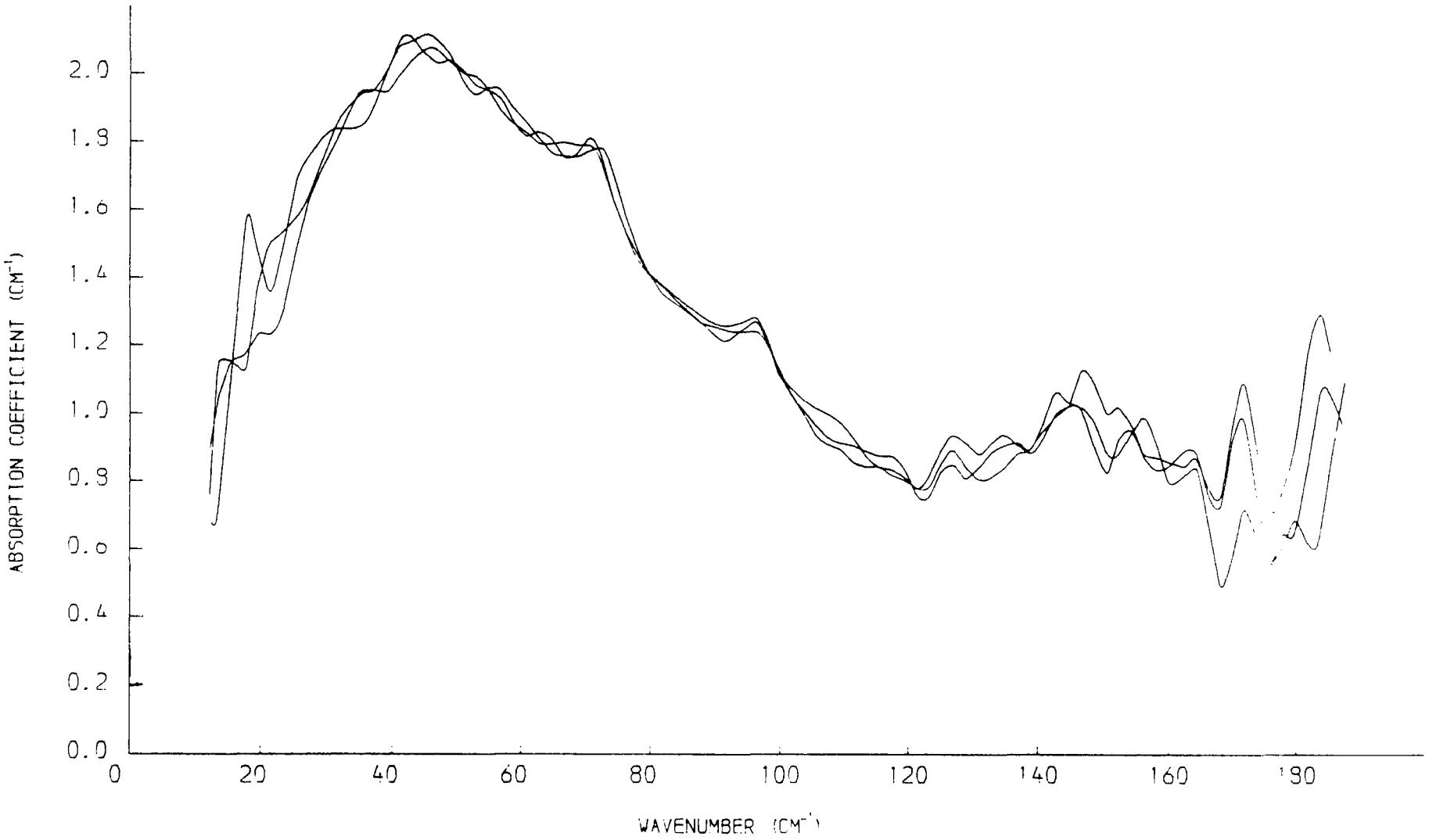

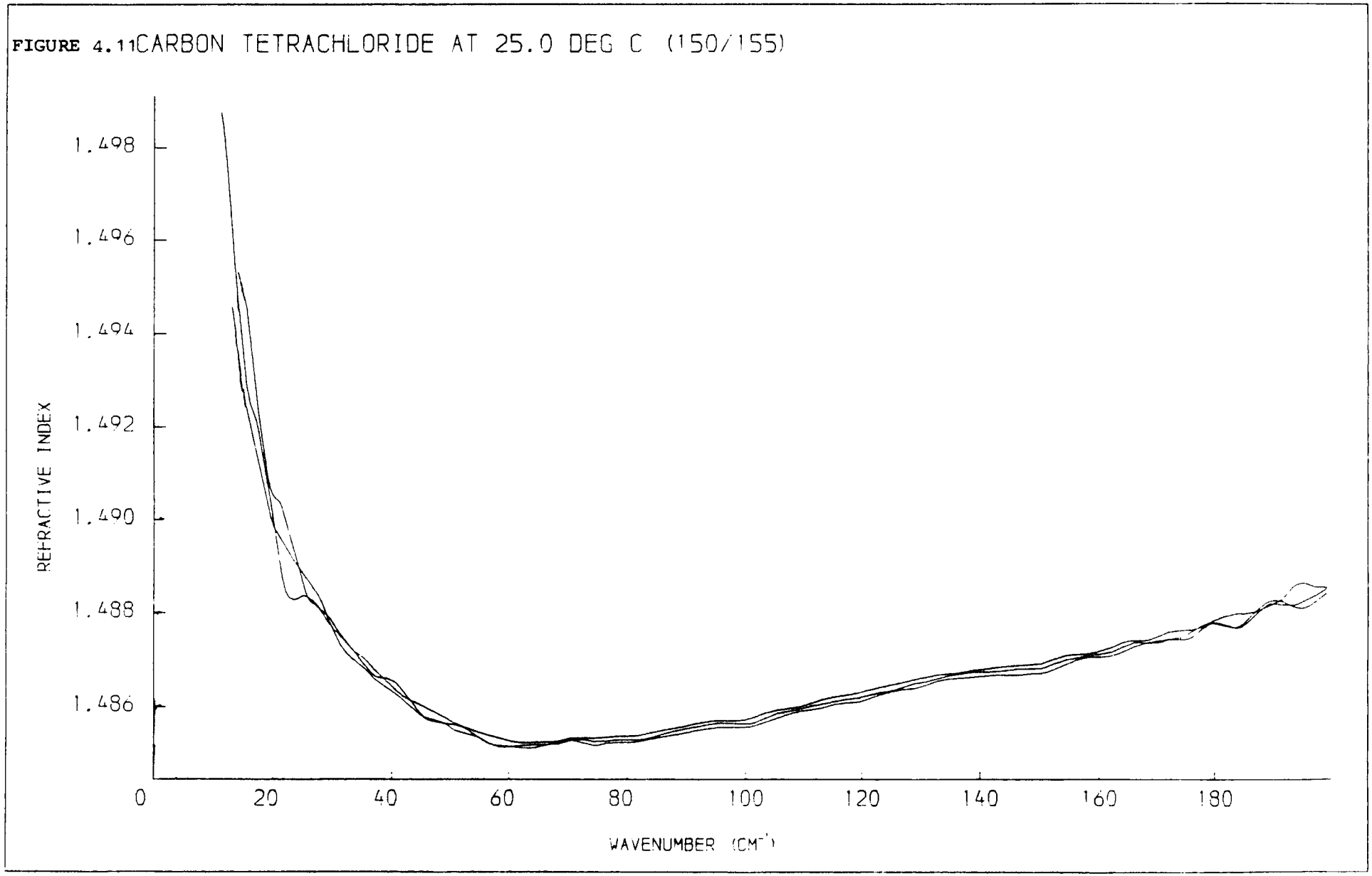
FIGURE 4.11CARBON TETRACHLORIDE AT 25.0 DEG C (150/155)
1.498
1.496
1.494
1.492
1.490
1.488
1.486
REFRACTIVE INDEX
0
20
40
60
80
100
120
140
160
180
WAVENUMBER (CM⁻¹)

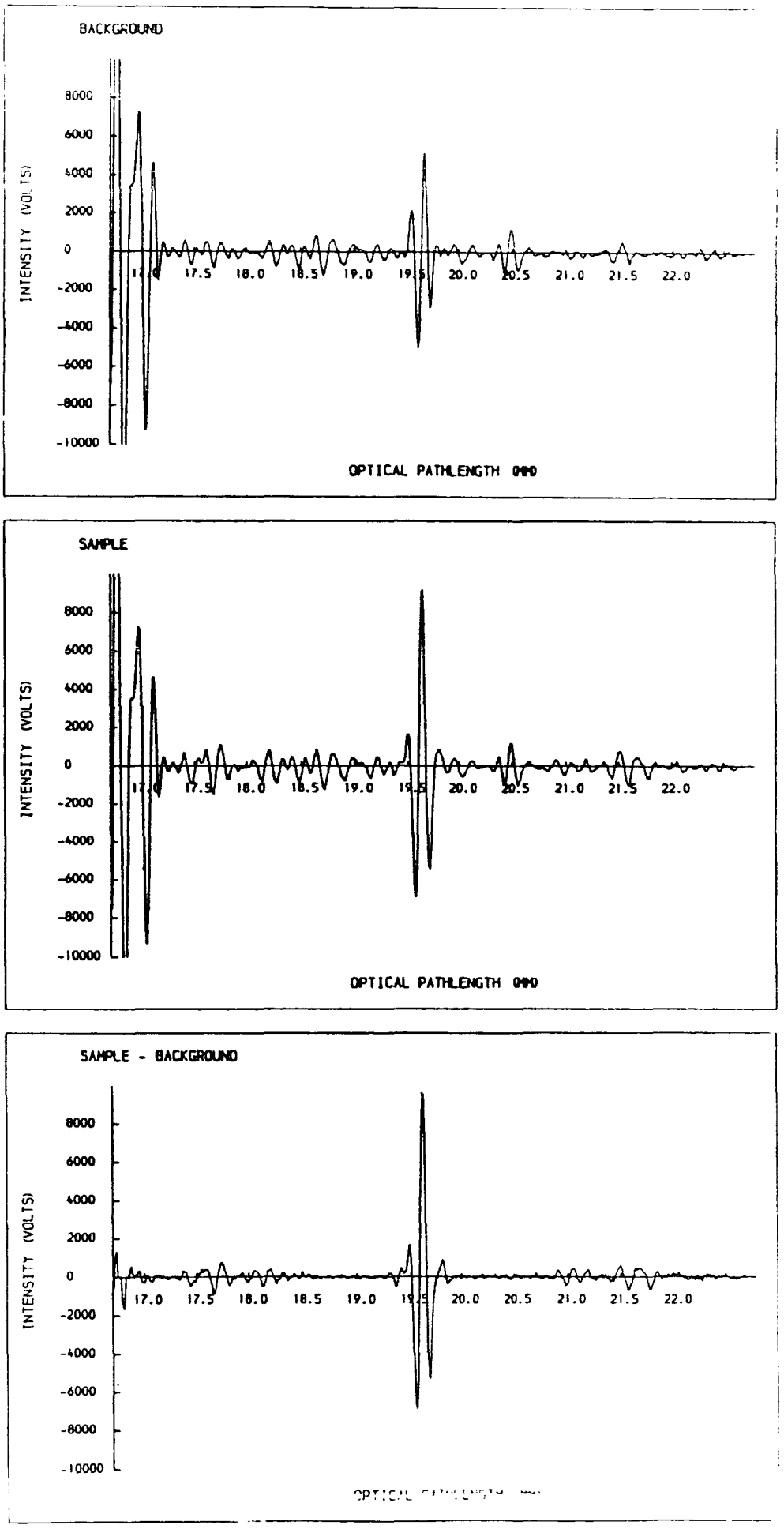

Figure 4.12 Subraction of overlapping interference patterns

subtracted from the second , giving an interferogram only containing contributions from the (1,1) signature. The subtracted background and sample interferograms obtained in this way were then analysed as previously.

4.1.3e Cleaning the New Liquid Cell

In order to reduce the possibility of contamination of liquid specimens the New liquid Cell was cleaned after each measurement. This was achieved by first removing the New Liquid Cell from the interferometer, the window, retaining screw and PTFE pads were then removed. The New Liquid Cell and window parts were then cleaned in a solvent that would not damage the 'O' ring (such as n-heptane) and then reassembled. This method of cleaning was preferred to simply washing the cell in situ, as the top PTFE pad did not give a perfect seal. Giving rise to the possibility of contaminants remaining under the top ring.

4.1.4 New Liquid Cell at Durham.

4.1.4a Implementation of The New Liquid Cell.

As the liquid cell was designed to be used with an NPL cube interferometer, a separate module that could be bolted onto the beam splitter box in place of the fixed mirror had to be built. An

adjustable mirror was mounted within the module, so that radiation from the beam splitter was reflected upwards through 90°, enabling the liquid cell to be attached to the top of the module, with the window horizontal. The presence of this mirror facilitated the incorporation of PM within the interferometer, with the associated advantages over AM[58,59,60]. The new instrumental layout is shown in Figure 4.13.

The optical pathlength of the fixed mirror arm was increased by fitting the liquid cell, therefore a spacer approximately equal to the increased pathlength was included in the moving mirror arm. The spacer length was such that the start position of the moving mirror was close to that required for the start of the FFT range of the (0,0) signature, this gave the maximum resolution required for all experiments.

A minor disadvantage of fitting the liquid cell, was that the polarizing system of Martin & Puplett[52] designed for the FS720 interferometer could not be used, as this required the use of 90° roof mirrors. A polarizing system could be implemented in the new system by fitting a second beam divider box to the instrument, between the focusing optics box and the present beam divider box. Moving the source box to the second beam divider box and using two free standing polarizing wire-grid beam dividers as in the NPL polarizing interferometer[51].

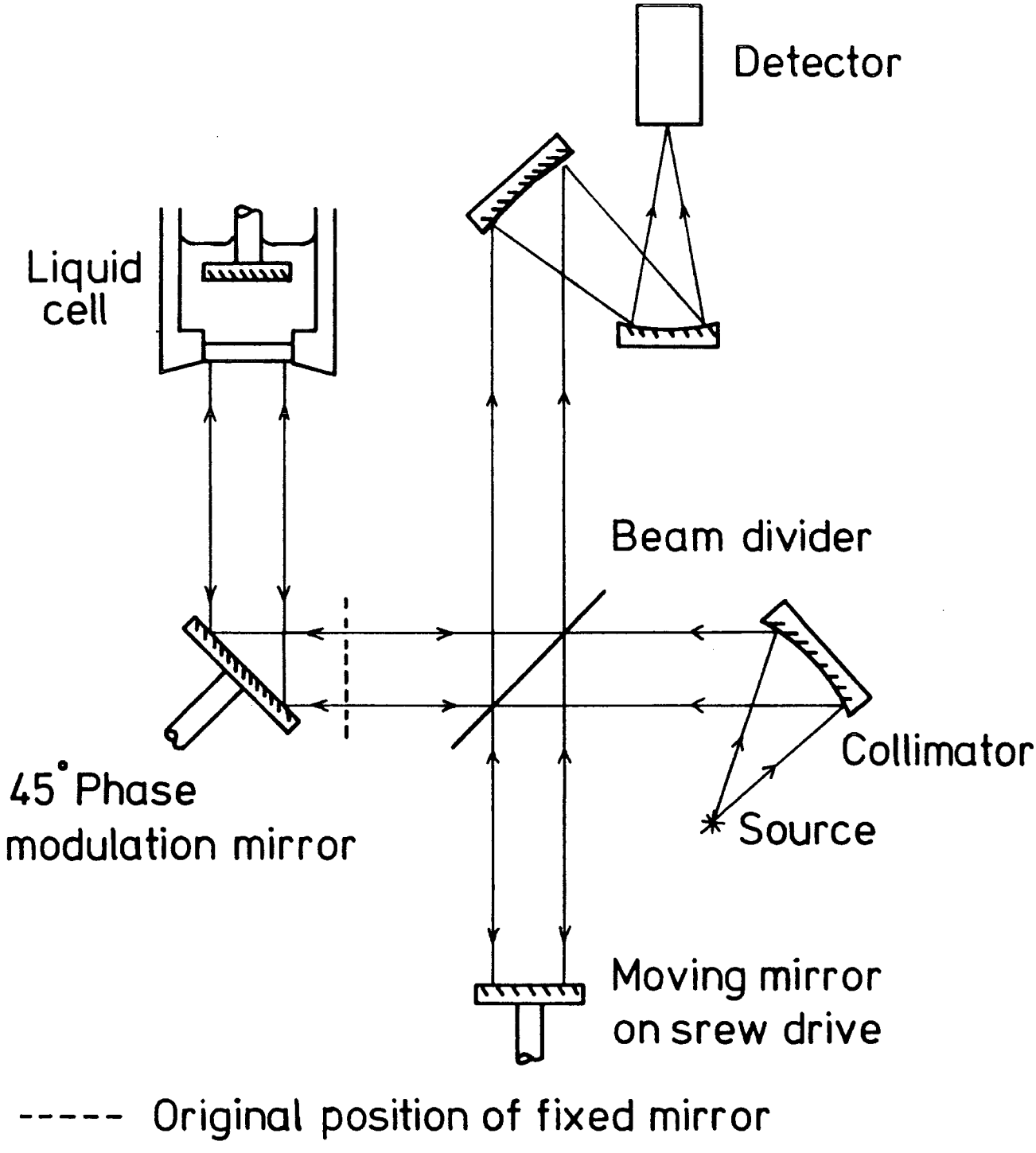

FIGURE 4.13: NEW LIQUID CELL MOUNTED ON THE DURHAM INTERFEROMETER

4.1.4b Optical Alignment.

The interferometer and New Liquid Cell were aligned as for the NPL system using the (0,0) and (1,1) signatures. When the interferometer was misaligned and the (0,0) signature was not resolved, a card with a cut out cross was placed between the collimator and BD. The resultant cross image was viewed between the BD and focussing optics using a 45° mirror and UV goggles. Any misalignment produced two cross images, by using the three adjusting screws of the PM unit, the image from the fixed mirror arm was made to coincide with that of the moving mirror arm. The optical alignment could then be further improved as in Section 4.1.3a.

4.1.4c Phase Adjustment.

Adjusting the amplifier phase by maximising the intensity of the (0,0) signature lobes was found to be very insensitive for the Ithaco amplifier. A more sensitive method is to switch the amplifier phase through 90°, set the signal to zero volts using the phase adjustment and switch the phase back through 90°.

4.1.4d Phase Modulation Adjustment.

The frequency and current of the PM mirror were set to the detector and experimental requirements as for the NPL system.

4.1.4e Practical Operation.

The liquid cell was set up and operated in the same way as on the NPL interferometers, but because the moving mirror unit uses a continually driven screw drive, a different approach to data collection was required. From Section 3.2.1, to compare the phase terms of two interferograms the start position of the interferograms must be known. Since this was not possible a reference point that was common to both interferograms was required. This can be accomplished by extending the range of the interferograms to include the (1,0) signature, as the reflection and transmission properties of the window liquid interface will not change during a TDFTS experiment.

To use the (1,0) signature as a reference, the distance from the ZPD to the sample point to higher optical pathlength must be calculated to a fraction of a sampling interval. Figure 4.14 shows a plot of the points about the (1,0) signature, for a 4 μm sampling interval, due to the fast rate of voltage change, a straight line can be drawn through the points about the crossover. An enlargement of the points about the crossover region is given in Figure 4.15, from which

$$\tan\theta' = \frac{961.362 + 841.726}{1.0}$$

$$= 1803.088$$

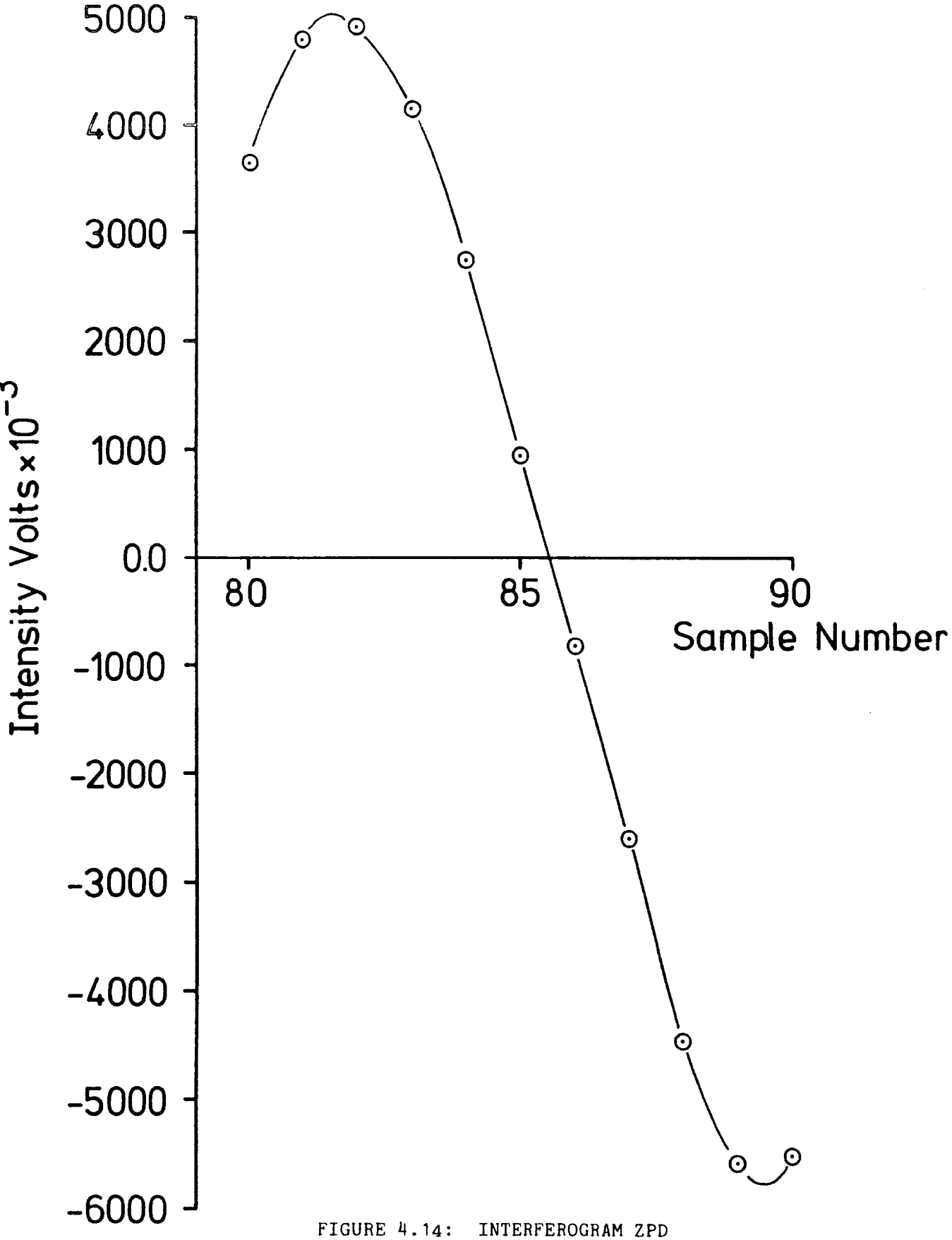

FIGURE 4.14: INTERFEROGRAM ZPD

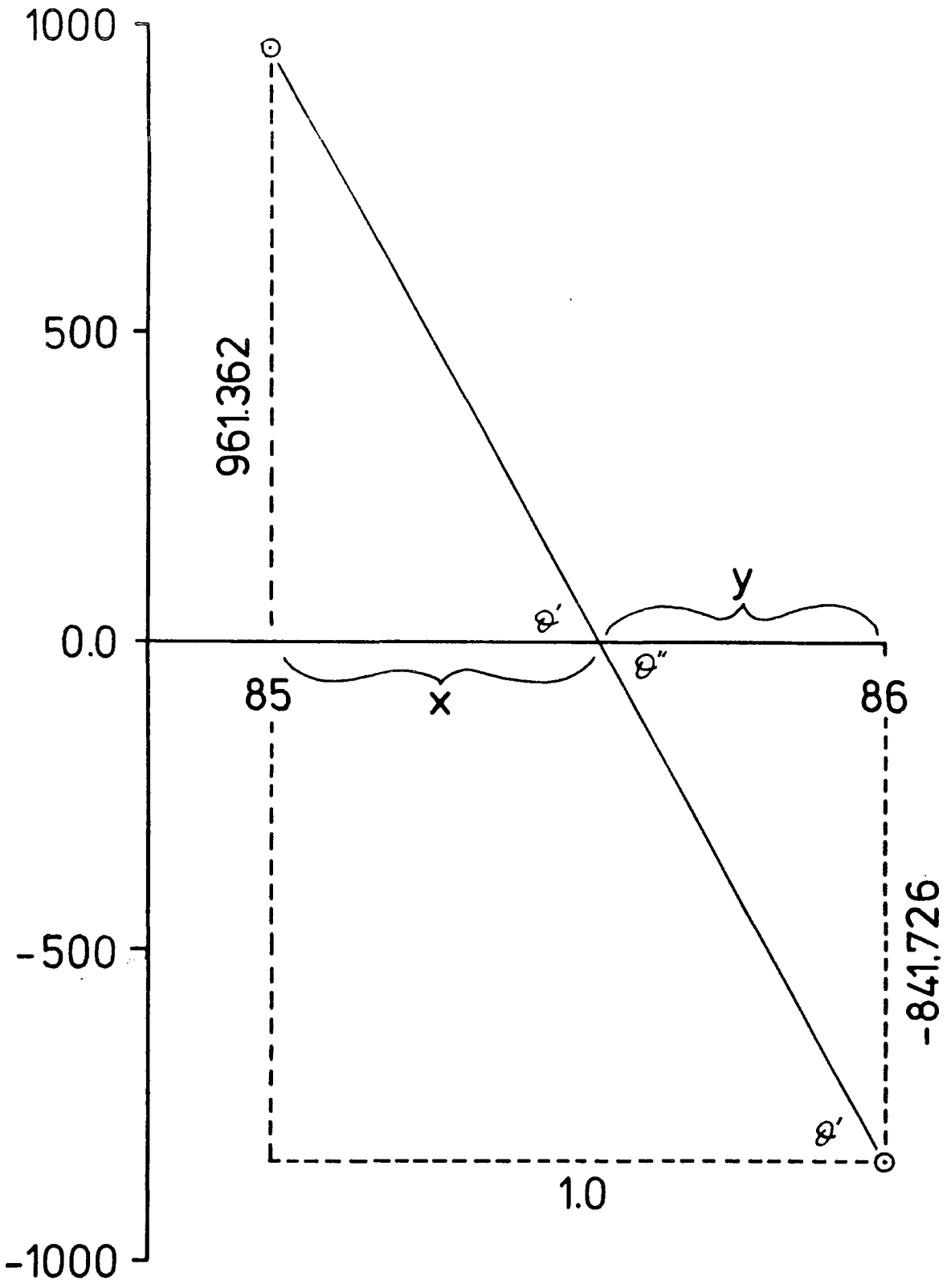

FIGURE 4.15: GEOMETRY OF THE ZPD

Interferogram mean level = -11.365×10^{-3} V

$$\therefore \tan\theta'' = \frac{841.726 - 11.365}{y}$$

But $\theta'' = \theta'$

$\therefore$ y = 0.461 Sampling Intervals. (S.I.)

From the interferogram:-

(1,0) ZPD = 86

(1,1) ZPD = 189

$\therefore$ Reference distance = 103.461 S.I.

The accuracy of this method of fringe shift determination is dependent on the determination of the interferogram average value and the dimensional stability of the interferometer. Any assymetry of the interference signatures will effect the average value. These effects can be reduced by not including approximately twenty five points on either side of each signature when calculating the mean level. For a typical interferogram this gave a difference of 0.0005 in the determination of $\bar{y}$.

4.1.4f Interferometer Dimensional Stability.

This was initially a problem at Durham when the liquid cell was first implemented, as there was no temperature control of the interferometer. Therefore, any room temperature changes also effected the interferometer, leading to dimensional instability occurring during experiments. Since the level of the measured refractive index of a sample is dependent on the measured fringe shift term, any dimensional changes would give erroneous refractive index results.

An estimate of the dimensional stability was made by measuring the movement of an interference signature ZPD position, with the moving mirror fixed, over a one hour period. The moving mirror was set as near as possible to the ZPD of the (0,0) signature and then left for one hour. At the end of this period the intensity of the detector signal was noted and the moving mirror scanned through the interference pattern, to determine the distance moved from the original position after one hour. The chart recorder was then calibrated at the same scan speed to 4 μm sampling intervals. From this trace shown in figure 4.16 the change in interferometer dimensions was found to be 0.09 mm.

For a transmission DFTS experiment on carbon tetrachloride at 25°C using a data collection time of 20 minutes per interferogram a variation of $\mp$ 0.1 in the level of the refractive index was found for

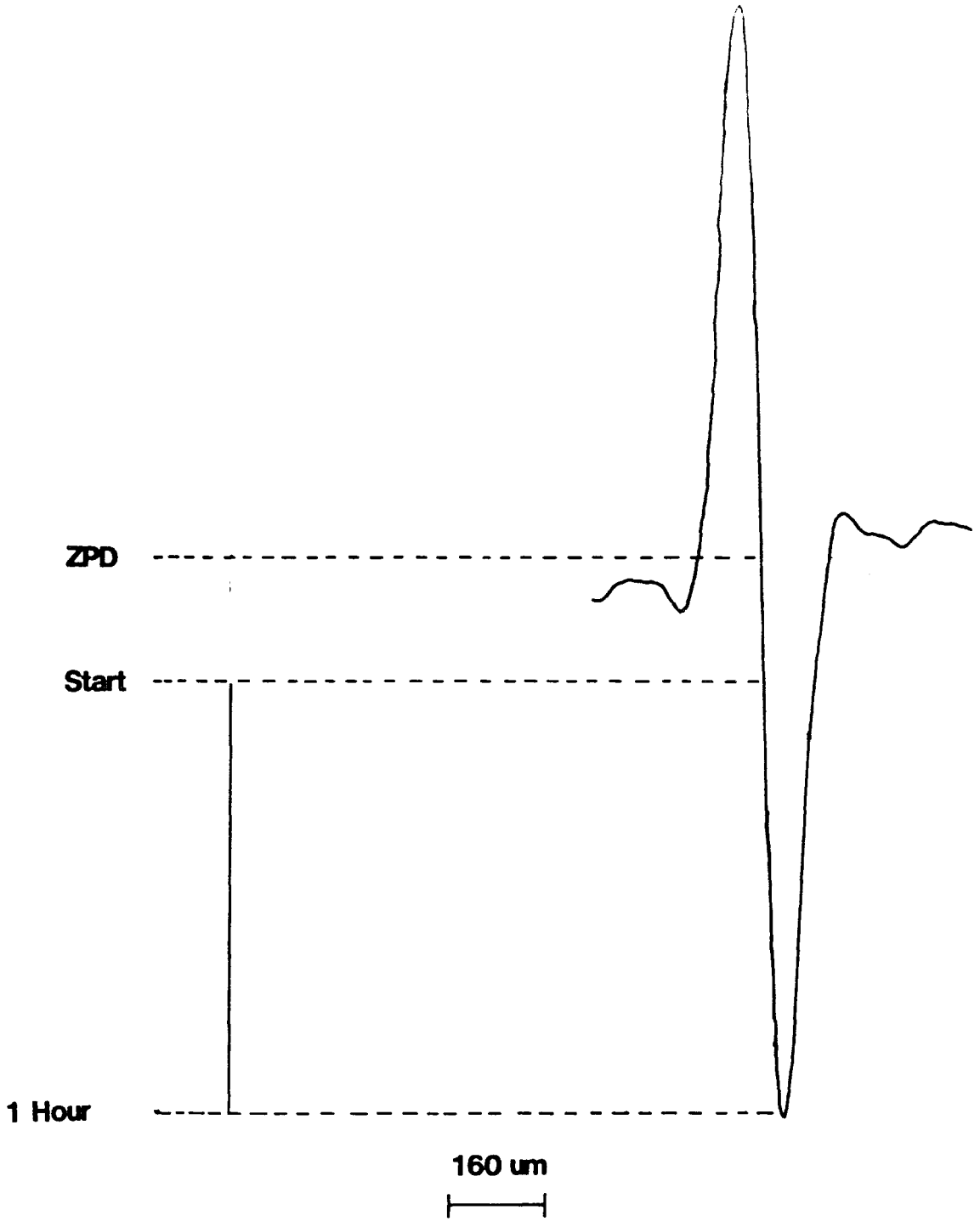

Figure 4.16 Change in interferometer dimensions

three determinations. This did not compare well with results from NPL where a variation of + 0.0001 in the refractive index level had been achieved.

The dimensional stability of the interferometer was improved by using copper coils mounted on copper blocks. These were fitted to the two arms of the interferometer and the beam divider box, the whole interferometer was then wrapped in cotton wool to provide thermal insulation. With the interferometer temperature controlled to 25°C a change of 0.013 mm in the dimensions occurred over a one hour period and a variation of ∓ 0.0003 in the refractive index level for three measurements on carbon tetrachloride was recorded, which did compare favourably with NPL results.

4.1.4g Data Collection.

A schematic layout of the Durham interferometer and data collection system is shown in Figure 4.17. The modulated detector signal is initially amplified by a preamplifier with a range of x1 to $x2^{10}$ and then by an Ithaco phase sensitive lock-in amplifier. The resultant amplified analogue signal is in the range ∓ 10 volts and is digitised by a 14 bit A to D (built by the Durham University Microprocessor Centre) which is triggered by the sampling interval selector unit. The output of the A to D is read into a Cifer micro-

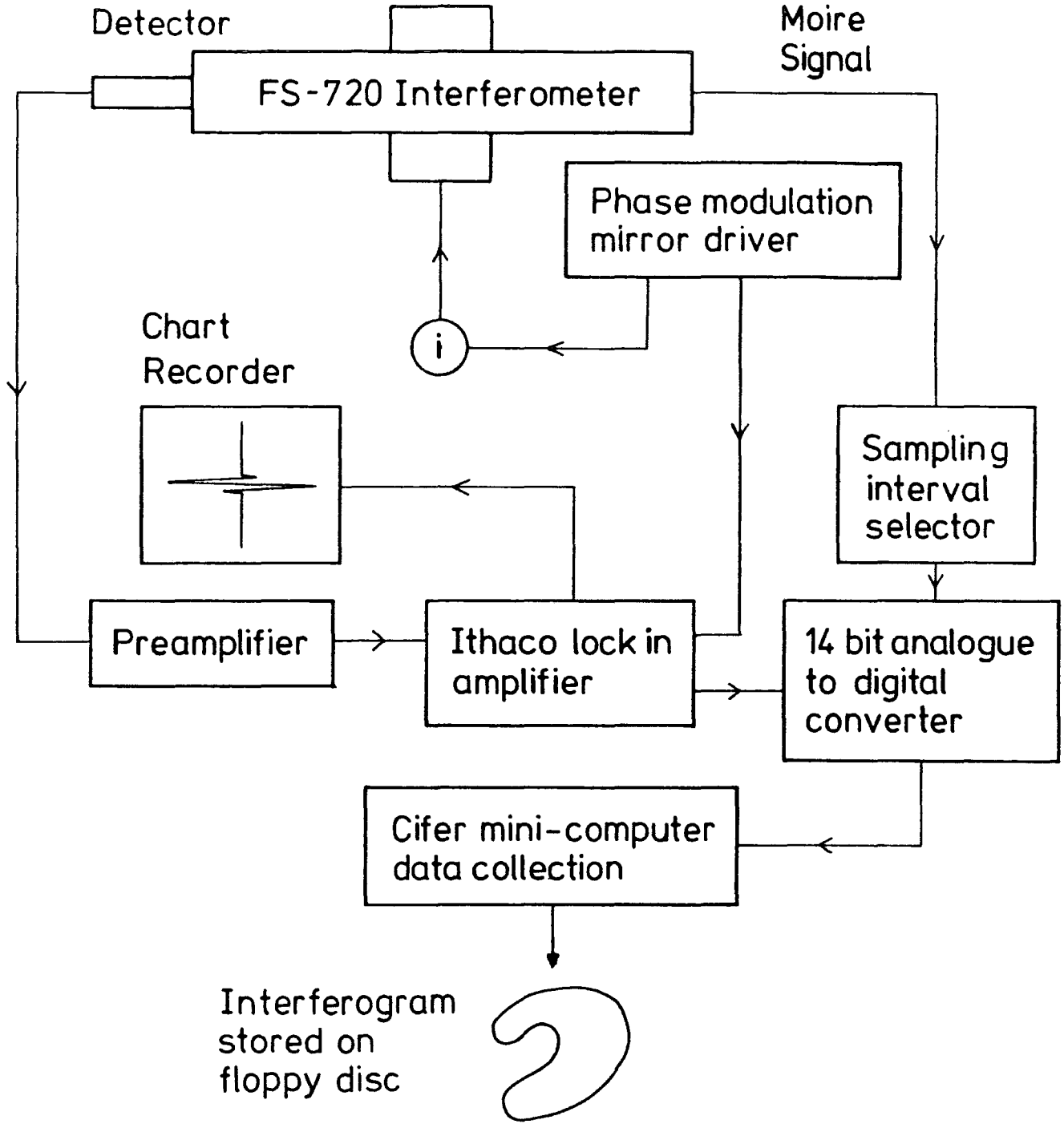

Figure 4.17 Durham interferometer data collection system

computer, where it is stored in a floppy disc file, with heading information to identify the interferogram and experimental parameters associated with it.

4.1.4h Computation of n and α.

Interferograms can be analysed on either the Cifer system or NUMAC, D.MTS facility using FORTRAN programs. A Cooley Tukey FFT program that will accept amplitude or phase modulated interferograms is used for transformation. Programs to analyse the real and imaginary FFT output for TDFTS, RDFTS, FIDFTS and TFTS on the Cifer system are interactive, D.MTS programs are non-interactive and must be consulted before use. The programs for both systems are listed in Tables 4.1a and b.

4.1.5 Comparison of NPL and Durham FTS Systems.

In order to check the reproducibility of data collected on the various interferometers used in this work, it was first necessary to compare the two computing systems used. This was achieved by analysing one set of data by both computing systems. Both Fourier transform programs use a Cooley-Tukey fast Fourier transform routine but the way in which the interferograms are manipulated before transformation differs. The major difference is in determining the ZPD position.

TABLE 4.1a: NUMAC PROGRAMS.

PROGRAM NAME	NO.	ACTION
C4: ASCI2	1	Read in Paper Tape.
PACKTP.O	2	Reformat data read in by 1.
SPLTINT.O	3	Separate reformated data into individual interferograms.
INTPLT.O	4	Plot interferograms.
Subtract.O	5	Subtract background interferogram from sample.
GPONFFT.O	6	Fast Fourier transform program outputs sin, cos, modulus or phase.
FFTAR.O	7	Averages output from 6, outputs average values or ratioed values (absorbance).
NANDALPHA.O	8	Calculates n and α from ϕ and ζ, corrects for phase branching when necessary.
NALPHPLOT.O	9	Plots n, α and averages.
OPCONS.O	10	Calculates ε' and ε'' from n and α, and plots values.
OPCONJN.O	11	Joins n and α data from two different spectral regions.
SUBSPEC.O	12	Subtracts solvent optical constants from solution optical constants.
OPCONINT.O	13	Adds microwave points to far-infrared data and interpolates n and α spectra.

TABLE 4.1a: (contd.)

PROGRAM NAME	NO.	ACTION
OPCONPLOT.0	14	Plots n, α, ε' and ε'' against cm^{-1} and ε' and ε'' against $\ell_n \bar{\nu}$
EPSRECALC.0	15	Scales solution data to liquid data. Also reduces number of data points for CCPLOT.0 & NEWFITF.0.
CCPLOT.0	16	Produces cole-cole plot.
FFT2.0	17	(K. ARNOLD) Fourier transform of microwave-far-infrared data.
MOMPLOT.0	18	(K. ARNOLD) Plots 2nd and 4th moments and $g^{(1)}$
NEWFITF.03	19	(P. JAMES and G.P. O'NEILL) Fitting to the 2nd order truncation of the Mori continued fraction.
WINDOW.0	20	Calculates n and α for new liquid cell window from reflection data.
LIQUIDREF.0	21	Calculates n and α for liquid by reflection technique.
FULLINT.0	22	Calculates n and α for a liquid where multiple reflections are recorded.

TABLE 4.1b: CIFER PROGRAMS.

PROGRAM NAME	NO.	ACTION
DATCOL1.FOR	1	Data collection Program. Reads interferometer amplifier output via A to D converta , starts and stops moving mirror stepping motor.
DATCOL2.FOR	2	As for 1, but without stepping motor control.
ZPD.FOR	3	Determins ZPD position in an interferogram within a specified range.
FSHIFT.FOR	4	Determins frindge shift value between two interferance frindges.
GPONFFT.FOR	5	Fast Fourier transform program as for NUMAC program 6.
AVERAGE.FOR	6	Averages output from 5.
TRANSPEC.FOR	7	Calculates absorption spectrum for a transmission experiment and gives line printer plot.
NANDALPH.FOR	7	Calculates n and α as for NUMAC.
NALPHAVE.FOR	8	Averages n and α spectra.
EPSCALC.FOR	9	Calculates ε' and ε''.
SPECPLOT.FOR	10	Plotting program, plots phase, modulus, refractiv index, absorption coeficient, dielectric loss and permittivity spectra.
WINDOW.FOR	11	Calculates New Liquid Cell window optical constants.
LIQDREF.FOR	12	Calculates n and α for liquid by reflection technique.

TABLE 4.1b: (contd.)

LLSRT.FOR	13	Performs linear least squares regresion treatment on 'raw' microwave data.
FKFIT.FOR	12	Fits microwave data to Fuoss-Kirkwood equation.

If we consider the schematic phase modulated interfergram in Figure 4.18 the "true" ZPD (TZPD) will occur at the point in the zero crossing corresponding to the mean level value. It is, however, unlikely that a sampled point will exactly coincide with the TZPD, so the sampled point nearest the TZPD is used in Fourier transformation of the interferogram. Birch and Parker[42] have shown that although the value of the computed phase spectrum depends on the sample point chosen, the computed refractive index spectrum is independent of the point chosen, as long as the distance from a chosen origin to that point is known.

In the NPL FFT program the negative sampled point nearest to the TZPD is taken as the ZPD, but in the Durham program the nearest point to the TZPD is used. For example, if the schematic interferogram were transformed, point A would be used by the NPL program and point B by the Durham program. The programs would therefore give the same modulus but different phase values for the same interferogram, but from Birch and Parker[42] the difference between the two spectra should be linear and related to the sample point chosen by the relationship.

$$2\pi\bar{\nu}\Delta x = \phi_{Diff} \qquad \ldots\ldots \quad 4.5$$

Δx = Interferogram sampling interval.

This situation arose for one of the interferograms chosen to

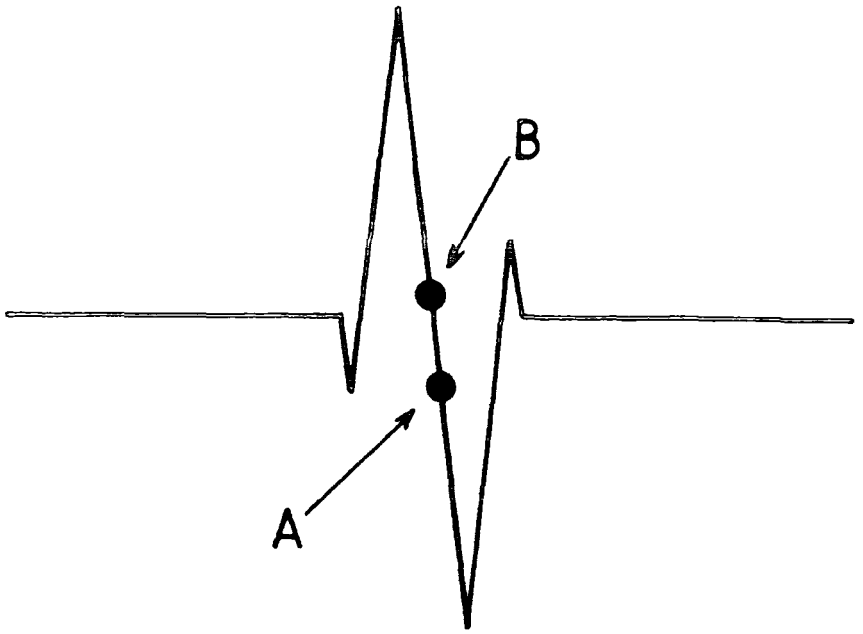

Figure 4.18 ZPD sampling points

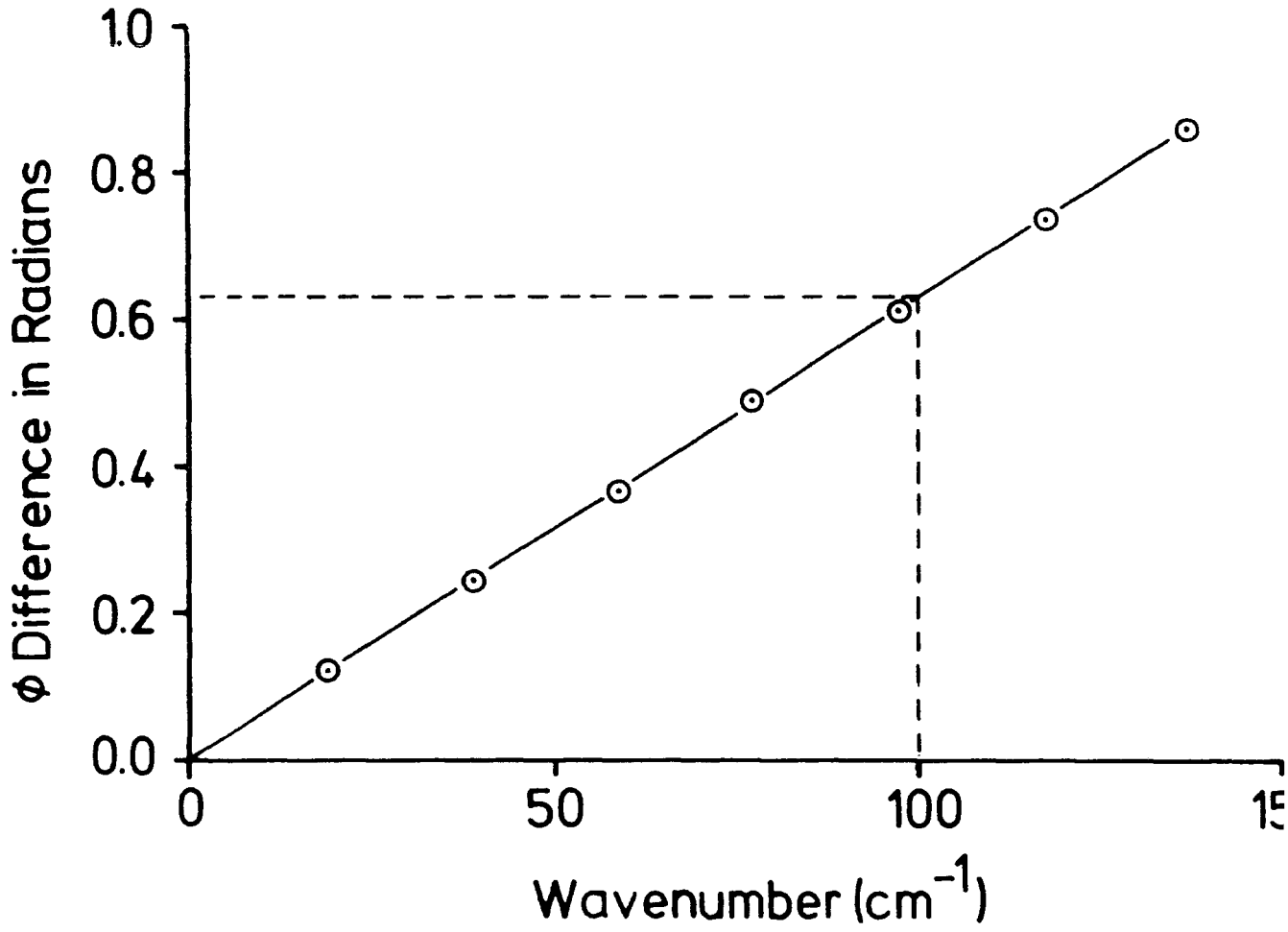

Figure 4.19 Phase difference against frequency

compare the two FFT programs, NPL tape 150. In Table 4.2 the phase values calculated by the two programs are tabulated at different frequencies, as can be seen they are not the same for tape 150. Figure 4.19 shows the plot of the phase difference against frequency for tape 150 which is a straight line, from equation 4.5 and Figure 4.20.

$$2\pi \times 100.0 \times \Delta x = 0.63$$

$$\therefore \Delta x = 0.001 \text{ cm}$$

which is the interferogram sampling interval, therefore the two ZPD positions are one sampling interval apart and the phase spectra are equivalent.

A final test on the data was made by computing the refractive index and absorption coefficient spectra from the two data sets. A selection of values are shown in Table 4.3 the difference in refractive index and absorption coefficient spectra calculated by the two programs is negligible when compared to the experimental errors (see Chapter 5). Spectra of carbon tetrachloride measured at the NPL and Durham using the respective computational systems show very good agreement.

TABLE 4.2:

$\bar{\nu}$ cm^{-1}	ϕ^{150} DURHAM	ϕ^{150} NPL	ϕ^{150} NPL-DHR	ϕ^{153} DURHAM	ϕ^{153} NPL	ϕ^{153} NPL-DHR
19.53	1.44279	1.5654	0.12261	1.40250	1.4004	-0.0021
39.06	1.43286	1.6783	0.24544	0.27509	0.27532	0.00023
58.58	1.33846	1.7066	0.36814	-0.94525	-0.94597	0.00072
78.13	1.34636	1.8372	0.49084	-1.64753	-1.6480	0.00047
97.66	1.56126	2.1748	0.61354	-1.94247	-1.9426	0.00013
117.19	1.90628	2.6427	0.73642	-1.84391	-1.8438	0.00011
136.72	2.26781	3.1270	0.85919	-1.56681	-1.5663	0.00051
156.25	2.71818	-2.5831	0.98190	-1.20448	-1.2042	0.00028
175.78	-2.97721	-1.8722	1.10501	-0.33767	-0.33652	0.00115
195.31	-2.19417	-0.9660	1.22817	+0.80318	0.80399	0.00081

ϕ^{150}_{DURHAM} : Refers to the phase of NPL Data tape 150 computed using Durham software.

TABLE 4.3:

ν cm^{-1}	η NPL	η DUR	η NPL-DUR	α NPL	α DUR
19.53	1.49004	1.49006	-0.00002	1.47595	1.47575
39.06	1.486403	1.48640	0.0	2.00505	2.004316
58.59	1.485162	1.48516	0.0	1.85965	1.85896
78.13	1.485250	1.48525	0.0	1.46037	1.45975
97.66	1.485575	1.48558	0.0	1.22576	1.22483
117.19	1.486089	1.48609	0.0	0.832004	0.83195
136.72	1.486614	1.486613	0.0	0.90452	0.90467
156.25	1.487004	1.487003	0.0	0.86220	0.86326
175.78	1.487585	1.48758	0.0	0.56935	0.57278
195.31	1.488102	1.48810	0.0	0.85219	0.85254

4.2 Low Frequency Measurements.

4.2.1 Introduction.

By using the DFTS methods previously outlined the optical constants of a liquid can be measured over a wide frequency range. The low frequency limit is dependent on the type of detector used, but frequencies below 60 GHz (2.0 cm^{-1}) are not normaly attainable. In order to determin the correlation function and carry out far-infrared band momement analysis, dielectric loss values down to zero frequency are required. Analysis of microwave values will also give the Debye relaxation time τ_D, therefore static permitivity and microwave measurements are required.

4.2.2 Static Permitivity Measurements.

Since the permitivity and capacitance of a liquid are equivalent, a plot of permitivity against capacitance will be a straight line, giving

$$\varepsilon_o = mC + c \qquad \ldots\ldots \quad 4.6$$

where m & c are constants.

If the capacitance values of liquids with known ε_o values are determined, the values for the constants m & c can be calculated. These values can then be used to convert capacitance measurements on

other liquids into permitivity values. The equipment used to measure the capacitance of the MeI solutions was a Wiss-Techn. Werkstatten D812 Weilheim Dipolmeter-DM01 operating at 2 kHz. Two liquids with literature ε_o values that were in the range expected for the MeI solutions were used to obtain M & C. They were cyclohexane (ε_o = 2.015)[62] and toluene (ε_o = 2.379)[62] .

The liquids were contained between two parallel plates in a temperature controlled cell that was maintained at 25 ∓ 1°C. The solutions were allowed 15 minutes to equilibrate before each measurement was made.

4.2.3 Microwave Measurements.

Measurements on the microwave absorption of MeI solutions were made in collaboration with Dr. A Price at UCW Aberystwyth. Two techniques were used, the region 4.0 to 18.0 GHz was covered using sweep frequency equipment, and two spot frequency measurements were made at 36 & 69 GHz.

4.2.3a Sweep Frequency Measurements.

The apparatus used to carry out sweep frequency measurements was supplied by Messrs. Systron Donner Ltd. and a block diagram of the apparatus is shown in Figure 4.20. The sweep frequency supply is

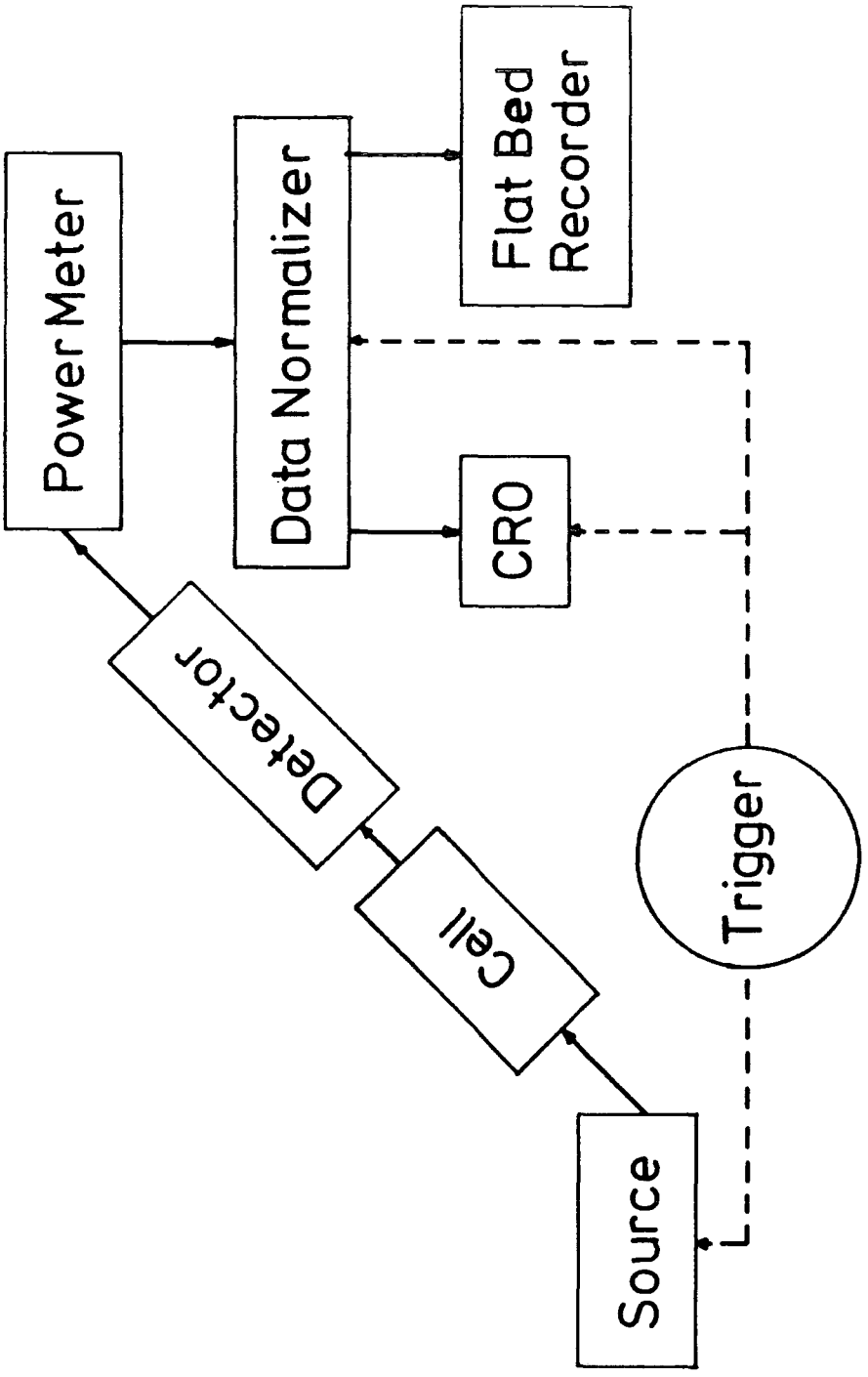

FIGURE 4.20: SWEEP FREQUENCY EQUIPMENT

generated using a multiband controller which powers two plug-in units with frequency ranges of 0.01 to 4.2 GHz and 4.0 to 18.0 GHz . The source, flat bed recorder and data normalizer are all triggered simultaneously. To reduce reflection effects the sample cell was placed at an angle to give a tapered upper liquid surface[63]. Measurements were made by first filling the cell with sufficient liquid to cover the bottom teflon window, using a micro syringe or a burette. A sweep frequency scan of the cell was then made and the result stored digitally in a 400 bit data normalizer. This initial trace was not flat due to reflections within the cell and was ratiod against subsequent frequency scans to remove these reflection effects.

Having obtained a good initial normalized trace on the X-Y recorder, the recorder attenuation axis was cal.ibrated by inserting standard Hewlett Packard attenuators between the cell and detector. Further known volumes of the liquid sample were then let into the cell and a frequency scan made for each addition. A typical recorder plot of attenuation for given liquid depth, against frequency over 4.0 to 18.0 GHz is shown in Figure 4.21. Since the sample cell is a waveguide of constant, known internal dimensions it is a simple matter to calculate the liquid depth in the cell, knowing the volume.

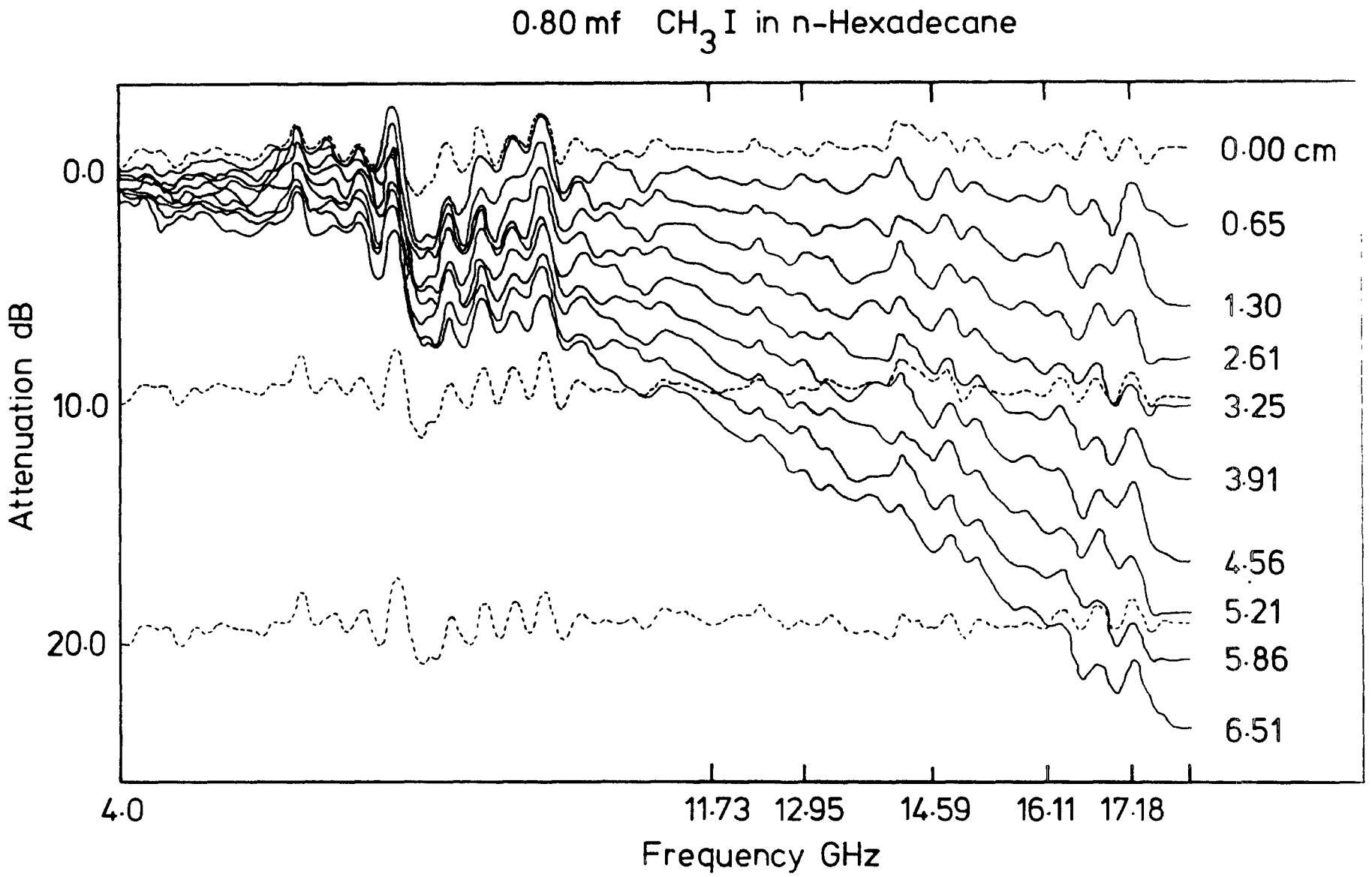

Figure 4.21 Sweep Frequency Plots

From the Kramer[63] relation

$$\frac{E_o}{E_i} = K\exp(-\alpha' d) \qquad \ldots\ldots \quad 4.7$$

where E_o and E_i are the output and input wave amplitudes, K is a function of the reflection coefficient at various interfaces, α' is the attenuation coefficient (cm^{-1}) and d is the sample depth (cm).

E_o/E_i is known as the power ratio T therefore

$$\ln T = \ln K - \alpha' d \qquad \ldots\ldots \quad 4.7$$

If dB is the measured attenuation

$$\ln T = \frac{2.303 dB}{20} \qquad \ldots\ldots \quad 4.8$$

substituting from equation 4.7

$$\frac{2.303 dB}{20} = \ln K - \alpha' d$$

$$dB = -\frac{\alpha' 2.303 d}{20} + \ln K$$

Therefore, a plot of dB against d will have a slope of

$$-\frac{\alpha' 2.303}{20}$$

According to Price[63] the plot will be linear if $\alpha' d > 1$ and contain

periodic variations (due to reflectors) if $\alpha'd<1$. A selection of plots obtained from the previous recorder plot are shown in Figure 4.22.

The gradient of each plot was determined by a linear least squares regression treatment, either using a Commodore SR9190R calculator or the program LLSRT on a Cifer micro computer, the output from which is shown in Figure 4.23.

4.2.3b Spot Frequency Measurements at 36 and 72 .

The apparatus used for 36 GHz measurements is shown schematically in Figure 4.24. Although power is supplied by a 36 GHz Klystron oscillator, the system frequency is dependent on the Q-band 8mm rectangular (0.28 x 0.14 Inch) dimensions and is measured waveguide using a tunable resonant cavity frequency meter. The dimensions of the cavity are varied by a micrometer, where resonance occurs energy is stored in the cavity and there is an associated sharp drop in power. Micrometer readings are converted to frequency using "Eliott" tables. The crystal detector was tuned to the system by maximising the detected signal.

Measurements were made by just covering the bottom teflon window of the waveguide with liquid and then setting the attenuator at approximately 25 dB. The associated reading on the power meter was

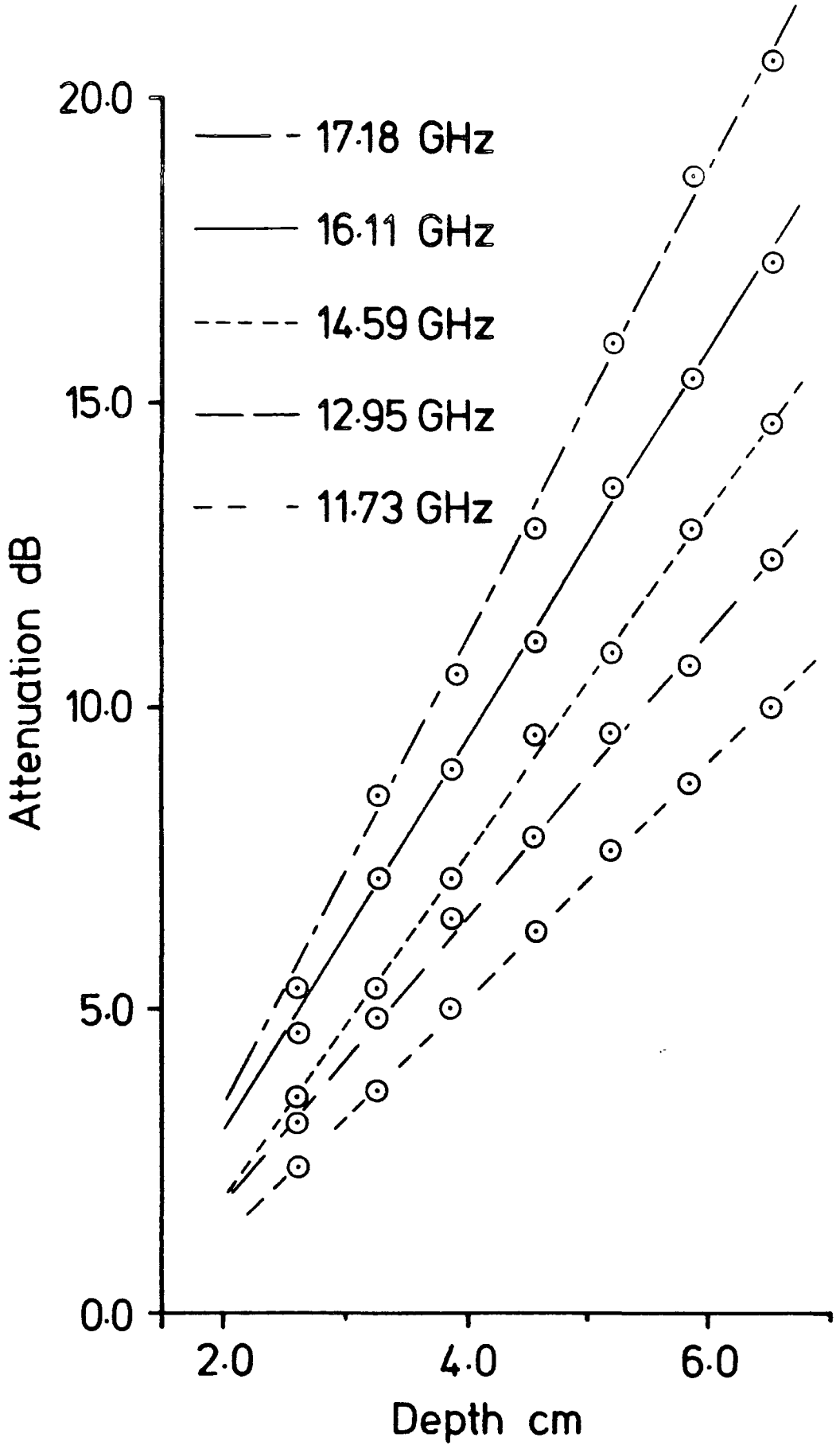

Figure 4.22 Attenuation against depth plots

FIGURE 4.23 0.162 mf METHYL IODIDE IN n-HEPTANE AT 69.86 GHz

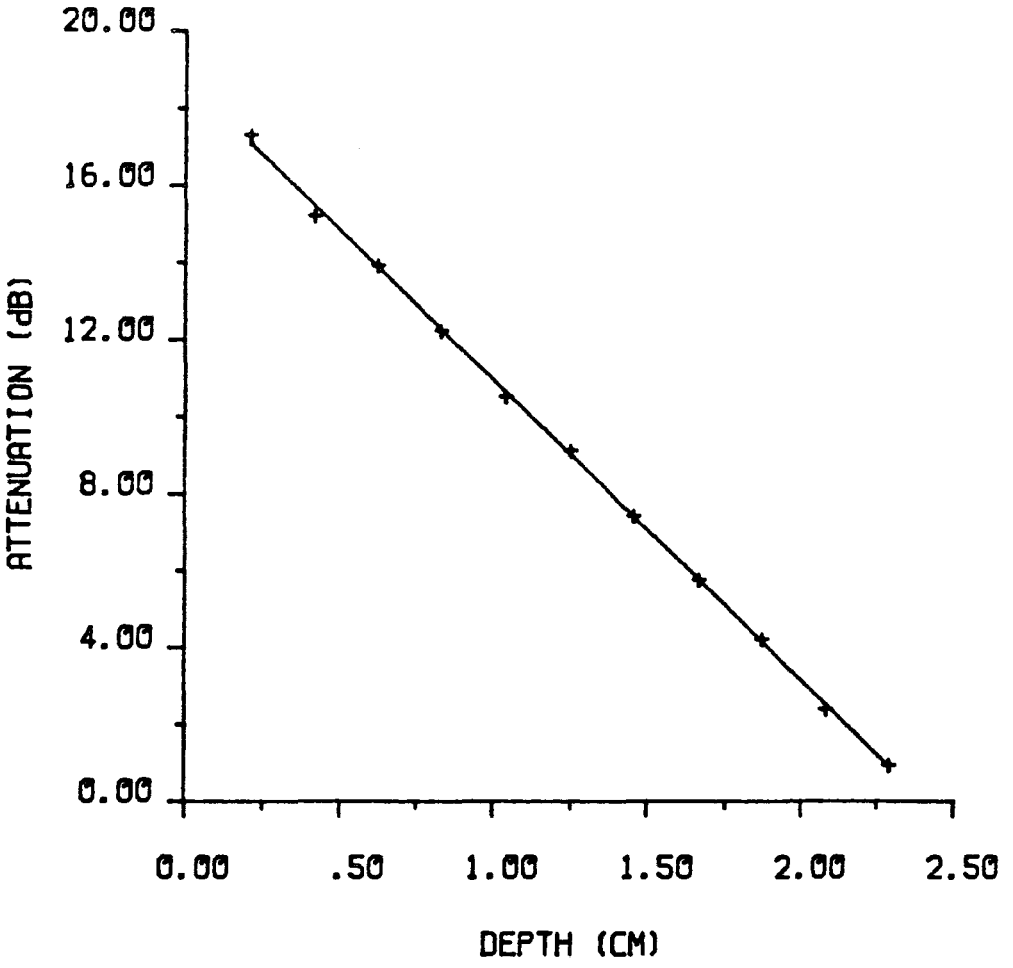

RESULTS FROM LEAST-SQUARES CALCULATION :-

CORRELATION COEFFICIENT = .9997

INTERCEPT = 18.709

SLOPE = -7.779

ATTENUATION COEFFICIENT = .895 CM^{-1}

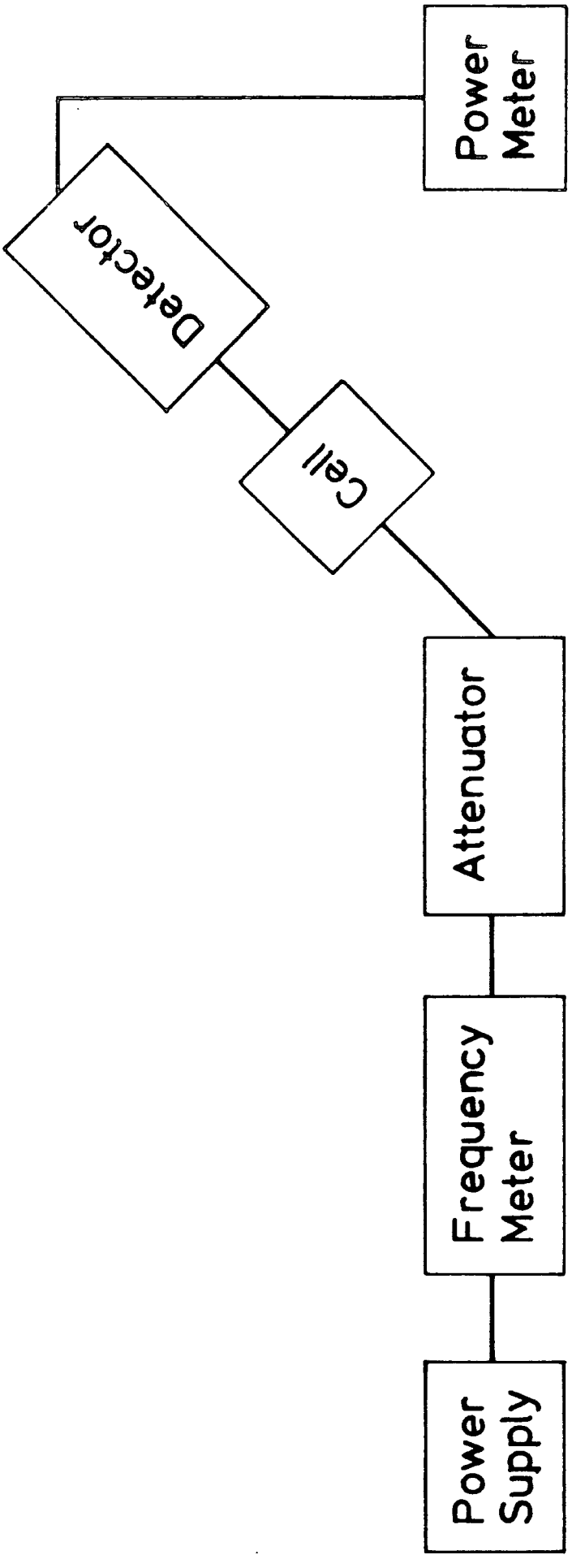

Figure 4.24 Spot frequency apparatus

noted, and maintained by varying the attenuator as further amounts of liquids were let into the cell. Thus non-linear effects due to the detector were minimal. Values of attenuation were measured on a vernia scale and had to be converted to decibels using "Eliott" tables. The attenuation coefficient of the liquid was calculated as for the sweep frequency measurements.

72 GHz measurements were made with a 72 GHz Klystron and an E-band 4mm (0.122 x 0.061 inches) waveguide set up as for the 36GHz system but with the attenuator between the cell and detector. In this case both the system frequency and attenuation were measured directly.

The reproducibility of these measurements is shown in Figures 4.25 and 4.26 for measurements made on separate days, and the error has been estimated to be $\mp$ 5%.

FIGURE 4.25 0.005 mf METHYL IODIDE IN CARBON TETRACHLORIDE AT 69.845 GHz

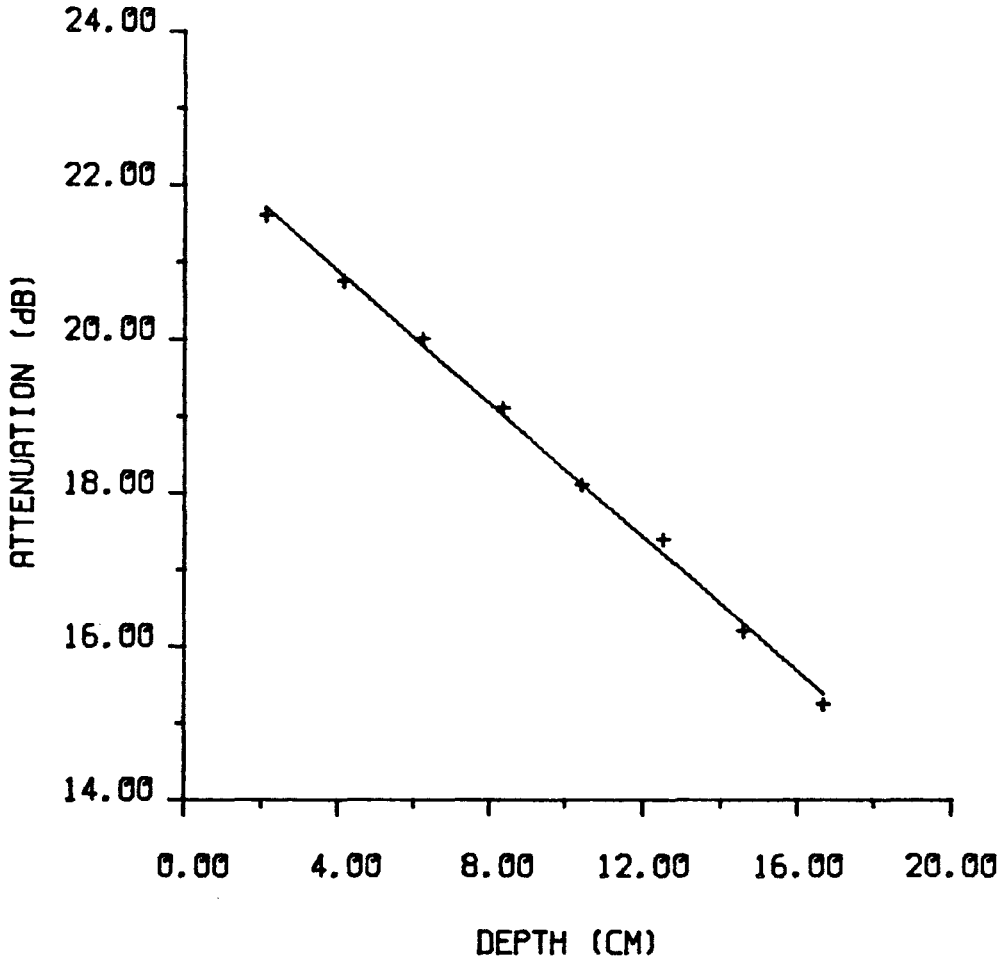

RESULTS FROM LEAST-SQUARES CALCULATION :-

CORRELATION COEFFICIENT = .9984

INTERCEPT = 22.621

SLOPE = -.434

ATTENUATION COEFFICIENT = .050 CM^{-1}

IGURE 4.26 0.005 MF METHYL IODIDE IN CARBON TETRACHLORIDE AT 69.825 GHZ

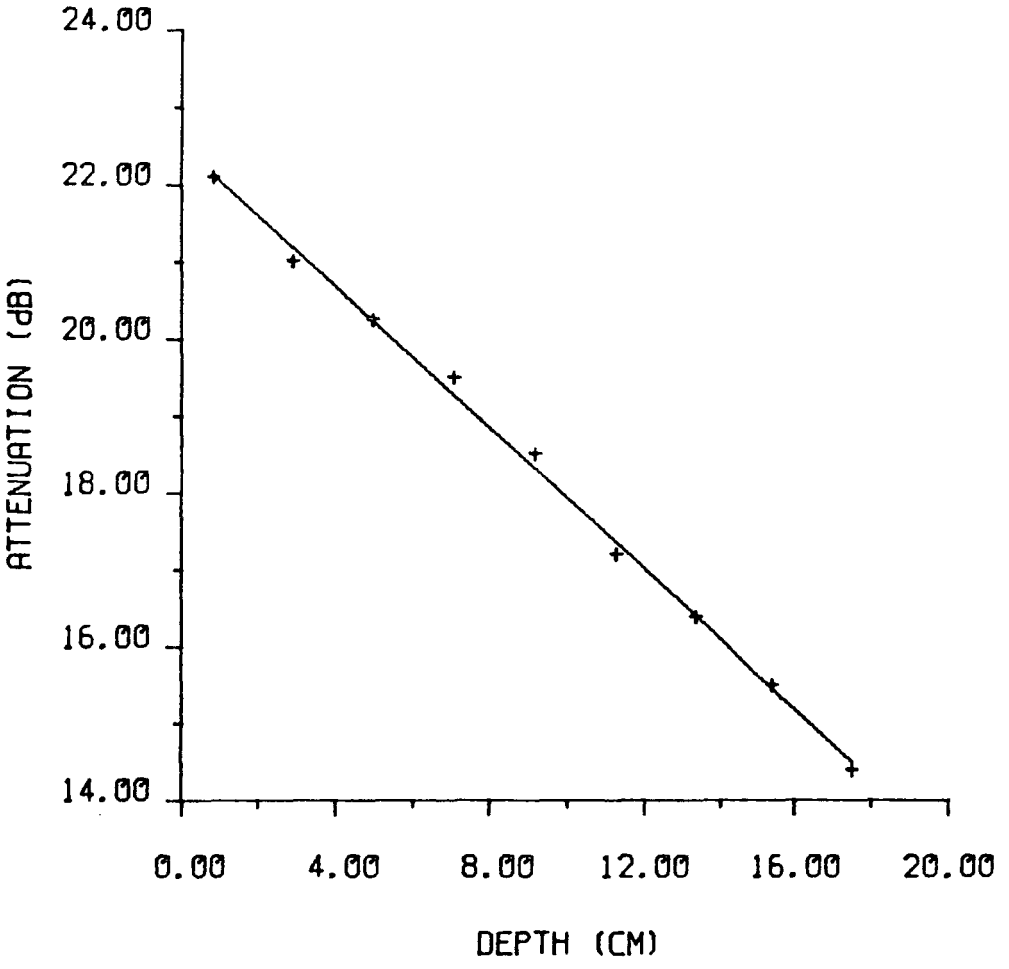

RESULTS FROM LEAST-SQUARES CALCULATION :-

CORRELATION COEFFICIENT = .9985

INTERCEPT = 22.519

SLOPE = -.458

ATTENUATION COEFFICIENT = .052 CM^{-1}

C H A P T E R 5

ERRORS

"Errors using inadequate data are much less than those using no data at all"

Charles Babbage 1792-1871

5.1 Introduction.

With physical measurements it is important to determine the associated experimental errors before any interpretation of the result is carried out. This is particularly important when using a technique that is capable of a high degree of accuracy, where it is desireable to identify the causes of experimental errors so they can be removed or reduced. This will enable the level of uncertainty associated with a measurement to be deduced.

5.2 Types of Experimental Error.

In a dispersive Fourier transform experiment there are two types of experimental error; random and systematic. Random errors give rise to fluctuations in a measurement, whilst systematic errors affect the magnitude of the experimental values. Having determined the types of error associated with a particular measurement, it is desirable to develop an experimental procedure that will remove or minimise the effects of these errors. Random errors can be reduced by taking care in making measurements and repeating experiments so that results can be averaged, to reduce the level of fluctuations. Systematic errors are more difficult to overcome since their effects on measurements are not easily detected. For example, a systematic error in the liquid pathlength will not produce a variation in each determination, but

will effect the level of the optical constants. Systematic errors are normally overcome by calibrating instruments using standard samples.

5.3 Errors Associated with Far-Infrared Liquid Cells.

A comprehensive assessment of the errors involved in measurements using the Free Layer and Leiden cells has been made by Afsar et al.[35,64]. It is intended in this Chapter to cover the New Liquid Cell.

5.4 Errors with the New Liquid Cell.

The possible sources of error arising from the interferometer and New Liquid Cell are given in Table 5.1; the errors have been categorised as random or systematic. In order to reduce these errors as much as possible, a general experimental procedure was followed for all measurements made. This involved careful alignment of the interferometer and New Liquid Cell, consistent treatment of micrometers prior to measurements, temperature control, and repeat experiments. The interferometer and New Liquid Cell were maintained to $\mp$ 0.1^{o}C for all experiments and the spectra presented in this thesis are an average of three determinations, thus allowing the reproducibility of each technique to be assessed. The level of reproducibility is shown on the averaged spectra by the following

TABLE 5.1

ERROR NO.	SOURCE OF ERROR	ERROR TYPE
1	Source Noise	R*
2	Source Energy Variation	R/S+
3	Detector Noise	R
4	Interferometer Moving Mirror (Screw Pitch, Step Size and Start Point)	R/S
5	Interferometer Alignment	S
6	Interferometer Phase	R (On Experimental Time Scale)
7	Gain Error (Linearity)	S
8	Analogue to Digital Conversion	R/S
9	Amplifier Noise	R
10	Fourier Transformation	S
11	New Liquid Cell Alignment	S
12	Liquid Pathlength	R/S
13	New Liquid Cell (Window/Mirror Quality)	S
14	New Liquid Cell Temperature	R/S
15	Solution Concentration	R

R* = Random S+ = Systematic

symbol, ⊞ . Where the averaged spectra covering different wavenumber ranges have been combined (see Section 6.3), the largest reproducibility value has been retained for the whole spectrum. An assessment of the systematic errors that could arise in each technique has been made and these are indicated by the following symbol, ⊕ .

5.4.1 Errors in Transmission Dispersive Fourier Transform Spectrometry.

In order to determine the systematic errors involved in a transmission experiment, we must consider the effects of experimental errors on the equations used to calculate the optical constants. Using results obtained for carbon tetrachloride at 25°C, (data reference Nos. NPL/150/155) to determine the magnitude and errors of the terms in these equations, it should be possible to assess the major sources of errors. Rewriting equation 3.35

$$\alpha(\tilde{\nu}) = \frac{1}{ds - db} \ln\left\{\frac{C_{s(\tilde{\nu})}}{C_{b(\tilde{\nu})}} GF\right\} \qquad \ldots\ldots 5.1$$

where GF takes ito account the amplifier gains used in recording the sample and background interferograms. Splitting equation 5.1 into two parts, the errors in the first term (1/(ds - db)) will be random and systematic. The random error will contribute to the reproducibility but the systematic error must be determined. The New Liquid Cell

micrometer can be read to ± 0.0005 cm so for ds = 1.4 cm and db = 0.8

$$\frac{1}{ds - db} = 1.667 \pm 0.0027 \text{ cm}^{-1}$$

The sample and background modulus spectra are shown in Figure 5.1; these spectra will be subject to all the errors except No.12 listed in Table 5.1.As before the random errors will be covered by the reproducibility and the level of systematic errors must be assessed. Since the spectra are determined alternately and they are ratioed in equation 5.1, errors 2, 4, 5, 8, 11 & 13 should be negligible providing there is no serious misalignment of the interferometer or New Liquid Cell. The gain error can be determined by calibrating the amplifier to known voltages, for this data the gains used give a gain factor of 1.0 ± 0.0. From Birch et al.[37] the absorption coefficient of carbon tetrachloride varies by approximately 0.01 cm^{-1} per ^{o}C in the 25^{o}C region. Since the New Liquid Cell is controlled to ± 0.1^{o}C, this gives a possible systematic error, due to temperature variation of ±0.001 cm^{-1}. Combining these errors gives a possible systematic error of ± 0.004 in the absorption coefficient. The major source of systematic error in the absorbance spectrum is therefore due to the sample pathlength determination. However, since the reproducibility of the absorption coefficient is ± 0.05 (see Figure 4.10), this level

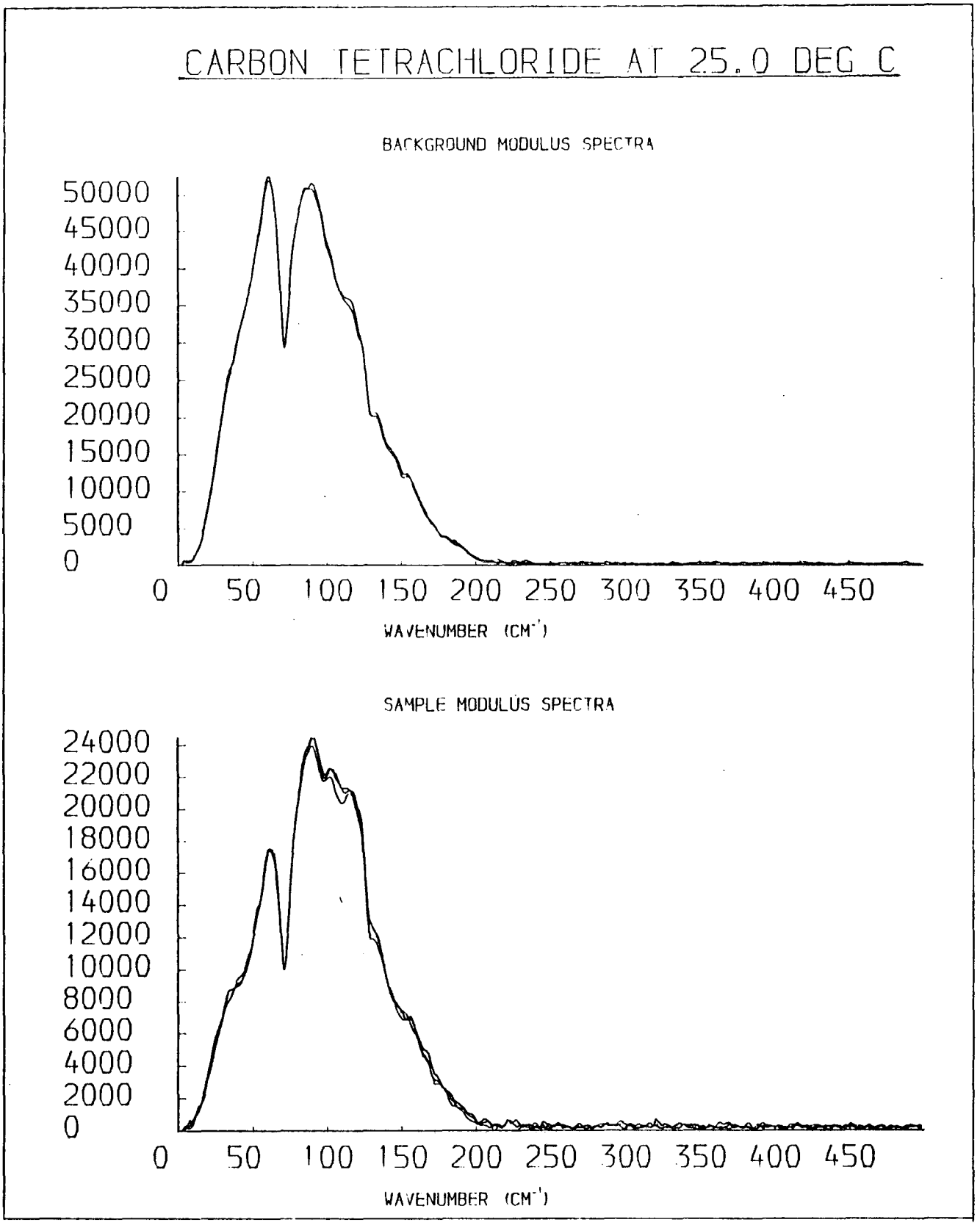

FIGURE 5.1 BACKGROUND AND SAMPLE MODULUS SPECTRA

of systematic error is negligible for these results.

Equation 3.36 can also be split into two parts, the phase term for the carbon tetrachloride data at 97.7 cm^{-1} is

$$\phi = \frac{-1.9426 - 2.1748 + M\pi}{4 \times \pi \times 97.7 \times 0.6(\mp 0.001)}$$

$$= -0.00559 \mp 0.000009$$

and the fringe shift term at 97.7 cm^{-1} is

$$FS = 2.6586\ (\mp 0.0005) - 1.7484\ (\mp 0.0005) + (0.0005 \times (302-333))$$

$$= 0.8947 \mp 0.001 \text{ cm}$$

$$\therefore n\ (97.7\ cm^{-1}) = 1.486 \mp 0.002$$

Together with an error due to temperature variations of $\mp$ 0.00007, since the random error for this data is $\mp$ 0.0005 (see Figure 4.11), these calculations show that the refractive index determination could be susceptible to a systematic error of $\mp$ 0.002. For the Durham method of fringe shift determination (see Section 4.1.4e) the systematic error would be the same.

5.4.2 Errors in Reflection Dispersive Fourier Transform Spectrometry.

To calculate the errors in a RDFTS experiment, the errors for the determination of the window optical constants must first be calculated.

5.4.2a Errors for the New Liquid Cell Window Optical Constants.

The major error in the cell window optical constants arises from determination of the window thickness, which can be measured to ∓ 0.0005 cm. Using the same data as in Section 3.2.2a and equations 3.49 & 3.50

$$n'(50\ cm^{-1}) = \frac{644.0264 - 3.14159}{4 \times 3.14159 \times 50.0 \times 0.3040\ (\mp\ 0.0005)}$$

$$n'(50\ cm^{-1}) = 3.355 \mp 0.006$$

and

$$\alpha'(50\ cm^{-1}) = 3.289\ (\mp\ 0.005)\ .\ \ln\left[\frac{1 - 0.2927\ (\mp\ 0.001)}{0.623}\right]$$

$$\alpha'(50\ cm^{-1}) = 0.417 \mp 0.003.$$

From the spectra in Figures 5.2 and 5.3 the random errors for the window refractive index and absorption coefficient are ∓ 0.005 and

FIGURE 5.3 REFLECTION DISPERSIVE MEASUREMENTS

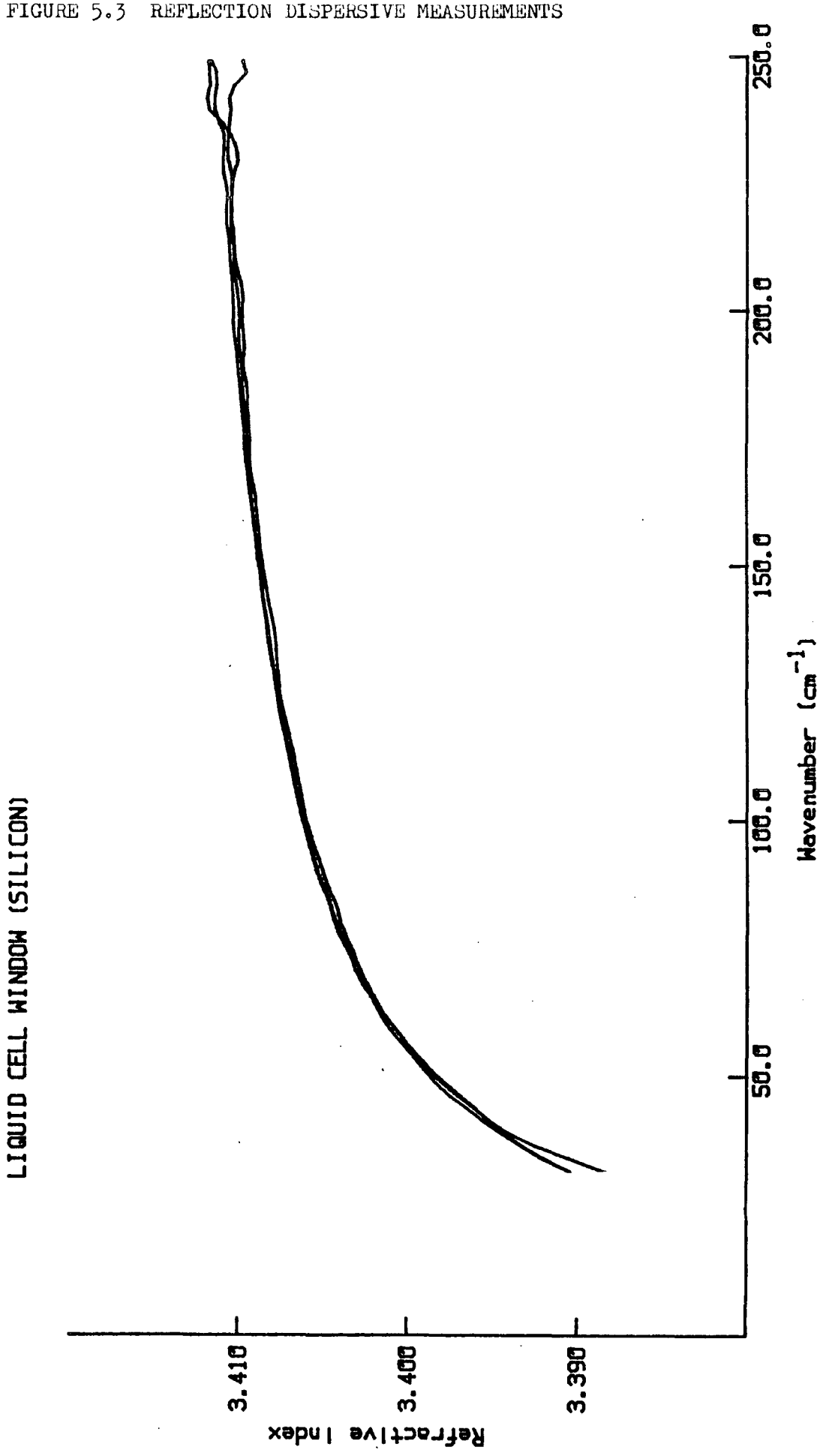

FIGURE 5.2 REFLECTION DISPERSIVE MEASUREMENTS

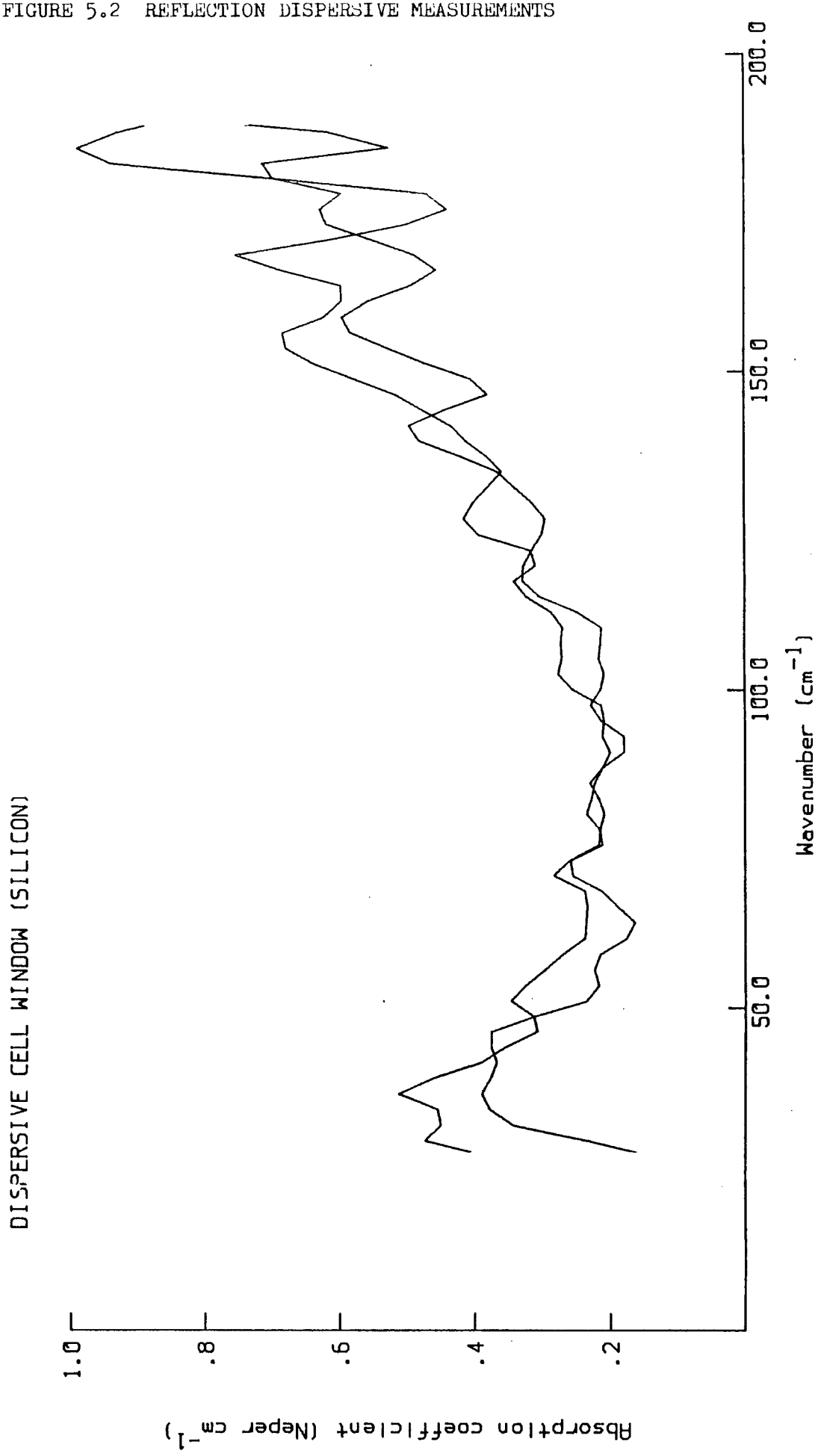

∓ 0.15 cm^{-1} respectively. The refractive index spectra are therefore more suceptable to systematic errors than random errors,whilst for the absorption coefficient spectra the converse is true.

5.4.2b Errors for the Liquid Optical Constants.

The liquid optical constants are determined using equation 3.55 from which it is clear that calculation of the experimental errors for this method is a rather laborious procedure. Calculation of the errors for one part of equation 3.55 are shown below as an example, again using the data from Section 3.22a, at 50 cm^{-1}.

$$\hat{r}_{01}^2 = \left(\frac{\hat{n}_o - \hat{n}_1}{\hat{n}_o + \hat{n}_1}\right)^2$$

$$\hat{r}_{01}^2 = \left\{\frac{[1 + i0] - [3.4 \mp 0.006 + i0.4 \mp 0.003]}{[1 + i0] + [3.4 \mp 0.006 + i0.4 \mp 0.003]}\right\}^2$$

$$\hat{r}_{01}^2 = \left\{\frac{-2.4 \mp 0.006 + i-0.4 \mp 0.003}{4.4 \mp 0.006 + i0.4 \mp 0.003}\right\}^2$$

$$\hat{r}_{01}^2 = \left\{\left[\frac{(-2.4 \mp 0.006 * 4.4 \mp 0.006) + (-0.4 \mp 0.003 * 0.4 \mp 0.003)}{(4.4 \mp 0.006)^2 + (0.4 \mp 0.003)^2}\right]\right.$$

$$\left. + i\left[\frac{(-0.4 \mp 0.003 * 4.4 \mp 0.006) + (-2.4 \mp 0.006 * 0.4 \mp 0.003)}{(4.4 \mp 0.006)^2 + (0.4 \mp 0.003)^2}\right]\right\}^2$$

$$\hat{r}_{01}^2 = \left\{\frac{10.72 \mp 0.03}{19.52 \mp 0.04} + i\,\frac{-0.8 \mp 0.02}{19.52 \mp 0.04}\right\}^2$$

$$\hat{r}_{01}^2 = (0.549 \mp 0.002 + i{-}0.041 \mp 0.001)^2$$

$$\hat{r}_{01}^2 = (0.549 \mp 0.002)^2 - (+0.041 \mp 0.001)^2 + i2(0.549 \mp 0.002 * -0.041 \mp 0.001$$

$$\hat{r}_{01}^2 = 0.300 \mp 0.002 + i{-}0.045 \mp 0.001$$

Errors for the other quantities in equation 3.55 have been calculated to give the systematic errors in n and k of water

$$n\ (50\ cm^{-1}) = 2.00 \mp 0.07 + i\ 0.48 \mp 0.02.$$

From Birch and Bennouna[44] the spectra of water obtained using the reflection technique have random errors for the refractive index and absorption index of ∓0.01 and ∓0.02 respectively. So systematic errors are greater than random errors for the refractive index data, whilst the systematic and random errors are the same for the absorption index data.

5.4 Conclusions.

The foregoing calculations have shown that for all the methods employed the systematic errors are predominant for refractive index determination and that random errors are the greatest for absorption coefficient determinations. This shows the importance of maintaining stable instrument dimensions during experiments and using a consistent method to measure liquid and instrument pathlengths, if accurate optical constant data is to be obtained.

C H A P T E R 6

THEORY

6.1 The Correlation Function Formalism

In chapter 1 the correlation function formalism was introduced, if we consider equation 1.4 in more detail, $\phi^{T}_{1R}(t)$ can be written as

$$\phi_{1R}(t) = \left\langle \sum_{i,j} \cos\theta_{ij}(t) \right\rangle \qquad \ldots\ldots \quad 6.1$$

$\phi_{1R}(t)$ is a cosine function of the angle between the permanent dipoles of two molecules i and j. The total microwave and far-infrared correlation function is given by[65]

$$\phi^{T}_{1R}(t) = \left\langle \sum_{i} [\cos\theta_i(o) \cdot \cos\theta_i(t)] \right\rangle + \left\langle \sum_{i \neq j} [\cos\theta_i(o) \cdot \cos\theta_j(t)] \right\rangle \qquad 6.2$$

'self' term — 'distinct' term

Equation 6.2 highlights one of the major problems in using the correlation function approach, that although the microwave and far-infrared band is free from vibrational relaxation, the 'distinct' term in equation 6.2 must be removed in order to obtain the single particle correlation function. A further problem of the far-infrared band is that it contains contributions due to collision induced dipole fluctuations due to solute-solute and solute-solvent collisions. The magnitude of this contribution to the far-infrared band is unknown, but attempts to quantitatively asses it have been made[66]. The correlation function is made up of two parts, a short time part (non-exponential) associated with the far-infrared, which is the initial

response of the system and is most sensitive to the molecular environment. Also a long time part (exponential) where the system has come to equilibrium, associated with the microwave region. Equation 1.14 can be simplified for low frequencies when $h\omega << kT$[21,67,68] giving

$$\phi^{T}_{1R}(t) = \frac{6kT}{8\pi^3 N\mu_o^2}\int_0^{\infty}\frac{D(\bar{\nu})\alpha(\bar{\nu})n(\bar{\nu})\exp(2\pi i\bar{\nu}ct)\,d\bar{\nu}}{\bar{\nu}^2} \qquad \ldots\ldots \quad 6.3$$

and the relaxation time of the correlation function is obtained from[65]

$$\tau^{T}_{1R} = \int_0^{\infty}\phi^{T}_{1R}(t)\,dt \qquad \ldots\ldots \quad 6.4$$

Another important feature of the microwave, far-infrared correlation function is that at zero time, a static correlation factor $g^{(1)}$ is obtained

$$\phi^{T}_{1R}(0) = g^{(1)} = \langle\sum_{i}[\cos\theta_i(0)\,.\,\cos\theta_j(0)]\rangle \qquad \ldots\ldots \quad 6.5$$

$g^{(1)}$ is obtained by integration of the microwave and far-infrared absorption cross section from[69,70]

$$g^{(1)} = \frac{1}{\mu^2_o}\frac{6hc}{4\pi^2 N}\int_0^{\infty}\frac{n(\bar{\nu})\alpha(\bar{\nu})D(\bar{\nu})\,d\bar{\nu}}{\bar{\nu}[1-\exp(-\frac{hc\bar{\nu}}{kT})]} \qquad \ldots\ldots \quad 6.6$$

6.2 Theories of Dielectric Relaxation.

Other methods of obtaining information on molecular motions from measurements of liquid absorption in the microwave far-infrared, involve theories for dipolar motion. The earliest attempt to do this was made by Debye[71].

6.2.1 Debye Theory for a Static Applied Field.

Debye[71] developed an expression for dipolar polarizability using the Langevin equation, which assumes there are no dipole-dipole forces, and the expression for the local field calculated by Lorentz, which assumes the molecules are distributed as for an ideal gas, giving the following expression for the total polarization

$$P = N_1 \left(P' + \frac{\mu^2}{3kT}\right)F \qquad \ldots\ldots \quad 6.7$$

where N_1 is the number of dipoles per unit volume
P' is the polarizability (N_1 F is the distortion polarization)
μ is the dipole moment
F is the electric field
k is the Boltzmann constant
T is the temperature in ^{o}K.

Since the applied field, and the field a molecule is experiencing are different (due to shielding and intermolecular forces), the local

field the molecule experiences must be calculated. To calculate the local field, a model of a molecule within a dielectric can be used. If we consider a dielectric between the parallel plates of a condenser, and imagine a single molecule within the dielectric about which is drawn a sphere, with dimensions that are large with respect to the molecule and small compared to the condenser plates. The dielectric outside the sphere can be considered to be homogeneous and of permittivity $\mathcal{E}_o$ and the dielectric within the sphere to be made up of individual molecules. The field the molecule experiences can then be divided into three parts as shown in Figure 6.1. They are the applied field F_1, the field due to polarization charges on the spherical surface F_2, and the field due to dipole-dipole interactions within the spherical region F_3, which will be zero in this instance as it is assumed there are no dipole-dipole forces.

From Hill[13]

$$F2 = \frac{4\pi P}{3\epsilon} \qquad \ldots\ldots \quad 6.8$$

where ϵ is the permittivity of free space giving an expression for the local field acting on the molecule of

$$F = F1 + F2 + F3 \qquad \ldots\ldots \quad 6.9$$

$$F = F1 + \frac{4\pi P}{3\epsilon} + 0$$

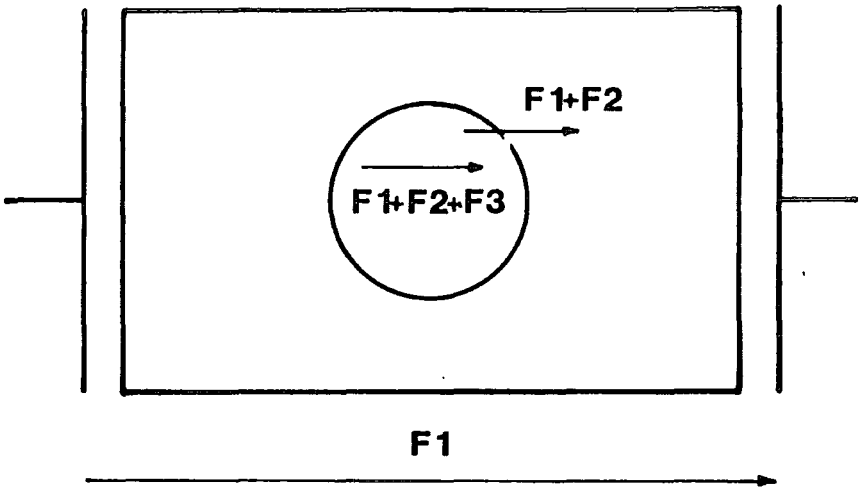

Figure 6.1 The Debye Local Field

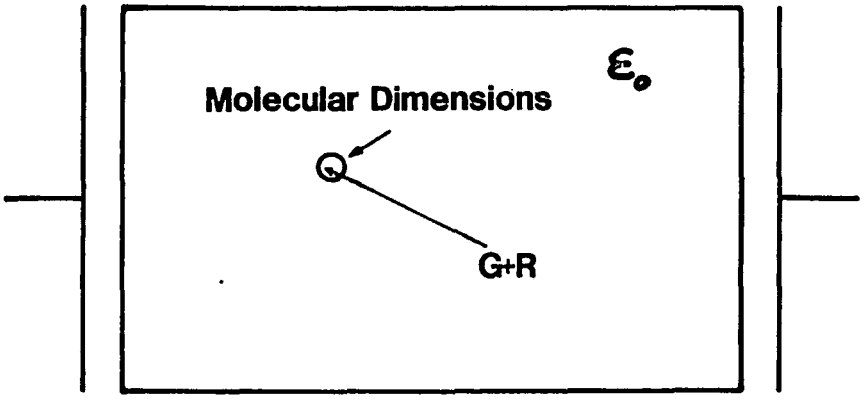

Figure 6.2 The Onsager Local Field

since

$$E_o = 1 + \frac{4\pi P}{\epsilon 1}$$

$$F = (E_o + 2)\frac{}{3} F1 \qquad \ldots\ldots \quad 6.10$$

Combining equations 6.7 and 6.10

$$\frac{\mathcal{E}_o - 1}{\mathcal{E}_o + 2} = \frac{4\pi N1(P' + \frac{\mu^2}{3kT})}{3\epsilon} \qquad \ldots\ldots \quad 6.11$$

where $\mathcal{E}_o$ is the static permittivity.

This is Debye's equation for static permittivity, the assumptions made in developing equations 6.7 and 6.10. Limit equation 6.11 to gases at low densities and dilute solutions of polar molecules in non polar solvents. A further difficulty of equation 6.11 is that it predicts ferroelectric behaviour due to the inadequacy of the Lorentz field to predict the local field in a dipolar dielectric. Onsager[14] improved equation 6.11 by using a more realistic model for the local field. He treated the molecule as a polarizable point dipole at the centre of a spherical cavity as in Figure 6.2. The cavity has molecular dimensions and is surrounded by a continuous medium of permittivity $\mathcal{E}_o$

The local field in the cavity can be split into two parts, the cavity field G from the external applied field, and the reaction field

R due to the dipole. These can be calculated for the Onsager model giving

$$\bar{G} = \frac{3\mathcal{E}_o}{2\mathcal{E}_o + 1} F \qquad \ldots\ldots \quad 6.12$$

and

$$\bar{R} = \frac{2(\mathcal{E}_o - 1)\bar{M}1}{2\mathcal{E}_o + 1a^3\epsilon} \qquad \ldots\ldots \quad 6.13$$

where a is the radius of the cavity defined by

$$\frac{4\ N_1 a^3}{3} = 1$$

and $\bar{M}$ is the total moment of the molecule. Using this model Onsager's equation for static permittivity is

$$\frac{(\mathcal{E}_o - \mathcal{E}_\infty)(2\mathcal{E}_o + \mathcal{E}_\infty)}{\mathcal{E}_o(\mathcal{E}_\infty + 2)^2} = \frac{4\pi N 1u^2}{9kT\epsilon} \qquad \ldots\ldots \quad 6.14$$

Onsager's equation does not predict ferroelectricity, but it is still assumed that there are no dipole-dipole interactions, i.e. $F_3 = 0$.

Two theories which include effects due to local forces, use statistical methods to calculate the dipolar polarizability and the local field. The Kirkwood[72] theory for non-polarizable dipoles is

$$\frac{(\varepsilon_o - 1)(2\varepsilon_o + 1)}{3\varepsilon_o} = \frac{4\ N\bar{M}M}{V\epsilon 3kT} \qquad \ldots\ldots\ 6.15$$

where N is the number of molecules
M is the electric moment of the molecule
$\bar{M}$ is the moment of the spherical cavity
V is the volume of the cavity

Frohlich[73] considers the z average and his equation for non-polarizable dipoles gives

$$\frac{(\varepsilon_o - 1)(2\varepsilon_o + 1)}{3\varepsilon_o} = \frac{4\pi N}{V\epsilon}\frac{\langle M.\bar{M}\rangle}{3kT} \qquad \ldots\ldots\ 6.16$$

The Kirkwood theory introduces a correlation parameter 'g', that is a measure of the local ordering, i.e. the 'static' angle between dipoles, (equivalent to $g^{(1)}$), $M = g\mu$ giving for equation 6.16

$$\frac{(\varepsilon_o - 1)(2\varepsilon_o + 1)}{3\varepsilon_o} = \frac{4\pi N\mu g}{V\epsilon 3kT} \qquad \ldots\ldots\ 6.17$$

Kirkwood accounts for distortion polarization by giving a polarizability of p' to each dipole and then uses Onsager's cavity field to give

$$\frac{(\varepsilon_o - 1)(2\varepsilon_o + 1)}{3\varepsilon_o} = \frac{4\pi N}{V\epsilon}\left(p' + \frac{g\mu^2_s}{3kT}\right) \qquad \ldots\ldots\ 6.18$$

where μ_s is the dipole moment in solution

$$\mu_s = \frac{(2\varepsilon_o + 1)(\varepsilon_\infty + 2)}{3(2\varepsilon_o + \varepsilon_\infty)}\,\mu_g \qquad \ldots\ldots \quad 6.19$$

Frohlich includes distortion polarization by assuming the dipoles are embedded in a polarizable continuum of permittivity ε_∞ giving

$$\frac{(\varepsilon_o - \varepsilon_\infty)(2\varepsilon_o + \varepsilon_\infty)}{\varepsilon_o(\varepsilon_\infty + 2)^2} = \frac{4\pi N g \mu^2}{9kTV\epsilon} \qquad \ldots\ldots \quad 6.20$$

If in Kirkwood's theory for distortion polarization the total local field were used instead of the cavity field equation 6.20 would be obtained.

6.3 Macroscopic-Microscopic Relationships.

In the theories presented it the previous sections, relationships between the experimentally measureable macroscopic parameters of a liquid system have been given. The problem for the experimentalist is to obtain information on the microscopic behaviour of molecules, from macroscopic measurements. This can be achieved through theories that have been developed in terms of the microscopic behaviour of a liquid system. Equations that have been developed to relate the microscopic relaxation time(τ_{mic}) of a molecule to the macroscopic (measured) relaxation time, are generally of the form

$$\tau_{mic} = D\tau_D \qquad \ldots\ldots \quad 6.21$$

where D is a correction factor that takes into account the local field and dielectric friction a single molecule is subjected to. This should include the shape of the cavity the molecule occupies and the forces acting on the cavity.

6.3.1 Debye's Diffusive Theory of Relaxation.

From Hill[13], Debye based his theory on Einstein's theory of Brownian motion. He considered the rotation of molecules to be interrupted by collisons with their neighbours and that the effect of these collisions could be described by a resistive couple proportional to the angular velocity of the molecule. The calculations were simplified for a molecule subject to a time dependent electric field E, by supposing the dipole axis rotates in a fixed plane that contains the direction of E as in Figure 6.3. Where the orientation of the molecule with respect to the applied field can be specified by and

If Figure 6.3 is considered to be a macroscopic system, the fraction of molecules in the angular interval $(\theta, \theta+d\theta)$ will be $f(\theta, t)d\theta$. Since all molecules specified by ϕ will be circularly symmetrically orientated they can be considered to behave as an ensemble and can be

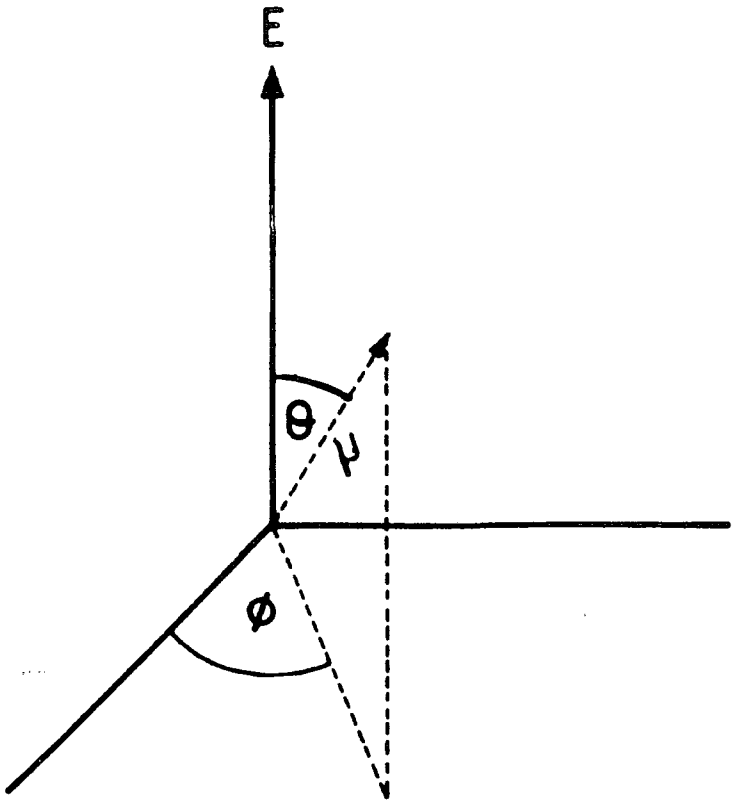

FIGURE 6.3 DIPOLE ROTATION IN A FIXED PLANE

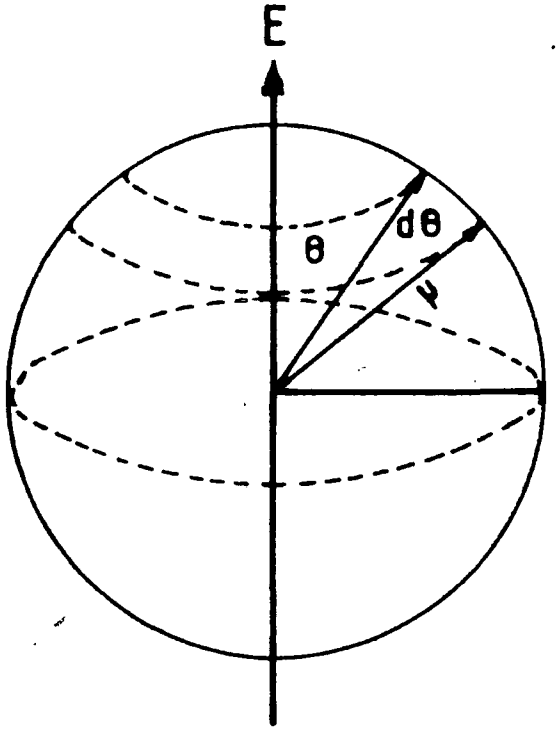

FIGURE 6.4 ROTATION WITHIN A UNIT SPHERE

represented by a distribution of points on a unit sphere as in Figure 6.4. Assuming that in the absence of an applied field the molecules follow a diffusive law, and if J_θ is the number of polar molecules which pass, in unit time, across unit length of the latitude θ = constant, in the direction of increasing θ, then

$$J_\theta = \underbrace{-K\frac{\partial f}{\partial \theta}}_{\text{DIFFUSIVE PROCESS}} + \underbrace{f\langle\dot{\theta}\rangle}_{\text{EFFECT OF APPLIED FIELD}} \quad \ldots\ldots \quad 6.22$$

$\langle\dot{\theta}\rangle$ is the average terminal angular velocity which is dependent on the orienting couple and the resistive (frictional) constant . The equation of motion of a polar molecule with moment of inertia I, due to the field E and the resistive constant can be written as

$$I\ddot{\theta} = -\mu E\sin\theta - \zeta\dot{\theta} \quad \ldots\ldots \quad 6.23$$

At equlibrium $\ddot{\theta}$ will tend to zero, with the result that the resistive constant will balance the couple, equation 6.23 then becomes

$$\zeta\dot{\theta} = -\mu E\sin\theta$$

and for the ensemble

$$\zeta\langle\dot{\theta}\rangle = -\langle\mu E\sin\theta\rangle$$

which can be written as

$$\zeta \langle \dot{\theta} \rangle = -\frac{\partial U}{\partial \theta} \qquad \ldots\ldots \quad 6.24$$

where U is the couple energy $\underset{\sim}{\mu} \cdot \underset{\sim}{E} = \mu E \cos\theta$ which means essentially the potential energy is balanced by the resistive constant.

Substituting equation 6.24 in equation 6.22 for an equilibrium distribution where $J_\theta = 0$

$$-K\frac{\partial f}{\partial \theta} = f\frac{\partial U}{\partial \theta}$$

which can be solved to give

$$f = A\exp\left(\frac{-U}{K\zeta}\right) \qquad \ldots\ldots \quad 6.25$$

where A is a constant.

For an equilibrium distribution we can use the Boltzmann law

$$f = A\exp\left(\frac{-U}{kT}\right) \qquad \ldots\ldots \quad 6.26$$

giving

$$K = \frac{kT}{\zeta} \qquad \ldots\ldots \quad 6.27$$

We must now determine a differential equation to give the distribution function for the non-equilibrium case. Since for a unit sphere the

length of the line θ = constant is $2\pi \sin\theta$, the rate of increase in the number of polar molecules between θ and $\theta + d\theta$ will be

$$\frac{\partial}{\partial t}(2\pi\sin\theta \cdot f d\theta) = -\frac{\partial}{\partial\theta}(2\pi\sin\theta \cdot J\theta)d\theta \qquad \ldots\ldots \quad 6.28$$

which gives

$$\frac{\partial f}{\partial t} = \frac{1}{\zeta\sin\theta}\frac{\partial}{\partial\theta}\left(kT\sin\theta\frac{\partial f}{\partial\theta} + f\mu F\sin^2\theta\right) \qquad \ldots\ldots \quad 6.29$$

which is the same as the Debye three dimensional diffusion equation determined by McConnell[1].

Equation 6.25 can be simplified to

$$f = A\left(1 + \frac{\mu F\cos\theta}{kT}\right) \qquad \ldots\ldots \quad 6.30$$

For an alternating applied field

$$F = F_o \exp(i\omega t)$$

If in equation 6.29 $\mu F \ll kT$, a solution for the non equilibrium case will be

$$f = A\left(1 + \frac{B\mu F\cos\theta}{kT}\right) \qquad \ldots\ldots \quad 6.31$$

where B is a constant, which is determined by substituting equation

6.31 in 6.29 neglecting high order terms than the first giving

$$B = \frac{1}{1 + i\omega\tau_{mic}}$$

where $\tau_{mic} = \frac{\zeta}{2kT}$

substituting into equation 6.31 this gives a distribution function of

$$f = A\left(1 + \frac{1}{1 + i\omega\tau_{mic}} \frac{\mu F\cos\theta}{kT}\right) \quad \ldots\ldots \quad 6.32$$

giving an average moment for the molecules in the direction of the field of

$$\langle \eta\cos\theta \rangle = \frac{\mu^2 F}{3kT(1 + i\omega\tau_{mic})} \quad \ldots\ldots \quad 6.33$$

Assuming as for Debye's static theory that F is the Lorentz field with $\mathcal{E}_o$ replaced by the frequency varying $\hat{\mathcal{E}}(\omega)$ the polarization will be complex and given by

$$\hat{P}(\omega) = N1\left\{\alpha + \frac{\mu^2}{3kT\ (1 + i\omega\tau_{mic})}\right\} \frac{\hat{\mathcal{E}}(\omega) + 2E}{3} \quad \ldots\ldots \quad 6.34$$

and the permittivity equation will now be

$$\frac{\hat{\mathcal{E}}(\omega) - 1}{\hat{\mathcal{E}}(\omega) + 2} \frac{M}{\rho} = \frac{4\pi N}{3\epsilon}\left(\alpha + \frac{1}{1 + i\omega\tau_{mic}} \frac{\mu^2}{3kT}\right) \quad \ldots\ldots \quad 6.35$$

where ρ is the density and M the molecular weight.

For ω = o equation 6.35 becomes Debye's equation for static permittivity. Equation 6.35 can be rewritten in terms of ε_o and ε_∞ to give

$$\frac{\hat{\varepsilon}(\omega) - \varepsilon_\infty}{\varepsilon_o - \varepsilon_\infty} = \frac{1}{1 + i\omega\tau_D} \qquad \ldots\ldots \quad 6.36$$

where

$$\tau_D = \frac{\varepsilon_o + 2}{\varepsilon_\infty + 2}\tau_{mic} \qquad \ldots\ldots \quad 6.37$$

Equation 6.36 is the same as equation 6.10, showing that Debye's diffusive theory gives the same relationships for the frequency varying permittivity and loss as for the static theory. The diffusive theory has however introduced a microscopic relaxation time, which from equation 6.37 is smaller than the macroscopic relaxation time. So Debye's diffusive theory enables a microscopic property to be determined from the measureable macroscopic properties of the system. Various other relationships between τ_{mic} and τ_D have been derived[74,75,76,77,78] for example

$$\tau_{mic} = \frac{(\varepsilon_o + 2\varepsilon_\infty)}{2\varepsilon_o + \varepsilon_\infty}\tau_D \qquad \text{(Nee and Zwanzig)}^{75} \qquad \ldots\ldots \quad 6.38$$

$$\tau_{mic} = \frac{(2\varepsilon_o + 2\varepsilon_\infty)}{3\varepsilon_o}\tau_D \qquad \text{(Cole-Glar..um)}^{76,77} \qquad \ldots\ldots \quad 6.39$$

6.3.2 The Corresponding Micro-Macro Correlation Theorem

A different approach to determin molecular properties from dielectric relaxation data has been made by Kivelson and Madden[79]. They point out that theories incorporating "local fields" do not give true molecular properties as although the sample cavity may be molecular, macroscopic theories are used. Kievelson and Madden assume that the medium is isotropic, that linear response theory holds and that intermolecular relaxations can be neglected. They use linear response theory to relate the macroscopic correlation function, $\phi_M(t)$ to the frequency varying dielectric constant,and the 'corresponding micro-macro correlation theorem'[79] to relate $\phi_M(t)$ to the microscopic correlation function $\phi_S(t)$. Keyes and Kivelson[80] give an expression relating the relaxation time of the two correlation functions as

$$\tau_M = \tau_S \frac{(1 + Nf)}{(1 + N\dot{f})} \qquad \ldots\ldots \quad 6.40$$

where N is the number of molecules, f is an equlibrium correlation in the orientation of the dipoles. (1 + Nf) is the Kirkwood g factor or $g^{(1)}$ and $\dot{f}$ is a dynamic orientation correlation factor. This was applied by Kivelson and Madden for spherical samples in a vacum,

assuming $\dot{f}=0$ they obtained

$$\tau_s = \tau_m \frac{(\varepsilon_\infty + 2)(\varepsilon_o + 2)}{\varepsilon_o - \varepsilon_\infty} \left[\frac{N \langle \mu \rangle^2}{3kTV}\right] 4\pi \qquad \ldots\ldots 6.41$$

where <u> is the magnitude of the permanent molecule dipole moment in the liquid and is estimated from

$$\frac{N\langle\mu^2\rangle}{3kTV} = \frac{4.85\mu_o{}^2 p}{M\left(\frac{T}{300}\right)} \qquad \ldots\ldots 6.42$$

where p is the mass density and $\mu^2{}_o$ the mean squared molecule dipole moment in Debyes which can be obtained from the dilute gas value μ_o or for dilute solutions in nonpolar solvents from

$$\mu_o{}^2 = \lim_{c \to 0} \frac{[\varepsilon_o(c) - \varepsilon_\infty(c)]}{[\varepsilon_\infty(c) + 2][\varepsilon_o(c) + 2]} \left[16.4\left(\frac{T}{300}\right)\right] \frac{1}{c} \qquad \ldots\ldots 6.43$$

where c is the molar concentration.

6.3.3 Kluk's Theory for the Microscopic Relaxation Time

Kluk[81] considered long range and short range interactions. He derived a relationship between the single particle correlation time and the macroscopic correlation time (τ_{MM}), by applying Frohlich's model of liquid dielectrics.

$$\tau_{mm} = \left[\frac{\left(1 + \frac{\varepsilon_\infty}{2\varepsilon_o^2}\right)}{\left(1 + \frac{1}{2\varepsilon_o}\right)}\right]\tau_D = f[\varepsilon_o, \varepsilon_\infty]\tau_D \qquad \ldots\ldots \quad 6.44$$

Equation 6.44 covers long range forces, for MeI liquid $f[\varepsilon_o, \varepsilon_\infty] = 0.9466$,then using the Mori formalism[82] in the same way as Kivelson and Madden with the dynamical variables from Gierke[83] and Frohlich's dielectric model he obtains a relationship between τ_D and τ_{mic} for molecules with C_{2v} or higher symmetry, via

$$\tau_{mic} = \tau_{mm}\, K^{-1} \qquad \ldots\ldots \quad 6.45$$

where K is the Kirkwood coefficient for an ellipsoidal cavity

$$K = \frac{VkT}{Nu_g^2}\frac{(\varepsilon_o - \varepsilon_\infty)(2\varepsilon_o + 1)}{[1 + D(\varepsilon_\infty - 1)]^2\varepsilon_o} \qquad \ldots\ldots \quad 6.46$$

giving

$$\tau_{mic} = \left[\frac{\left(1 + \frac{\varepsilon_\infty}{2\varepsilon_o^2}\right)}{\left(1 + \frac{1}{2\varepsilon_o}\right)}\right] K^{-1}\tau_D \qquad \ldots\ldots \quad 6.47$$

6.4 Band Moments.

Gordon[68] has shown that the short time part of the correlation function can be represented in a power series in time. The coefficients of which are frequency moments of the spectrum, and each is an equilibrium property of the system. For a symmetric top molecule the first terms of the series are given by[84]

$$\phi^{T}_{1R}(t) = g^{(1)} - \frac{2\,kT}{I_B}\left(\frac{t^2}{2!}\right) + \left[8\left(\frac{kT}{I_B}\right)^2\left(1 + \frac{I_A}{I_B} + \frac{\langle o(v)^2\rangle}{k^2T^2}\right)\right]\frac{t^4}{4!} + \ldots \quad \ldots\ldots \quad 6.48$$

and

$$\phi^{T}_{1R}(t) = g^{(1)} - M2R\,\frac{t^2}{2!} + M4R\,\frac{t^4}{4!} + \ldots. \quad \ldots\ldots \quad 6.49$$

where I_A and I_B are the moments of inertia of the molecule parallel and perpendicular respectively to the C_3 axis, $\langle o(v)^2\rangle$ is the mean square torque on a molecule due to other molecules and M_{2R} and M_{4R} are the second and fourth moments of the spectrum. The second moment is a single molecule property dependent only on the temperature of the system, whereas the fourth moment contains a term reflecting the molecular environment of the molecule. For the microwave, far-infrared band the moments are given by[69]

$$MnR = \int_0^\infty I_{(\bar{\nu})}(\bar{\nu} - \bar{\nu}_o)^n \, d\bar{\nu} \qquad \ldots\ldots \quad 6.50$$

where $\bar{\nu}$ is the frequency in wavenumbers (cm^{-1}).

6.5 Models for Molecular Reorientation.

Using the fundimental laws of motion mathematical models can be developed that will describe the motion of a molecule. The effectiveness of these models is usually tested by using them to derive a property such as absorption coefficient or correlation function that can then be compaired to the same property derived from physical measurements. Debye's diffusive theory (see 6.3.1.1) is one such model.

6.5.1 Problems with Debye's Diffusive Theory.

From McConnell[1] equations for the refractive index and absorption coefficient, in terms of ε_o, ε_∞ and τ_D can be derived from equation 6.37 giving, for $\omega\tau_D >> 1$

$$n(\omega) = \varepsilon_\infty^{\frac{1}{2}} \left[1 + \frac{(\varepsilon_o - \varepsilon_\infty)(\varepsilon_o + 3\varepsilon_\infty)}{8\varepsilon_\infty^2 \omega^2 \tau_D^2} \right] \qquad \ldots\ldots \quad 6.51$$

$$\alpha(\omega) = \frac{\varepsilon_o - \varepsilon_\infty}{c\tau_D \varepsilon_\infty^{\frac{1}{2}}} \qquad \ldots\ldots \quad 6.52$$

The $n(\bar{\nu})$ and $\alpha(\bar{\nu})$ values obtained from equations 6.51 and 6.52 are shown schematically in Figure 6.5. As can be seen $n(\bar{\nu})$ follows the same form as for $\varepsilon'(\omega)$ in Figure 1.5 but after an initial rise $\alpha(\bar{\nu})$ attains a nearly constant value, known as the Debye plateau. Experimental measurements of $\alpha(\bar{\nu})$ in the far-infrared region do not show this plateau and in fact show a drop in α after a peak in the far-infrared. this shows the inadequacy of the Debye theory in predicting the far-infrared absorption.

6.5.2 Corrections to Debye's Diffusive Theory.

In developing his theory Debye made certain simplifications, which were:-

i. Neglect of Dipole-Dipole interactions for polar molecules.

ii. Neglect of effects due to inertia.

iii. Polar molecules were assumed to be spherical.

Taking these assumptions into account should improve the ability of Debye theory to predict the Far-infrared absorption. From McConnell[1], intermolecular interactions cannot be treated adequately at present, but effects due to inertia can be dealt with. In Debye's theory the effects due to inertia are neglected in equation 6.23 when $I\ddot{\Theta}$ is set to zero, Rocard[85] has corrected for this by rewriting equation 6.23 as

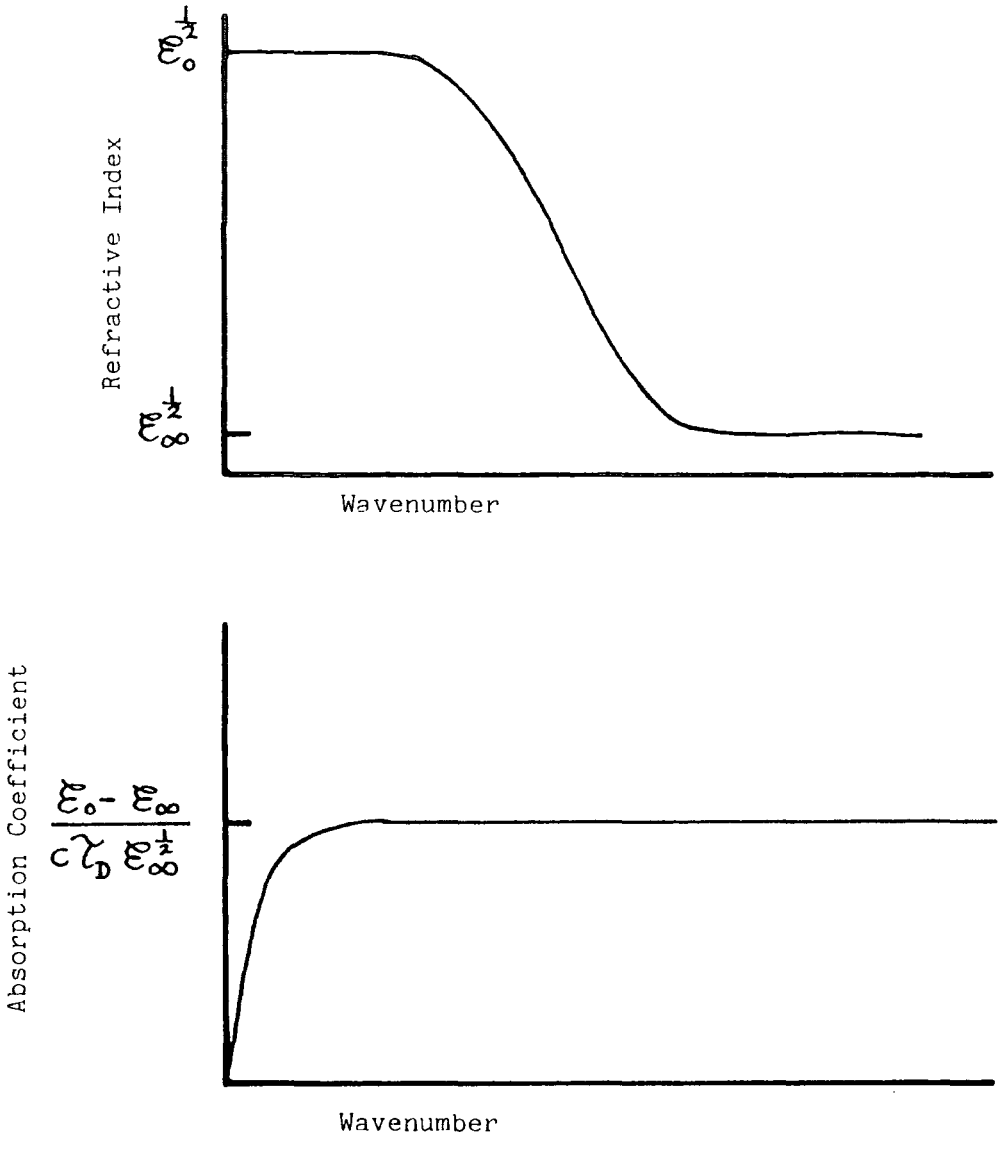

Figure 6.5 $n(\tilde{\nu})$ and $\alpha(\tilde{\nu})$ obtained from the Debye equation

$$I\ddot{\theta} = -\mu E_o \sin\omega t - \zeta\dot{\theta} \qquad \ldots\ldots \quad 6.53$$

which can be used to give a modified Debye equation of

$$\frac{\hat{\varepsilon}(\omega) - \varepsilon_\infty}{\varepsilon_o - \varepsilon_\infty} = \frac{1}{(1 + i\omega\tau_D)(1 + i\omega\tau_F)} \qquad \ldots\ldots \quad 6.54$$

where τ_F is the friction time defined by

$$\tau_F = \frac{I}{\zeta}$$

A similar correction was made by Powles[87] who expressed equation 1.21 as

$$I\ddot{\theta} = -\mu E_o e^{i\omega t} \sin\theta - \zeta\dot{\theta} \qquad \ldots\ldots \quad 6.55$$

This gives a corrected Debye equation of

$$\frac{\varepsilon(\omega) - \varepsilon_\infty}{\varepsilon_o - \varepsilon_\infty} = \frac{1}{(1 + i\omega\tau_D + (1 - \lambda)i\omega\tau_F - \tau_F\tau_D\omega^2)} \qquad \ldots\ldots \quad 6.56$$

where $0 < \lambda < 1$

Whilst these corrections do give a reduction in the intensity of α after the Debye α_{max} with increasing frequency, they still do not give the correct form of the Far-infrared absorption.

6.5.3 The Gordon M and J Diffusion Models

The Gordon M and J models[87] are essentually inertia corrected Debye models, in these models hard core instant collisions take place at random times. For the M-diffusion model these collisions randomise the direction of the angular momentum of the molecule and in the J-diffusion case both the direction and magnitude of the angular momentum are randomised. The number of collisions (n) between time 0 and time t is given by a Poisson distribution.

$$P(n,t) = \frac{1}{n!}\left(\frac{t}{t_c}\right)^n \exp\left(\frac{-t}{t_c}\right) \qquad \ldots\ldots \quad 6.58$$

where t_c is the mean time between collisions.

Brot[20] considers the J-diffusion model to be the most realistic of the two, but although the model fits microwave data well and gives a return to transparency in the far-infrared it does not fit experimental far-infrared data, as can be seen in figure 6.6.

6.5.4 The Mori Formalism.

The Mori Formalism is a model for moelcular reorientation developed by Evans and co-workers[67,82,84] by solving the generalised Langevin equation for molecular rotation of a dynamical array of interacting molecules. The microwave, far-infrared spectrum is

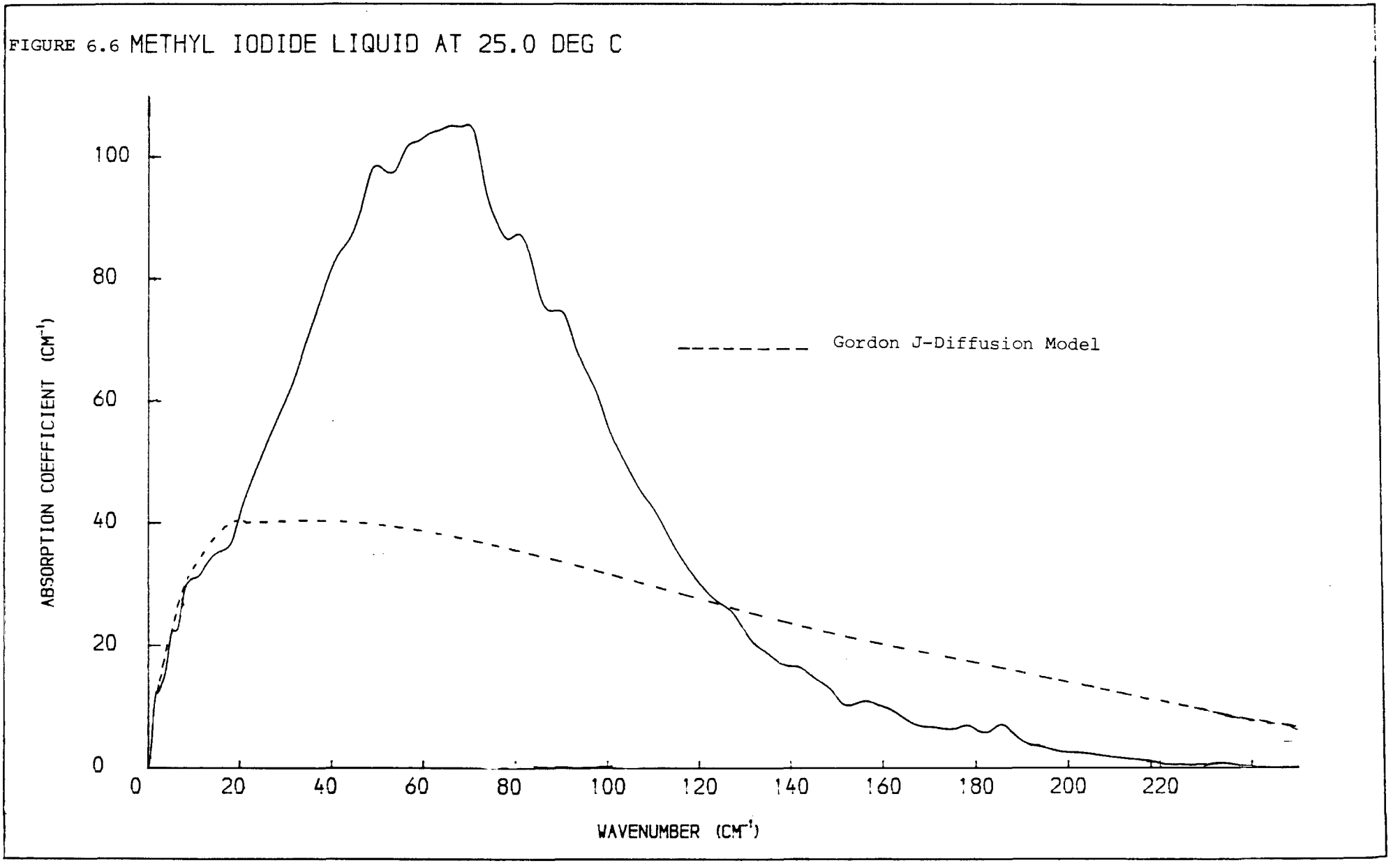
FIGURE 6.6 METHYL IODIDE LIQUID AT 25.0 DEG C
ABSORPTION COEFFICIENT (CM⁻¹)
WAVENUMBER (CM⁻¹)
Gordon J-Diffusion Model
0
20
40
60
80
100
120
140
160
180
200
220

deduced by approximating the associated orientational correlation function with a hierarely of response functions (memory functions), which with the correlation function form the Mori series. The Mori series is then truncated with an empirical function to give a spectrum containing equilibrium averages proportional to the intermolecular mean square torque. An excellent description of the calculations involved in developing the model for 2nd order truncation of the series has been given by James[9]. The general form of the Langevin equation is

$$u(t) + \int_{o}^{t} K_u^{n}(t - \tau_{mic})\ (\tau_{mic})\ d\tau_{mic} = \Gamma(t) \qquad \ldots\ldots\ 6.59$$

where $K_u^{n}(t)$ is a memory function.

For the rotational autocorrelation function

$$\dot{\phi}_u(t) = -\int_{o}^{t} K_u^{o}(t - \tau_{mic})\phi_u(\tau_{mic})\ d\tau_{mic} \qquad \ldots\ldots\ 6.60$$

and the Mori series representation for spectral density obtained by Laplace transformation is

$$\phi_u(p) = \frac{g(o)}{p + K_u^{o}(p)} = \frac{g(o)}{\dfrac{p + K_u^{o}(o)}{p + K_1(p)}} = \ldots. \qquad \ldots\ldots\ 6.61$$

where p is the Laplace variable ($i\omega$) 2nd order truncation of the Mori series using an exponential memory function of the form

$$K_u^1(t) = K_u^1(o) \exp(-\gamma t)$$

gives the absorption coefficient

$$\alpha(w) = \frac{A\omega^2 K_u^1(o) K_u^o(o) \gamma}{\gamma^2[K_u^o(o) - \omega^2]^2 + [\omega^3 - \omega(K_u^1(o) + K_u^o(o)]^2} \quad \ldots\ldots \quad 6.62$$

where

$$A = \frac{4\ N\mu^2}{3kTV} = \frac{\mathcal{E}_o - \mathcal{E}_{oo}}{n(\omega)c}\ (i)^2$$

and γ^{-1} is a torque relaxation time.

For a symmetric top or linear molecule the memory functions K_u^o and K_u^1 can be related to the band moments using equation 1.51 in the form[88]

$$\phi_{1R}(t) = g^{(1)} - a1\frac{t^2}{2!} + a2\frac{t^4}{4!} + \ldots\ldots \quad \ldots\ldots \quad 6.63$$

where

$$a1 = K_u^o \text{ and } a2 = K_u^1$$

So K_u^o is the second moment and K_u^1 is related to the intermolecular mean square torque through the fourth moment. Equation 1.55 is solved by least squares fitting with $K_u^o(o)$ fixed at the value of the

theoretical rotational second moment. From the theoretical and experimental n and α spectra presented in figures 7.67 and 7.68 this model would appear to give a very good fit to the far-infrared absorption.

6.5.5 The Gaussian Cage Model of Molecular Reorientation

The bend or kink seen in $\ln \phi^{T}_{1R}$ correlation functions (See figure 8.20), has been interpreted as being due to partial reversal of angular momentum[89]. This effect is ascribed to a molecule within a transient cage formed by the local liquid structure, moving to the edge in a certain time, where the torques acting on it will tend to reverse the angular momentum. A gaussian cage model that reproduces this effect has been developed by Lynden-Bell and Steel[89].The model is based on molecules with large intermolecular torques undergoing librations in a cage formed by the local liquid structure.the librations have a Gaussian distrobution of frequency with a width Δ and average frequency Ω_0. Using the method of Kubo[89] the correlation function ($C_L(t)$) is expressed in terms of a cumulant expansion

$$C_L(t) = \exp[K_L(t)] \qquad \ldots\ldots \quad 6.64$$

where $K_L(t)$ is the cumulant function.

K_L is calculated by using the Tokuyami and Mori generalised Langevin equation[89] for reorientation of linear or spherical top molecules giving

$$C_L(t) = \exp[-\int_0^t (t - \tau)\psi_L(\tau)\, d\tau] \qquad \ldots\ldots \quad 6.65$$

where ψ_L is the second derivative of the total cumulant function K_L with its sign reversed. To a first approximation

$$\psi_L = \frac{kT}{I} L(L+1)C_\omega(\tau) \qquad \ldots\ldots \quad 6.66$$

where $C_\omega(\tau)$ is the angular velocity autocorrelation function.

The Gaussian cage model gives a functional form for $\psi_L(t)$ for the hindered (high torque) limit, and $C_\omega(\tau)$ is modified for a range of librational frequencies giving

$$\psi_L(t) = L(L+1)\frac{kT}{I}\cos(\Omega_o t)\exp(-\frac{\Delta^2 t^2}{2}) \qquad \ldots\ldots \quad 6.67$$

where Δ and Ω_o are as previously defined.

and

$$ln C_L(t) = -L(L+1)\frac{kT}{I}\int_0^t (t-\tau)\cos(\Omega_o\tau)\exp(\frac{-\Delta^2\tau^2}{2})\, d\tau \qquad \ldots\ldots \quad 6.68$$

Experimental $ln \phi^T_{1R}(t)$ functions can be fitted to equation 6.68[90] to give the model parameters Ω_o and Δ, which describe the "Gaussian cages". The model also gives information on the intermolecular mean

squared torques from

$$\Omega_o^2 + \Delta^2 = \left\{ N^2 - a \right\} \frac{KT}{I} \qquad \ldots\ldots \quad 6.69$$

where a = 1 for spherical molecules and 2 for linear molecules, $(N^2>a)$ and N^2 is the intermolecular mean squared torque $< N^2 >$ for rotation about the x and y axes divided by $(KT)^2$.

C H A P T E R 7

RESULTS

7.1 Microwave Analysis.

Results for the attenuation coefficient (α') of methyl iodide in various solvents determined from microwave measurements are given in Tables 7.1 to 7.7. The microwave relaxation time τ_D was obtained from this data using a modified Fuoss-Kirkwood equation[63]

$$\nu \text{ Max} = \left[\frac{3\varepsilon_o + \varepsilon_\infty}{\varepsilon_o + 3\varepsilon_\infty}\right]^{\frac{1}{2}} \frac{1}{2\pi\tau_D} \qquad \ldots\ldots \quad 7.1$$

Where ν_{Max} is the frequency at which ε'' shows a maximum, and is evaluated from

$$\cosh^{-1}\left[\frac{(\alpha'/\nu)_{Max}}{\alpha'/\nu}\right] = \beta \ln\left(\frac{\nu_{Max}}{\nu}\right) \qquad \ldots\ldots \quad 7.2$$

where α'/ν is assumed to be proportional to ε'', giving the square rooted factor in equation 7.1 and β is an empirical parameter ($0<\beta<1$). A plot of the left hand side of equation 7.2 against $\ln(\nu)$ will give a straight line of gradient β, cutting the x axis at $\ln(\nu_{Max})$. Since the equation only holds for frequencies below ν_{Max} only values of α'/ν below $(\alpha'/\nu)_{Max}$ were used in the analysis. Plots of α'/ν against $\ln(\nu)$ and the corresponding plot from equation 7.2 are shown in Fig. 7.1. Since the square rooted term in equation 7.1 is very close to unity for MeI solutions (see Table 7.8), for solutions where values for ε_o or ε_∞ were not available, the following relationship

METHYL IODIDE AT 298 K

Concentration		Frequency		Attenuation Coefficient	Correlation Coefficient
mf	Mole l^{-1}	GHz	cm^{-1}	cm^{-1}	
1.00	16.049	7.20	0.240	0.2224	0.9968
		9.45	0.315	0.3320	0.9730
		11.68	0.390	0.5185	0.9991
		13.91	0.464	0.6909	0.9980
		15.75	0.525	0.8375	0.9952
		33.88	1.130	3.5207	0.9975
		69.86	2.330	16.6964	0.9961

METHYL IODIDE IN CARBON TETRACHLORIDE AT 298 K

Concentration		Frequency		Attenuation Coefficient	Correlation Coefficient
mf	Mole l^{-1}	GHz	cm^{-1}	cm^{-1}	
0.000	0.000	69.85	2.330	0.0240	0.9918
0.005	0.052	33.87	1.130	0.0181	0.9908
		69.83	2.329	0.0528	0.9986
		69.83	2.329	0.0500	0.9985
0.016	0.167	33.88	1.130	0.0482	0.9975
		69.85	2.329	0.1179	0.9997
0.162	1.781	6.95	0.232	0.0268	0.9970
		10.43	0.348	0.0474	0.9919
		12.08	0.403	0.0695	0.9930
		14.26	0.476	0.0986	0.9987
		16.56	0.552	0.1351	0.9952
		18.00	0.600	0.1472	0.9948
		33.88	1.130	0.4585	0.9996
		69.85	2.330	0.9107	0.9989
0.370	4.413	7.23	0.241	0.0700	0.9964
		9.83	0.328	0.1193	0.9949
		11.70	0.390	0.1580	0.9997
		13.65	0.455	0.2142	0.9986
		15.19	0.507	0.2621	0.9992
		16.73	0.558	0.3188	0.9989
		18.00	0.600	0.3429	0.9992
		33.88	1.130	1.0101	0.9971
		69.84	2.329	2.0833	0.9980
0.637	8.527	7.13	0.238	0.1192	0.9997
		8.84	0.295	0.1666	0.9917
		10.79	0.360	0.2579	0.9980
		11.83	0.394	0.3085	0.9997
		13.36	0.446	0.3930	0.9971
		14.63	0.488	0.4612	0.9999
		16.23	0.541	0.5582	0.9959
		18.00	0.600	0.6238	0.9994
		33.88	1.130	2.6102	0.9983
		69.85	2.330	4.5775	0.9978

METHYL IODIDE IN CARBON DISULPHIDE AT 298 K

Concentration		Frequency		Attenuation Coefficient	Correlation Coefficient
mf	Mole l^{-1}	GHz	cm^{-1}	cm^{-1}	
0.100	1.653	6.69	0.223	0.0236	0.9894
		8.52	0.284	0.0456	0.9849
		11.23	0.376	0.0515	0.9974
		13.15	0.437	0.0591	0.9959
		15.05	0.502	0.0794	0.9956
		33.88	1.130	0.3759	0.9989
		69.86	2.330	0.8370	0.9999

METHYL IODIDE IN n-HEPTANE AT 298 K

Concentration		Frequency		Attenuation Coefficient	Correlation Coefficient
mf	Mole l^{-1}	GHz	cm^{-1}	cm^{-1}	
0.005	0.034	33.87	1.130	0.0079	0.5854
		69.86	2.330	0.0265	0.9991
0.016	0.111	33.88	1.130	0.0302	0.9931
		69.86	2.330	0.0797	0.9993
0.162	1.219	7.69	0.257	0.0218	0.9932
		11.98	0.400	0.0442	0.9977
		14.60	0.487	0.0624	0.9994
		18.00	0.600	0.0836	0.9933
		33.88	1.130	0.3436	0.9995
		69.86	2.330	0.8958	0.9997
0.370	4.413	11.06	0.369	0.0704	0.9994
		12.58	0.420	0.0805	0.9984
		14.41	0.481	0.1122	0.9973
		15.63	0.521	0.1309	0.9981
		17.45	0.582	0.1465	0.9880
		34.20	1.130	0.5691	0.9991
		67.79	2.330	1.5829	0.9999
0.637	8.527	5.58	0.186	0.0488	0.9952
		10.09	0.337	0.1318	0.9091
		11.30	0.377	0.1714	0.9999
		12.52	0.418	0.2091	0.9994
		13.74	0.458	0.2274	0.9987
		14.96	0.499	0.2756	0.9996
		16.17	0.540	0.3193	0.9996
		34.20	1.130	1.4742	0.9928
		67.82	2.330	2.9903	0.9995
0.800	10.106	6.97	0.232	0.1373	0.9971
		9.61	0.321	0.2145	0.9920
		11.62	0.388	0.2746	0.9984
		13.22	0.441	0.3404	0.9934
		14.57	0.486	0.4370	0.9971
		16.23	0.541	0.5463	0.9984
		18.00	0.600	0.6123	0.9991
		33.88	1.130	2.4143	0.9970
		69.86	2.330	5.0494	0.9990

7.5

METHYL IODIDE IN n-DECANE AT 298 K

Concentration		Frequency		Attenuation Coefficient	Correlation Coefficient
mf	Mole l^{-1}	GHz	cm^{-1}	cm^{-1}	
0.005	0.0026	69.86	2.330	0.0417	0.9818
0.016	0.083	33.88	1.130	0.0353	0.9450
		33.88	1.130	0.0286	0.9836
		69.86	2.330	0.0592	0.9994
0.162	0.9341	11.76	0.392	0.0302	0.9959
		14.18	0.473	0.0344	0.9973
		15.65	0.522	0.0424	0.9902
		33.88	1.130	0.1928	0.9966
		69.86	2.330	0.5217	0.9998
0.370	4.413	10.54	0.352	0.0610	0.9761
		11.76	0.392	0.0686	0.9985
		12.98	0.433	0.0763	0.9992
		14.20	0.474	0.0939	0.9967
		15.41	0.514	0.1077	0.9995
		16.57	0.553	0.1277	0.9935
		34.20	1.130	0.5508	0.9989
		67.82	2.330	1.0510	0.9988
0.637	8.527	5.67	0.189	0.0442	0.9986
		10.54	0.352	0.1223	0.9997
		11.76	0.392	0.1621	0.9999
		13.59	0.453	0.2188	0.9995
		15.17	0.506	0.2523	0.9997
		16.27	0.543	0.2884	0.9993
		17.85	0.595	0.3200	0.9969
		34.20	1.130	1.1582	0.9975
		67.82	2.330	2.0880	0.9997
0.800	10.106	11.76	0.392	0.2674	0.9998
		12.80	0.427	0.3205	0.9963
		14.23	0.475	0.3983	0.9989
		15.50	0.517	0.4370	0.9999
		16.97	0.566	0.5754	0.9994
		34.20	1.130	3.2744	0.9971
		67.65	2.330	1.7171	0.9985

7.6

METHYL IODIDE IN n-HEXADECANE AT 298 K

Concentration		Frequency		Attenuation Coefficient	Correlation Coefficient
mf	Mole l^{-1}	GHz	cm^{-1}	cm^{-1}	
0.016	0.083	34.20	1.13	0.0235	0.9999
		67.26	2.33	0.0520	0.9993
0.162	0.9341	34.20	1.13	0.1337	0.9985
		67.26	2.33	0.3201	0.9999
0.370	4.413	11.97	0.3994	0.0358	0.9981
		15.50	0.5172	0.0563	0.9960
		34.20	1.13	0.2547	0.9999
		67.26	2.33	0.6004	0.9985
0.637	8.527	11.91	0.3974	0.1232	0.9989
		13.86	0.4624	0.1782	0.9972
		15.44	0.5151	0.2112	0.9988
		16.78	0.5598	0.2587	0.9916
		34.20	1.13	0.9421	0.9999
		67.26	2.33	1.8963	0.9995
0.800	10.106	11.73	0.3913	0.2237	0.9996
		12.95	0.4319	0.2692	0.9984
		14.59	0.4867	0.3303	0.9991
		16.11	0.5375	0.3740	0.9991
		17.18	0.5730	0.4571	0.9974
		34.20	1.13	1.4735	0.9981
		67.26	2.33	3.3998	0.9967

7.7

METHYL IODIDE IN SANTOTRAC 40

Concentration % V/V	Frequency GHz	Frequency cm^{-1}	Attenuation Coefficient cm^{-1}	Correlation Coefficient
0.00	67.67	2.2570	0.0287	0.9984
0.25	67.67	2.2570	0.0500	0.9998
0.50	67.67	2.2570	0.7170	0.9998
5.00	34.20	1.1410	0.1944	0.9989
	67.67	2.2570	0.3917	0.9999
25.00	11.79	0.3933	0.1488	0.9983
	13.01	0.4339	0.1839	0.9978
	14.23	0.4745	0.1978	0.9953
	16.05	0.5354	0.2568	0.9976
	34.20	1.1410	0.9526	0.9972
	67.67	2.2570	1.8171	0.9996
50.00	11.79	0.3933	0.2774	0.9996
	13.62	0.455	0.3661	0.9986
	15.44	0.514	0.4385	0.9999
	16.97	0.566	0.4736	0.9944
	34.20	1.1410	1.6381	0.9988
	67.67	2.2570	4.1689	0.9987
80.00	11.79	0.3933	0.4235	0.9998
	13.01	0.4339	0.5208	0.9969
	14.83	0.4948	0.6747	0.9987
	16.30	0.5436	0.7588	0.9983
	34.20	1.1410	6.2409	0.9973
	67.67	2.2570	6.6617	0.9929

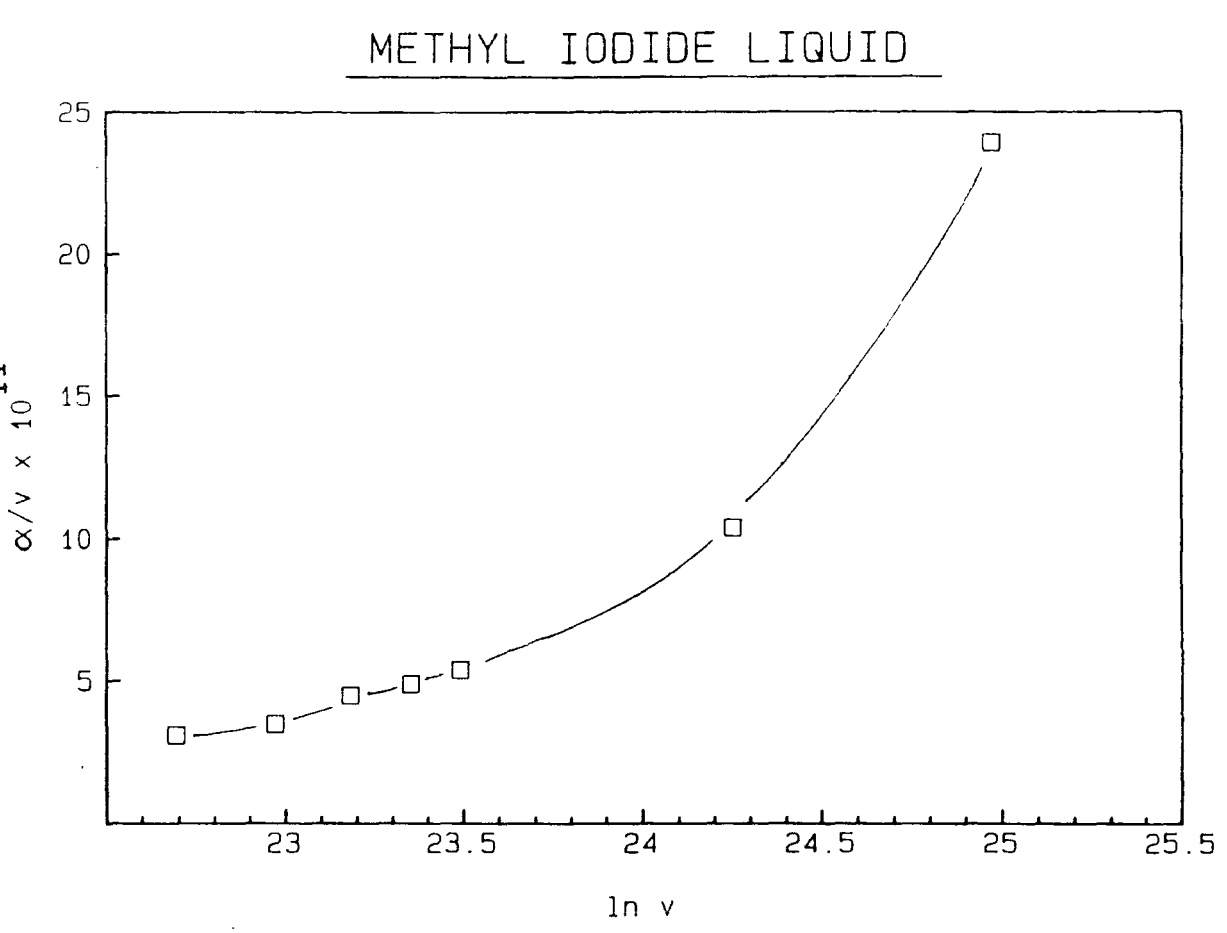

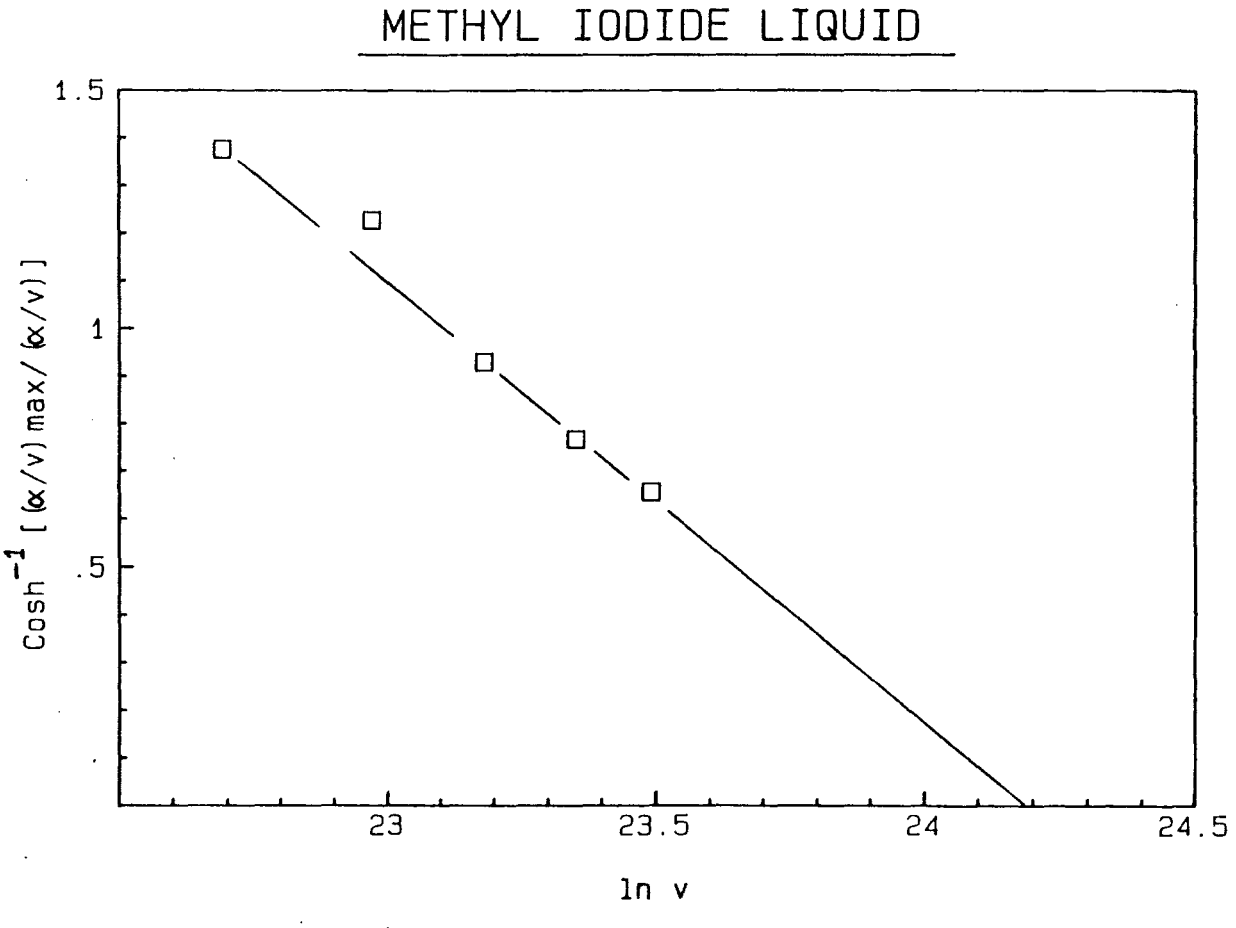

Figure 7.1 α/ν against $\ln\nu$ and corresponding plot from Equ. 7.2

was used.

$$\nu_{Max} = \frac{1}{2\pi\tau_D}$$

Where ε'' data was available for the microwave and far-infrared regions (see Section 7.4), ν_{Max} from the peak in ε'' was measured directly and used to calculate τ_D using an unmodified Fuoss Kirkwood equation. Values of τ_D for the above methods are given in Table 6.8. and values of ε_o and ε_∞ are given in table 7.9

7.2 Far-Infrared Data.

Using the theory and techniques given in Chapters 3 & 4, the optical constants of MeI in the same range of solvents used in section 6.1, were determined. The far-infrared region covered was from 3 to 200 cm^{-1}, using three ranges. These were approximately 3 to 15 cm^{-1} (cooled detector), 10 to 40 cm^{-1} (cooled detector) and 20 to 200 cm^{-1} (Golay detector). These ranges were joined together in the overlap regions to give complete far-infrared spectra as in Figures 7.2. and 7.3. In all cases any mismatch between the individual spectra was less than the experimental error (see Chapter 5).

RELAXATION TIMES OF MeI

Solvent	Concentration mf	τ_D ps	β	τ_{OBS} ps	$\tau_{D‡}$ ps	β‡
	1.0	1.8	0.79	4.1	5.0	0.92
	0.005			1.1		
	0.016			1.2		
	0.162	1.9	0.99	1.3	3.4	0.8
n-HEPTANE	0.370	1.9	1.00	1.3	3.8	1.0
	0.670	2.9	1.07		4.3	1.0
	0.800	2.8	1.05		4.6	1.0
	0.016			1.2		
	0.162	2.1	1.00	1.9	2.1	1.0
n-DECANE	0.370	3.4	1.25	2.32	3.4	1.1
	0.670	2.9	1.07		3.5	0.9
	0.800	2.0			4.5	1.0
	0.016			2.7		
	0.162			1.4		
	0.370	2.3	1.00	1.4	2.3	1.0
n-HEXADECANE	0.637	2.3	1.00		3.1	1.1
	0.800	2.3	0.93		3.8	1.0
	25.0*	2.5	0.98		3.5	1.0
SANTOTRAC 40	50.0*	1.7	0.80		6.9	1.0
	80.0*	1.2	0.80		7.9	1.5
	0.162	3.43	1.09	3.3	2.2	0.8
CARBON TETRACHLORIDE	0.370	3.1	0.95		3.1	1.0
	0.637	2.3	0.89		5.2	1.1
CARBON DISULPHIDE	0.100	2.5	0.90	3.1	2.5	0.9

‡ 72 + 36 GHz points removed.

* Concentration in Vol % CH_3I

7.9

DILECTRIC PROPERTIES OF MeI

Solvent	Concentration mf	ϵ_o	ϵ_∞	$\epsilon_o - \epsilon_\infty$
	1.0	6.850	2.936	3.914
n-HEPTANE	0.005	1.015	1.005	0.010
	0.016	1.040	1.010	0.030
	0.162	1.461	1.099	0.362
	0.370	1.900	1.234	0.666
n-DECANE	0.016	1.048	1.017	0.031
	0.162	1.281	1.062	0.219
	0.370	1.530	1.069	0.461
n-HEXADECANE	0.016	1.022	1.006	0.016
	0.162	1.218	1.049	0.169
	0.370	1.337	1.095	0.242
CARBON TETRACHLORIDE	0.162	1.459	1.136	0.323
CARBON DISULPHIDE	0.100	1.537	1.268	0.269

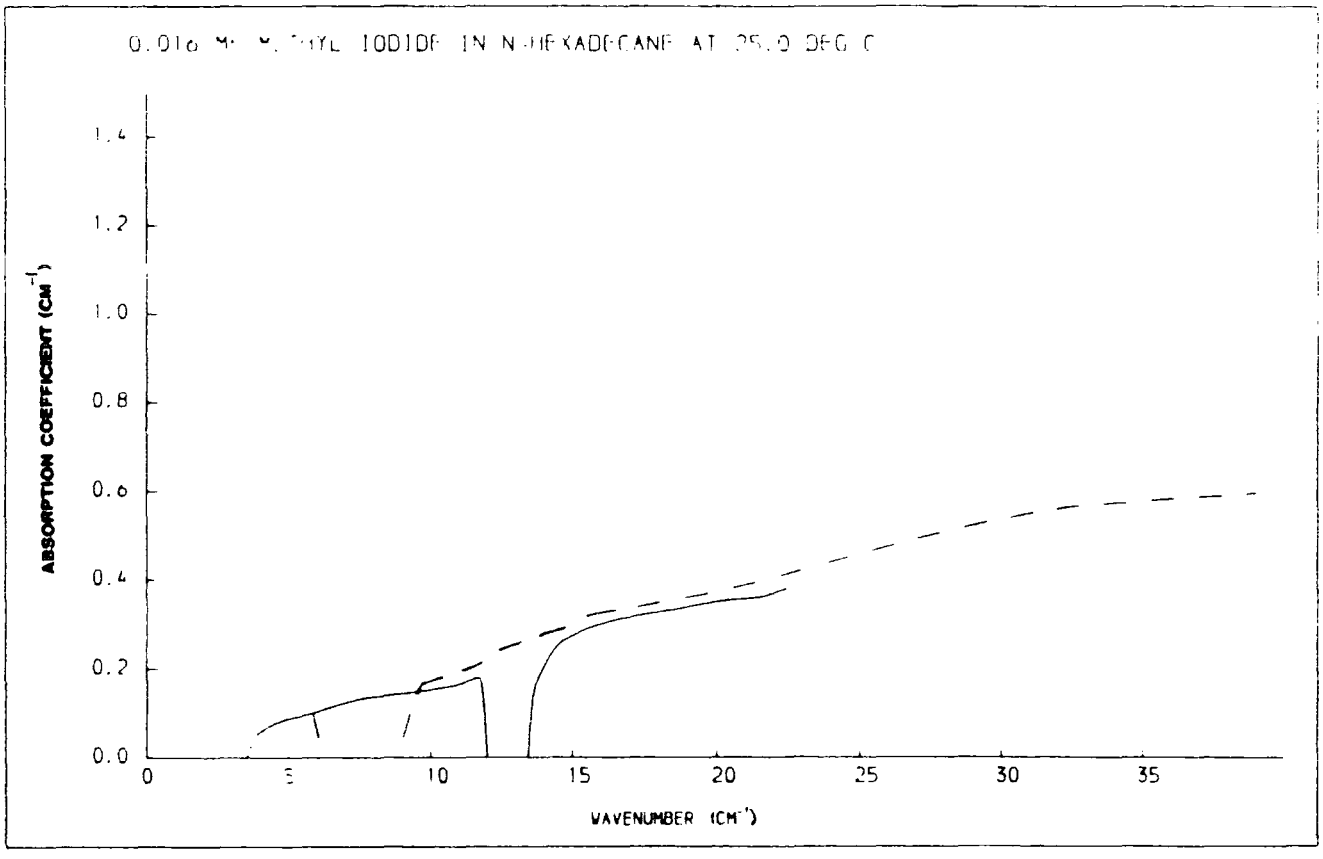

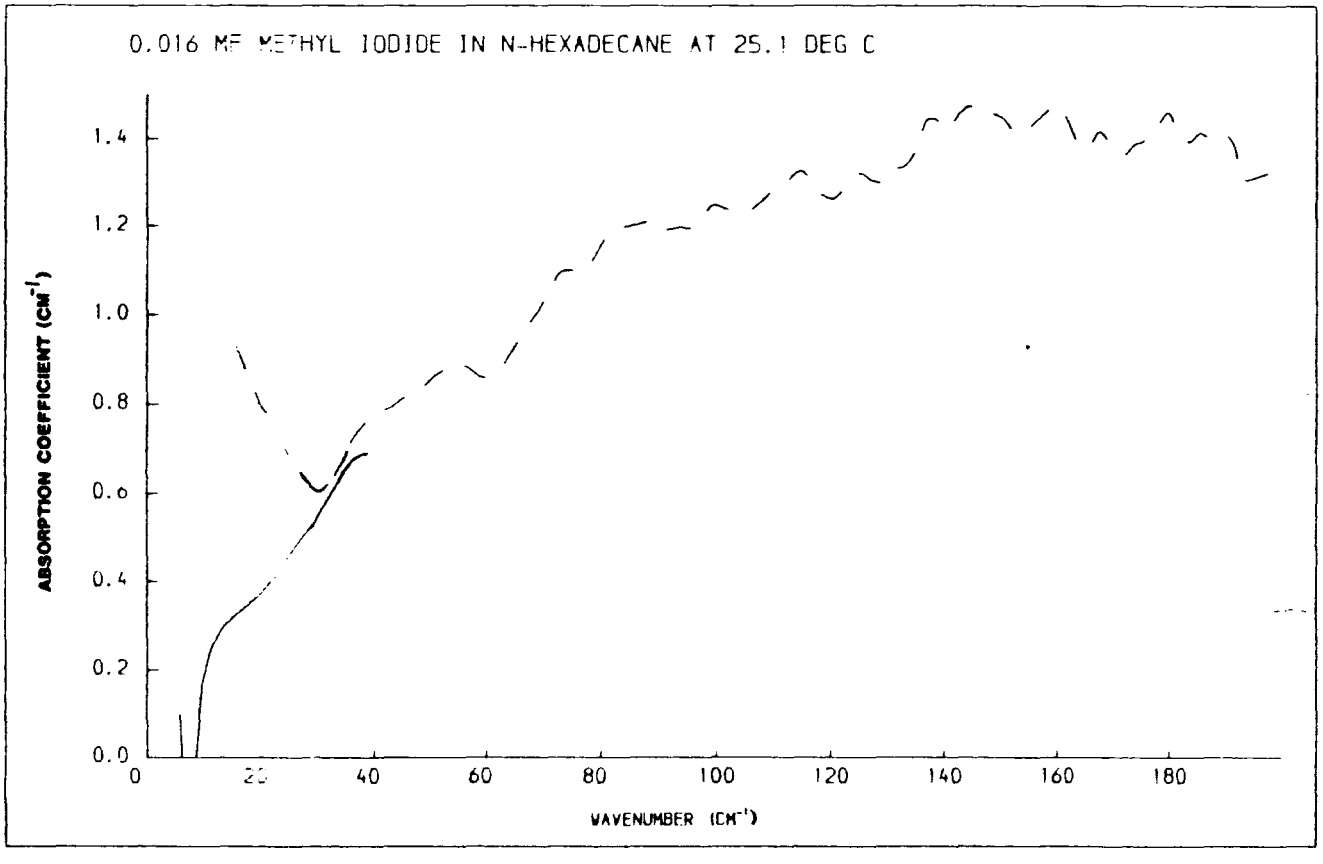

Figure 7.2 Joining of n and α spectra

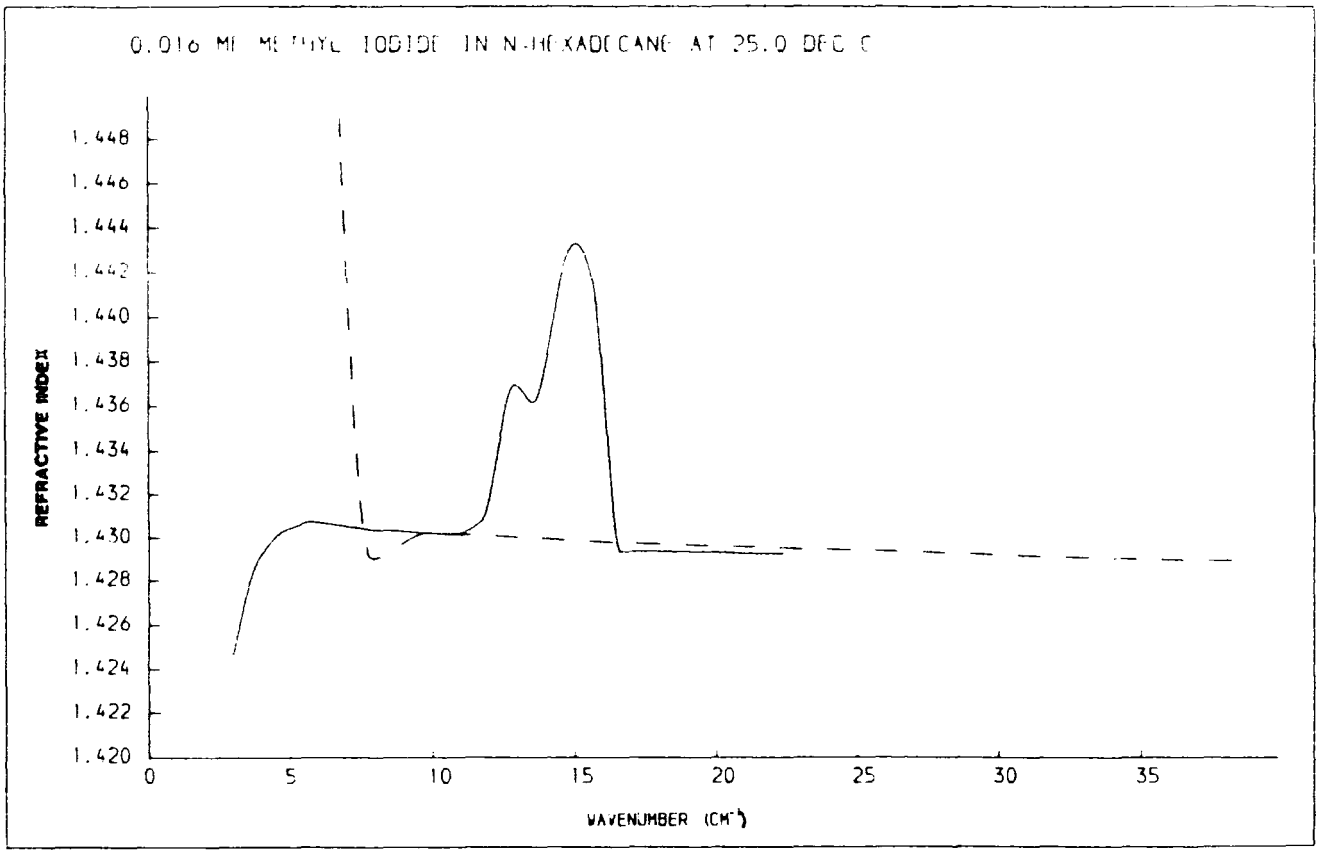

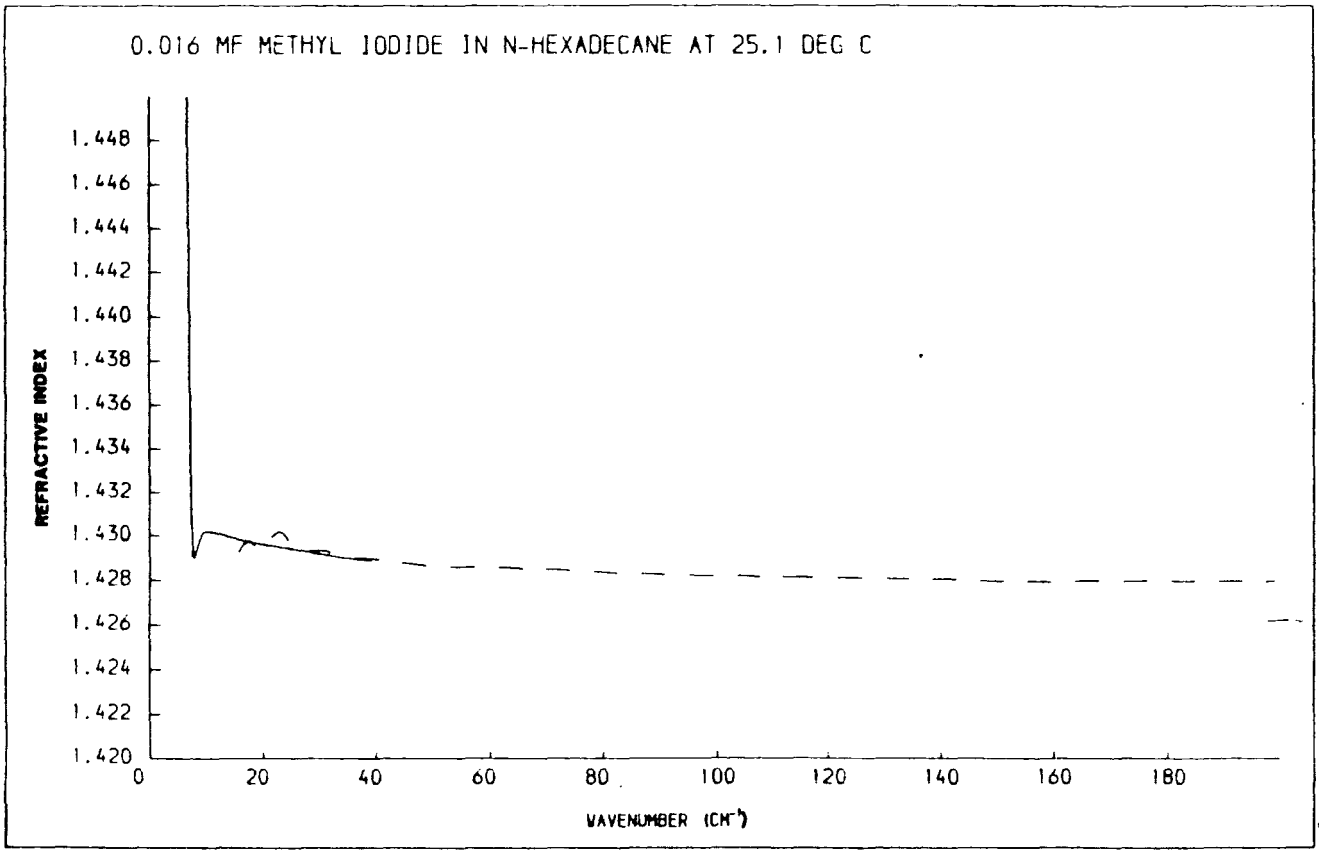

Figure 7.3 Joining of n and α spectra

7.3 Combination of Far-Infrared and Microwave Data.

Before analysis of the far-infrared and microwave spectra could take place, data from the two regions had to be combined, and the solvent contribution to the solution data removed.

7.3.1 Joining of Microwave and Far-Infrared Spectra.

The frequency ranges of the recorded microwave and far-infrared spectra were such that there was no overlap between the two regions. Depending on the solution measured the upper limit of the microwave data was approximately 2 cm^{-1} and the far-infrared data extended down to approximately 3 cm^{-1}, In order to carry out Hilbert[21] or Fourier transforms on the combined data, (see Sections 7.3.3 & 7.4.2), the complete frequency range must be sampled at a constant frequency interval and contain no gaps. The far-infrared data was sampled at a constant interval but the microwave data was at random frequency intervals. To overcome both of these problems the microwave and far-infrared data were combined and an interpolation carried out[8] to resample the data at a constant interval. The accuracy of the interpolation procedure was such that the interpolated data compared exactly with the uninterpolated data. The effects due to interpolating across the gap between the microwave and far-infrared

regions on subsequent analysis have been assessed by Arnold[8] and will be discussed where relevant.

7.3.2 Subtraction of Solvent Contribution to Solution Spectra.

The refractive index and absorption coefficient spectra determined for the methyl-iodide solutions are made up of a solvent and solute contribution. Since we are studying the effect of the solvent on the solute and wish to compare pure liquid data to solution data, the solvent contribution must be removed from the solution data. In normal transmission Fourier transform-spectrometry this is achieved by using the solvent as a background and ratioing solution and solvent modulus spectra. This method can lead to errors, since generally the same pathlength is used for both measurements and the solvent will be oversubtracted from the solution. In DFTS experiments the solution and solvent spectra are determined separately. This enables the solvent data to be scaled to the "true" contribution to the solution data, before subtraction. From equation 3.12 the optical constants are made up of a phase term and an absorption term. Assuming the Ber-Lambert law holds, the absorption term for the solvent can be scaled to concentration and then subtracted from the solution absorption term

$$\mathfrak{E}_c'' = \mathfrak{E}_b'' - (\mathfrak{E}_a'' * C_a) \qquad \ldots\ldots \quad 7.4$$

where the subscripts a, b and c stand for solvent, solution and solute respectively and

$$C = \frac{\text{Number of solvent molecules in solution}}{\text{Number of solvent molecules in pure solvent}} \qquad 7.5$$

The procedure for scaling and subtraction of the phase term is not clear, but the following argument has been used to deal with this problem.

From Hill[13], for a liquid held between two parallel plates of a condenser, when an electric field is applied to the condenser

$$\mathcal{E}_o = 1 + \frac{4\pi P}{\epsilon E} \qquad \ldots\ldots \quad 7.6$$

If the liquid contains Ni molecules per unit volume and the average moment induced in each one due to polarization is M,

$$P = Ni\ M \qquad \ldots\ldots \quad 7.7$$

and for an average electric field E acting on each molecule

$$M = \alpha_T E \qquad \ldots\ldots \quad 7.8$$

where α_T is the total polarizability of the molecules and is made up of electronic, atomic and orientation contributions.

$$\alpha_T = \alpha_e + \alpha_a + \alpha_{or} \qquad \ldots\ldots \quad 7.9$$

If we limit this discussion to microwave and far-infrared frequencies the total polarizability can be simplified to

$$\alpha_T = \alpha_{or} \qquad \ldots\ldots \quad 7.10$$

Equation 7.6 now becomes

$$\mathcal{E}_o = 1 + \frac{4\pi N_i \alpha_{or} F}{E \epsilon} \qquad \ldots\ldots \quad 7.11$$

If we now measure the $\mathcal{E}_o$ of a solvent and solution, $\mathcal{E}_o{}^a$ and $\mathcal{E}_o{}^b$ these can be expressed in terms of equation 7.1 as follows

$$\mathcal{E}_o^a = 1 + \frac{4\pi N_i^a \alpha_{or}^a F}{\epsilon E} \qquad \ldots\ldots \quad 7.12$$

and

$$\mathcal{E}_o^b = 1 + \frac{4\pi N_i^b \alpha_{or}^b F}{\epsilon E} \qquad \ldots\ldots \quad 7.13$$

But we require $\mathcal{E}_o^c$ of the solute, so must remove the polarizability due to the solvent molecules in 7.13 since

$$N_i^b \alpha_{or}^b = N_i^c \alpha_{or}^c + N_i^a \alpha_{or}^a$$

The number of solvent molecules in equation 7.12 will be less than in equation 7.11, therefore ε_o of the solute will be

$$\varepsilon_o^c = 1 + (\varepsilon_o^b - 1) - \left\{(\varepsilon_o^a - 1) * C_a\right\} \qquad \ldots\ldots \quad 7.15$$

where C_a is as for equation 7.5.

Applying equation 7.15 to the frequency varying permitivity gives the general expression

$$\varepsilon_c'(\bar{\nu}) = 1 + (\varepsilon_b' - 1)(\bar{\nu}) - \left\{(\varepsilon_a' - 1) * C_a\right\}(\bar{\nu}) \qquad \ldots\ldots \quad 7.16$$

The removal of the solvent contribution to the optical constants of MeI solutions using equations 7.4 and 7.16 can be seen in Figs. 7.4 and 7.5. In carrying out this subtraction it is assumed that the solvent optical constants have not been changed by interaction with the solute; and the errors assosiated with the solute spectra are the sum of the errors for the solution and solvent spectra.

7.3.3 Kramers Kronig Analysis.

Measurements made in the microwave region were on attentuation only, therefore there was no permitivity data available for this region. To overcome this problem the Kramers Kronig relations[91,92] were used. These give

$$n(\bar{\nu}) - n_\infty = H\left\{k(\bar{\nu})\right\} \qquad \ldots\ldots \quad 7.17$$

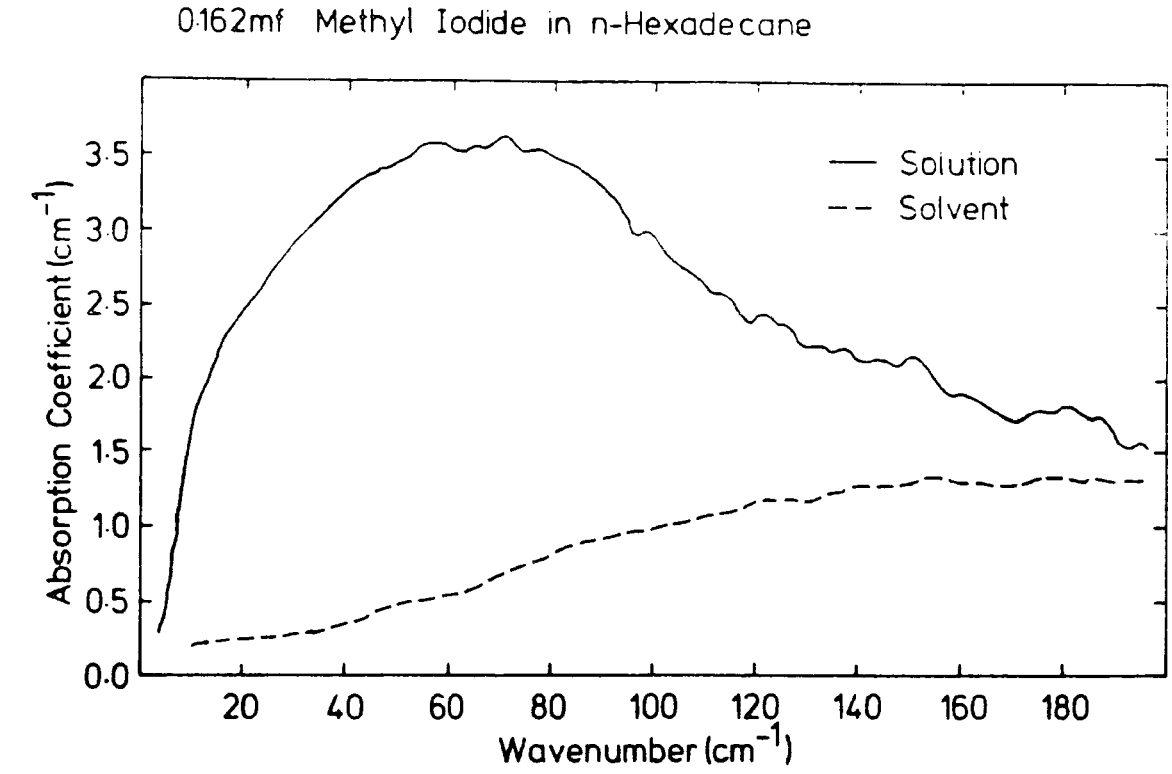

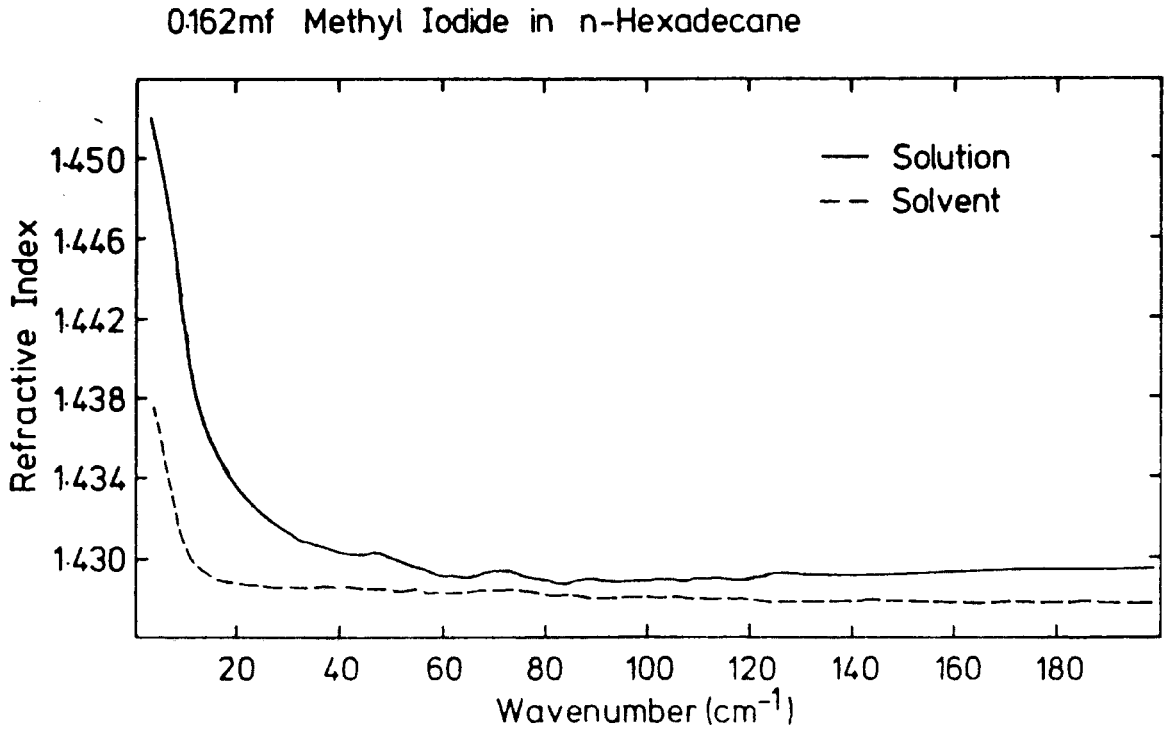

Figure 7.4 Subtraction of solvent

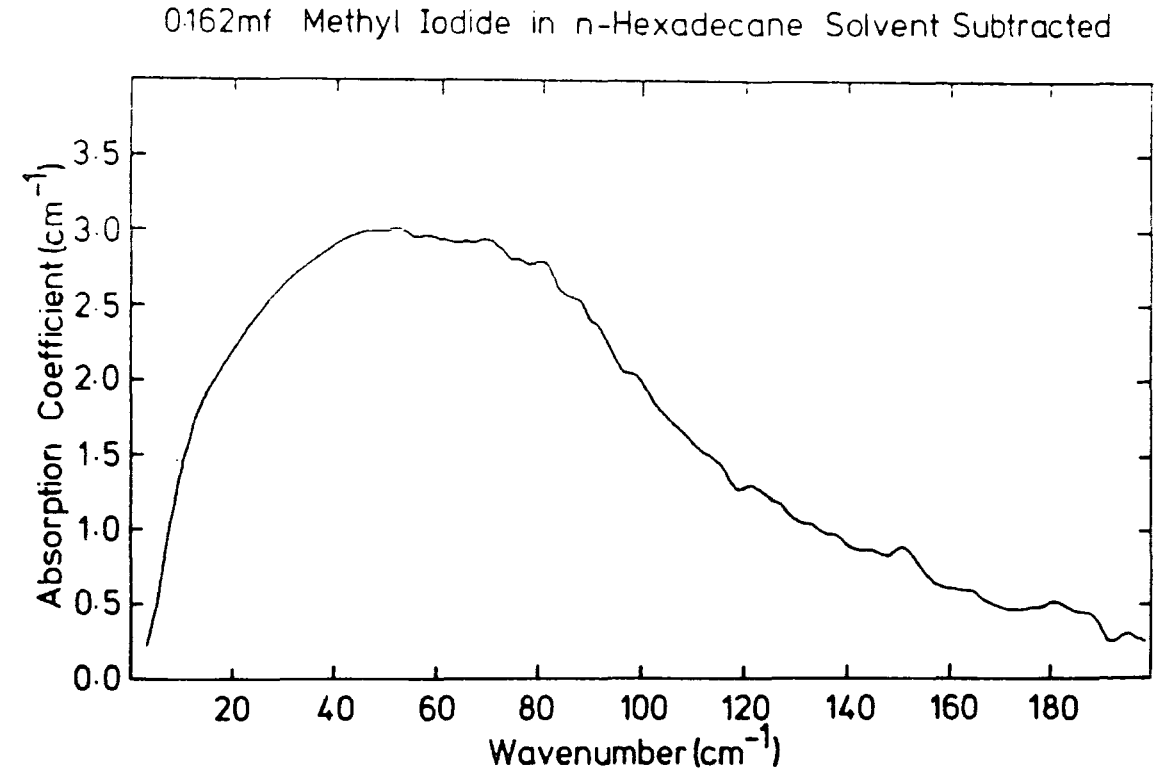

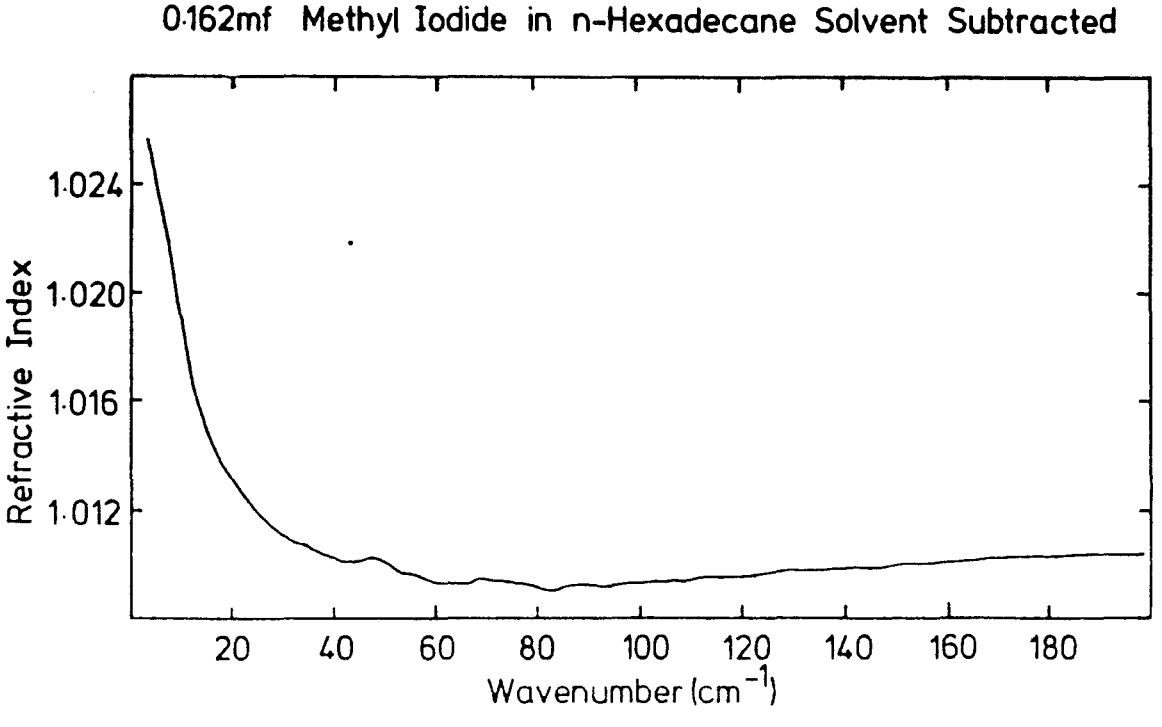

Figure 7.5 Solute Spectra

where H stands for Hilbert transformation of the bracketed function over the microwave and far-infrared region. n_{∞} is determined by using equation 7.17 with the measured refractive index at approximately 60 cm^{-1}, then by substituting the value of n_{∞} in equation 7.17 $n(\tilde{\nu})$ can be determined in the microwave region. The result of Hilbert transformation on $k(\tilde{\nu})$ for a 0.162 mf solution of MeI in n-heptane n-decane and n-hexadecane are shown in Figures 7.6 to 7.8 As can be seen the $n(\tilde{\nu})$ from equation 7.17 agrees very well with the measured $n(\tilde{\nu})$. The measured and calculated ε_0 values for 0.162 mf MeI in n-heptane of 1.461 and 1.475 respectively also agree very well. This supports Arnold's[8] method of fixing the $n(\tilde{\nu})$ level by using ε_0 values when no measured $n(\tilde{\nu})$ values are available.

7.4 Results from Combined Microwave and Far-Infrared Data.

The optical constant spectra for MeI and the solvents carbon tetrachloride, n-heptane, n-decane and n-hexadecane are shown in Figures. 7.9 & 7.14 and spectra for MeI in solvent solutions with the solvent contribution removed are shown in Figures. 7.15 to 7.35. From these and other solute spectra the following results were obtained.

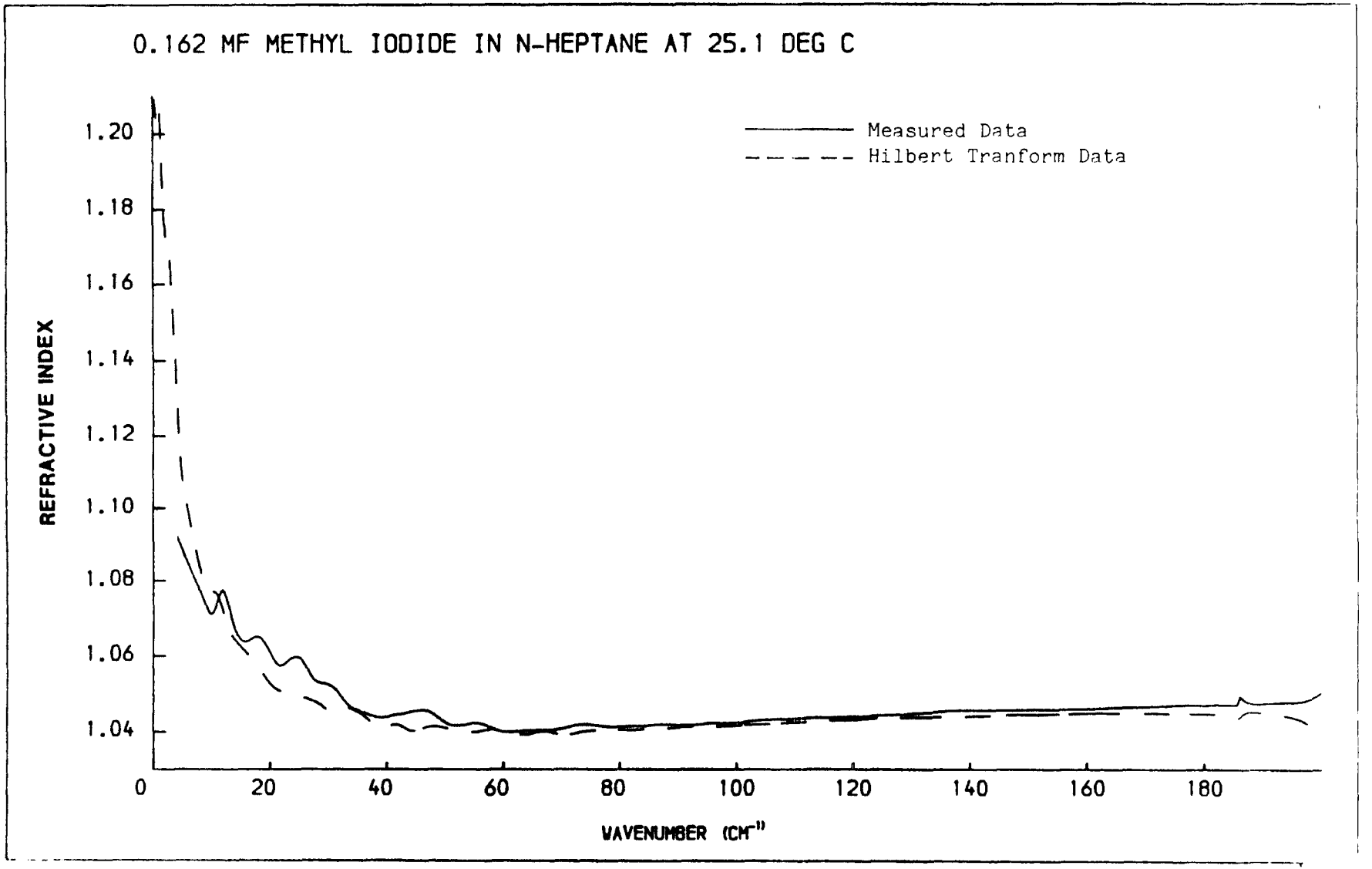

Figure 7.6 Kramers Kroning Results

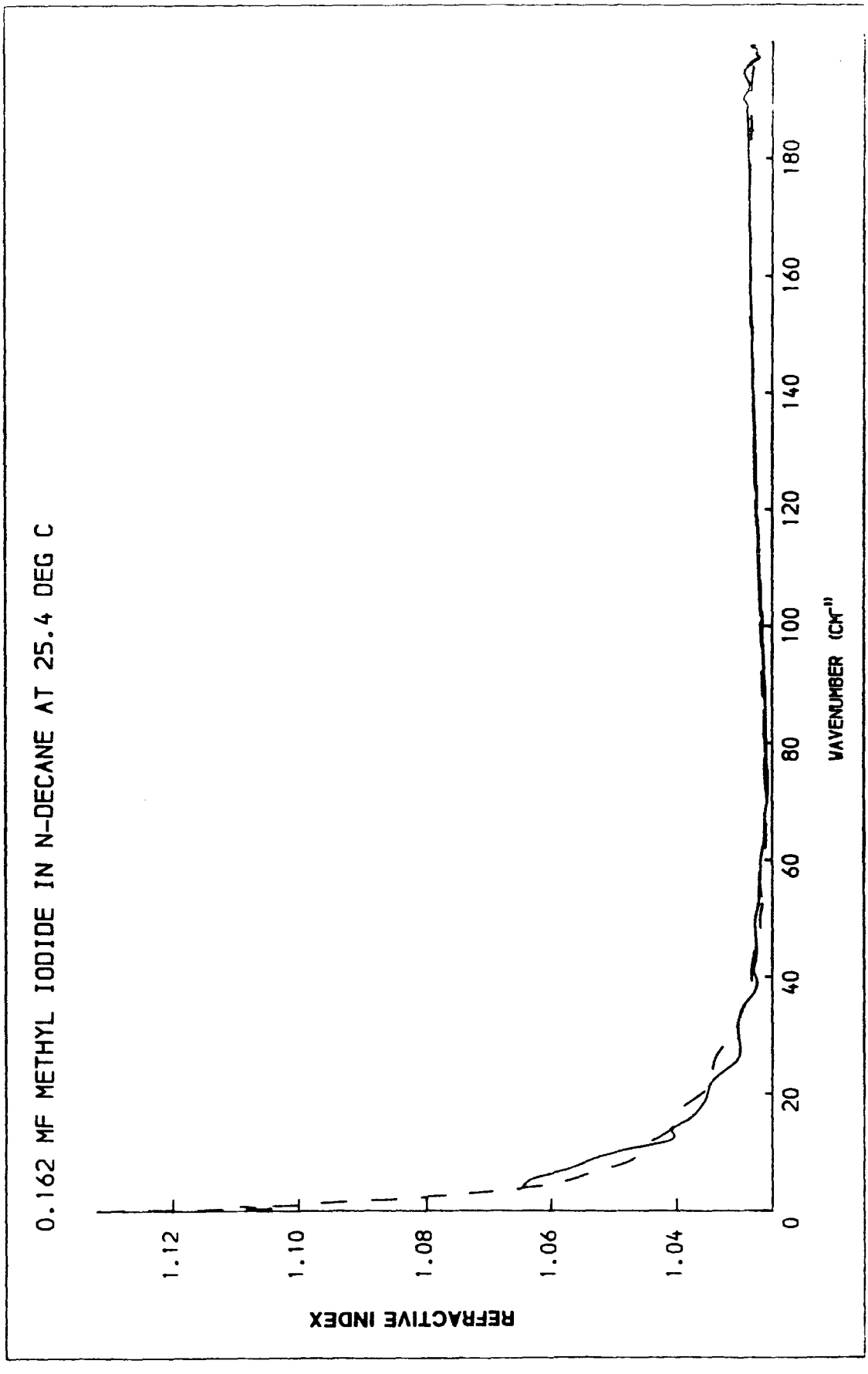

Figure 7.7 Kramers Kroning Results

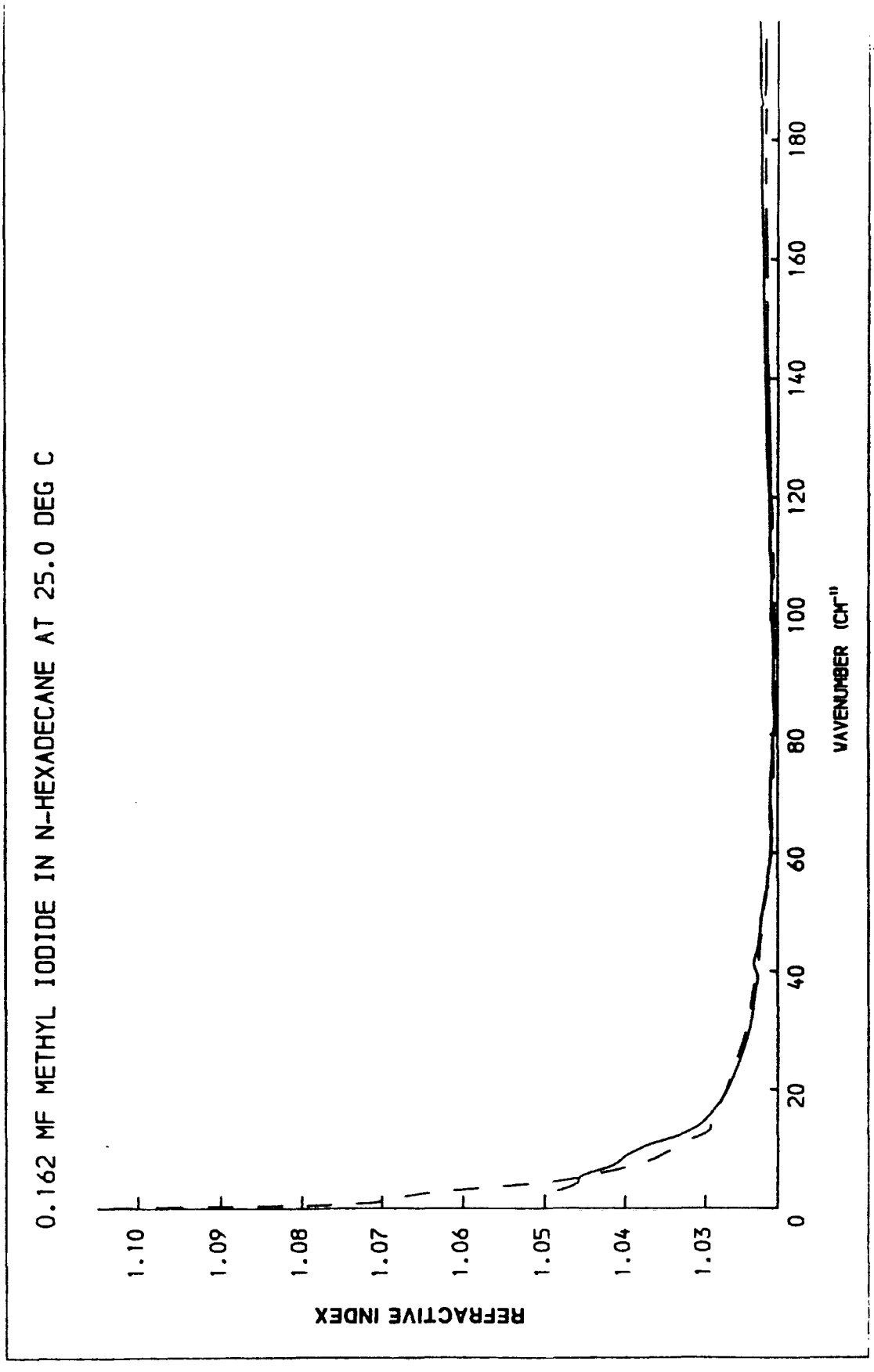

Figure 7.8 Kramers Kroning Results

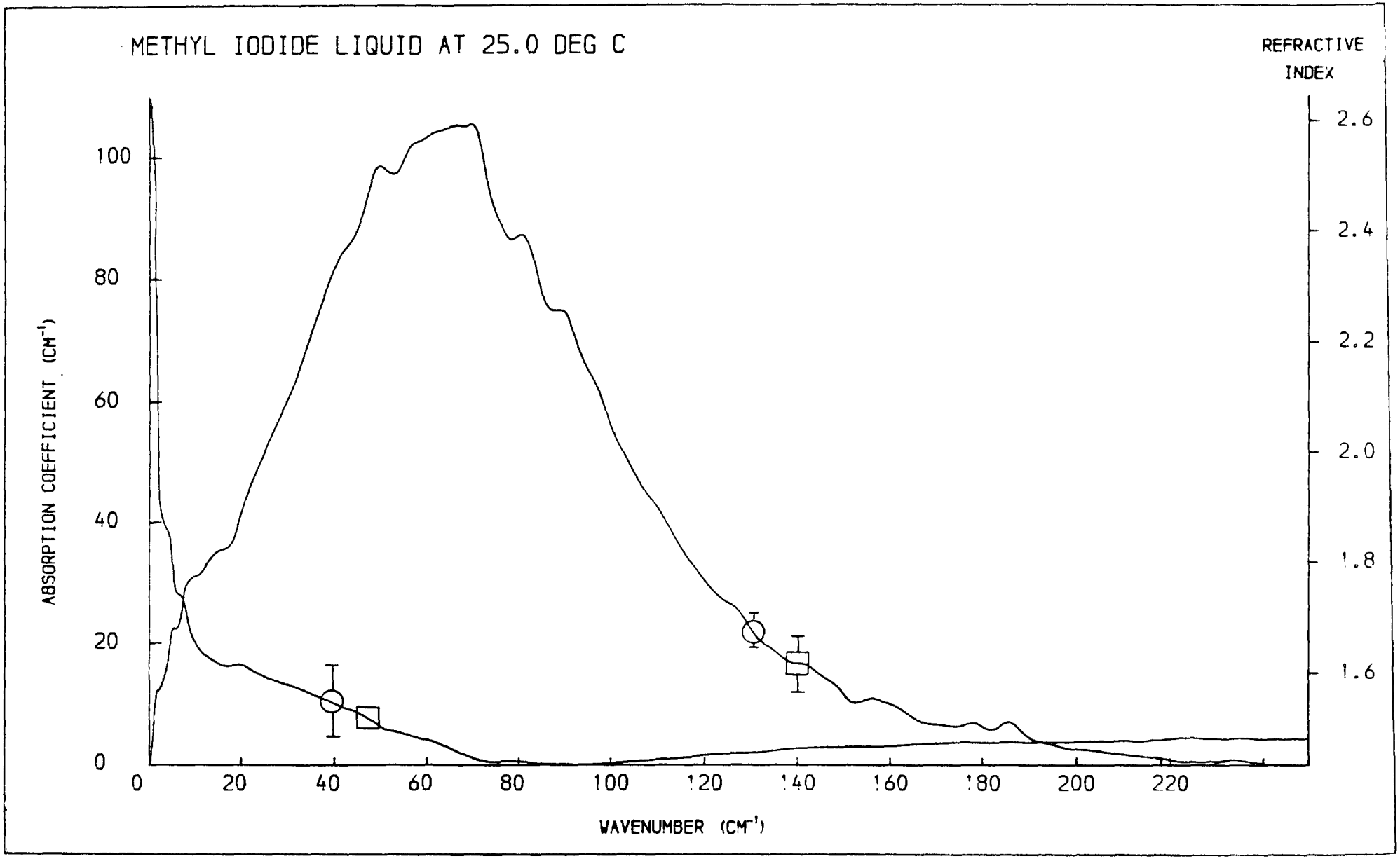
METHYL IODIDE LIQUID AT 25.0 DEG C
REFRACTIVE INDEX
2.6
2.4
2.2
2.0
1.8
1.6
ABSORPTION COEFFICIENT (CM⁻¹)
100
80
60
40
20
0
0
20
40
60
80
100
120
140
160
180
200
220
WAVENUMBER (CM⁻¹)

FIGURE 7.9

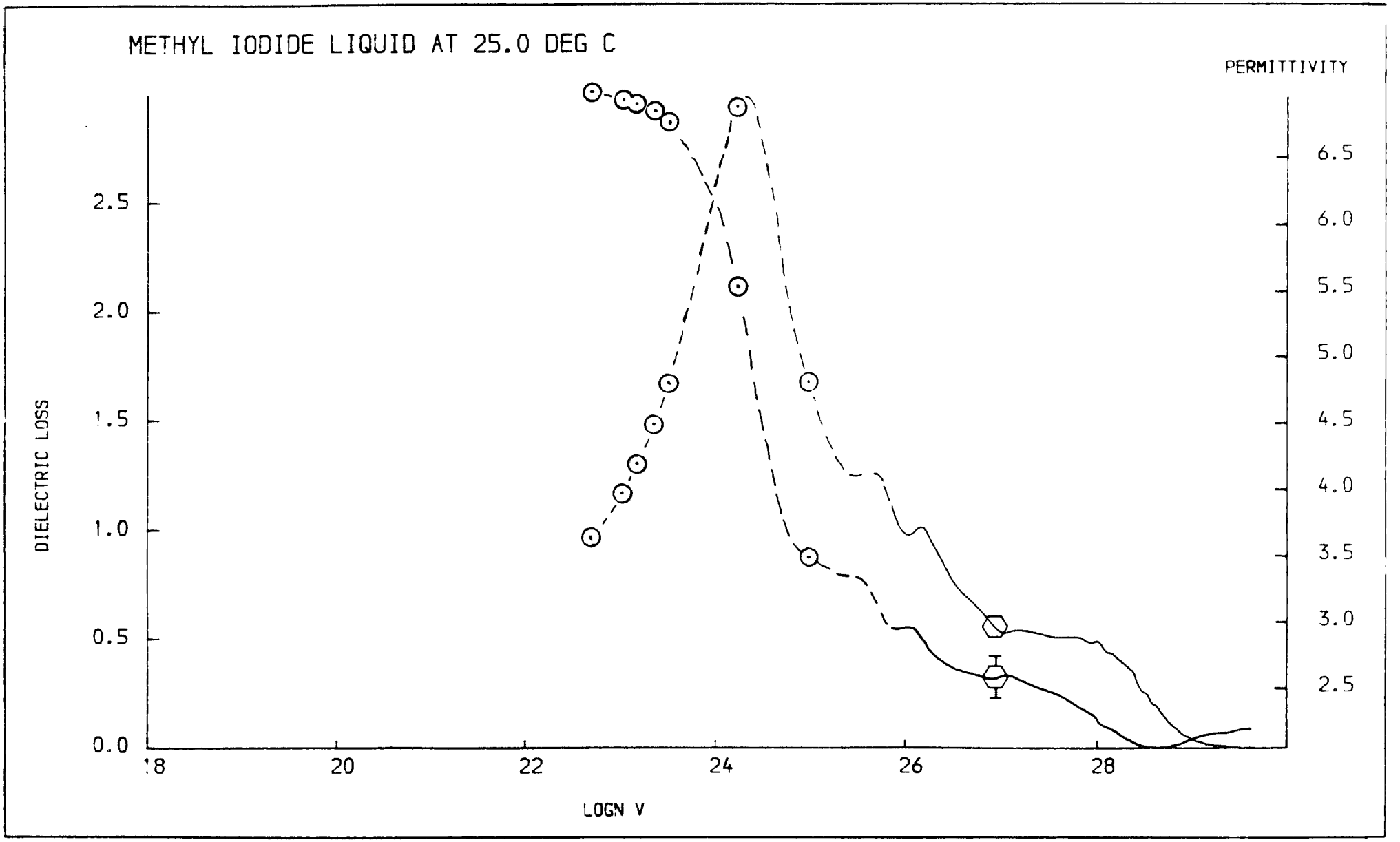
METHYL IODIDE LIQUID AT 25.0 DEG C
PERMITTIVITY
DIELECTRIC LOSS
LOGN V
0.0
0.5
1.0
1.5
2.0
2.5
18
20
22
24
26
28
2.5
3.0
3.5
4.0
4.5
5.0
5.5
6.0
6.5

FIGURE 7.10

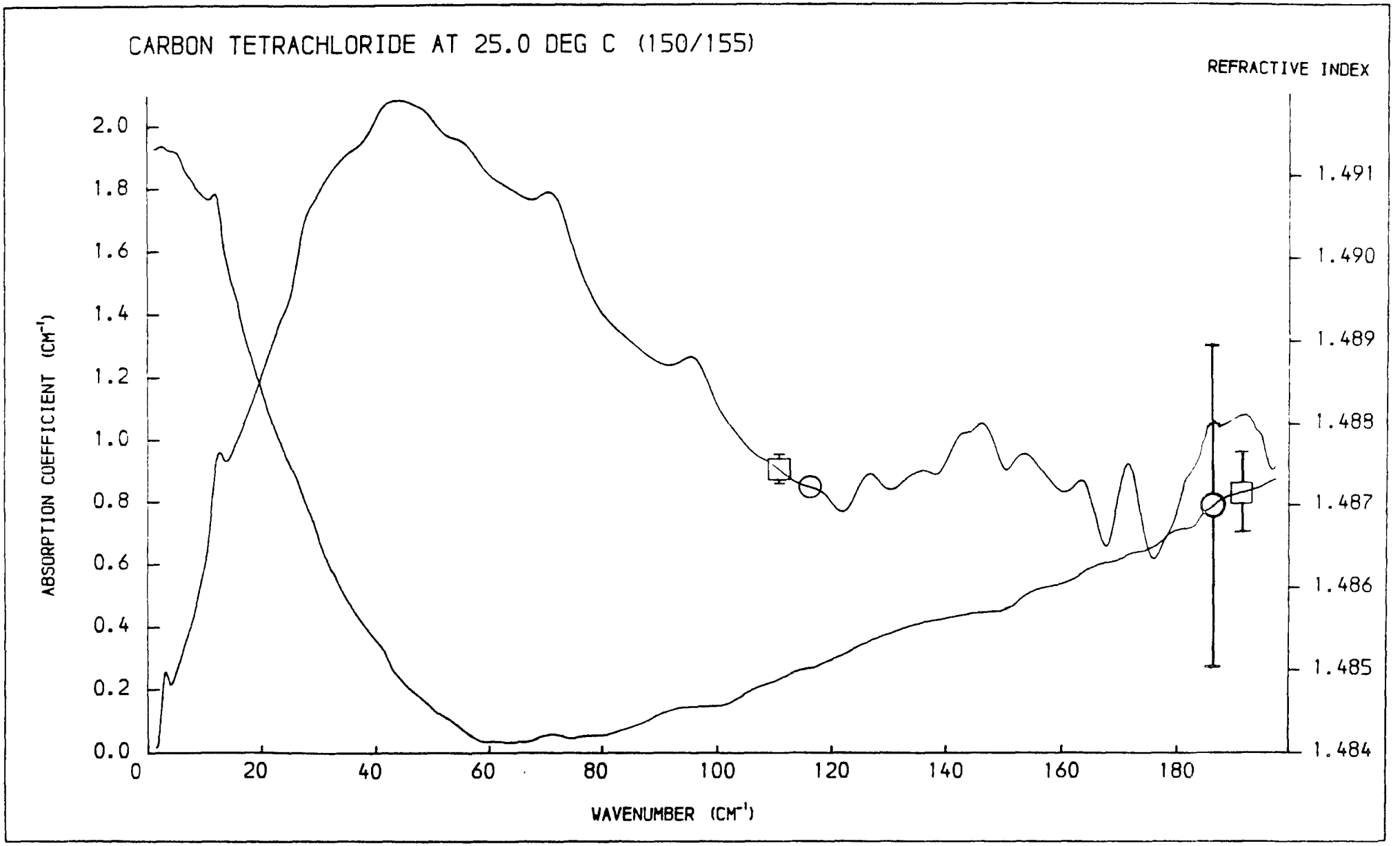
CARBON TETRACHLORIDE AT 25.0 DEG C (150/155)
REFRACTIVE INDEX
ABSORPTION COEFFICIENT (CM⁻¹)
2.0
1.8
1.6
1.4
1.2
1.0
0.8
0.6
0.4
0.2
0.0
1.491
1.490
1.489
1.488
1.487
1.486
1.485
1.484
0
20
40
60
80
100
120
140
160
180
WAVENUMBER (CM⁻¹)

FIGURE 7.11

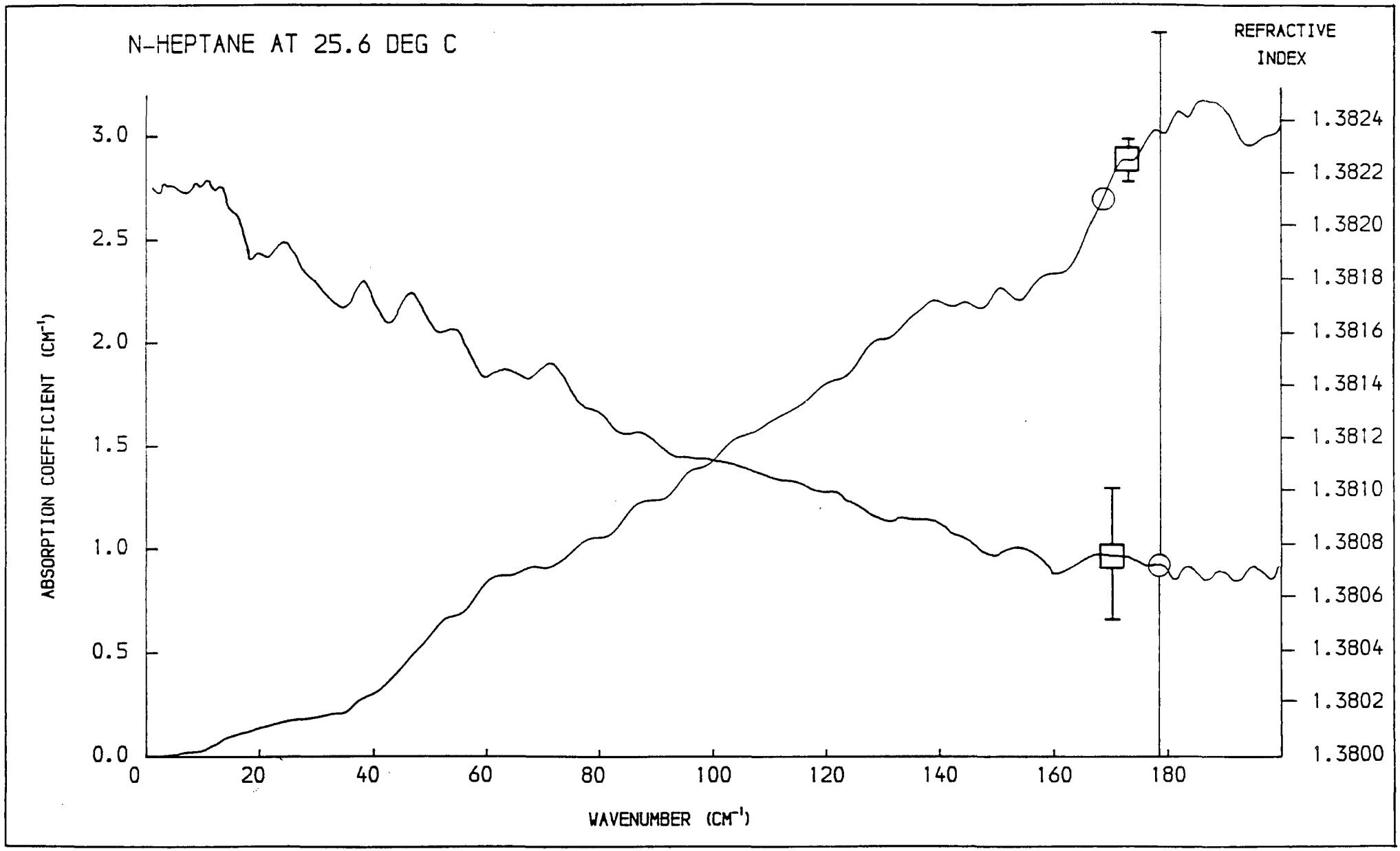
N-HEPTANE AT 25.6 DEG C
REFRACTIVE INDEX
ABSORPTION COEFFICIENT (CM⁻¹)
WAVENUMBER (CM⁻¹)
0.0
0.5
1.0
1.5
2.0
2.5
3.0
0
20
40
60
80
100
120
140
160
180
1.3800
1.3802
1.3804
1.3806
1.3808
1.3810
1.3812
1.3814
1.3816
1.3818
1.3820
1.3822
1.3824

FIGURE 7.12

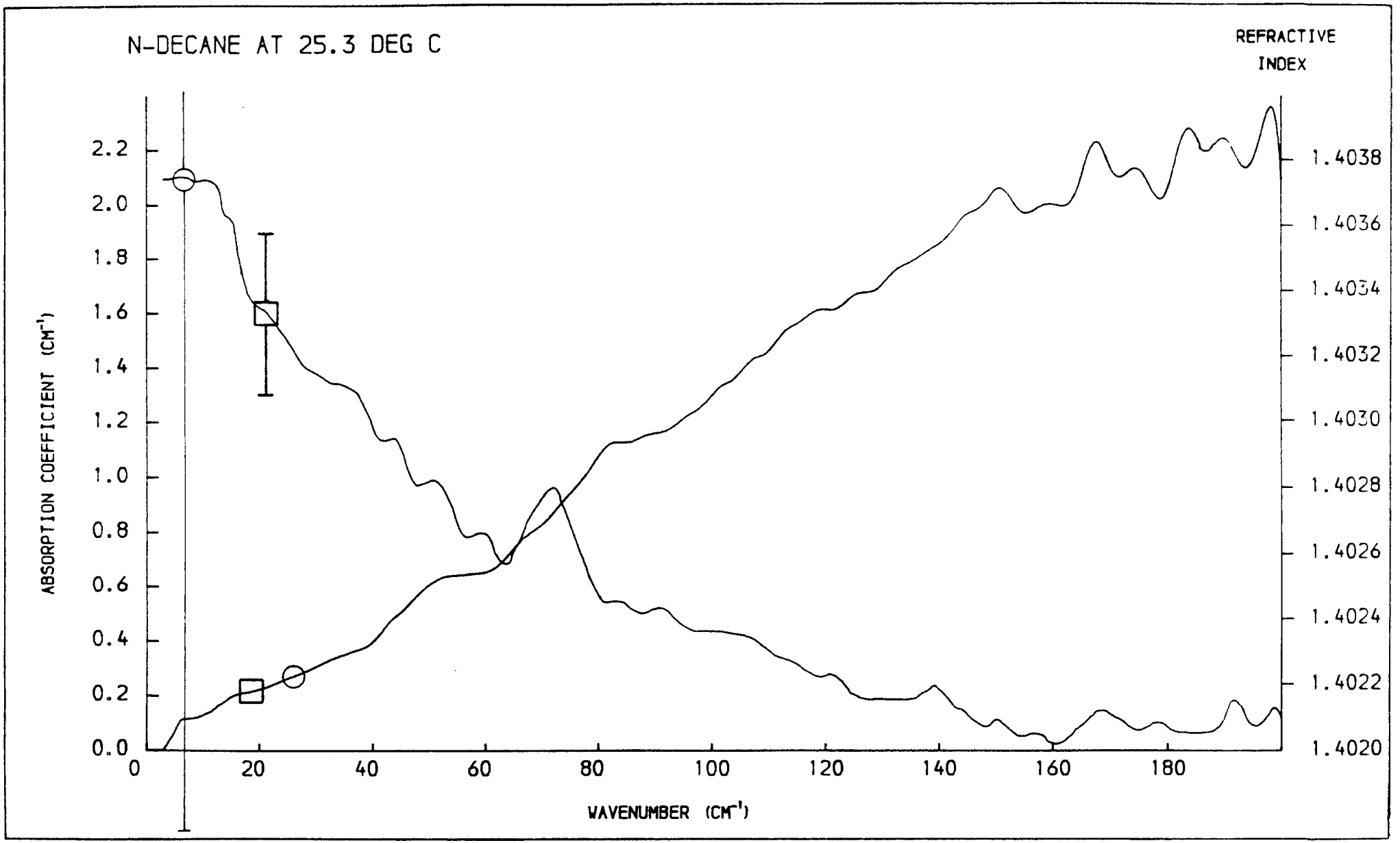
N-DECANE AT 25.3 DEG C
REFRACTIVE INDEX
ABSORPTION COEFFICIENT (CM⁻¹)
2.2
2.0
1.8
1.6
1.4
1.2
1.0
0.8
0.6
0.4
0.2
0.0
1.4038
1.4036
1.4034
1.4032
1.4030
1.4028
1.4026
1.4024
1.4022
1.4020
0
20
40
60
80
100
120
140
160
180
WAVENUMBER (CM⁻¹)

FIGURE 7.13

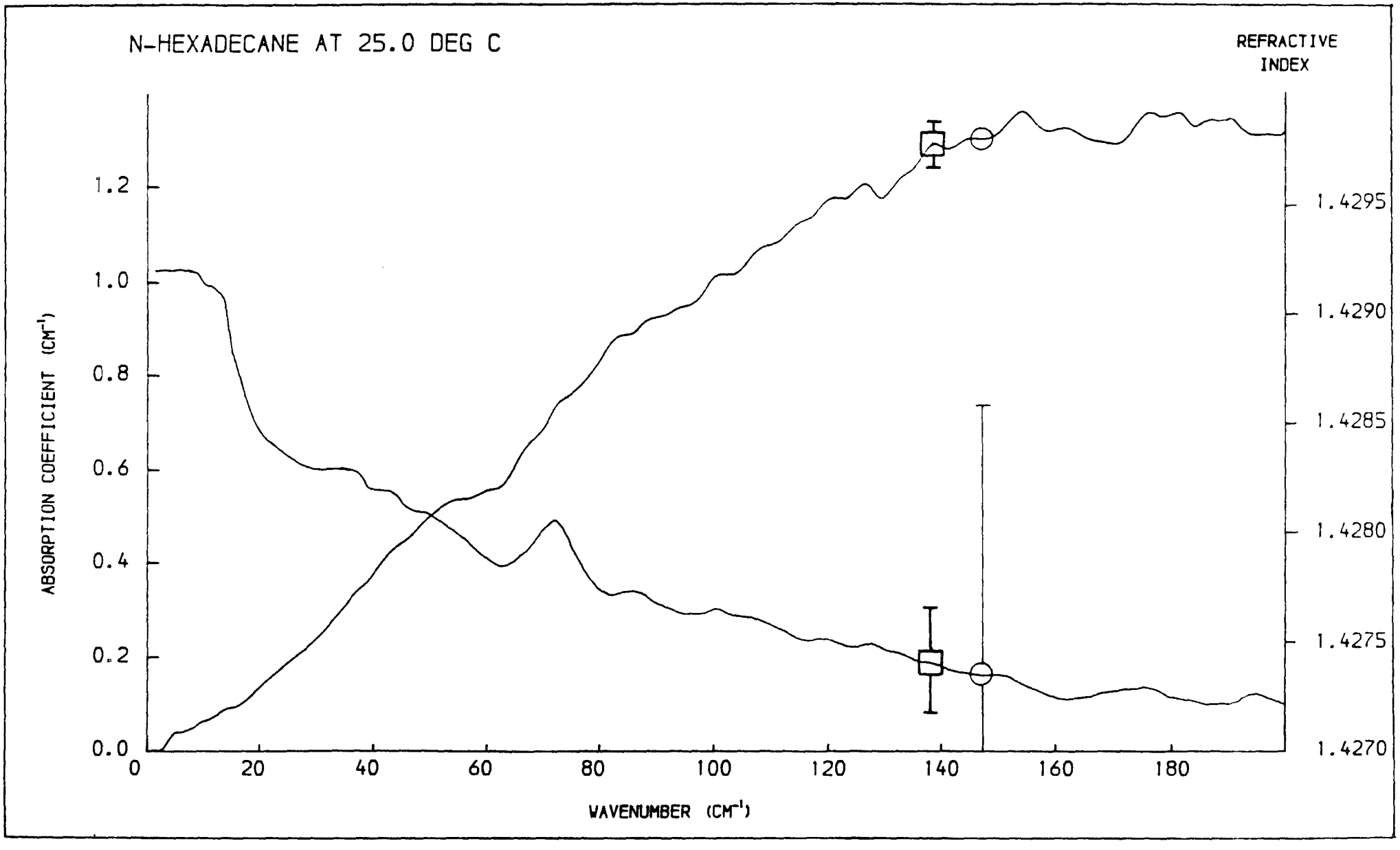
N-HEXADECANE AT 25.0 DEG C
REFRACTIVE INDEX
ABSORPTION COEFFICIENT (CM⁻¹)
WAVENUMBER (CM⁻¹)
0.0
0.2
0.4
0.6
0.8
1.0
1.2
0
20
40
60
80
100
120
140
160
180
1.4270
1.4275
1.4280
1.4285
1.4290
1.4295

FIGURE 7.14

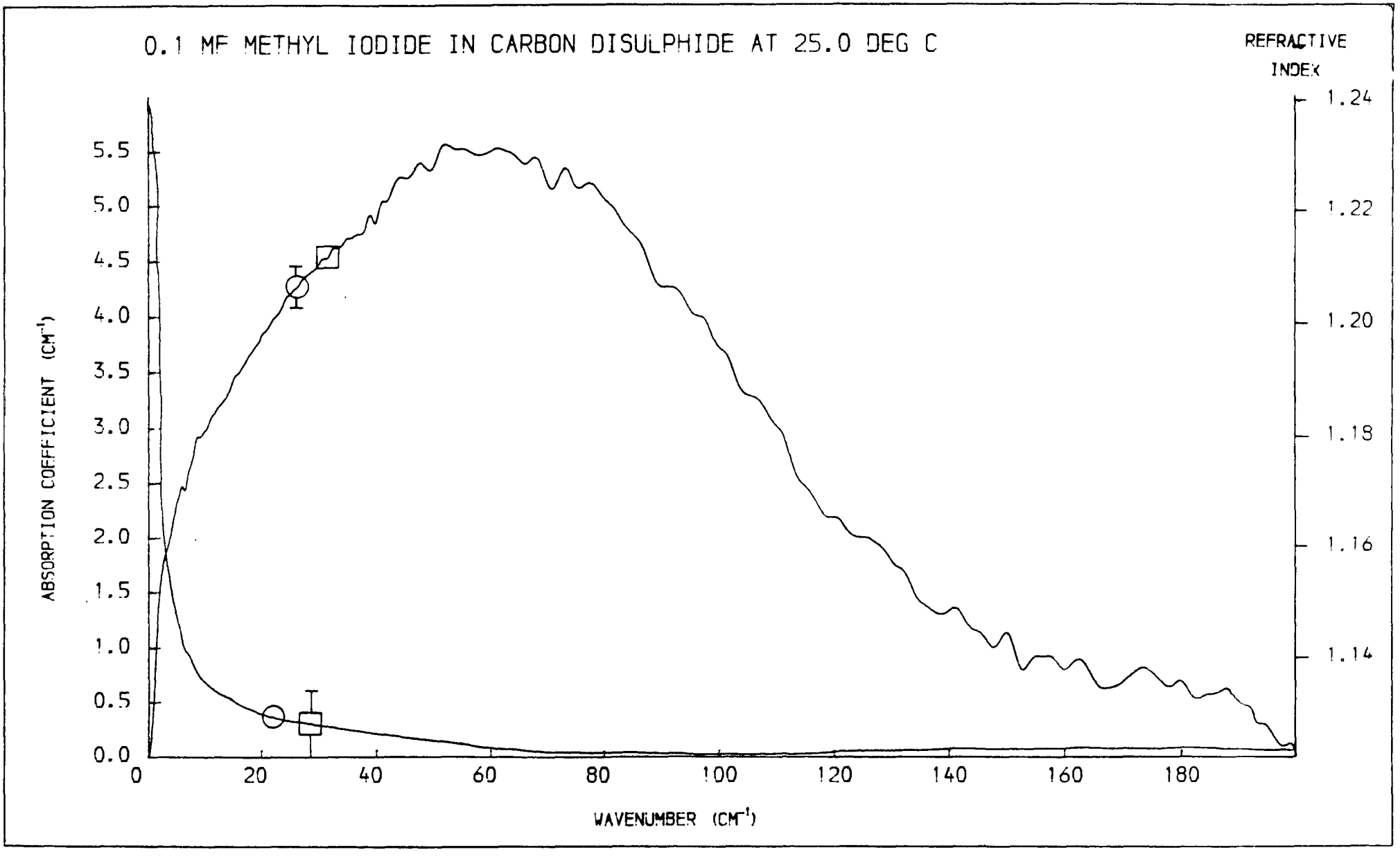
0.1 MF METHYL IODIDE IN CARBON DISULPHIDE AT 25.0 DEG C
REFRACTIVE INDEX
1.24
1.22
1.20
1.18
1.16
1.14
ABSORPTION COEFFICIENT (CM⁻¹)
5.5
5.0
4.5
4.0
3.5
3.0
2.5
2.0
1.5
1.0
0.5
0.0
0
20
40
60
80
100
120
140
160
180
WAVENUMBER (CM⁻¹)

FIGURE 7.15

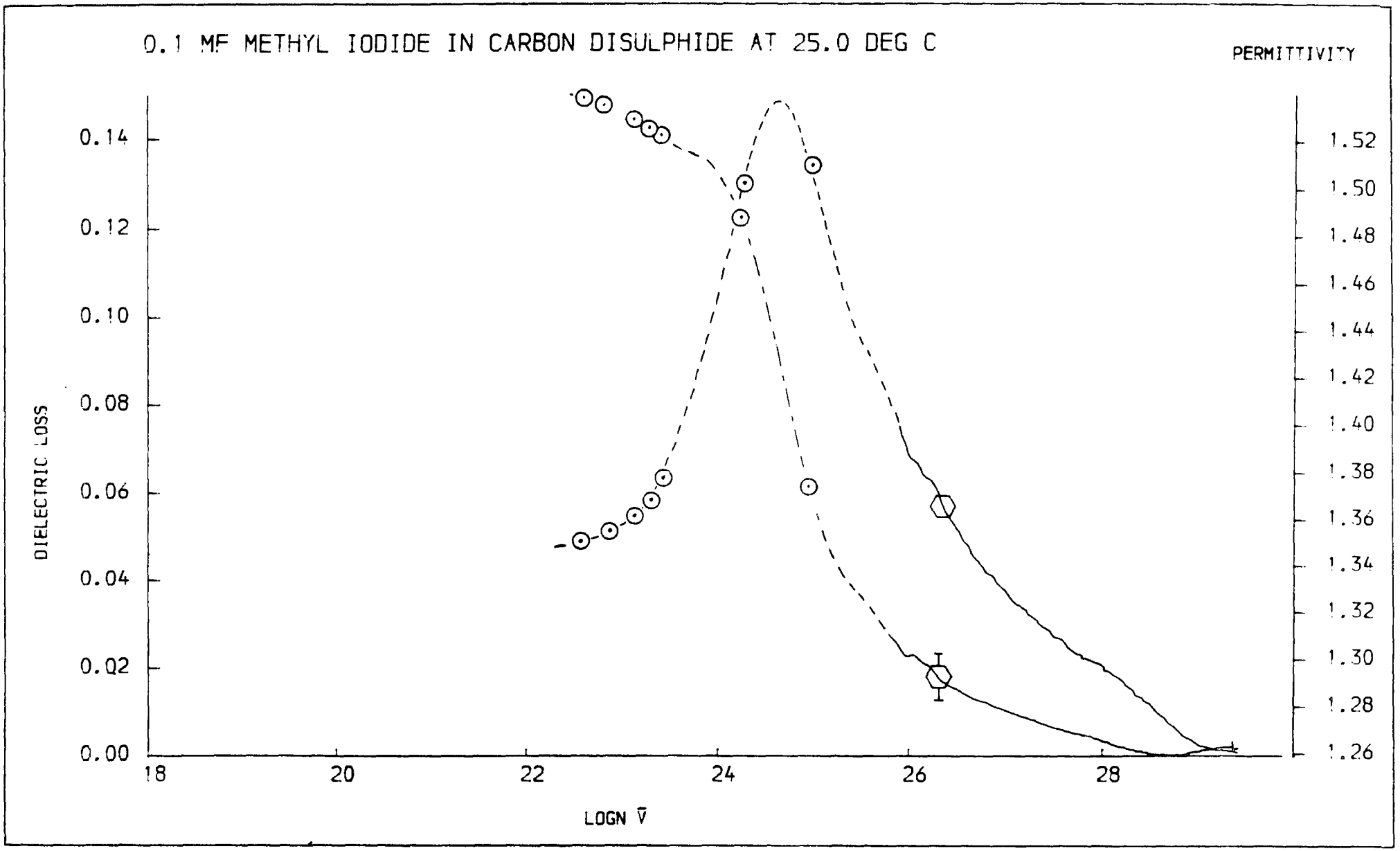
0.1 MF METHYL IODIDE IN CARBON DISULPHIDE AT 25.0 DEG C
PERMITTIVITY
DIELECTRIC LOSS
0.14
0.12
0.10
0.08
0.06
0.04
0.02
0.00
1.52
1.50
1.48
1.46
1.44
1.42
1.40
1.38
1.36
1.34
1.32
1.30
1.28
1.26
18
20
22
24
26
28
LOGN $\bar{\nu}$

FIGURE 7.16

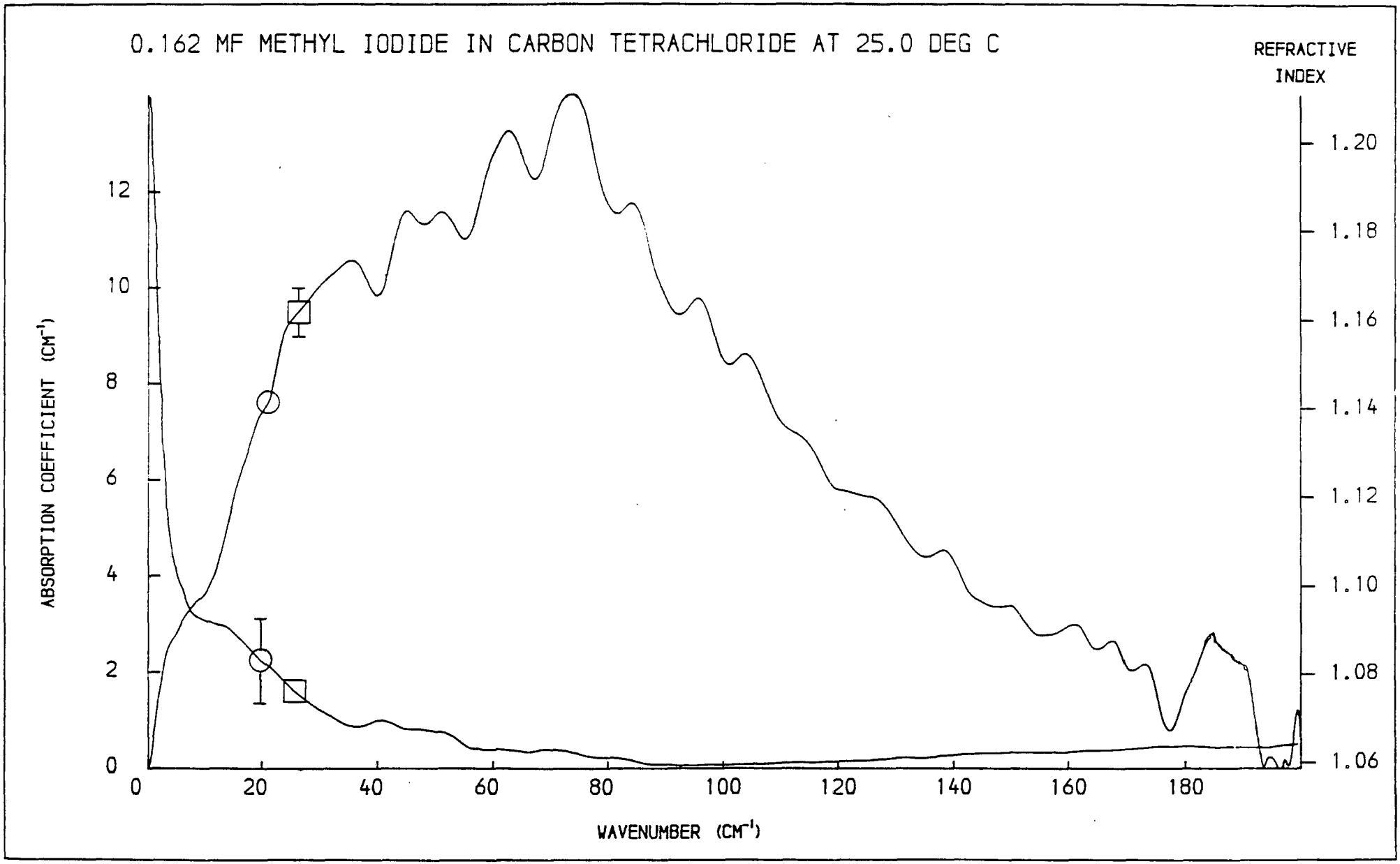
0.162 MF METHYL IODIDE IN CARBON TETRACHLORIDE AT 25.0 DEG C
REFRACTIVE INDEX
ABSORPTION COEFFICIENT (CM⁻¹)
WAVENUMBER (CM⁻¹)
0
2
4
6
8
10
12
0
20
40
60
80
100
120
140
160
180
1.06
1.08
1.10
1.12
1.14
1.16
1.18
1.20

FIGURE 7.17

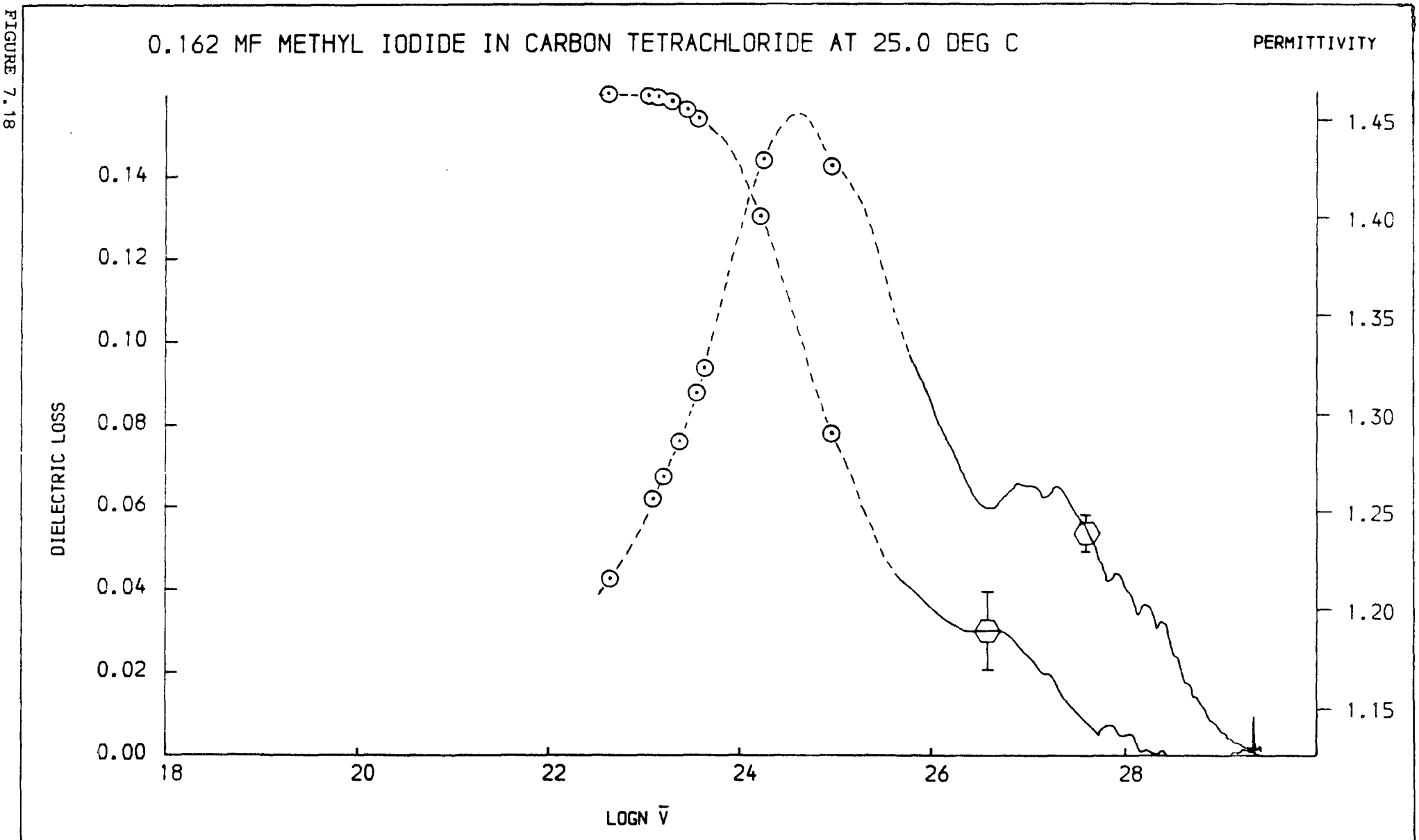
0.162 MF METHYL IODIDE IN CARBON TETRACHLORIDE AT 25.0 DEG C
PERMITTIVITY
DIELECTRIC LOSS
0.00
0.02
0.04
0.06
0.08
0.10
0.12
0.14
1.15
1.20
1.25
1.30
1.35
1.40
1.45
18
20
22
24
26
28
LOGN $\bar{V}$

FIGURE 7.18

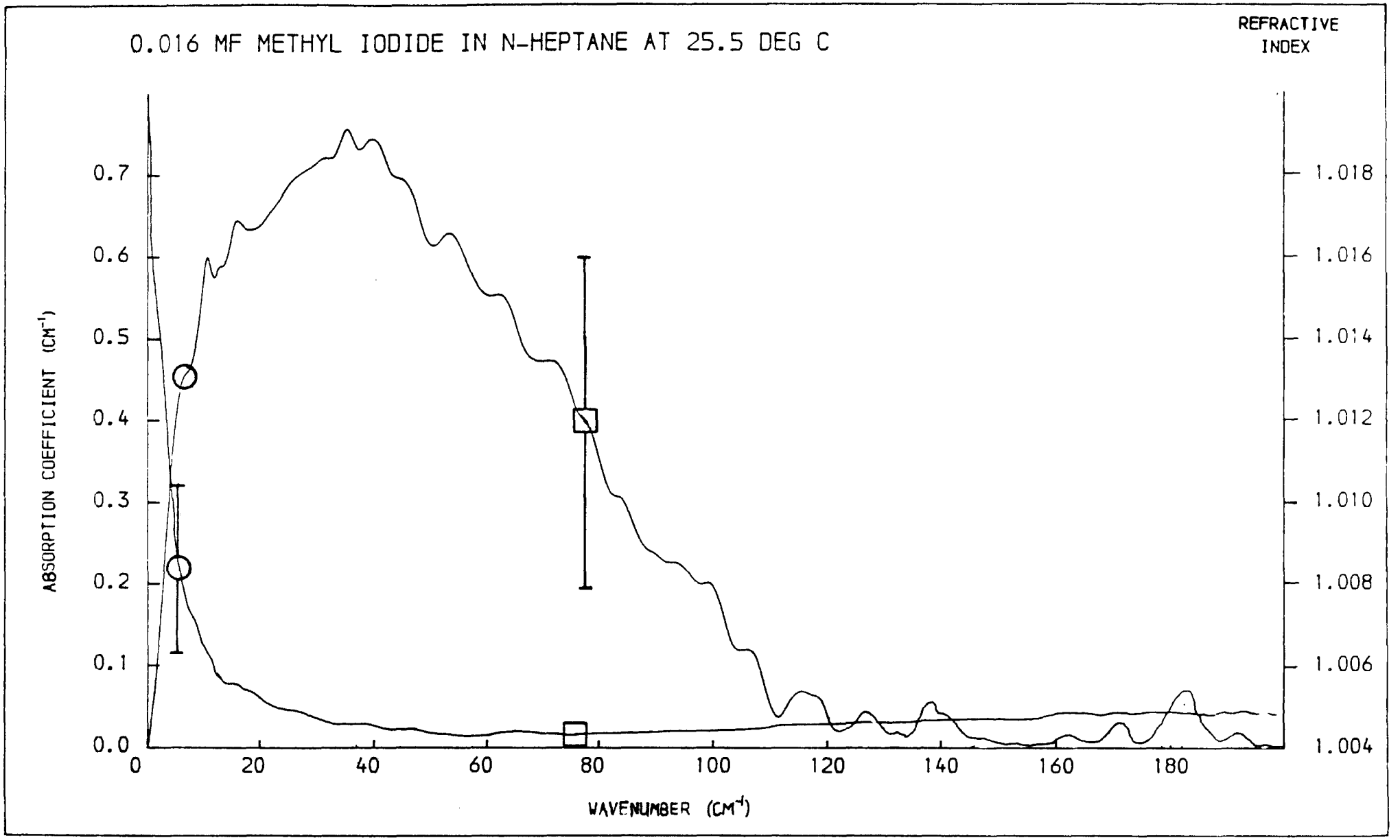
0.016 MF METHYL IODIDE IN N-HEPTANE AT 25.5 DEG C
REFRACTIVE INDEX
ABSORPTION COEFFICIENT (CM⁻¹)
0.0
0.1
0.2
0.3
0.4
0.5
0.6
0.7
1.004
1.006
1.008
1.010
1.012
1.014
1.016
1.018
0
20
40
60
80
100
120
140
160
180
WAVENUMBER (CM⁻¹)

FIGURE 7.19

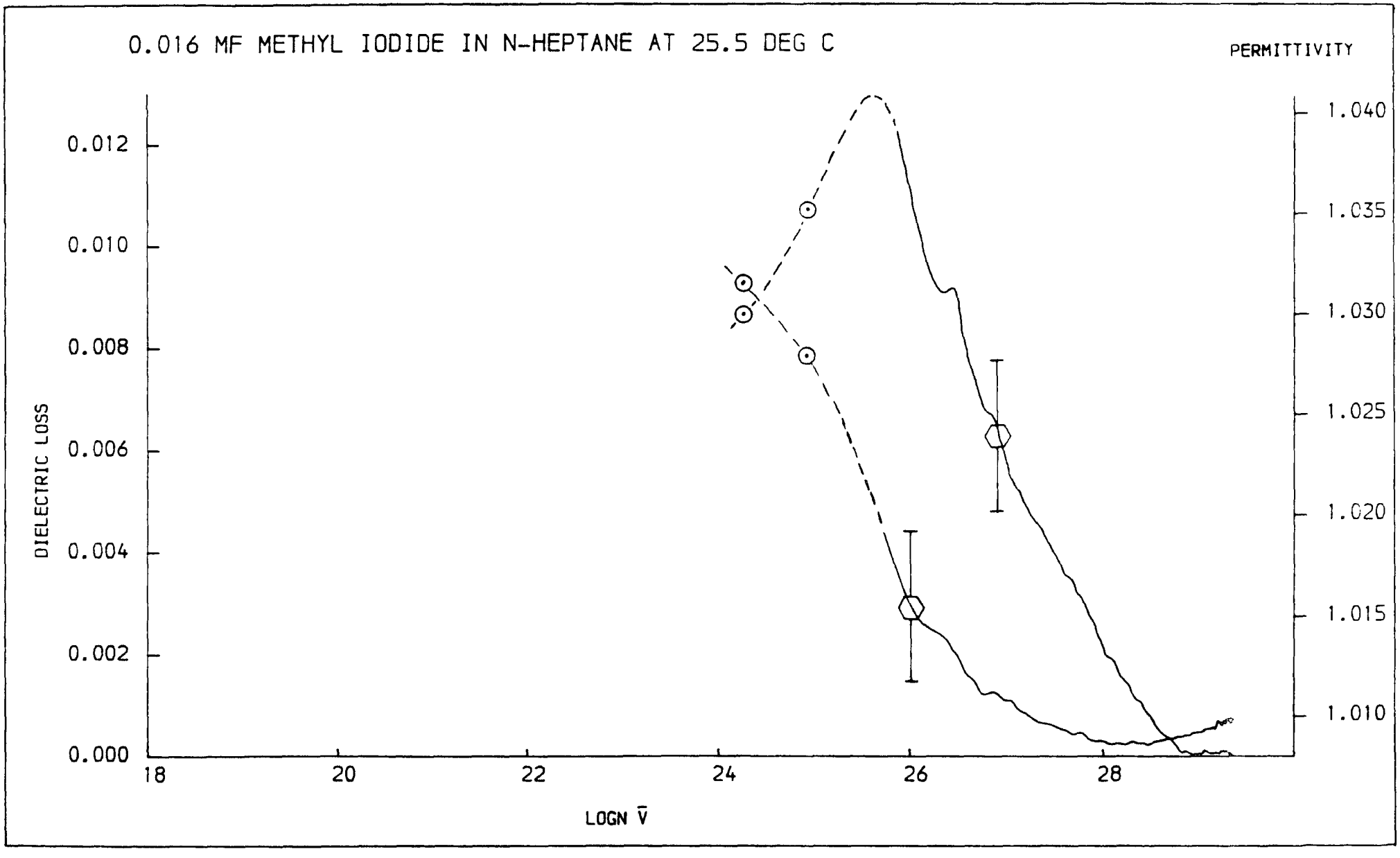
0.016 MF METHYL IODIDE IN N-HEPTANE AT 25.5 DEG C
PERMITTIVITY
DIELECTRIC LOSS
0.012
0.010
0.008
0.006
0.004
0.002
0.000
1.040
1.035
1.030
1.025
1.020
1.015
1.010
18
20
22
24
26
28
LOGN V̄

Figure 7.20

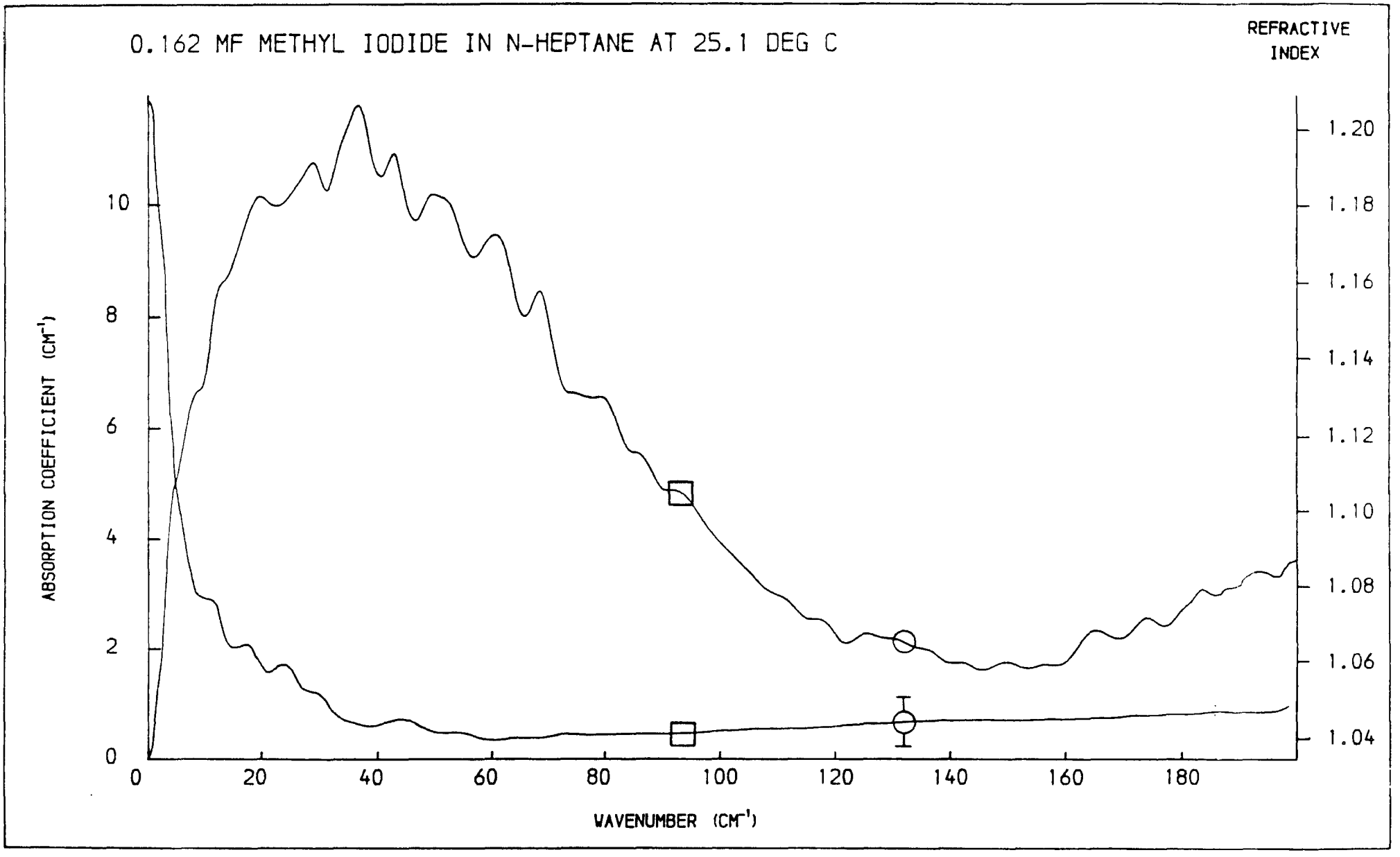
0.162 MF METHYL IODIDE IN N-HEPTANE AT 25.1 DEG C
REFRACTIVE INDEX
ABSORPTION COEFFICIENT (CM⁻¹)
WAVENUMBER (CM⁻¹)
0
2
4
6
8
10
0
20
40
60
80
100
120
140
160
180
1.04
1.06
1.08
1.10
1.12
1.14
1.16
1.18
1.20

FIGURE 7.21

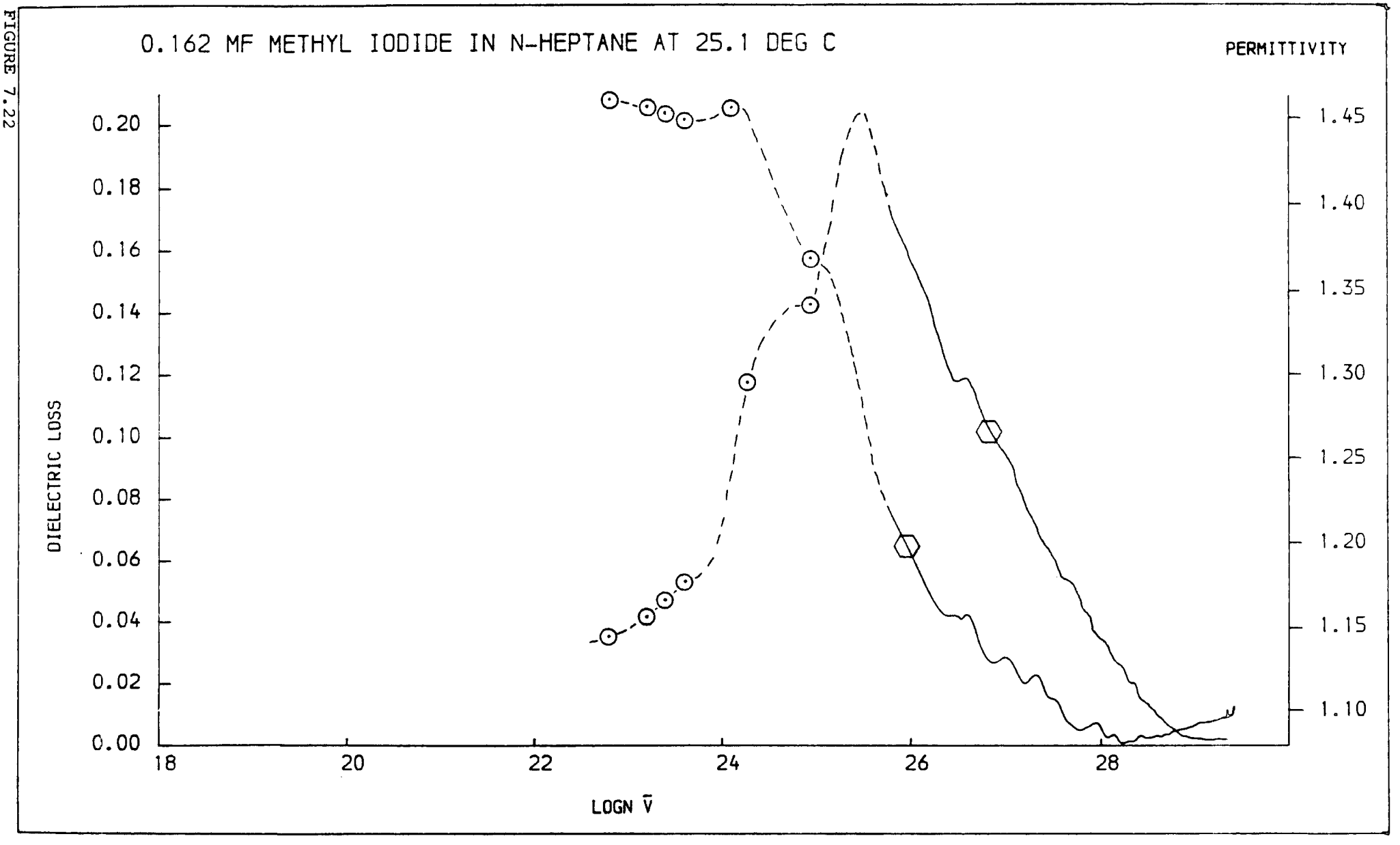
0.162 MF METHYL IODIDE IN N-HEPTANE AT 25.1 DEG C
PERMITTIVITY
DIELECTRIC LOSS
0.20
0.18
0.16
0.14
0.12
0.10
0.08
0.06
0.04
0.02
0.00
1.45
1.40
1.35
1.30
1.25
1.20
1.15
1.10
18
20
22
24
26
28
LOGN $\bar{V}$

FIGURE 7.22

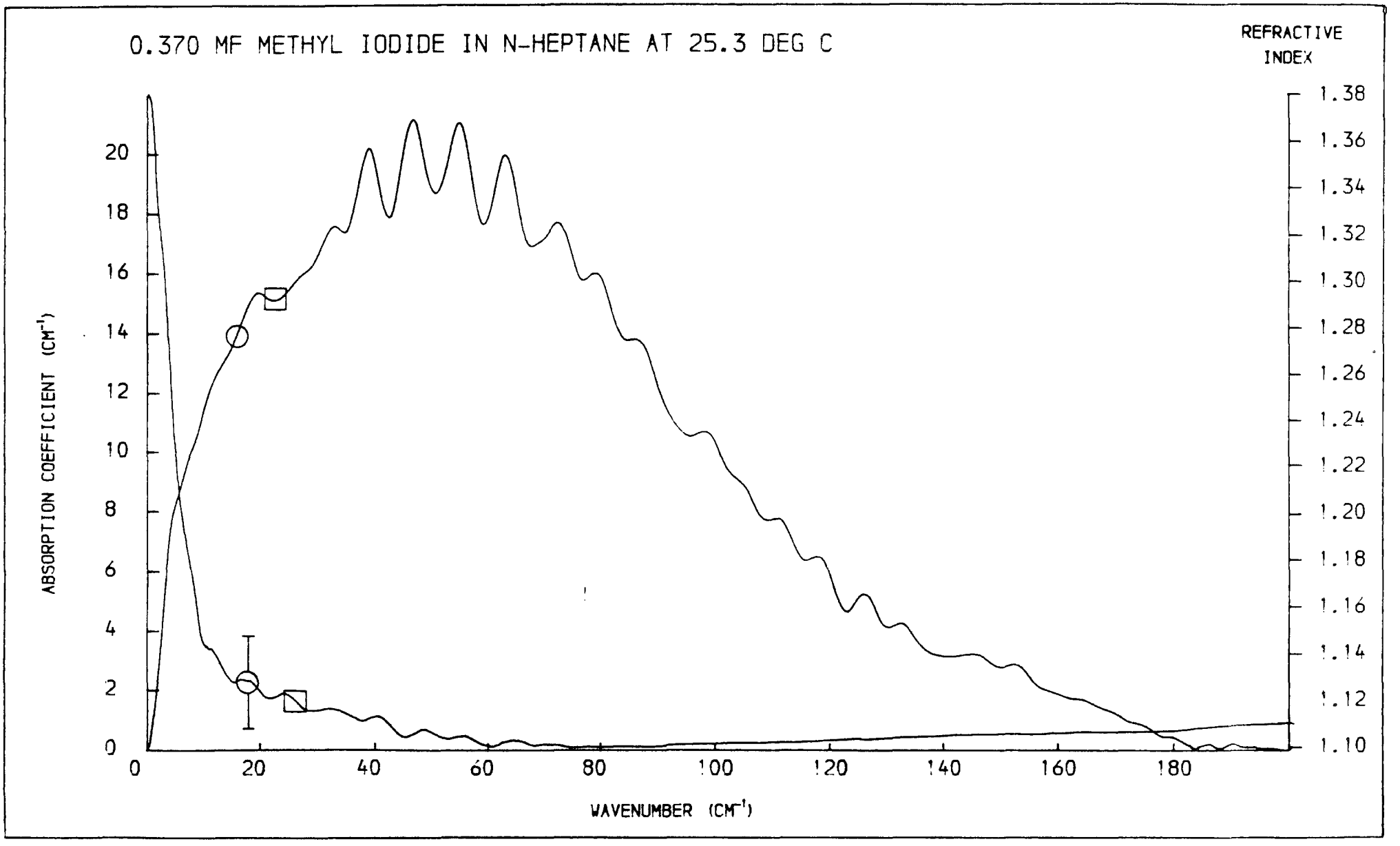
0.370 MF METHYL IODIDE IN N-HEPTANE AT 25.3 DEG C
REFRACTIVE INDEX
1.38
1.36
1.34
1.32
1.30
1.28
1.26
1.24
1.22
1.20
1.18
1.16
1.14
1.12
1.10
ABSORPTION COEFFICIENT (CM⁻¹)
0
2
4
6
8
10
12
14
16
18
20
0
20
40
60
80
100
120
140
160
180
WAVENUMBER (CM⁻¹)

FIGURE 7.23

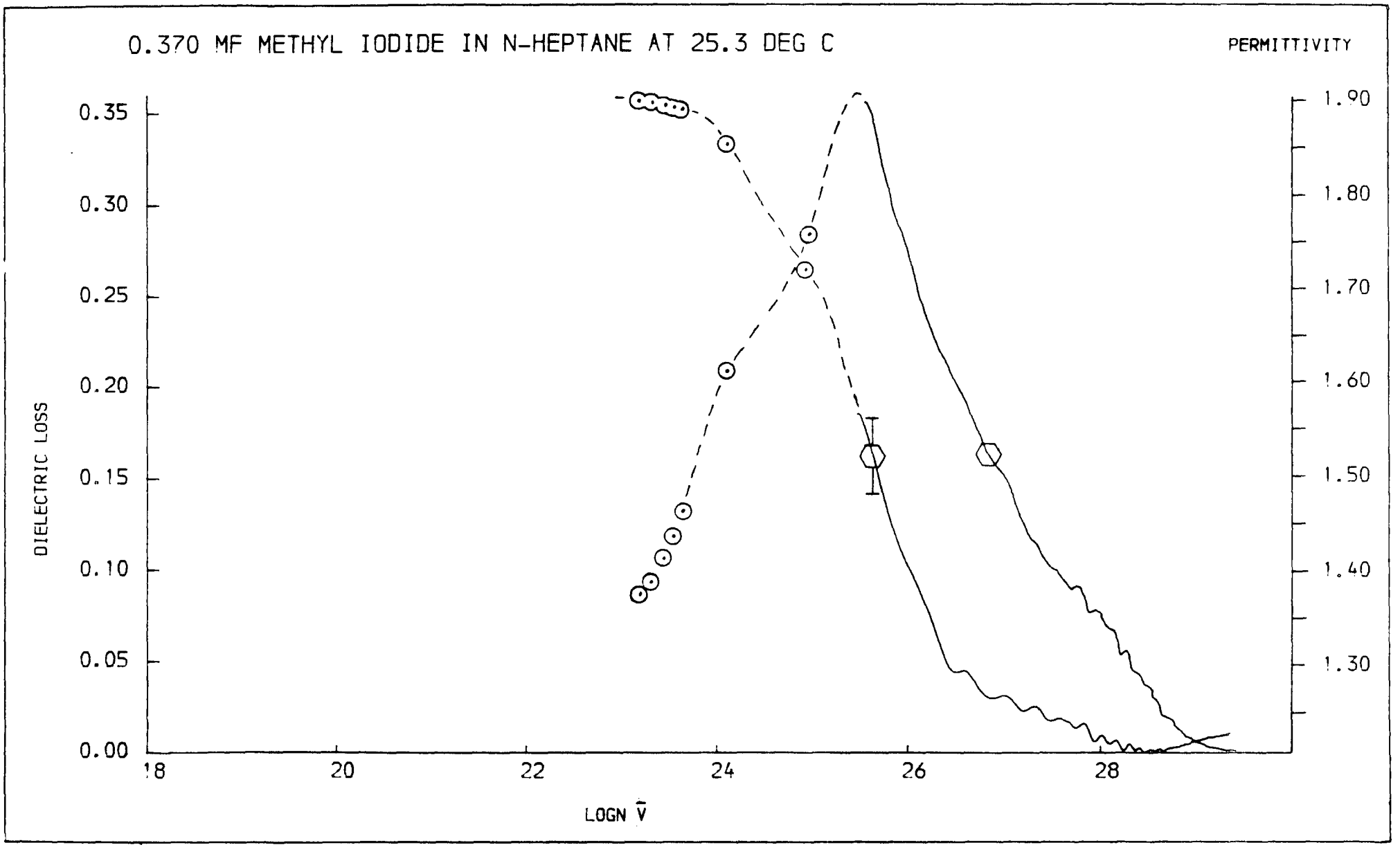
0.370 MF METHYL IODIDE IN N-HEPTANE AT 25.3 DEG C
PERMITTIVITY
DIELECTRIC LOSS
0.35
0.30
0.25
0.20
0.15
0.10
0.05
0.00
1.90
1.80
1.70
1.60
1.50
1.40
1.30
18
20
22
24
26
28
LOGN $\bar{\nu}$

FIGURE 7.24

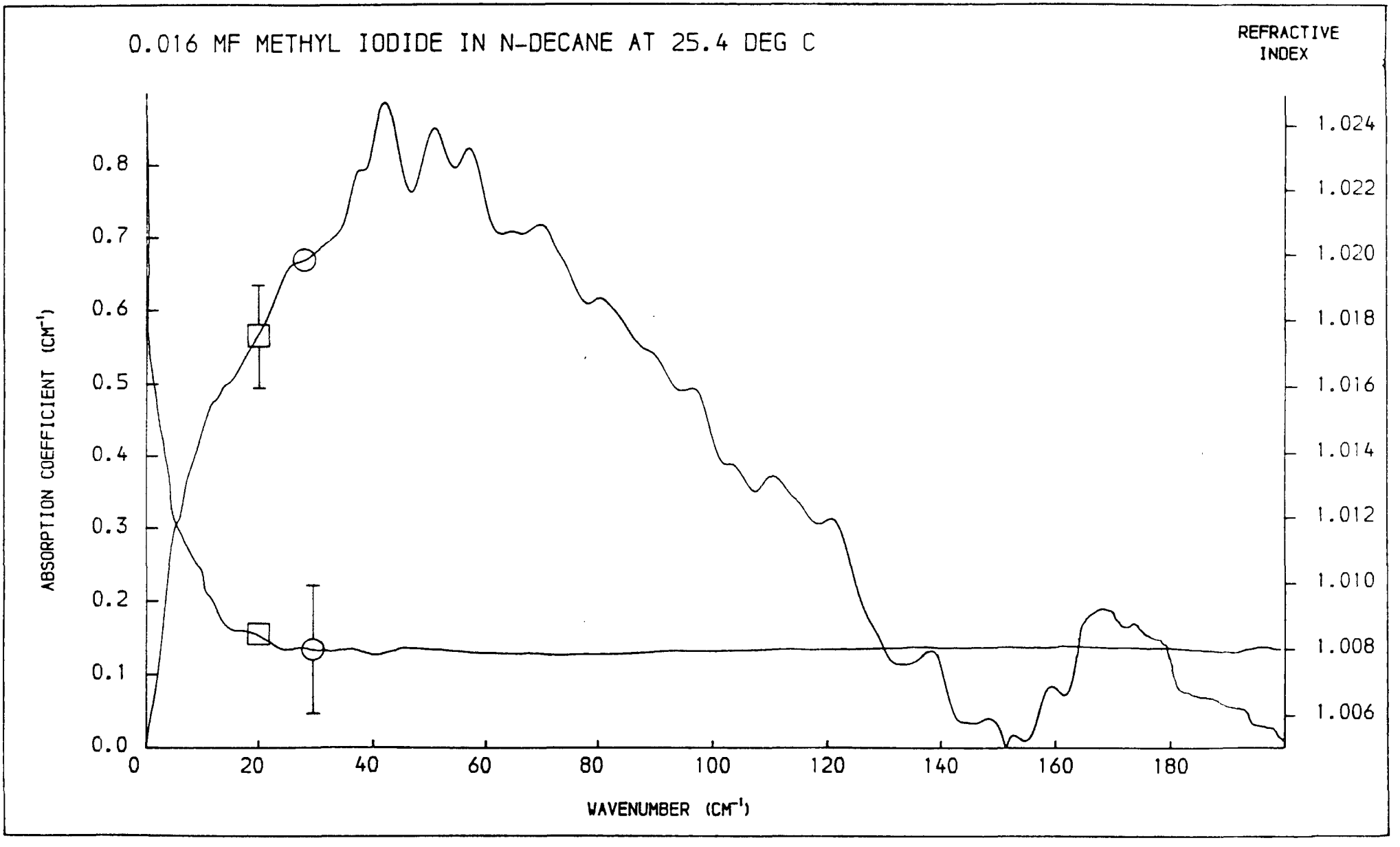
0.016 MF METHYL IODIDE IN N-DECANE AT 25.4 DEG C
REFRACTIVE INDEX
ABSORPTION COEFFICIENT (CM⁻¹)
0.0
0.1
0.2
0.3
0.4
0.5
0.6
0.7
0.8
1.006
1.008
1.010
1.012
1.014
1.016
1.018
1.020
1.022
1.024
0
20
40
60
80
100
120
140
160
180
WAVENUMBER (CM⁻¹)

FIGURE 7.25

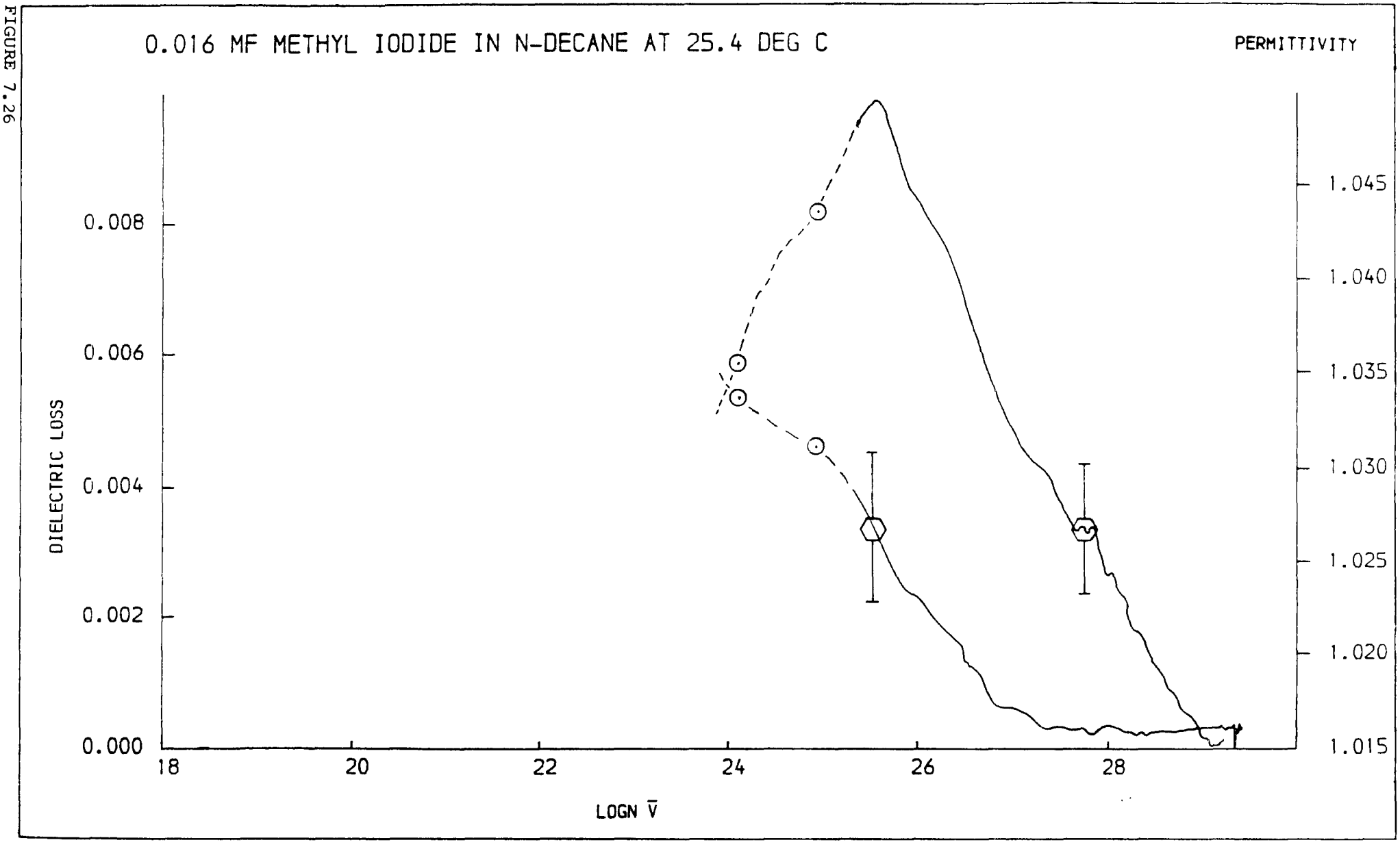
0.016 MF METHYL IODIDE IN N-DECANE AT 25.4 DEG C
PERMITTIVITY
DIELECTRIC LOSS
0.000
0.002
0.004
0.006
0.008
1.015
1.020
1.025
1.030
1.035
1.040
1.045
18
20
22
24
26
28
LOGN V̄

FIGURE 7.26

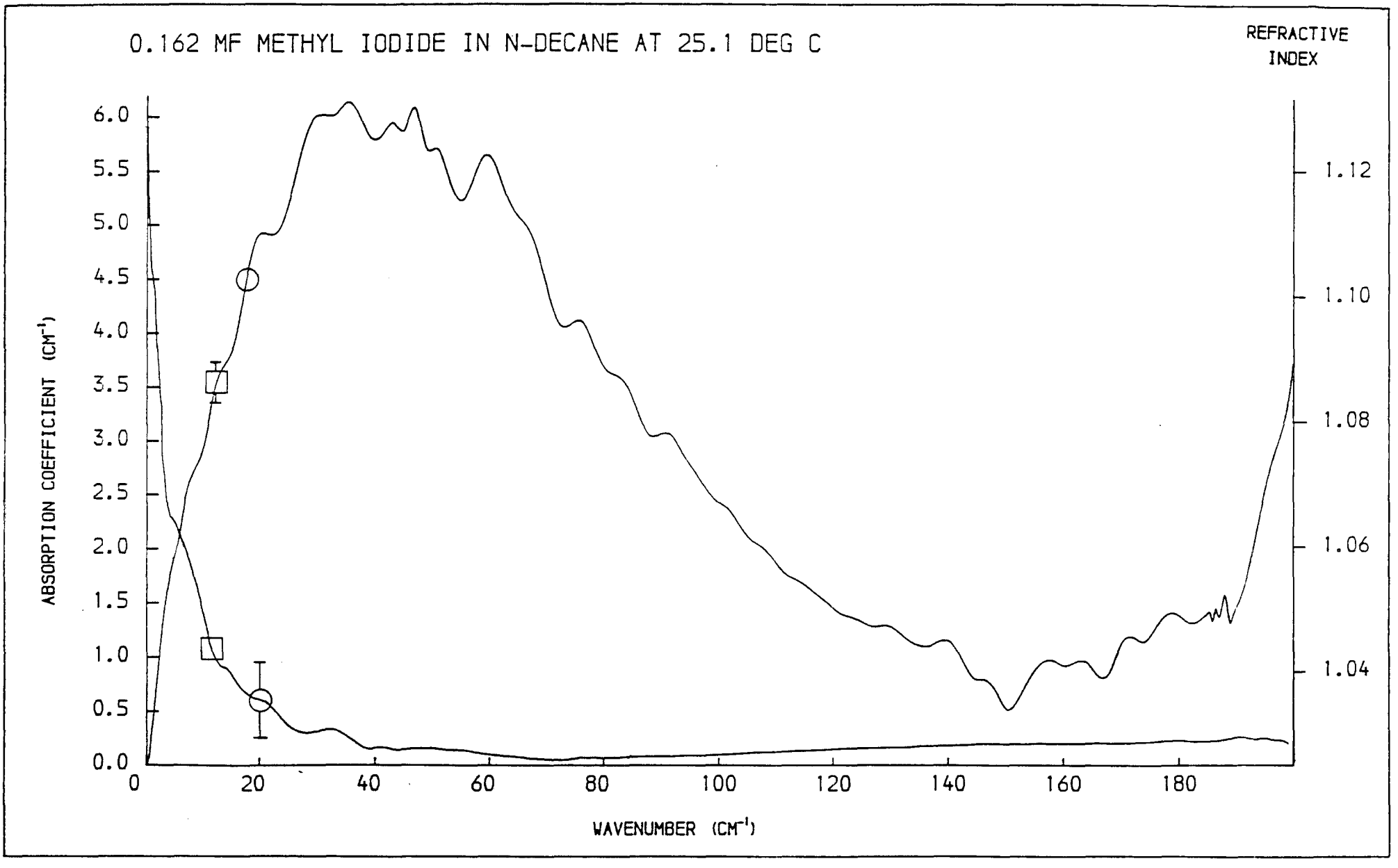
0.162 MF METHYL IODIDE IN N-DECANE AT 25.1 DEG C
REFRACTIVE INDEX
ABSORPTION COEFFICIENT (CM⁻¹)
WAVENUMBER (CM⁻¹)
0.0
0.5
1.0
1.5
2.0
2.5
3.0
3.5
4.0
4.5
5.0
5.5
6.0
0
20
40
60
80
100
120
140
160
180
1.04
1.06
1.08
1.10
1.12

FIGURE 7.27

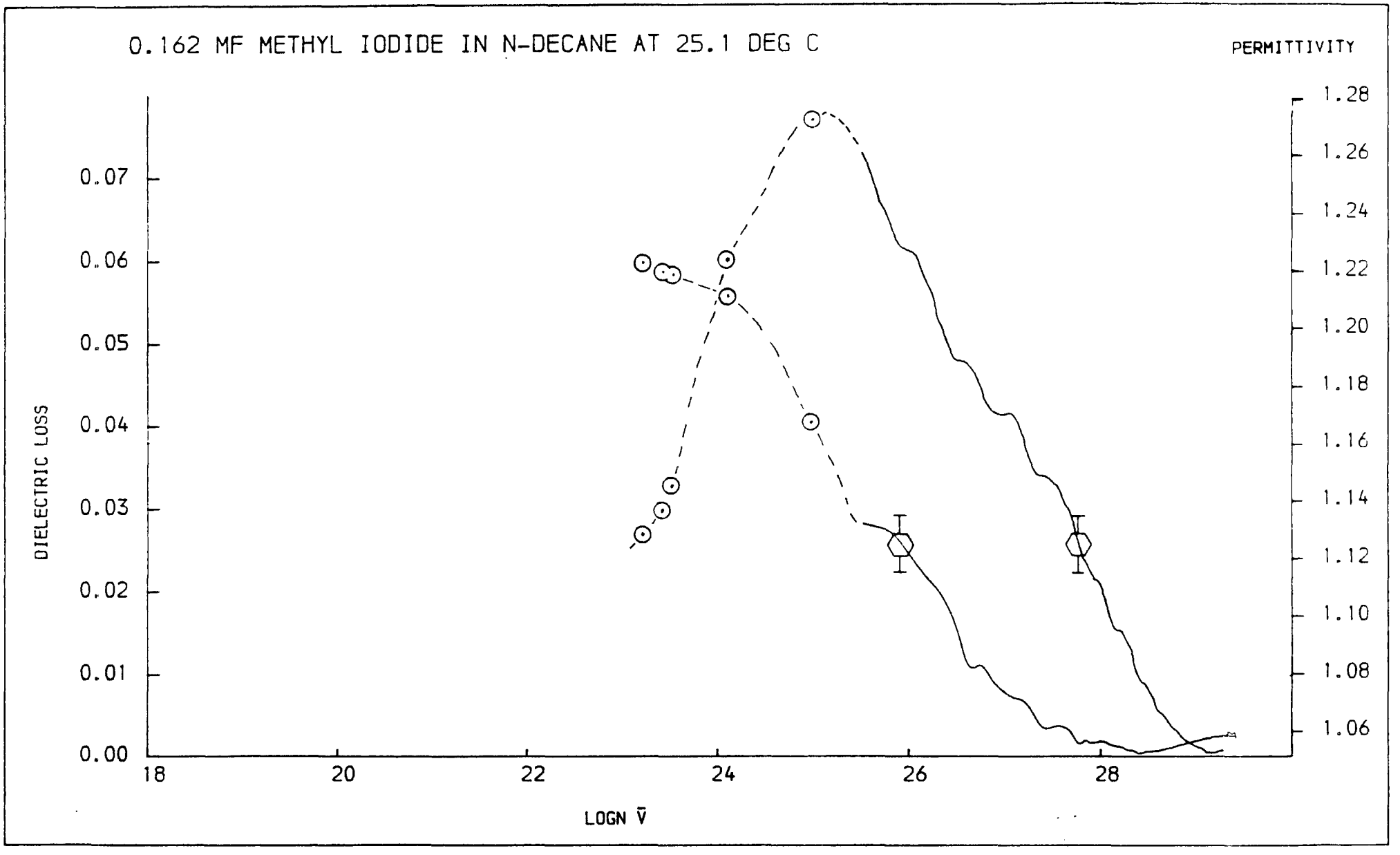
0.162 MF METHYL IODIDE IN N-DECANE AT 25.1 DEG C
PERMITTIVITY
DIELECTRIC LOSS
0.00
0.01
0.02
0.03
0.04
0.05
0.06
0.07
1.06
1.08
1.10
1.12
1.14
1.16
1.18
1.20
1.22
1.24
1.26
1.28
18
20
22
24
26
28
LOGN $\bar{\nu}$

FIGURE 7.28

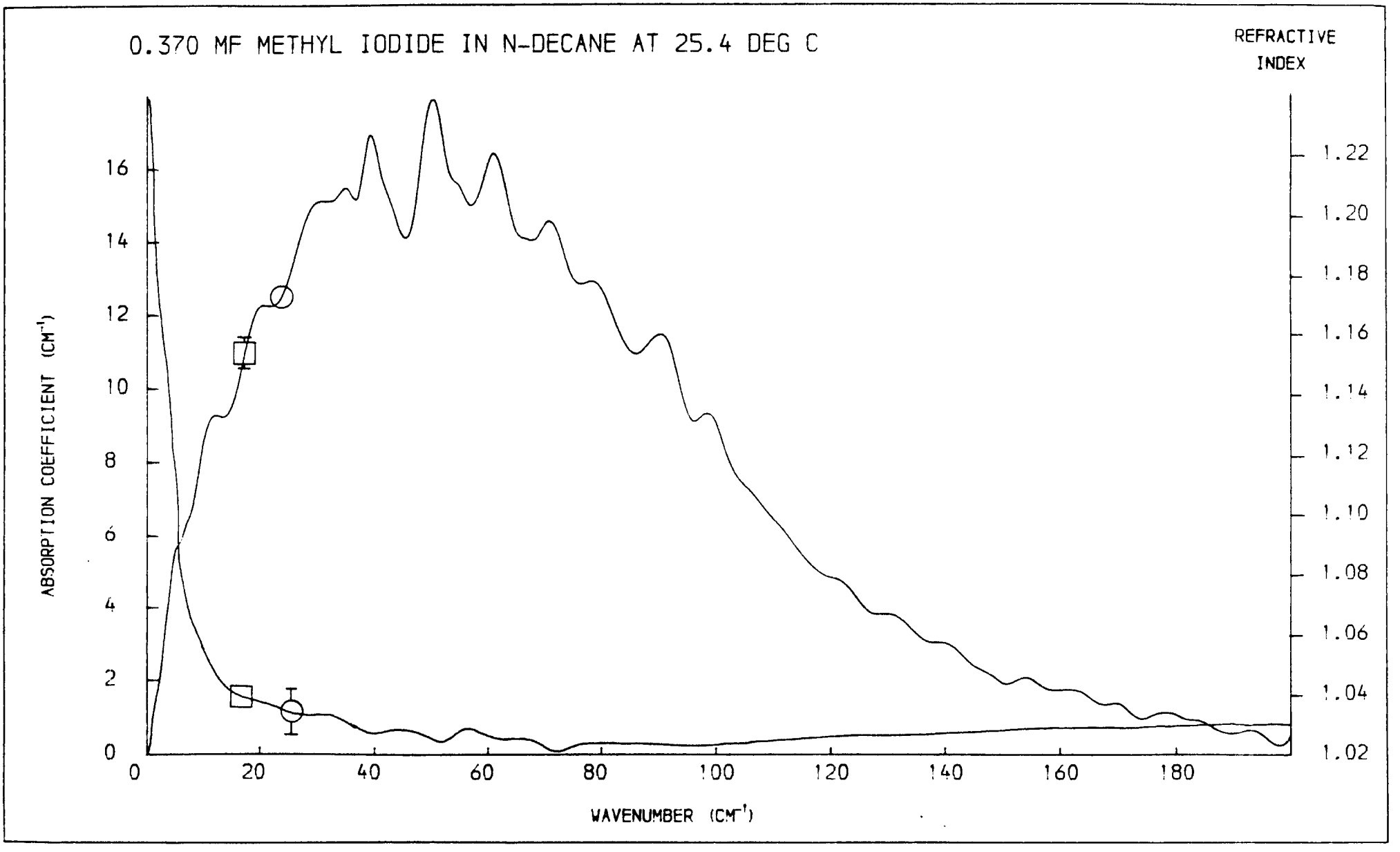
0.370 MF METHYL IODIDE IN N-DECANE AT 25.4 DEG C
REFRACTIVE INDEX
ABSORPTION COEFFICIENT (CM⁻¹)
WAVENUMBER (CM⁻¹)
0
2
4
6
8
10
12
14
16
0
20
40
60
80
100
120
140
160
180
1.02
1.04
1.06
1.08
1.10
1.12
1.14
1.16
1.18
1.20
1.22

FIGURE 7.29

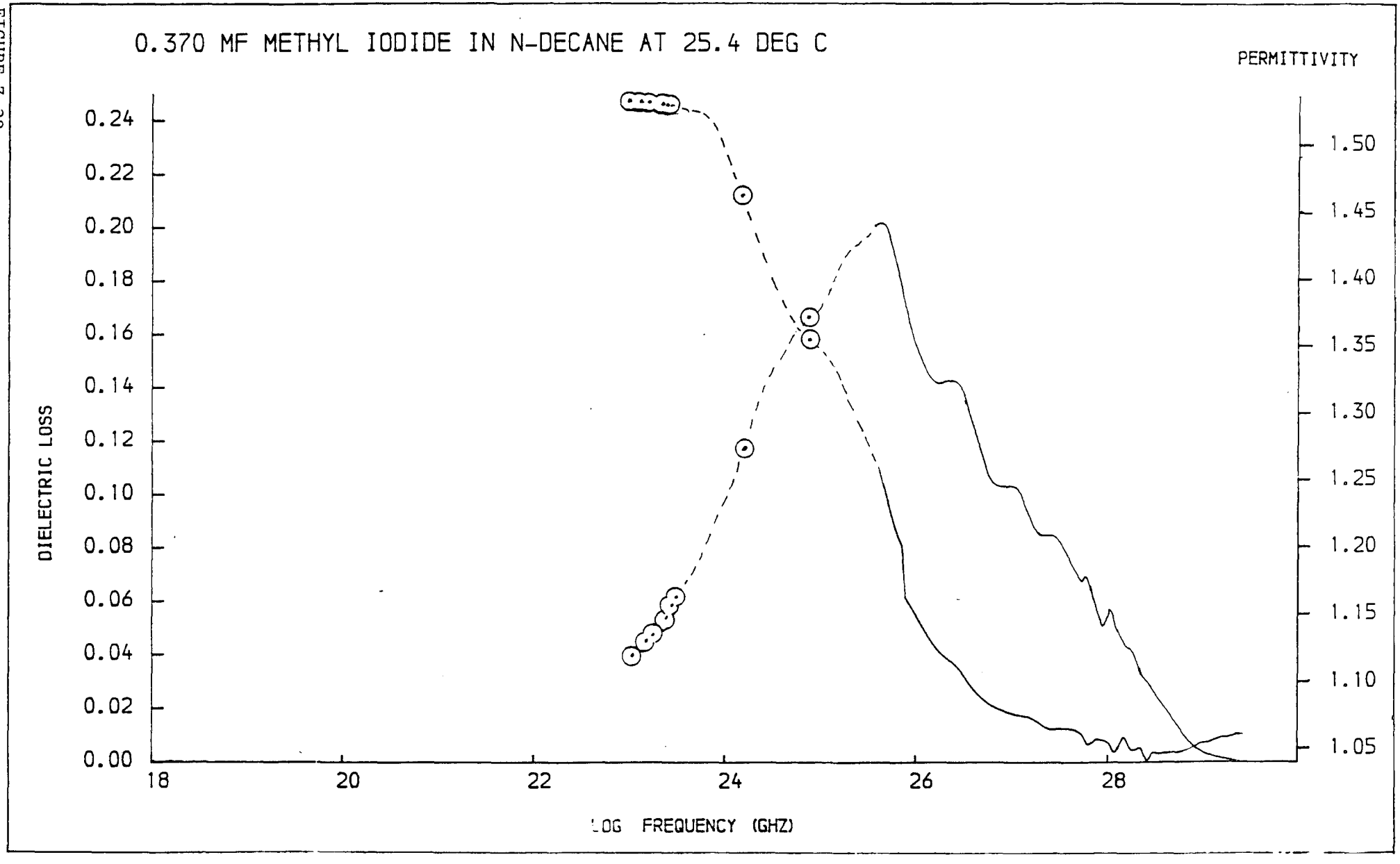
0.370 MF METHYL IODIDE IN N-DECANE AT 25.4 DEG C
PERMITTIVITY
DIELECTRIC LOSS
0.24
0.22
0.20
0.18
0.16
0.14
0.12
0.10
0.08
0.06
0.04
0.02
0.00
1.50
1.45
1.40
1.35
1.30
1.25
1.20
1.15
1.10
1.05
18
20
22
24
26
28
LOG FREQUENCY (GHZ)

FIGURE 7.30

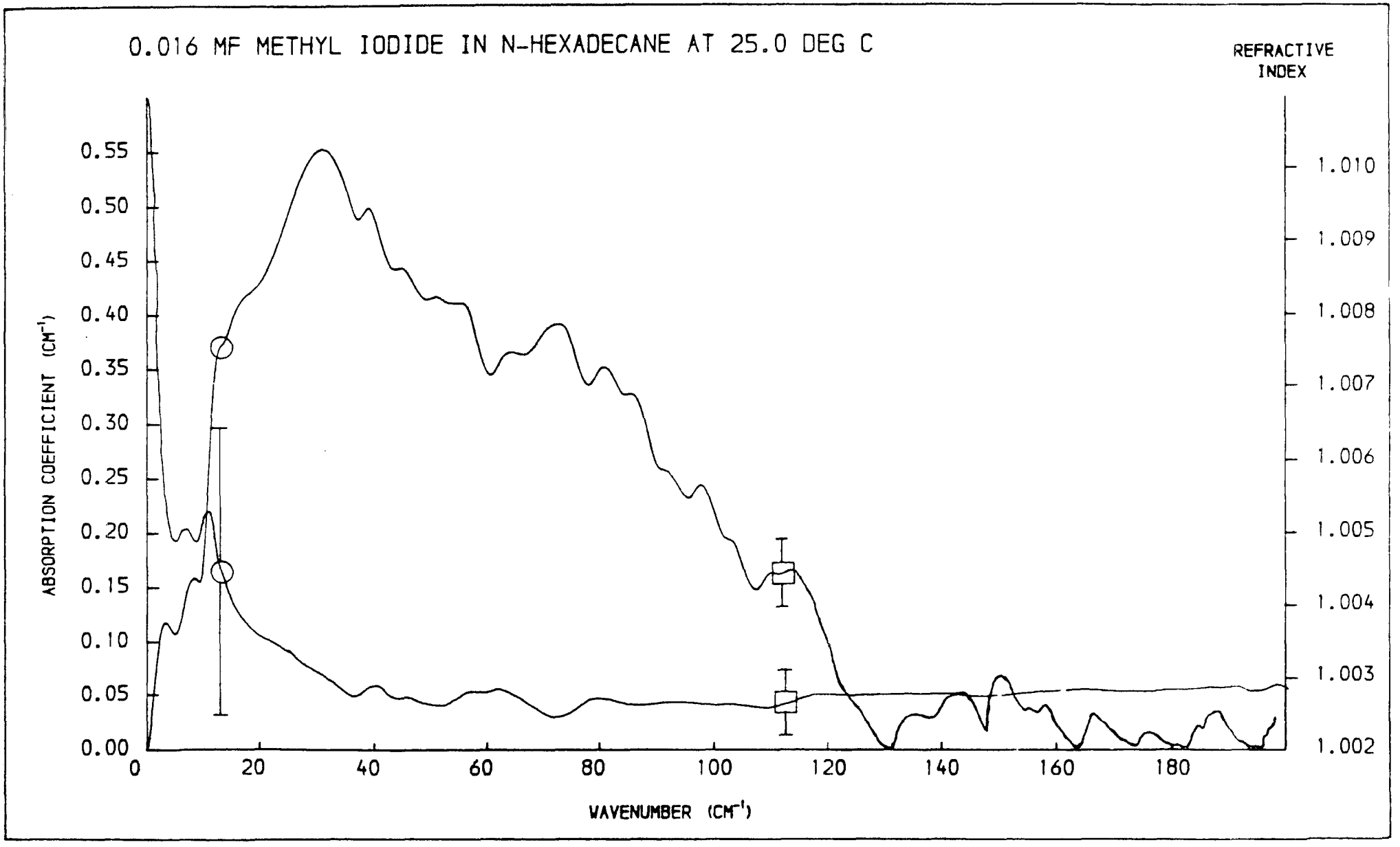
0.016 MF METHYL IODIDE IN N-HEXADECANE AT 25.0 DEG C
REFRACTIVE INDEX
ABSORPTION COEFFICIENT (CM⁻¹)
0.55
0.50
0.45
0.40
0.35
0.30
0.25
0.20
0.15
0.10
0.05
0.00
1.010
1.009
1.008
1.007
1.006
1.005
1.004
1.003
1.002
0
20
40
60
80
100
120
140
160
180
WAVENUMBER (CM⁻¹)

FIGURE 7.31

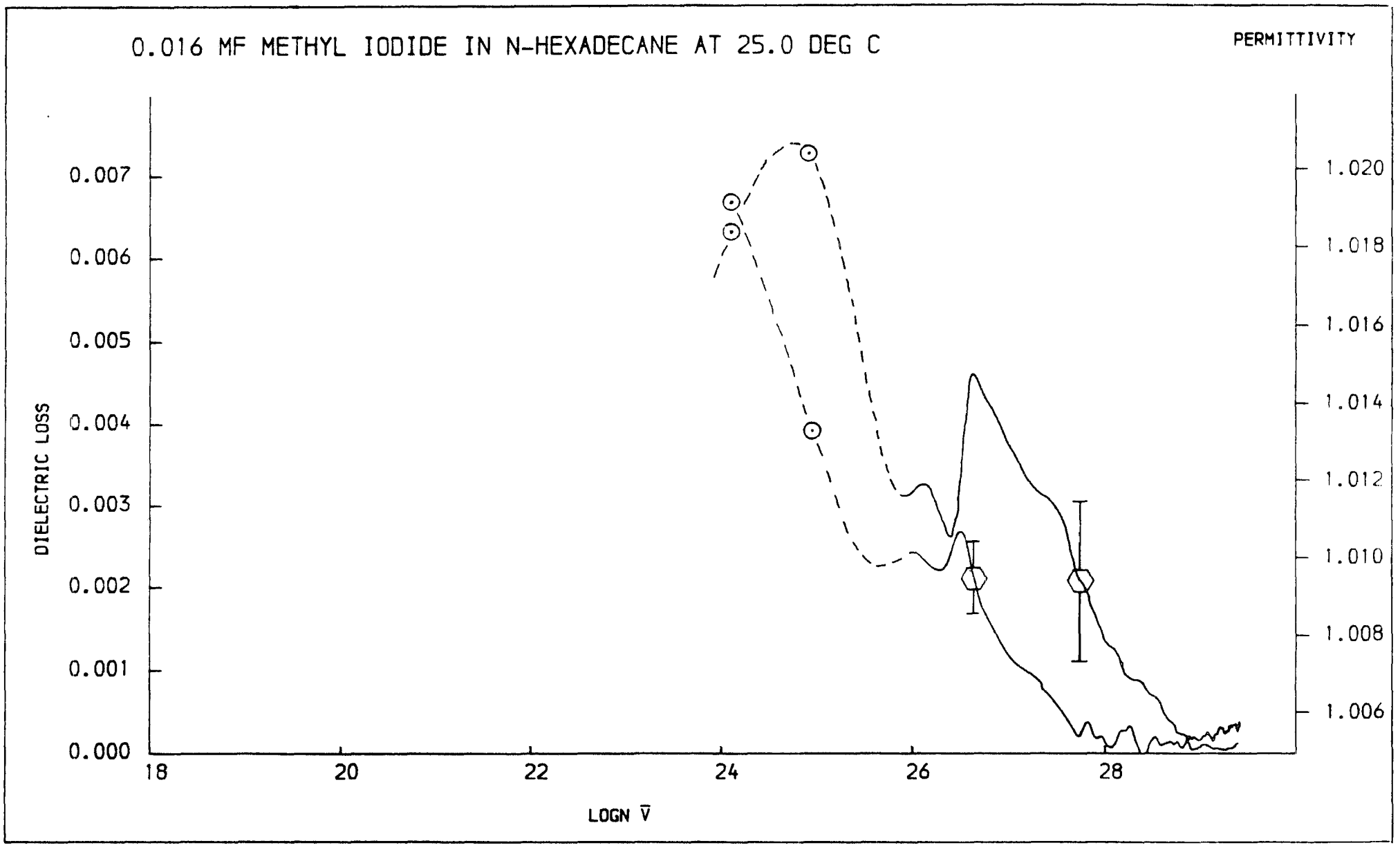
0.016 MF METHYL IODIDE IN N-HEXADECANE AT 25.0 DEG C
PERMITTIVITY
DIELECTRIC LOSS
0.007
0.006
0.005
0.004
0.003
0.002
0.001
0.000
1.020
1.018
1.016
1.014
1.012
1.010
1.008
1.006
18
20
22
24
26
28
LOGN $\bar{V}$

FIGURE 7.32

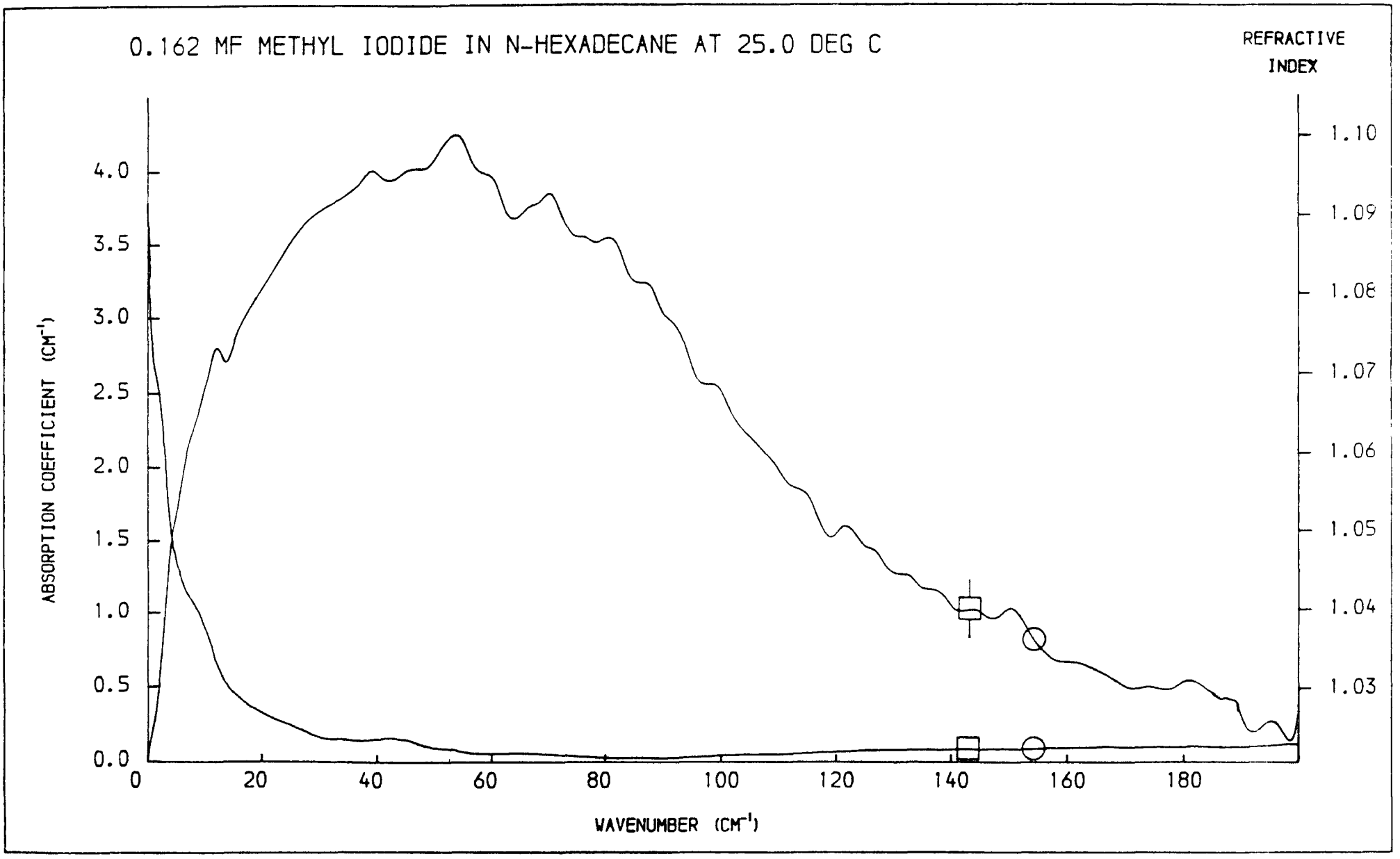
0.162 MF METHYL IODIDE IN N-HEXADECANE AT 25.0 DEG C
REFRACTIVE INDEX
ABSORPTION COEFFICIENT (CM⁻¹)
WAVENUMBER (CM⁻¹)
0.0
0.5
1.0
1.5
2.0
2.5
3.0
3.5
4.0
0
20
40
60
80
100
120
140
160
180
1.03
1.04
1.05
1.06
1.07
1.08
1.09
1.10

FIGURE 7.33

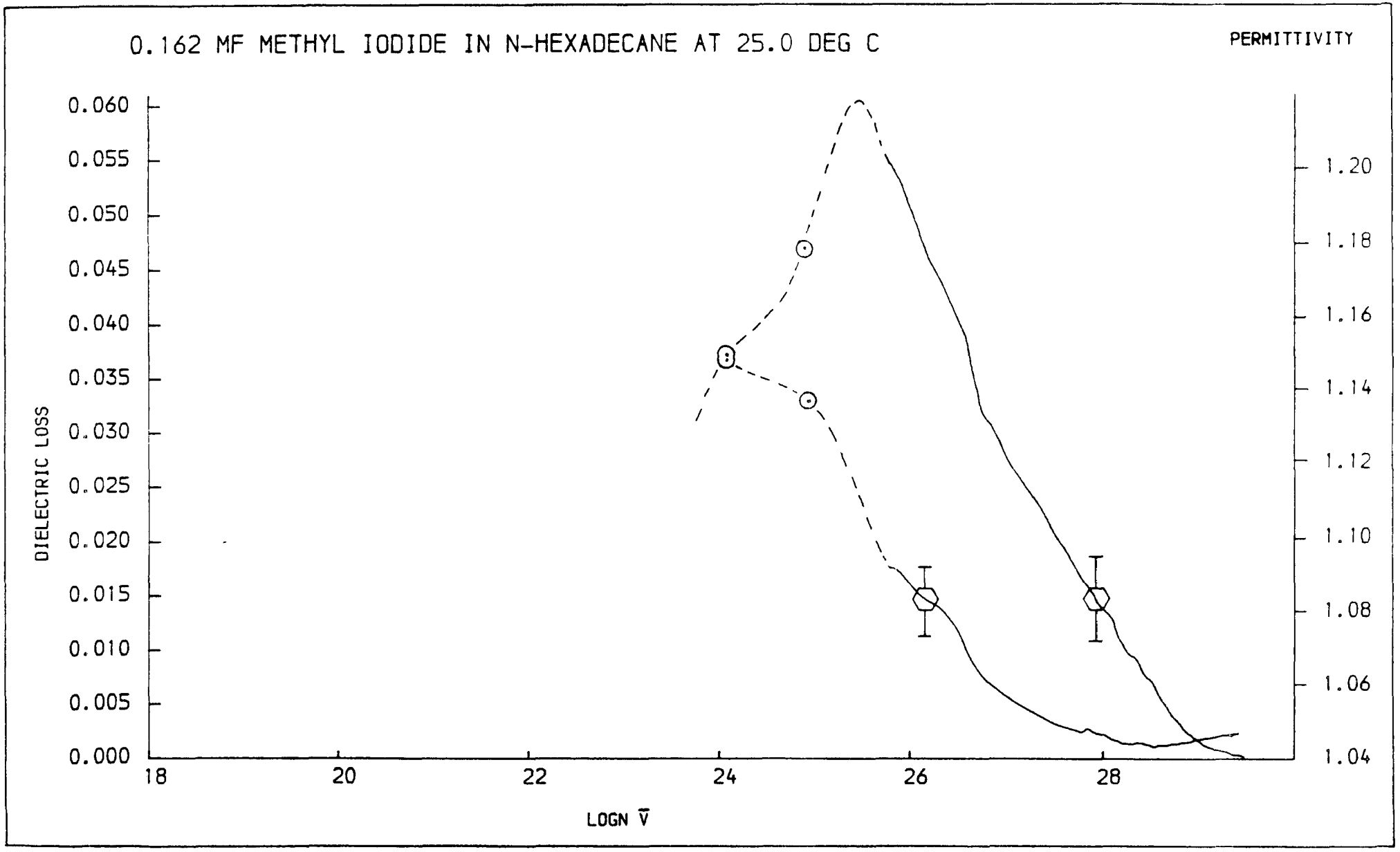
0.162 MF METHYL IODIDE IN N-HEXADECANE AT 25.0 DEG C
PERMITTIVITY
DIELECTRIC LOSS
0.060
0.055
0.050
0.045
0.040
0.035
0.030
0.025
0.020
0.015
0.010
0.005
0.000
1.20
1.18
1.16
1.14
1.12
1.10
1.08
1.06
1.04
18
20
22
24
26
28
LOGN V̄

FIGURE 7.34

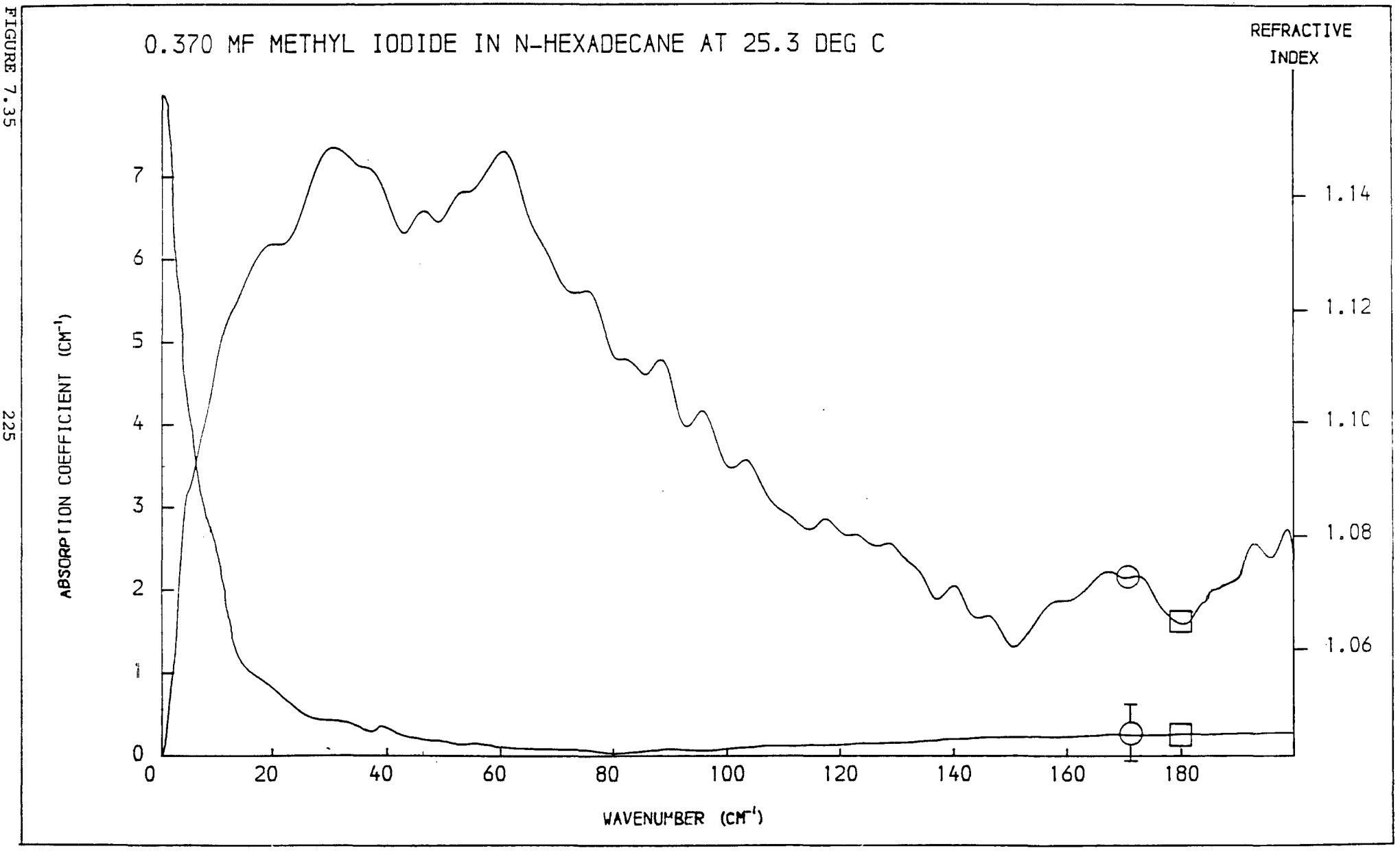
0.370 MF METHYL IODIDE IN N-HEXADECANE AT 25.3 DEG C
REFRACTIVE INDEX
ABSORPTION COEFFICIENT (CM⁻¹)
WAVENUMBER (CM⁻¹)
0
1
2
3
4
5
6
7
0
20
40
60
80
100
120
140
160
180
1.06
1.08
1.10
1.12
1.14

FIGURE 7.35

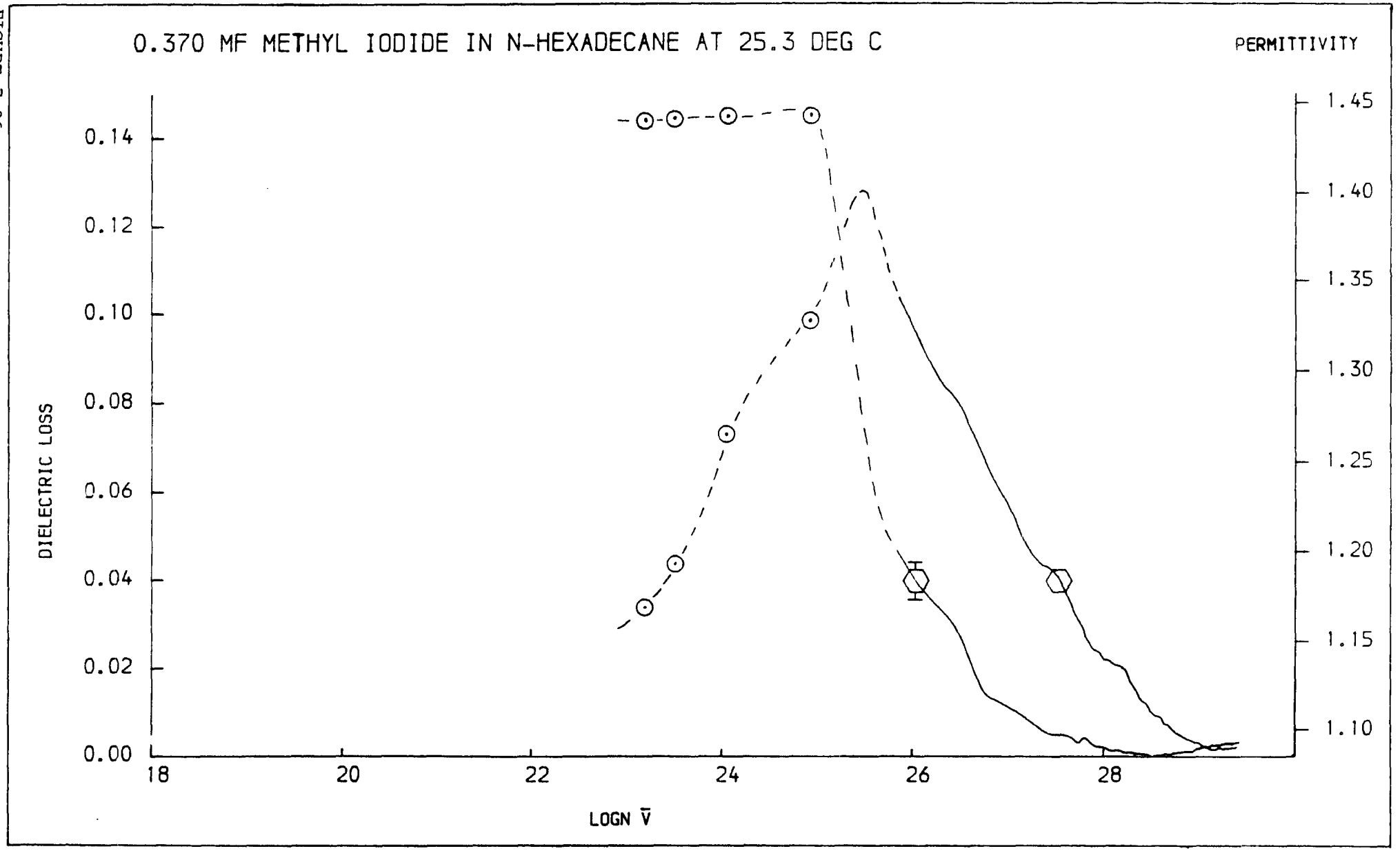
0.370 MF METHYL IODIDE IN N-HEXADECANE AT 25.3 DEG C
PERMITTIVITY
DIELECTRIC LOSS
0.14
0.12
0.10
0.08
0.06
0.04
0.02
0.00
1.45
1.40
1.35
1.30
1.25
1.20
1.15
1.10
18
20
22
24
26
28
LOGN $\bar{V}$

FIGURE 7.36

7.4.1 Analysis of the Absorption Coefficient Spectra.

Measurements were made of the absorption coefficient peak position, half height width (FWHH) and the area of the band between 0 and 200 cm^{-1}. These results are presented in Table 7.10. Using Gordon's sum rule for a symmetric top molecule[95], the liquid dipole moment can be calculated from this data.

$$Ai = \frac{2\,\mu^2_{Calc} I(1/I_b)}{3c^2} \qquad \ldots\ldots \quad 7.18$$

where Ai is the integrated absorption intensity per molecule. This calculated dipole moment can be compared with the Onsager[14] enhanced dipole moment, obtained from

$$\mu^* = \frac{(2\varepsilon_o + 1)(\varepsilon_\infty + 2)}{3(\varepsilon_o + \varepsilon_\infty)}\,\mu_{gas} \qquad \ldots\ldots \quad 7.19$$

These values are given in Table 7.11.

7.4.2 Fourier Transformation of the Far-Infrared Absorption.

From Section 1, Fourier transformation of $\varepsilon''/$ will give the orientational correlation function, ϕ_{1R}. Plots of ϕ_{1R} and $\ln\phi_{1R}$ are shown in Figs. 7.37 to 7.44. The correlation time τ^T_{1R} can be obtained from equation 6.4 by integration of the area under the

ABSORPTION COEFFICIENT PROPERTIES OF MeI

Solvent	Concentration mf	$\bar{\nu}_{MAX}$ cm^{-1}	FWHH cm^{-1}	A1 cm Mol^{-1} x 10^{-20}
	1.0	62 ± 2	77 ± 1	95.1 ± 5%
	0.005	35 ± 5	40 ± 1	46.8 ± 10%
n-HEPTANE	0.016	37 ± 2	75 ± 1	58.4 ± 5%
	0.162	36 ± 2	82 ± 1	63.3 ± 5%
	0.370	40 ± 5	92 ± 1	74.9 ± 5%
	0.016	48 ± 2	93 ± 1	109.5 ± 10%
n-DECANE	0.162	40 ± 2	80 ± 1	70.7 ± 5%
	0.370	50 ± 2	93 ± 1	78.9 ± 5%
	0.016	32 ± 4	78 ± 2	94.0 ± 10%
n-HEXADECANE	0.162	53 ± 2	103 ± 1	87.6 ± 5%
	0.370	46 ± 2	97 ± 1	75.2 ± 5%
CARBON TETRACHLORIDE	0.162	70 ± 2	100 ± 1	94.4 ± 5%
CARBON DISULPHIDE	0.100	59 ± 2	77 ± 1	92.6 ± 10%

7.11

DIPOLE MOMENT DATA IN DEBYES (μ_o = 1.65)

Solvent	Concentration mf	μ_{calc}	μ^*	μ^* (ε_∞ = 2.936)
	1.0	2.5_4	2.35_5	
n-HEPTANE	0.005	1.5_0	1.65	1.62_6
	0.016	1.6_7	1.65	1.63_7
	0.162	1.7_4	1.66	1.78_4
	0.370	1.9_0	1.70	1.89_9
n-DECANE	0.016	2.2_9	1.65	1.64_0
	0.162	1.8_4	1.66	1.72_7
	0.370	1.9_5	1.66	1.80_5
n-HEXADECANE	0.016	2.1_2	1.65	1.62_9
	0.162	2.0_5	1.65	1.70_5
	0.370	1.9_0	1.66	1.74_6
CARBON TETRACHLORIDE	0.162	2.1_3	1.67	1.78_4
CARBON DISULPHIDE	0.100	2.1_1	1.69	1.80_7

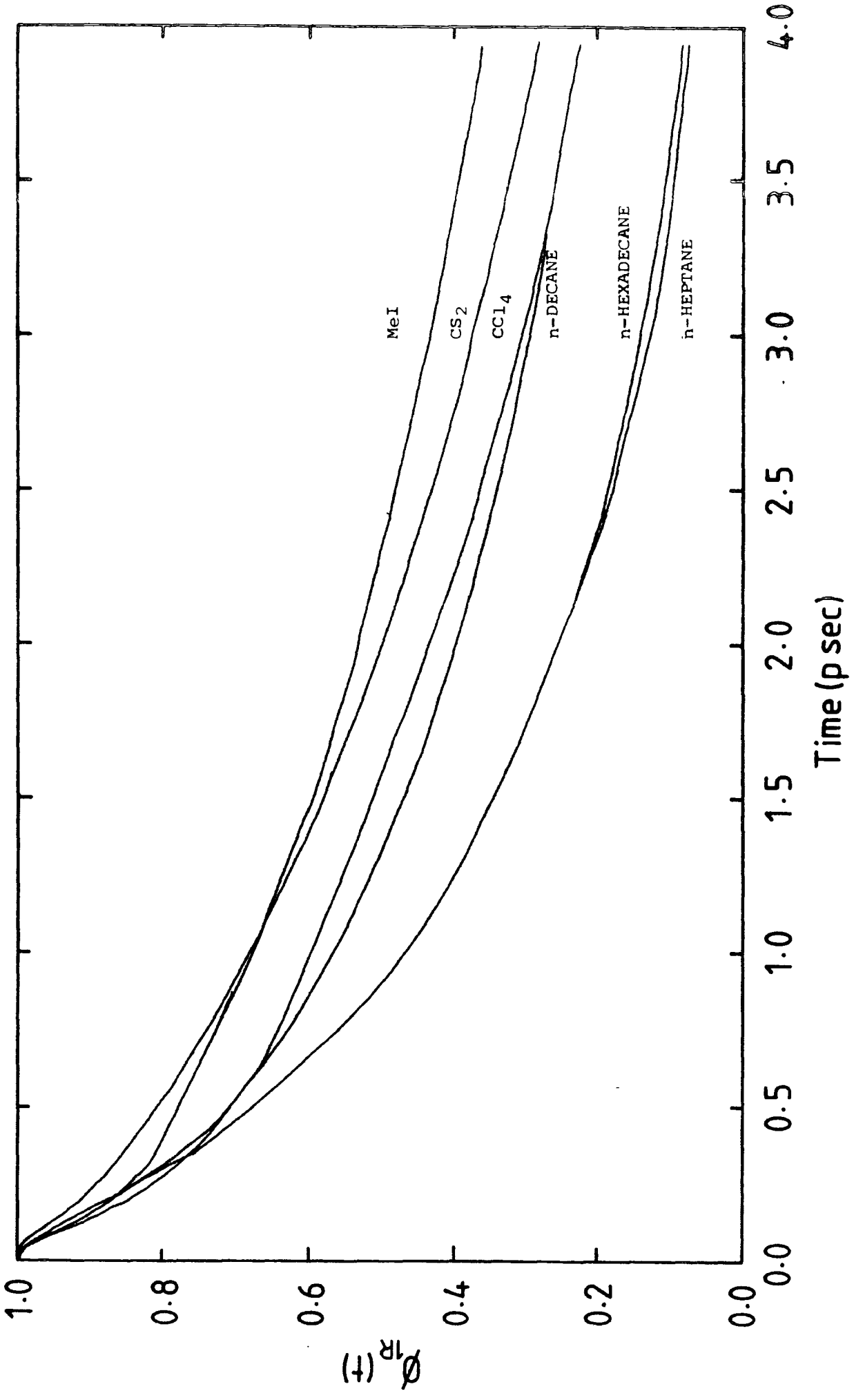

Figure 7.37 Correlation Functions for Me I liquid and in a range of solvents

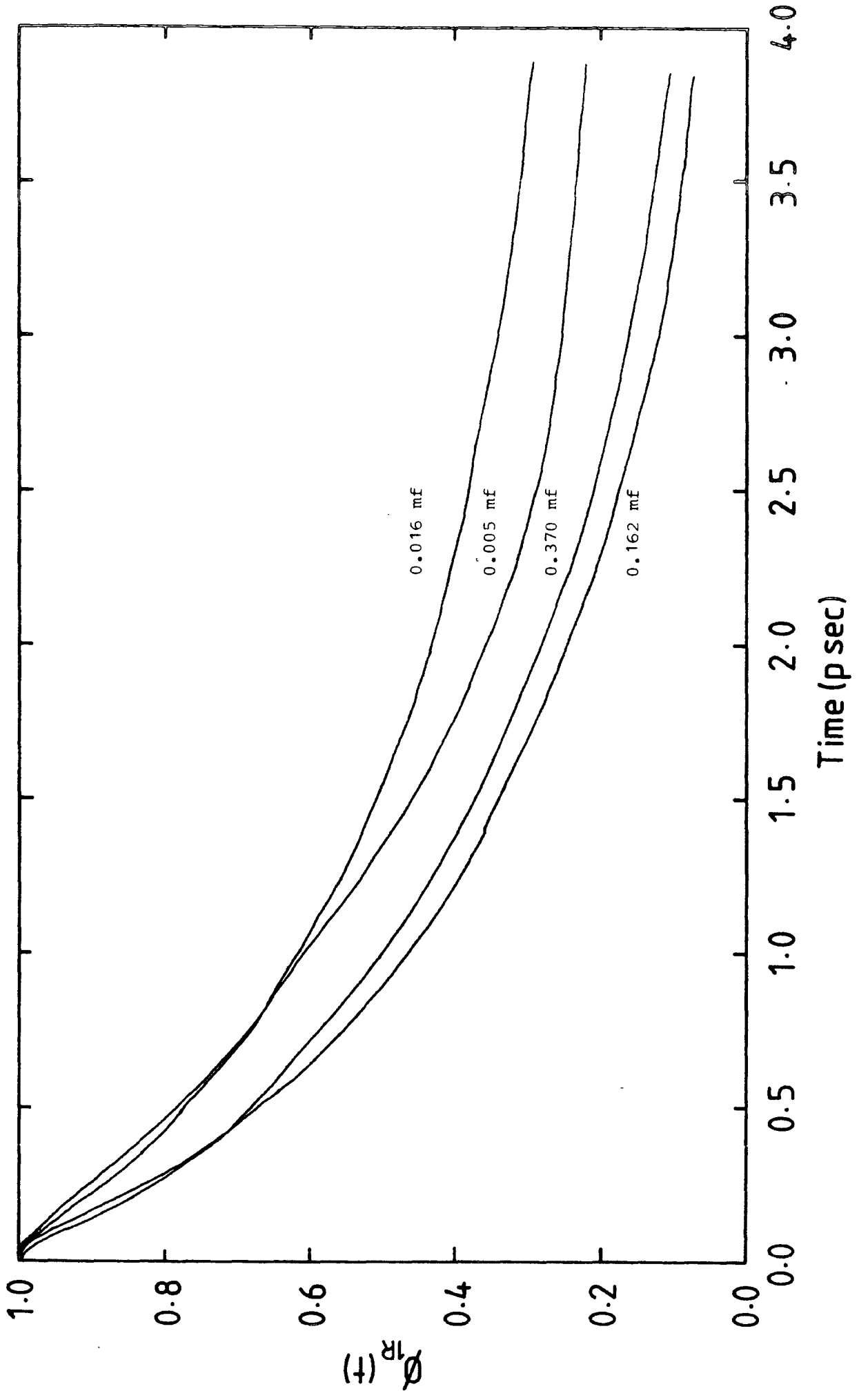

Figure 7.38 Correlation Functions for MeI in n-heptane solutions

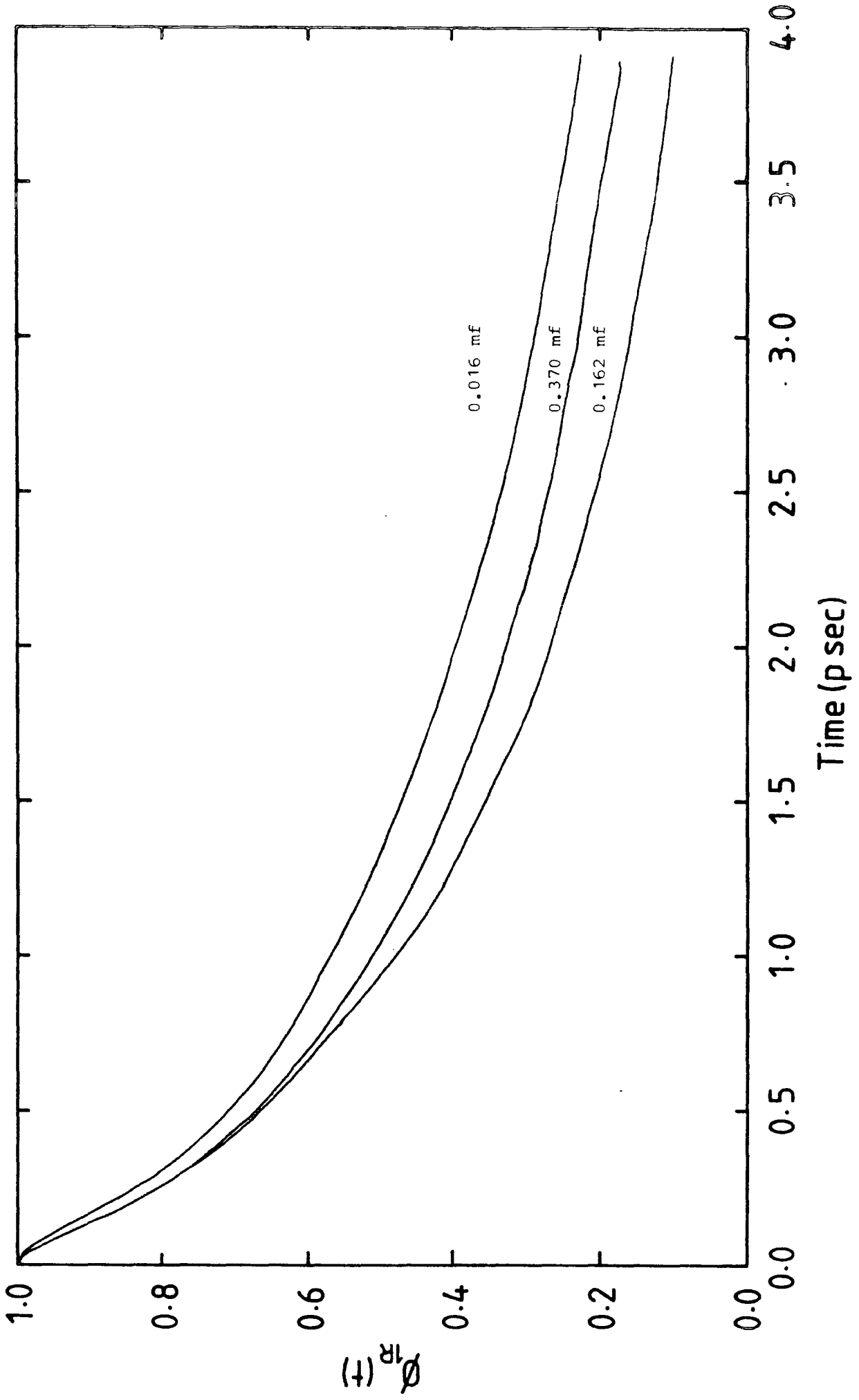

Figure 7.39 Correlation functions for Me I in n-decane solution

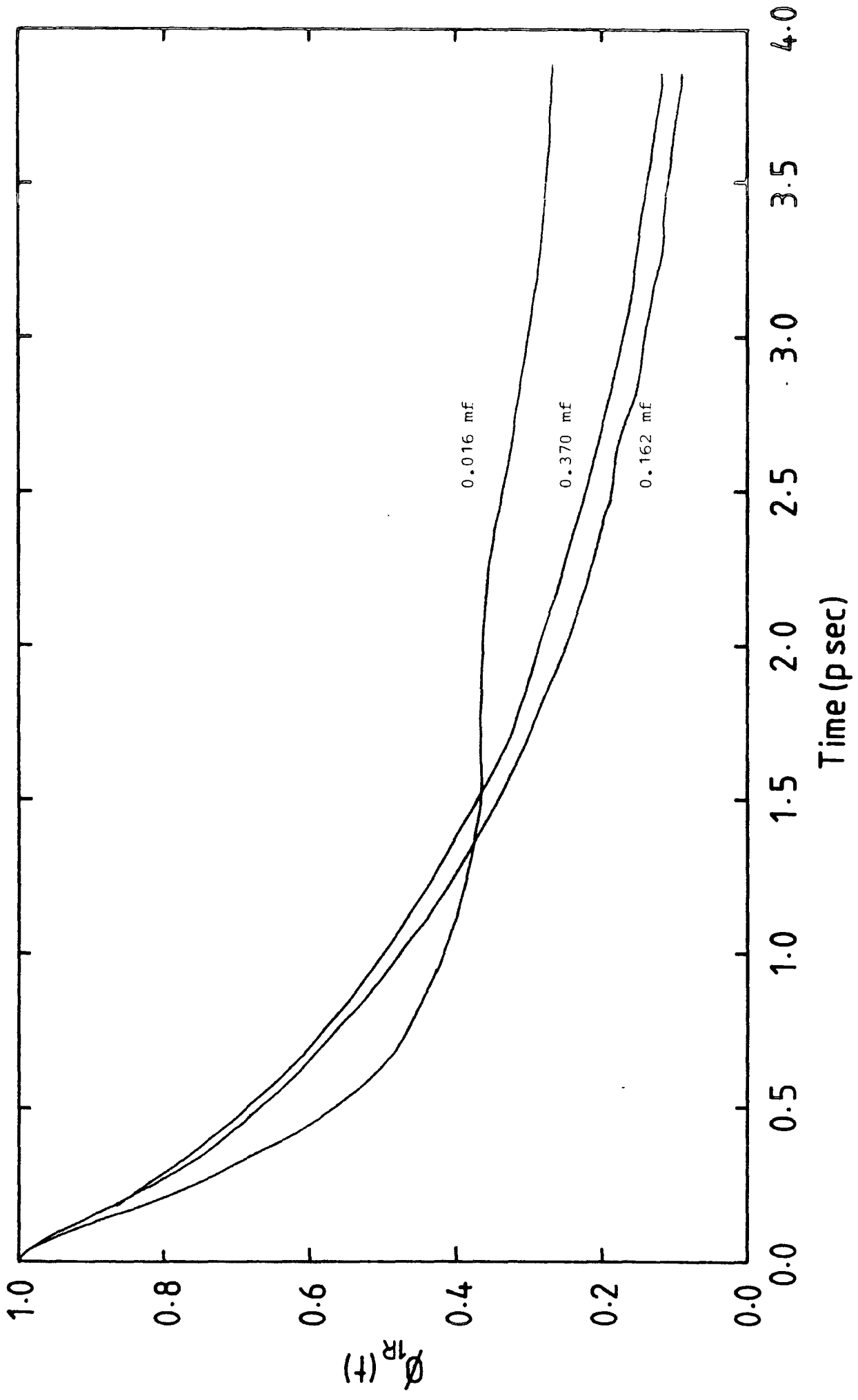

Figure 7.40 Correlation functions for Me I in n-hexadecane solution

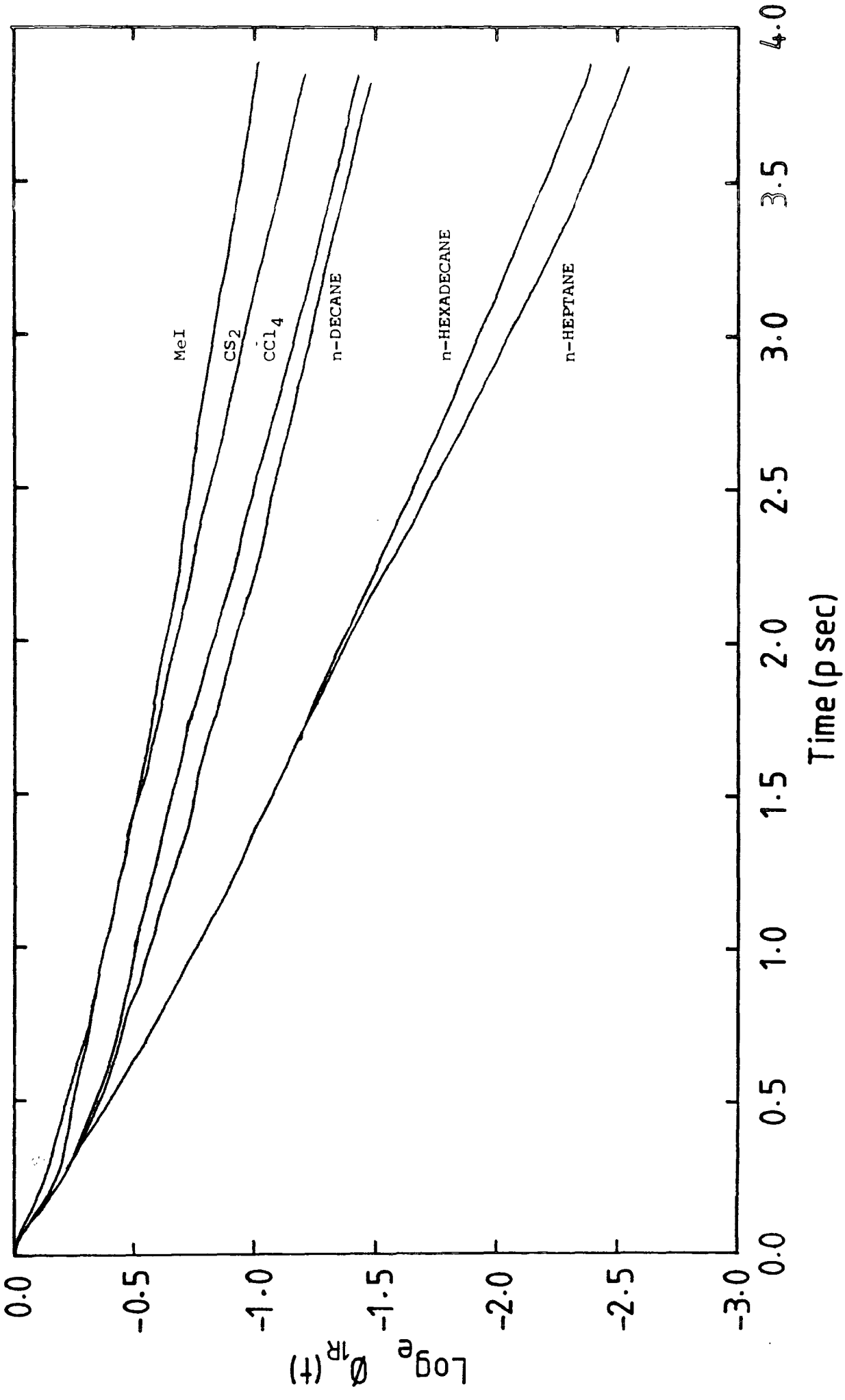

Figure 7.41 Me I liquid and in a range of solvents

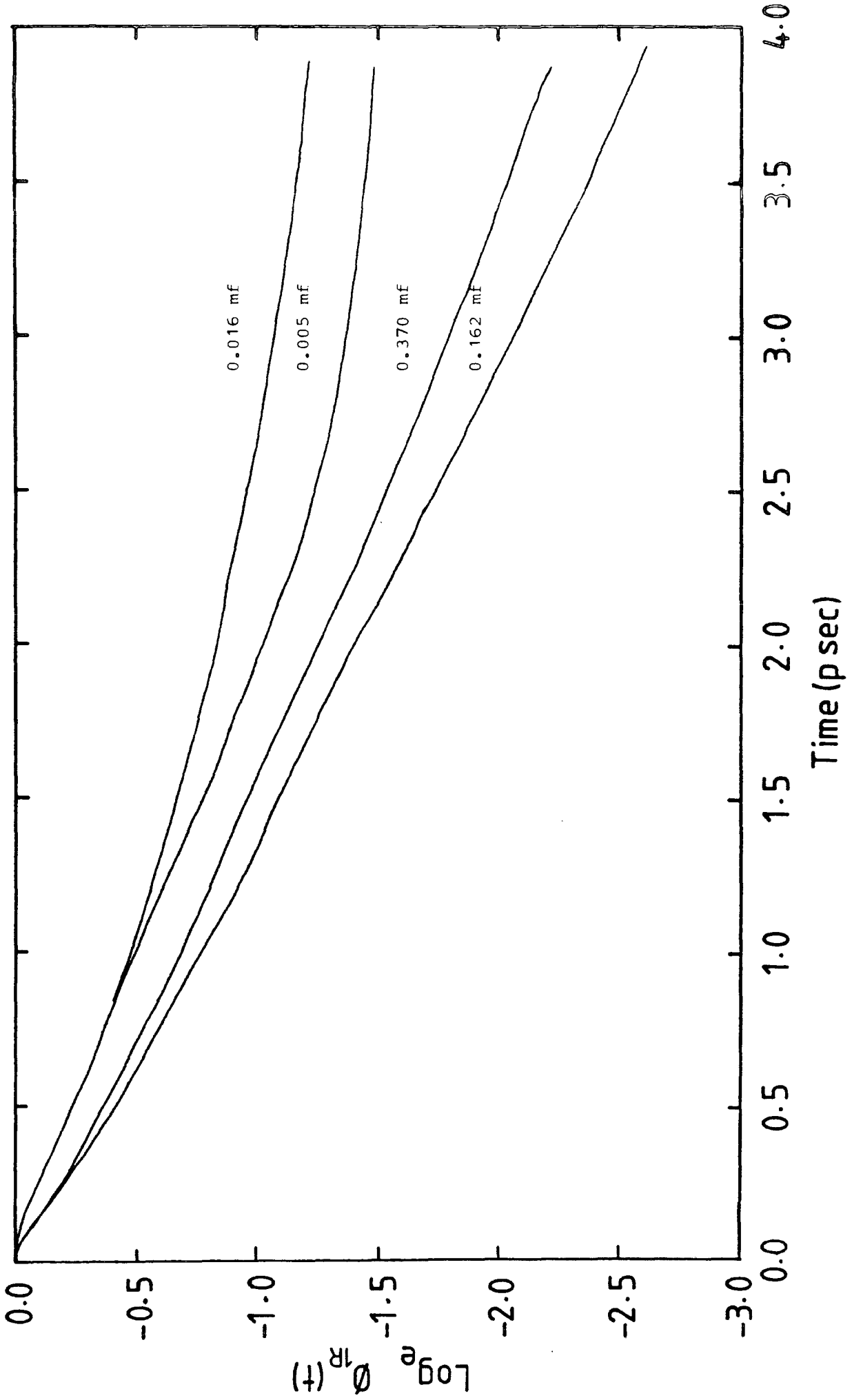

Figure 7.42 Me I in n-heptane solutions

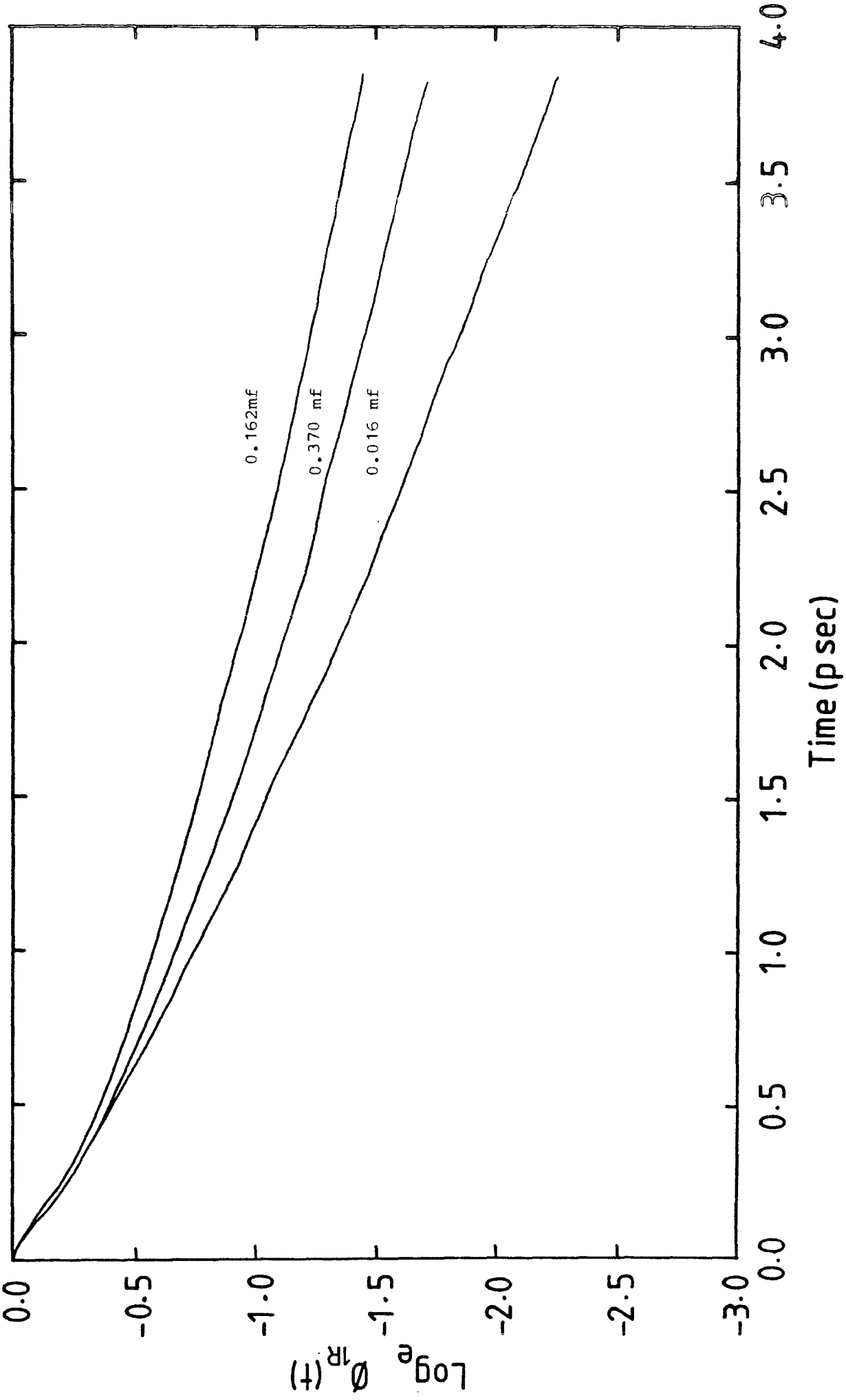

Figure 7.43 Me I in n-Decane solutions

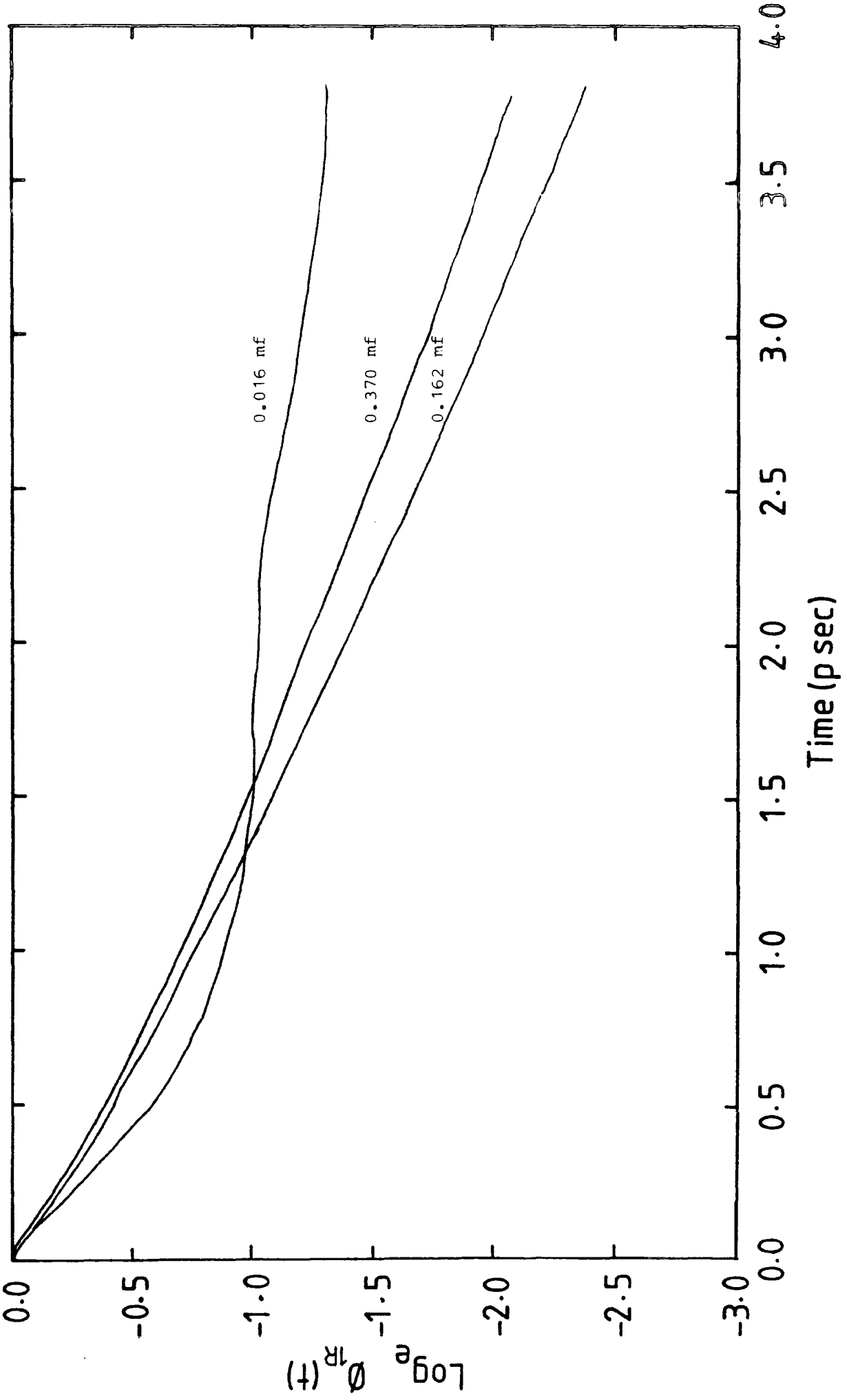

Figure 7.44 Me I in n-hexadecane solutions

correlation function, or from the slope of the ln plot of ϕ_{1R} or the time taken to reach 1/e , the results of these three methods are given in Table 7.12.

7.4.3 Band Moment Analysis.

The second (M_{2R}) and fourth (M_{4R}) spectral moments can be obtained from dielectric loss data using equation 6.50. A selection of the normalised moments obtained from the spectra in section 7.4 are shown in Figures 7.45 and 7.54. Values for the moments, $g^{(1)}$ and Kirkwood Froilick g factor g^{KF} calculated from equation 6.20 are presented in Table 7.13.

7.4.4 Intermolecular Mean Squared Torques.

From equations 6.48 and 6.49

$$M_{4R} = 8\left[\frac{kT}{I_B}\right]^2 \left[1 + \left(\frac{IA}{I_B}\right) + \frac{\langle o(\nu)^2 \rangle}{k^2T^2}\right] \qquad \ldots\ldots \quad 7.20$$

So the intermolecular mean squared torque can be obtained from the fourth moment, also from Ried[94] they can be determined from the position of the peak in the absorption coefficient spectrum. Values obtained from both of these techniques and the Mori model of Evans etal[84] are given in Table 7.14.

CORRELATION FUNCTION RELAXATION TIMES

Solvent	Concentration mf	τ^{A}_{IR} ps	τ^{B}_{IR} ps	τ^{C}_{IR} ps
	1.0	3.7	3.9	5.2
n-HEPTANE	0.005	3.1	1.9	6.7
	0.016	3.5	2.7	5.5
	0.162	1.7	1.4	1.6
	0.370	1.9	1.5	1.8
n-DECANE	0.016	1.6	1.4	2.0
	0.162	2.7	2.3	3.4
	0.370	2.3	1.7	3.0
n-HEXADECANE	0.016	3.0	1.5	3.7
	0.162	1.6	1.4	1.5
	0.370	2.0	1.5	2.0
CARBON TETRACHLORIDE	0.162	2.7	2.5	3.1
CARBON DISULPHIDE	0.100	3.1	3.1	3.5

IR measured by; A = Integral, B = $\frac{1}{e}$, C = Gradient

BAND MOMENT ANALYSIS

Solvent	Concentration mf	M_2R cm^{-2} ±10%	M_2R* cm^{-2} ±10%	M_4R $10^4 cm^{-4}$ ±20%	M_4R* $10^4 cm^{-4}$ ±20%	g_o	g_o*	g_{K-F}
CH_3I	1.0	247.79	325.28	143.99	195.54	2.00	0.77	0.66
CCl_4	0.162	396.66	427.66	300.62	323.86	1.20	1.01	0.92
CS_2	0.100	184.05	277.56	152.46		1.10	0.87	0.77
	0.005	119.16		24.31		1.97	1.96	1.73
n-HEPTANE	0.016	154.42		44.23		1.87	1.84	1.61
	0.162	154.95		76.61		1.92	1.64	1.53
	0.370	284.21		158.21	177.69	1.35	1.02	0.94
	0.016	171.40		81.85		1.56	1.54	2.20
n-DECANE	0.162	258.58		129.25		1.32	1.20	1.27
	0.370	312.57		184.98		1.19	1.02	0.94
	0.016	220.34		92.54		1.87	1.85	1.66
n-HEXADECANE	0.162	243.54		115.63		1.19	1.10	1.48
	0.370	282.80		161.60		1.38	1.18	1.09

* Values using the internal field correction of Hill[95] are included when different to uncorrected values. $\frac{(2KT)}{I} = 207.307\ cm^{-2}$.

FIGURE 7.45 M_{2R} FOR MeI LIQUID

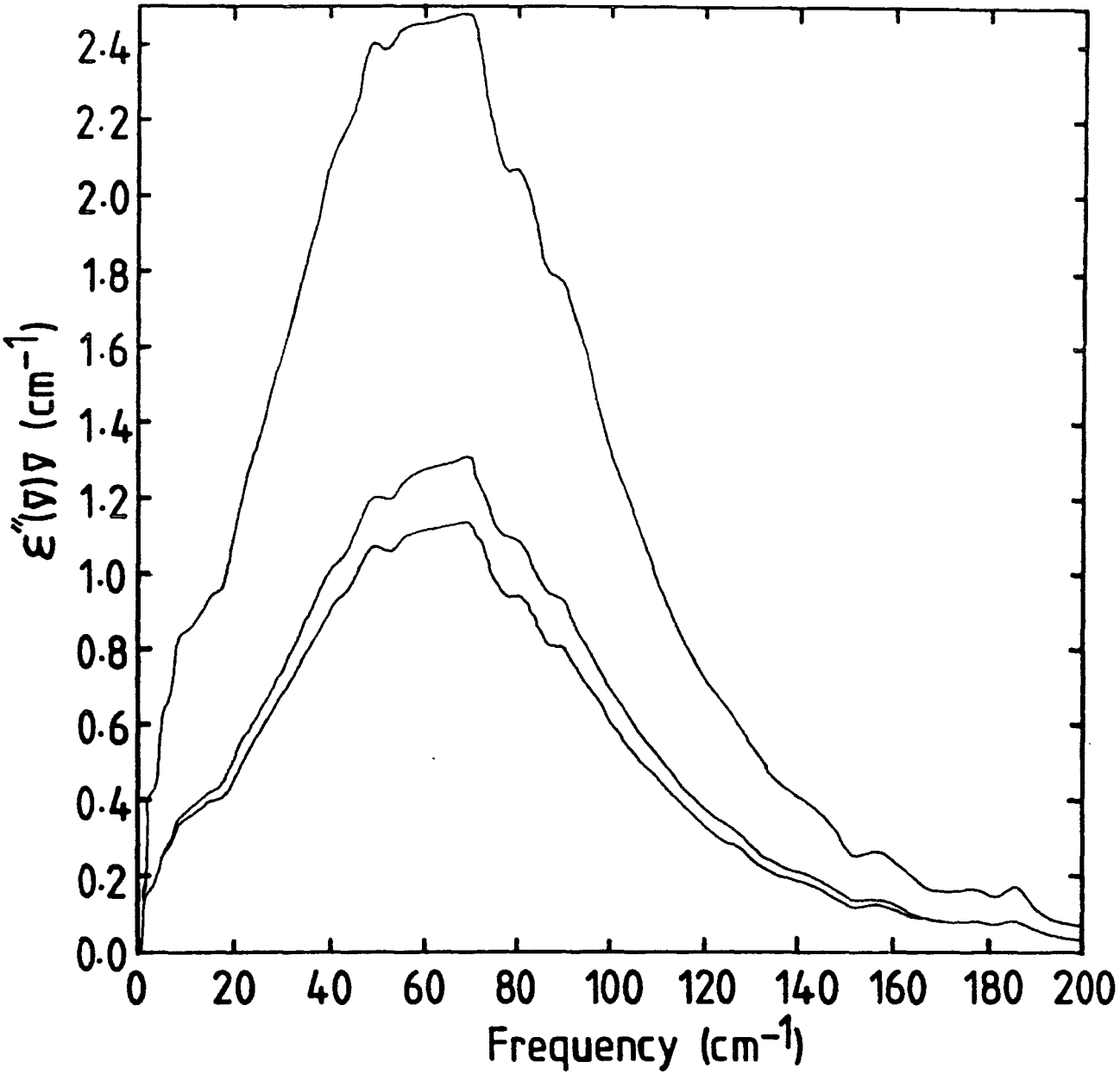

FIGURE 7.46 M_{4R} FOR MeI LIQUID

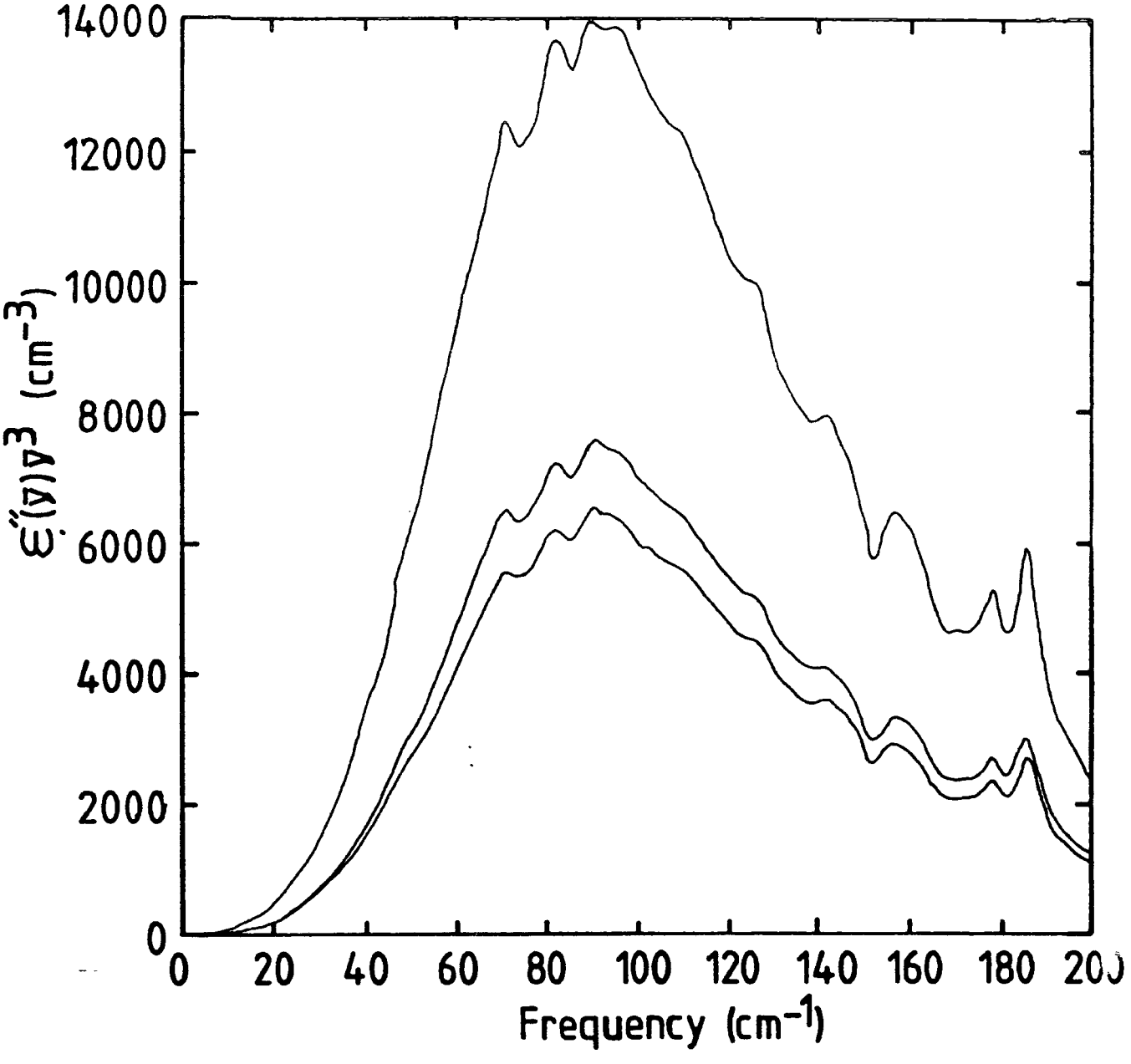

FIGURE 7.47 0.162 mf MeI IN CARBON TETRACHLORIDE

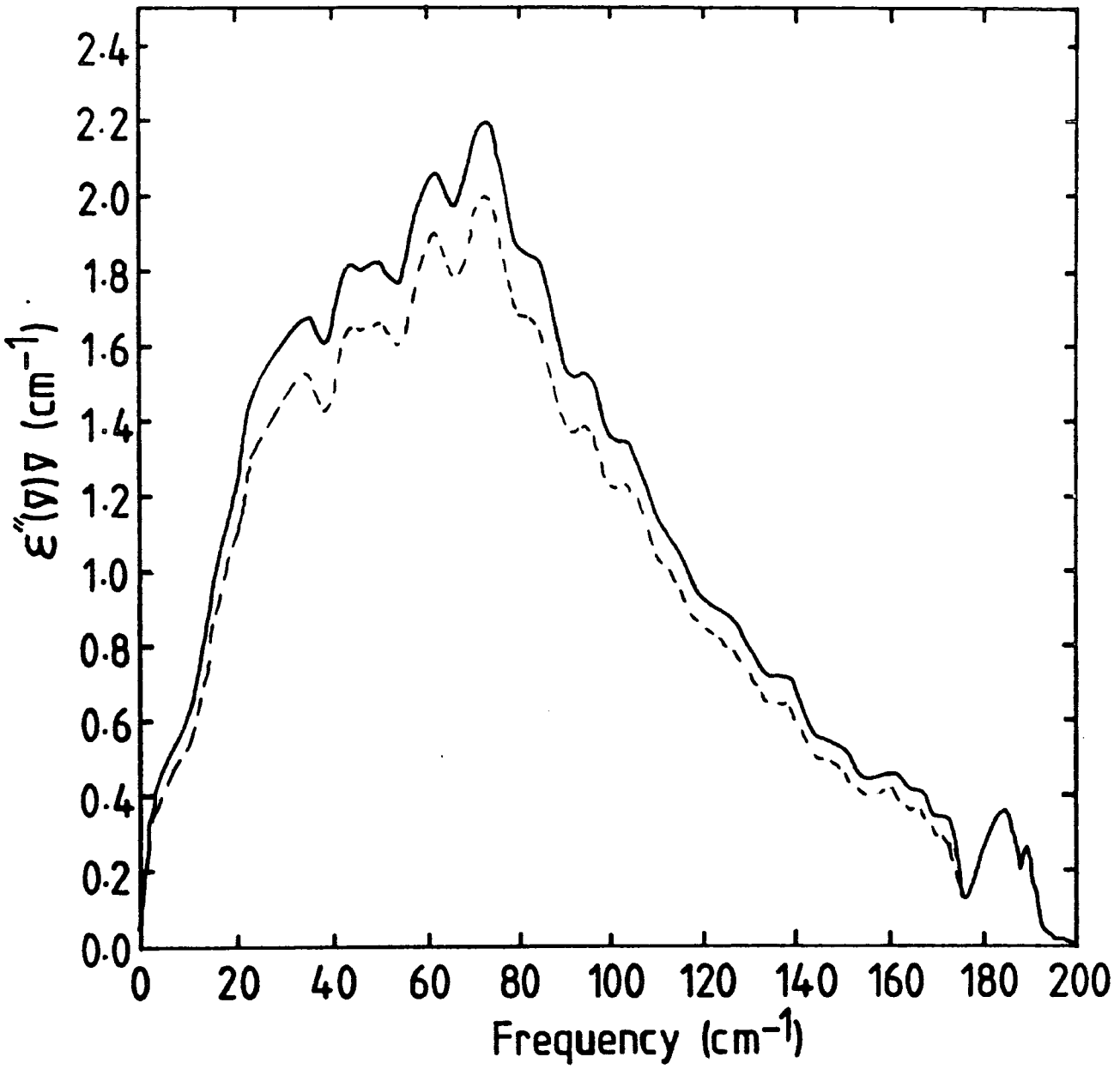

FIGURE 7.48 0.162 mf MeI IN CARBON TETRACHLORIDE

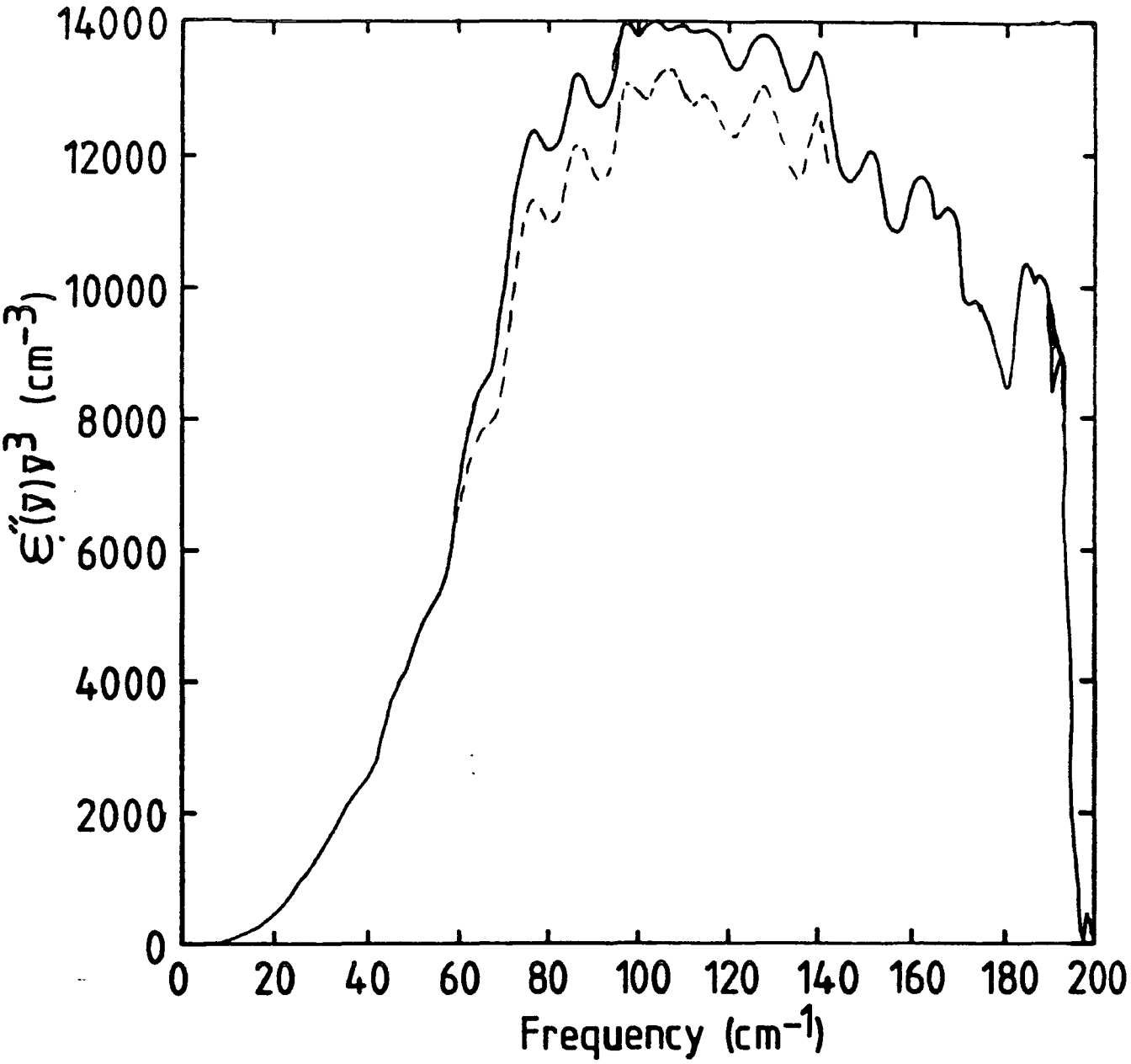

FIGURE 7.49 0:162 mf MeI IN n-HEPTANE

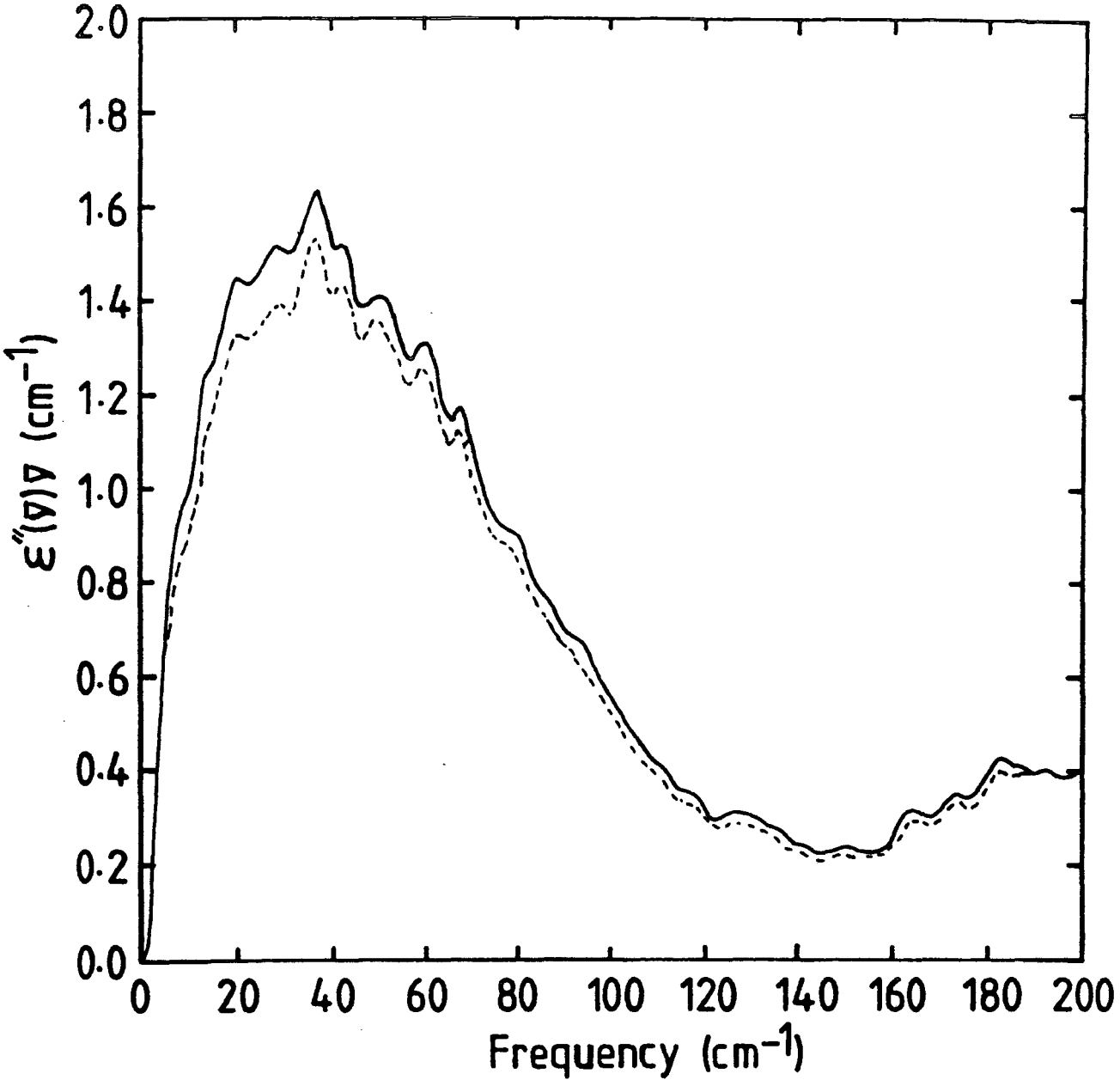

Figure 7.50 0:162 mf MeI IN n-HEPTANE

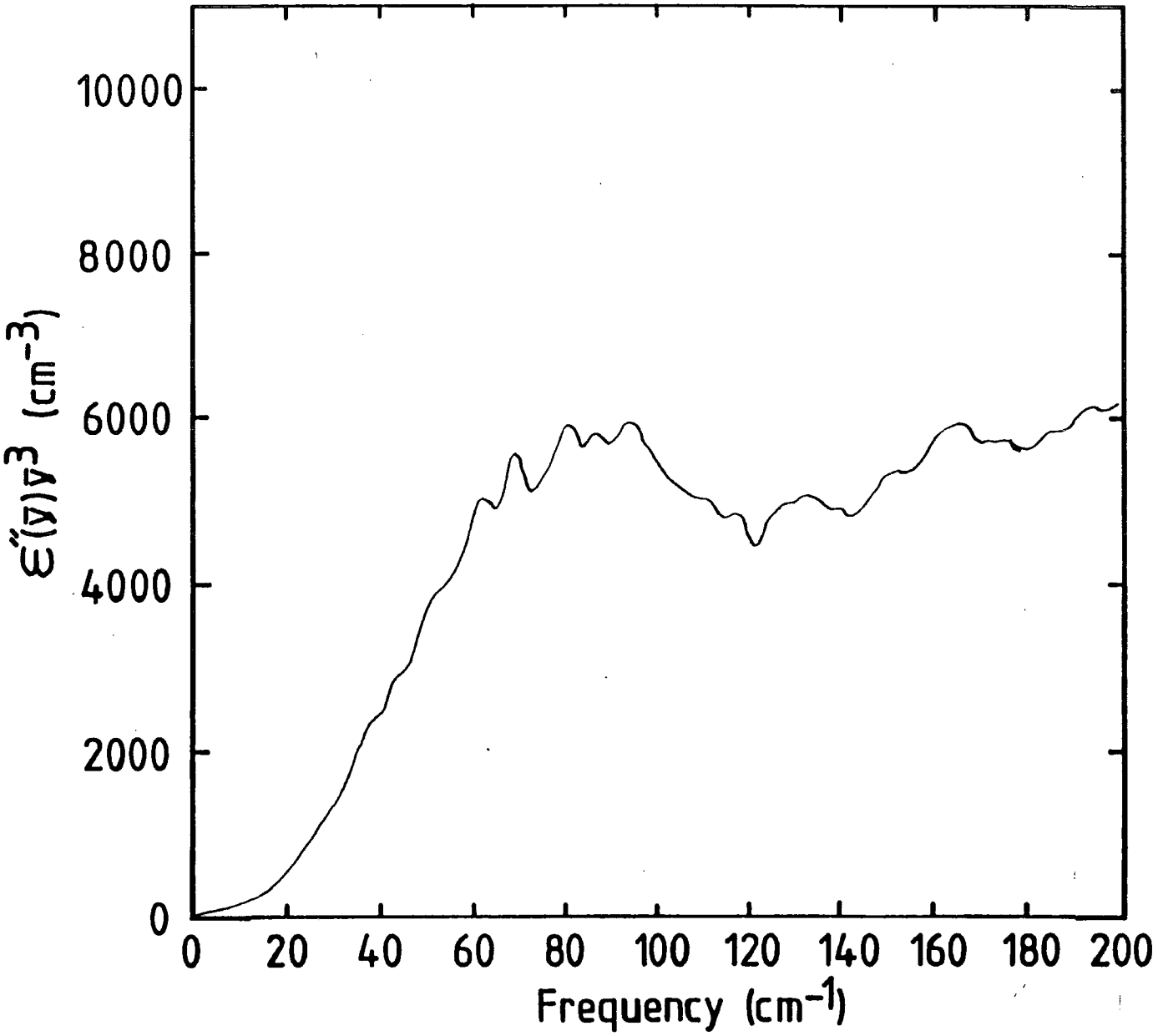

FIGURE 7.51 0.370 mf MeI IN n-DECANE

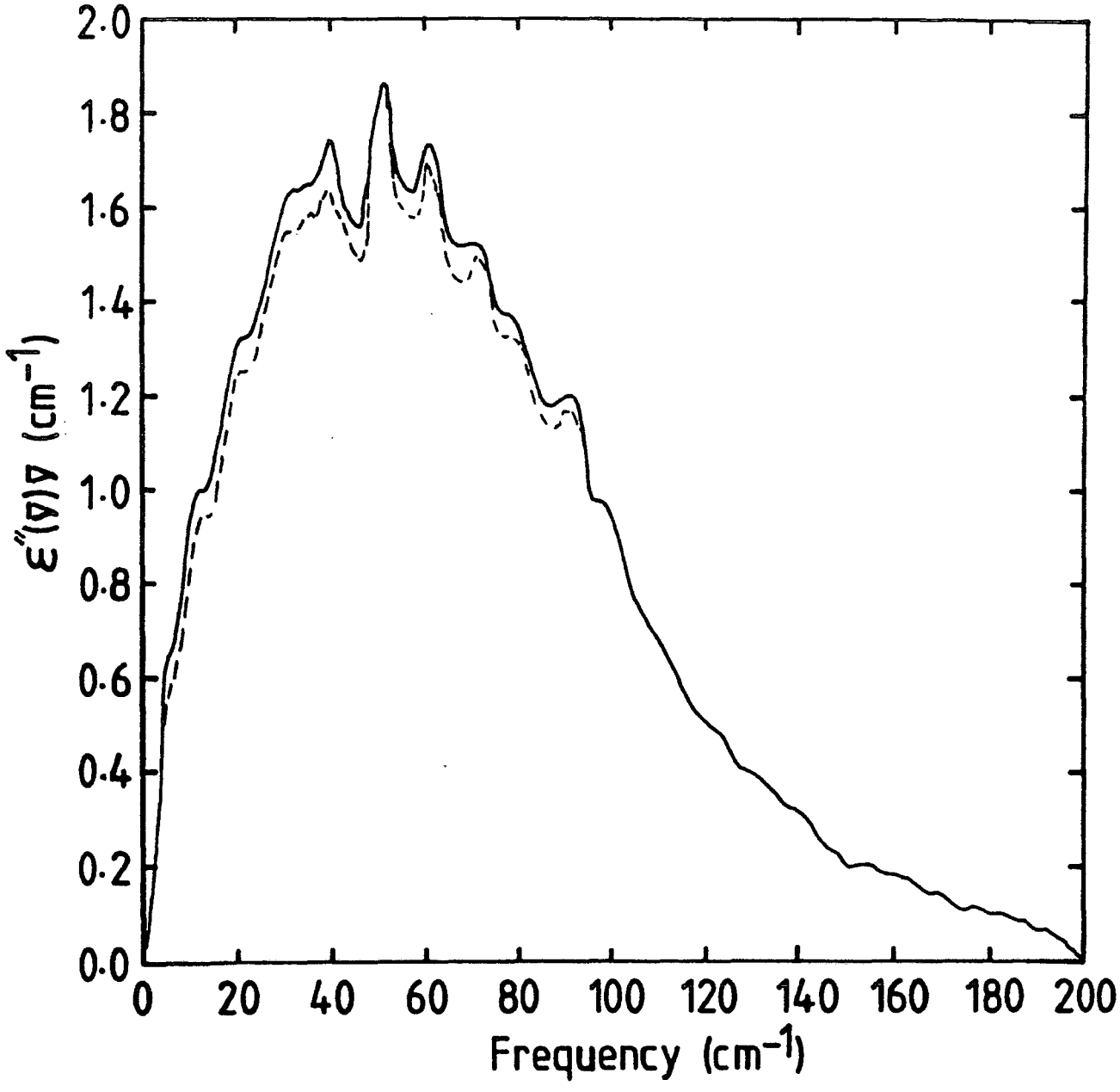

FIGURE 7.52 0.370 mf MeI IN n-DECANE

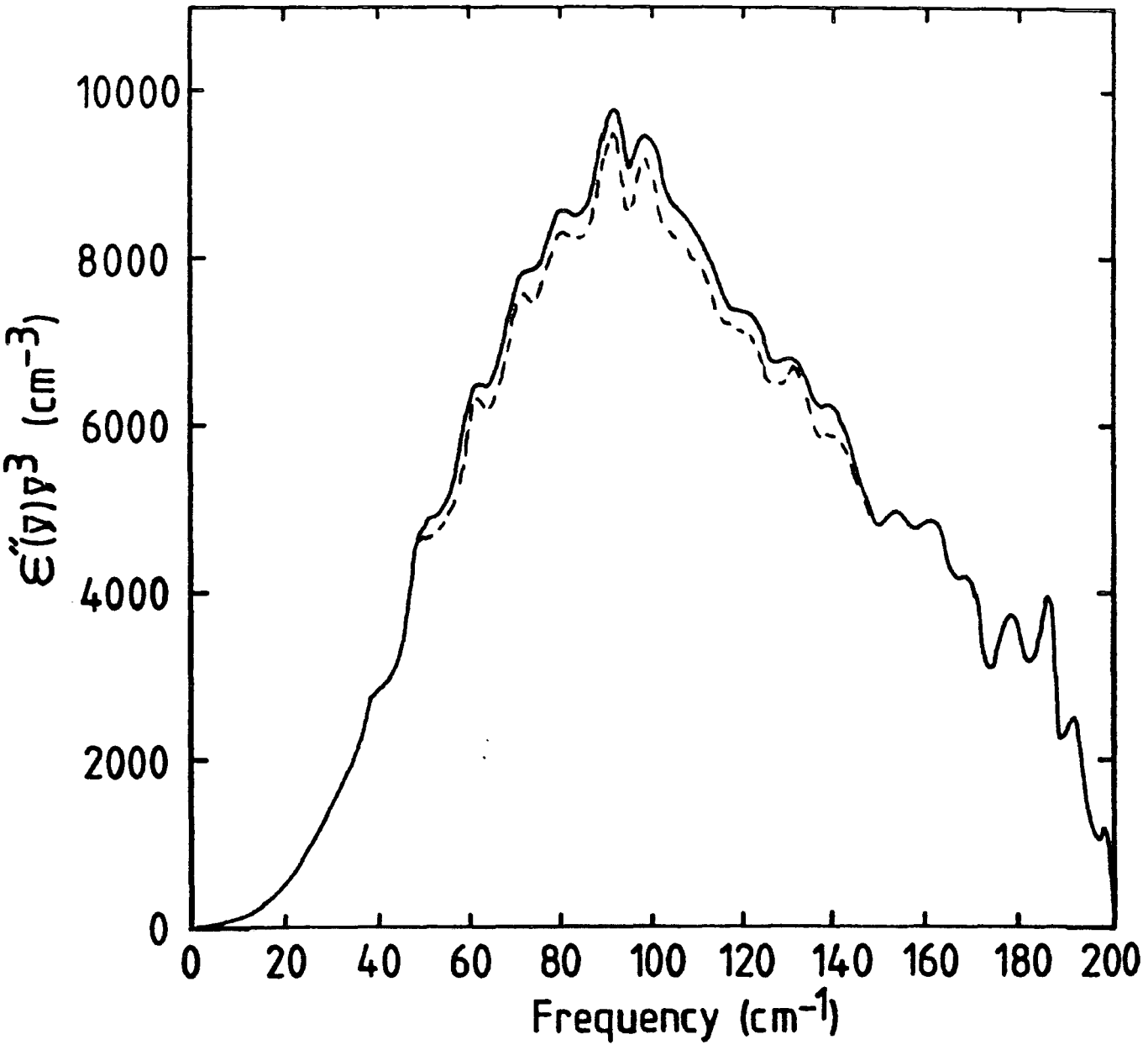

FIGURE 7.53 0.162 MeI IN n-HEXADECANE

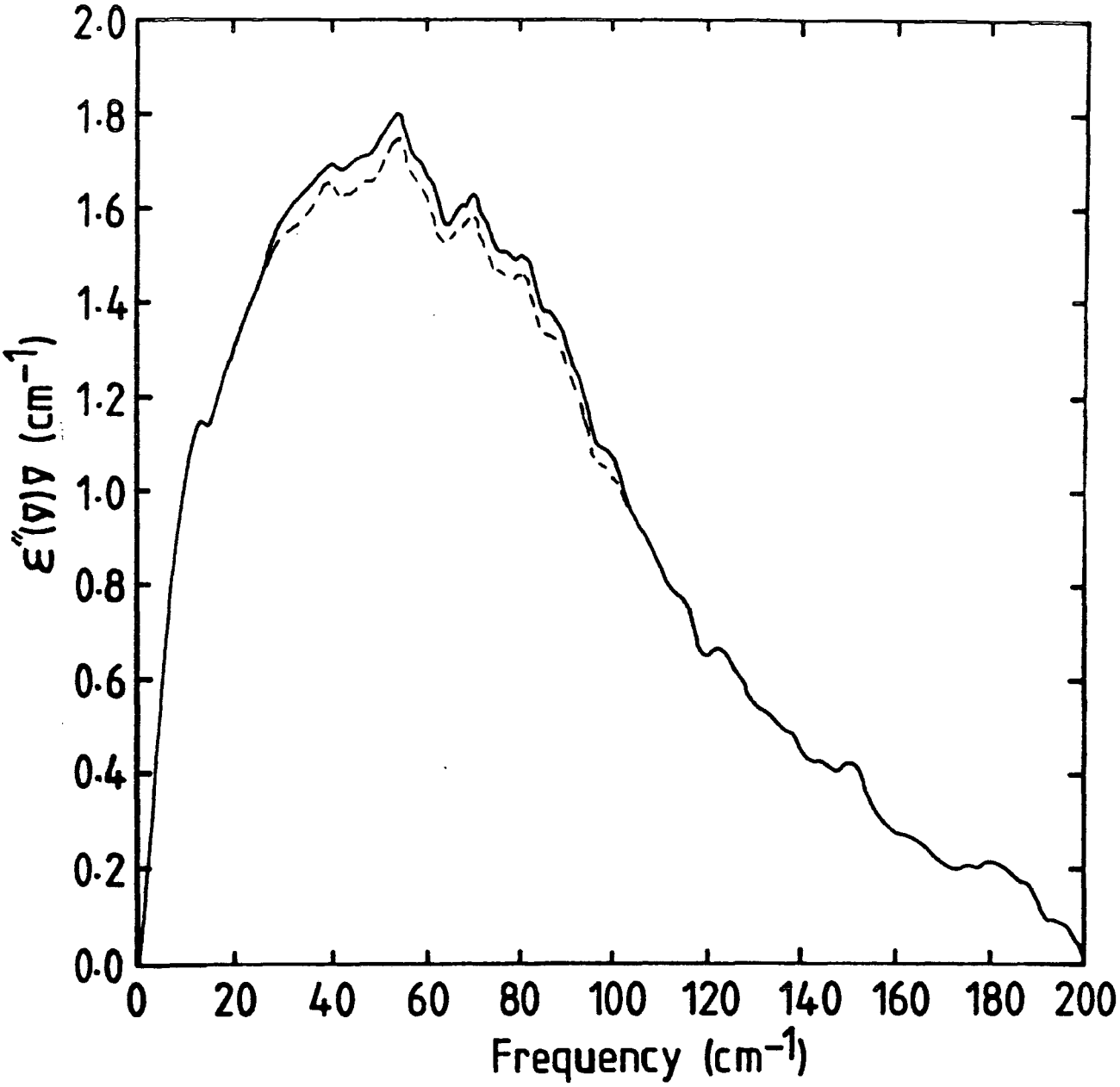

FIGURE 7.54 0.162 mf MeI IN n-HEXADECANE

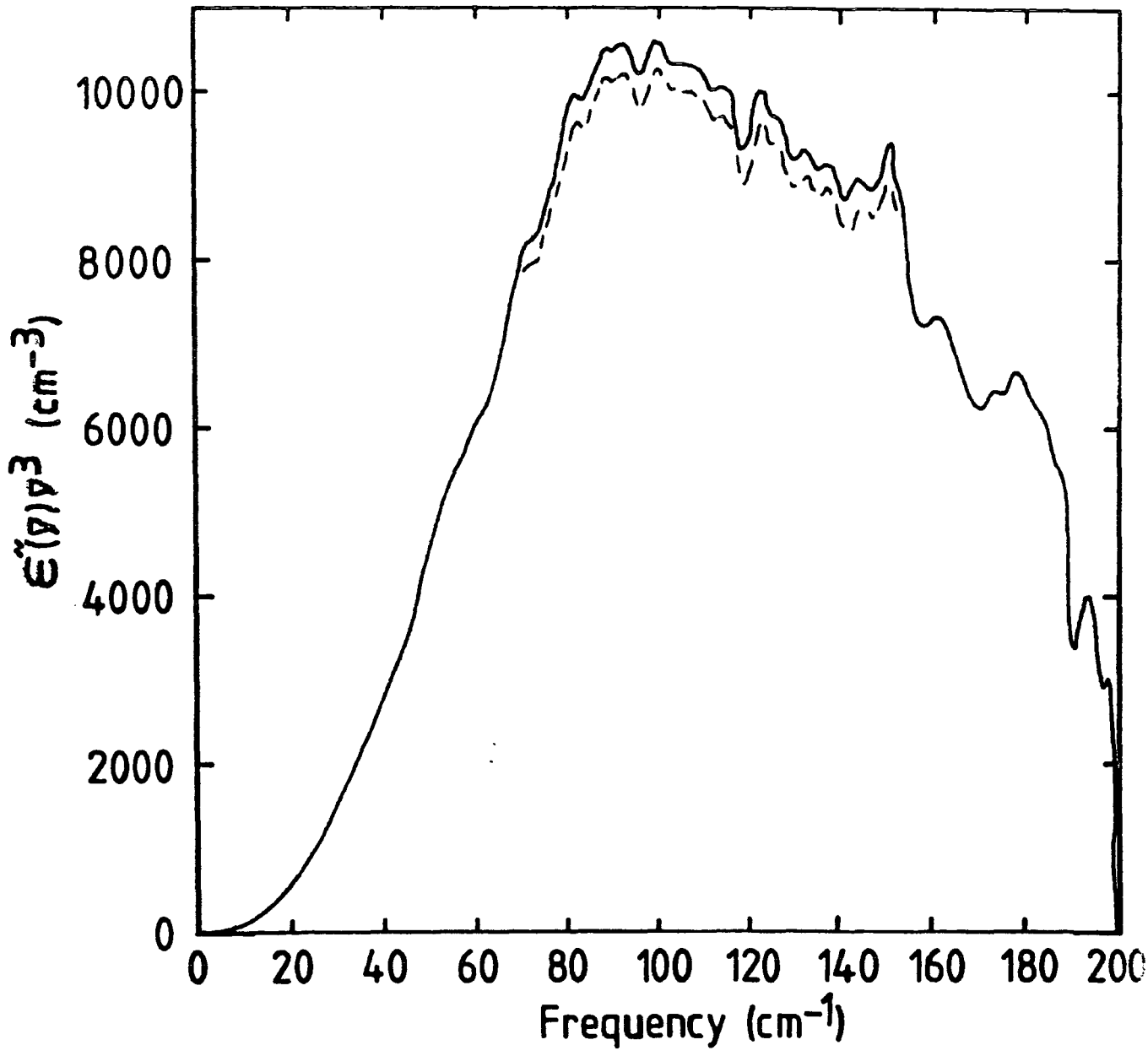

INTERMOLECULAR MEAN SQUARED TORQUE VALUES

Solvent	Concentration mf	$\langle [O(V)]^2 \rangle$ $10^{-4}cm^{-2}$	$\langle [O(V)]^2 \rangle^*$ $10^{-4}cm^{-2}$	$\langle [O(V)]^2 \rangle^{\#}$ $10^{4}cm^{-2}$	$\langle [O(V)]^2 \rangle^{+}$ $10^{-4}cm^{-2}$
CH_3I	1.0	270	373	343	225
CCl_4	0.162	583	630	758	231
CS_2	0.100	287		409	308
	0.005	31			1894
n-HEPTANE	0.016	71		201	280
	0.162	136			189
	0.370	299	338	469	195
	0.016	115		593	263
n-DECANE	0.162	241		303	220
	0.370	352		512	185
	0.016	168		466	284
n-HEXADECANE	0.162	219		1180	227
	0.370	305		396	181

* With Hill correction

\# Two parameter Mori Model

\+ Three parameter Mori Model

7.4.5 Cole-Cole Plots.

From Section 1.3.1 when both permitivity and dielectric loss data are available, the measured optical constants can be represented in the form of Cole-Cole plots. These are shown for various solutions in Figures 7.55 to 7.66.

7.4.6 Fitting to the 2nd order Mori Formalism.

From Section 6.4.4 the far-infrared absorption coefficient and refractive index spectra can be fitted to a model for molecular reorientation. In this work both two and three parameter fits have been made using measured absorption coefficient and refractive index spectra and solely absorption coefficient spectra respectively. Typical fits (good and poor) to experimental data are given in Figures 7.67 and 7.70 and the results of fitting to the liquid and solution data are given in Table 7.15. When represented in the form of Cole-Cole plots a better indication of the quality of a fit is obtained as can be seen in Figures 7.71 and 7.72

7.4.7 Viscosities.

Literature[64] values for the viscosity of methyl iodide and solvents used in this work are shown in Figure 7.73.

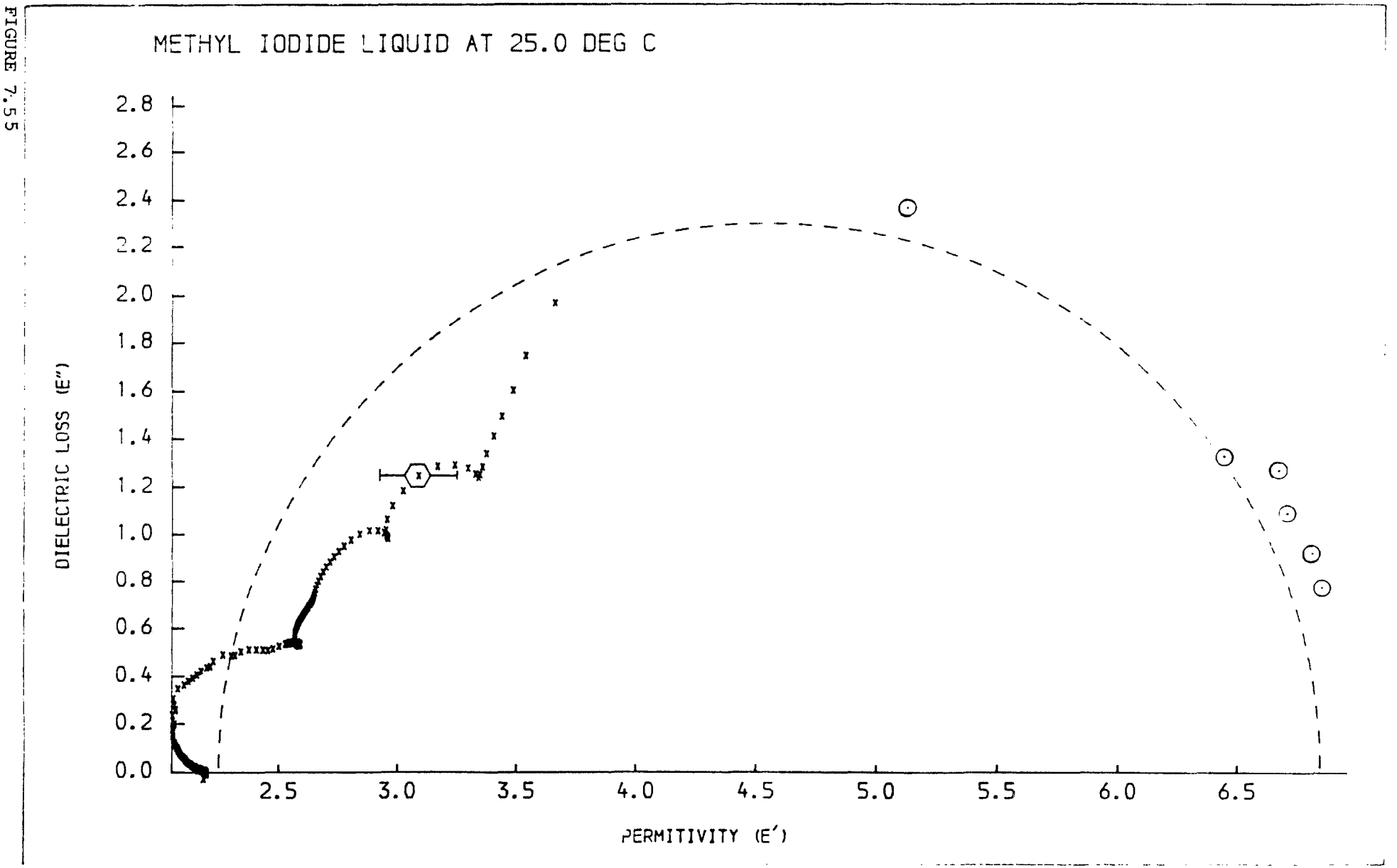
METHYL IODIDE LIQUID AT 25.0 DEG C
DIELECTRIC LOSS (E")
2.8
2.6
2.4
2.2
2.0
1.8
1.6
1.4
1.2
1.0
0.8
0.6
0.4
0.2
0.0
2.5
3.0
3.5
4.0
4.5
5.0
5.5
6.0
6.5
PERMITIVITY (E')

FIGURE 7.5 5

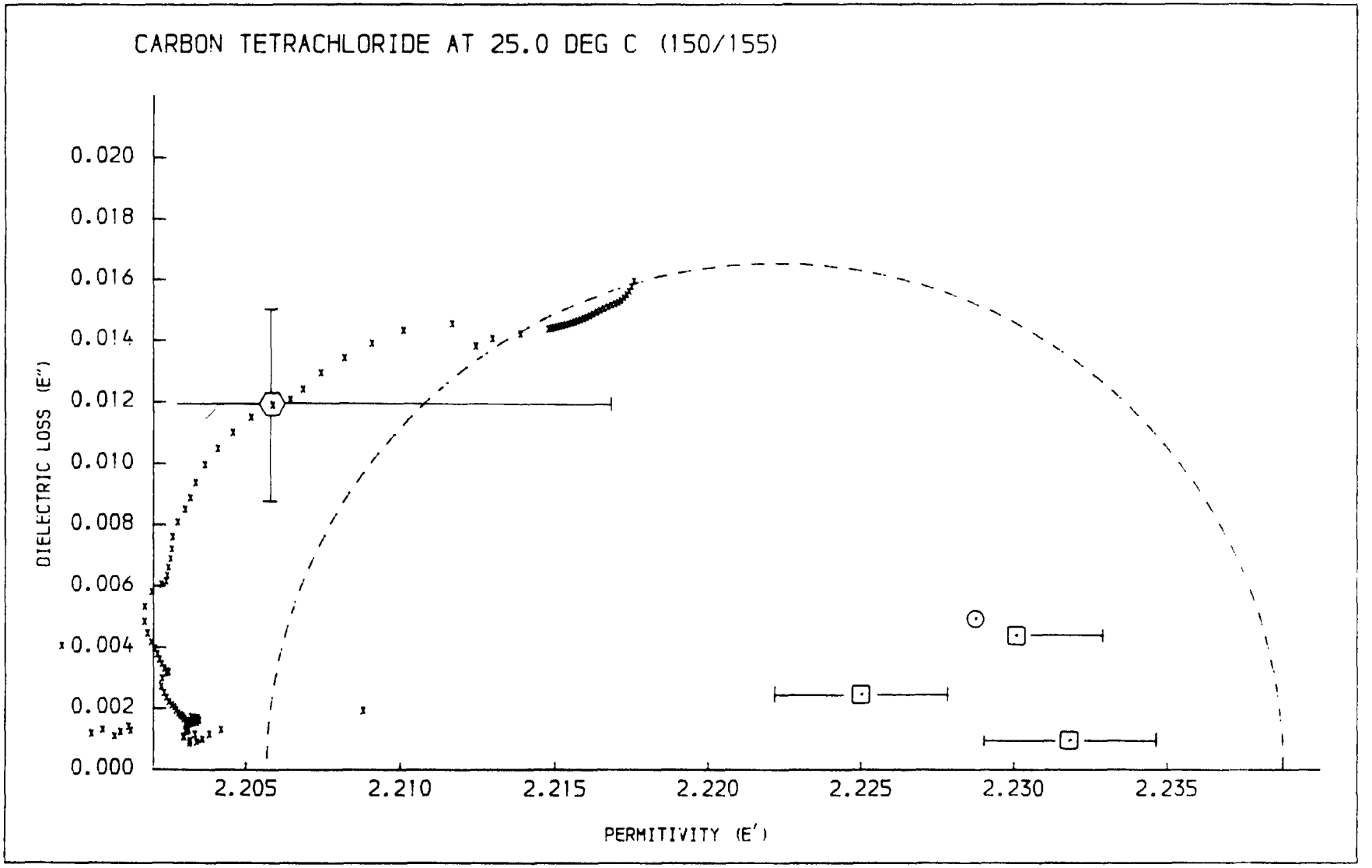
CARBON TETRACHLORIDE AT 25.0 DEG C (150/155)
DIELECTRIC LOSS (E'')
0.020
0.018
0.016
0.014
0.012
0.010
0.008
0.006
0.004
0.002
0.000
2.205
2.210
2.215
2.220
2.225
2.230
2.235
PERMITIVITY (E')

FIGURE 7.56

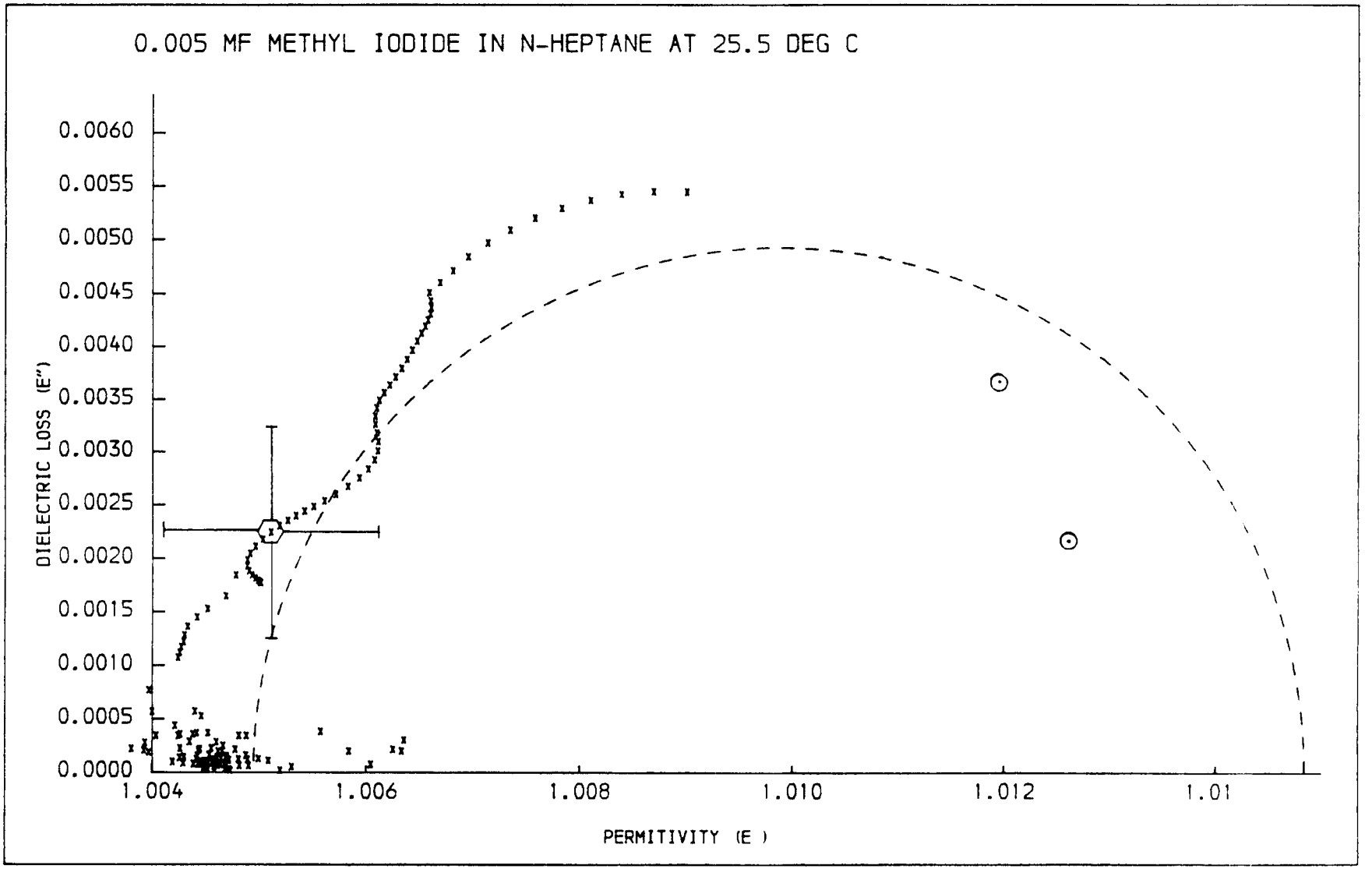
0.005 MF METHYL IODIDE IN N-HEPTANE AT 25.5 DEG C
DIELECTRIC LOSS (E")
0.0060
0.0055
0.0050
0.0045
0.0040
0.0035
0.0030
0.0025
0.0020
0.0015
0.0010
0.0005
0.0000
1.004
1.006
1.008
1.010
1.012
1.01
PERMITIVITY (E)

FIGURE 7.57

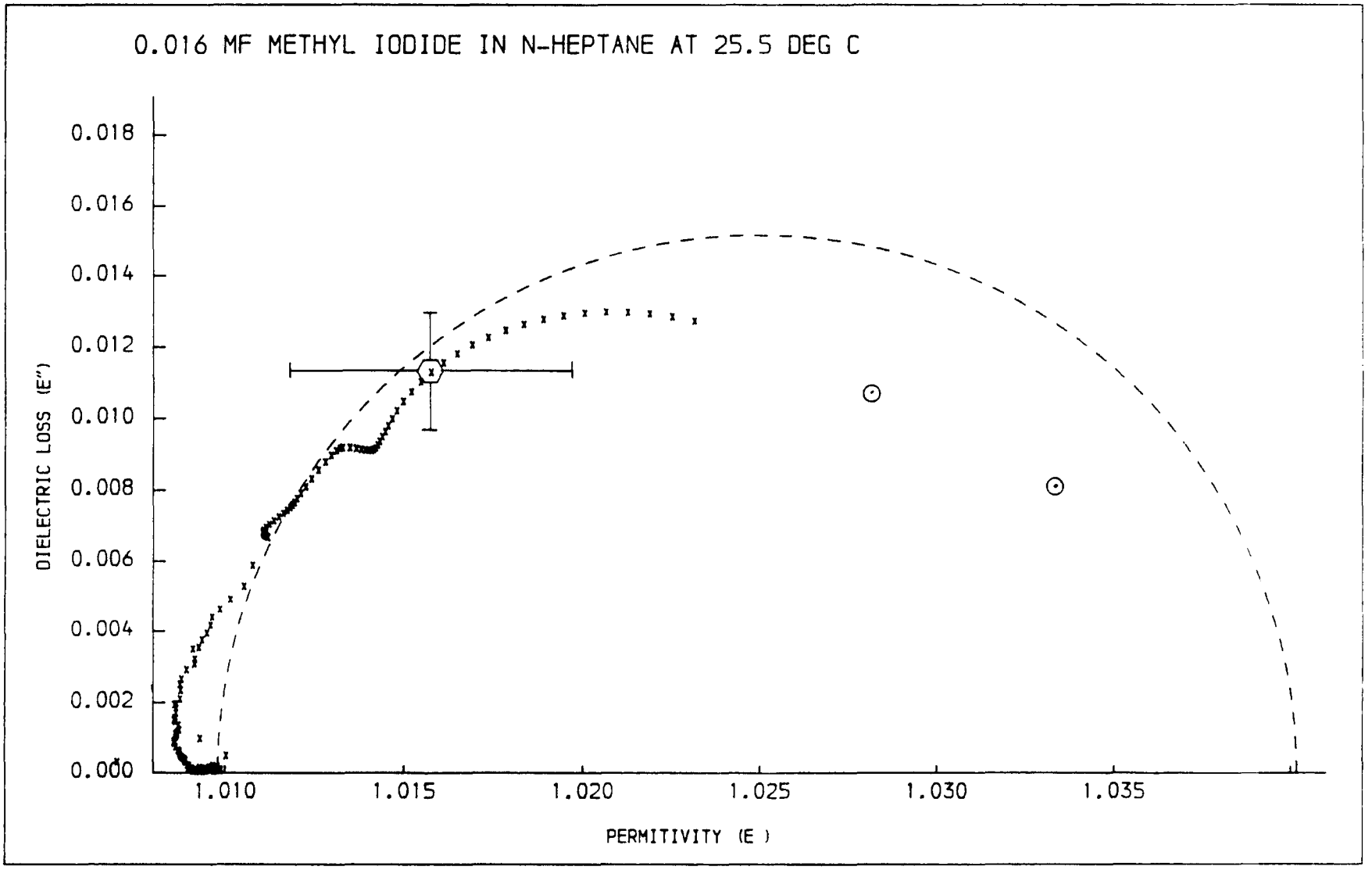
0.016 MF METHYL IODIDE IN N-HEPTANE AT 25.5 DEG C
DIELECTRIC LOSS (E")
0.018
0.016
0.014
0.012
0.010
0.008
0.006
0.004
0.002
0.000
1.010
1.015
1.020
1.025
1.030
1.035
PERMITIVITY (E)

FIGURE 7.58

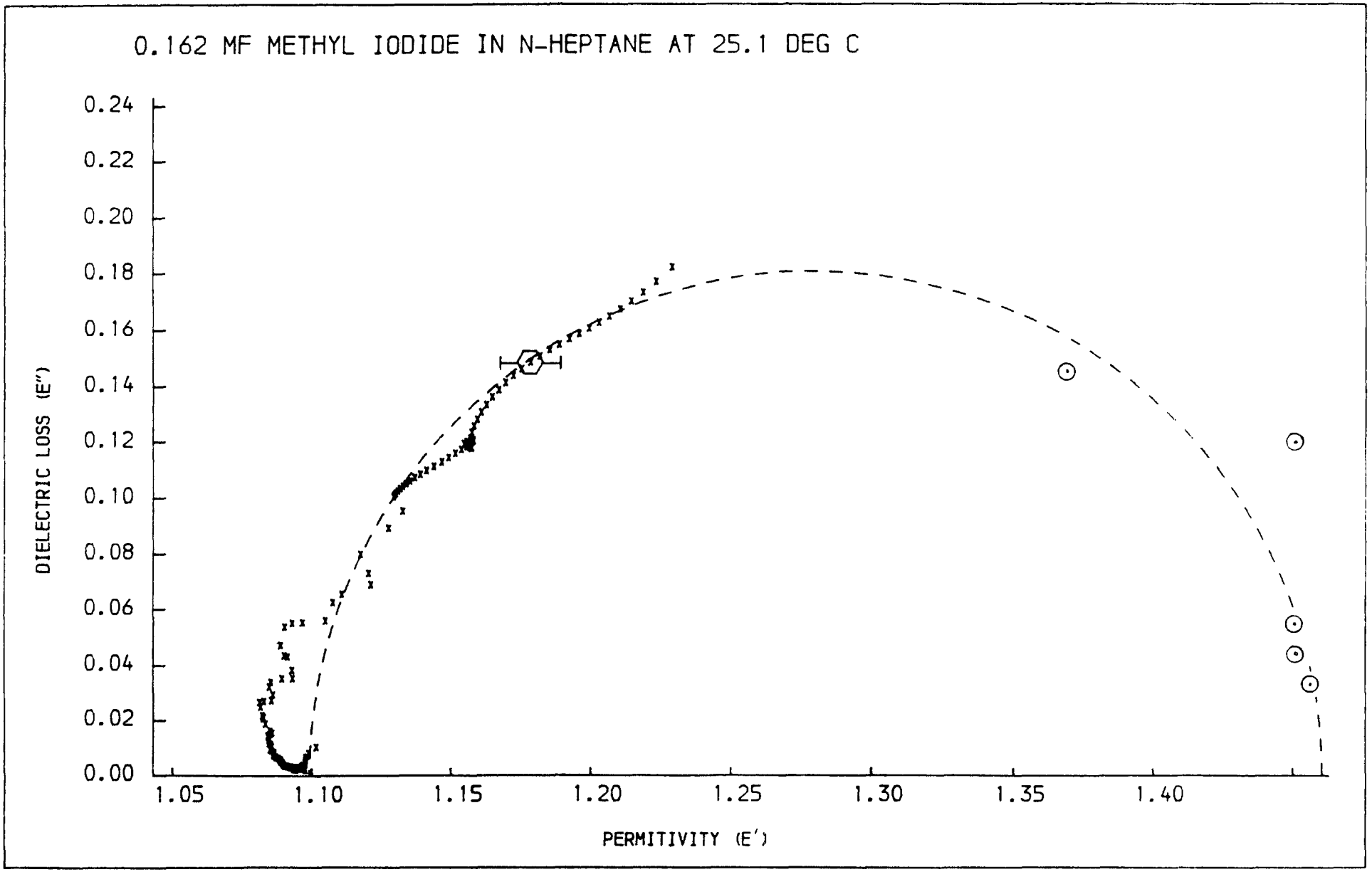
0.162 MF METHYL IODIDE IN N-HEPTANE AT 25.1 DEG C
DIELECTRIC LOSS (E")
0.24
0.22
0.20
0.18
0.16
0.14
0.12
0.10
0.08
0.06
0.04
0.02
0.00
1.05
1.10
1.15
1.20
1.25
1.30
1.35
1.40
PERMITIVITY (E')

FIGURE 7.59

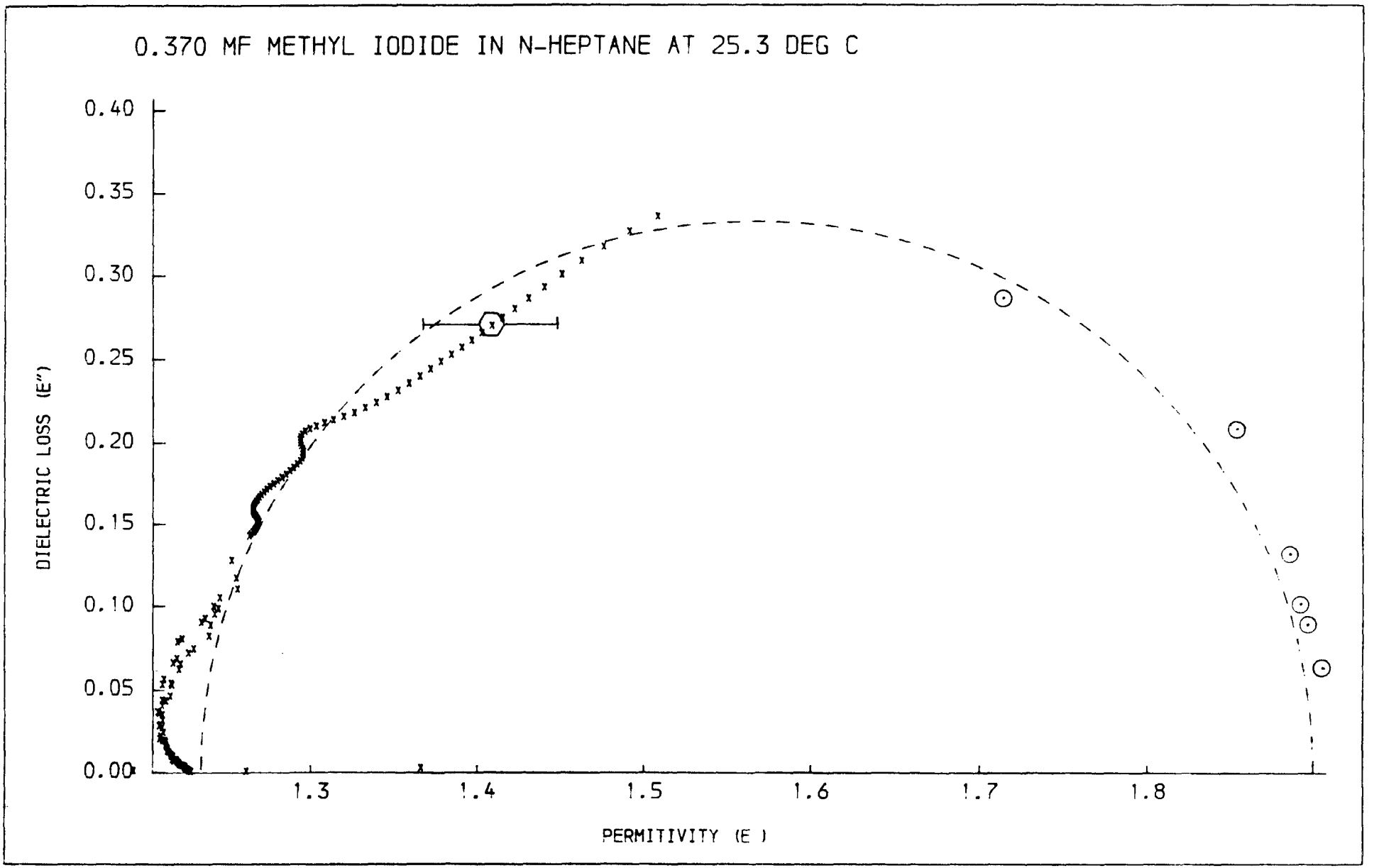
0.370 MF METHYL IODIDE IN N-HEPTANE AT 25.3 DEG C
0.40
0.35
0.30
0.25
0.20
0.15
0.10
0.05
0.00
DIELECTRIC LOSS (E")
1.3
1.4
1.5
1.6
1.7
1.8
PERMITIVITY (E')

FIGURE 7.60

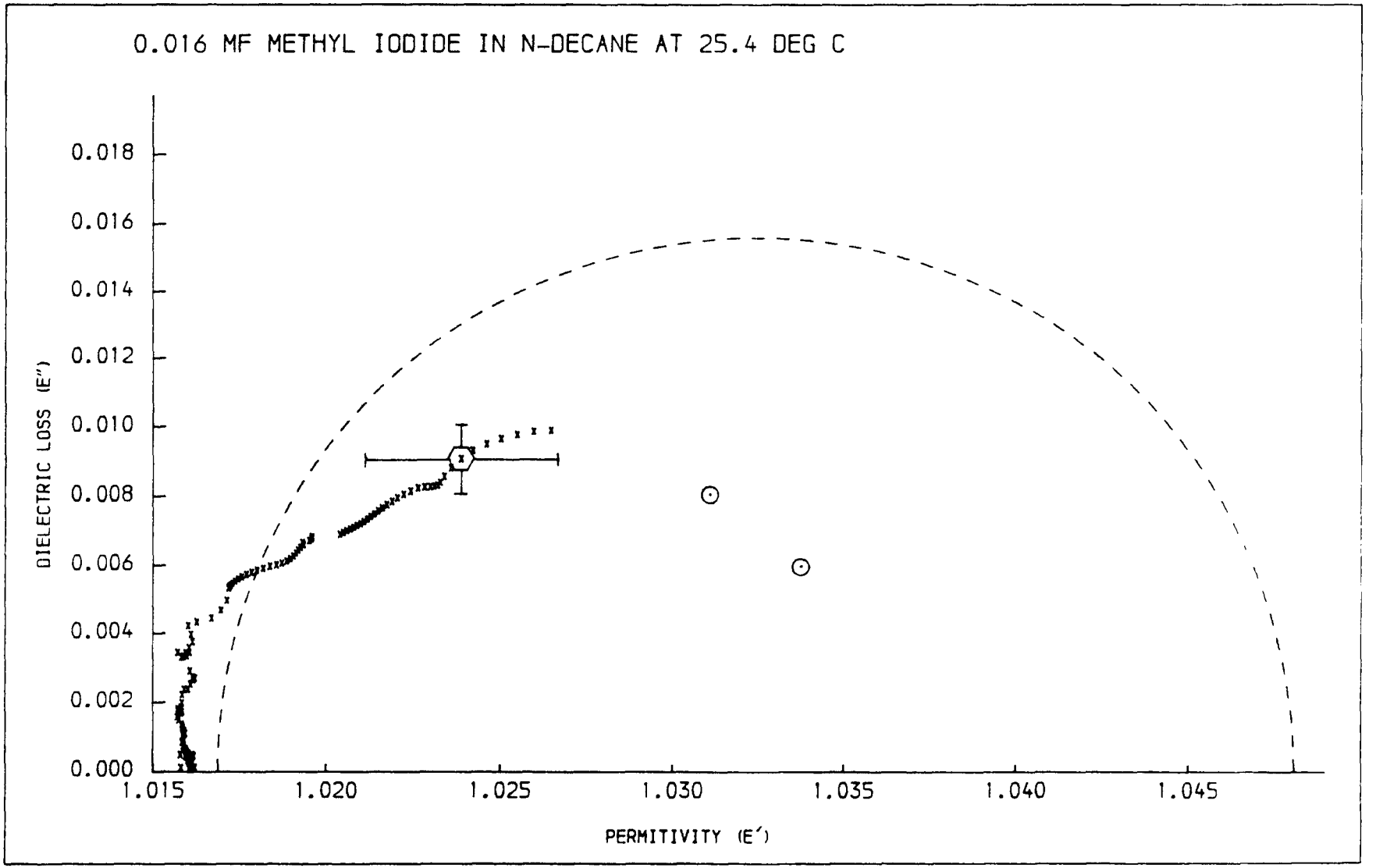
0.016 MF METHYL IODIDE IN N-DECANE AT 25.4 DEG C
DIELECTRIC LOSS (E'')
0.018
0.016
0.014
0.012
0.010
0.008
0.006
0.004
0.002
0.000
1.015
1.020
1.025
1.030
1.035
1.040
1.045
PERMITIVITY (E')

FIGURE 7.61

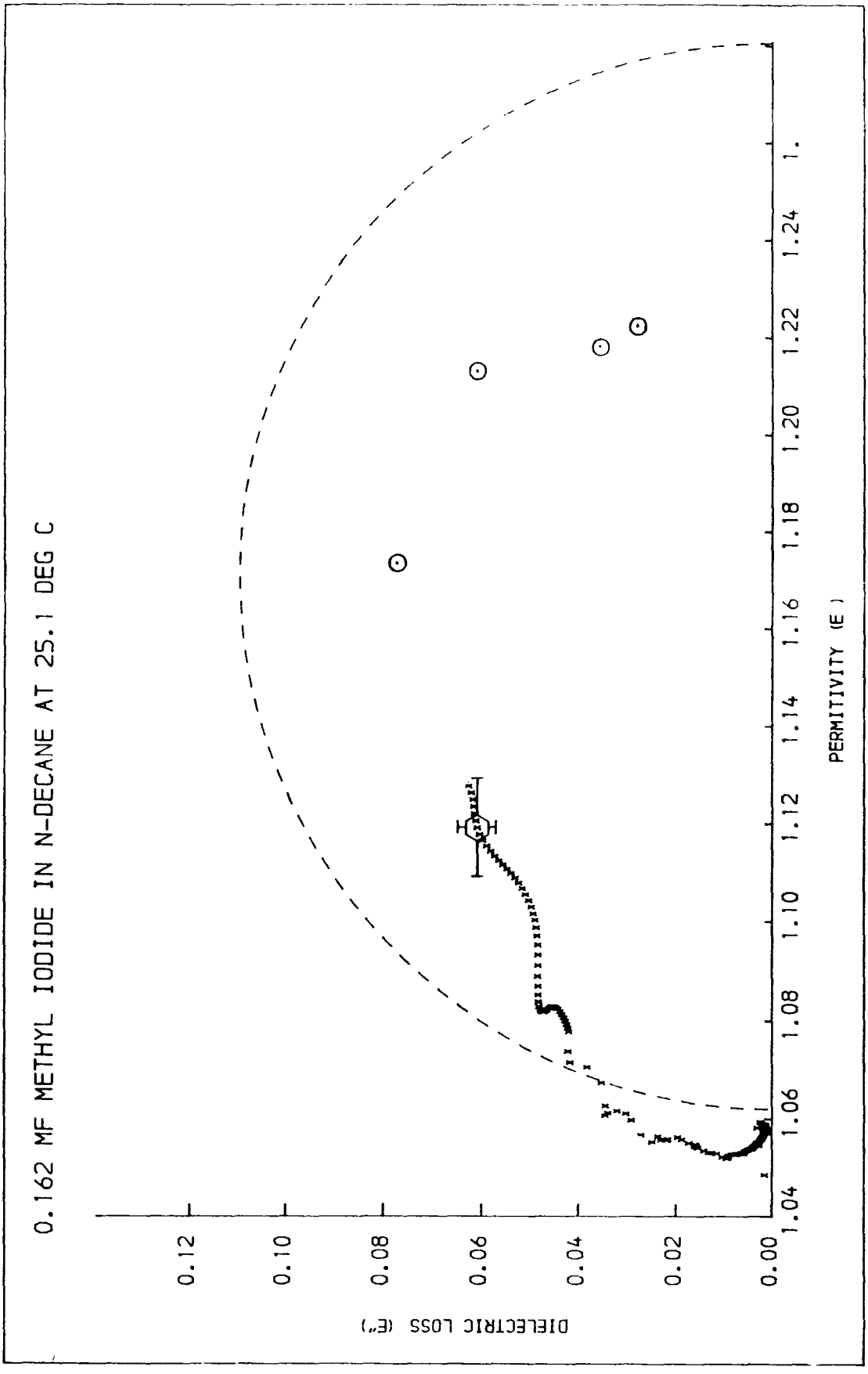
0.162 MF METHYL IODIDE IN N-DECANE AT 25.1 DEG C
DIELECTRIC LOSS (ε")
0.12
0.10
0.08
0.06
0.04
0.02
0.00
1.04
1.06
1.08
1.10
1.12
1.14
1.16
1.18
1.20
1.22
1.24
1.
PERMITIVITY (ε')

FIGURE 7.62

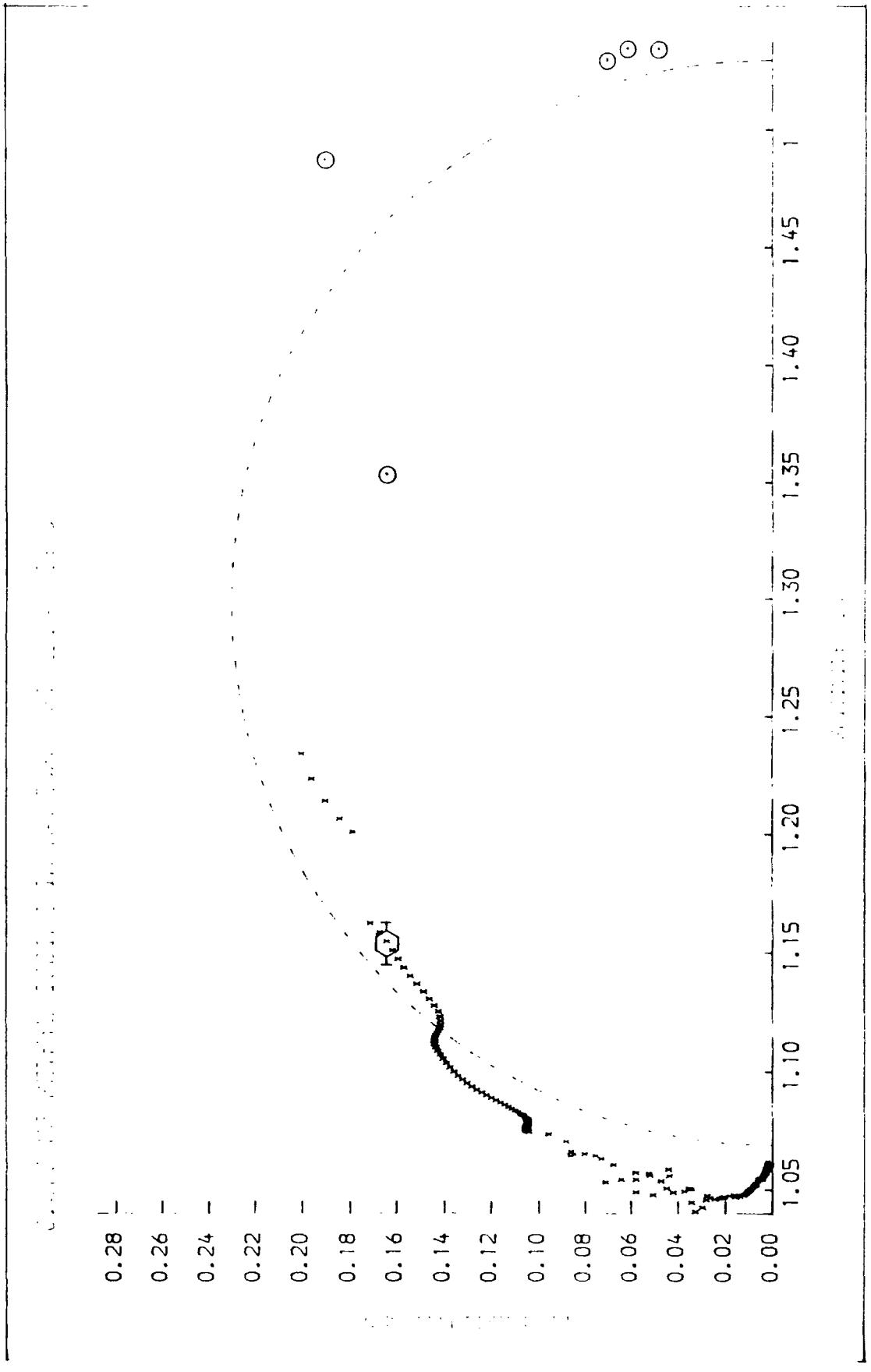
0.28
0.26
0.24
0.22
0.20
0.18
0.16
0.14
0.12
0.10
0.08
0.06
0.04
0.02
0.00
1.05
1.10
1.15
1.20
1.25
1.30
1.35
1.40
1.45
1

FIGURE 7.63

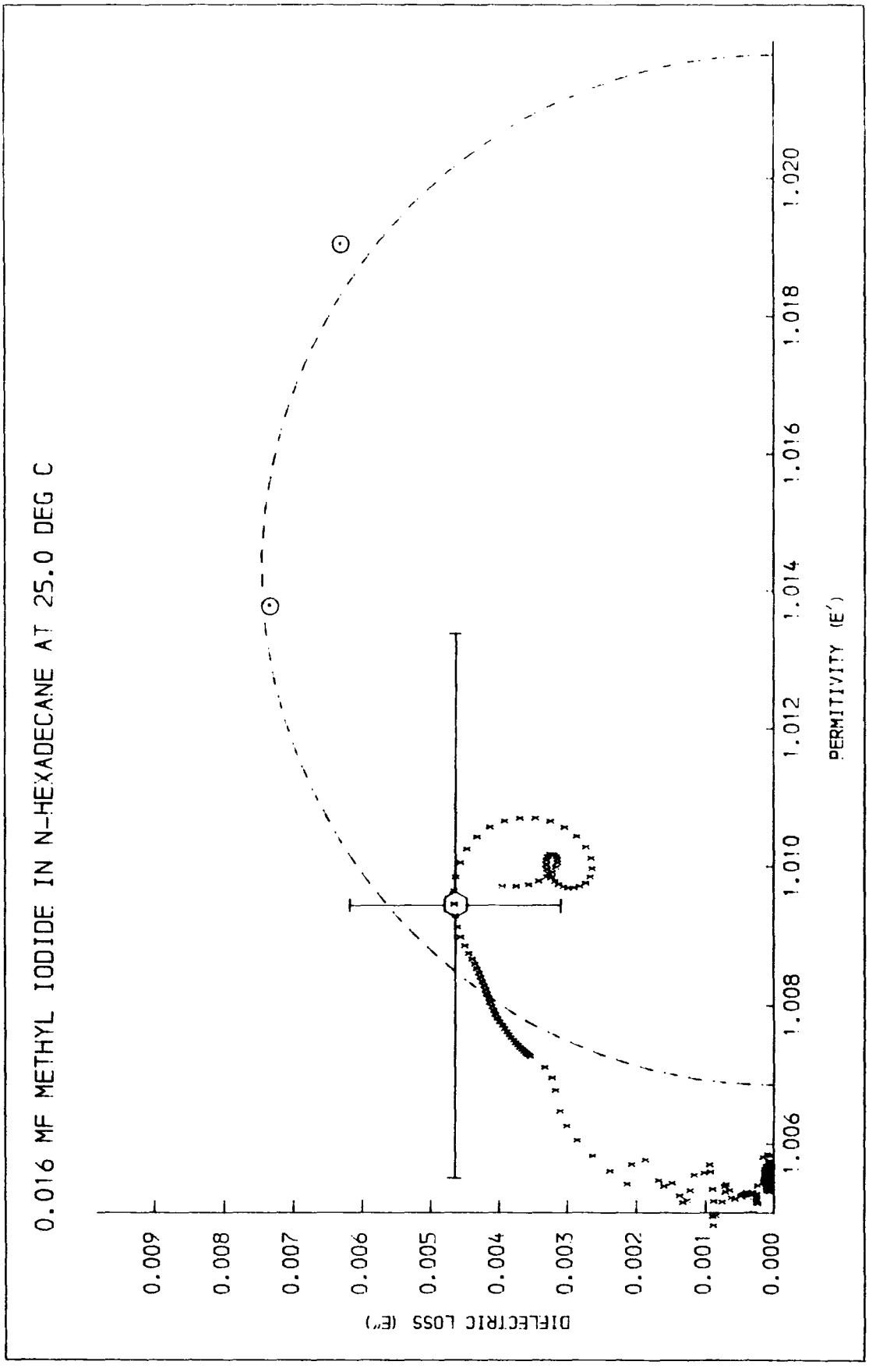
0.016 MF METHYL IODIDE IN N-HEXADECANE AT 25.0 DEG C
DIELECTRIC LOSS (ε″)
0.009
0.008
0.007
0.006
0.005
0.004
0.003
0.002
0.001
0.000
1.006
1.008
1.010
1.012
1.014
1.016
1.018
1.020
PERMITIVITY (ε′)

FIGURE 7.64

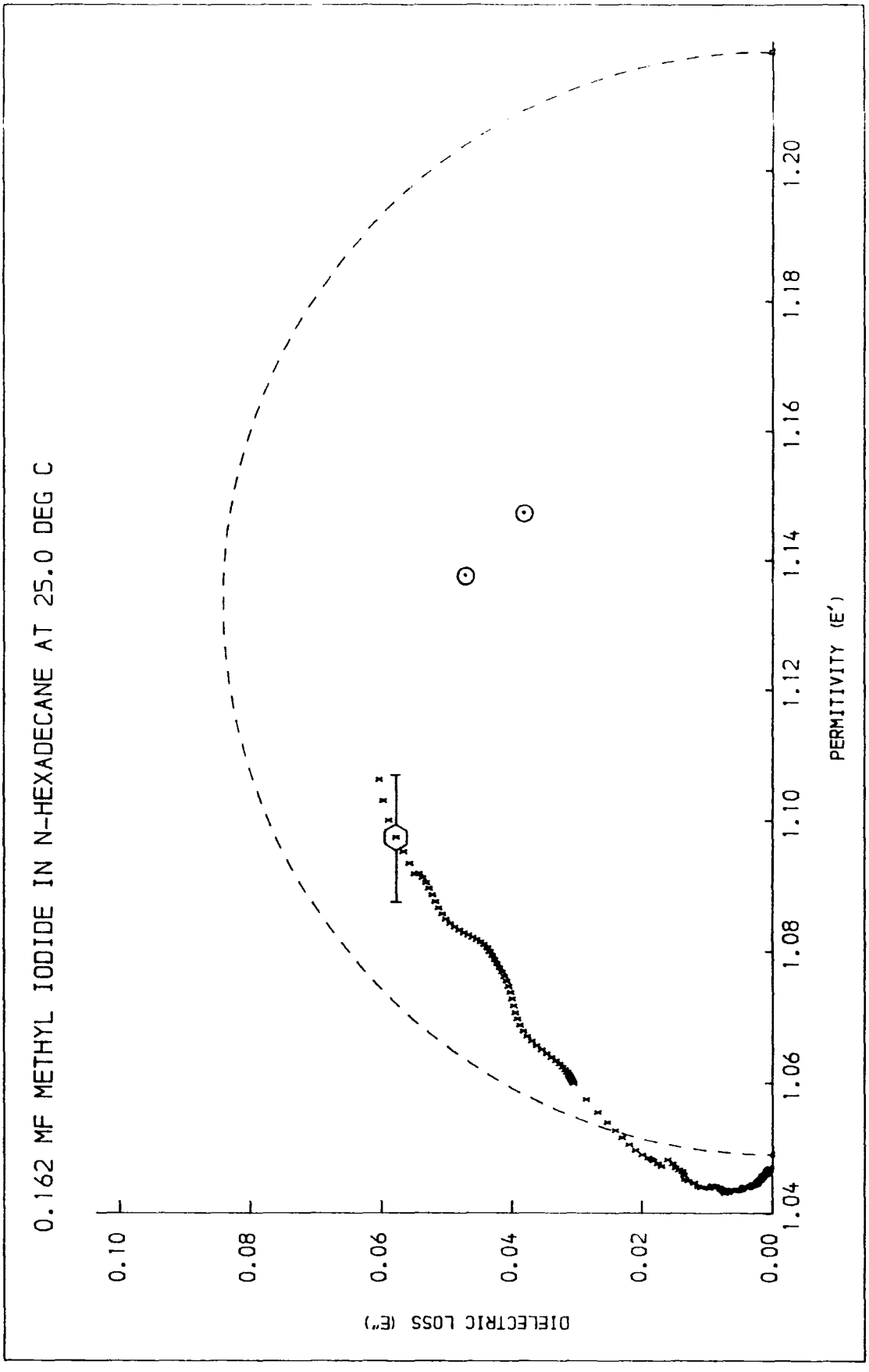
0.162 MF METHYL IODIDE IN N-HEXADECANE AT 25.0 DEG C
DIELECTRIC LOSS (ε")
0.10
0.08
0.06
0.04
0.02
0.00
1.04
1.06
1.08
1.10
1.12
1.14
1.16
1.18
1.20
PERMITIVITY (ε')

FIGURE 7.65

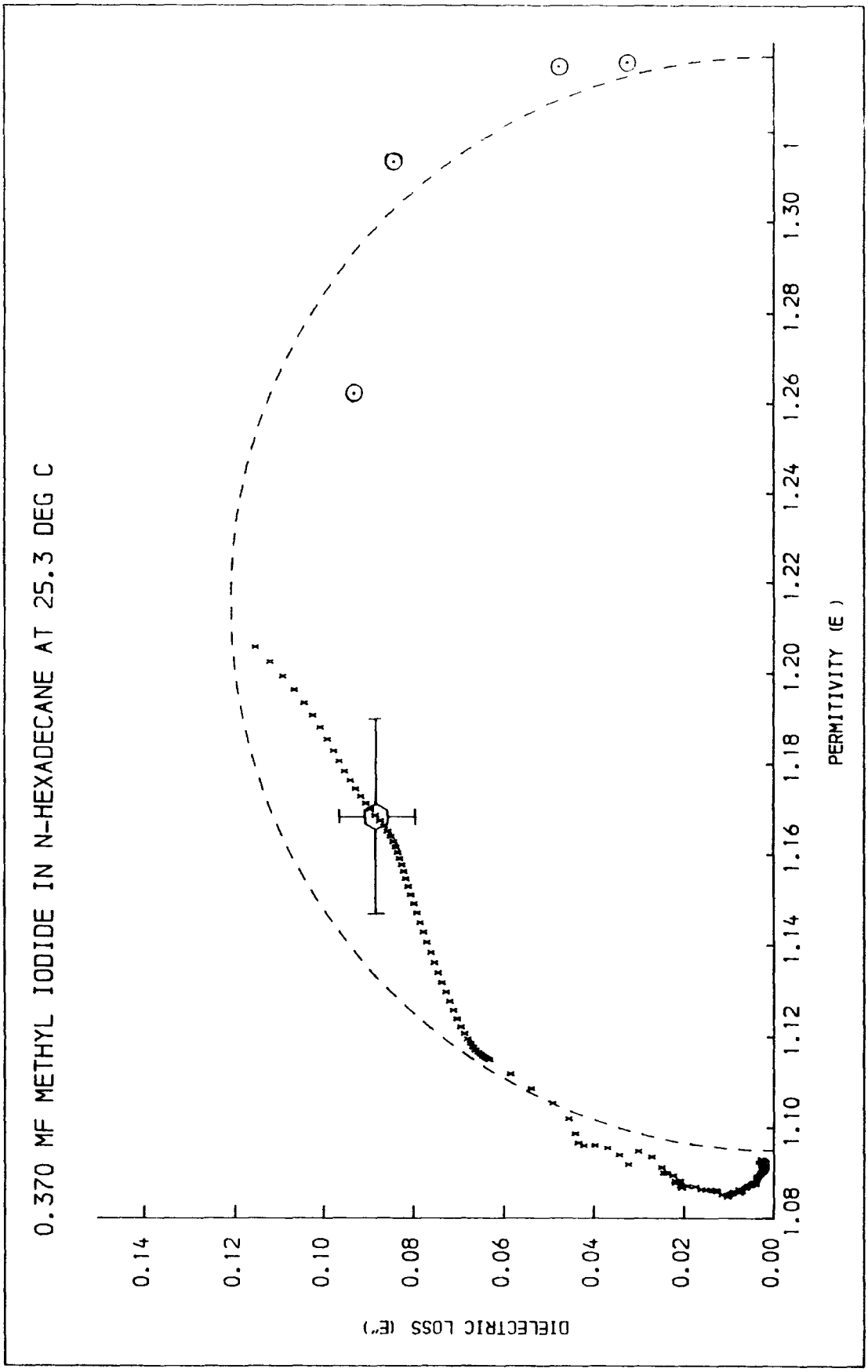
0.370 MF METHYL IODIDE IN N-HEXADECANE AT 25.3 DEG C
DIELECTRIC LOSS (ε")
0.14
0.12
0.10
0.08
0.06
0.04
0.02
0.00
1.08
1.10
1.12
1.14
1.16
1.18
1.20
1.22
1.24
1.26
1.28
1.30
1
PERMITIVITY (ε')

FIGURE 7.66

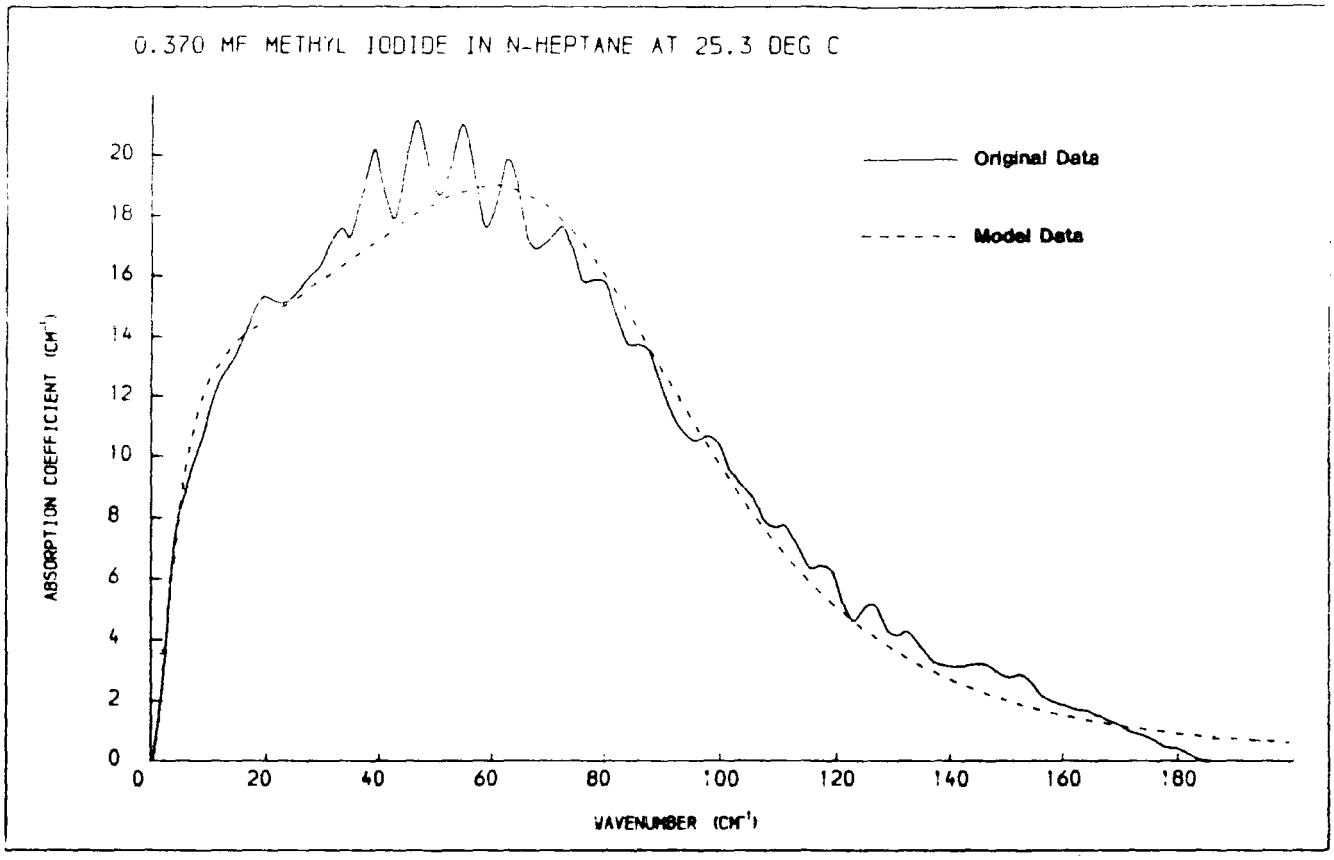
0.370 MF METHYL IODIDE IN N-HEPTANE AT 25.3 DEG C
Original Data
Model Data
ABSORPTION COEFFICIENT (CM⁻¹)
WAVENUMBER (CM⁻¹)
0
2
4
6
8
10
12
14
16
18
20
0
20
40
60
80
100
120
140
160
180

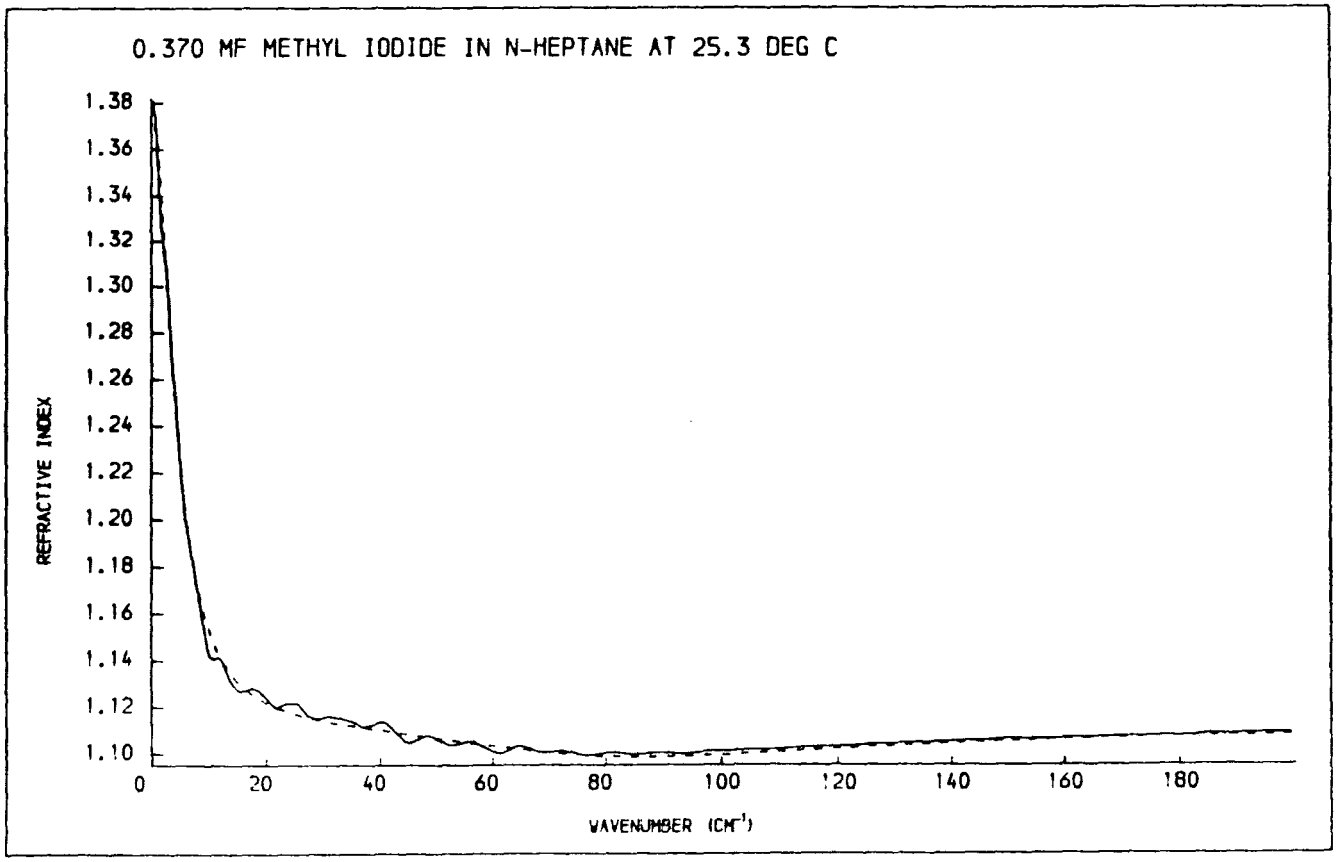
0.370 MF METHYL IODIDE IN N-HEPTANE AT 25.3 DEG C
REFRACTIVE INDEX
WAVENUMBER (CM⁻¹)
1.10
1.12
1.14
1.16
1.18
1.20
1.22
1.24
1.26
1.28
1.30
1.32
1.34
1.36
1.38
0
20
40
60
80
100
120
140
160
180

FIGURE 7.67

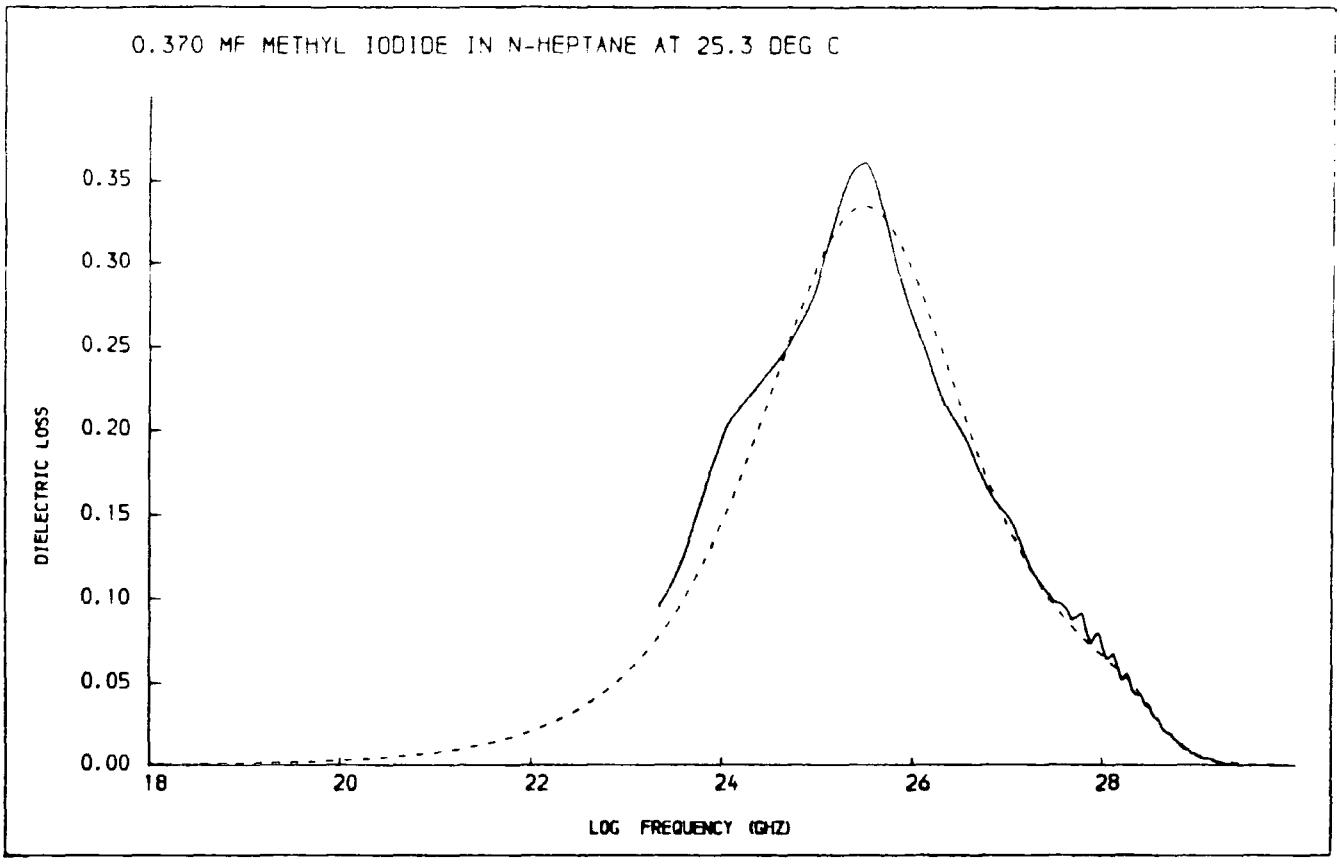
0.370 MF METHYL IODIDE IN N-HEPTANE AT 25.3 DEG C
DIELECTRIC LOSS
0.35
0.30
0.25
0.20
0.15
0.10
0.05
0.00
18
20
22
24
26
28
LOG FREQUENCY (GHZ)

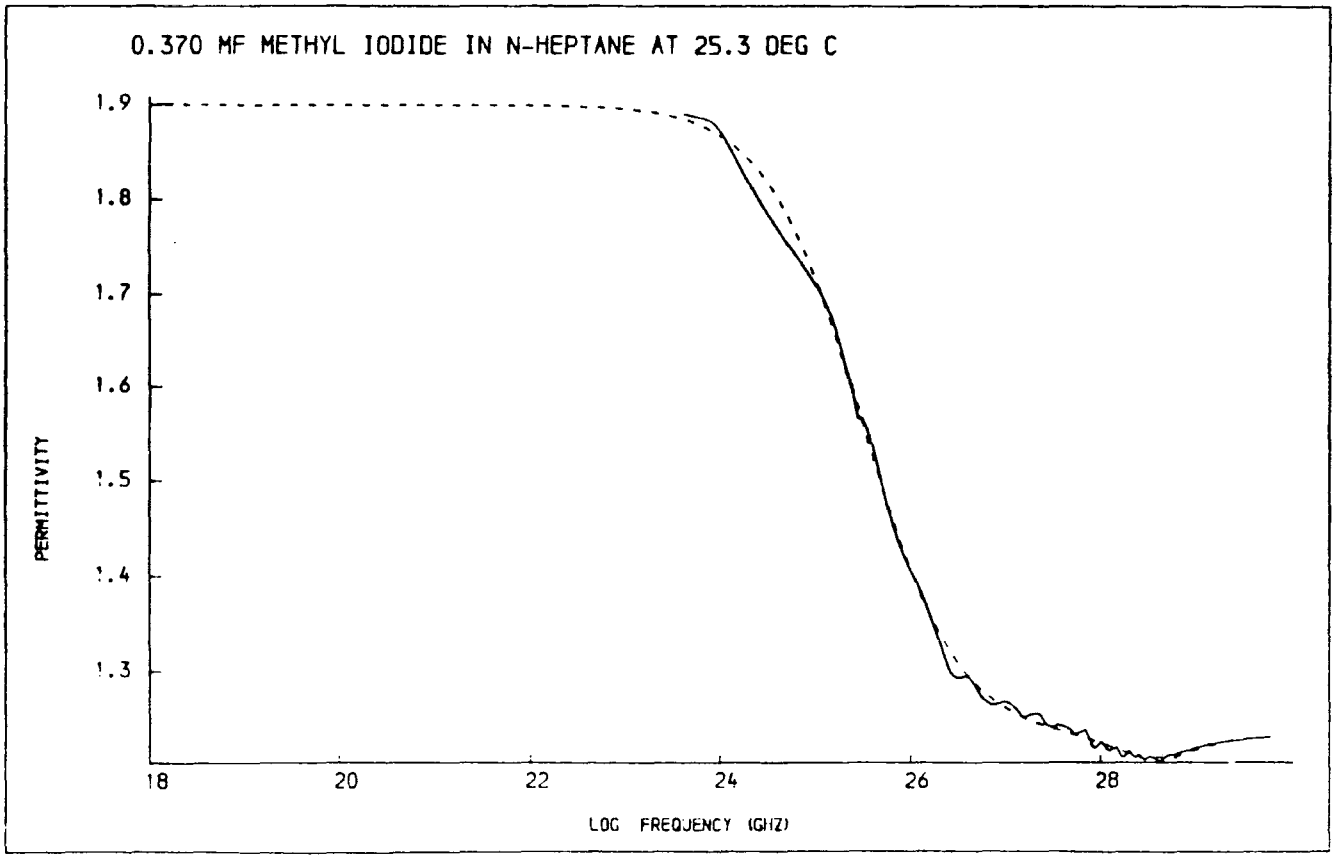
0.370 MF METHYL IODIDE IN N-HEPTANE AT 25.3 DEG C
PERMITTIVITY
1.9
1.8
1.7
1.6
1.5
1.4
1.3
18
20
22
24
26
28
LOG FREQUENCY (GHZ)

FIGURE 7.68

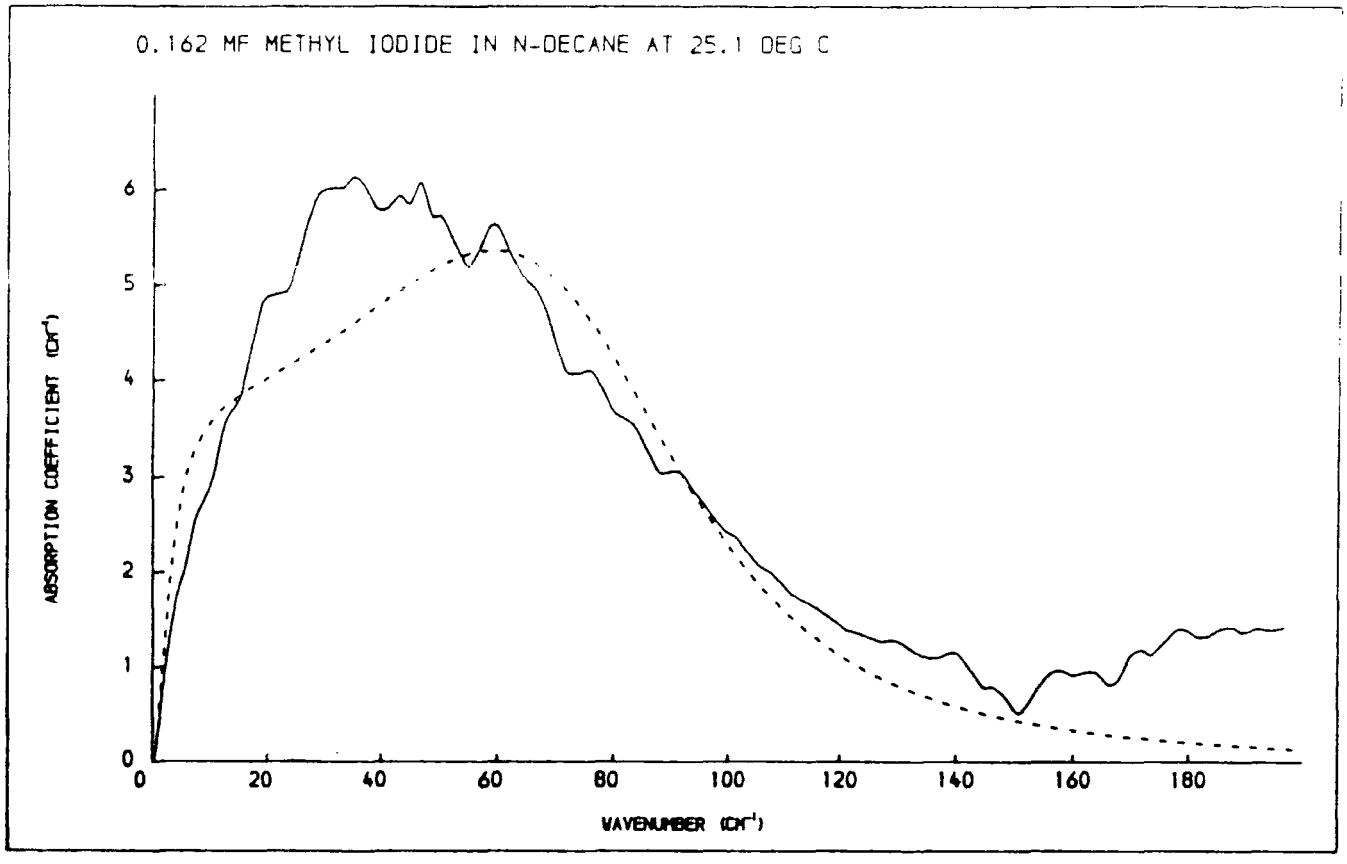
0.162 MF METHYL IODIDE IN N-DECANE AT 25.1 DEG C
ABSORPTION COEFFICIENT (CM⁻¹)
0
1
2
3
4
5
6
0
20
40
60
80
100
120
140
160
180
WAVENUMBER (CM⁻¹)

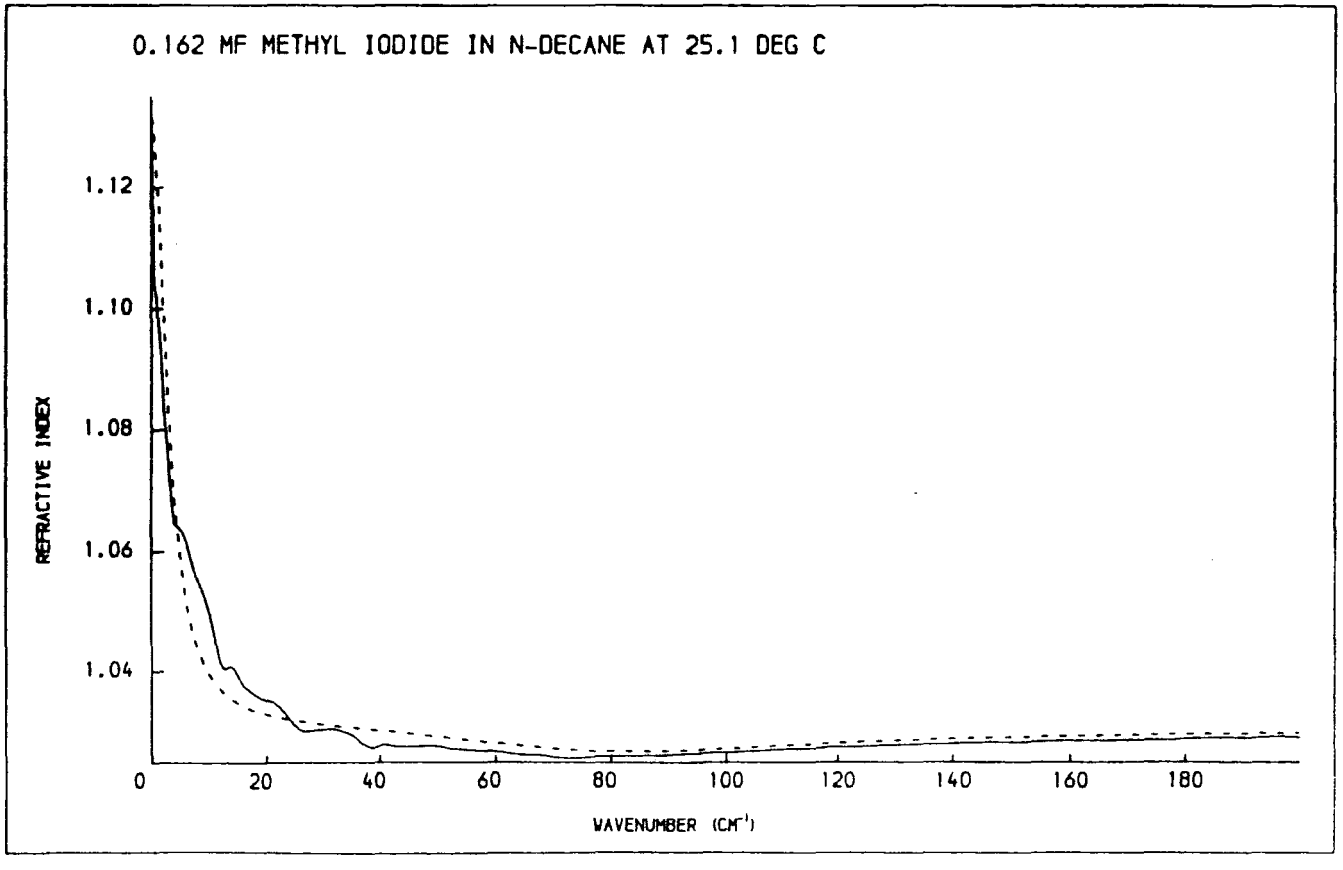
0.162 MF METHYL IODIDE IN N-DECANE AT 25.1 DEG C
REFRACTIVE INDEX
1.04
1.06
1.08
1.10
1.12
0
20
40
60
80
100
120
140
160
180
WAVENUMBER (CM⁻¹)

FIGURE 7.69

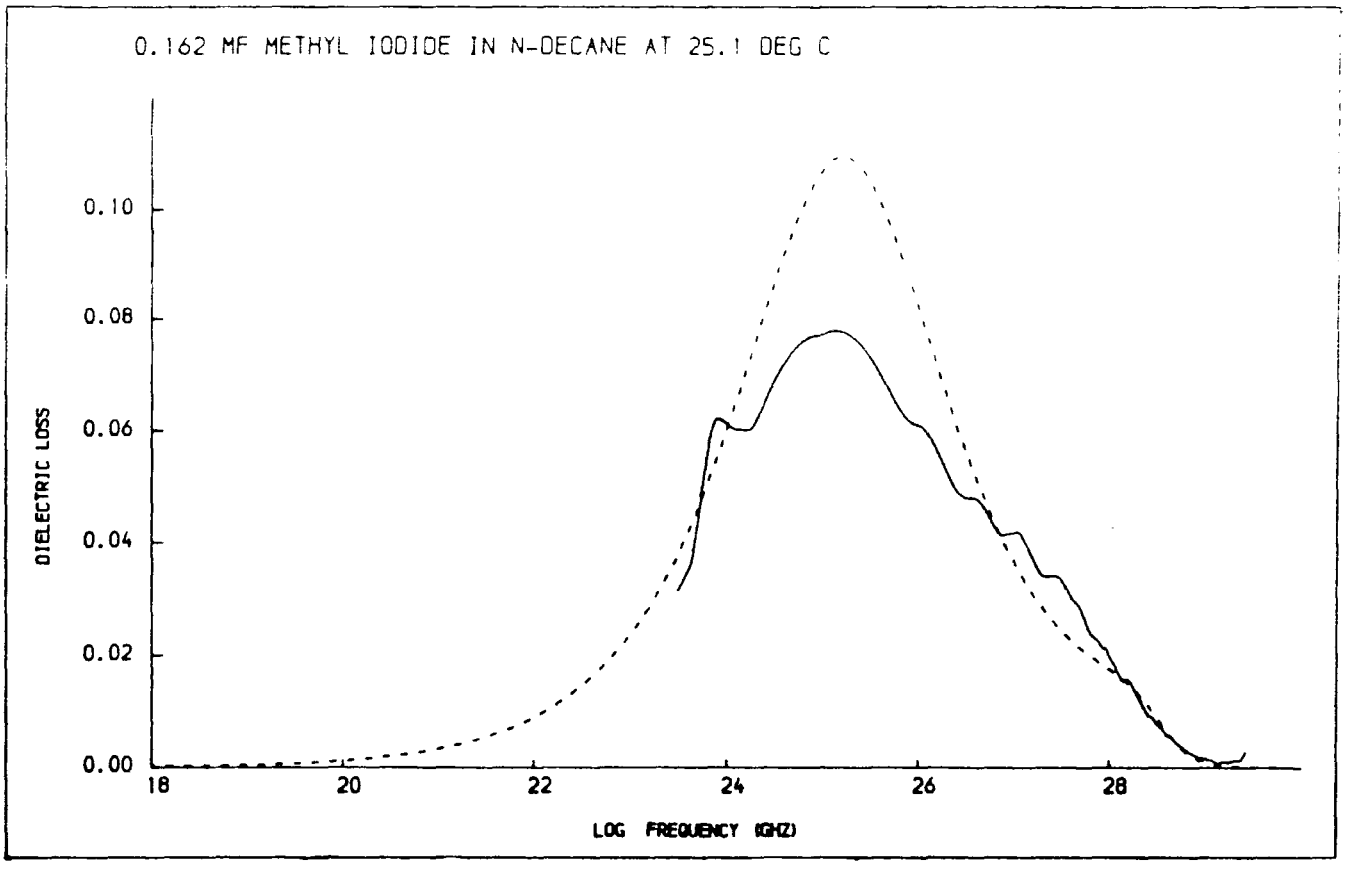
0.162 MF METHYL IODIDE IN N-DECANE AT 25.1 DEG C
DIELECTRIC LOSS
0.10
0.08
0.06
0.04
0.02
0.00
18
20
22
24
26
28
LOG FREQUENCY (GHZ)

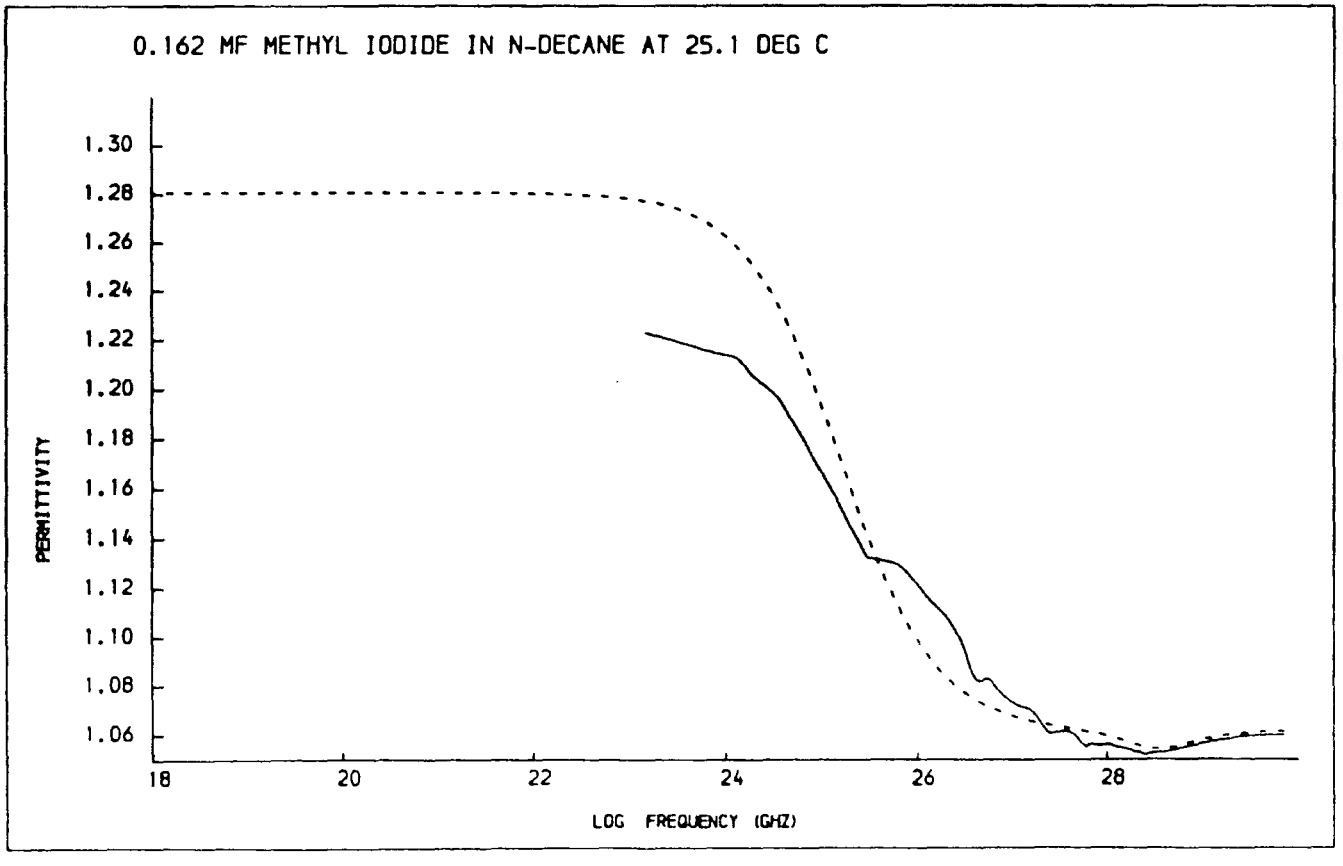
0.162 MF METHYL IODIDE IN N-DECANE AT 25.1 DEG C
PERMITTIVITY
1.30
1.28
1.26
1.24
1.22
1.20
1.18
1.16
1.14
1.12
1.10
1.08
1.06
18
20
22
24
26
28
LOG FREQUENCY (GHZ)

FIGURE 7.70

NEWFIT RESULTS FOR MeI

NPAR	NTYPE	IFAIL	XPS	$\chi 10^{13}$	$K_1(0) \times 10^{26}$	$K_0(0)cm^{-2}$	$M_4R \times 10^4 cm^{-4}$	Solvent & Concentration mf
3	10	0	-1	1.11	2.349	263.13	181.04	
2	10	0	-1	1.00	2.015	207.31	121.97	Liquid
3	0	0	1	1.10	2.333	263.27	179.96	
2	0	0	1	0.989	2.004	207.31	121.33	
3	10	0	-1	1.47	3.201	412.08	388.56	
2	10	0	1	1.11	2.060	207.31	124.60	Carbon
3	0	0	-1	1.47	3.196	411.74	387.65	Tetrachloride
2	0	0	-1	1.11	2.058	207.31	124.48	0.162
3	10							
2	10	0	1	1.51	2.720	207.31	163.15	Carbon
3	0	0	1	1.61	3.097	238.07	213.38	Disulphide
2	0	0	1	1.51	2.719	207.31	163.08	0.1

NEWFIT RESULTS MeI IN n-HEPTANE

NPAR	NTYPE	IFAIL	XPS	$\chi 10^{13}$	$K_1(0) \times 10^{26}$	$K_0(0)cm^{-2}$	$M_4R \times 10^4 cm^{-4}$	Concentration mf
3	10	2	0					
2	10	2	0					
3	0	2	0					0.005
2	0	0	1	12.86	16.307	207.31	956.66	
3	10	0	1	1.72	1.965	191.49	109.67	
2	10	0	1	2.06	2.464	207.31	148.19	
3	0	0	-1	1.72	1.962	191.07	109.26	0.016
2	0	0	1	2.08	2.496	207.31	150.07	
3	10							
2	10	0	1	1.62	1.691	207.31	103.05	
3	0							0.162
2	0	0	1	1.62	1.698	207.31		
3	10	0	1	1.73	2.648	312.94	243.24	
2	10	0	1	1.45	1.747	207.31	106.32	
3	0	0	1	1.74	2.652	313.26	243.84	0.370
2	0	0	1	1.45	1.752	207.31	106.61	

NEWFIT RESULTS MeI IN n-DECANE

NPAR	NTYPE	IFAIL	XPS	$\gamma 10^{13}$	$K_1(0) \times 10^{26}$	$K_0(0)cm^{-2}$	$M_4R \times 10^4 cm^{-4}$	Concentration mf
3	10	0	1	1.66	2.871	245.88	204.91	
2	10	0	1	1.45	2.339	207.31	140.89	0.016
3	0	0	1	1.66	2.872	246.78	205.75	
2	0	0	1	1.45	2.330	207.31	140.37	
3	10	0	1	1.55	2.345	235.11	160.84	
2	10	0	-1	1.36	1.962	207.31	118.88	0.162
3	0	0	1	1.54	2.335	234.85	159.99	
2	0	0	1	1.36	1.959	207.31	118.70	
3	10	0	-1	1.64	2.660	336.88	263.79	
2	10	0	1	1.33	1.662	207.31	101.35	0.370
3	0	0	1	1.66	2.669	339.39	266.70	
2	0	0	1	1.33	1.659	207.31	101.18	

NEWFIT RESULTS MeI IN n-HEXADECANE

NPAR	NTYPE	IFAIL	XPS	$\aleph 10^{13}$	$K_1(0) \times 10^{26}$	$K_0(0)cm^{-2}$	$M_4R \times 10^4 cm^{-4}$	Concentration mf
3	10	0	1	1.86	3.224	259.21	242.14	
2	10	0	-1	1.60	2.516	207.31	151.23	0.162
3	0	0	1	1.85	3.217	259.49	241.90	
2	0	0	1	1.60	2.511	207.31	150.94	
3	10	0	1	3.65	5.863	358.45	604.89	
2	10	0	1	1.75	2.024	207.31	122.50	0.370
3	0	0	1	3.59	5.770	357.24	593.44	
2	0	0	1	1.74	2.025	207.31	122.55	
3	10	0	-1	2.90	3.323	591.73	588.92	
2	10	0	-1	1.13	0.668	207.31	43.30	0.016
3	0	0	1	1.75	2.461	286.73	207.01	
2	0	0	-1	1.42	1.630	207.31	99.49	

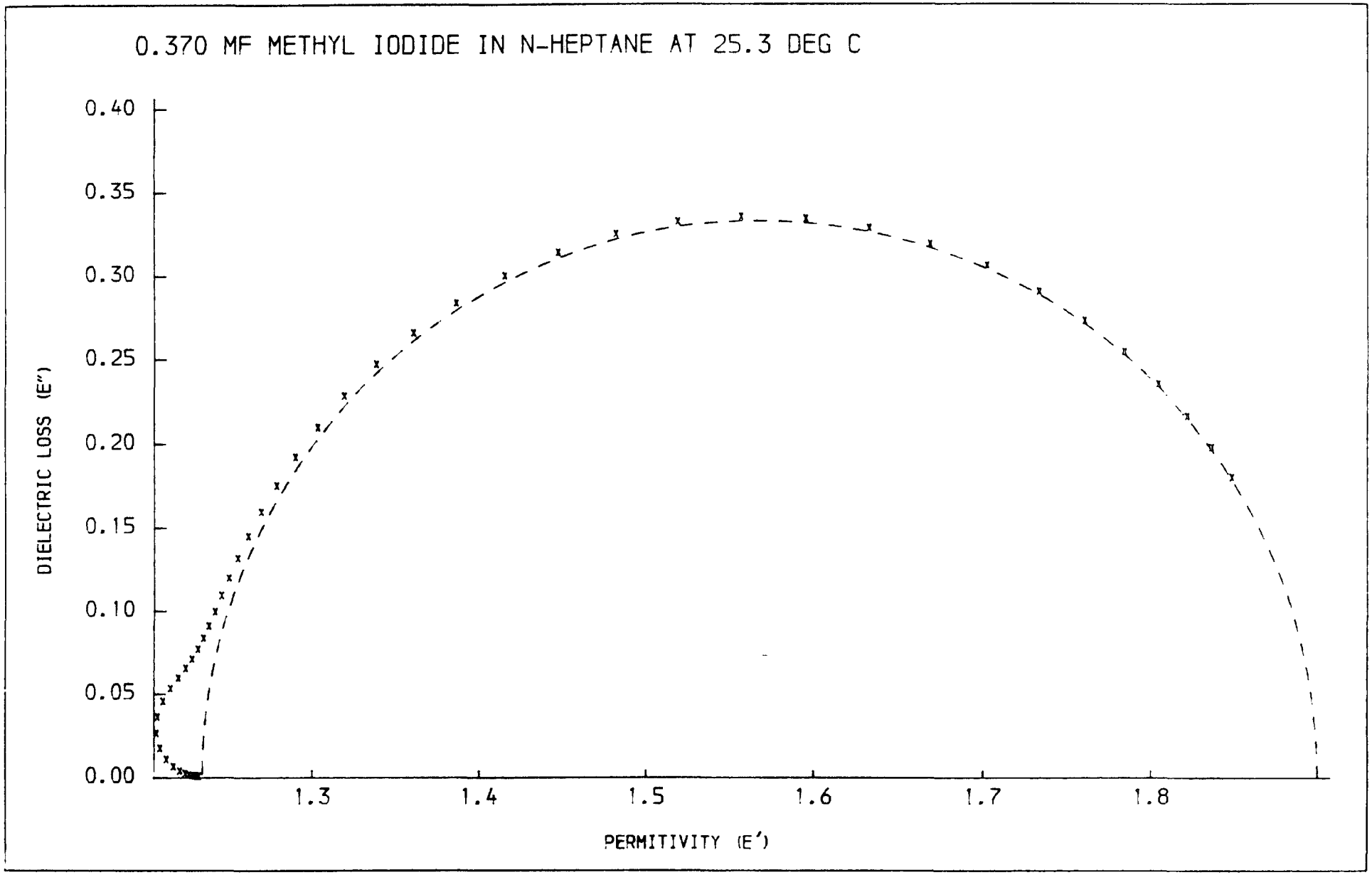
0.370 MF METHYL IODIDE IN N-HEPTANE AT 25.3 DEG C
0.40
0.35
0.30
0.25
0.20
0.15
0.10
0.05
0.00
DIELECTRIC LOSS (E")
1.3
1.4
1.5
1.6
1.7
1.8
PERMITIVITY (E')

FIGURE 7.71

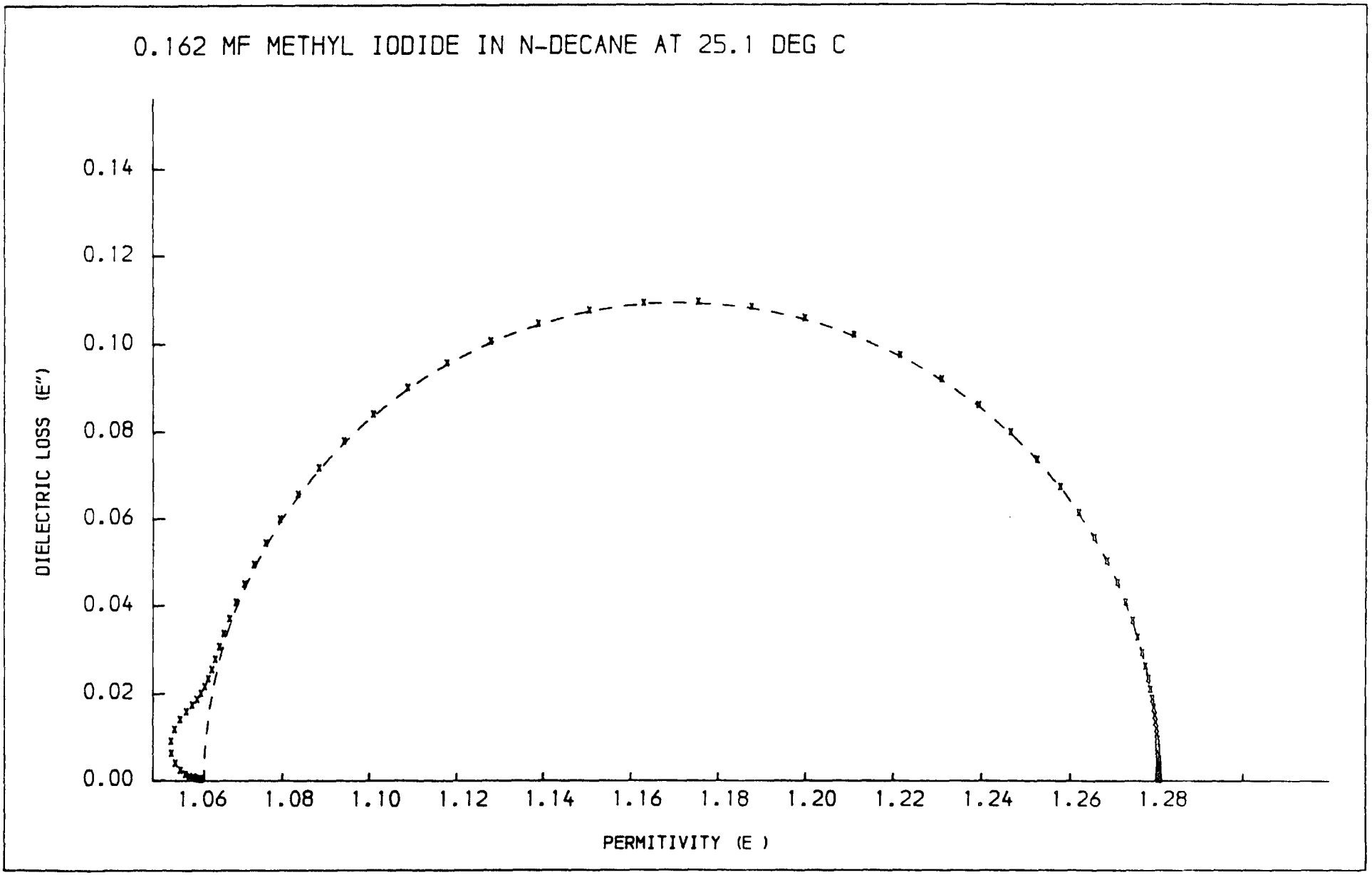
0.162 MF METHYL IODIDE IN N-DECANE AT 25.1 DEG C
DIELECTRIC LOSS (E")
0.14
0.12
0.10
0.08
0.06
0.04
0.02
0.00
1.06
1.08
1.10
1.12
1.14
1.16
1.18
1.20
1.22
1.24
1.26
1.28
PERMITIVITY (E)

FIGURE 7.72

FIGURE V.73 Variation of Viscosity With Temperature

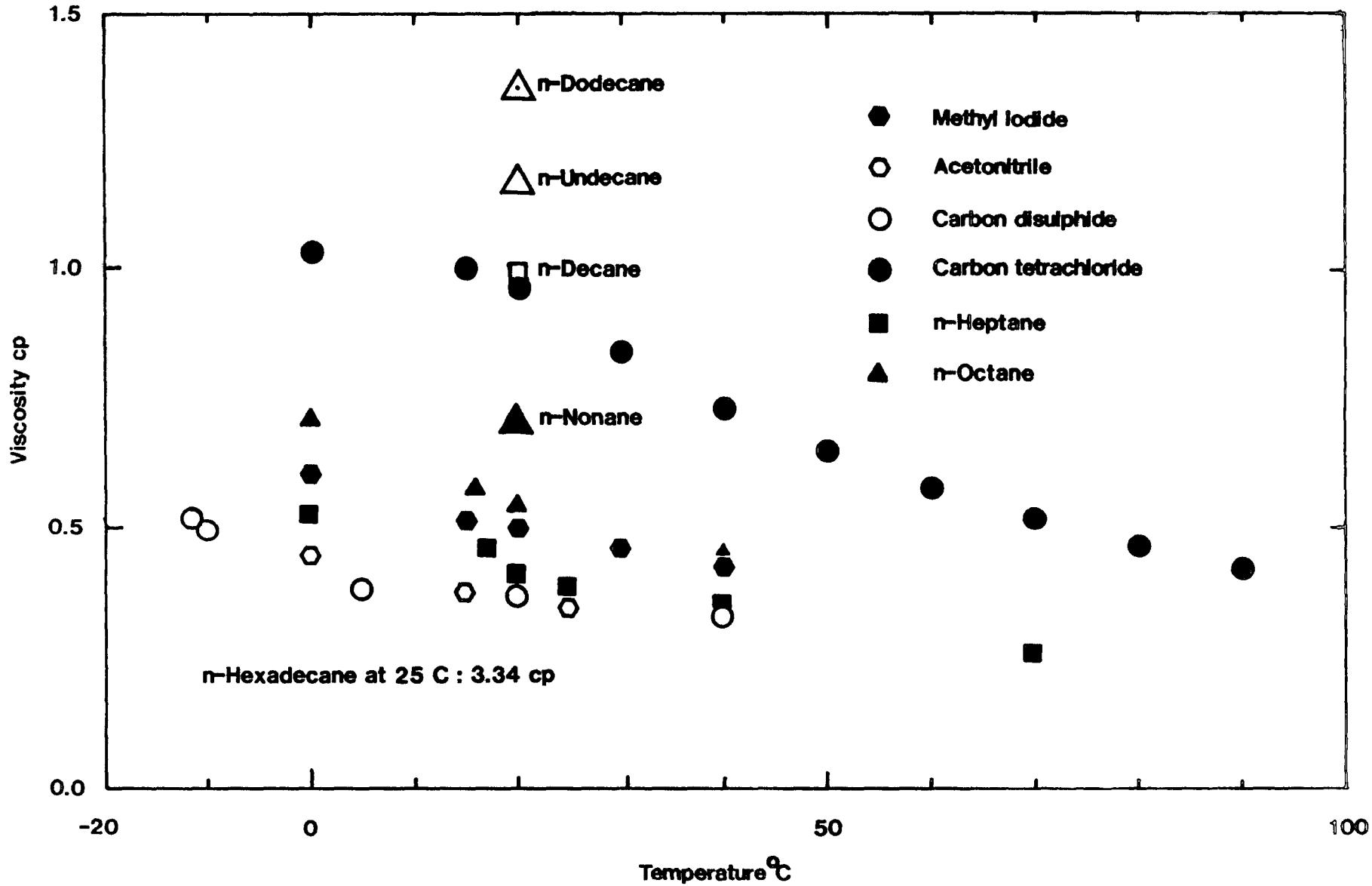

C H A P T E R 8

DISCUSSION

8.1. Literature Investigations of Dynammics and Interactions in MeI

The dynamics and physical properties of MeI in hydrocarbon solvents have been studied previously using Raman spectroscopy by Pacynko et al[96]. In this investigation the correlation functions $\phi_{2R}(t)$ and $\phi_{\nu}(t)$ were determined using the ν_3(C-I) band of MeI at one concentration, in a range of n-alkanes. The results show that τ_{2R} is reduced from the liquid value by the n-alkane environment , but increases towards the liquid value with increasing chain length. When τ_{2R} values were plotted against solution viscosity as reproduced in figure 8.1, they fell into two groups, indicating near free rotation in C_5 to C_{10} (short τ_{2R}, long τ_{ν}) and more hindered rotation in C_{12} to C_{16} (longer τ_{2R}, shorter τ_{ν}). A distinct correlation between the reorientational motion of the molecule and the relative free volume was found.

In a Raman scattering study on the fast axial rotation of methyl halides and acetonitrile by Gompf et al[97], the degenerate methyl stretching E band (ν_4), has been used to examine the small angle diffusion and J-diffusion models. Examination of the diffusional constants $D_{\parallel}(CH_3I)$ and $D_{\parallel}(CD_3I)$ indicated that the spinning motion about the axis is not diffusional, but controlled by inertia. However, the temperature and pressure variation of the model parameters indicated the diffusion model does not give a realistic description of fast axial rotation. Using the memory function formalism, the J-diffusion correlation functions $g_1^{(2)}(t)$ and $g_2^{(2)}(t)$ were fitted to the experimental correlation function of the ν_4 band. It was found that the model did not fit the detailed shape of the experimental correlation function unless the Coriolis coupling

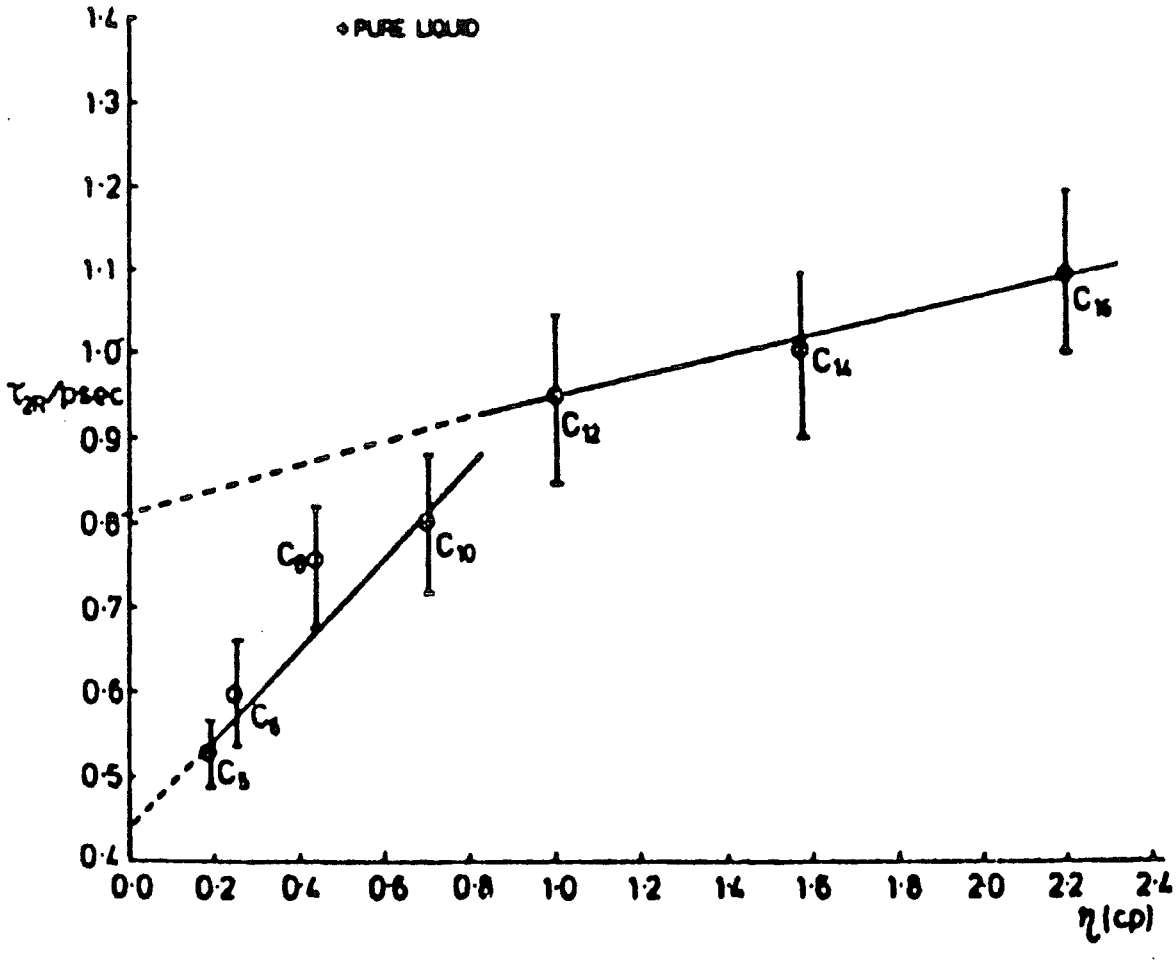

Figure 8.1 τ_{2R} values plotted as a function of viscosity reproduced from Pacynko etal[97]

constant was allowed to vary, but this gave doubtful values for the Coriolis coupling constant and J-diffusion parameters.

In a more recent publication by Bohm etal[98] the tumbling and spinning motion of the acetonitrile molecule has been simulated. The resulting single particle angular velocity and angular momentum correlation functions gave good agreement with experimental data and show the tumbling motion to be subject to a 'cage' effect due to neighbouring molecules. They found the motion about and perpendicular to the symmetry axis to be very different, which indicates that the use of the J diffusion model, (which assumes both types of motion to be the same), is highly questionable for acetonitrile.

K.Sato et al[4] have measured the far-infrared integrated intensities for MeI in carbon tetrachloride and carbon disulphide (0.2 to 1.1 M at room temperature) and obtained Beers law corrected values of $99.7*10^{-2}$ and $99.4*10^{-2}$ cm mol^{-1} respectively. These values were used to obtain liquid phase dipole moments from equation 7.18 which were 1.88 and 1.84 D. More comprehensive microwave and far-infrared studies on MeI have been made by Kluk etal[5] and Kocot etal[6]. In the microwave study by Kluk etal on MeI liquid at different temperatures, values for ε_0, ε_∞ and τ_D were reported which are in very good agreement with those determined in this work. They found the τ_{sp} determined using equation 6.47 agreed with $3\tau_{20}$ values from Raman scattering, which they interpret as indicative of diffusional rotation about the molecular axis. For this to be true ln ϕ^T must be totally exponential as in figure 8.2, but from figures 7.41 to 7.44 this is not the case for the short time part of ln ϕ^T. Therefore rotational diffusion can only be valid for the long time motion. Kocat etal determined $\bar{\nu}_{max}$, α_{max}, α integrated intensity and τ_{1R} for MeI liquid,

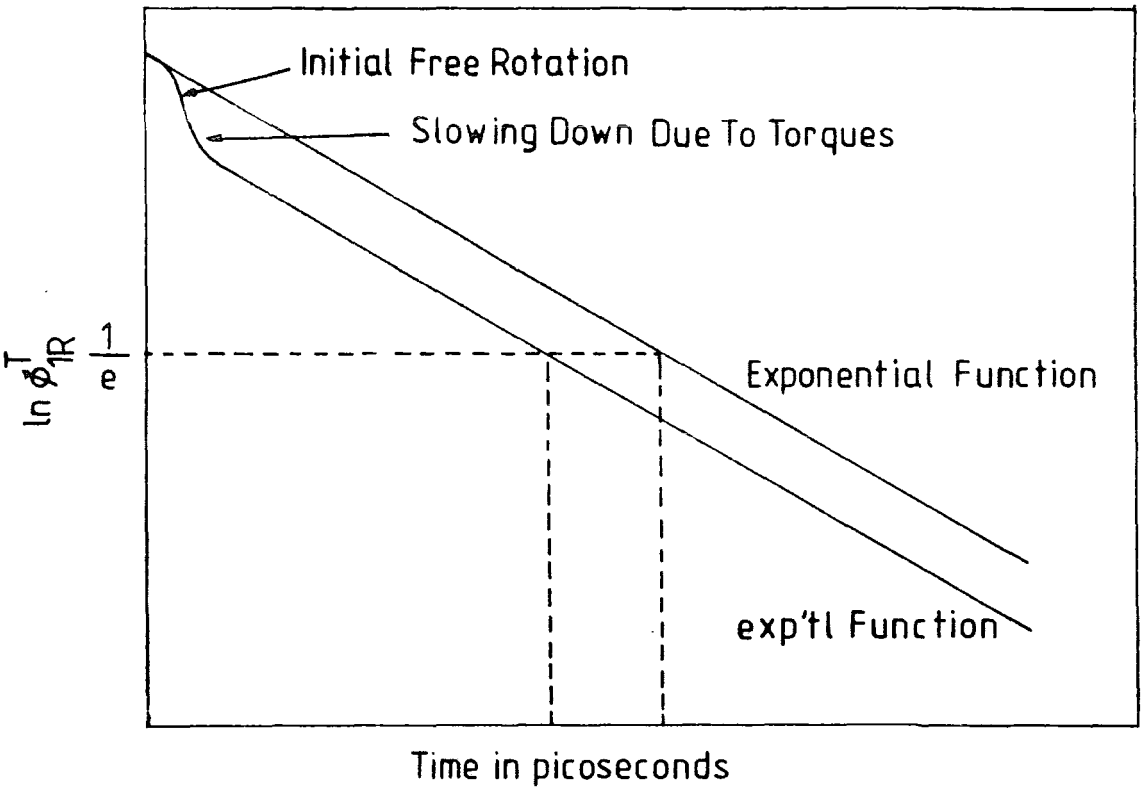

Figure 8.2 ϕ_{1R}^{T} functions

Figure 8.3 Effect of far-infrared absorption on microwave absorption

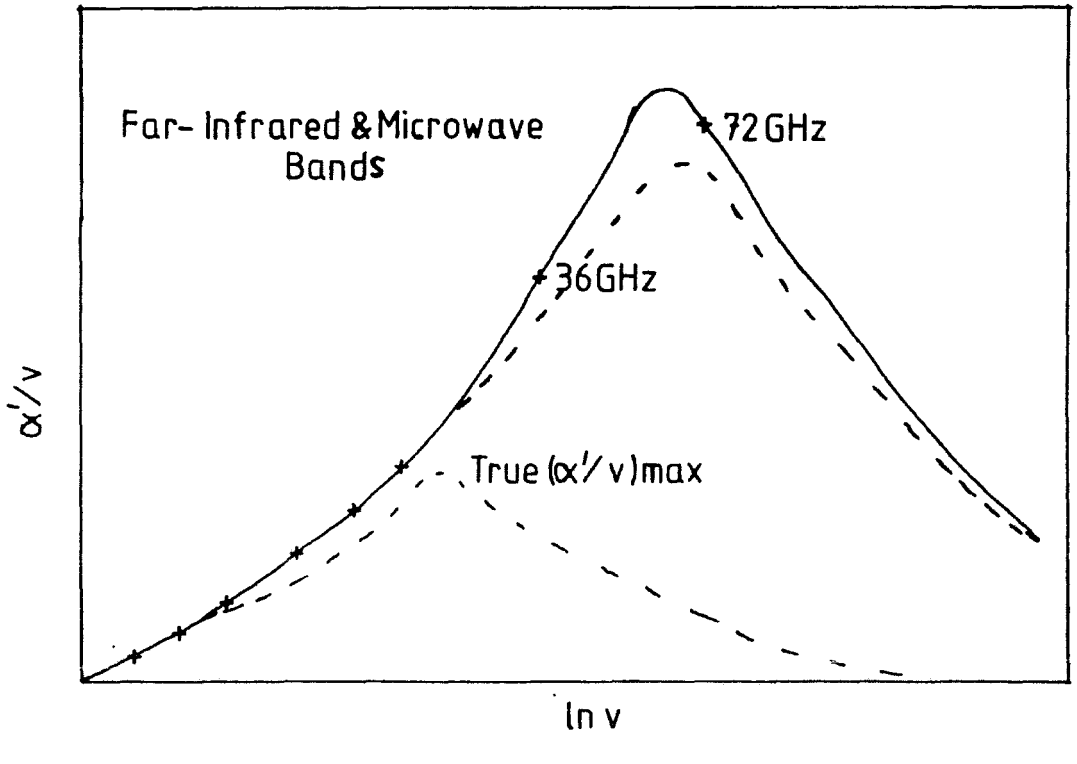

all of which are in close agreement with the values determined in this work. A summary of the literature microwave and far-infrared results for MeI is given in table 8.1.

8.2. Effects of Solvent Environment and Concentration on MeI

8.2.1 Relaxation Times

Microwave relaxation times τ_D were calculated using equation 7.1, but initially values obtained for MeI liquid did not agree with literature values. Also for the solution data the τ_D values gave a different trend with concentration when compared to the τ_D^{obs} values as can be seen in table 7.8, this is believed to occur, because of perturbation of the microwave absorption by the far-infrared absorption[99]. Which is demonstrated in figure 8.3, where the increased absorption in the microwave region due to the far-infrared band moves the microwave ν_{max} to a higher frequency giving a faster relaxation time than the "true" microwave relaxation time. As a simple check, for solution data where there were sufficient microwave points the ones to higher frequency (36 and 72 GHz) were removed and the remaining points reanalysed. The Fuoss-Kirkwood analysis of the reduced data sets always gave ν_{max} values at lower frequencies than for the full data sets, and therefore slower relaxation times, which agreed with literature values for the MeI liquid data.

The microwave τ_D and far-infrared τ_{1R}^T relaxation times of MeI in different solvent environments given in chapter 7, are plotted against concentration in figures 8.4 to 8.7. For all the solvents, the microwave τ_D relaxation times become faster with decreasing MeI concentration, as found by Arnold et al[65] for acetonitrile. The other relaxation times plotted in figures 8.4 to 8.7, cover a smaller

8.1

PROPERTY	LITERATURE VALUE	EXPERIMENTAL VALUE
ϵ_o	6.89	6.850
ϵ_∞	2.80	2.936
τ_D	4.1	5.0
$V_{Max} cm^{-1}$	61	62
$\alpha_{Max} cm^{-1}$	102	105
$Ai \times 10^{20} cm\ mol^{-1}$	90.0	91.4

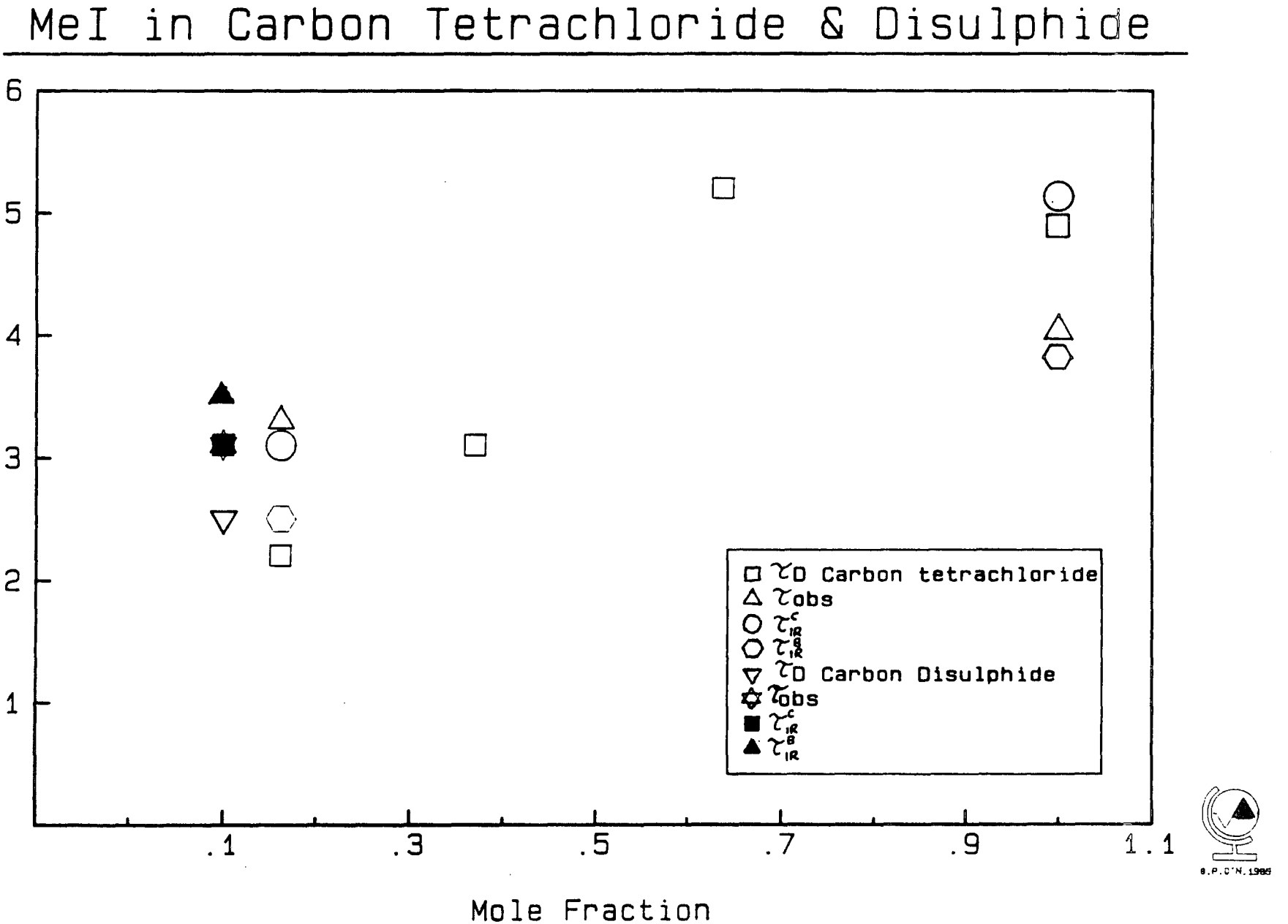
MeI in Carbon Tetrachloride & Disulphide
Time in picoseconds
Mole Fraction
6
5
4
3
2
1
.1
.3
.5
.7
.9
1.1
τD Carbon tetrachloride
τobs
τc IR
τB IR
τD Carbon Disulphide
τobs
τc IR
τB IR

Figure 8.4

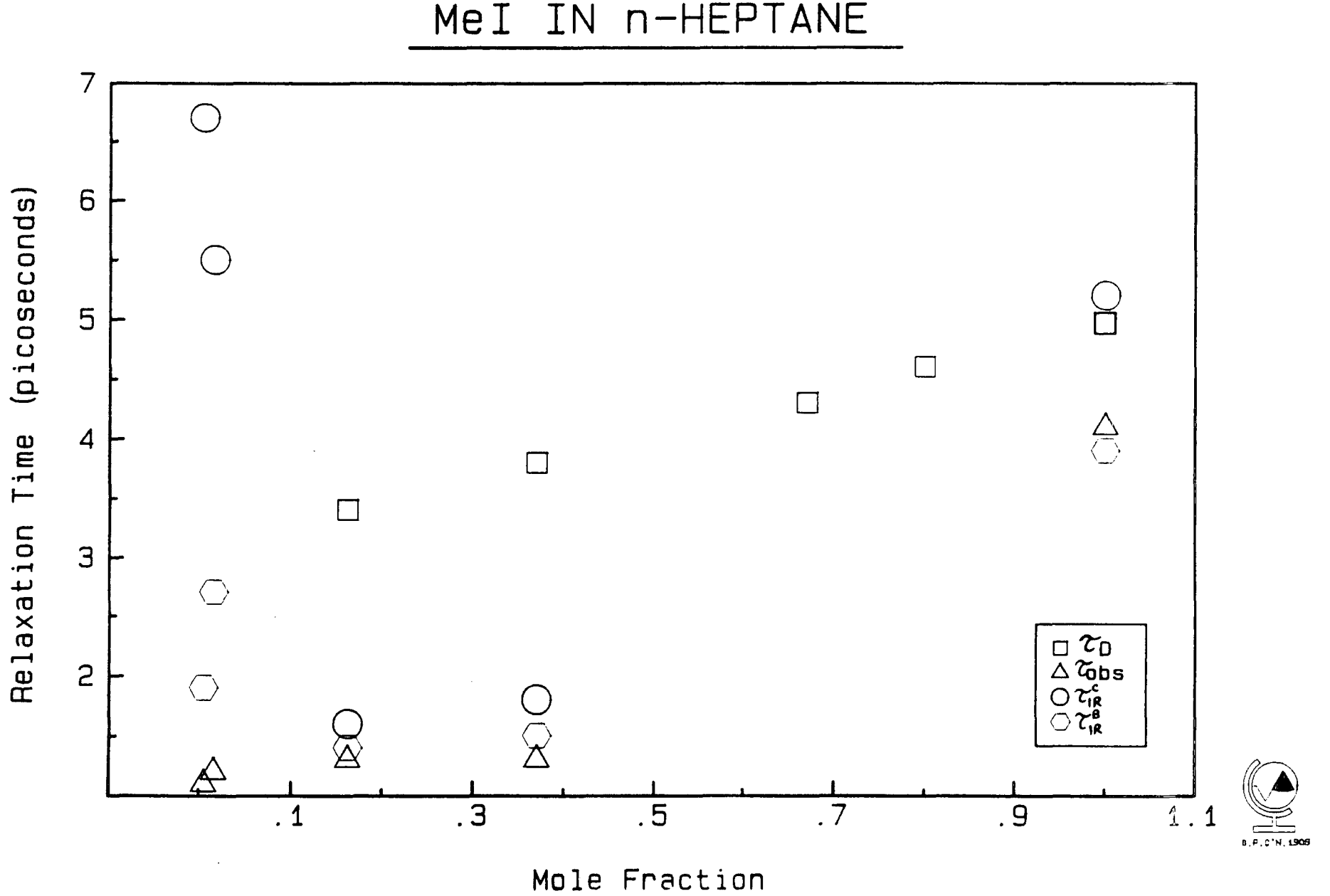
MeI IN n-HEPTANE
Relaxation Time (picoseconds)
Mole Fraction
2
3
4
5
6
7
.1
.3
.5
.7
.9
1.1
τ_D
τ_{obs}
τ^c_{IR}
τ^B_{IR}

Figure 8.5

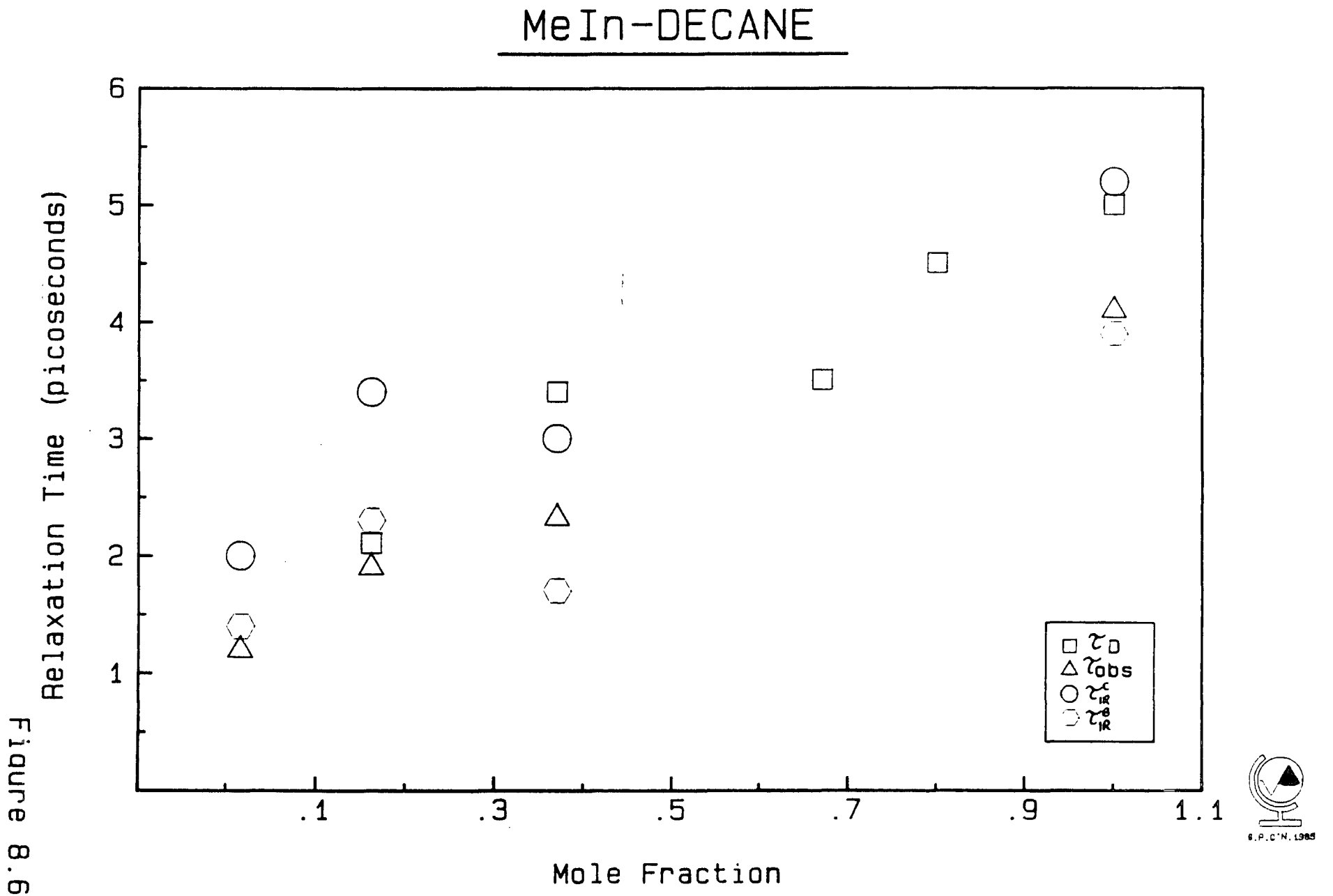
MeIn-DECANE
Relaxation Time (picoseconds)
Mole Fraction
1
2
3
4
5
6
.1
.3
.5
.7
.9
1.1
τ_D
τ_{obs}
τ^c_{IR}
τ^s_{IR}

Figure 8.6

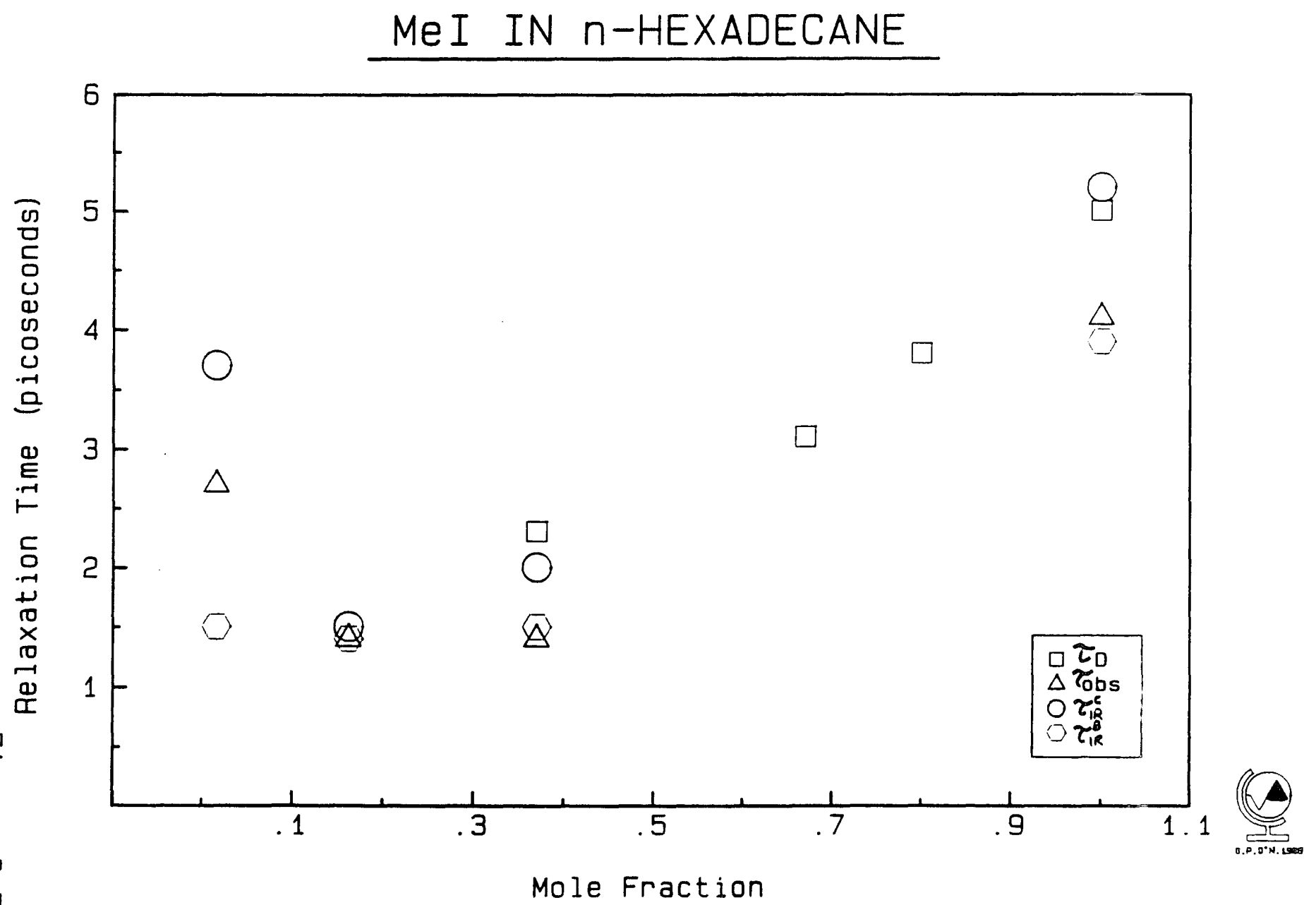
MeI IN n-HEXADECANE
Relaxation Time (picoseconds)
6
5
4
3
2
1
.1
.3
.5
.7
.9
1.1
Mole Fraction
τ_D
τ_{obs}
τ_{IR}^{c}
τ_{IR}^{B}

Figure 8.7

concentration range, therefore trends with concentration for them are less clear. However, the solution times are all faster than for the liquid and are generally constant or decrease slightly with decreasing MeI concentration over the range measured. For the n-alkane range of solutions, τ_D times become faster with increasing chain length, whilst τ_{1R}^T times become slower with increasing chain length. For the liquid values, τ_D and τ_{1R}^c times are very similar and slower than τ_{1R}^b and the τ_D^{obs} times which are also similar, this trend can be seen in the respective solution values as well.

The total correlation function relaxation times determined from the time to reach 1/e (τ_{1R}^b) and the slope of the correlation function (τ_{1R}^c) are plotted in figures 8.8 and 8.9. The time derived from the 1/e measurement is always faster than the corresponding time from the slope of the correlation function, demonstrating the influence of the inital non-exponential short time motion of the system on the correlation function. This effect is shown schematically in figure 8.2, from which it is clear that for the experimental correlation function the initial non exponential part, which is similar to that of a free rotor, causes it to reach 1/e faster than it would for the corresponding totally exponential correlation function, which would be due to strongly hindered motion. The point of inflection in the experimental angular momentum correlation function is due to the hindering effect of the intermolecular torques and is interpreted as evidence of a cage effect. This effect has also been observed by Bohm etal[98] for modelled correlation functions of acetonitrile. This difference between the two methods of measurement, points to the possibility that the two times are reflecting motions occurring on different time scales. τ_{1R}^c the long time diffusional rotation of the

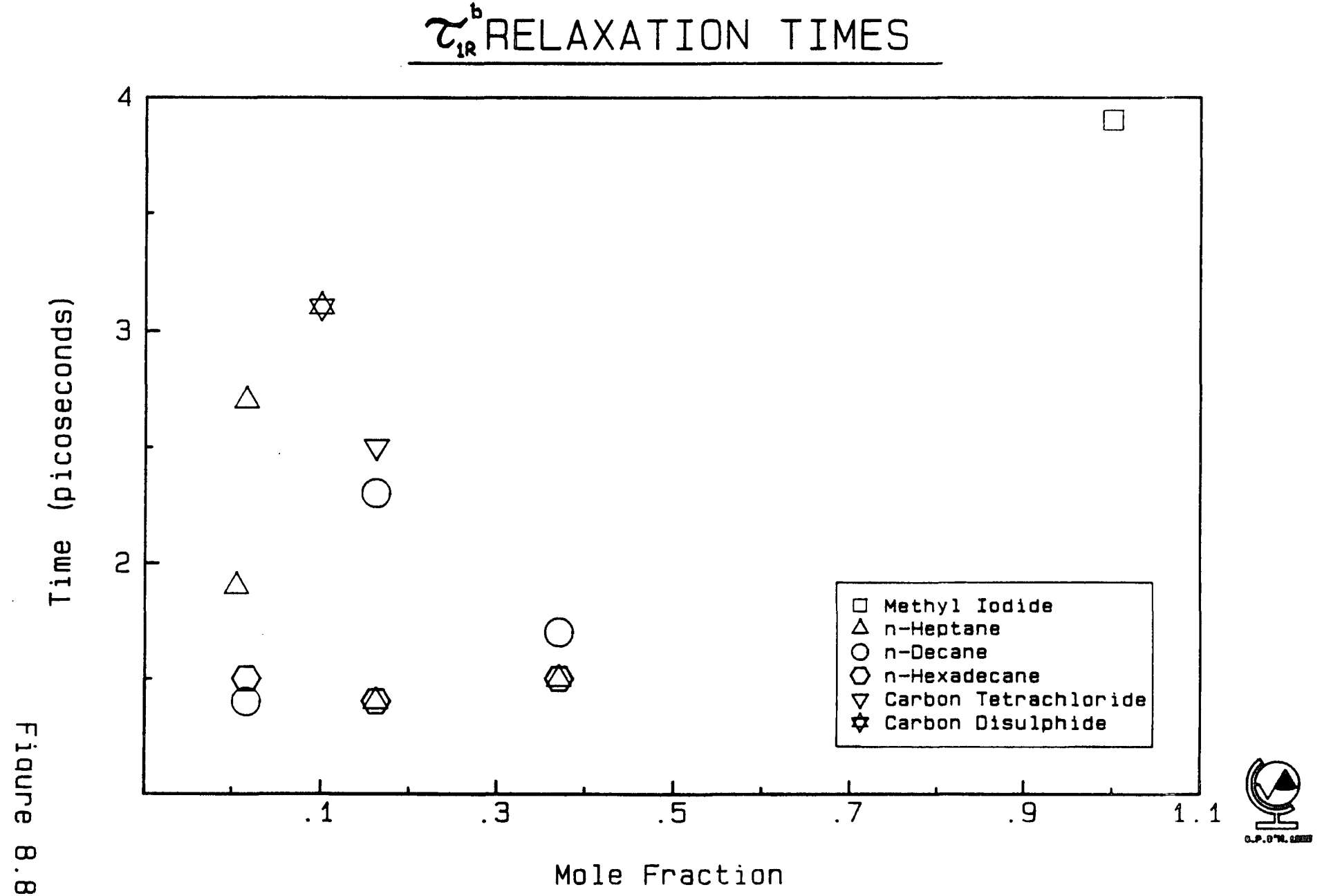
τ_{1R}^{b} RELAXATION TIMES
Time (picoseconds)
4
3
2
.1
.3
.5
.7
.9
1.1
Mole Fraction
Methyl Iodide
n-Heptane
n-Decane
n-Hexadecane
Carbon Tetrachloride
Carbon Disulphide

Figure 8.8

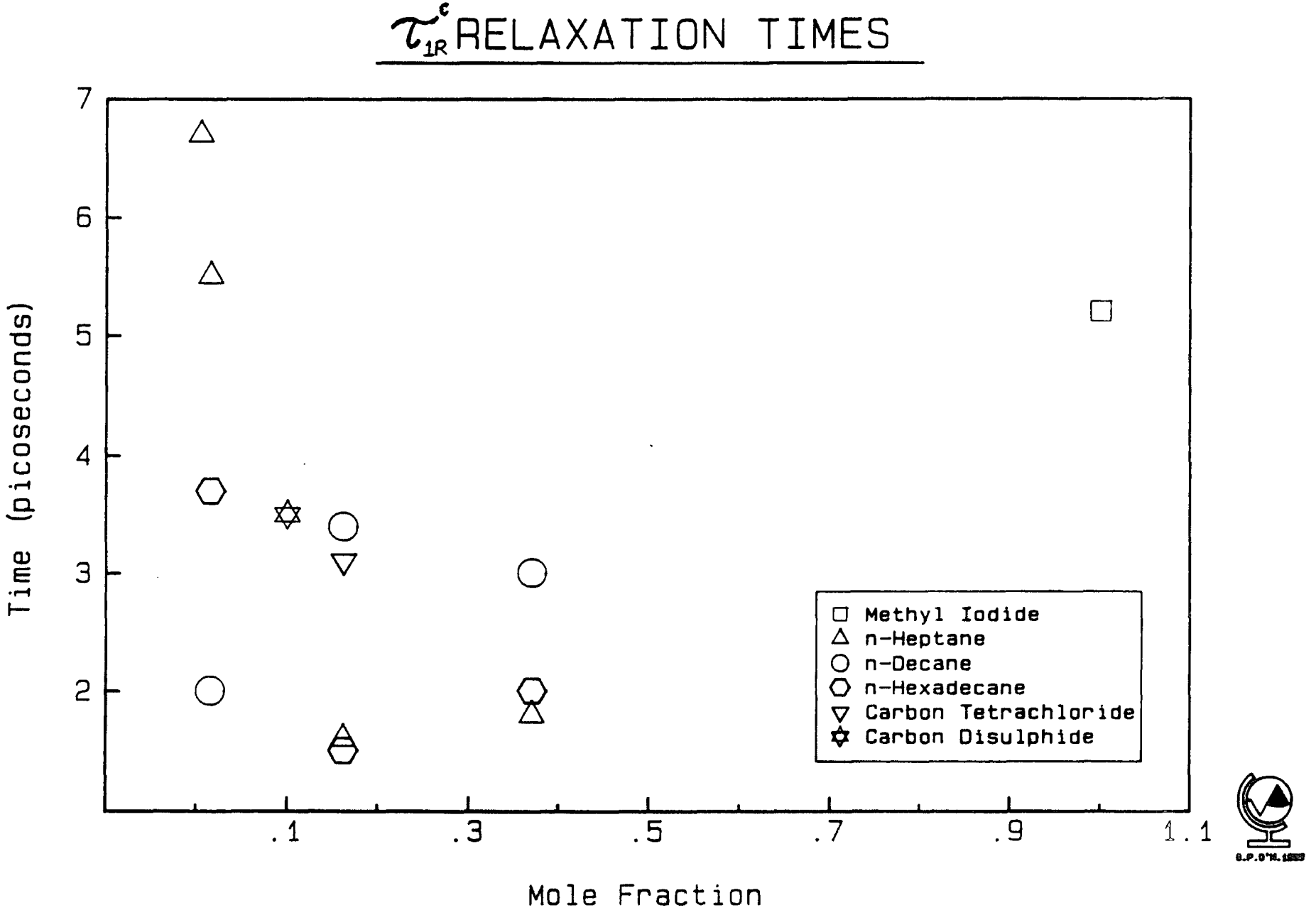
τ^c_{1R} RELAXATION TIMES
Time (picoseconds)
7
6
5
4
3
2
.1
.3
.5
.7
.9
1.1
Mole Fraction
Methyl Iodide
n-Heptane
n-Decane
n-Hexadecane
Carbon Tetrachloride
Carbon Disulphide

Figure 8.9

system and τ^{b}_{1R} a combination of long and short time motion. For n-heptane the differences between τ^{s}_{1R} and τ^{b}_{1R} increase with decreasing MeI concentration, indicating that the short time motion of the system is becoming more dominant at low MeI concentrations, possibly because the MeI molecules are separated on dilution and are able to rotate freely for a longer time interval. For n-decane and n-hexadecane there are smaller differences between the times, which also change little with dilution, indicating that the short time motion is still restricted by the local intermolecular torques as in the liquid. Therefore the effect of the local environment upon the time development of the MeI molecular motion, can be seen in the angular momentum correlation function. From this and the similarity between τ^{obs}_{D} and τ^{b}_{1R} values and also τ_{D} and τ^{s}_{1R} values the short time and long time motions of the system are reflected in the microwave-far-infrared spectrum with the short time motion being more dominant in the far-infrared absorption.

Considering the relaxation times and the macroscopic viscosities for the solvents given in figure 7.73, there would appear to be no correlation between the macroscopic viscosity and the MeI relaxation times.

8.2.2 The Far Infrared Absorption

Results from analysis of the far-infrared absorption given in chapter 7 are plotted in figures 8.10 and 8.11 from which, the $\bar{\nu}_{max}$ position shows a decrease with decreasing MeI concentration, with the n-decane and n-hexadecane values being closer to the liquid value than the n-heptane values. The n-alkane values are all lower than the values for carbon tetrachloride and carbon disulphide which are both

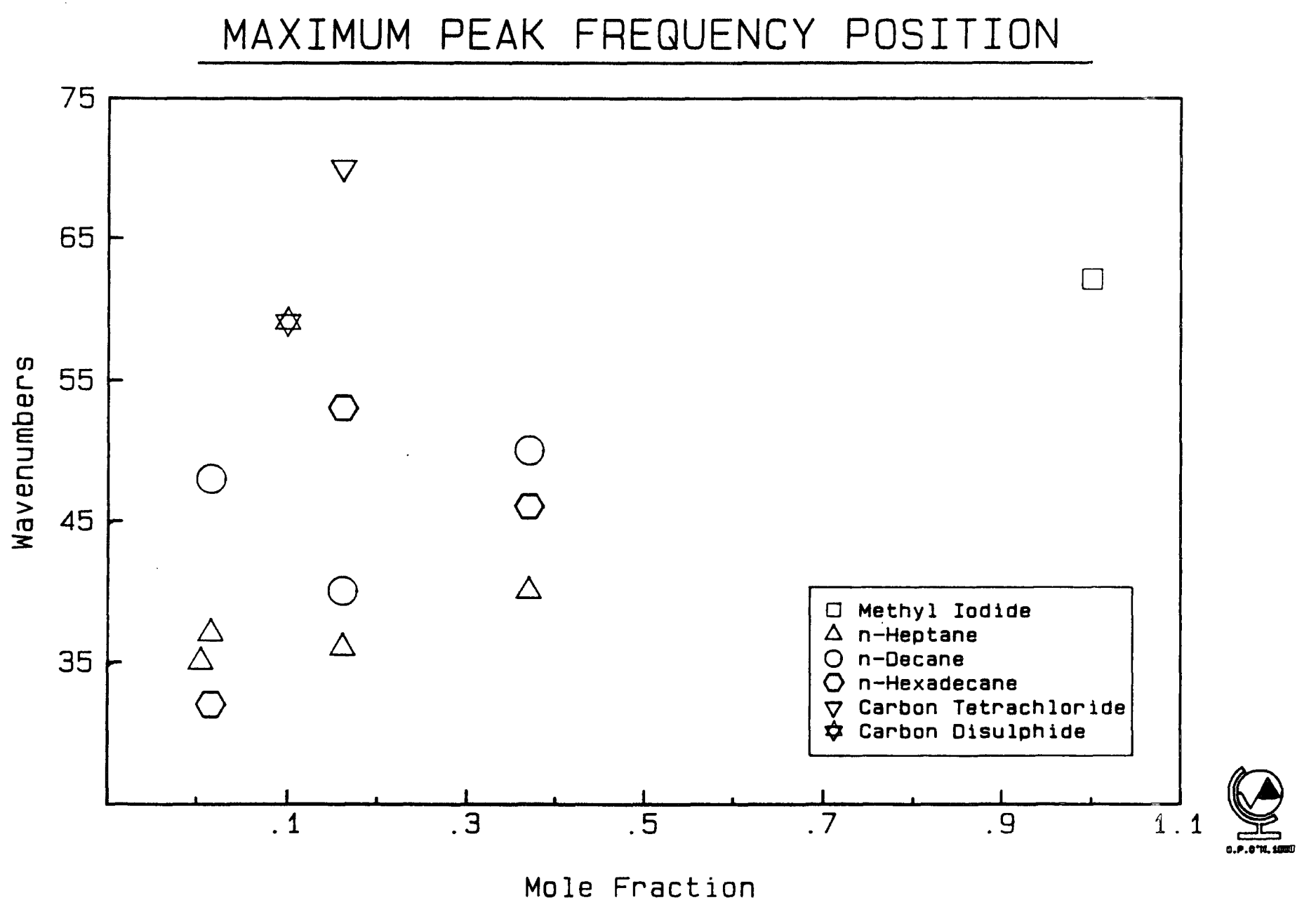
MAXIMUM PEAK FREQUENCY POSITION
75
65
55
45
35
Wavenumbers
.1
.3
.5
.7
.9
1.1
Mole Fraction
Methyl Iodide
n-Heptane
n-Decane
n-Hexadecane
Carbon Tetrachloride
Carbon Disulphide

Figure 8.10

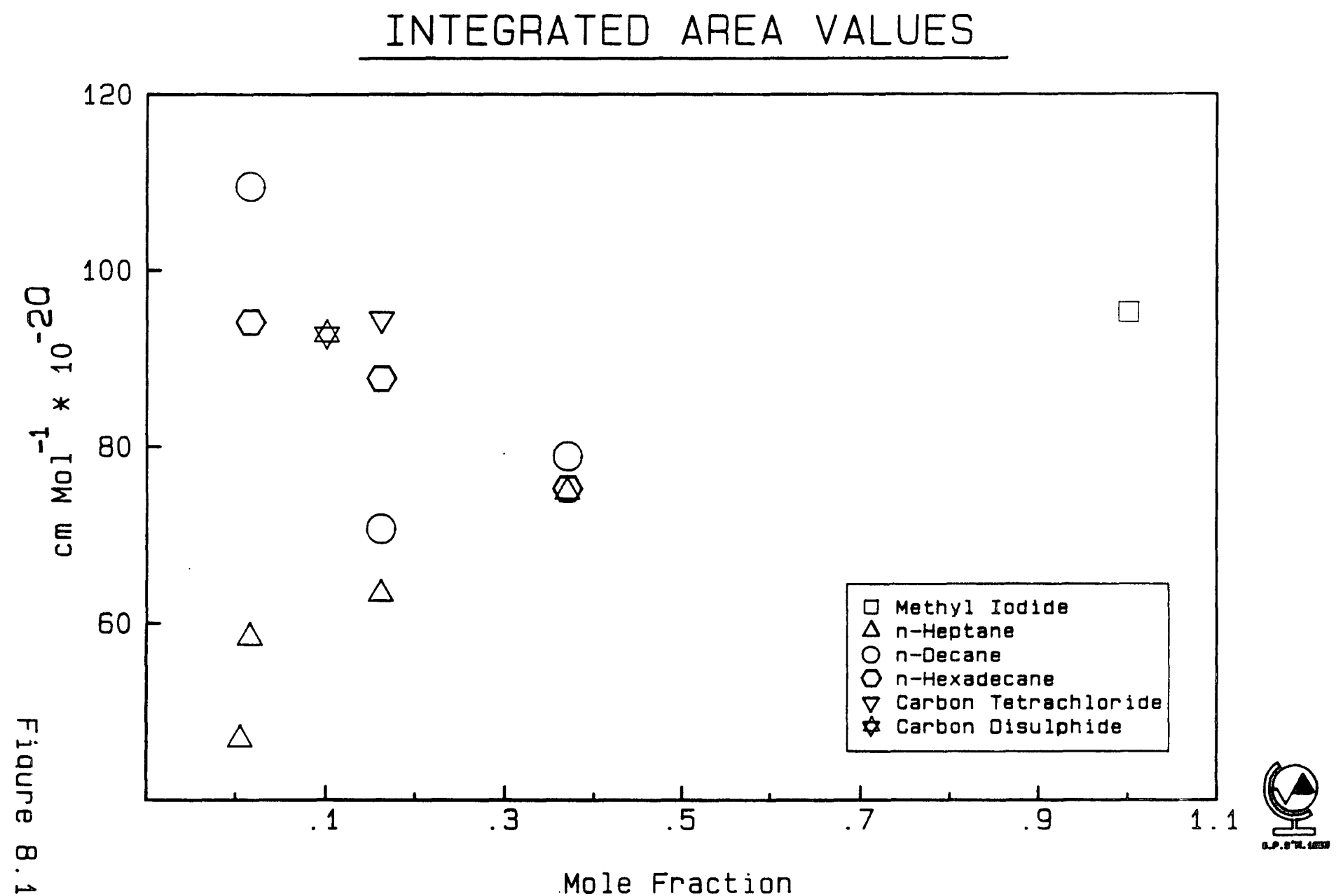
INTEGRATED AREA VALUES
120
100
80
60
cm Mol-1 * 10-20
.1
.3
.5
.7
.9
1.1
Mole Fraction
Methyl Iodide
n-Heptane
n-Decane
n-Hexadecane
Carbon Tetrachloride
Carbon Disulphide

Figure 8.11

similar to the liquid values from Evans[94]. The peak frequency of a far-infrared band is proportional to the fourth moment and therefore also the intermolecular torques. So the peak frequency measurements indicate that the torques experienced in n-decane and n-hexadecane solutions are similar to those in the liquid, whilst those in n-heptane solutions are lower.

The absorption coefficient integrated area and FWHH values show some very interesting trends between the solvents, when compared to the liquid values. The FWHH values for n-heptane solutions go from less than to greater than the liquid value, whilst the Ai values increase with MeI concentration towards the liquid value. This trend suggests that there is a substantial induced component in the liquid Ai value which is being removed on dilution in n-heptane, possibly because the MeI molecules are being separated by the solvent. Therefore interactions between the MeI molecules would be reduced as would the induced effects, leading to a narrower number of rotational frequencies (smaller FWHH values) and a smaller "total" dipole (smaller Ai values). A different trend is seen for n-decane and n-hexadecane, here the FWHH values are all greater than the liquid value and the Ai values go from less than to greater than the liquid value with decreasing concentration. This indicates that there is a broader range of rotational frequencies for the longer chain alkane solutions and that induced effects are becoming greater as the MeI concentration decreases. This suggests that, for the long chain alkanes as the number of MeI molecules decreases they are being forced into solute "pools" within the solvent environment. These effects are also reflected in the dipole moment values calculated from the Ai values. The liquid μ_{calc} value is much greater than the dipole moment value

calculated from equation 6.11, both of which are greater than μ_o, as found by Kocot etal[6]. Pointing to an induced dipole contribution to the permanent molecular dipole. For the solvents the n-heptane μ_{calc} values become very similar to the μ_* values with reducing concentration indicating a reduction in induced effects for this solvent. However, for n-decane and n-hexadecane, μ_{calc} values are all greater than μ_* and remain constant with decreasing MeI concentration, again indicating that interaction induced effects are still apparent at low MeI concentrations for these two alkanes.

8.2.3 Moments and Torques

THe second moment values given in table 7.11, are plotted in figure 8.12, as can be seen the liquid value is higher than the theoretical value for rotational energy, as found by Arnold[8] for acetonitrile. De Santis etal[100] have studied the second moment of N_2 liquid obtained from Rayleigh scattering experiments. They have shown that the increase in the second moment above the value for rotational energy is due to cross terms. Therefore the reduction in the second moment in n-decane solutions could be interpreted as being due to the removal of cross terms with dilution. The fourth moment values are plotted in figure 8.13, since these values are more heavily weighted by the high frequency tail of the far-infrared band, they should be more sensitive to induced effects. They do in fact, show a slight increase over the liquid value for all the n-alkanes at 0.37mf, and then a steady decrease with decreasing MeI concentration, though the n-decane and n-hexadecane values remain very similar and greater than the n-heptane values. The torque values are proportional to the fourth moment values and in fact show exactly the same trend, as can be seen

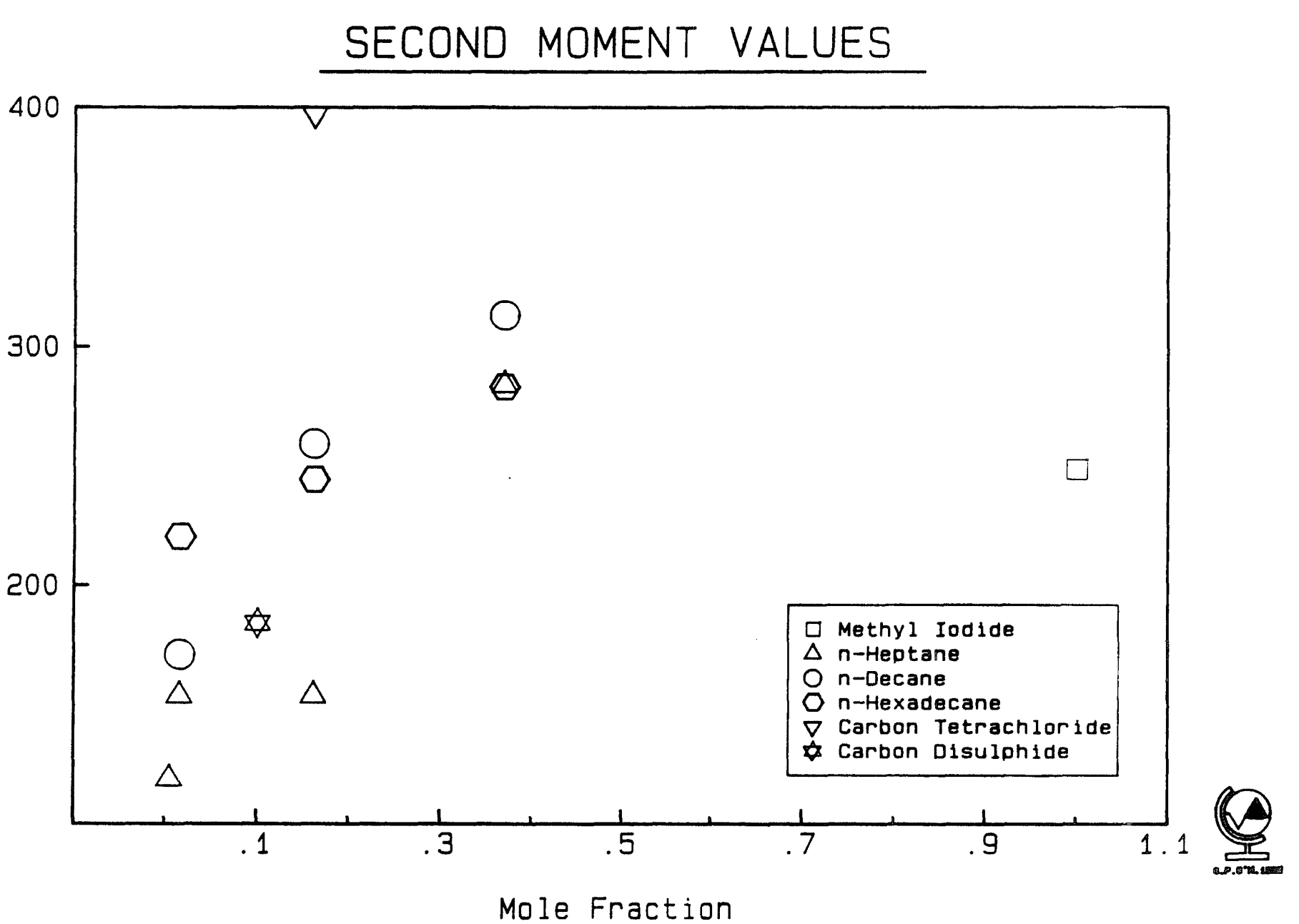
SECOND MOMENT VALUES
400
300
200
cm-2
.1
.3
.5
.7
.9
1.1
Mole Fraction
Methyl Iodide
n-Heptane
n-Decane
n-Hexadecane
Carbon Tetrachloride
Carbon Disulphide

Figure 8.12

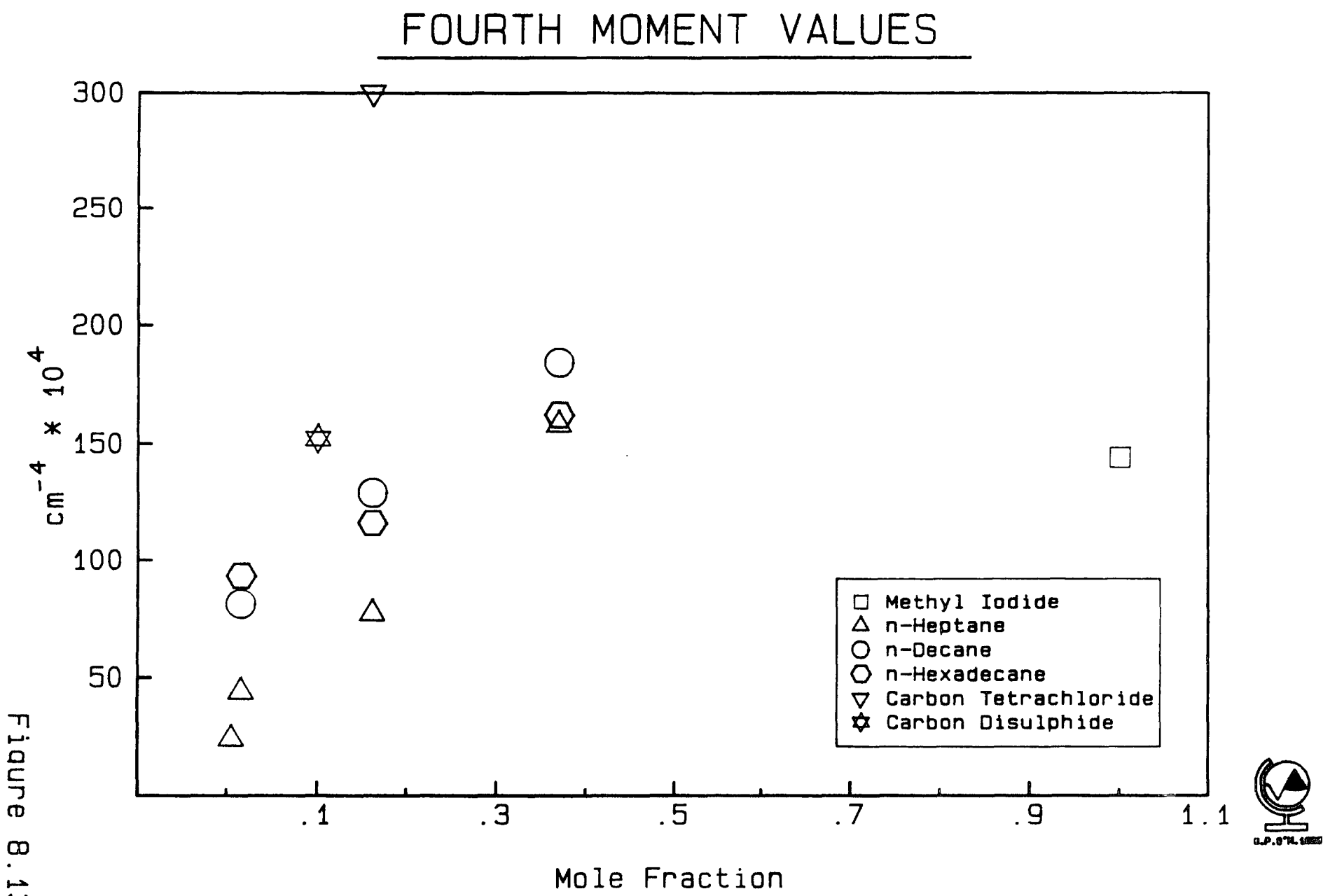
FOURTH MOMENT VALUES
300
250
200
150
100
50
cm-4 * 10^4
.1
.3
.5
.7
.9
1.1
Mole Fraction
Methyl Iodide
n-Heptane
n-Decane
n-Hexadecane
Carbon Tetrachloride
Carbon Disulphide

Figure 8.13

from figure 8.14. The MeI molecules in n-decane and n-hexadecane are therefore experiencing similar torques which are greater than for n-heptane solutions, suggesting there are more molecules closer together in n-decane and n-hexadecane than in n-heptane. This difference in solute environment has also been observed by Pacynko etal[96]. They suggest that for the longer chain length alkanes the MeI molecules are forming solute "pools" within the alkane environment which would account for the higher than expected torque values in n-decane and n-hexadecane solutions. The moment and torque values for carbon tetrachloride are higher than the liquid values which may be due to the high polarisability of the carbon tetrachloride molecules causing added induced effects due to the solvent molecules.

8.2.4 Correlation Factors

The $g^{(1)}$ and g^{KF} values given in table 7.13 for MeI in n-alkanes show the same trend of values >1 at high MeI concentrations, which increase as the MeI concentration is reduced. There is very good agreement between the $g^{(1)}$ and g^{KF} values, though for the liquid the Hill internal field correction[95] has a marked effect on the $g^{(1)}$ value. The correction changes the $g^{(1)}$ value from one indicative of a parallel alignment between molecules to a value that indicates nearly anti parallel alignment which is in agreement with the g^{KF} value. As for the moments (see table 7.13), the Hill correction has little effect on the $g^{(1)}$ function for the n-alkane results. The angular form of the $g^{(1)}$ function is shown in figure 8.15, and the resulting static angular alignment for MeI molecules are given in table 8.2. From these results the molecules go from a random arrangement($\theta=90^{o}$) towards a parallel one($\theta=0^{o}$) with decreasing MeI concentration. $g^{(1)}$ values can

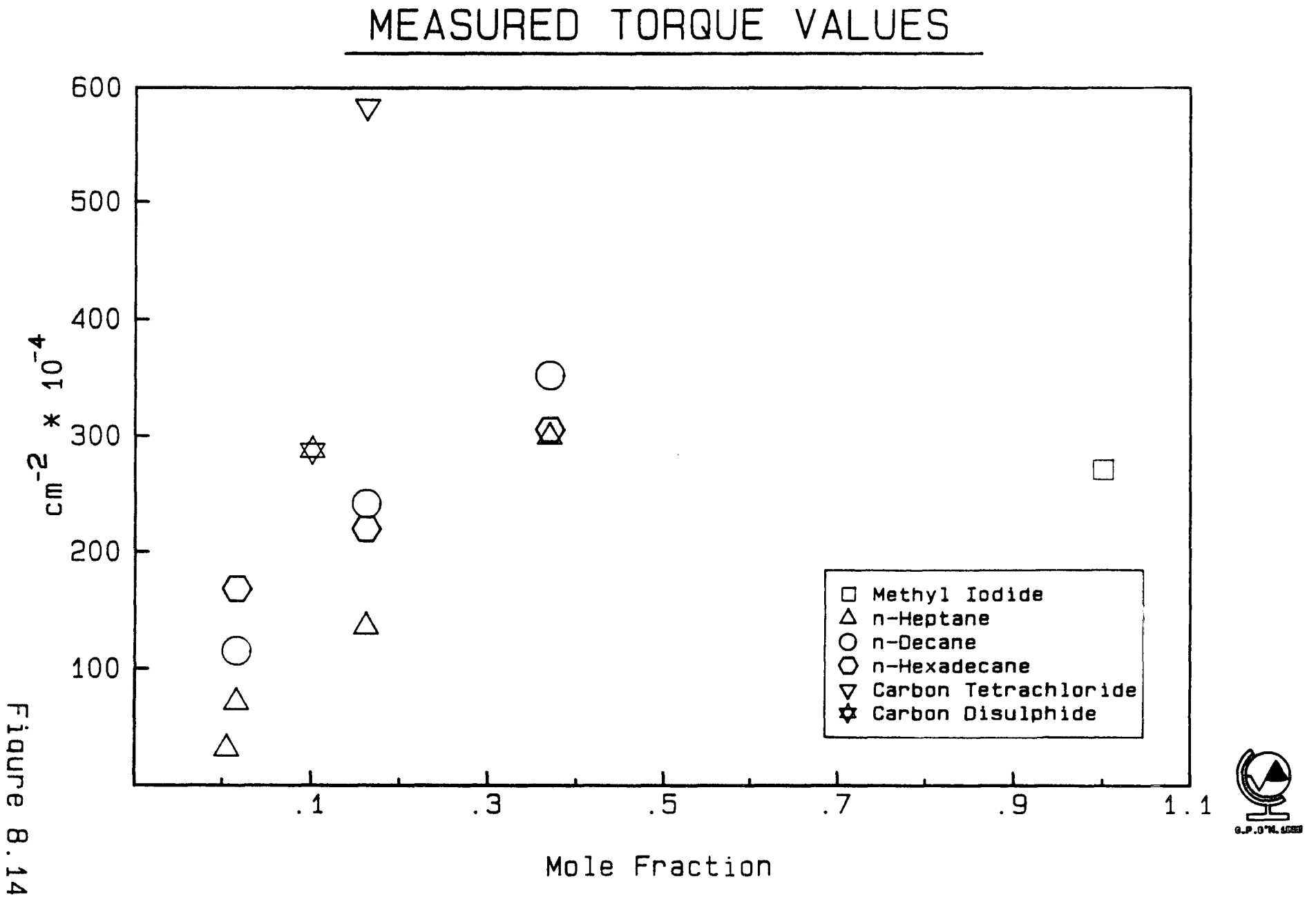
MEASURED TORQUE VALUES
600
500
400
300
200
100
cm-2 * 10-4
.1
.3
.5
.7
.9
1.1
Mole Fraction
Methyl Iodide
n-Heptane
n-Decane
n-Hexadecane
Carbon Tetrachloride
Carbon Disulphide

Figure 8.14

$$g^{(1)} = 1 + Z \sum \langle \cos \theta_{ij} (\theta) \rangle$$

(Z = Cluster Number)

For : Z = 1

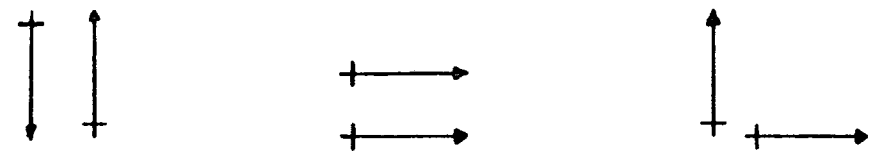

$g^{(1)} = 0$ $g^{(1)} = 2$ $g^{(1)} = 1$

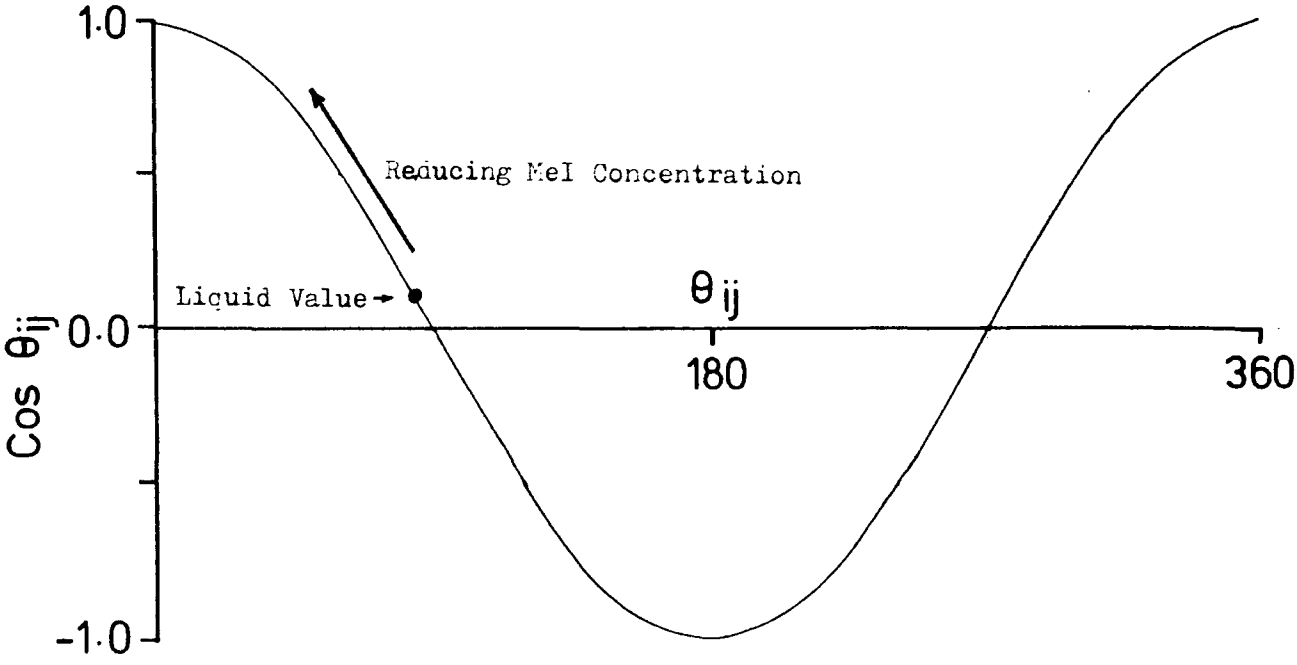

FIGURE 8.15 THE ANGULAR FORM OF THE $g^{(1)}$ FUNCTION

8.2

CORRELATION FACTORS

SOLVENT	CONCENTRATION mf	θ_o DEGREES	θ^{KF} DEGREES
	1.0	103	109
	0.005	16	43
	0.016	32	52
n-HEPTANE	0.162	50	58
	0.370	88	93
	0.016	57	0
n-DECANE	0.162	78	74
	0.370	88	93
	0.016	31	49
n-HEXADECANE	0.162	84	61
	0.370	79	85
CARBON TETRACHLORIDE	0.162	89	95
CARBON DISULPHIDE	0.1	97	103

also be calculated using equation 6.40 the Glarum Powles form of which is given below.

$$\frac{\tau_D^{mw}}{\tau_{sp}} = \left[\frac{3\varepsilon_o}{2\varepsilon_o - \varepsilon_\infty}\right] \frac{g^{(1)}}{(1+N\dot{f})} \qquad \ldots\ldots \quad 8.1$$

Fixing $(1+N\dot{f})$ at 1 (ie no dynamic correlations) and using g^{KF} and the experimentally measured $g^{(1)}$ values in equation 8.1 gives the values given in table 8.3. Comparing the $g^{(1)}$ values to those in table 7.13 it is clear that there is a large difference between the $g^{(1)}$ values from equation 8.1 and those determined from equations 6.20 and 6.48. Indeed results for $g^{(1)}$ or τ_{sp} that agree with measured values can only be obtained if $\dot{f} \neq 1$, which would mean that dynamic correlations are significant, (the interpretation of such dynamic correlations is not clear). For equation 8.1, both microwave and far-infrared relaxation times give very similar results for the respective $g^{(1)}$, τ_{sp}, $(1+N\dot{f})$ and the ratio τ_D/τ_{sp}. The ratio value is close to 3 for the solution data and 1.5 for MeI liquid, though considering the disagrement between the measured values and those from equation 8.1, any interpretation of this ratio must be in some doubt.

8.2.5 Interaction Induced Effects

An extensive computer simulation of the dielectric properties of Acetonitrile using a 3 site model, has been carried out by Edwards, Madden and McDonald[101,102], in which the total correlation function was separated into reorientational and collision induced parts. The contribution to the reorientational correlation function of interaction induced dipoles was found to account for 40% of the far-infrared absorption intensity. Absorption coefficient spectra were

SOLVENT	g(1)	τ_{SP}	(1+Nf̊)	τ_D/τ_{SP}
*MeI	1.6	3.9	0.45	1.3
*n-Heptane	0.8	0.9	1.95	3.6
*n-Decane	0.45	0.64	1.17	3.3
*n-Hexadecane	0.3	0.38	1.40	3.9
#MeI	1.5	2.7	0.5	1.5
#n-Heptane	0.41	0.35	3.9	3.9
#n-Decane	0.64	0.74	1.9	3.1
#n-Hexadecane	0.37	0.48	2.8	2.9

* Using τ_D + g^{KF} values with τ_{SP} = 1.8ps

Using τ^T_{IR} and $g^{(1)}$ values with τ^T_{SP} = 1.4ps

obtained from these correlation functions, the combined form of which, was in very good agreement with the experimental absorption coefficient spectrum of Arnold et al[65]. The modelled results indicated that the collision induced part of the spectrum was similar to that of a non-polar solvent and that the far infrared band is mainly due to reorientational dipole density (permanent and induced). However, Arnold etal[94] found only a small enhancement in intensity for acetonitrile above that predicted from the Gordon sum rule. This can be accounted for by cancellation effects of the induced dipoles for many body interactions[103]. For the MeI in n-alkane solutions two trends with concentration can be seen for the integrated area of the far-infrared absorption, this may give some insight into the effect of molecular environment on induced effects. From the Ai values in figure 8.4, we again see a separation of the n-alkane data into two groups, the n-decane and n-hexadecane values being similar to the liquid value, whilst the n-heptane Ai values show a reduction with reducing MeI concentration. This trend can be clearly seen in figure 8.16, where the Beers law corrected spectra for MeI in n-heptane at three concentrations are presented. All three bands show very good agreement from the microwave region up to the peak in the far-infrared band. However, for the remainder of the band profile, the three spectra are different, so it is the tail of the far-infrared band that is causing changes in the Ai values with concentration, since the tail of the far-infrared absorption is considered to be sensitive to induced effects, it can be conjectured that figure 8.16 is showing the reduction of induced effects with dilution. Interestingly the Ai value for 0.016 mf MeI in n-heptane is approximately 50% of the liquid value which is of the order of the value for induced effects calculated by

FIGURE 8.16 METHYL IODIDE IN N-HEPTANE AT 25.5 DEG C

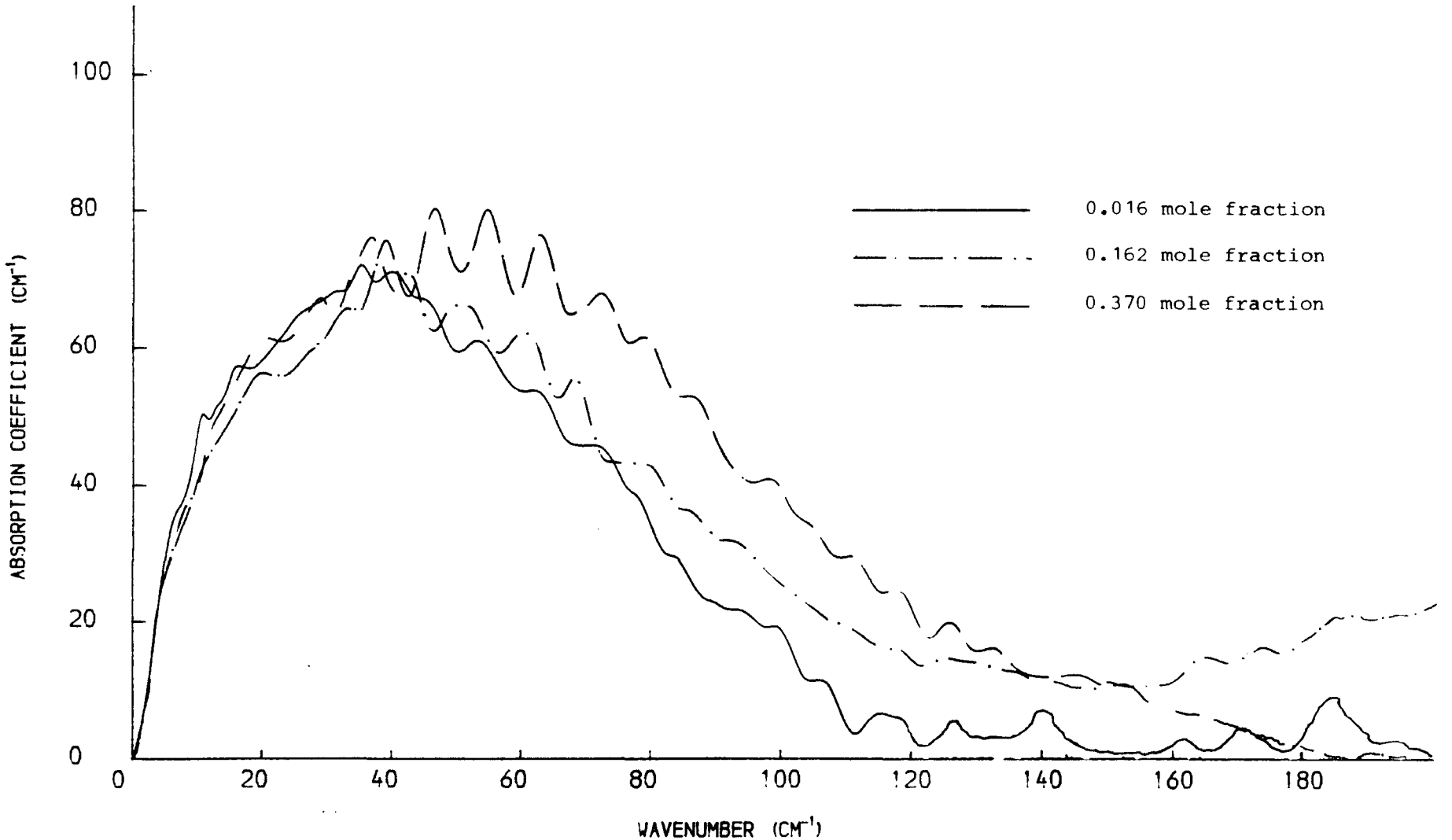

Edwards etal[101,102]. The Ai values show that the MeI far-infrared spectrum is infact subject to induced effects, unlike CH_3CN where the much larger dipole moment and cancellation effects proberably swamp and reduce any induced effects.

8.2.6 Cole-Cole Plots

Gerschel et al[11] have studied methyl chloride over the microwave-far-infrared range and produced cole-cole plots. These gave an enhancement over the Debye semi-circle between the microwave and far-infrared processes, which has been interpreted as evidence of a third reorientational process, and a more pronounced deviation near to ε_∞ corresponding to the far-infrared absorption. Subtraction of the librational and reorientational dielectric loss peaks leaves a small residual peak at 6 to 7cm^{-1}, due to the insensitivity of this band to temperature and density changes it has been assigned to a resonance process.

The experimental Cole-Cole plots determined in this work have a bulge in the bottom left hand corner of the plots corresponding to far-infrared frequencies and show deviations from the Debye semicircle which tend to be inside the semicircle. In these Cole-Cole plots the ε_∞ values used are those determined from the measured ε' spectra at 200 cm^{-1}. This could account for the differences between these plots and those of Gerschel. However, for measurements made on dichloromethane Gerschel et al[104] found the resultant Cole-Cole plot did not give a deviation outside of the Debye semicircle, but infact came inside of the circle. This difference is attributed to the differences in diploar interactions between the two liquids, The differences in the Cole-Cole plots of MeI could therefore point to

differences in dipolar interactions for the different solvent environments.

8.3. Solvent Spectra

In chapter 7 The far-infrared spectra of the solvents used in this work were presented, the non-polar carbon tetrachloride and carbon disulphide produce weak far-infrared spectra, due to induced effects, which have the same shape as for the far more intense liquid MeI absorption. The n-alkanes however, show a very broad absorption peaking at about 200cm^{-1}. The absorption coefficient and refractive index spectra of the n-alkanes are compared in figure 8.17. The refractive index spectra show an increase with chain length, reflecting the increasing density of the solvents and the absorption coefficient shows a reduction with increasing chain length. Since the far-infrared absorption for non-polar liquids is entirely due to induced effects, this indicates that induced effects are reduced as chain length increases. Which could be due to slower motion of the longer alkane chains leading to a reduction in the number of collisions between molecules giving a reduction in collisional effects. This ties in with the theory for MeI to be trapped by the less mobile long chain alkanes, forming solute "pools" where the MeI molecules will experience a similar environment to the liquid. The permittivity and dielectric loss spectra of the n-alkanes are plotted in figure 8.18, the permittivity spectra are similar to the refractive index spectra, but the dielectric loss spectra show very interesting details. These can be seen more clearly in figure 8.19, the n-alkane spectra are similar with in the case of n-heptane peaks at about

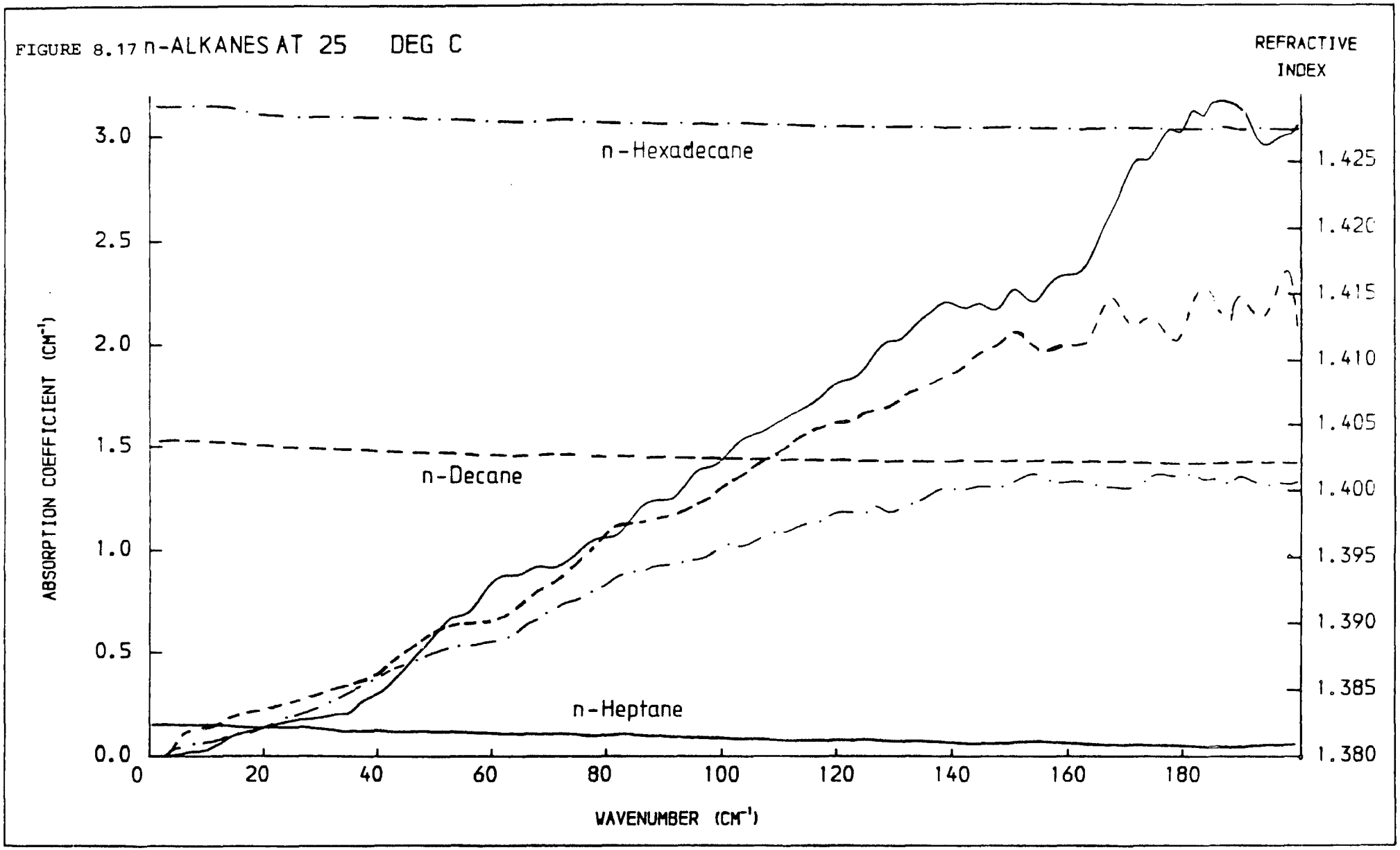
FIGURE 8.17 n-ALKANES AT 25 DEG C
REFRACTIVE INDEX
n-Hexadecane
n-Decane
n-Heptane
ABSORPTION COEFFICIENT (CM⁻¹)
WAVENUMBER (CM⁻¹)
3.0
2.5
2.0
1.5
1.0
0.5
0.0
0
20
40
60
80
100
120
140
160
180
1.425
1.420
1.415
1.410
1.405
1.400
1.395
1.390
1.385
1.380

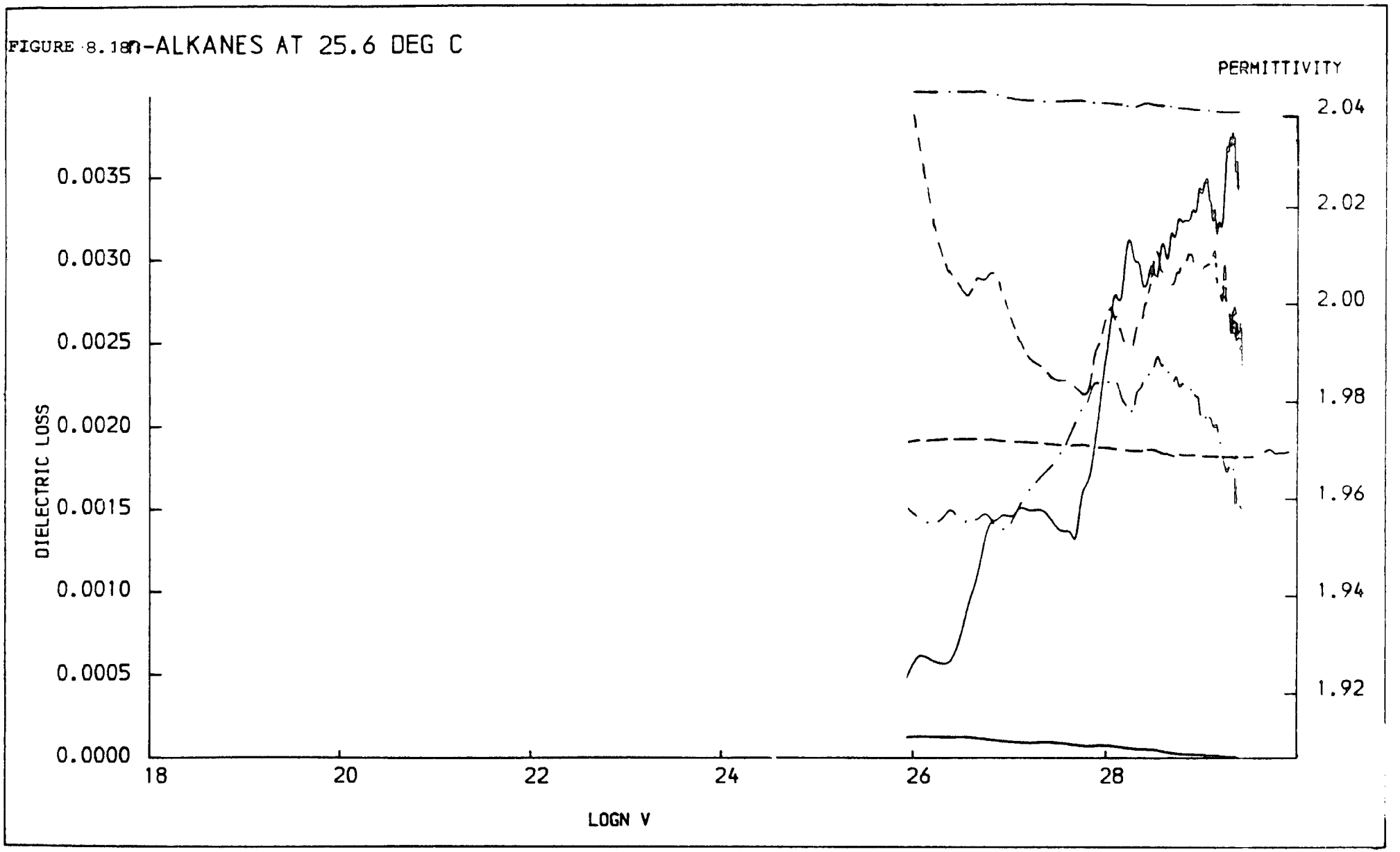
n-ALKANES AT 25.6 DEG C
PERMITTIVITY
2.04
2.02
2.00
1.98
1.96
1.94
1.92
0.0035
0.0030
0.0025
0.0020
0.0015
0.0010
0.0005
0.0000
DIELECTRIC LOSS
18
20
22
24
26
28
LOGN V

FIGURE 8.18

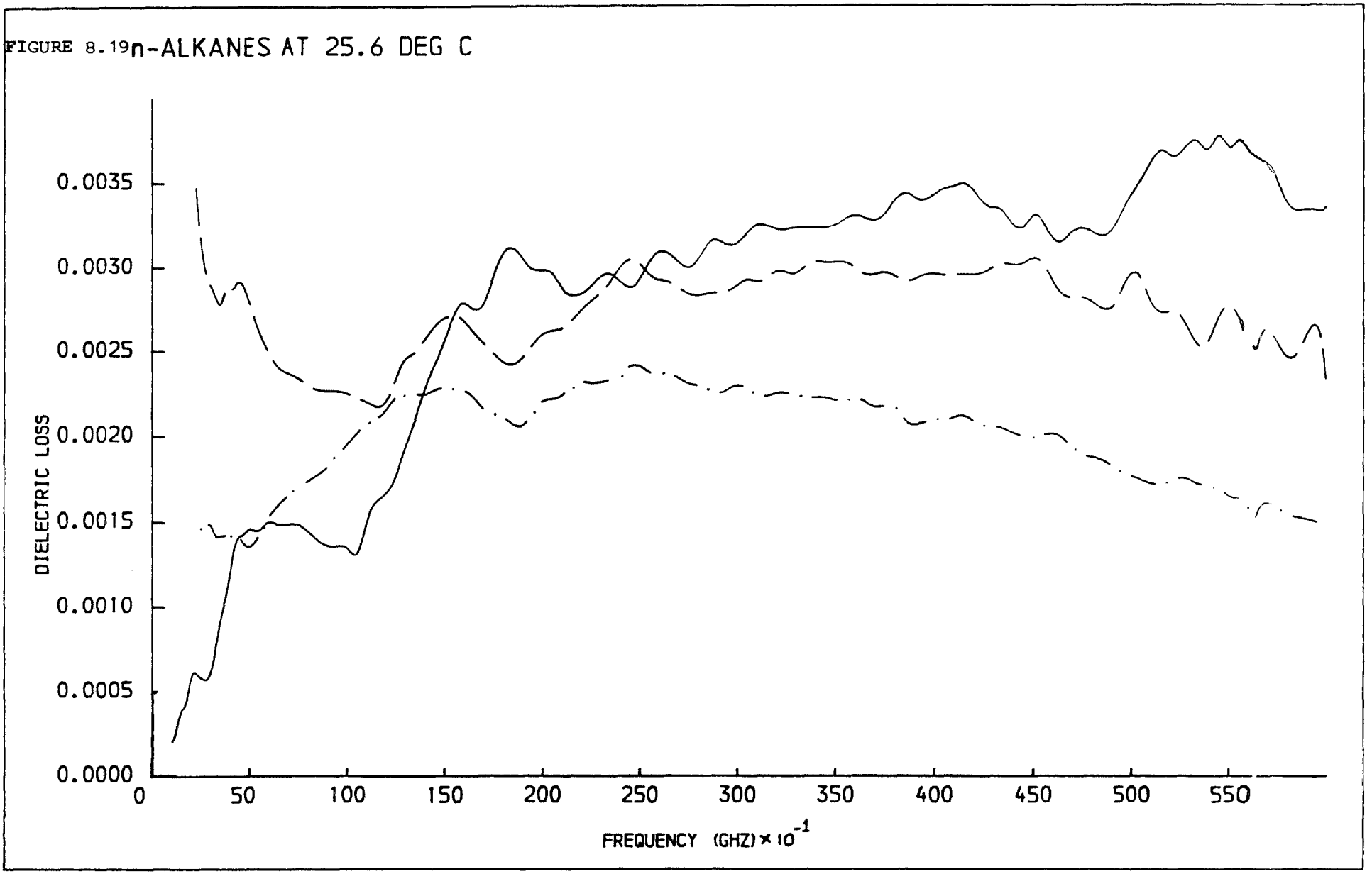
FIGURE 8.19 n-ALKANES AT 25.6 DEG C
DIELECTRIC LOSS
0.0035
0.0030
0.0025
0.0020
0.0015
0.0010
0.0005
0.0000
0
50
100
150
200
250
300
350
400
450
500
550
FREQUENCY (GHZ) × 10^-1

500GHz, 1800GHz and 5500 GHz on top of a broad absorption centred at about 3500GHz. The assosiated relaxation times calculated from $1/2\pi\tilde{\nu}_{max}$ would be 0.3ps, 0.1ps, 0.05ps (broad band) and 0.03ps, the physical interpretation of such results is not clear. Scaife etal[105] have measured a lower resolution dielectric loss spectrum of n-heptane showing one peak at about 2THz, with a peak value similar to that in figure 8.18. Richter and Schiel[106] have obtained the dipole correlation function for n-hexane, which shows two different slopes, indicating two processes, but in this case the relaxation times are 2.9 and 7.9ps. They interpret the steep initial decay of the correlation function, up to 0.3ps, as being caused by fast intra and intermolecular vibrational motions. The two peaks that would correspond to the two slopes in the correlation function would be positioned at 19GHz and 50GHz both of which would be outside the lower range of the spectra in figures 8.18 and 8.19. But in these spectra the wing of such a band can be seen, Richter and Schiel consider these two bands to be due to induced dipoles caused by comformational changes in the n-alkane chain.

8.4 Model Fitting

From chapter 6 the Debye, and Gordon M and J-diffusion models do not fit experimental far-infrared data due to non-inclusion of inertial effects, but the second order truncated Mori model of Evans etal[67,82,84] gives an apparently good fit. Generally the three parameter Mori model gave a better fit than the two parameter and in cases of a good fit, second moment, fourth moment and torque values of the same order as those measured in this work were obtained as can be seen from tables 7.13 to 7.15. However, overall the fourth moment and

torque values do not show good agreement with measured values and in fact show opposite trends with concentration. So, although the absorption coefficient and refractive index spectra are fitted well by the Mori model, the model parameters do not agree with experamental results, also the model gives no indication of interaction induced dipole rotation and fluctuations, and the mathematical validity of the model has been questioned[109].

The Gausian cage model developed by Lynden-Bell and Steele[89] is a more physically meaningful model and has parameters that give information on the molecular motions and torques. Unfortunately, experimental correlation functions for MeI in n-alkanes have not been fitted to equation 6.68, in this work. Recently however, Yarwood[108] has fitted some of the rotational correlation functions presented in chapter 7, to equation 6.68. His results are reproduced in table 8.4, and a comparison of the observed and fitted correlation functions is shown in figure 8.20. From these results, for MeI liquid and in solutions, there is very good agreement between the experimental rotational correlation functions and those produced by fitting to equation 6.68. However, the modelled and experimental absorption spectra do not show such good agreement as can be seen from figures 8.21 and 8.22. This is most likely to be due to the complexity of the processes giving rise to the far-infrared absorption, (40% of the intensity being due to induced effects, see 8.2.5), not being fully reflected in the modelled data. Nevertheless the model parameters given in table 8.4, follow similar trends to the corresponding properties measured in this work, using the model parameters the following can be inferred. The large Ω_o/Δ valuefor the liquid,

TABLE 8.4 Results of Gaussian Cage Fit for CH_3I in Various Solvents

SOLVENT (T/K)	Conc. (mf)	$\Omega_o/psec^{-1}$	Ω_o/cm^{-1}	$\Delta^2/psec^{-2}$	Δ/cm^{-1}	Ω_o/Δ	N^2
Liquid (298)	1.0	9.4	50.0	21.6	24.7	2.03	31.9
CS_2	0.1	11.0	58.4	39.9	33.5	1.74	45.8
n-heptane (298)	0.16	7.0	37.2	18.0	22.5	1.65	20.2
n-decane (298)	0.16	10.8	57.3	31.2	29.7	1.93	42.3
hexadecane (298)	0.16	9.0	47.8	33.4	30.5	1.57	33.1

FIGURE 8.20 EXPERIMENTAL AND MODELLED CORRELATION FUNCTIONS

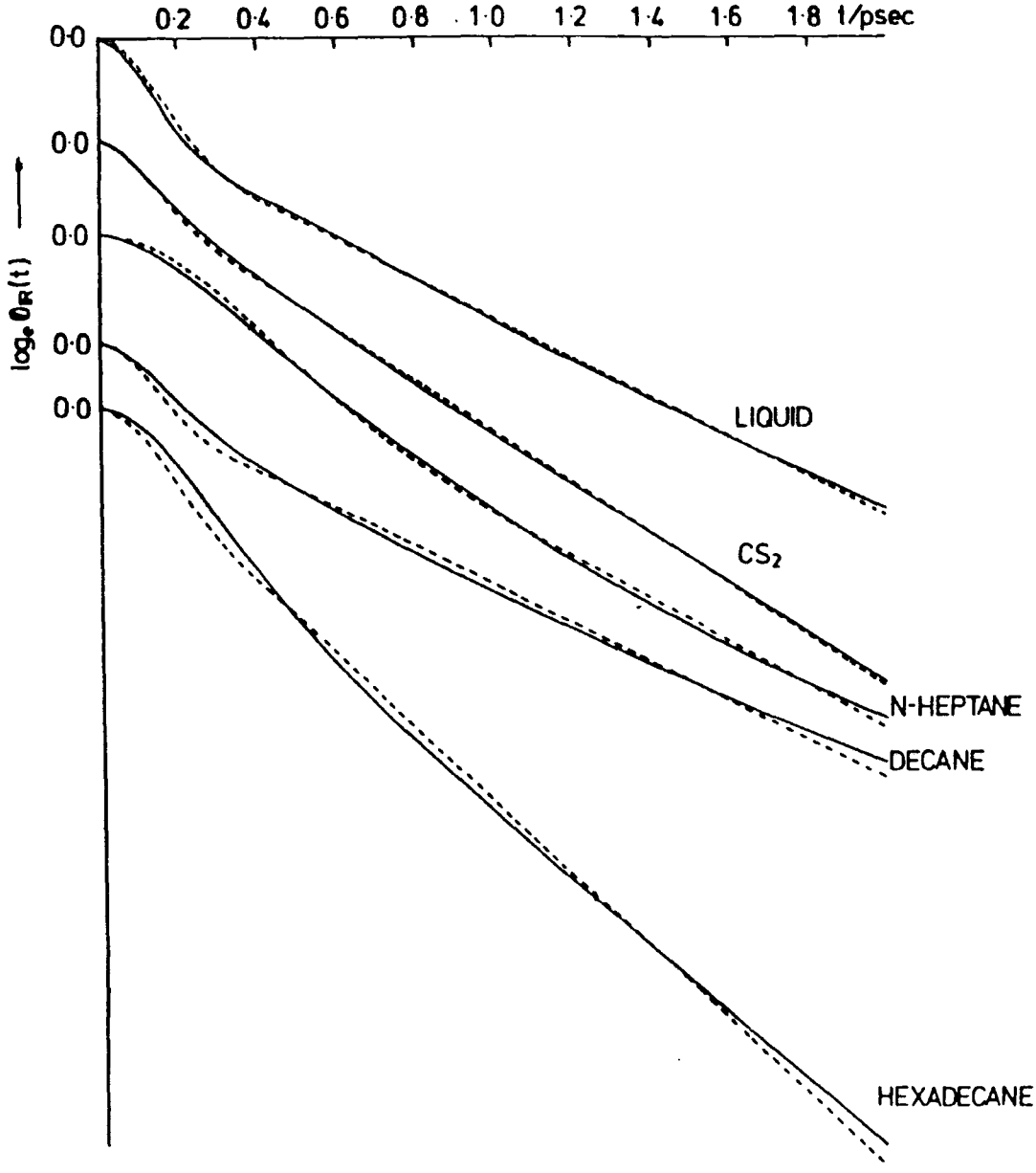

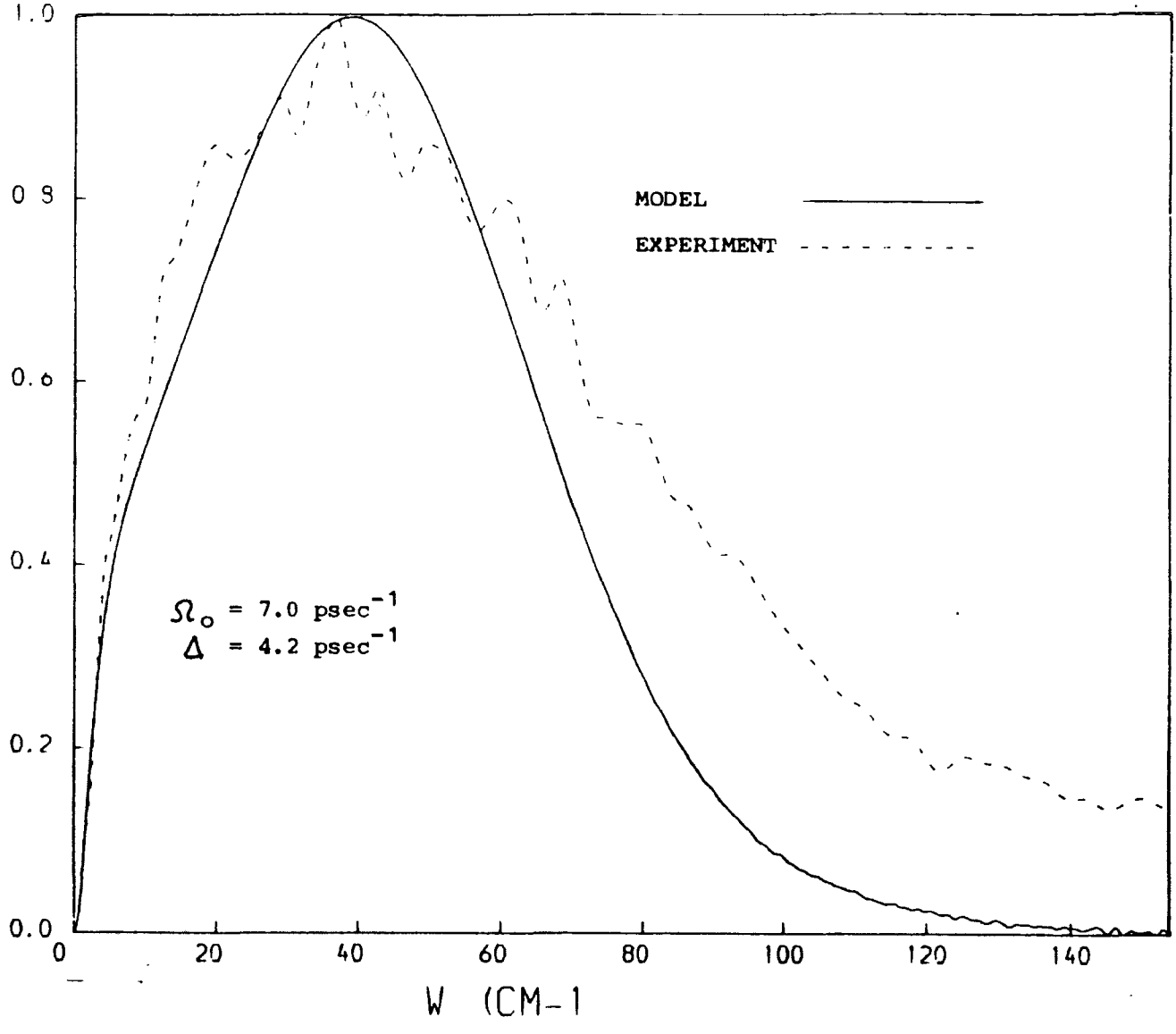

FIGURE 8.21 GAUSSIAN CAGE MODEL FIT TO 0.162 mf MeI IN n-HEPTANE

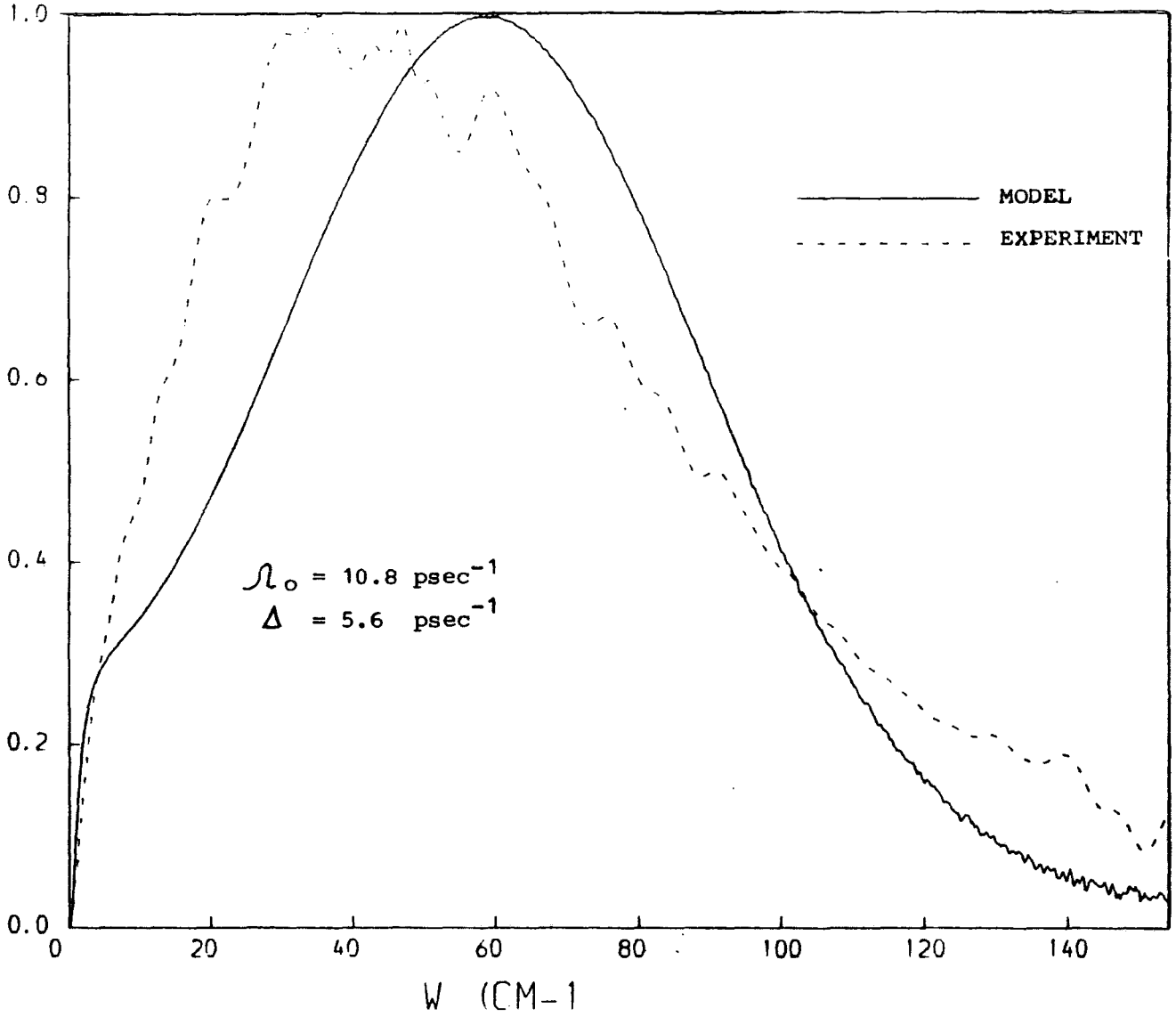

FIGURE 8.22 GAUSSIAN CAGE FIT TO 0.162 mf MeI IN n-DECANE

indicates a high librational frequency (large Ω_0) and or a narrow distrubution of frequencies (small Δ). Therefore the liquid molecular environment is very homogeous. As the MeI liquid is diluted by a solvent, the molecular environment would be expected to become less homogeneous, which would be reflected by a reduction in Ω_0/Δ , (Δ becoming larger), this is infact the case for carbon disulphide, n-decane and n-hexadecane solutions, but not for n-decane solution where the value is similar to the liquid, indicating a more homogeneous environment for this solvent. The torque values show the same trend as for measurements in this work with n-decane and n-hexadecane solution values being similar to the liquid whilst the n-heptane value is lower. This indicates a very hindered MeI molecular environment for the long chain alkanes which becomes much less hindered in the short chain alkanes. So although the model absorption spectra do not agree with the measured spectra perfectly, the above shows the model parameters to give good agreement with experamental results, showing that the cage effect in the MeI tumbling motion has been correctly modelled.

8.5 Conclusions

8.5.1 The New Liquid Cell Performance

The results section has shown the excellent level of accuracy and reproducability in far-infrared optical constant measurements of liquids, achievable using the New Liquid Cell. Practical operation and setting up of the cell has been straightforward and its versatility demonstrated by making measurements on high and low loss liquids.

8.5.2 MeI in Hydrocarbon Solvents

One of the most difficult problems in obtaining information on the microscopic behaviour of the MeI molecule, is the calculation of the single molecule properties. This can be seen in equation 6.2, for the single particle correlation function to be determined, the distinct term in the equation must be removed. One way of achieving this is to isolate the MeI molecule in a non-polar environment, where it will only be subject to forces due to interaction with the solvent environment. The effect of dilution can be seen in the T_D and T_{1R} values plotted in figures 8.4 to 8.10, both relaxation times become faster with dilution indicating less hindered motion, and there are differences between solvents at low concentrations showing the effect of the solvent on the solute single particle relaxation time. However, there is the added complication that for n-decane and n-hexadecane the MeI molecules may be forming solute pools and single particle times are not being measured.

The $g^{(0)}$ values given in table 7.13 also show the effects of dilution, as the MeI molecules are separated by the solvent molecules, the intermolecular forces are reduced. This allows neighbouring MeI molecules to be better aligned with the probing electromagnetic field giving smaller angles between molecules. Moment and torque values also reflect this reduction in intermolecular forces with dilution, and show differences between solvent environments.

All the results in this work for MeI in n-alkanes show a separation of molecular properties into two groups which are dependent on chainlength. In n-heptane, MeI would appear to be well dispersed and as the MeI concentration is reduced, so too, are interactions between the MeI molecules, as evidenced by lower intermolecular

torques and faster relaxation times. There is also evidence of a reduction of induced effects with reducing concentration, in the wings of the far-infrared absorption for n-heptane solutions. In n-decane and n-hexadecane solutions, despite dilution the MeI molecules still behave as in the liquid environment. This indicates that the MeI molecules are not being dispersed by the solvent, but are in fact forming localised areas of high MeI concentration within which the molecules experience the same environment as in the liquid. This difference in the molecular environment for MeI in the n-alkanes has also been observed in the parameters obtained from the gausian cage model.

8.6 Future Work

8.6.1 The Gausian Cage Model

Since the Gausian cage model has successfully modelled the molecular parameters for MeI, the most obvious progression of the work presented in this thesis, would be to fit more of the experimental correlation functions presented in chapter 7, to equation 6.68. This should give a better understanding of the environmental changes taking place and possibly enable the types of reorientational motion and interactions of molecules in the liquid phase to be elucidated. As the model does not fit the wings of the measured far-infrared bands, it would appear to be unable to fully account for induced effects. Further work on spectra such as those for n-heptane solutions with the model may give a better insight into the phenomena of induced effects.

8.6.2 Further Experimental Work

A large number of solution spectra that have been recorded, have not been reported in this work because the full far-infrared range has not been recorded. Further experimental measurements on carbon tetrachloride solutions and more importantly Santotrac 40 solutions, will enable a broader range of molecular environments to be included in future studies.

8.6.3 Solvent Spectra

From section 8.4 it is clear that the n-alkanes have a complicated far-infrared absorption, which at present is not fully understood and merits further investigation. The absorption bands that have been assigned to induced dipoles caused by conformational changes have not been fully resolved in this work. However, accurate low frequency far-infrared measurements using cooled detectors should enable these bands to be fully resolved and allow conformational changes within the n-alkanes to be studied.

REFERENCES

1. J. McConnell, 'Rotational Brownian Motion and Dielectric Theory', Academic Press, London, 1980.

2. J.Sakai and M.Katayana, Chem.Phys.Lett. **35**(3), 395,(1975).

3. M.W. Evansand J. Yarwood,Advances in Molecular Relaxationand Interaction Processes, **21**, 1, (1981).

4. K. Sato, Y. Ohkubo, T. Moritsu, S. Ikawa and M. Kimura, Bull.Chem.Soc.Japan, **51**(9), 2493, (1978).

5. A.Kocot, S.Gandor and E.Kluk; Acta Phys.Pol. **A58**, 149, (1980).

6. A.Kocot, S.Gandor, K.Leibler etal. Mol.Phys.**53**,1481(1984)

7. C.J.Reid and M.W.Evans, Mol. Phys. **40**, 1357 (1980)

8. K.E. Arnold, PhD. Thesis, Univ. of Durham 1981 and references in thesis.

9. P.L. James, PhD. Thesis, Univ. of Durham 1982

10. A. Gershel, K. Leibler, Z. Kisiel, L. Pszczolkowski, C. R. Acad. Sc. Paris **295**, II, 1051, (1982)

11. A. Gershel, T. Grochulski , Z. Kisiel, L. Pszczolkowski and K.Leibler, Mol. Phys., **54**, 97, (1985)

12. A. Gershel, I. Dimicoli, J. Jaffre and A. Riou, Mol. Phys. **32**, 679, (1976)

13. N.E. Hill, W.E. Vaughn, A.H. Price and M. Davies, 'Dielectric Properties and Molecular Behaviour'; Van Nostrand, London (1969)

14. L. Onsager, J.Amer.Chem.Soc. **58**, 1486, (1936)

15. J.R. Birch and T.J. Parker "DFTS" Infrared and Millimeter Waves Vol. 2, Ed. K.J. Button, Academic Press, New York (1979)

16. K.S. Cole and R.H. Cole, J.Chem.Phys. 9, 341, (1941)

17. R. Zwanzig, Am.Rev.Phys.Chem. **16**, 67, (1965)

19. R. Kubo, J.Phys.Soc. Japan **12**, 570, (1957)

20. C. Brot, Dielectric and Related Molecular Processes, Vol.2. The Chemical Society (1975)

21. G.P. O'Neill, A. Khuen and J. Yarwood, J. Mol. Struct. **80**, 383, (1982)

21. J. Chamberlain, "The Principles of Interferometric Spectroscopy" (1979) John Wiley & Sons, Chichester, New York, Brissane, Toronto.

22. P. Jacquinot, J.Opt.Soc.Amer. **44**, 761, (1954)

23. P. Fellgett, Thesis. Univ. of Cambridge (1951)

24. J.R. Birch, NPL Report Des 64 (1980)

25. J.E. Chamberlain, A.E. Costley and H.A. Gebbie, Spectrochimica Acta, **23A**, 2255, (1967)

26. J. Chamberlain, M.S. Zafar and J.B. Hasted, Nature (London) Phys.Sci. **242**, 116, (1973)

27. M.S. Afsar, J.B. Hasted and J. Chamberlain; Nature (London) Phys.Sci. **243**, 106, (1973)

28. G.W. Chantry, J.M. Evans, J.W. Fleming and H.A. Gebbie, Infrared Phys. **9**, 31, (1969)

29. M.N. Afsar and J.B. Hasted, J.Opt.Soc.Am. **67**, 902, (1977)

30. J. Yarwood, C. Barker, P.L. James, G.P. O'Neill, W.A. Scott and R.N. McKenzie, J.Phys.E.Sci.Instrum. **14**, 161, (1981)

31. M.N. Afsar, D.D. Honijk, W.F. Passchier and J. Goulon, IEEE Trans. Microwave Theory Tech. **MTT-25**, 505, (1977)

32. N.W.B. Stone and G.W. Chantry, Adv. Infrared Raman Spectroscopy, **3**, 43, (1977)

33. D.D. Honijk, W.F. Passchier, M. Mandel and M.N. Afsar, Infrared Phys. **17**, 9, (1977)

34. W.F. Passchier, D.D. Honijk and M. Mandel, Infrared Phys. **15**, 95, (1975)

35. W.F. Passchier, D.D. Honijk, M. Mandel and M.N. Afsar, Infrared Phys, **17**, 381, (1977)

36. D.D. Honijk, W.F. Passchier, M. Mandel and M.N. Afsar, Infrared Phys, **16**, 257, (1976)

37. J.R.Birch, G.P.O'Neill, J.Yarwood and M.Bennouna, J.Phys.E.Sci. Instrum, **15**, 684, (1982)

38. J. Chamberlain, Infrared Phys. **12**, 145, (1972)

39. J.R. Birch and C.E. Bulleid, Infrared Phys. **17**, 279, (1977)

40. J.R. Birch and T.J. Parker, Infrared Phys. **19**, 103, (1979)

41. R.N. Bracewell, "The Fourier Transform and its Applications" 2nd edition. McGraw-Hill Kogakusha, Tokyo, 1978

42. D.D. Honijk, W.F. Passchier, M. Mandel and M.N. Afsar, J.Phys.D, **10**, 509 (1977)

43. M.N. Afsar and J.B. Hasted, Infrared Phys. **18**, 835 (1978)

44. J.R. Birch and M. Bennouna, Infrared Phys. **21**, 229, (1981)

45. S.D. Conte and C. de Boor, "Elementary Numerical Analysis", P.32 McGraw-Hill, New York and Kogakusha, Tokyo.

46. G.W. Chantry, H.M. Evans, J. Chamberlain and H.A. Gebbie, Infrared Phys. **9**, 85, (1969)

47. O.K. Filippov and V.M. Pivovarov, Optics adn Spectroscopy, **16**, 282 (1964)

48. J. Chamberlain, G.W. Chantry, F.D. Findlay, H.A. Gebbie, J.E. Gibbs, N.W.B. Stone and A.J. Wright, Infrared Phys, **6**, 195, (1966)

49. J.W. Fleming, NPL Report No. Mat. App. 31

50.a. C.L. Mok Infrared Phys. **19**, 437, (1979)

50.b. J.A. Beunen, J.O.S.A. **71**, 184, (1981)

51. J.R. Birch and K.F. Ping, Infrared Phys. **24**, 309, (1984)

52. D.H. Martin and E. Puplett, Infrared Phys. **10**, 105 (1969)

53.a. M.J.E. Golay, Rev. Scient. Instrum. **18**, 347 (1947)

53.b. M.J.E. Golay, ibid. **20**, 816 (1949)

54. E.H. Putley, J.Phys.Chem.Solids. **22**, 241 (1961)

55. B.V. Rollin, Proc.Phys.Soc. **77**, 1102 (1961)

56. F.J. Low, J.Opt.Soc.Amer. **51**, 1300 (1961)

57. P.L. James, M.Sc., Thesis, Univ of Durham (1976)

58. J. Chamberlain, Infrared Phys. **11**, 25 (1971)

59. J. Chamberlain and H.A. Gebbie, Infrared Phys. **11**, 57, (1971)

60. J. Chamberlain and H.A. Gebbie, Applied Optics, **10**, 1184 (1971)

61. J. Chamberlain, G.W. Chantry and N.W.B. Stone, Chem.Soc.Rev. **4**(4), 569, (1975)

62. CRC Handbook of Chemistry and Physics, CRC Press, Florida, 1980

63. A.H. Price and G.H. Wegdam, J.Phys.E, **10**, 478, (1977)

64. W.F. Passchier, D.D. Honijk and M. Mandel, Infrared Phys. **16**, 389, (1976)

65. K.E. Arnold, J. Yarwood and A.H. Price, Mol.Phys. **48**(3), (1983)

66. A. Gerschel, I. Darmon and C. Brot, Mol.Phys.**23**, 317, (1972).

67. M.W. Evans, Adv.Molec.Relaxation Int.Processes, **10**, 203, (1975)

68. R. Gordon, J.Chem.Phys. **43**, 1307, (1965)

69. L.C. Rosenthal and H.L.Strauss, **64**, 282, (1976)

70. J.S. Anderson, W.E. Vaughan, L.C. Rosenthal and H.L. Strauss, J.Chem.Phys. **65**, 2481, (1976)

71. P. Debye, 'Polar Molecules', Reinhold Publishing Corporation, New York, (1929)

72. J.G. Kirkwood, J.Chem.Phys. **7**, 911 (1936)

73. H. Frohlich, Theory of Dielectrics, Oxford University Press, London, (1949)

74. G. Bossis, Physica A, **110**, 408, (1982)

75. T.W. Nee and R. Zwanzig, J.Chem.Phys. **53**, 6352, (1970)

76. S.H. Glarum, J.Chem.Phys. **33**, 1371, (1960)

77. R.H. Cole, J.Chem.Phys. **42**, 637, (1965)

78. E. Fatuzzo, P.R. Mason, Proc.Phys.Soc. **90**, 741, (1967)

79. D. Kivelson and P. Madden, Mol.Phys. **30**(6), 1749, (1975)

80. T. Keyes and D. Kivelson, J.Chem.Phys. **56**, 1057, (1972)

81. E. Kluk, Alta.Phys. Pol. **A58**, 51, (1980)

82. H. Mori, Prog.Theor.Phys. **33**, 423, (1965)

83. T.D. Gierk, J.chem.Phys. **65**, 3873, (1976)

84. G.J.Evans and M.W.Evans, J.Chem.Soc.Faraday Trans.II, **72**, 1169 (1976)

85. M.Y. Rocard, J.Phys. Radium **4**, 247, (1933)

86. J.G. Powles, Trans. Faraday Soc. **44**, 802, (1948)

87. R.G. Gordon, J.Chem.Phys. **44**, 1830, (1966)

88. J.H.R. Clarke, Adv. Infrared and Raman Spectroscopy, (Eds. Clarke and Hester), **4**, Ch.4, Heyden, (1978)

89. R.M.Lynden-Bell and W.A.Steele, J.Phys.Chem. **88**, 6514, (1984)

90. J. Yarwood in Press (1985)

91. R. Kronig, J.Opt.Soc.Amer, **12**, 547, (1926)

92. H.A. Kramers, Atti Congr.Int.Fisici. Como, **2**, 545, (1927)

93. R.G. Gordon, J.Chem.Phys. **38**, 1724, (1963)

94. C.J. Ried and M.W. Evans, J.Chem.Soc.Faraday II, **76**, 289, (1980)

95. N.E. Hill, J.Phys. **C5**, 415, (1972)

96. W.F. Pacynko, J. Yarwood and D.J. Gardiner, Chem.Phys. **78**, 319, (1983)

97. J.Gompt, H.Versmold and H.Langer, Ber. Bunsenges. Phys. Chem. **86**, 1114, (1982)

98. H.J. Bohm, R.M. Lynden-Bell, P.A. Madden and I.R. McDonald Mol.Phys. **51**(3), 761, (1984)

99. A.H. Price, Personal Communication.

100. A. DeSantis, E. Moretti and M. Sampoli, Mol.Phys. 46(6), 1271, (1982)

101. D.M.F. Edwards, P.A. Madden and I.R.McDonald, Mol.Phys. **51**(5), 1141, (1984)

102. D.M.F. Edwards, P.A. Madden, Mol.Phys. **51**(5), 1163, (1984) J.Chem.Phys, **77**(3), 1197, (1982)

103. T.I. Cox and P.A. Madden, Chem.Phys.Lett. **77**(3), 511, (1981).

104. Z. Kisiel, K. Leibler, A. Gerschel, J.Phys.E, **17**, 240, (1984).

105. W.G. Scaif, J.K. Vij, G. Evans and M.W. Evans, J.Phys.D.Appl. Phys. **15**, 1279, (1982)

106. W. Richter and D. Schiel in press (1985).

107. B.K.P. Scaif, Adv.Mol.Relaxation interact Processes, **24**, 75, (1982)

108. J. Yarwood, in press (1986).

APPENDIX I

RESEARCH COLLOQUIA, SEMINARS AND LECTURES ORGANIZED BY THE DEPARTMENT OF CHEMISTRY DURING THE PERIOD 1979 TO 1982

(* indicates those attended)

21 November, 1979.*

Dr. J. Muller (University of Bergen). "Photochemical Reactions of Ammonia".

28 November, 1979.*

Dr. B. Cox (University of Stirling). "Macrobicyclic Cryptate Complexes. Dynamics and Selectivity".

5 December, 1979.

Dr. G.C. Eastmond (University of Liverpool). "Synthesis and Properties of Some Multicomponent Polymers".

12 December, 1979.*

Dr. C.I. Ratcliffe (University of London). "Rotor Motions in Solids".

19 December, 1979.*

Dr. K.E. Newman (University of Lausanne). "High Pressure Multinuclear NMR in the Elucidation of the Mechanisms of Fast, Simple Reactions".

30 January, 1980.*

Dr. M.J. Barrow (University of Edinburgh). "The Structures of Some Simple Inorganic Compounds of Silicon and Germanium - Pointers to Structural Trends in Group IV".

6 February, 1980.

Dr. J.M.E. Quirke (University of Durham). "Degradation of Chlorophyll-a in Sediments".

23 April, 1980.

B. Grievson B.Sc. (University of Durham). "Halogen Radiopharmaceuticals".

14 May, 1980.*

Dr. R. Hutton (Waters Associates, U.S.A.). "Recent Developments in Multi-milligram and Multi-gram Scale Preparative High Performance Liquid Chromatography".

21 May, 1980.

Dr. T.W. Bentley (University of Swansea). "Medium and Structural Effects in Solvolytic Reactions".

10 July, 1980.

Professor P. des Marteau (University of Heidelburgh). "New Developments in Organonitrogen Fluorine Chemistry".

7 October, 1980.*

Professor T. Felhner (Notre-Dame University, U.S.A.). "Metalloboranes - Cages or Coordination Compounds?".

15 October, 1980.*

Dr. R. Adler (University of Bristol). "Doing Chemistry Inside Cages - Medium Ring Bicyclic Molecules".

12 November, 1980.*

Dr. M. Gerloch (University of Cambridge). "Magnetochemistry is about Chemistry".

19 November, 1980.

Dr. T. Gilchrist (University of Liverpool). "Nitroso Olefins as Synthetic Intermediates".

3 December, 1980.

Dr. J.A. Connor (University of Manchester). "Thermochemistry of Transition Metal Complexes".

18 December, 1980.*

Dr. R. Evans (University of Brisbane, Australia). "Some Recent Communications to the Editor of the Australian Journal of Failed Chemistry".

18 February, 1981.*

Professor S.F.A. Kettle (University of East Anglia). "Variations in the Molecular Dance at the Crystal Ball".

25 February, 1981.

Dr. K. Rowden (University of Sussex). "The Transmission of Polar Effects of Substituents".

4 March, 1981.

Dr. S. Craddock (University of Edinburgh). "Pseudo-linear Pseudohalides".

11 March, 1981.*

Dr. J.F. Stoddart (I.C.I. Ltd./University of Sheffield). "Stereochemical Principles in the Design and Function of Synthetic Molecular Receptors".

17 March, 1981.*

Professor W. Jencks (Brandels University, Massachusetts). "When is an Intermediate not an Intermediate?".

18 March, 1981.

Dr. P.J. Smith (International Tin Research Institute). "Organotin Compounds - A Versatile Class of Organo-metallic Compounds".

9 April, 1981.

Dr. W.H. Meyer (RCA Zurich). "Properties of Aligned Polyacetylene".

6 May, 1981.*

Professor M. Szware, F.R.S. "Ions and Ion Pairs".

10 June, 1981.*

Dr. J. Rose (I.C.I. Plastics Division). "New Engineering Plastics".

17 June, 1981.

Dr. P. Moreau (University of Montpellier). "Recent Results in Perfluoroorganometallic Chemistry".

14 October, 1981.*

Professor E. Kluk (University of Katowice). "Chemiluminescence & Photooxidation".

22 October, 1981.*

Dr. P.J. Corish (Dunlop). "What Would Life be Like Without Rubber".

28 October, 1981.*

Dr. R.J.H. Clark (University College, London). "Resonance Raman Spectroscopy".

29 October, 1981.

Miss J.M. Cronyn (University of Durham). "Chemistry in Archaeology".

6 November, 1981.

Dr. W. Moddeman (Monsanto Labs., St. Louis, Missouri). "High Energy Materials".

12 November, 1981.*

Professor A.I. Scott (University of Edinburgh). "An Organic Chemist's View of Life Through the N.M.R. Tube".

18 November, 1981.

Professor M.J. Perkins (Chelsea College). "Spin Trapping and Nitroxide Radicals".

19 November, 1981.

Professor B.L. Shaw (University of Leeds). "Big Rings and Metal-Carbon Bond Formation".

25 November, 1981.

Dr. M. Baird (University of Newcastle). "Intramolecular Reactions of Carbenes and Carbenoids".

30 November, 1981.*

Dr. B.T. Heaton (University of Kent). "N.M.R. Studies of Carbonyl Clusters".

2 December, 1981.*

Dr. G. Beamson (University of Durham). "Photoelectron Spectroscopy in a Strong Magnetic Field".

3 December, 1981.*

Dr. W.O. Ord (Northumbria Water Authority). "The Role of the Scientist in a Regional Water Authority".

20 January, 1982.

Dr. M.R. Bryce (University of Durham). "Organic Metals".

27 January, 1982.*

Dr. D.L.H. Williams (University of Durham). "Nitrosation and Nitrosoamines".

28 January, 1982.*

Professor I. Fells (University of Newcastle). "Balancing the Energy Equations".

3 February, 1982.

Dr. D. Parker (University of Durham). "Modern Methods of Determining Enantiomeric Purity".

10 February, 1982.*

Dr. D. Pethrick (University of Strathclyde). "Conformation of Small and Large Molecules".

11 February, 1982.

Dr. D.W. Turner (University of Oxford). "Photoelectrons in a Strong Magnetic Field".

17 February, 1982.*

Professor D.T. Clark (University of Durham). "Studies of Surfaces by ESCA".

18 February, 1982.*

Professor R.K. Harris (University of East Anglia). "N.M.R. in the 1980's".

24 February, 1982.*

Dr. L. Field (University of Oxford). "Application of N.M.R. to Biosynthetic Studies on Penicillin".

25 February, 1982.

Professor R.O.C. Norman (University of York). "Turning Points and Challenges for the Organic Chemist".

3 March, 1982.

Dr. P. Bamfield (I.C.I. Organics). "Computer Aided Design in Synthetic Organic Chemistry".

4 March, 1982.

Dr. R. Whyman (I.C.I. Runcorn). "Making Metal Clusters Work".

17 March, 1982.

Professor R.J. Haines (University of Cambridge/Natal). "Clustering Around Ru, Fe and Rh".

7 April, 1982.*

Dr. a. Pensak (Dupont, U.S.A.). "Computer Aided Synthesis".

5 May, 1982.

Dr. G. Tennant (University of Edinburgh). "The Aromatic Nitro Group in Heterocyclic Reactions".

7 May, 1982.

Dr. C.D. Garner (University of Manchester). "Molybdenum Centres in Enzymes".

26 May, 1982.

Dr. A. Welch (University of Edinburgh). "Conformation and Distortion in Carbometallo-boranes".

14 June, 1982.*

Professor C.M.J. Stirling (University College of Wales, Bangor). "How Much Does Strain Affect Reactivity?".

28 June, 1982.

Professor D.J. Burton (University of Iowa, U.S.A.). "Some Aspects of the Chemistry of Fluorinated Phosphonium Salts and Their Phosphonates".

2 July, 1982.*

Professor H.F. Koch (Ithaca College, University of Cornell, U.S.A.). "Proton Transfer to and Elimination Reactions from Localized and Delocalized Carbanions".

13 September, 1982.

Professor R. Neidlein (University of Heidelberg). "New Aspects and Results of Bridged Annulene Chemistry".

27 September, 1982.

Dr. W.K. Ford (Xerox Research Centre, Webster, New York). "The Dependence of the Electronic Structures of Polymers on Their Molecular Architecture".

13 October, 1982.

Dr. W.J. Feast (University of Durham). "Approaches to the Synthesis of Conjugated Polymers".

14 October, 1982.

Professor H. Suhr (University of Tubingen). "Preparative Chemistry in Non-Equilibrium Plasmas".

27 October, 1982.*

Dr. C.E. Housecroft (Oxford High School and Notre Dame University). "Bonding Capabilities of Butterfly-Shaped Fe_4 Units: Implications for C-H Bond Activation in Hydrocarbon Complexes".

28 October, 1982.

Professor M.F. Lappert, F.R.S. (University of Sussex). "Approaches to Asymmetric Synthesis and Catalysis Using Electron-Rich Olefins and Some of Their Metal Complexes".

APPENDIX II

CONFERENCES ATTENDED DURING THE PERIOD 1979 TO 1982

1. Annual Congress of the Chemical Society and the Royal institute of Chemistry, Durham University, April 1980

2. Royal Society of Chemistry, Statistical Mechanics and Thermodynamics Group, "The Structure of Molecular Liquids", Cambridge, April 1981.

3. Spectroscopy Group of the Institute of Physics, "Special Techniques for the Submillimetre Region", Westfield College, London, April 1981.

4. European Molecular Liquids Group, "Analytical and Computational Studies of Basic Problems in Molecular Liquids", Dublin Institute for Advanced Studies, April 1982.

APPENDIX III

J. Phys. E: Sci. Instrum., Vol. 14, 1981. Printed in Great Britain

A new cell for liquid phase refractive index determinations in the submillimetre spectral region

J Yarwood†, C Barker†, P L James†, G P O'Neill†, W A Scott‡ and R N McKenzie‡
† Chemistry Department, University of Durham, Durham City, UK
‡ Beckman-RIIC Ltd, Glenrothes, Fife, Scotland, UK

Received 8 May 1980

Abstract A simple refractive index cell for use in the spectral range between 0·2–20 mm^{-1} is described. The module is designed to be compatible with a Beckman-FS720 interferometer and it is extremely easy to align and use. The cell has the advantage of high energy throughput and low reflection losses from the thin polymer front window. The results obtained for liquid tetrabromoethane and p-difluorobenzene agree within 1–2% of the published data, the random error in our measurements being about ±1%.

1 Introduction

There are a number of spectroscopic problems of physical, chemical and biochemical importance for which a knowledge of the dispersion of the refractive index in the far infrared region is important. For example, Chamberlain (1968) has shown that one might be able to establish more easily whether an absorption band is due to a relaxation process or a resonance phenomenon. There are many spectral features which occur in the submillimetre region whose exact origin is still obscure. These include (i) bands associated with ion–ion and ion–molecule interactions in alkyl salt (Yarwood and Barker 1975, 1977, Yarwood *et al* 1978a) or metal salt solutions (Popov *et al* 1971, Popov and Handy 1972, Edgell 1972) in solvating or (supposedly) non-solvating media, (ii) absorption associated with hindered rotational and translational motions of both polar (Evans 1975b, Evans *et al* 1977, 1978a, b, 1979, Yarwood *et al* 1978b, 1979) and non-polar (Evans 1975a, Evans and Davies 1976) liquids, (iii) bands (probably of a composite nature) arising due to the formation of electron donor–acceptor complexes (Yarwood 1973).

In addition, refractive index data are of use in the study of band integrated intensities (Chamberlain 1965, Chamberlain and Gebbie 1966) and are essential (Yarwood *et al* 1979) if one is to make comparison of infrared and microwave data in the interesting overlap region at submillimetre wavelengths (since the relationship between the absorption coefficient $\alpha(\bar{\nu})$ and the dielectric loss $\epsilon''(\bar{\nu})$ depends on the refractive index).

The problem of making accurate refractive index measurements on condensed phases in the 60–6000 GHz (0·2–20 mm^{-1}) region has been solved, in principle, by the use of a dispersive Michelson interferometer (Chamberlain *et al* 1969, Chantry 1971, Chamberlain 1979) with the specimen placed in one of the active arms. This allows the attenuation and phase shift caused by the specimen to be determined and the optical constants can then be calculated (Birch and Parker 1979a, b). The earliest work was performed with the liquid forming a gravity held layer over one of the interferometer mirrors but more recently it has been shown how a closed cell leads to certain advantages. In particular, the gravity held arrangement leads to liquid pathlength variations due to losses by evaporation from volatile liquids. Furthermore, for highly absorbing samples, it is often not possible to make layers thin enough (due to surface tension and viscosity effects). The one closed cell which has been described (Honijk *et al* 1976, 1977) is quite sophisticated in design but is complicated to use in practice and has the disadvantage of a thick front window (silicon) which leads to high energy losses. Our aim was to design and test a cell which is simple to align and use with a commercially available interferometer (a Beckman-RIIC Ltd model FS720) and which produces refractive index data with an overall accuracy of about ±1% for a wide range of highly absorbing liquids and solutions.

2 Cell design and construction

In order to achieve these aims we designed a system with the following features:

(i) The liquid sample is enclosed by a thin, inert (plastic) window which is easily removable without removing the cell or disturbing the optical alignment. Energy loss through the window is very small.

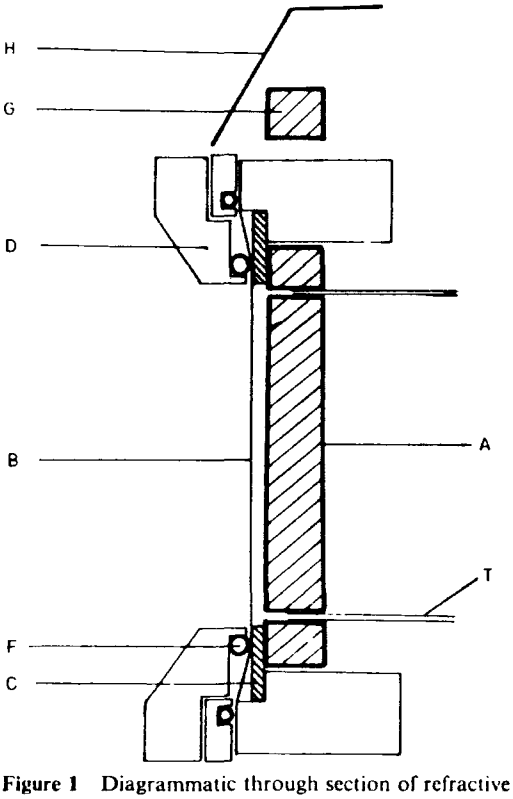

Figure 1 Diagrammatic through section of refractive index cell.

0022-3735/81/020161+05 $01.50

(ii) There is provision for variable sample thickness down to and *below* the thickness which may be achieved using a gravity held liquid.
(iii) Accurate measurement of the dispersive interferogram maximum displacement (on introduction of the sample) is achieved by simply leaving part of the cell mirror uncovered.
(iv) The cell mirror has as large an area as possible and is capable of sensitive adjustment to ensure that the sample is perpendicular to the interferometer beam.
(v) The instrument is easily converted between dispersive and non-dispersive modes with only minor optical adjustments.

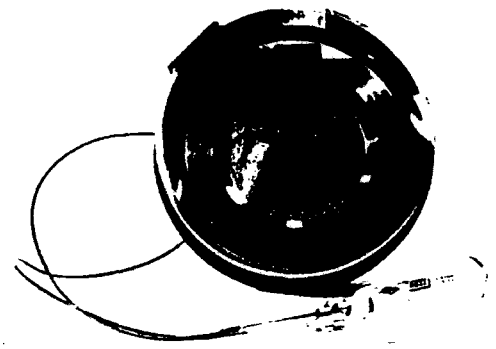

(*a*)

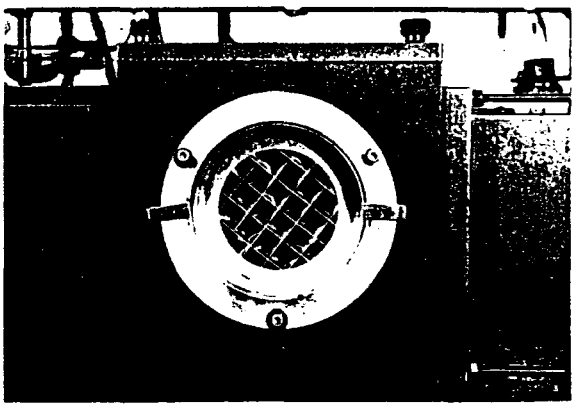

(*b*)

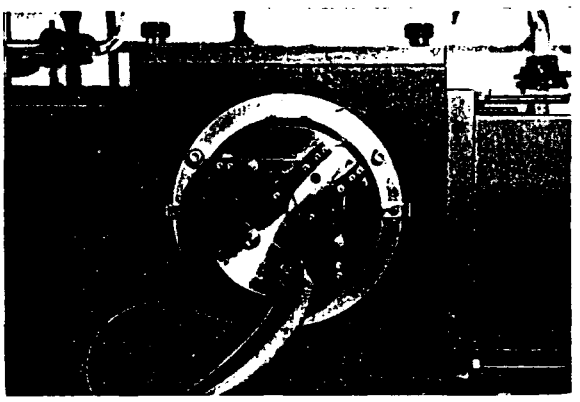

(*c*)

Figure 2 The completed refractive index cell: (*a*) the whole cell showing the reference mirror and cell window holder; (*b*) the vacuum membrane and supporting grid; (*c*) the whole module mounted in the FS720 interferometer.

Figure 1 shows a diagrammatic representation of the cell module which we have designed. The rear wall of the cell consists of a circular, gold covered plane mirror (A) which forms the 'fixed' mirror of the interferometer system. This mirror is covered by a thin plastic (mylar or polyethylene) window (B) which is mounted in a stretched configuration on a frame (D) with aid of the O ring (F). This frame is then screwed down over the mirror, in such a way that the spacer gasket (C) is sealed between the window and the mirror A. Both the window and spacer thicknesses are variable. After optical alignment using a standard Beckman fixed mirror three-point adjustable mounting, the sample is introduced through the Teflon tubes (T) which are bonded directly into the back of the glass mirror (A). By mounting the mirror (A) slightly off centre on the main mounting plate we have been able to include in the beam, a small rectangular reference mirror (G) which, if not covered by the diaphragm (H), provides a small reference 'marker' on the dispersive interferogram (see §3). The two mirrors are produced from separate pieces of material but are lapped and polished together to ensure that they are coincident in the beam direction. The constructed cell is shown in figure 2(*a*).

The cell described above is isolated from the main part of the interferometer by a plastic vacuum membrane (see figure 2(*b*)) which is held over a wire grid and sealed against the mounting flange with an O ring device. This supported membrane (usually of 25 gauge mylar beam splitter material) is used to enable the rest of the interferometer to be evacuated without significantly reducing the energy throughput. The space between the vacuum membrane and the cell window (about 10 mm) is flushed with dry nitrogen.

3 Operation and calculations

Cell operation is straightforward in every way. One has only to be sure that the cell is aligned properly and that the window holding the liquid sample against the mirror is not 'bowing' in such a way that the sample is of variable thickness. This

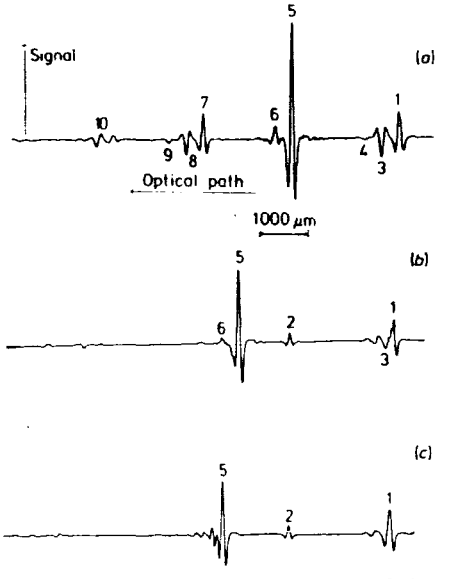

Figure 3 Interferograms produced by FS720 with dispersive cell (of 1 mm thickness) using a 100 gauge mylar beam splitter and a liquid helium cooled germanium bolometer. (*a*) Empty cell; (*b*) liquid p-difluorobenzene; (*c*) liquid tetrabromoethane.

Table 1 Optical path differences of observed fringes relative to reflection from top surface of cell window (fringe 1).

Fringe	Phase change	Optical path difference	Recorded† path difference (μm)	Predicted‡ PD (μm)	% error
2	π	$2d+2t$	2052 ± 4	2036	0·8
3	0	$2t+\bar{x}_w$	354 ± 6	357	0·6
4	0	$4t+2\bar{x}_w$	682 ± 10	713	4·3
5	π	$2t+2d+\bar{x}_w+\bar{x}_s$	2170 ± 6	2189	0·9
6	π	$4t+2d+2\bar{x}_w+\bar{x}_s$	2522 ± 6	2545	0·9
7	3π	$2t+4d+\bar{x}_w+2\bar{x}_s$	4010 ± 6	4021	0·3
8	2π	$4t+4d+2\bar{x}_w+2\bar{x}_s$	4366 ± 10	4378	0·3
9	2π	$6t+4d+3\bar{x}_w+2\bar{x}_s$	4721 ± 7	4734	0·3

† Obtained from 'sample' interferogram.
‡ Using $t=102$ μm, $\bar{n}_w=1{\cdot}748\pm0{\cdot}015$ and d value of 916 ± 12 μm.

problem can be overcome, if it arises (and it is easily recognised, see below) by adjusting the height of an external liquid reservoir. Some chemicals (notably acetone and tetrabromoethane) tend to etch off the gold covering from the mirror but this is easily replaced using a standard gold evaporator.†

Typical interferograms produced using the cell with a standard FS720 interferometer and liquid helium cooled bolometer are shown in figure 3. The numbered fringes on each trace may be correlated with the expected optical path differences shown in table 1 and with the ray diagrams shown in figure 4. The average refractive indices are referred to as

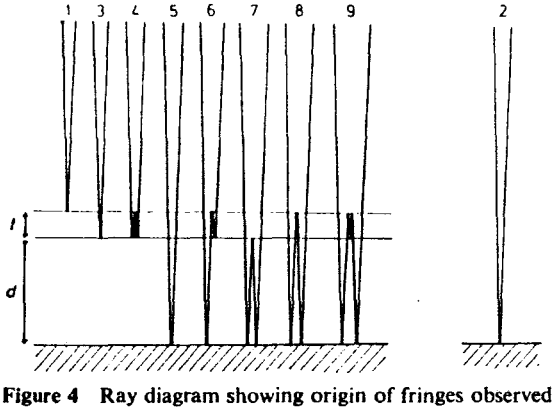

Figure 4 Ray diagram showing origin of fringes observed in the interferogram.

$\bar{n}_\omega$ and $\bar{n}_s$ for window and sample materials respectively while the thicknesses of the optical layers are t and d respectively. The refractive index of the liquid at wavenumber $\bar{\nu}$ is determined (Chamberlain *et al* 1969) by the relation.

$$n(\bar{\nu})=1+\frac{\bar{x}_s}{2d}+\frac{1}{4\pi\bar{\nu}d}[\phi_s(\bar{\nu})-\phi_0(\bar{\nu})+2m\pi] \qquad (1)$$

where $\phi_s(\bar{\nu})$ and $\phi_0(\bar{\nu})$ are the phase functions of the sample and background spectra. If $\Delta(\bar{\nu})\,(=2d[\bar{n}(\bar{\nu})-1])$ and $\delta_0(\bar{\nu})$ are the phase differences introduced by sample and instrumental imperfections (respectively) then the true phase difference is given by,

$$\Phi_s(\bar{\nu})=2\pi\bar{\nu}[\Delta(\bar{\nu})+\delta_0(\bar{\nu})] \qquad (2)$$

The integer m is introduced in equation (1) because the phase difference $\phi_s(\bar{\nu})$ is the *principal* value of the true phase difference given in equation (2). It is expected that $m=0$ except in regions of very high absorption where the optical thickness $n(\bar{\nu})d$ may deviate by more than $\frac{1}{4}\bar{\nu}$ from the mean optical thickness $\bar{n}d$ (Chamberlain *et al* 1969). Since the phase functions $\phi_s(\bar{\nu})$ and $\phi_0(\bar{\nu})$ are easily determined from the respective spectra, the calculation of $n(\bar{\nu})$ from equation (1) requires only the determination of the average optical path difference ($\bar{x}_s$) caused by the introduction of the sample into the second beam of the interferometer. The procedure is as follows (referring to figure 4 and table 1):

(i) the cell pathlength, d, is first determined from the fringe spacing (3)–(5), given by $2d+\bar{x}_s$ (but with $\bar{x}_s=0$ for an empty cell interferogram);

(ii) the window thickness t is then calculated from the distance (1)–(2) $(=2d+2t)$ on a full cell interferogram;

(iii) the average optical path difference of the window material, $\bar{x}_w$, is then easily calculated using the distance (1)–(3) $(=2t+\bar{x}_w)$;

(iv) finally, since the fringe spacing (2)–(5) (for a full cell interferogram) is simply $\bar{x}_w+\bar{x}_s$, the value of $\bar{x}_s$ (and if necessary $\bar{n}_s$ since $\bar{x}_s=2d(\bar{n}_s-1)$) can be easily computed.

The other fringes, given in table 1 and shown in figure 3 may then be employed to perform an internal consistency check on the fringe assignments and associated calculations.

4 Results and discussion

Table 1 shows that there is very good agreement between calculated and observed fringe positions and this serves to confirm the fringe assignments shown in figure 4. At least some part of the errors given in table 1 are probably due to the effects of phase changes on reflection at the various boundaries. These will affect the distances measured in order to calculate $\bar{x}_s$ and d and lead to discrepancies between observed and calculated fringe positions. It should be noted that equation (1) gives a refractive index which is also uncorrected for these effects. The only way of avoiding such effects is to use the 'full interferogram' methods (Honijk 1976, 1977, Birch and Parker 1979a) of computation but large shifts in refractive index are not expected. In this work it was considered undesirable to use this technique because we wish to check our data against previous measurements which also employed equation (1). It is worth noting, however,

† We are grateful to Dr M J Morant and Mr J Gibson of our Applied Physics Department for helping us with this and various related optical measurements.

that the full-interferogram method also has the advantage of automatically eliminating problems associated with the reflection fringes (1), (3) and (6) - which, for example, in this work limit the phase resolution obtainable since such fringes have to be either 'edited' out or omitted from the calculation of $\phi_R(\bar{\nu})$ and $\phi_0(\bar{\nu})$.

Figure 3 demonstrates that we have encountered no major problems with 'bowing' of the front window. This is expected to give rise to loss of optical alignment and subsequent loss of fringe modulation and definition. There is *some* loss of modulation depth for the extremely dense tetrabromoethane ($\rho^{20} = 2{\cdot}96 \times 10^3$ kg m^{-3}) (figure 3(*c*)) but for liquids with more 'normal' densities this is not a problem (figure 3(*b*)).

The refractive index dispersion curves shown in figure 5 indicate that our results for the two 'test' liquids are within ~1–2% of the previously published data at approximately the same temperature (Davies 1974, Chamberlain *et al* 1967). The overall 'level' of refractive index is some 2% higher than that fixed (using a laser operating at 2·97 mm^{-1}) at the National Physical Laboratory. There are several sources of possible systematic error between our data and those published previously. These include differences in temperature between the two sets of measurements. However since this could not have been more than 5°C and since the variation of n with temperature is only about 0·0005 per degree (Int. Critical Tables, Vol. VII) this could not lead to more than about 0·2% error. Another possible source of error is the determination of the thickness of liquid (d) and the central fringe displacement, $\bar{x}$. These determinations have been checked using the techniques employed by Chamberlain and those advocated more recently (Birch and Parker 1979b) and found to give results within about 1% of each other. We are therefore convinced that our results are not subject to any obvious systematic error (in comparison with the techniques used to obtain the published data). The shapes of the dispersion curves are virtually identical. Since no error bars are given on the NPL curves it is difficult to say, however, whether the two sets are within the experimental random error. From the errors given in table 1, however, it seems likely that this *is* the case. Certainly Chantry (1971) regards a ±1% error as being entirely acceptable using this technique. The results are therefore regarded as being satisfactory when one considers the simplicity of our hardware. We now propose to make some minor modifications (such as installing variable temperature control) before using the cell to make measurements on more chemically useful systems.

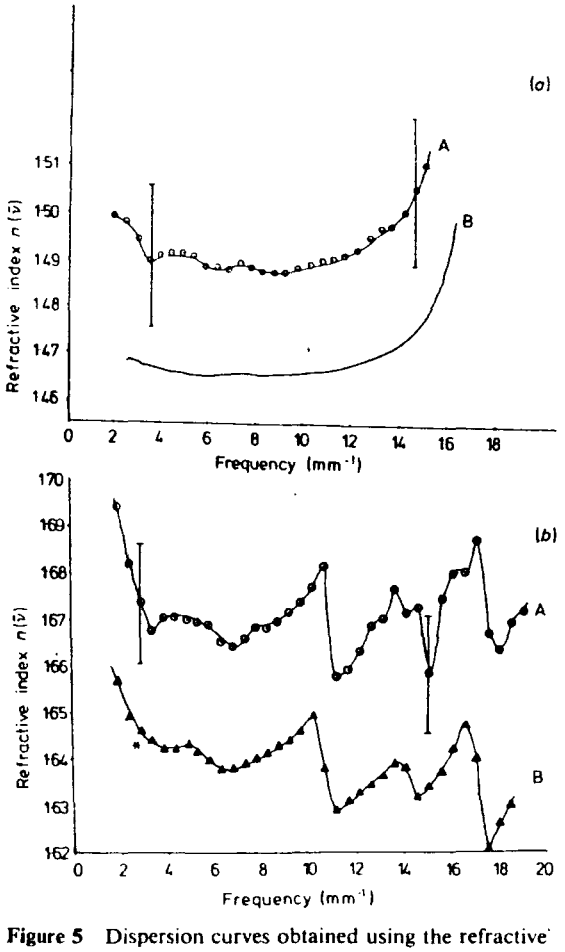

Figure 5 Dispersion curves obtained using the refractive index cell. (*a*) p-difluorobenzene; (*b*) tetrabromoethane. The temperature is 23 ± 1°C in each case. Our data is labelled A and the NPL data is labelled B.

Acknowledgments

We are grateful for valuable discussions with Dr J R Birch and the late Dr J. Chamberlain. Professor D H Martin and Dr P Ade helped us to put our cooled detector into operation and thanks are also due to the SRC and Beckman RIIC Ltd for their continued support of this project with equipment grants and CASE studentship awards.

References

Birch J R and Parker T J 1979a Dispersive Fourier transform spectroscopy
Infrared and Millimetre Waves Vol. 2 ed K J Button (New York: Academic) Chapter 3

Birch J R and Parker T J 1979b The role of the origin of computation in the determination of phase spectra by dispersive Fourier transform spectroscopy
Infrared Phys. **19** 103

Chamberlain J 1968 On the submillimetre wave refraction of liquids
Chem. Phys. Lett. **2** 464

Chamberlain J, Gibbs J E and Gebbie H A 1969 The determination of refractive index spectra by Fourier spectrometry
Infrared Phys. **9** 185

Chamberlain J E 1965 On a relation between absorption strength and refractive index
Infrared Phys. **5** 175

Chamberlain J E 1979 *Principles of Interferometric Spectroscopy* (New York: Wiley) Chapter 7

Chamberlain J E and Gebbie H A 1966 Dispersion measurements on polytetrafluoro-ethylene in the far infrared
Appl. Optics **5** 393

Chamberlain J E, Gibbs J E and Gebbie H A 1967 Submillimetre dispersion of liquid tetrabromoethane
Spectrochimica Acta **23A** 2255

Chantry G W 1971, *Submillimetre Spectroscopy* (New York: Academic) Chapter 4 and Appendix 4

Davies M M 1974 Infrared absorptions in non-dipolar liquids
Molecular Motions in Liquids (Dordrecht: Reidel) pp 615–35

Edgell W F 1972 Infrared and Raman studies of ions and ion pairs
Ions and Ion Pairs in Organic Reactions Vol. I ed M Szwarc (New York: Wiley-Interscience) Chapter 4 and references therein

Evans G J, Reid C J and Evans M W 1978a Far-infrared absorption of CH_2Cl_2 in isotropic and cholesteric solvents
J. Chem. Soc., Faraday Trans. II **74** 343

Evans M W 1975a Investigation of the intermolecular dynamics of non-polar molecules using the rotational velocity correlation function
J. Chem. Soc., Faraday Trans. II **71** 71

Evans M W 1975b Comparison in the time region 0–1·2 ps of model and experimental absorptions of liquid and rotator phases in the far-infrared
J. Chem. Soc., Faraday Trans. II **71** 2051

Evans M W and Davies G J 1976 Use of generalised Langevin theory to describe far infrared absorptions in non-dipolar liquids. Effect of pressure and temperature on the intermolecular mean square torques in liquid CS_2 and CCl_4
J. Chem. Soc., Faraday Trans. II **72** 1194 1206

Evans M W, Evans G J and Davies G J 1977 Absorption of dipolar liquids in the far infrared–a sensitive measure of the Mori continued fraction
J. Chem. Soc. Faraday Trans. II **73** 1071

Evans M W, Evans G J and Davies G J 1979 Zero-THz absorptions and the rotational Langevin equation
***J. Chem. Soc. Faraday Trans. II* 75 1428**

Evans M W, Reid C J, Yadav R A, Evans G J and Davies G J 1978b Liquid state dynamics of CH_2Cl_2
J. Chem. Soc. Faraday Trans. II **74** 2143

Honijk D D, Passchier W F, Mandel M and Afsar M N 1976 Determination of complex refractive index spectra of liquids in the far-infrared region (5–500 cm^{-1}) with dispersive Fourier transform spectrometry
Infrared Phys. **16** 257

Honijk D D, Passchier W F, Mandell M and Afsar M N 1977 Determination of complex refractive indices with Fourier transform interferometry. V Methods for determination of complex refractive index spectra of liquids in the 5–500 cm^{-1} region using a variable pathlength, variable temperature cell
***Infrared Phys.* 17 9**

Popov A I and Handy P R 1972 Spectroscopic studies of ionic solvation, XII Ionic solvation in pyridine and substituted pyridine solutions
***Spectrochimica Acta* 28A 1545**

Popov A I, Wong M K and McKinney W J 1971 Spectroscopic studies of ionic solvation, VIII Alkali metal salts in acetone solutions
***J. Phys. Chem.* 75 56**

Yarwood J 1973 Measurement and interpretation of vibrational spectra of molecular complexes
Spectroscopy and Structure of Molecular Complexes ed J Yarwood (London: Plenum) Chapter 2

Yarwood J and Barker C 1975 Vibrational spectroscopic studies on ion–molecule interactions in non-aqueous solutions Part I. Far-infrared studies on tetra-n-butyl ammonium chloride in benzene
J. Chem. Soc. Faraday Trans. II **71** 1322

Yarwood J and Barker C 1977 Studies of ion–ion and ion–molecule interactions using far infrared interferometry
Faraday Symp., Chem. Soc. **11** 136

Yarwood J, James P L, Arndt R, Evans M W and Evans G J 1979 Studies of molecular motions and vibrational relaxation in acetonitrile IV Far-infrared and molecular dynamics in carbon tetrachloride solution
Mol. Phys. **38** 699

Yarwood J, James P L and Barker C 1978a Studies of ion–ion and ion–solvent interactions using far-infrared spectroscopy Part 3. Comparison of observed spectra with results of simple model calculations
Faraday Diss. Chem. Soc. **64** 188

Yarwood J, James P L, Döge G and Arndt R 1978b Comparison of infrared and Raman vibrational relaxation functions of the ν_1 and ν_3 modes of acetonitrile
Faraday Diss. Chem. Soc. **66** 252

APPENDIX IV

Journal of Molecular Structure, 80 (1982) 383—388
Elsevier Scientific Publishing Company, Amsterdam — Printed in The Netherlands

FAR INFRARED AND MICROWAVE SPECTRAL STUDIES ON THE MOLECULAR DYNAMICS AND INTERACTIONS OF METHYL IODIDE IN CARBON DISULPHIDE SOLUTION

G.P. O'NEILL, A. KHUEN and J. YARWOOD
Department of Chemistry, University of Durham, Durham City, DH1 3LE (Gt. Britain)

J.R. BIRCH
Division of Electrical Science, National Physical Laboratory, Teddington, Middx., TW11 OLW (Gt. Britain)

A.H. PRICE
Edward Davies Chemical Laboratory, U.C.W., Aberystwyth, Dyfed, SY23 1NE (Gt. Britain)

ABSTRACT

The far-infrared and microwave spectra of methyl iodide in dilute solution (0.1 mf) in carbon disulphide have been used to measure the relaxation times and correlation function for dipole reorientation in this particular medium. It is shown that rotation is faster than in the liquid phase due to removal of intermolecular correlations. The short time part of the correlation function is shown to be distinctly non-exponential and this part of the power spectrum is fitted to a model which enables the intermolecular mean square torque to be determined. The spectral second moment agrees well with that calculated using the classical rotational energy indicating that induced dipole absorption is not of major importance in this solution.

(1) BACKGROUND AND THEORY

It has recently been demonstrated (1-4) how a combination of far-infrared and microwave absorption measurements may be employed to study the reorientational motion and interactions of molecules in polar fluids. The advantages of spectral data in the 0.1-250 cm^{-1} region are as follows:-

(a) one avoids, of course, the complications (1,2) associated with the separation of vibrational and rotational correlation functions using infrared or Raman vibration/rotation spectra.

(b) Provided that the frequency range is wide enough one is able to calculate the total correlation function for dipole rotation which is

$$\phi_{IR}^{T}(t) = \frac{<\sum_{i,j}[\vec{\mu}_i(o).\vec{\mu}_j(t)]>}{<\sum_{i,j}[\vec{\mu}_i(o)\vec{\mu}_j(o)]>} \propto \int_0^\infty \frac{D(\bar{\nu})\alpha(\bar{\nu})n(\nu)\exp(2\pi\bar{\nu}ct)d\bar{\nu}}{\bar{\nu}[1-\exp(-h\bar{\nu}c/kT)]} \qquad (1)$$

0022-2860/82/0000—0000/$02.75

where $D(\bar{\nu})$ is the 'internal' field correction (3), and $n(\bar{\nu})$ the refractive index.

$\phi^T_{1R}(t)$ gives a direct measure of the relaxation time, τ^T_{1R}, since

$$\tau^T_{1R} = \int_0^\infty \phi^T_{1R}(t)dt \qquad (2)$$

and this may be easily followed as a function of concentration, solvent or temperature. Such correlation functions will also be important in checking the future development of liquid phase intermolecular potentials using molecular dynamics computer simulations (4).

(c) Since the far-infrared power absorption coefficient $\alpha(\bar{\nu})$ can be measured very accurately between about 5 and 250 cm^{-1}, the high frequency part of the spectrum is very well defined. This means that the intermolecular mean square torque is relatively easily measured using a straightforward band moment analysis (5) or by fitting the $\alpha(\bar{\nu})$ to a suitable model (6) (see below).

(d) Since, therefore, the short time part of $\phi^T_{1R}(t)$ is extremely well known and, since it is usually only this part which deviates from an exponential decay law, that is

$$\phi^T_{1R}(t) = \exp(-t/\tau^T_{1R}) \text{ for long times,} \qquad (3)$$

it is clear that the far-infrared spectrum provides an extremely stringent test of models for molecular rotation (6,7), the more sophisticated of which are only exponential at long times.

It is noted that the correlation function (eqn. 1) is obtained by Fourier transformation of $\alpha/\bar{\nu}^2$ ($\equiv \epsilon''(\bar{\nu})/\bar{\nu}$) at low frequencies ($h\bar{\nu} \ll kT$). This means that the spectral profile required is heavily weighted towards the low frequency data. It is therefore essential to have data in the 0.1-5 cm^{-1} region, where conventional far infrared sources and detectors are relatively poor. The required data may be obtained from one of two sources.

(i) low frequency $\alpha/\bar{\nu}$ data may be obtained by the method described by Price and Wegdam (8). This data also enables a 'Debye' relaxation time τ_D to be obtained - quite independently from the far infrared data.

(ii) Alternatively, and especially if one has no access to microwave data, one can use the technique advocated by Khuen (9) which involves making a measurement of the rotational band profile or, more realistically, a value of τ_{1R}, from the infrared spectrum. It may then be reliably assumed that, at long times, $\phi^T_{1R}(t)$ follows equation (3) and that therefore the spectrum is Lorentzian. For $\bar{\nu}$ between 0.1 and 5 cm^{-1} we then have

$$I(\bar{\nu}) = \frac{A}{1 + b^2(\bar{\nu}-\bar{\nu}_o)^2} \qquad (4)$$

where A is the band intensity, $\bar{\nu}_o$ the band centre and b is $2/\Delta\bar{\nu}_{\frac{1}{2}}$. $\Delta\bar{\nu}_{\frac{1}{2}}$ is the band

half-width (FWHM) in cm^{-1} related to τ_{1R} by

$$\tau_{1R}^{T} = (\pi c \Delta\bar{\nu}_{\frac{1}{2}})^{-1} = (10.6 \times 10^{-12}/\Delta\bar{\nu}_{\frac{1}{2}}) \text{ sec.}$$

The power absorption spectrum $\alpha(\bar{\nu})$ may then be obtained from the absorption cross section $I(\bar{\nu})$ since,

$$I(\bar{\nu}) = \frac{3n(\nu)\alpha(\bar{\nu})kT}{16\pi^4\bar{\nu}^2 c} \qquad (5)$$

So $\alpha(\bar{\nu}) \propto I(\bar{\nu})\bar{\nu}^2/n(\bar{\nu})$

The frequency dependent index of refraction $n(\bar{\nu})$ may be obtained either by direct measurement (10) or by a Kramers-Kronig analysis (11) of the absorption data.

These two techniques are compared in this paper. The intermolecular mean square torques $< O(V)^2 >$ are obtained for a symmetric top molecule from a band moment analysis. The short time part of the correlation function may be written (5) as,

$$\phi_{1R}^{T}(t) = 1 - a_1 t^2/_{2!} + a_2 t^4/_{4!} + \ldots.$$

$$= 1 - M_{2R} t^2/_{2!} + M_{4R} t^4/_{4!} + \ldots. \qquad (6)$$

where $M_{2R} = 2kT/I_B$ (7a)

$$M_{4R} = 8\left(\frac{kT}{I_B}\right)^2 \left(1 + \frac{I_A}{4I_B}\right) + \frac{2 < O(V)^2 >}{I_B^2} \qquad (7b)$$

and $$M_{nR} = \frac{\int_0^\infty (\bar{\nu}-\nu_o)^n I(\bar{\nu}) d\bar{\nu}}{\int I(\bar{\nu}) d\bar{\nu}} \qquad (8)$$

Since $2kI/I_B$ is known $< O(V)^2 >$ is easily calculated provided that the data are sufficiently accurate at high frequencies.

Alternatively the $\alpha(\bar{\nu})$ data may be fitted to a model based on truncation of the Mori continued fraction solution of the generalised Langevin equation (6,12). Using third order truncation, it has been shown (12) that,

$$\alpha(\omega) = \frac{A'\omega^2 K_o(0) K_1(0) \gamma}{\gamma^2[K_o(0)-\omega^2]^2 + \omega^2[\omega^2-(K_o(0)+K_1(0)]^2} \qquad (9)$$

with $A' = \frac{\varepsilon_o - \varepsilon_\infty}{cn(\omega)}$ and $\omega = 2\pi c\bar{\nu}$.

The parameters $K_o(0)$ and $K_1(0)$ are respectively $-a_1$ and $a_1 - a_2/a_1$ and so can again be used to measure $< O(V)^2 >$. The $1/\gamma$ parameter is a torque correlation time.

(2) EXPERIMENTAL

The equipment and methods of analysis have been described previously in some detail for both far-infrared (10) and microwave (8) measurements. The materials were of 'Analar' grade and they were thoroughly dried over molecular sieves prior to use.

RESULTS AND DISCUSSION

Figure 1 shows the power absorption coefficient $\alpha(\bar{\nu})$ in the region of interest (including a selection of microwave data). In figure 2 we show the absorption cross section $(\alpha(\bar{\nu})/\bar{\nu}^2$; see equations 5 and 6) and the refractive index in the range required to calculate $\phi_{IR}^{I}(t)$ via equation (1).

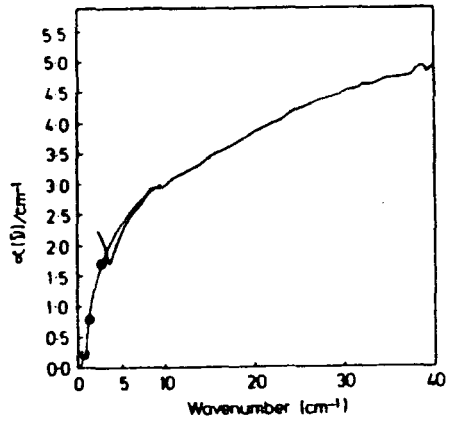

Fig. 1. Far infrared and microwave spectra of CH_3I in CS_2 (0.1 mf). The dotted line shows low frequency Lorentzian of equation 4 with $\Delta\bar{\nu}_{\frac{1}{2}} = 6\ cm^{-1}$.

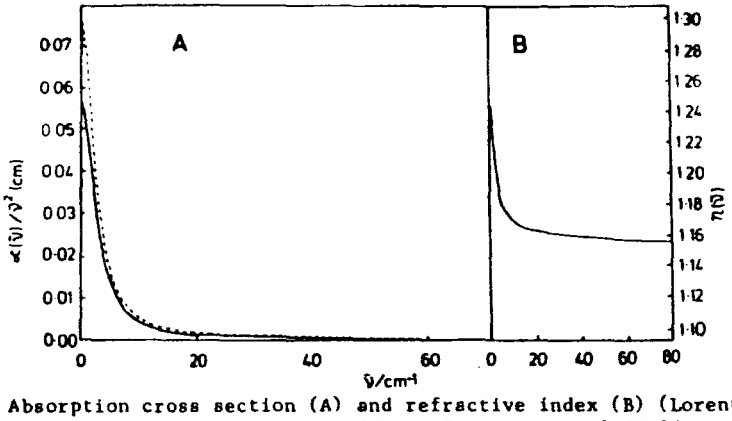

Fig. 2. Absorption cross section (A) and refractive index (B) (Lorentzian curve in fig. 1). The dotted curve shows the effect of the internal field correction on $\epsilon''(\bar{\nu})/\bar{\nu}$.

Figure 3 shows the resulting correlation functions for $D(\bar{\nu}) = 1$ and for $D(\bar{\nu})$ given by Rosenthal and Strauss (ref. 3, eqn. 9). Although the correction has little effect on $\phi(t)$ it does effect other parameters and is used to provide the results reported herein. The correlation function shown is that calculated using a low frequency pure Lorentzian band (eqn. 4) with a half width corresponding to the rotational relaxation time (1.8 psec) obtained (9) from infrared spectroscopy. The corresponding $\phi(t)$ obtained with microwave data is very similar but the relaxation time obtained (2.7-2.8 psec) is longer - presumably due to the presence of intermolecular correlations between neighbouring molecules which are expected to be more important

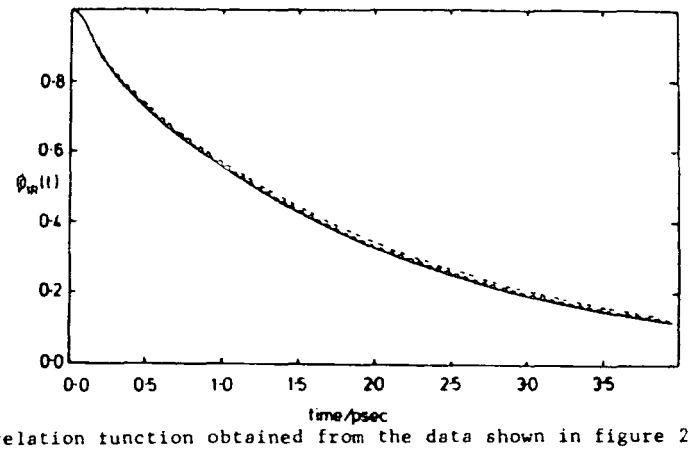

Fig. 3. Correlation function obtained from the data shown in figure 2. The dotted curve shows the effect of an internal field correction.

for microwave spectra. The τ_{1R}^{T} values are considerably faster than those observed in the liquid phase where values range between 3.5 and 4.5 psec (2,14). This difference is again caused by removal of intermolecular correlations and by a decrease in viscosity (11). The 2nd and 4th moments obtained via equation (8) and the intermolecular means square torques are given in table 1. Since the only difference between results obtained using microwave and infrared data at low frequencies is below about 5 cm^{-1}, it is expected that the two sets of data will lead to very similar moments and torques. It should be noticed that the 2nd moments obtained (with an internal field correction) agree very well with the classical average rotational kinetic energy given in eqn. (7a). Furthermore, the torque calculated agrees very well with that obtained for the liquid by Bansal et al. (17) from Raman data. These results indicate a relatively small contribution from induced dipole fluctuations to the far I.R. data.

Figure 4 shows the result of fitting equation 9 to the $\alpha(\bar{\nu})$ data. The parameters $K_1(o)$ and γ are given in table 1 and it is noted that the torque obtained in this way is in very reasonable agreement with that obtained by direct integration. The quality of the fit is very good with the observed $\epsilon_o - \epsilon_\infty$ again indicating that the spectrum arises mainly from permanent dipole rotation. The torques are in good agreement with those obtained for other molecules of similar size, shape and dipole moment (ref. 13, p.113).

TABLE 1

Optical data, relaxation times and intermolecular mean square torques for 0.1 mf CH_3I in CS_2 (298 K)

ϵ_o^a	n_{1R}^2	τ_{1R}^T/ps	τ_{1R}^{sp}/ps	τ_{2R}^{sp}/ps
1.537	1.339[x]	1.80[x]	1.8	1.1
	1.226[y]	2.78[y]		

$10^{-24}M^{b}_{2R}/s^{-2}$	$10^{-48}M_{4R}/s^{-4}$	$10^{-24}K_1(o)/s^{-2}$	$10^{-12}\nu/s^{-1}$	$10^{-4}\langle O(V)^2\rangle/cm^{-2}$
		262.6	14.1	298[c]
7.28[x]	2164[x]			326[x]
7.43[y]	2203[y]			332[y]
($209.5\ cm^{-2}$)	($175.2 \times 10^{4}\ cm^{-4}$)			

x. with low frequency infrared (Lorentzian) profile. y. with low frequency microwave data. a. solution value (3.18) - solvent value (1.643). b. $2kT/I_B \equiv 207.3\ cm^{-2}$. c. Value obtained from $K_1(o)$.

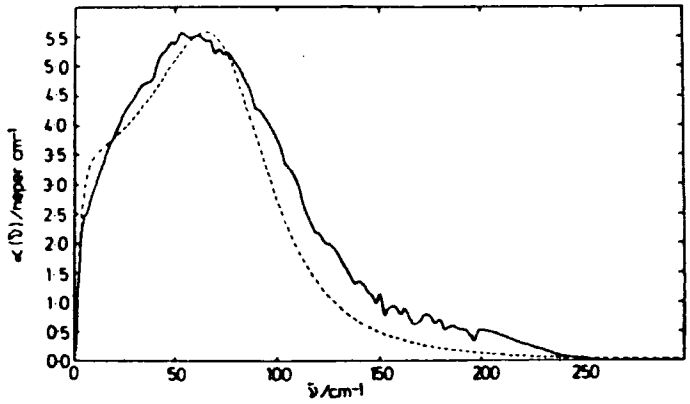

Fig. 4. Comparison of $\alpha(\tilde{\nu})$ with the model embodied in equation 9 (third order truncation of Mori continued fraction).

ACKNOWLEDGEMENT

S.R.C. are thanked for equipment grants and for a studentship to G.P.O. This work was supported by a NATO fellowship (to A.K.).

REFERENCES

1. J. Yarwood and R. Arndt, Molecular Association (Ed. R. Foster), Vol. 2 (Wiley, London, 1978, pp.267-325.
2 J. Yarwood and M.W. Evans, Adv. Mol. Rel. Int. Processes, 21(1981) pp.1-87.
3 L.C. Rosenthal and H.L. Strauss, J. Chem. Phys., 64(1976)282.
4 M.W. Evans, unpublished results; D.J. Adams, E.M. Adams, P. Carley and G.J. Hills, Proc. Meeting on Polar Liquids, Aberystwyth, Sept. 1979.
5 J.H.R. Clarke, Adv. Infrared and Raman Spectroscopy, (Eds. Clark and Hester), Vol. 4 Chapter 4 (Heyden, 1978).
6 M.W. Evans, Adv. Mol. Rel. Int. Processes, 10(1977)203.
7 M.W. Evans, G.J. Evans, J. Yarwood, P.L. James and R. Arndt, Mol. Phys., 38(1979) 699.
8 A.H. Price and G.H. Wegdam, J. Phys., E10(1977)481.
9 A. Khuen, NATO Fellowship Report, University of Durham 1980.
10 J. Yarwood, P.L. James, J.R. Birch and M.N. Afsar, Infrared Phys., 21(1981)9.
11 D.R. Jones, H.C. Andersen and R. Pecora, Chem. Phys., 9(1975)339.
12 M.W. Evans and G.J. Evans, J. Chem. Soc., Faraday Trans., 72(1976)1169.
13 J. Yarwood, Ann. Rev. Phys. Chem., C (1980), pp.99-130.
14 A. Kocot, S. Gandor and E. Kluk, Acta Phys. Polon., A58(1980)149.
15 K.E. Arnold, J. Yarwood and A.H. Price, Mol. Phys. (in press).
16 G.J. Davies, J. Chamberlain and M. Davies, J. Chem. Soc., Faraday Trans. II, 69(1973)1223.
17 M.L. Bansal, S.K. Deb and A.P. Ray, Chem. Phys. Lett. (in press).

APPENDIX V

J. Phys. E: Sci. Instrum., Vol. 15, 1982. Printed in Great Britain

A variable-thickness variable-temperature liquid cell for dispersive Fourier transform spectrometry

J R Birch†, G P O'Neill‡, J Yarwood‡ and M Bennouna§
† Division of Electrical Science, National Physical Laboratory, Teddington, Middlesex TW11 0LW, UK
‡ Department of Chemistry, University of Durham, Science Laboratories, South Road, Durham DH1 3LE, UK
§ Groupe de Recherche 4 du CNRS, 'Physique des Liquides et Electrochimie', Université P et M Curie, 4 Place Jussieu, 75230 Paris, Cedex 05, France

Received 21 December 1981, in final form 1 February 1982

Abstract. The design of a variable-thickness variable-temperature liquid cell suitable for use in the determination of the optical constants of liquids at millimetre and submillimetre wavelengths by the techniques of transmission and reflection dispersive Fourier transform spectrometry is described. Its construction is considerably more simple than those of earlier cells of this type, and this avoids many of their operational difficulties. The results of measurements of the temperature variation of the optical constants of carbon tetrachloride between 20 and 120 cm^{-1} are presented to illustrate the use of the cell.

1. Introduction

The determination of the spectral variation of the optical constants of liquids at millimetre and submillimetre wavelengths by dispersive Fourier transform spectrometry (Birch and Parker 1979) was originally developed through the use of two independent measurement methods. The first measurements were made in transmission on relatively transparent liquids using the free-layer method (Chamberlain *et al* 1967, 1969, Davies *et al* 1970) in which a relatively transparent liquid specimen formed a free gravity-held plane-parallel layer on the surface of the fixed mirror of a two-beam interferometer. This method was modified to allow the study of more absorbing liquids by the approximate methods of editing (Chamberlain *et al* 1967, Davies *et al* 1970), subtraction (Chamberlain *et al* 1973a, Afsar *et al* 1976a) and double subtraction (Afsar *et al* 1976b), while the dispersive reflection method (Chamberlain *et al* 1973b) was developed for the study of virtually opaque liquids such as water (Zafar *et al* 1973). Although the free-layer method has the advantage of experimental simplicity it is susceptible to serious systematic errors. These can arise from the difficulty of achieving a plane-parallel layer, from vibrations of the free liquid surface, from the problems of determining the specimen thickness and from the presence of the liquid vapour in the optical path above the liquid. In addition, surface tension effects limit the minimum thickness for which a continuous film can be maintained to about 100 μm and this prohibits the study of very heavily absorbing liquids by this method. These limitations led to the development of variable-thickness cells in which the liquid specimen was totally enclosed between a plane-parallel transparent window and a movable plane mirror. By totally containing the liquid these cells avoided all of the problems associated with the free surface of the liquid and also allowed layer thicknesses down to about 10 μm to be attained. In addition, by allowing the study of the complex reflectivity of the interface between the cell window and a liquid, dispersive reflection measurements could be performed on heavily absorbing liquids. Thus, such cells combined both transmission and reflection measurement capabilities in one apparatus, a significant development.

The detailed constructions of the two cells of this type that were originally developed (Afsar *et al* 1977, Honijk *et al* 1977) have not been described thoroughly in the literature, although diagrams have appeared in review articles (Stone and Chantry 1977, Stone 1978, Birch and Parker 1979). However, the nature of the sophisticated close-fitting piston-within-cylinder mechanisms used to contain the liquid and to control the cell thicknesses meant that it was difficult to adjust the alignment of the cell mirror to give a plane-parallel layer and also that these mechanisms were susceptible to being jammed by small particulate matter or viscous residues from improperly cleaned cells. In the present work a new large-aperture variable-thickness variable-temperature liquid cell is described. It has a particularly simple design that avoids the complexities and operational difficulties of the earlier cells, while maintaining their measurement capabilities.

2. The cell

The construction of the cell is illustrated in figure 1. It essentially consisted of a stainless-steel body in the form of a hollow cylinder fitted with a plane-parallel single-crystal silicon window at its lower end. The silicon was n type with a resistivity of about 0.6 Ωm, a diameter of 60 mm and a thickness of 2.6 mm. In order to minimise the possibility of damage to this brittle material it was supported at its edges between two annular PTFE pads to prevent contact with any of the metal parts of the cell.

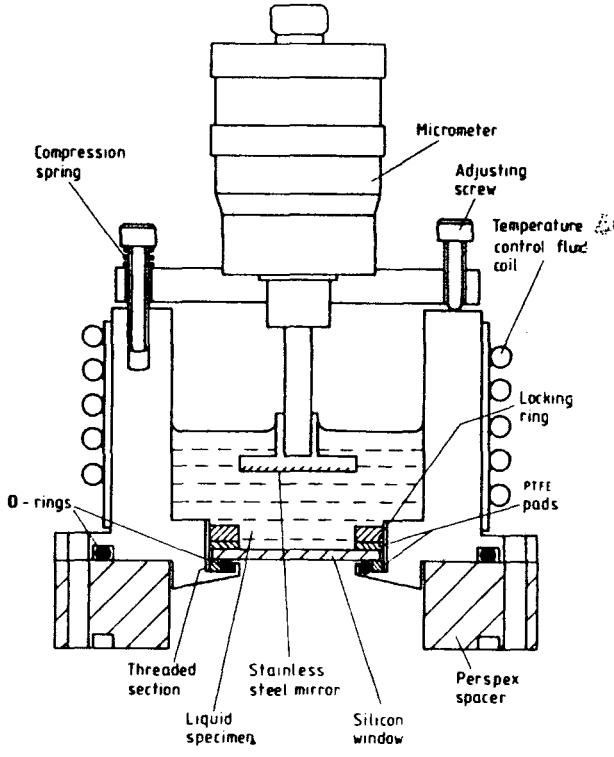

Figure 1. Construction of the liquid cell.

0022-3735/82/060684 + 05 $02.00

This gave the cell a clear aperture of 45 mm diameter. A locking ring which screwed into a threaded section of the cell body firmly clamped the window between the PTFE pads and forced it against an O-ring seal concentric with the lower pad to provide the vacuum and liquid seal for the cell. In this clamped position the clamping ring and PTFE pads largely prevented any liquid from coming into contact with the O-ring and thus avoided the possibility of contamination of the liquid by any material leached out of the ring. The cell mirror was a lapped stainless-steel flat which was a tight push fit over the anvil of a nonrotating micrometer (type 197-101 supplied by Mitutoyo (UK) Ltd). The micrometer was fitted in the top plate of the cell so that the mirror could be positioned over the window as shown. The travel of the micrometer was 50 mm and the design of the cell such that the distance between the mirror and the window could be varied from a few tens of micrometres to about 45 mm. The scale gradation of this micrometer was 0.005 mm and it was estimated that it could be set to give a chosen specimen thickness, or change of thickness, to better than 0.001 mm. The top plate of the cell was firmly clamped down onto the main body of the cell by six equispaced screws, three of which screwed into the main body of the cell through clearance holes in the top plate. These were spring loaded as shown in the figure to force the rounded ends of the other three screws onto the rim of the main body. These were screwed through tapped holes in the top plate and were used to align the mirror in the cell. In order to maintain the simplicity of the cell design a vapour seal was not provided between the cell body and its top plate as this would have needed to have been flexible in order to accommodate the motion of the mirror alignment mechanism. Instead, masking tape was stuck around the outside of the cell as required over the small gap between the cell and its top plate. This was easily removed and provided an adequate seal for all relatively nonvolatile liquids. The bottom surface of the cell, that facing the incident radiation from the interferometer, was machined to a conical form so that radiation reflected from it would not be able to contribute to the detected interference function. The specimen to be studied was introduced into the cell through a small hole in the top plate by the use of a syringe. A volume of the specimen liquid sufficient to cover the cell mirror was used. This ensured that the upper surface of the liquid, although free, was not in the optical path. The specimen temperature was maintained at the desired value by passing fluid (water or paraffin) from a constant-temperature bath through a copper coil clamped to the outside of the cell body. Currently, the cell has been used at temperatures between 283 and 323 K (10 and 50°C).

In operation the cell was positioned at the end of the fixed-length arm of a two-beam interferometer as shown in figure 2. The instrument was constructed with the cell vertically upwards as the upper surface of the liquid was not contained. The cell was connected to the rest of the interferometer via a 25 mm thick perspex spacer shown in figure 1. This acted as a thermal isolator, preventing direct thermal contact between the two, which were generally at different temperatures. The interferometer is shown in the configuration appropriate to the use of polarising wire-grid beam-dividers, although the cell has been used in interferometers having thin-film dielectric beam-dividers when measurements were required in the spectral range above 250 cm^{-1}. In the wire-grid configuration the interferometer cannot be used with polarisation modulation as in the original instrument of Martin and Puplett (1970) as the first wire grid, which acts as a polariser to the input radiation and an analyser to the output radiation, spatially separates the two orthgonally polarised output beams. Thus, phase modulation of the radiation within the interferometer was used with the periodic path difference variation introduced at the plane mirror set at 45° to the optic axis in the moving mirror arm.

The use of the cell is best described with reference to figure 3. The upper part of this shows the primary rays which propagate between the three interfaces of a filled cell when

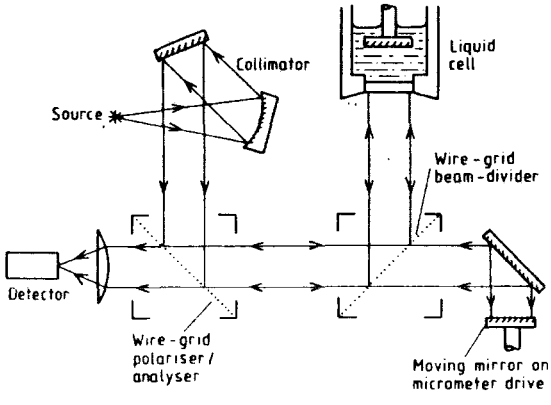

Figure 2. A schematic representation of a polarising wire-grid interferometer incorporating the liquid cell in its fixed length arm.

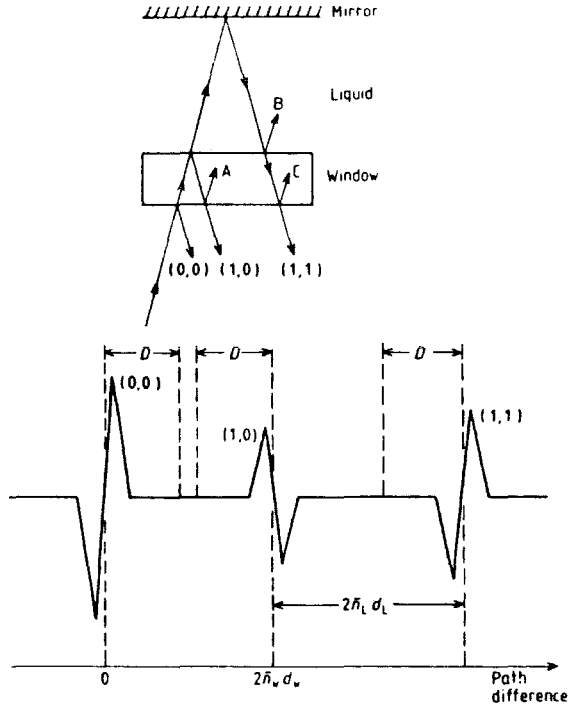

Figure 3. The upper part of the figure shows the primary rays which propagate between the three interfaces of a filled cell when radiation is incident on it. The rays labelled (0, 0), (1, 0) and (1, 1) according to the notation of Honijk *et al* (1977) are the primary rays of interest, which are reflected back into the interferometer; each gives rise to a localised interference signature in the recorded interference pattern, as illustrated in the lower part of the figure.

radiation is incident on it, and which result in the rays (0, 0), (1, 0) and (1, 1) being reflected back into the interferometer (the notation follows that of Honijk *et al* (1977)). These reflected rays travel different optical paths and each in turn gives rise to a localised interference signature in the detected interferogram when the optical path length in the moving mirror arm equals its own. This is illustrated in the lower part of the figure, in which the signature corresponding to the (0, 0) ray has been arbitrarily labelled as occurring at zero optical path difference. The signature corresponding to the (1, 0) ray then occurs at a path difference of about $2\bar{n}_w d_w$, where $\bar{n}_w$ is the mean refractive index of the window material over the spectral range of interest, and d_w is the window thickness. Similarly, the signature corresponding to the (1, 1) ray occurs at a further path difference of about $2\bar{n}_L d_L$, where $\bar{n}_L$ is the mean refractive index of the liquid specimen and d_L its thickness. The rays A, B and C that re-enter the cell give rise to an infinite series of internally reflected rays that eventually reflect back into the interferometer, but one can generally arrange the experimental parameters so that their effects are not resolved in the recorded interference functions.

In principle, any pair of interference signatures from this cell can be used to give the optical constants of a liquid specimen. In practice, the requirement that random and systematic uncertainties in a measurement be minimised means that one prefers to work with combinations of the three signatures shown in figure 3. Thus, in transmission measurements on reasonably transparent liquids the cell has been used for a series of measurements on polar molecules in non-polar solvents, in a continuation of earlier dilution studies aimed at distinguishing the single-molecule contribution to the rotational correlation function from interaction-induced intermolecular contributions (Birch *et al* 1981). In these studies measurements were made on two different thicknesses of the specimen, recording only the (1, 1) signature in each case, the optical constants being derived from the ratio of the complex spectra obtained by Fourier transformation of the two signatures. The smaller of the two thicknesses is chosen so that there is no significant intrusion into the recorded interference function by structure associated with the (1, 0) interference signature. This requires that

$$2\bar{n}_L d_L \gtrsim D \qquad (1)$$

where the spectral resolution desired in the measurement requires the range of path difference values within $\pm D$ of the (1, 1) signature to be used.

The results of some such measurements on pure carbon tetrachloride are presented in figures 4 and 5. In the two parts of figure 4 three independent determinations of the refraction and absorption spectra at 33.8°C are shown for the spectral region between 20 and 120 cm^{-1}, the measurements being taken using the interferometer shown in figure 2 together with a quartz window Golay cell. The measurements are shown superimposed to allow the levels of random uncertainties in the measured spectra to be estimated. In the refraction spectrum this was $\sim \pm 0.0001$, while in the absorption spectrum it was typically less than ± 0.05 neper cm^{-1}. At these low levels of random uncertainty it is important to be aware of the susceptibility of the measurement method to systematic error. This will be dealt with in a subsequent publication. Figure 5 shows the average refraction and absorption spectrum of CCl_4 at this temperature, determined from these independent measurements, together with those similarly determined at 10.7 and 50.5°C. The broad absorption band present at all these temperatures arises from collision-induced dipole fluctuations which occur because of the finite polarisability of the CCl_4 molecules. For this molecule it is expected that the wavenumber of maximum absorption should decrease with increasing temperature, as it has been shown (Evans and Davies 1976) that the intermolecular mean square

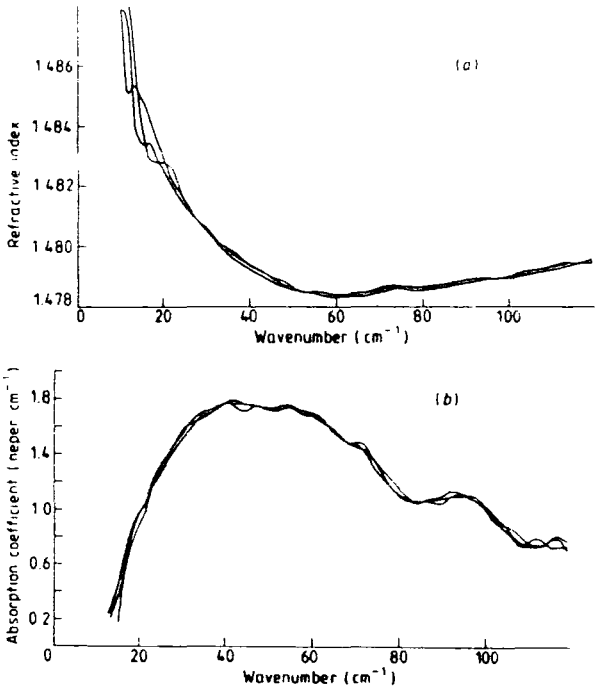

Figure 4. The results of dispersive transmission determinations of the optical constants of carbon tetrachloride at 33.8°C between about 20 and 120 cm^{-1} made using the cell: (*a*) the refraction spectrum, (*b*) the power absorption spectrum. Each part shows three independent determinations superimposed so that the levels of reproducibility can be estimated. Each independent determination is shown as a continuous curve created by joining adjacent spectral points by straight lines.

torque decreases with temperature. The band is also expected to broaden since the induced dipole fluctuations are modulated by molecular rotation and translation. If the total intensity remains approximately constant this should lead to a decrease in the maximum value of the absorption coefficient with increasing temperature. These features, together with the expected decrease in refractive index with increasing temperature, are clearly observed in the present data, although the temperature range covered was insufficient to produce a well defined frequency shift.

The cell has also been used for reflection measurements on highly absorbing liquids, in which the complex Fresnel reflectivity of the interface between the upper surface of the window and the liquid is effectively determined. The particular experimental method used for this has been recently developed (Birch and Bennouna 1981) and offers some distinct advantages over earlier reflection methods (Chamberlain *et al* 1973b, Afsar and Hasted 1977, 1978) including a halving of the experimental observation time and a reduced susceptibility to random and systematic uncertainties. The measurement only requires the (0, 0) and (1, 0) signatures from a full cell to be recorded, and therefore, the sole requirement on the liquid thickness is that it be sufficient that all rays which enter the liquid are so strongly attenuated that their corresponding interference signatures are not resolved in the detected interferogram. In practice, therefore, the cell mirror is not required and it would not usually be assembled with the cell for such measurements. In a similar

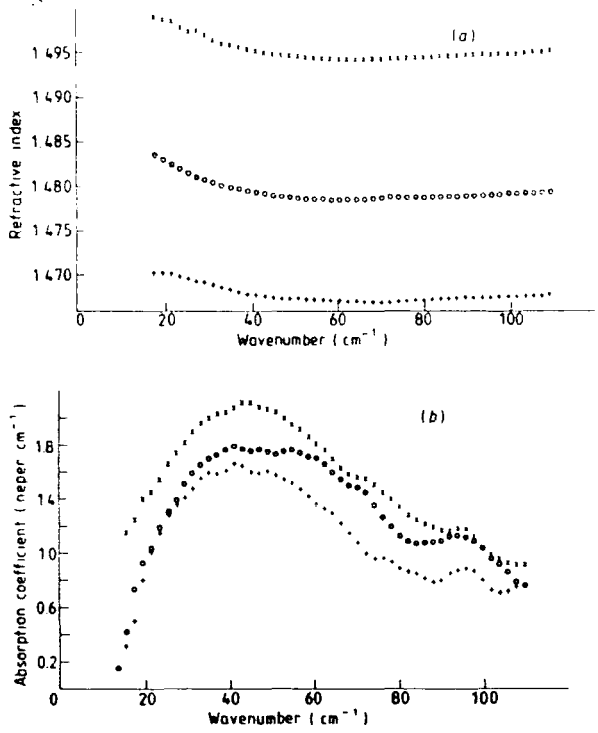

Figure 5. The refraction and absorption spectra of carbon tetrachloride determined with the cell at 10.7, 33.8 and 50.5°C: (*a*) the refraction spectrum, (*b*) the power absorption spectrum. Each spectrum is the average of three independent determinations. In both parts × refers to 10.7°C, ⊙ to 33.8°C and + to 50.5C.

manner to the transmission experiment outlined above it is necessary to assume that the interference structure associated with the two signatures does not overlap to any significant extent, and this is equivalent to the inequality

$$\tilde{n}_w d_w \geqslant D \qquad (2)$$

where D has the same meaning as before. Using this reflection method the cell has been used in a study of the optical constants of water and some concentrated aqueous salt solutions between 25 and 450 cm^{-1} (Birch and Bennouna 1981, Bennouna *et al* 1981).

3. Conclusions

The design of a cell suitable for use in the determination of the optical constants of liquids at millimetre and submillimetre wavelengths by dispersive Fourier transform spectrometry has been described. The cell can be used in transmission and reflection experiments and is therefore suitable for the study of the spectral variation of the optical constants of liquids ranging from the virtually transparent to the virtually opaque.

References

Afsar M N, Chamberlain J and Hasted J B 1976a The measurement of the refraction spectrum of a lossy liquid in the far infrared region
Infrared Phys. **16** 587–99

Afsar M N and Hasted J B 1977 Measurements of the optical constants of liquid H_2O and D_2O between 6 and 450 cm^{-1}
J. Opt. Soc. Am. **67** 902–4

Afsar M N and Hasted J B 1978 Submillimetre wave measurements of optical constants of water at various temperatures
Infrared Phys. **18** 835–41

Afsar M N, Hasted J B and Chamberlain J 1976b New techniques for dispersive Fourier transform spectrometry of liquids
Infrared Phys. **16** 301–10

Afsar M N, Honijk D D, Passchier W F and Goulon J 1977 Dispersive Fourier transform spectrometry with variable-thickness variable-temperature liquid cells
IEEE Trans. Microwave Theory and Tech. **MTT-25** 505–8

Bennouna M, Cachet H, Lestrade J C and Birch J R 1981 The determination of the complex refractive indices of some concentrated aqueous salt solutions at submillimetre wavelengths
Chem. Phys. **62** 439–45

Birch J R, Afsar M N, Yarwood J and James P L 1981 The far-infrared dispersion of acetonitrile in dilute solution in carbon tetrachloride
Infrared Phys. **21** 9–15

Birch J R and Bennouna M 1981 An improved experimental method for reflection dispersive Fourier transform spectrometry of very heavily absorbing liquids
Infrared Phys. **21** 229–34

Birch J R and Parker T J 1979 'Dispersive Fourier transform spectrometry' in *Infrared and Millimetre Waves* vol. 2 ed. K J Button (New York: Academic)

Chamberlain J, Afsar M N and Hasted J B 1973a Direct measurements of the refraction spectrum of ethanol at submillimetre wavelengths
Nature Phys. Sci. **245** 28–30

Chamberlain J, Costley A E and Gebbie H A 1967 Submillimetre dispersion of liquid tetrabromoethane
Spectrochim. Acta **23A** 2255–60

Chamberlain J, Gibbs J E and Gebbie H A 1969 The determination of refractive index spectra by Fourier spectrometry
Infrared Phys. **9** 185–209

Chamberlain J, Zafar M S and Hasted J B 1973b Direct measurement of refraction spectrum of liquid water at submillimetre wavelengths
Nature Phys. Sci. **243** 116–7

Davies M, Pardoe G W F, Chamberlain J and Gebbie H A 1970 Submillimetre- and millimetre-wave absorptions of some polar and non-polar liquids measured by Fourier transform spectroscopy
Trans. Faraday Soc. **66** 273–92

Evans M W and Davies G J 1976 Effect of pressure and temperature on the intermolecular mean square torque in liquid CS_2 and CCl_4
J. Chem. Soc., Faraday Trans. II **72** 1206–13

Honijk D D, Passchier W F, Mandel M and Afsar M N 1977 The determination of complex refractive indices with Fourier transform interferometry—V Methods for the determination of complex refractive index spectra of liquids in the far infrared spectral region (5–500 cm^{-1}) using a variable-pathlength variable-temperature cell
Infrared Phys. **17** 9–24

Martin D H and Puplett E 1970 Polarised interferometric spectrometry for the millimetre and submillimetre spectrum
Infrared Phys. **10** 105–9

Stone N W B 1978 Expanding field of far infrared Fourier transform spectroscopy in the laboratory, industry and the environment
Appl. Opt. **17** 1332–41

Stone N W B and Chantry G W 1977 'Advances in far infrared interferometric spectroscopy' in *Advances in Infrared and Raman Spectroscopy* vol. 3 ed. R J H Clark and R E Hester (London: Heyden)

Zafar M S, Hasted J B and Chamberlain J 1973 Submillimetre wave dielectric dispersion in water
Nature Phys. Sci. **243** 106–9